The Synthesis and Photophysics of Liquid Crystalline Complexes of Gold(III) and Their Porphyrin Dyads

Alice Jane McEllin

PhD

University of York

Chemistry

September 2022

Abstract

Cyclometallated complexes have for many years been of interest, particularly for use in organic light emitting diodes (OLEDs) due to the availability of triplet excited states. Over the last 20 years investigation into cyclometallated gold(III) alkynyl complexes has been an active area of research, with the introduction of long alkoxy chains on the cyclometallating ligand in the 4,4'- and 3,3',4,4'-positions of the phenyl ring giving liquid crystal phases. Combination of the fluidity and organisation of mesophases with photoactive cyclometallated complexes is of interest due to the possibility of polarised emission.

A systemic investigation into the mercuration and auration of various isomers of 2,6-*bis*(alkoxyphenyl)pyridine was undertaken to investigate the effect of substituent position on product formation and yield. Pure monomercury (**2-[Hg]**, **3-[Hg]**, **5-[Hg]** and **2,5-[Hg]**) and dimercurated complexes (**2,3-[Hg$_2$]** and **2,5-[Hg$_2$]**) were isolated in high yield (>60%) when a substituent is present at the 2,2-positions; a striking change from the low yields of impure monomercury complexes previously reported. The first example of a mercury-free auration for this class of ligands is also reported, for use of a palladium(II) intermediate and a rhodium(III) catalysed auration for 2,2',3,3'-tetrasubstituted ligands.

Complexes substituted in the 2,2'-, 2,2',3,3'- and 2,2',5,5'-positions were linked to a range of phenylacetylide ligands and the mesophase and photophysical properties investigated. Formation of mesophases was determined to depend strongly on molecular shape, with 'disc-like' **2,3-[Au]-3-*n*** giving columnar phases and 'rod-like' **2,5-[Au]-1-*n*** giving SmA phases. Weak triplet emission (PLQYs <0.1%, lifetimes <100 ns)) was reported, with emission in the yellow and green regions. Connection to zinc and free base di- and tetrasubstituted porphyrins gave gold-porphyrin dyads. The mesophase and photophysical behaviours were disappointing, with no phases formed, while only red fluorescence from the porphyrin was observed, with the exception of **3,4-[Au]-ZnP**, which also showed gold-based phosphorescence in the yellow region.

Contents

List of Figures

13

15

List of Tables

Accompanying Material

XRD data tables, .cif files, characterisation data and assigned ^{1}H and ^{13}C{^{1}H} NMR spectra for the pincer ligands, mercury(II) complexes and chlorogold(III) complexes can be found at the following link: (https://bit.ly/3LpAm4d).

Acknowledgements

First, and foremost, I need to thank my supervisor Professor Duncan Bruce for all his support and guidance during my PhD. I also need to thank my IPM, Professor Jason Lynam, for his support and, in particular, for his training and assistance in carrying out DFT calculations on Gaussian and Viking.

I would also like to thank Dr Luke Wilkinson and Fraser Arnold for additional support and help with use of Viking and Gaussian. Calculations on this project were undertaken on the Viking Computer Cluster, which is a high-performance computer facility provided by the University of York. I am grateful for computational support from the University of York High Performance Computing service, Viking and the Research Computing team.

Elemental analysis was carried out by Dr Graeme McAllister, mass spectrometry by Karl Heaton and single crystal X-ray structures were recorded and refined by Dr Adrian Whitwood and Theo Tanner, with the exception of **2-[Au]-Cl**, where data was collected by Peter N. Horton of the UK National Crystallography Service. MicroED on the gold porphyrin dyads was kindly done by Emily Thompson and Dr. Huw Jenkins. I also want to thank the chemistry department technical staff for their remarkable willingness to collect data on their instruments on organomercury complexes! I would like to thank Heather Fish and Dr Alexander Heyam for assistance and training on using the NMR spectrometers and Heather in particular for setting up the ^{199}Hg NMR routine – a big ask to let organomercury near the 500 MHz spectrometer!

I must thank Dr Stephen Cowling for training on SAXS, DSC and microscopy and assistance in identifying liquid crystal phases; Dr Laurence Abbott for training and assistance with fluorescence measurements and to Dr Daniel Shaw for providing the laser key when required!

Author's Declaration

I declare that this thesis is a presentation of original work and I am the sole author, except were reference has been made to work contributed by others, indicated below. The work presented in this thesis was carried out in the Department of Chemistry at the University of York between October 2018 and September 2022. This work has not previously been presented for an award at this, or any other, University. All sources are acknowledged as References.

Significant contributions from other researchers:

- Dr Adrian Whitwood and Theo Tanner collected and solved crystal structures for several ligands, gold complexes, mercury complexes and porphyrins.
- Emily Thompson and Dr. Huw Jenkins collected and solved the crystal structures for **2,3-[Au]-di-ZnP** and **2,3-[Au]-di-P**.
- Dr Christopher Goult preformed the work relating to attempted direct auration *via* microwave methods and the related computational studies.
- MChem student Liam Curtis synthesised complexes **2,5-[Au]-1-12** and **2,5-[Au]-1-14** and undertook characterisation for both these complexes and **2,3-[Au]-3-14**.
- Several of the phenylacetylene ligands used were previously synthesised by Dr Rachel Parker and MChem students Rachel Stracey and Liam Curtis.
- Low temperature photophysical measurements for **2-[Au]-Cl** were performed by Prof. J. A. Gareth Williams.

Some of the material presented within this thesis has previously been published in:

Chapter 1: A General Introduction to Liquid Crystals, Photophysics and OLEDs

1.1   Introduction to Liquid Crystals

There is widespread familiarity with the three main states of matter: the solid state, the liquid state and the gas state, and they are distinguished by the degree of molecular order. Thus, the crystalline solid state has absolute orientational and positional order in three dimensions, while the isotropic liquid state has no long-range molecular ordering. However, in 1888 Reinitzer determined that cholesteryl benzoate, a derivative of cholesterol, displayed two melting points. The first at 145.5 °C gave rise to a cloudy liquid and the second at 178.5 °C to a clear liquid.[1, 2] Recognising that this was of potential interest he sent samples to Lehmann, who had been using a heating stage under a polarising optical microscope to study phase behaviour, and who recognised it as a new phase of matter, initially using the term soft crystals, then crystal fluids and finally the term used today: liquid crystals.[3] While initially only of academic interest, the use in a prototype liquid crystal displays (LCD) in the late 1960s and early 1970s[4-9] and the discovery of the first room-temperature liquid crystal, *p*-methoxybenzylidene-*p*-*n*-butylaniline (MBBA), in 1969,[4] followed by the first of the cyanobiphenyls, 4-cyano-4'-pentylbiphenyl (5CB), at the University of Hull in 1972, made them of great industrial interest.[10]
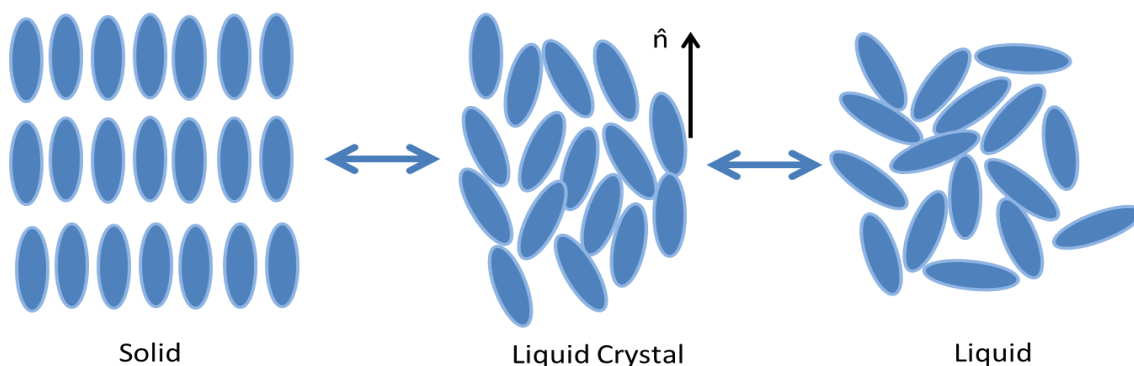
Figure 1.1: The generic structures of the solid, isotropic liquid and liquid crystal phase.

Liquid crystal phases (or mesophases) lie between the crystalline solid and isotropic liquid phases (Figure 1.1) and therefore display intermediate degrees of orientational and positional order. Liquid crystals (or mesogens) can be subdivided into two broad classes: thermotropic mesogens, where phase changes are induced primarily as a function of temperature and the lyotropic mesogens where phase changes are induced as a function of concentration in a solvent. The latter will not be investigated in this work and are therefore not considered further. For thermotropic liquid crystals the solid-mesophase phase transition is defined as the melting temperature, T_m and the mesophase-isotropic liquid phase transition the clearing temperature, T_c.

1.1.1 Thermotropic Liquid Crystals

For formation of a thermotropic liquid crystal phase, the presence of molecular anisotropy is important, which is defined as when one molecular dimension is very different to the other two. The most common shapes for low molecular weight mesogens are calamitic (rod-like – one long axis) and discotic (disc-shaped – one short axis) (Figure 1.2), with molecular shape determining phase morphology. Mesophases can be classified as enantiotropic; a phase occurring above the melting point that is thermodynamically stable and possesses reversible melting and clearing transitions, or monotropic, which only form on supercooling below the melting point and are therefore kinetically, rather than thermodynamically stabilised.

Rod-Shaped   Disc-Shaped

l

w

l

w

$l»w$ $w»l$
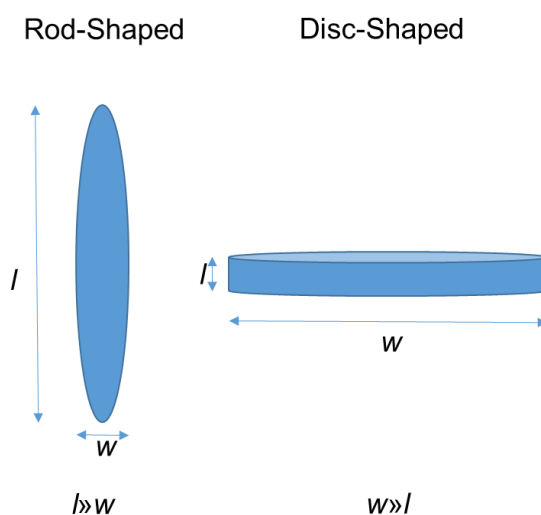
Figure 1.2: Generic shape of calamitic (rod-like) and discotic (disc-shaped) liquid crystals.

The degree of phase ordering is defined by the order parameter, S (*Eqn 1.1*):

Eqn 1.1
$$S = \frac{1}{2}(3\cos^2\theta - 1)$$

where θ is the angle an individual molecule makes with the preferred direction of alignment – the director, $\hat{\mathbf{n}}$, being then averaged over all molecules. When alignment is perfect, the order parameter is 1 (*e.g.* in the crystalline solid) and when the order parameter is 0, there is no preferred alignment (*e.g.* in the isotropic liquid). The order parameter will tend to decrease with increasing temperature in the liquid crystal phase, due to decreased molecular alignment as molecules gain more kinetic energy (Figure 1.3). On reaching the clearing temperature there is a discontinuity where the order parameter suddenly becomes zero on the phase transition to the order-less isotropic liquid. For a nematic phase (see below), S would typically take a values between 0.3 and 0.4 at the transition to the isotropic liquid.
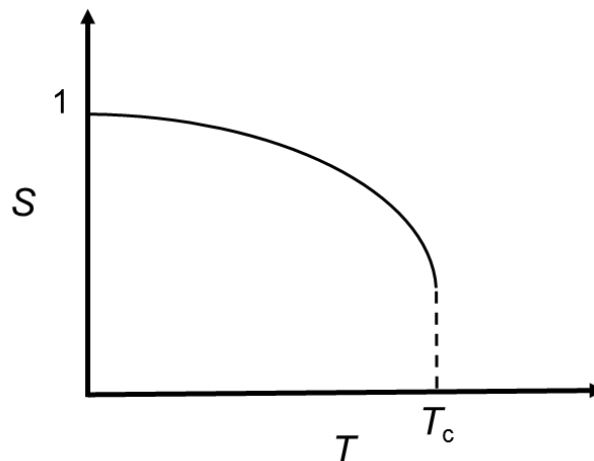
Figure 1.3: Value of the order parameter, S, as a function of temperature.

1.1.1.1 *Calamitic Mesogens*

Calamitic mesogens have a longer length than they do breadth resulting in a rod-shape and typically contain a rigid core appended by one or more flexible chains (Figure 1.7).[11] The simplest of the phases formed by calamitic molecules is the nematic phase (N) (Figure 1.4), where the molecules align, on average, with a preferred orientation known as the director, $\hat{\mathbf{n}}$.[12] There is a chiral version of this phase, the chiral nematic phase (N*), (known previously as the cholesteric phase as the first known molecules displaying this phase were all cholesterol derivatives), where the presence of chiral mesogens or dopants

imparts chirality to the mesophase due to steric packing constraints, resulting in helical structure formation with a defined pitch (Figure 1.5). The director precesses through 360° over this distance.
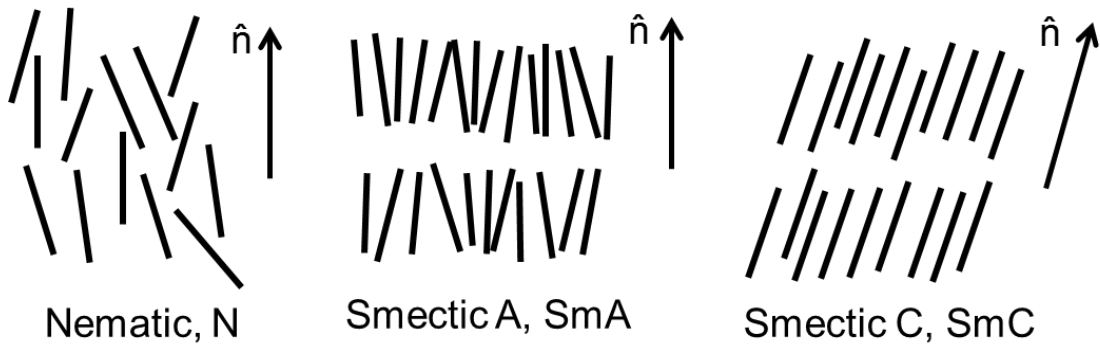
Figure 1.4: Generic structures of the nematic, smectic A and smectic C phases.
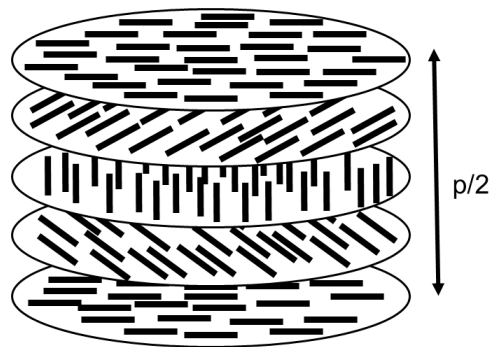
Figure 1.5: Generic structure of the chiral nematic phase, N*.

A degree of positional ordering is introduced in the smectic phases due to molecular features encouraging the formation of layer structures.[13] The least ordered smectic phase is the smectic A phase (SmA), where the director lies orthogonal to the layer plane, while in the smectic C (SmC) the director is tilted relative to the layer plane (Figure 1.4). Hexagonal arrangements in the layers due to increased ordering gives the smectic B phase (SmB) and the tilted analogues smectic I and F (SmI and SmF) (Figure 1.6), with chiral versions possible for the SmC, SmI and SmF phases, where the director precesses helically over several layers. A particular calamitic mesogen can exhibit one or more mesophases, which must be determined experimentally. The normal thermodynamic ordering of phases, which represents decreasing order with increasing temperature, is: SmB, SmF, SmI, SmC, SmA, N, Iso. Knowledge of this order can aid in phase identification, noting that many materials would show between one and three phases.
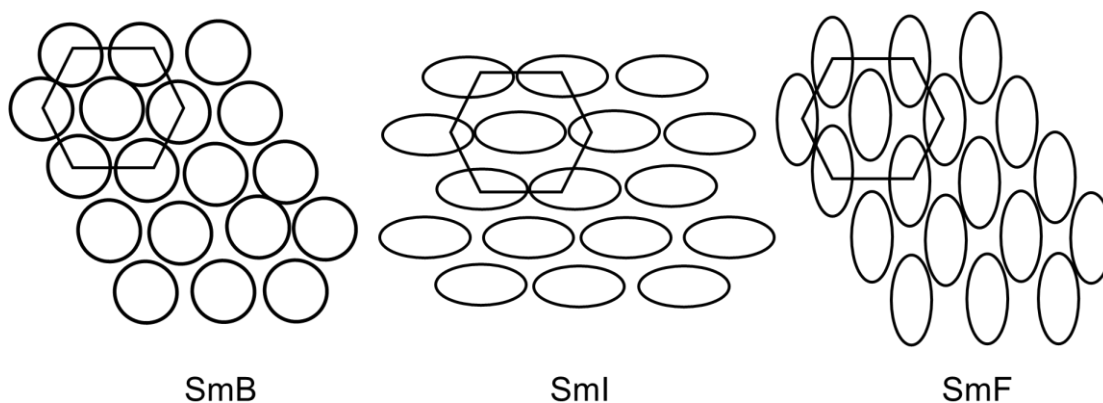
Figure 1.6: Generic structures of the smectic B, I and F phases, showing the hexagonal lattice of the mesogenic molecules in the layers. The smectic I phase is tilted towards the side and the smectic F towards the apex.

C 24.0 N 35.0 Iso   C 31.0 N 55.0 Iso

C 56.0 SmC 105.5 SmA 131.0 N 136.0 Iso
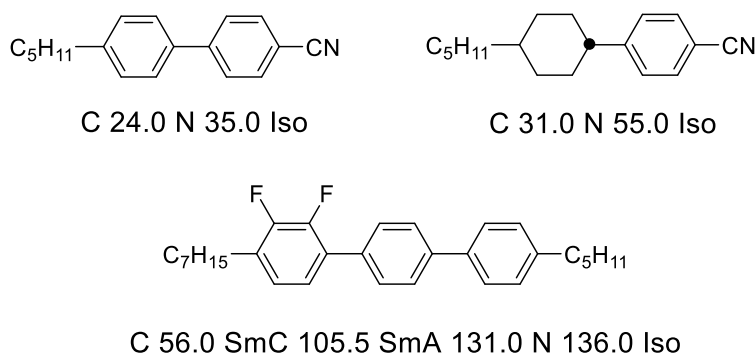
Figure 1.7: Structures of some typical calamitic mesogens.[12, 13]

1.1.1.2   *Discotic Mesogens*

The first identified discotic mesogen was reported in 1977 by Chandrasekhar *et al.;* a hexaalkenoate of benzene.[14] Discotic molecules have a planar core, most frequently aromatic, surrounded by flexible chains, with generally a minimum of six required for phase formation (Figure 1.8).[15] The simplest phase of disc-like molecules is the discotic nematic (N_D), which is equivalent to the nematic phase in that the molecules align in a preferred orientation (Figure 1.9), but do not display any further ordering. It is, however, very much rarer than the nematic phase of calamitic materials. Slightly more order is displayed in the columnar nematic phase (N_{col}), where aggregation into columns is observed, but no positional columnar ordering occurs.

C 68.3 Col$_r$ 86.0 Iso   C 69.0 Col$_h$ 122.0 Iso

C 68.0 Col$_r$ 97.0 Iso   C 98.2 N$_D$ 131.2 Iso
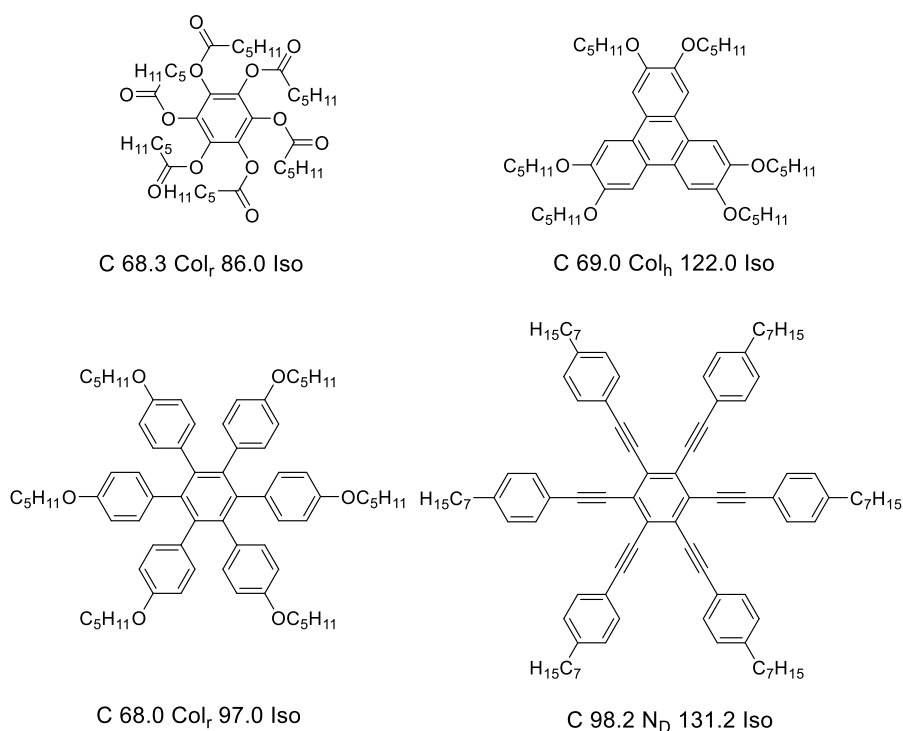
Figure 1.8: Examples of some typical discotic mesogens.[14, 15]

Discotic Nematic, N$_D$ Columnar Nematic, N$_{Col}$ Hexagonal Columnar, Col$_h$
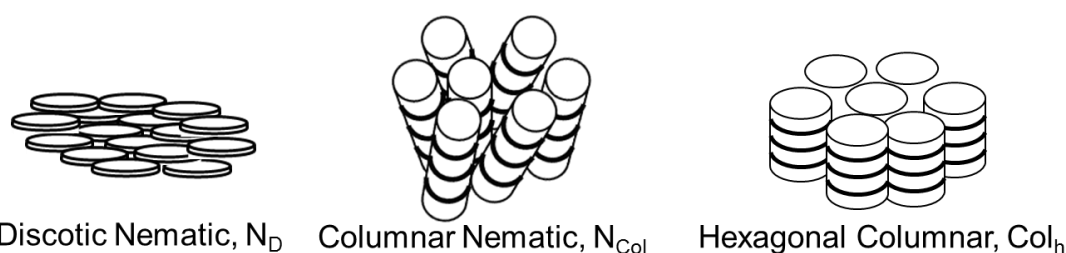
Figure 1.9: Generic structures of the discotic nematic phase, columnar nematic phase and the hexagonal columnar phase.

More frequency found are the columnar phases, where the molecules stack in columns, which are then arranged on a two-dimensional lattice, the symmetry of which defines the phase (Figure 1.10).[11, 15] The two most common are the hexagonal columnar phase (Col$_h$) and the rectangular phases (Col$_r$), however the oblique (Col$_o$) columnar phase is also known. One space-group is possible for hexagonal columnar (*p6mm*) and oblique columnar (*p1*) phases, while several are possible for the rectangular columnar phases (*e.g. p2gg, p2mg* and *c2mm*) (Figure 1.10).[16]

Hexagonal   Simple Rectangular   Oblique

p6mm   *p2gg*   *p1*

Centred Rectangle   Simple Rectangular

c2mm   *p2mg*
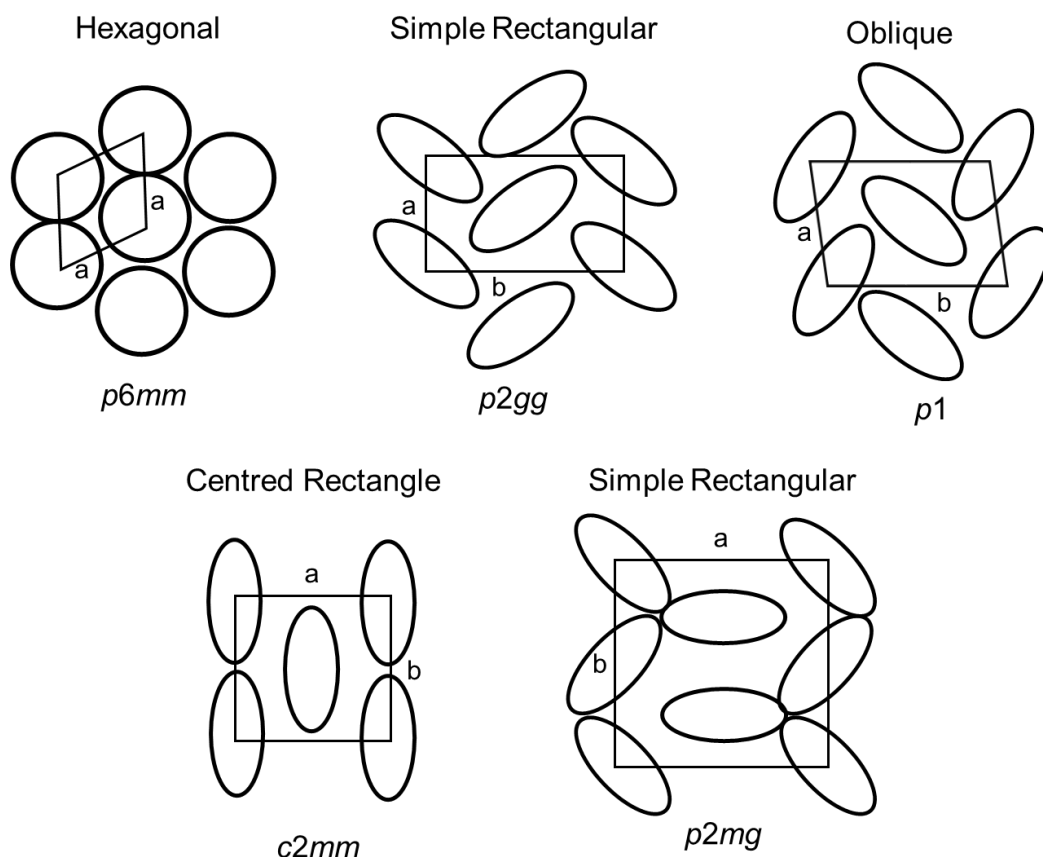
Figure 1.10: The ordering in the columnar phases.[16]

1.1.1.3   *Metallomesogens*

Metallomesogens are metal-containing molecules that exhibit a mesophase, with the introduction of the metal expanding not only the possible geometries due to the high coordination numbers possible in some complexes, particularly when considering the examples of lanthanide and octahedral transition metal complexes, but also possible localised self-assembly due to metal-metal interactions and metal-ligand interactions.[17,] [18] Furthermore, metals are capable of introducing several potentially desirable properties for multifunctional materials, for example magnetism, redox and electronic properties, which are capable of being tuned depending on the nature of the metal, oxidation state and the ligand nature. Of particular relevance for this thesis is the possibility of expanding the photophysical properties of the materials, including the introduction of phosphorescence when heavy metal atoms are present. These are of particular interest in Organic Light Emitting Diodes, OLEDs, due to the combination of optoelectronic and magnetic properties, with 100% theoretical internal quantum efficiency, when heavy metal atoms are present. The mesophase implies anisotropy and self-organisation, which

can enhance charge transport properties, while fluidity is retained to give a dynamic, multifunctional soft material.

The first metallomesogens were reported in 1923 by Vorländer when he determined that Schiff-base complexes of diaryl mercury(II) displayed smectic behaviour (Figure 1.11a).[19] Greater interest developed in the mid-1970s when Malthête and Billard published work on liquid crystalline derivatives of ferrocene (Figure 1.11b)[20] and Giroud and Mueller-Westerhoff on dithiolene complexes of nickel(II) and platinum(II) (Figure 1.11c).[21]
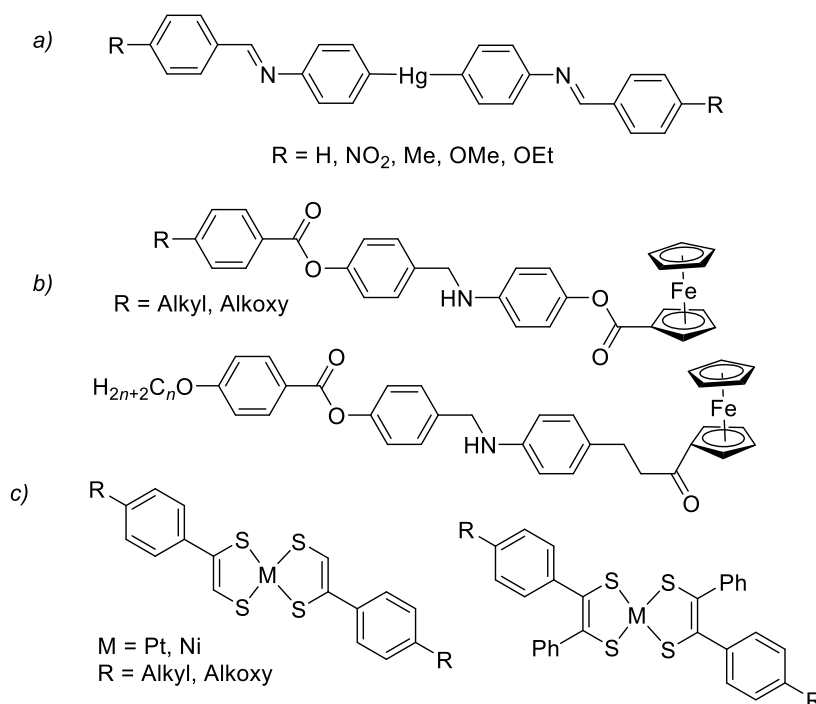
Figure 1.11: Structure of Schiff-base complex of diaryl mercury(II), accepted as the first metallomesogens (a),[19] structures of liquid crystalline derivatives of ferrocene (b),[20] and dithiolene complexes of nickel(II) and platinum(II) (c).[21]

Most early work investigated square-planar or linear complexes due to the greater ease of introduction of the anisotropy needed to produce calamitic and discotic mesogens; indeed, porphyrins and the related phthalocyanines proved to display natural geometries for the formation of discotic mesophases, detailed in Section 4.4. For higher coordination numbers, such as octahedral complexes of transition metals, strategies have had to be developed to overcome the bulky nature of the central metal core. The two main strategies have been the use of a highly anisotropic ligand, often rod-shaped, with small axillary ligands or use of ligands that are highly functionalised with aliphatic chains (Figure 1.12).

The former typically give nematic and smectic phases, while the later typically give columnar phases.
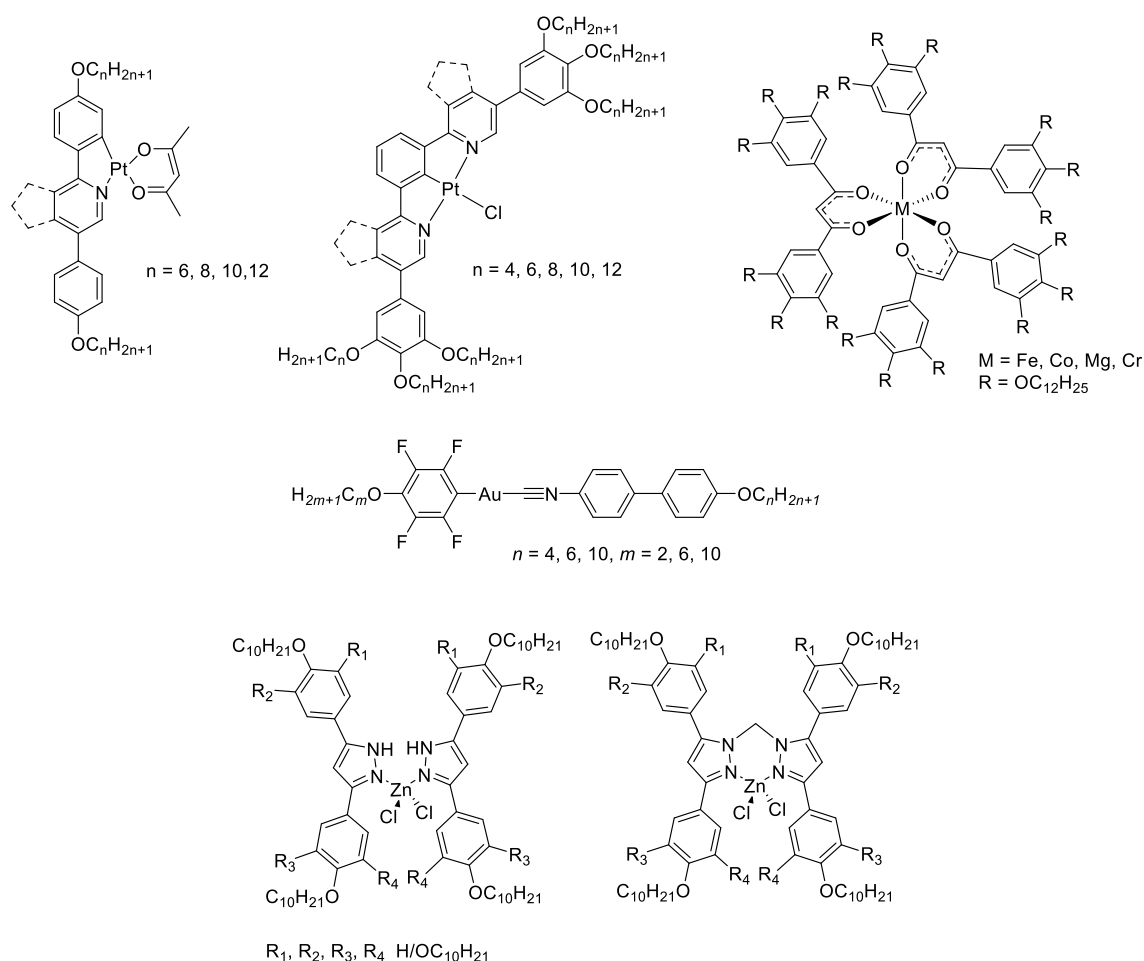
Figure 1.12: Examples of metallomesogens showing how ligand geometry can be used to induce mesophases.[22-28]

1.1.2 Characterisation of Liquid Crystals

There are three main methods that are used to characterise liquid crystal phases: Polarising Optical Microscopy (POM), Differential Scanning Calorimetry (DSC) and Small-Angle X-ray Scattering (SAXS).[29] POM is the fastest method and in the hands of a skilled operator can allow identification of mesophase(s) present. DSC, conversely, does not allow phase identification, but instead measures phase transition temperatures and enthalpies and is used to complement POM. SAXS is a powerful tool, but also the most involved and challenging to undertake, allowing investigation of molecular position and alignment in phases and can be used in conjunction with information gained from

POM to enable phase identification and hence provides another complementary method of identification.

1.1.2.1 Polarising Optical Microscopy (POM)

The most commonly used characterisation technique to investigate the nature of mesophases is polarising optical microscopy (POM).[11, 30, 31] Liquid Crystals are by their very nature anisotropic, which results in birefringence due to the presence of two molecular refractive indexes, causing the incident light wave to be split into two waves: the ordinary ray, $n_\perp$ or n_o, which travels perpendicular to the director and the extraordinary ray, $n_\parallel$ or n_e, which travels parallel to the director. The waves travel through the sample at different speeds and angles resulting in optical birefringence (Figure 1.13). The quantity $n_\parallel$ - $n_\perp$ is termed the birefringence, Δn, and when $\Delta n > 0$ the phase has positive birefringence, while when $\Delta n < 0$ the birefringence is negative.
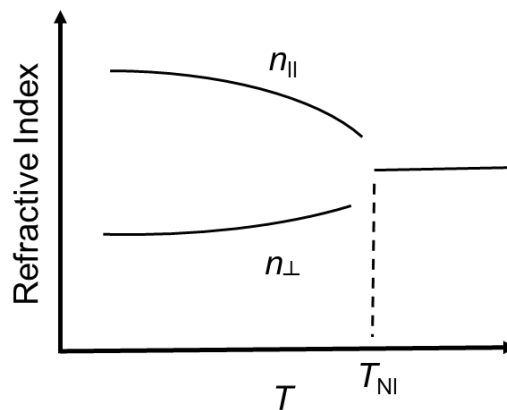
Figure 1.13: The optical birefringence of a liquid crystalline sample as a function of temperature.

In a polarising optical microscope the sample is placed on a heating platform, allowing temperature control, between two polarisers orientated at 90° angle to each other (Figure 1.14). The incident light ray is plane polarised by the first polariser. If the sample is isotropic with no birefringence present or homeotropically aligned so the viewing angle is down the optical axis, the ray of light passes through the sample unchanged and is therefore blocked by the second polariser (analyser) and no light is transmitted. However, for a birefringent sample the wave is split, resulting in loss of plane polarisation, allowing passage through the second polariser enabling viewing of an interference pattern.
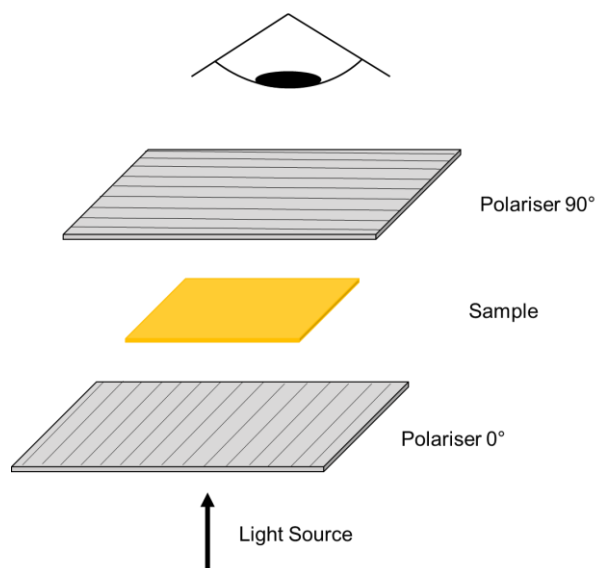
Figure 1.14: Simplified diagram of a polarising optical microscope.

The optical texture arising from the interference can allow mesophase identification due to the presence of characteristic defects and symmetry-dependent phase elasticity.[31] Defects are typically caused by the meeting of different sample domains due to sudden localised changes in director direction; on meeting these cause point defects (observed as black spots) or disclination defects (observed as line defects). Phases are typically identified, where possible, through a combination of texture and defects formed on cooling, with more than one texture possible for a given phase.

Nematic samples display Schlieren textures, where a 'thread-like' network of black disclinations is present on a coloured background, giving raise to the phase name. The black threads meet in four- and two-brush defects (Figure 1.15a). The nematic phase also exhibits a high level of fluidity and the presence of Brownian motion.
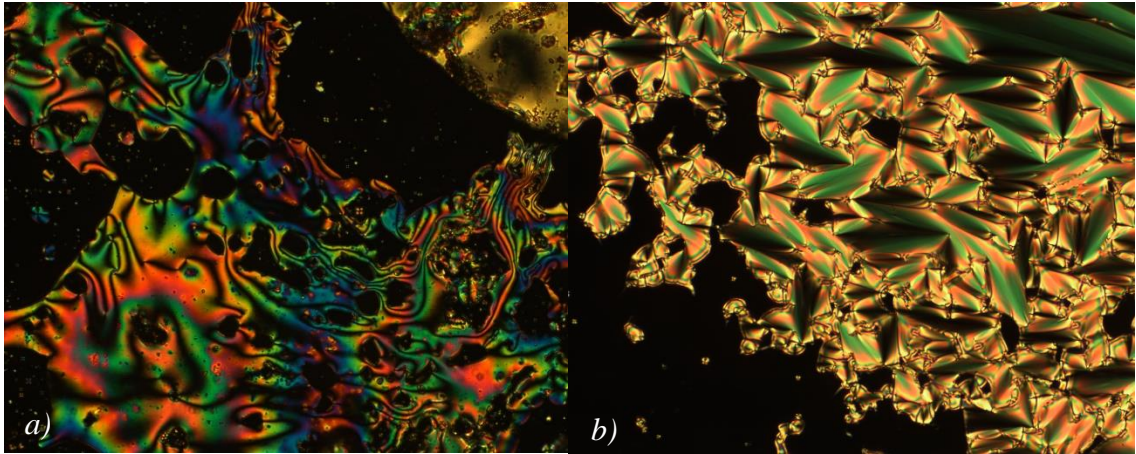
Figure 1.15: POM images of a typical nematic phase showing a Schlieren texture (a) and a smectic A phase showing a focal-conic texture (b).

The increased ordering in a smectic A phase to give regions of molecules where the director is aligned perpendicular to the optical axis and regions where it is parallel, results in formation of two textures: focal-conic defects due to the lamella nature of the phase and an optically-extinct black zone for the latter (Figure 1.15b). On director tilt angle introduction for smectic C phase the focal-conic texture is retained, through it can appear broken. The director tilting also results in Schlieren texture formation in the formally optically extinct black areas, through only four-brush defects are present.

Columnar phases form fan-like structures or straight-line (spine) defects (Figure 1.16), with the former formed by homogeneous columnar alignment and the latter by optical extinction of two homeotropic domains, with the optical axis perpendicular to the axis of the column.[15]
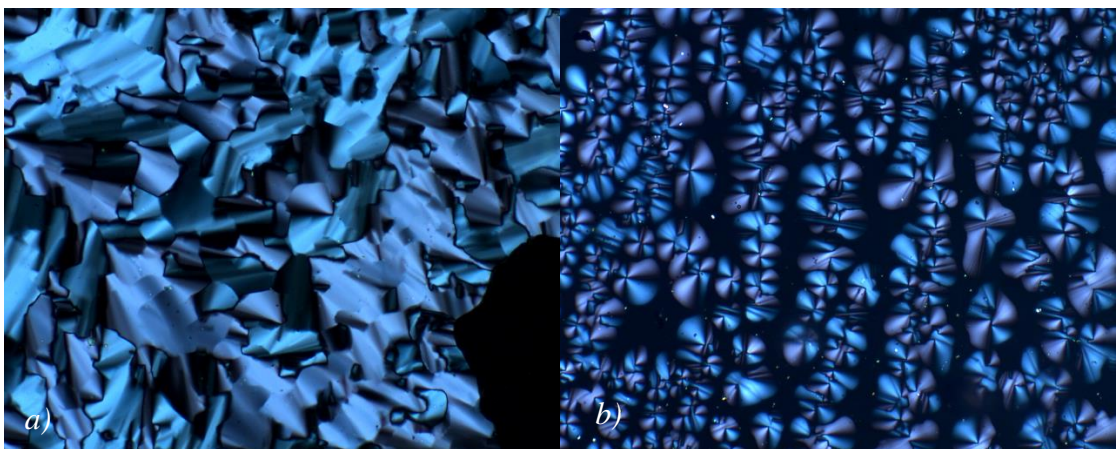
Figure 1.16: Typical textures of a hexagonal columnar phase showing straight-line defects (a) or fan-like structures (b).

1.1.2.2　　　　　*Differential Scanning Calorimetry (DSC)*

Differential Scanning Calorimetry measures material heat capacity as a function of temperature compared to a known reference, allowing enthalpy changes and precise transition temperatures to be determined. Using a known indium calibration sample, the DSC instrument heats a defined mass of sample, in an aluminium pan, over a set temperature range, with an identical, empty, sealed pan in an adjacent furnace (Figure 1.17). Both furnaces are heated independently, but the energy required to keep them at a constant temperature is monitored using a platinum sensor, with exothermic and endothermic phase transitions requiring more or less power to achieve this. Plotting this power difference as a DSC trace (Figure 1.18) allows viewing of phase transitions, with the integrated peak area giving the phase transition enthalpy.
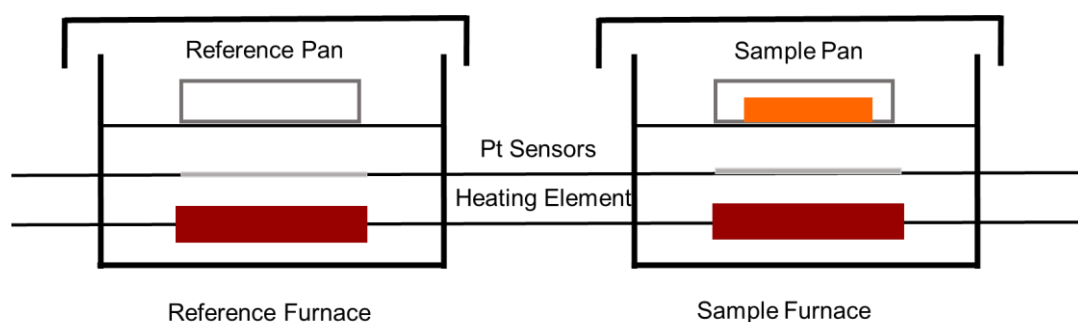
Figure 1.17: Simplified diagram of a DSC experiment.

Used in conjunction with POM this can not only provide exact thermal data, but can also sometimes identify phase transitions that cannot be identified readily by POM due to subtle texture changes. However, it does not allow phase identification and occasionally phase transitions which have very small enthalpies will not be apparent.[11, 32] By assuming that $\Delta G = 0$ at a transition, the enthalpy change can be used to calculate a change in entropy, ($\Delta S = \Delta H/T$), which provides information about the change in ordering at the transition.
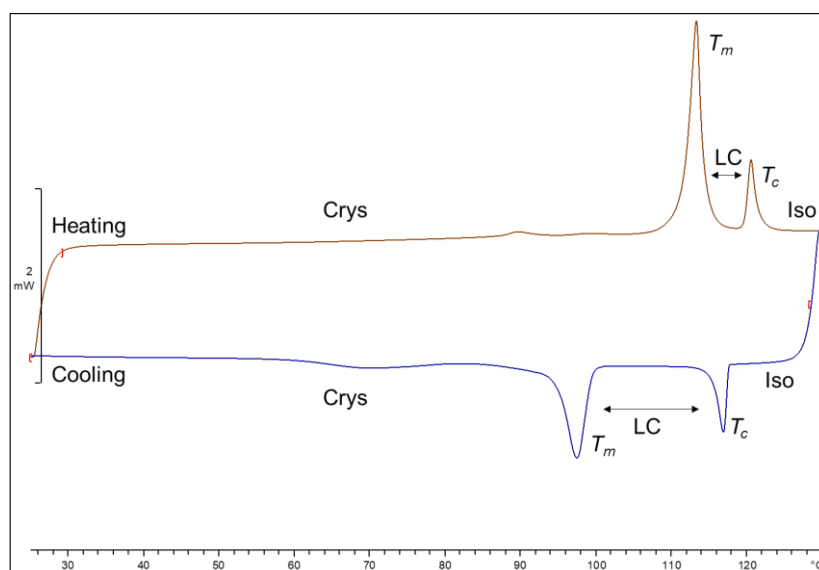
Figure 1.18: Example DSC trace of a liquid crystalline compound, where T_m is the melting point temperature and T_c is the clearing point temperature.

1.1.2.3 Small-Angle X-ray Scattering (SAXS)

The third, and final, characterisation method is small-angle X-ray scattering, which enables structural parameters of the phase itself to be determined, due to the small degree of intermolecular ordering present in the phase(s).[15, 33, 34]

The basis of X-ray diffraction is defined by the Bragg equation (*Eqn 1.2*), which states that X-rays reflected from adjacent planes, separated by a distance *d*, interfere constructively to give a diffraction pattern when the path difference, $2d\sin\theta$, where θ is the angle between incident radiation and plane, is an integer multiple of the experimental wavelength, λ (Figure 1.19). When the distance is not an integer wavelength multiple destructive interference occurs.

Eqn 1.2 $$n\lambda = 2d\sin\theta$$

The change in the angle of radiation is 2θ and this is one of the parameters that is measured by an XRD experiment.

47
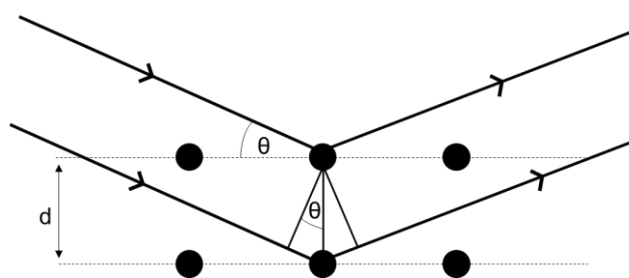
Figure 1.19: Illustration of Braggs law in an ordered medium.

The sample to be investigated is loaded in a 0.9 mm diameter capillary tube and placed in a temperature-controlled furnace. The X-ray beam is passed through the temperature-controlled sample to a detector, which records the resulting diffraction pattern (Figure 1.20).

Diffraction patterns for the nematic phase, which lacks long-range order typically consist of two diffuse concentric circles, one in the wide-angle region, (representing a small, wide-to-side periodicity), and the other in the small-angle region, representing the effective molecular length.[33] Radial integration allows determination of the diffraction pattern as a function of 2θ (°), which can be converted into the *d*-spacing (Å) or even scattering vector q (Å^{-1}). In the smectic phases sharpening of small-angle reflections is observed and, in addition, higher-order lamella reflection(s) can sometimes be observed. For the smectic A and C phase, due to the presence of long-range order in one-dimension, sharp d_{001} reflections are observed in the wide-angle region relating to the layer thickness (Figure 1.21).[33] Depending on the degree of long-range ordering, weaker higher-order peaks, d_{002}, and occasionally d_{003}, can also be observed. All assignment of SAXS data should be undertaken with reference to POM and DSC data.
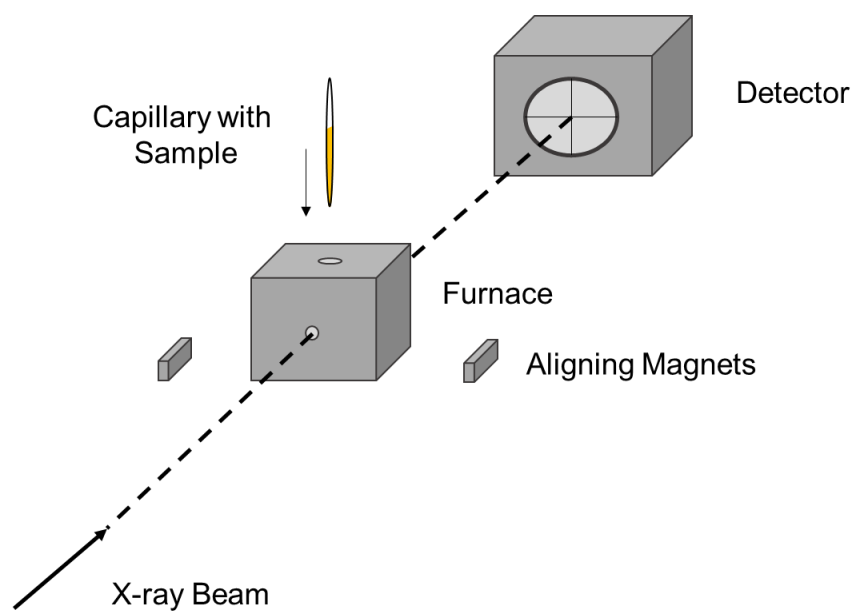
Figure 1.20: Simplified diagram of a small angle X-ray scattering experiment.
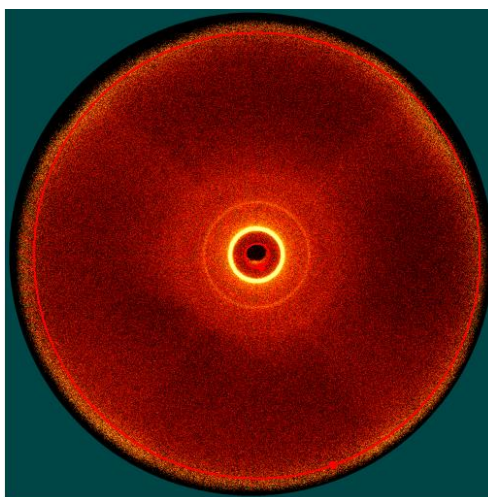
Figure 1.21: SAXS diffraction pattern for a smectic A mesophase.
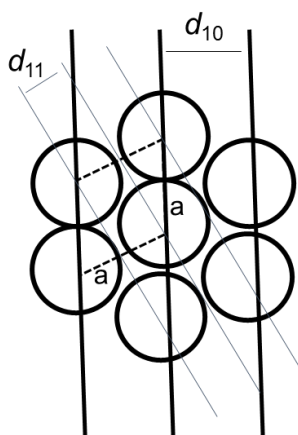
Figure 1.22: Determination of the unit cell parameters for hexagonal columnar mesophases.[15]

In columnar phases the relationship between the peak spacing is symmetry dependent.[15, 35] For a hexagonal columnar mesophase (Figure 1.22) the unit cell parameter, a, can be obtained by Equation 1.3:

Equ. 1.3
$$d_0 = \frac{2a}{\sqrt{3}}$$

The Miller indices are associated with the unit cell parameter by Equation 1.4, where h, k = 0, 1, 2... (integer Bragg indices):

Equ. 1.4
$$d_{HK0} = \sqrt{h^2 + k^2 + hk}$$

This results in the following sharp diffraction peaks at the following characteristic d-spacings of $1:\sqrt{3}:\sqrt{4}:\sqrt{7}$ for the d_{10}, d_{11}, d_{20} and d_{21} reflections respectively, and, with reference to POM, can be taken as assignment of hexagonal symmetry. Due to the rapid reduction of peak intensity with increasing d, generally only 2 - 4 peaks are observed, with only the d_{100} peak a strong reflection. Occasionally, however, only a single reflection is seen and, in such cases it is important not to over interpret that observation.
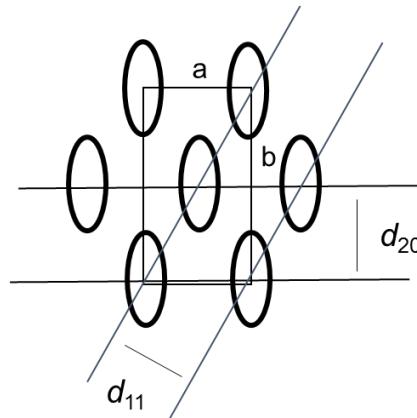
Figure 1.23: Determination of the unit cell parameters for rectangular columnar mesophases.[15]

Indexation of rectangular columnar phases is more challenging, with two lattice parameters, a and b, (Figure 1.23) determined due to lower phase symmetry.

Equ 1.5
$$a_r = 2d_{20} \text{ and } b_r = d_{11} \cdot \frac{2d_{20}}{\sqrt{4d_{20}^2 - d_{11}^2}}$$

This gives rise to the following equation:

$$\frac{1}{d_{hk}^2} = \frac{h^2}{a_r^2} + \frac{k^2}{b_r^2}$$

With characteristic d-spacings of $1:\sqrt{2}:\sqrt{4}:\sqrt{5}:\sqrt{8}$ for the d_{100}, d_{110}, d_{200}, d_{210} and d_{220} reflections respectively. Indexation of rectangular columnar phases to determine the space-group is challenging as it relies on the presence of sufficient reflections to observe systematic absences and rarely are the required number of reflections present. Frequently, the presence of two strong reflections in the small-angle region, indexed to d_{11} and d_{20} is taken, with reference to POM, as identification as a rectangular columnar phase.

1.2 Introduction to Emissive Metal Complexes

Many compounds, both organic and inorganic, are emissive and find use in optical devices, electronics, medicine and bioimaging.[36-42] Organic compounds are frequently chromophores, displaying florescence through the presence, for example, of aromatic units. However, upon complexation to certain metals, particularly transition metals, the nature of the emissive behaviour can be modified due both to the influence of the metal and also the introduction of different types of metal-ligand interaction. These are now discussed.

1.2.1 Photophysics Basics

A chromophore will absorb radiation at wavelengths where the incident energy matches the energy gap between the ground state, S_0 and an accessible excited state, which is normally an excited state of the same multiplicity to avoid breaking the spin selection rule. For most molecules this is a singlet-to-singlet transition, $S_0 \rightarrow S_1 \rightarrow S_2...$ etc. (spin, $s = 0$). Frequently the excited state is generated in a vibronically excited form, but relaxes rapidly down to the lowest vibrational level through vibrational relaxation, with excess energy dispersed to the surroundings. The molecule can then relax back down to the ground state by a radiative emission at a slightly lower wavelength than the incident light (Figure 1.24); for states of the same multiplicity this emission is known as florescence and is distinguished by a short lifetime and small Stokes shift (energy difference). Again the ground state is formed in a vibrationally excited state, which decays rapidly by

vibrational relaxation. An isoenergetic, non-radiative transition between states of the same spin multiplicity, known as internal conversion (IC), is also possible. This can be between the first excited state, S_1 and the ground state, S_0 or between the second excited state, S_2 and the first excited state, S_1, with further deactivation either radiatively or non-radiatively to the ground state. Such transitions can be displayed on a simple Jabłoński diagram (Figure 1.25).
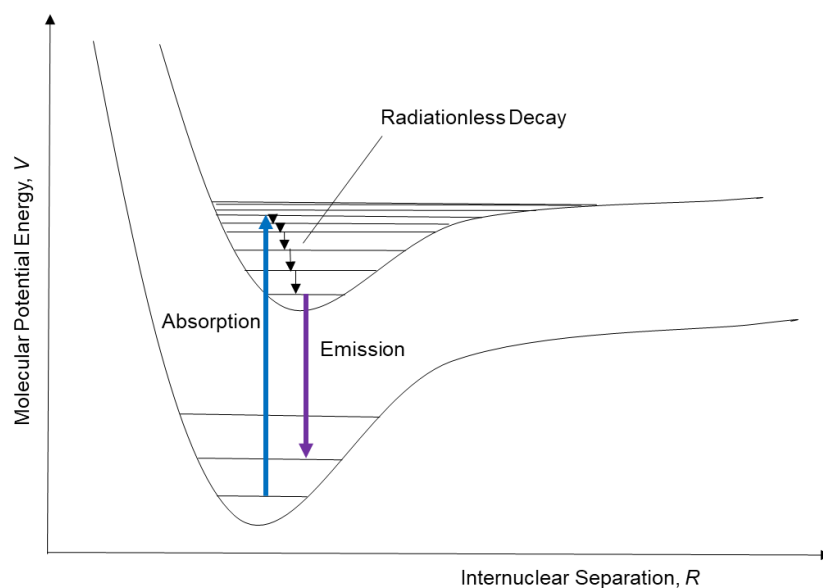
Figure 1.24: The process of absorption of light on a potential energy diagram.
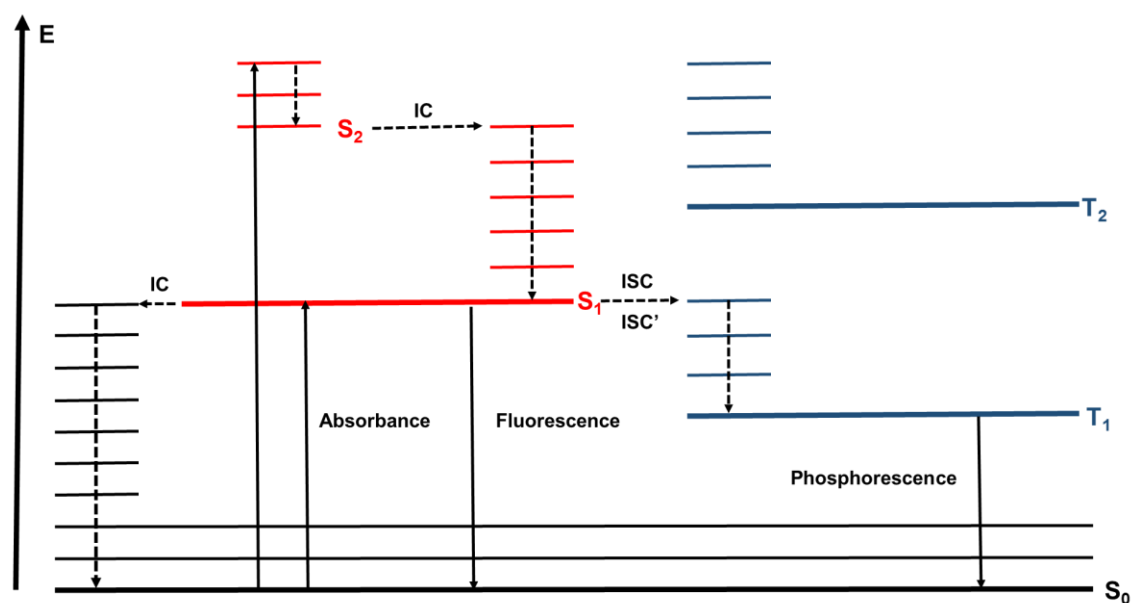
Figure 1.25: Simple Jabłoński diagram.

For most organic molecules, triplet states do not play a large role due to the low probability of triplet state formation due to the spin selection rule, $\Delta S = 0$, which states that the total molecular spin must be conserved at all times. However, if there are heavy atoms in the molecule, population of triplet states becomes of increased importance due to spin-orbital coupling (SOC) - a relativistic interaction between spin angular momentum and orbital angular momentum. Spin-orbital coupling is directly proportional to Z^4, where Z is the nuclear charge and causes a partial lifting of the spin selection rule allowing triplet state generation from singlet states by a process known as intersystem crossing (ISC). Deactivation by phosphorescence can then arise through a spin-forbidden radiative transition between the triplet excited state and the singlet ground state, can restore the ground state. Phosphorescence is distinguished by a longer excited-state lifetime (10^{-3} - 10^2 s compared to 10^{-9} - 10^{-7} s for fluorescence) and larger Stokes shift than fluorescence. It is also easily quenched by the presence of dioxygen, due to energy transfer from the phosphor to the triplet dioxygen molecule, requiring measurement in anaerobic conditions. This also provides a useful test for the nature of the emission, so that if a band disappears, or weakens significantly in intensity, on exposure to dioxygen it can be assigned as of triplet emission.

1.2.2   Emissive Metal Complexes

Cyclometallated complexes can be frequently luminescent, with possible applications as optical chemosensors,[43-45] photocatalysts,[46-51] biological labelling reagents,[52, 53] phosphorescent emitters in OLEDs[39-41, 54-57] and molecular photochemical devices for solar energy conversion.[58-60] Access to the triplet states is highly desirable in many applications including OLEDs, resulting in a large interest in potential materials.

Colouration in simple transition metal complexes is frequent due to electron movement between d-orbitals, but the interaction of metal and ligand molecular orbitals can introduce additional transitions (metal-to-ligand charge transfer (MLCT), ligand-to-ligand charge transfer (LLCT) and metal-to-metal charge transfer bands (MMCT), the latter where more than one metal centre is present in a complex). Heavy metal containing complexes ($Z > 20$) typically display phosphorescence due to fast ISC due to spin-orbital coupling.

Use of platinum(II),[28, 61-87 88-91] iridium(III)[22, 23, 84, 90-101] and increasingly gold(III) in emissive metal complexes are common, with gold(III) and platinum(II) being isoelectric. Many other metal complexes are also emissive, with lanthanide(III) complexes providing sharp emission bands of high colour purity from the 4f-shell. These complexes are discussed in further depth in the following review and are not considered further in this work.[102] The photophysical properties of gold(III) complexes will be discussed in Section 3.1.

There have been multiple examples of emissive platinum(II) complexes with many containing either C^N[28, 61, 62, 75, 80-82, 87, 90, 91, 103] N^N[77-79, 104] or N^C^N[64, 65, 74, 83, 88, 89] cyclometallating ligands to give neutral species or N^N^N cyclometallating ligands to give cationic complexes.[61, 63, 67-70, 76] Due to the high level of spin-orbit coupling complexes tend to display phosphorescence with lifetimes in the microsecond regions. Emission colour can be tuneable, depending on the structure, with excimeric emission and intermolecular metal-to-metal-to-ligand charge transfer, MMLCT, frequently important due to formation of short Pt···Pt contacts due to the preferred square-planar structure for platinum(II).[67, 68, 70, 88, 89] Quantum yields up to 0.7 have been reported.[87]

R = H, Me, C(O)OMe

R = C_6H_5, C_6H_4Cl-4, $C_6H_4CH_3$-4, $C_6H_4OCH_3$-4, $C_6H_4NO_2$-4, benzo-15-crown-5, C_6H_3-$(OCH_3)_2$-3,5
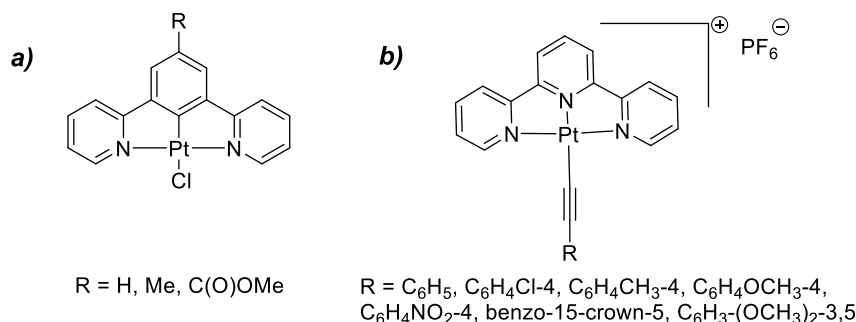
Figure 1.26: Structure of an emissive platinum(II) complex with a N^C^N-coordinating dipyridylbenzene ligand (a)[64] and structure of a platinum(II) complex with a N^N^N- coordinating tripyridyl ligand.[67]

Previously, low-lying metal-centred d-d states in platinum(II) complexes provided an efficient route of thermal deactivation,[105, 106] with the result that cyclometallating ligands are required to raise the d-d state energy so that emission can occur from $^3\pi$-π^* and MLCT states, with the ligand nature effecting the nature of the emission. N^N^C cyclometallating ligands have been shown to primarily give MLCT, while use of N^C^N resulted in a change to $^3\pi$-π^*.[64] An example of an emissive platinum(II) complex with a N^C^N-coordinating dipyridylbenzene ligand (Figure 1.26a) emitted in the green to

yellow region at 480 – 580 nm, with high quantum yields of 0.60-0.58.[64] At concentrations $>10^{-5}$ mol dm^{-3} additional excimer emission was observed at ~700 nm. Increasing the electron-donating ability of the substituent resulted in red-shifting due to a narrowing HOMO-LUMO gap. Similar complexes have been used in OLEDs with moderately large EQEs (4 to 16%).[65] Use of a N^N^N-coordinating tripyridyl ligand (Figure 1.26b) gave an emissive anionic complex, which emitted in the yellow to red regions, 560 – 660 nm, though not all complexes were emissive at room temperature.[67] Emission was assigned as ^{3}MLCT, with possibly some mixed ^{3}LLCT states. Emission colour properties have been shown to be tuneable,[68-70] with aggregation states frequently important in emission.

Iridium(III) is commonly complexed to phenylpyridine ligands,[90, 95-98] with colour tuning achieved by variation of substituents. The quantum yield and lifetimes can also be tuned by use of appropriately located electron-donating and electron-withdrawing substituents, PLQYs up to 50% have been achieved and lifetimes in the microsecond region.[100] Related ligands used include ligands based on 1-phenylisoquinoline,[93] benzothiazole[22, 23] and diazine complexes.[23] Iridium(III) complexes are regularly used in OLEDs, which are reviewed in further detail in the following references.[23] Moderately high external quantum efficiencies (EQEs) of 10-20% are frequently achieved,[22, 93] with one complex having a very high reported EQE of 31% (Figure 1.27).[97]
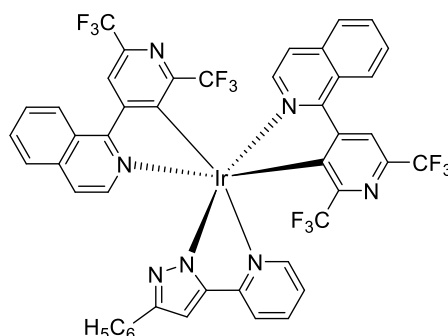
Figure 1.27: Structure of iridium complex, with pyrazol-pyridine and (2,6-bis(trifluoromethyl)pyridin-4-yl)isoquinoline ligands, which displays a very high EQE of 30.6%.[97]

1.3   An Introduction to OLEDs

The phenomenon of electroluminescence, where luminescence is induced by the application of an electric current, was first demonstrated in silicon carbide (SiC) in

1907[107] and in an organic compound in 1955 when Bernanose *et al.* applied an alternating current, with high voltage, to thin films of acridine orange and quinacridone.[108] In 1960 researchers at Dow Chemicals developed an alternating current driven electroluminescent cell based on anthracene,[109] but the requirements (>100 V) of this and other early device examples made them undesirable for practical applications,[110, 111] with later, slow improvements.[112] Then in 1987 Tang and VanSlyke developed the first OLED device with a drive voltage below 10 V, from *tris*(8-hydroxyquinolato)aluminium(III), giving a green luminescence.[113] Since this there has been a large amount of interest in OLEDs.[114]

1.3.1 Device Structure

OLEDs work by the injection of electrons into the LUMO at the device cathode to form an electronically excited state.[114] At the same time holes are introduced in the HOMO at the anode resulting in formation of an exciton. Radiative relaxation causes light emission as either fluorescence or phosphorescence, depending on the nature of the luminescent material. The simplest device therefore consists of three layers (Figure 1.28): a thin film of luminescent material sandwiched between two electrodes, a thin cathode of metal (either calcium or aluminium or an alloy, such as Li/Al, that has the same properties) and a semi-transparent anode of indium tin oxide (ITO), generally backed on to either glass or plastic; the latter offers the possibility of flexible devices.
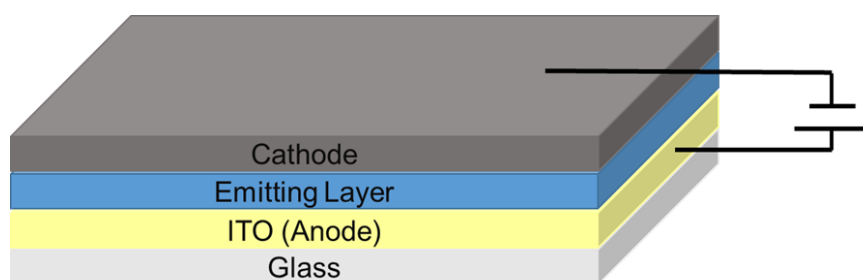
Figure 1.28: Structure of a simple OLED device.

While this is the most basic structure possible, generally multi-layer devices are used to improve performance (Figure 1.29). The OLED device efficiency is dependent on the efficiency of charge-carrier injection, charge balance, excited state multiplicity (singlet or triplet), photoluminescent quantum yield (PLQY) and extraction of emitted light. The use of additional layers enables improved matching of work-functions and material energy levels to improve performance (Figure 1.30). Hole- and electron-injection layers (HIL and EIL) and hole- and electron-transport layers (HTL and ETL) minimise the

energy gap between the electrodes and emissive layer creating an easier pathway for charge carrier movement. Hole/electron/exciton blocking layers (HBL and EBL) are also used frequently to confine charge recombination to the emission layer, which often consists of the emissive material doped into a polymer matrix, with, again, energy-level matching important to prevent charge trapping on the host; careful matching enables energy transfer to the emitter.
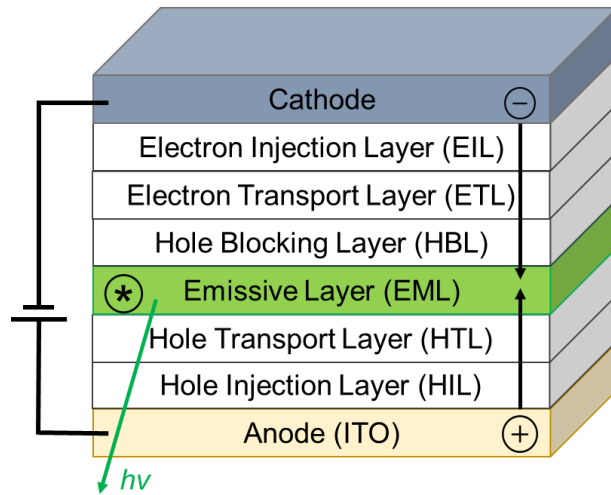
Figure 1.29: Generic structure of a multilayer OLED device.
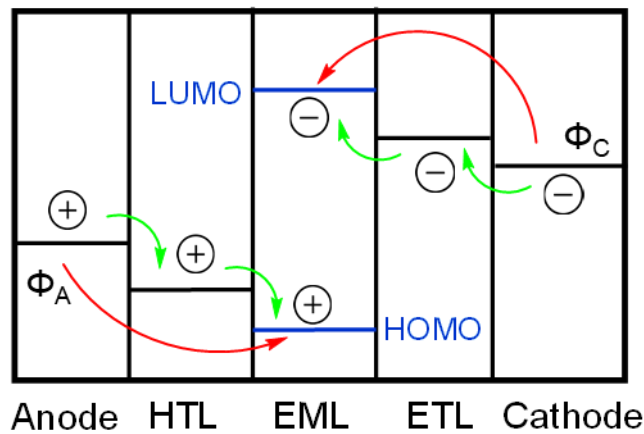
Figure 1.30: Energy levels in a multilayer OLED device, showing charge carrier movement in the device.

The theoretical internal quantum efficiency (IQE) is dependent on the emission nature: fluorescence or phosphorescence. Due to the method of charge injection in an OLED device, holes and electrons are injected independently, meaning there is no inherent spin correlation present. This means that singlet and triplet states can be formed with equal

probability leading to a statistical 1:3 ratio (singlet to triplet). In the absence of SOC, this inherently restricts the IQE of a singlet emitter to a maximum of 25% as only the singlet state can decay radiatively. On the other hand when SOC occurs, the triplet states can also decay and so emission quantum yields can reach a theoretical maximum of 100%. Hence, use of phosphorescent emitting materials in order to allow access to emission from the triplet states is highly desirable and many proposed emissive materials contain heavy metals due to the increased SOC.[114, 115]

A useful triplet emitter should then ideally have a lifetime in the general region of ~1 μs to avoid self-quenching and generate a high PLQY.[114, 116] It should also be charge neutral to avoid migration in an electric field, avoid self-quenching by triplet-triplet annihilation and finally, be capable of being processed by either vacuum deposition (sublimation) or spin coating (organic solvent soluble).

The external quantum efficiency (EQE) is a measure of the efficiency of the device and is normally much lower than the emission quantum yield, typically taking a value of 20-30% for the triplet emitter. This indicates that only a small amount of the produced light in the emissive layer will actually exit the device for productive use.[117, 118]

1.3.2   OLEDs vs LCDs

OLEDs present several potential advantages over liquid crystal displays (LCD), which have until now dominated the device market.[114, 119] Thus, OLEDs have a faster response time, improved colour contrast, can be made much thinner and require no backlight, lowering power consumption and opening the possibility of use in light, flexible, portable devices. OLEDs also show improvements in viewing angle and contrast ratio. However OLEDs have a few current major disadvantages when compared to LCDs. The operational lifetime, particularly for blue OLEDs due to the inherently high-energy emission, is significantly shorter, resolution is lower and manufacturing cost is currently high making the final product outside many purchasers' price range. LCDs can also be recycled, while OLEDs cannot.[114] Nevertheless, OLEDs are now frequently available commercially in high-end TV screens and in mobile phone displays, based mainly on cyclometallated iridium(II) complexes.[2]

Liquid-crystalline OLEDs are of potential interest as the increased molecular ordering in the liquid-crystalline phase can lower the drive voltage with the presence of a well-correlated pathway along which the charge carriers move.[119-121] For example, conductivity anisotropies of ~10^5 are known in columnar mesophases.[122] The peripheral alkyl/alkoxy chains are also capable of acting as spacers mitigating self-quenching effects, and the fluid nature can allow dynamic effects and self-healing properties.[115] Finally, alignment in liquid-crystalline phases of calamitic materials can lead to polarised emission,[92, 115] with the first example of a polarised OLEDS being reported in 1995.[123] Currently displays require addition of a polariser to produce the required polarised light, which blocks ~50% of the produced light. In the interest of increased device efficiency and decreased energy usage an inherently polarising emission layer, enabling dispensation of one polariser, is highly desirable.

1.4 Aims of Project

This project aims to build on the work previously undertaken, by Parker, on the investigation of the thermal and photophysical properties of gold(III) complexes substituted in the 4,4′- and 3,3′,4,4′-positions with dodecyloxy chains.[54] It was shown that the introduction of long chains in these positions resulted in formation of columnar mesophases and gave green and yellow triplet emission respectively, with, excitingly, quantum yields in solution up to 34%. These complexes were successfully used as dopants in OLEDs.

Porphyrins are known to be strongly photophysically active and therefore the attachment of these units to gold(III) complexes is of interest to investigate the resulting photophysical, and liquid crystalline, properties in the hope of development of further suitable dopants for OLEDs. Due to the steric constraints attachment to the porphyrin unit requires, substitution of the gold(III) complexes in the 2,2′-positions of the phenyl unit of the C^N^C ligand is helpful. Therefore, the chemical reactivity of a range of novel C^N^C ligands on mercuration and auration are investigated, along with the complexes' spectroscopic properties, with particular emphasis on the attempted development of a mercury-free route of synthesis to C^N^C cyclometallated gold(III) complexes. The resulting phenyl alknyl complexes', as well as the gold-porphyrin dyads', liquid

crystalline and photophysical properties are investigated with a view towards determining the suitability as potential OLED dopants.

1.5   References

1.   F. Reinitzer, *Monatsh. Chem.*, 1888, **9**, 421-441.
2.   F. Reinitzer, *Liq. Cryst.*, 1989, **5**, 7-18.
3.   O. Lehmann, *Z. Phys. Chem.*, 1889, **4**, 462.
4.   H. Kelker and B. Scheurle, *Angew. Chem. Int. Ed.*, 1969, **8**, 884-885.
5.   G. H. Heilmeier, L. A. Zanoni and L. A. Barton, *Appl. Phys. Lett.*, 1968, **13**, 46-47.
6.   G. H. Heilmeier, Z. L. A. and L. A. Barton, *Proc. IEEE*, 1968, **56**, 1162-1171.
7.   G. H. Heilmeier, L. A. Zanoni and L. A. Barton, *IEEE Trans. Electron Devices*, 1970, **17**, 22-26.
8.   M. F. Schiekel and K. Fahrenschon, *Appl. Phys. Lett.*, 1971, **19**, 391-393.
9.   R. A. Soref, *Appl. Phys. Lett.*, 1973, **22**, 165-166.
10.   G. W. Gray, K. J. Harrison and J. A. Nash, *Electron. Lett.*, 1973, **9**, 130-131.
11.   P. J. Collings and M. Hird, *Introduction to Liquid Crystals Chemistry and Physics*, Taylor & Francis Ltd, London, 1997.
12.   R. J. Mandle, E. Bevis and J. W. Goodby, *Handbook of Liquid Crystals*, 2014, DOI: 10.1002/9783527671403.hlc037, 1-27.
13.   J. W. Goodby, *Handbook of Liquid Crystals*, 2014, DOI: 10.1002/9783527671403.hlc061, 1-26.
14.   S. Chandrasekhar, B. K. Sadashiva and K. A. Suresh, *Pramana*, 1997, **9**, 471–480.
15.   P. A. Heiney, *Handbook of Liquid Crystals*, 2014, DOI: 10.1002/9783527671403.hlc069, 1-47.
16.   D. M. Collard and C. P. Lillya, *J. Am. Chem. Soc.*, 1991, **113**, 8577-8583.
17.   F. Scandola, C. Chiorboli, A. Prodi, E. Iengo and E. Alessio, *Coord. Chem. Rev.*, 2006, **250**, 1471-1496.
18.   D. Pucci and B. Donnio, *Handbook of Liquid Crystals*, 2014, DOI: 10.1002/9783527671403.hlc077, 1-67.
19.   D. Vorländer, *Ber. Dtsch. Chem. Ges*, 1910, **43**, 3120-3135.
20.   J. Malthete and J. Billard, *Mol. Cryst. Liq. Cryst.*, 1979, **34**, 117-121.
21.   A. M. Giroud and U. T. Mueller-Westerhoff, *Mol. Cryst. Liq. Cryst.*, 1977, **41**, 11-13.
22.   G. Ge, J. He, H. Guo, F. Wang and D. Zou, *J. Organomet. Chem.*, 2009, **694**, 3050-3057.
23.   Y.-X. Hu, X. Xia, W.-Z. He, Z.-J. Tang, Y.-L. Lv, X. Li and D.-Y. Zhang, *Org. Electron.*, 2019, **66**, 126-135.
24.   H. Zheng and T. M. Swager, *J. Am. Chem. Soc.*, 1994, **116**, 761–762.
25.   S. T. Trzaska, H. F. Hsu and T. M. Swager, *J. Am. Chem. Soc.*, 1999, **121**, 4518–4519.
26.   T. M. Swager and H. Zheng, *Mol. Cryst. Liq. Cryst.*, 1995, **260**, 301-306.
27.   E. Cavero, S. Uriel, P. Romero, J. L. Serrano and R. Giménez, *J. Am. Chem. Soc.*, 2007, **129**, 11608-11618.
28.   R. R. Parker, J. P. Sarju, A. C. Whitwood, J. A. G. Williams, J. M. Lynam and D. W. Bruce, *Chem. Eur. J.*, 2018, **24**, 19010-19023.

29.   J.-G. An, S. Hina, Y. Yang, M. Xue and Y. Liu, *Rev. Adv. Mater. Sci.*, 2016, **44**, 398-406.

30.   S. J. Cowling, *Handbook of Liquid Crystals*, 2014, DOI: 10.1002/9783527671403.hlc012, 1-38.

31.   O. D. Lavrentovich, *Handbook of Liquid Crystals*, 2014, DOI: 10.1002/9783527671403.hlc027, 1-53.

32.   C.-C. Huang, *Handbook of Liquid Crystals*, 2014, DOI: 10.1002/9783527671403.hlc034, 1-8.

33.   D. M. Agra-Kooijman and S. Kumar, *Handbook of Liquid Crystals*, 2014, DOI: 10.1002/9783527671403.hlc014, 1-38.

34.   N. Godbert, A. Crispini, M. Ghedini, M. Carini, F. Chiaravalloti and A. Ferrise, *J. Appl. Crystallogr.*, 2014, **47**, 668-679.

35.   V. Percec, M. Glodde, G. Johansson, V. S. K. Balagurusamy and P. A. Heiney, *Angew. Chem.*, 2003, **115**, 4474-4478.

36.   O. Birel, S. Nadeem and H. Duman, *J. Fluoresc.*, 2017, **27**, 1075-1085.

37.   L.-L. Li and E. W.-G. Diau, *Chem. Soc. Rev.*, 2013, 291-304.

38.   M. Imran, M. Ramzan, A. K. Qureshi, M. A. Khan and M. Tariq, *Biosensors (Basel)*, 2018, **8**.

39.   J. Bauri, R. B. Choudhary and G. Mandal, *J. Mater. Sci.*, 2021, 18837–18866.

40.   X. Li, Y. Xie and Z. Li, *Chem. Asian. J.*, 2021, **16**, 2817-2829.

41.   M. C. Tang, M. Y. Chan and V. W. Yam, *Chem. Rev.*, 2021, **121**, 7249-7279.

42.   A. Mahmood, J.-Y. Hu, B. Xiao, A. Tang, X. Wang and E. Zhou, *J. Mater. Chem. A*, 2018, **6**, 16769-16797.

43.   T. W. Bell and N. M. Hext, *Chem. Soc. Rev.*, 2004, **33**, 589-598.

44.   A. Bencini and V. Lippolis, *Environ. Sci. Pollut. Res.*, 2016, **23**, 24451-24475.

45.   Q. Zhao, F. Li and C. Huang, *Chem. Soc. Rev.*, 2010, **39**, 3007.

46.   S. Navalón, A. Dhakshinamoorthy, M. Álvaro and H. Garcia, *ChemSusChem*, 2013, **6**, 562-577.

47.   S. Fukuzumi, J. Jung, Y. Yamada, T. Kojima and W. Nam, *Chem. Asian J.*, 2016, **11**, 1138-1150.

48.   M. Wang, Y. Na, M. Gorlov and L. Sun, *Dalton Trans.*, 2009, 6458-6467.

49.   S. Gautam, H. Agrawal, M. Thakur, A. Akbari, H. Sharda, R. Kaur and M. Amini, *J. Environ. Chem. Eng.*, 2020, **8**.

50.   M. I. Litter, *Appl. Cat., B*, 1999, **23**, 89-114.

51.   H. Hennig, *Coord. Chem. Rev.*, 1999, **182**, 101–123.

52.   Q. Zheng, H. Dai, M. E. Merritt, C. Malloy, C. Y. Pan and W.-H. Li, *J. Am. Chem. Soc.*, 2005, **127**, 16178-16188.

53.   K. K.-W. Lo and S. P.-Y. Li, *RSC Adv.*, 2014, **4**, 10560.

54.   R. R. Parker, D. Liu, X. Yu, A. C. Whitwood, W. Zhu, J. A. G. Williams, Y. Wang, J. M. Lynam and D. W. Bruce, *J. Mater. Chem. C*, 2021, **9**, 1287-1302.

55.   V. K. Au, D. P. Tsang, K. M. Wong, M. Y. Chan, N. Zhu and V. W. Yam, *Inorg. Chem.*, 2013, **52**, 12713-12725.

56.   M. C. Tang, W. K. Kwok, S. L. Lai, W. L. Cheung, M. Y. Chan and V. Wing-Wah Yam, *Chem. Sci.*, 2019, **10**, 594-605.

57.   L.-K. Li, M.-C. Tang, S.-L. Lai, M. Ng, W.-K. Kwok, M.-Y. Chan and V. W.-W. Yam, *Nat. Photonics*, 2019, **13**, 185-191.

58.   V. N. Kozhevnikov, M. M. Ustinova, P. A. Slepukhin, A. Santoro, D. W. Bruce and D. N. Kozhevnikov, *Tetrahedron Lett.*, 2008, **49**, 4096-4098.

59.   A. S. Polo, M. K. Itokazu and N. Y. Murakami Iha, *Coord. Chem. Rev.*, 2004, **248**, 1343-1361.

60. H. Gao, R. Yu, Z. Ma, Y. Gong, B. Zhao, Q. Lv and Z. A. Tan, *J. Polym. Sci.*, 2022, **60**, 865-916.

61. E. C.-H. Kwok, M.-Y. Chan, K. M.-C. Wong and V. W.-W. Yam, *Polyhedron*, 2016, **120**, 54-59.

62. J. Shi, Y. Wang, M. Xiao, P. Zhong, Y. Liu, H. Tan, M. Zhu and W. Zhu, *Tetrahedron*, 2015, **71**, 463-469.

63. F. Camerel, R. Ziessel, B. Donnio, C. Bourgogne, D. Guillon, M. Schmutz, C. Iacovita and J. P. Bucher, *Angew. Chem. Int. Ed.*, 2007, **46**, 2659-2662.

64. J. A. G. Williams, A. Beeby, E. S. Davies, J. A. Weinstein and C. Wilson, *Inorg. Chem.*, 2003, **43**, 8609−8611.

65. M. Cocchi, D. Virgili, V. Fattori, D. L. Rochester and J. A. G. Williams, *Adv. Funct. Mater.*, 2007, **17**, 285-289.

66. R. Akiyoshi, Y. Hirota, D. Kosumi, R. Ohtani, M. Nakamura, L. F. Lindoy and S. Hayami, *Dalton Trans.*, 2018, **47**, 14288-14292.

67. V. W.-W. Yam, R. P.-L. Tang, K. M.-C. Wong and K.-K. Cheung, *Organometallics*, 2001, **20**, 4476-4482.

68. V. W. Yam, K. H. Chan, K. M. Wong and N. Zhu, *Chem. Eur. J.*, 2005, **11**, 4535-4543.

69. E. C. Kwok, M. Y. Chan, K. M. Wong, W. H. Lam and V. W. Yam, *Chem. Eur. J.*, 2010, **16**, 12244-12254.

70. V. W.-W. Yam, K. M.-C. Wong and N. Zhu, *J. Am. Chem. Soc*, 2002, **124**, 506-6507.

71. J. K.-W. Lee, C.-C. Ko, K. M.-C. Wong, N. Zhu and V. W.-W. Yam, *Organometallics*, 2007, **26**, 12-15.

72. M. Ghedini, A. Crispini, D. Pucci and G. Barberio, *Organometallics*, 1999, **18**, 2116-2124.

73. T. Kaharu, T. Tanaka, M. Sawada and S. Takahash, *J. Mater. Chem.*, 1994, **4**, 859-865.

74. W. Lu, B.-X. Mi, M. C. W. Chan, Z. Hui, C.-M. Che, N. Zhu and S.-T. Lee, *J. Am. Chem. Soc*, 2004, **126**, 4958-4971.

75. Y. Wang, Y. Liu, J. Luo, H. Qi, X. Li, M. Nin, M. Liu, D. Shi, W. Zhu and Y. Cao, *Dalton Trans.*, 2011, **40**, 5046-5051.

76. H. S. Lo, S. K. Yip, N. Zhu and V. W. Yam, *Dalton Trans.*, 2007, 4386-4389.

77. D. Pucci, G. Barberio, A. Crispini, O. Francescangeli, M. Ghedini and M. La Deda, *Eur. J. Inorg. Chem.*, 2003, **2003**, 3649-3661.

78. Y. Li, A. Y. Tam, K. M. Wong, W. Li, L. Wu and V. W. Yam, *Chem. Eur. J.*, 2011, **17**, 8048-8059.

79. M. Krikorian, S. Liu and T. M. Swager, *J. Am. Chem. Soc.*, 2014, **136**, 2952-2955.

80. A. S. Mocanu, M. Iliş, F. Dumitraşcu, M. Ilie and V. Cîrcu, *Inorg. Chim. Acta*, 2010, **363**, 729-736.

81. A. Diez, S. J. Cowling and D. W. Bruce, *Chem. Commun.,* 2012, **48**, 10298-10300.

82. A. Santoro, A. C. Whitwood, J. A. G. Williams, V. N. Kozhevnikov and D. W. Bruce, *Chem. Mater.*, 2009, **21**, 3871-3882.

83. V. N. Kozhevnikov, B. Donnio and D. W. Bruce, *Angew. Chem. Int. Ed.*, 2008, **47**, 6286-6289.

84. D. N. Kozhevnikov, V. N. Kozhevnikov, M. Z. Shafikov, A. M. Prokhorov, D. W. Bruce and J. A. Williams, *Inorg. Chem.*, 2011, **50**, 3804-3815.

85. D. N. Kozhevnikov, V. N. Kozhevnikov, M. M. Ustinova, A. Santoro, D. W. Bruce, B. Koenig, R. Czerwieniec, T. Fischer, M. Zabel and H. Yersin, *Inorg. Chem.*, 2009, **48**, 4179-4189.

86. A. Santoro, M. Wegrzyn, A. C. Whitwood, B. Donnio and D. W. Bruce, *J. Am. Chem. Soc.*, 2010, **132**, 10689–10691.

87. M. Spencer, A. Santoro, G. R. Freeman, A. Diez, P. R. Murray, J. Torroba, A. C. Whitwood, L. J. Yellowlees, J. A. Williams and D. W. Bruce, *Dalton Trans.*, 2012, **41**, 14244-14256.

88. V. N. Kozhevnikov, B. Donnio, B. Heinrich and D. W. Bruce, *Chem. Commun.*, 2014, **50**, 14191-14193.

89. V. N. Kozhevnikov, B. Donnio, B. Heinrich, J. A. G. Williams and D. W. Bruce, *J. Mater. Chem. C*, 2015, **3**, 10177-10187.

90. X. Wu, M. Zhu, D. W. Bruce, W. Zhu and Y. Wang, *J. Mater. Chem. C*, 2018, **6**, 9848-9860.

91. A. Santoro, Doctor of Philosophy in Chemistry, University of York, 2010.

92. X. Wu, G. Xie, C. P. Cabry, X. Xu, S. J. Cowling, D. W. Bruce, W. Zhu, E. Baranoff and Y. Wang, *J. Mater. Chem. C*, 2018, **6**, 3298-3309.

93. S. Okada, K. Okinaka, H. Iwawaki, M. Furugori, M. Hashimoto, T. Mukaide, J. Kamatani, S. Igawa, A. Tsuboyama, T. Takiguchi and K. Ueno, *Dalton Trans.*, 2005, 1583-1590.

94. E. Baranoff, J.-H. Yum, M. Graetzel and M. K. Nazeeruddin, *J. Organomet. Chem.*, 2009, **694**, 2661-2670.

95. G. Nasr, A. Guerlin, F. Dumur, L. Beouch, E. Dumas, G. Clavier, F. Miomandre, F. Goubard, D. Gigmes, D. Bertin, G. Wantz and C. R. Mayer, *Chem. Commun.*, 2011, **47**, 10698-10700.

96. H.-Y. Li, L. Zhou, M.-Y. Teng, Q.-L. Xu, C. Lin, Y.-X. Zheng, J.-L. Zuo, H.-J. Zhang and X.-Z. You, *J. Mater. Chem. C*, 2013, **1**, 560-565.

97. N. Su, S. Li, K. Yang, F. Zhou, J. Song, L. Zhou and J. Qu, *Dyes Pigm.*, 2021, **195**.

98. T.-Y. Li, J. Wu, Z.-G. Wu, Y.-X. Zheng, J.-L. Zuo and Y. Pan, *Coord. Chem. Rev.*, 2018, **374**, 55-92.

99. A. Santoro, A. M. Prokhorov, V. N. Kozhevnikov, A. C. Whitwood, B. Donnio, J. A. G. Williams and D. W. Bruce, *J. Am. Chem. Soc.*, 2011, **133**, 5248-5251.

100. A. M. Prokhorov, A. Santoro, J. A. Williams and D. W. Bruce, *Angew. Chem. Int. Ed.*, 2012, **51**, 95-98.

101. Y. Wang, C. P. Cabry, M. Xiao, L. Male, S. J. Cowling, D. W. Bruce, J. Shi, W. Zhu and E. Baranoff, *Chem. Eur. J.*, 2016, **22**, 1618-1621.

102. K. Binnemans, *J. Mater. Chem.*, 2009, **19**, 448-453.

103. Y. Wang, Q. Chen, Y. Li, Y. Liu, H. Tan, J. Yu, M. Zhu, H. Wu, W. Zhu and Y. Cao, *J. Phys. Chem. C*, 2012, **116**, 5908-5914.

104. M. Kato, C. Kosuge, K. Morii, J. S. Ahn, H. Kitagawa, T. Mitani, M. Matsushita, T. Kato, S. Yano and M. Kimura, *Inorg. Chem.*, 1999, **38**, 1638-1641.

105. T. K. Aldridge, E. M. Stacy and D. R. McMillin, *Inorg. Chem.*, 1994, **33**, 722-727.

106. T.-C. Cheung, K.-K. Cheung, S.-M. Peng and C.-M. Che, *J. Chem. Soc., Dalton Trans.*, 1996, 1645-1651.

107. H. J. Round, *Electr. World*, 1907, **49**, 309.

108. A. Bernanose, *Br. J. Appl. Phys.*, 1955, **6**, 54-55.

109. W. Helfrich and W. G. Schneider, *Phys. Rev. Lett.*, 1965, **14**, 229-231.

110. D. F. Williams and M. Schadt, *Proc. IEEE*, 1970, **58**, 476-476.

111. J. Dresner, *RCA Rev.*, 1969, **30**, 332-333.
112. P. S. Vincett, W. A. Barlow, R. A. Hann and G. G. Roberts, *Thin Solid Films*, 1982, **94**, 171-183.
113. C. W. Tang and S. A. VanSlyke, *Appl. Phys. Lett.*, 1987, **51**, 913-915.
114. J.-H. L. H.-W. Chen, B.-Y. Lin, S. Chen, S.-T. Wu, *Light: Sci. Appl.*, 2018, **7**, 17168.
115. Y. Wang, J. Shi, J. Chen, W. Zhu and E. Baranoff, *J. Mater. Chem. C*, 2015, **3**, 7993-8005.
116. T. Hofbeck and H. Yersin, *Inorg. Chem.*, 2010, **49**, 9290-9299.
117. J. Frischeisen, D. Yokoyama, A. Endo, C. Adachi and W. Brütting, *Org. Electron.*, 2011, **12**, 809–817.
118. J. Lu, Y. Zheng and J. Zhang, *RSC Adv.*, 2015, **5**, 18588–18592.
119. S. R. Forrest, *Nature*, 2004, **428**, 911-118.
120. J. Nelson, *Science*, 2001, **293**, 1059-1060.
121. L. Schmidt-Mende, A. Fechtenkötter, K. Müllen, E. Moons, R. H. Friend and J. D. MacKenzie, *Science*, 2001, **293**, 1119-1122.
122. S. Laschat, A. Baro, N. Steinke, F. Giesselmann, C. Hagele, G. Scalia, R. Judele, E. Kapatsina, S. Sauer, A. Schreivogel and M. Tosoni, *Angew. Chem. Int. Ed.*, 2007, **46**, 4832-4887.
123. P. Dyreklev, M. Berggren, O. Inganäs, M. R. Andersson, O. Wennerström and T. Hjertberg, *Adv. Mater.*, 1995, **7**, 43-45.

Chapter 2: The Synthesis and Characterisation of Mercury(II) and Gold(III) Complexes

2.1   Synthesis of Gold(III) Complexes in the Literature

The first example of a gold(III) C^N^C complex (where C^N^C is 2,6-diphenylpyridine) was reported by Che *et al.* in 1998 (Figure 2.1).[1] The authors synthesised [Au(C^N^C)Cl] *via* a Hg(C^N^CH)Cl intermediate. The final complex, [Au(C^N^C)Cl], formed *via* a transmetalation reaction of Hg(C^N^CH)Cl with K[AuCl₄]. Since this point many other complexes have been investigated.[2-6] Unfortunately it is still currently impossible to synthesise gold(III) C^N^C complexes of this form directly, without pre-activation of the ligand (Section 2.3).
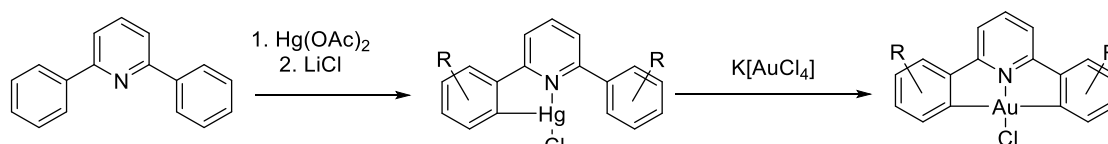
Figure 2.1: Synthesis of [Au(C^N^C)Cl] via Hg(C^N^CH)Cl.

Ligand exchange results in formation of gold(III) C^N^C complexes with various auxiliary ligands. The standard method for exchange of the auxiliary ligand to form the alkynyl complex is *via* reaction of the chlorogold(III) complex with CuI, triethylamine and an excess of the ligand under anhydrous and anaerobic conditions.[7, 8]
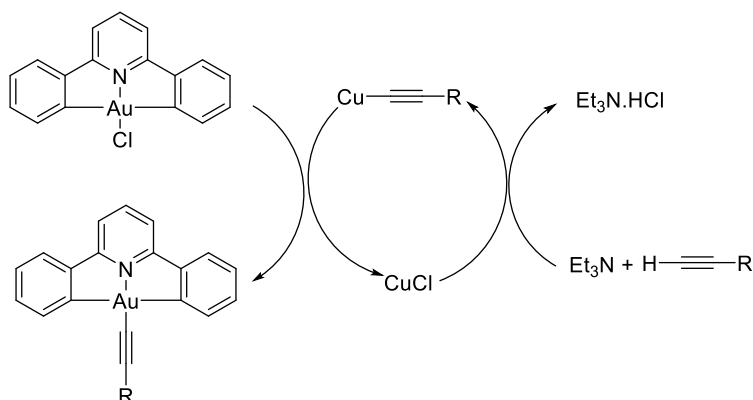
Figure 2.2: Diagram showing the catalytic cycle for formation of gold(III) alkynyl complexes, catalysed by CuI.

The reaction proceeds through a copper-catalysed reaction (Figure 2.2), the first step of which resembles a Sonogashira-like reaction. The terminal acetylene reacts with the copper iodide in the presence of a base (Et$_3$N) to give a copper-acetylide, which undergoes a transmetalation reaction with the gold(III) chloride to give the product, regenerating the catalyst in the process.

Alternately, Roşca *et al* demonstrated that [Au(C^N^C)OH] (formed *via* either reaction of CsOH with the chlorogold complex or *via* addition of AgO$_2$CCF$_3$ and then KOH) was capable of reaction under mild conditions with C-H and N-H compounds, aryl boronic acids and terminal alkynyls to give perfluoroalkyl, *N*-heterocycle and alkynyl complexes (Figure 2.3).[9]
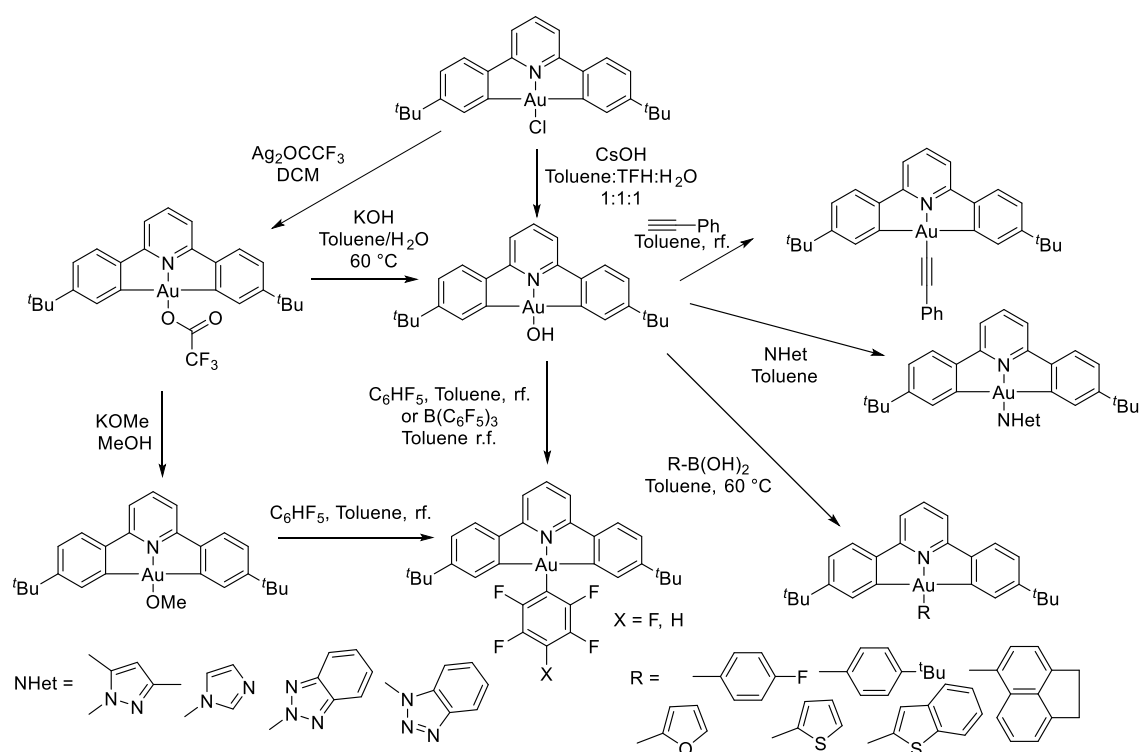
Figure 2.3: Synthesis of various novel gold(III) complexes from the gold chloride and the gold hydroxide.[9]

2.2   The Synthesis of Mercury(II) Complexes in the Literature

Organomercury complexes were first prepared over 125 years ago and were among the first prepared organometallic compounds, due to their historical use in medicines, with thimerosal still widely used as a preservative in vaccines, intravenous drugs and in antitoxins (Figure 2.4). Other wide historical uses include use as pesticides and in industrial applications, many of which have been banned due to toxicity issues.[10]
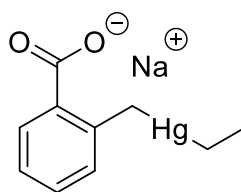
Figure 2.4: The structure of thimerosal.

Formerly, organomercury complexes have been used in the synthesis of other compounds as intermediates due to ready availability, functional group tolerance and chemical and thermal stability, easily undergoing transmetalation reactions with other metals, such as palladium. However in more recent years, the less toxic and more reactive Grignard and organolithium complexes have become the regents of choice in many of the former synthetic uses of organomercury complexes, with replacement of the remaining uses desirable.[11, 12]

Mercury(II) acetate readily mercurates electron-rich arenes. Ligand metathesis with lithium chloride gives the chloromercury complex, with the first examples reported in 1989.[13-15] The mechanism exhibits characteristics of typical aromatic substitution and is facilitated by highly toxic mercury salts and electron-donating groups on the ring.[11] Mixtures of the *ortho-*, *para-* and *meta-*isomers are not uncommon. Organomercury complexes have been widely used in the development of general routes for the synthesis of aryl-gold(III) complexes containing nitrogen-atoms.[1, 7, 8, 12]
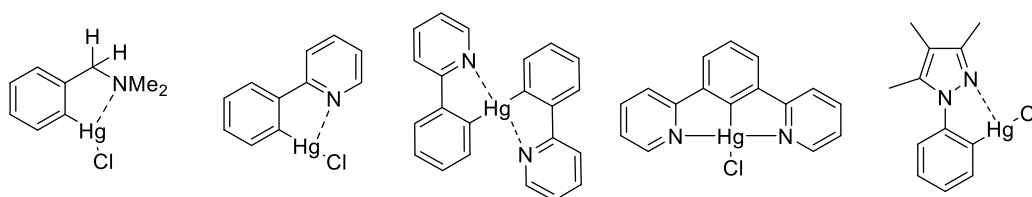
Figure 2.5: Examples of cyclometallated mercury(II) complexes, displaying secondary bonds to nitrogen.

Mercury(II) forms two strong predominantly co-linear, *sp*-hybridised, bonds in both inorganic (XHgX′) and organic (RHgX and RHgR′) compounds, however significant distortions from linearity can occur occasionally.[16] Hg-C bonds are normally assumed to have high Hg $6s$ orbital character.[12] Mercury readily forms weak, highly fluxional, secondary bonds with heteroatoms, particularly nitrogen, though others including oxygen

are also known,[12, 16] resulting in a high effective coordination number of mercury, with such bonds causing the aforementioned distortions from linearity[16] and downfield shifting in ^{1}H NMR spectra when present.[12] The formation of secondary bonds is due to vacant $6p$ and $6d$ orbitals, which are available for coordination to heteroatom lone pairs. Formation of five-membered metallacycles are particularly favourable (Figure 2.5).[17-22]
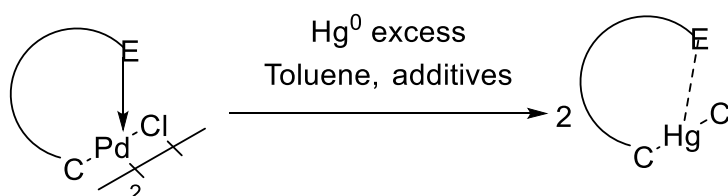
Figure 2.6: Formation of mercury(II) metallacycles from palladium(II) complexes, where E is a heteroatom.[19]

Interaction of azapalladacycles with metallic mercury formed *C,N*-mercuracycle organomercuric(II) chloride during redox transmetalation reactions (Figure 2.6). A labile N-Hg bond was assigned as a weak non-covalent bond or a closed shell interaction.[19] Lin *et al* showed that *C*-metalation of *N*-substituted triazoles occurred in the presence of Hg(OAc)$_2$ to form *C,N*-mercuracycles in near quantitative yield.[23] The reaction occurred by initial *N*-coordination of mercury, followed by an acetate assisted deprotonation-metalation due to intramolecular hydrogen-bonding, while simultaneously a weak C-Hg bond formed (Figure 2.7). Hg(OAc)$_2$ was shown to be unique in this behaviour, with alternate bases investigated not reacting (Ag$_2$O, Ag(OAc), Pd(OAc)$_2$, HgCl$_2$, KOH and K$_2$CO$_3$).
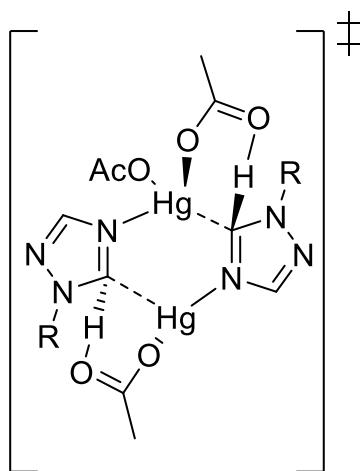
Figure 2.7: Transition state for reaction of mercury acetate in a concerted metalation-deprotonation pathway.[145]

2.3 Literature Examples of Direct Auration

There are few examples of direct auration of ligands with gold(III) in the literature, with most examples relating to 2-phenylpyridine, however given the high level of inherent toxicity of current methods, a method of direct auration is desirable.
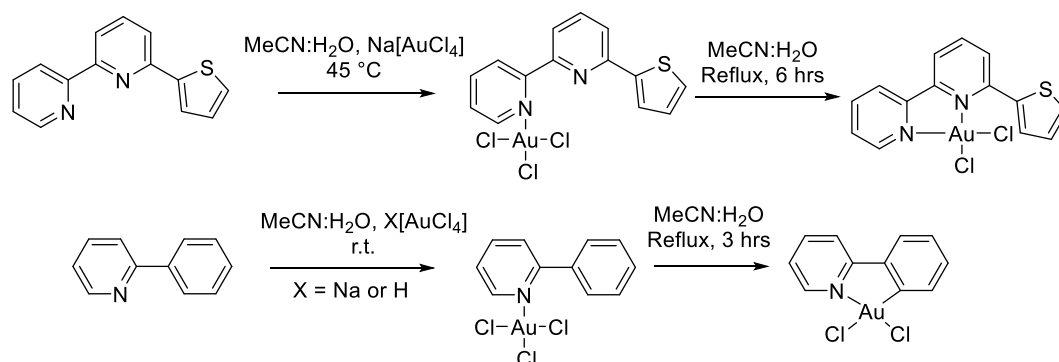
Figure 2.8: Direct auration of 6-(2''-thienyl)-2-2'-bypyridine (top) or 2-phenylpyridine (bottom).[24, 25]

An early example of direct auration of 2-phenylpyridine or 6-(2''-thienyl)-2-2'-bypyridine (Figure 2.8) with H[AuCl$_4$] or Na[AuCl$_4$] in water at 45 °C gave [AuCl$_3$(HL)], followed by a 'roll-over' reaction by heating to reflux in acetonitrile at 100 °C to give the cyclometallated product, [AuLCl$_2$]. A non-bonding interaction between the heteroatoms of the ligand and the metal was determined to be key in the success of the reaction.[24, 25] An attempted direct double C-H activation required refluxing for >100 hours before any observation of cyclometallated product.[24] Variations of this method were later used in some other examples (Figure 2.9).[26-29] A direct C-H bond activation was observed in the reaction of 2-benzylpyridines in water at room temperature with AuCl$_3$.2H$_2$O or K[AuCl$_4$], with subsequent heating to reflux in water:acetonitrile (4:1) resulting in formation of the desired cyclometallated species.[29] Limited information is provided for the direct synthesis of [Au(ppy)Cl$_2$] and [Au(ppy)(en)](ClO$_4$)$_2$ (where ppy is 2-phenylpyridine and en is ethylenediamine) under harsh conditions by a Russian group.[27] Parish *et al.* later determined that the use of *ortho*-mercurated derivatives of 2-phenylpyridines and 2-phenyl-4-(methylcarboxylato)quinolone) was more effective than

direct auration, a common trend in work with gold(III), resulting in increased use of the, now, standard method detailed in Section 2.1.[28]
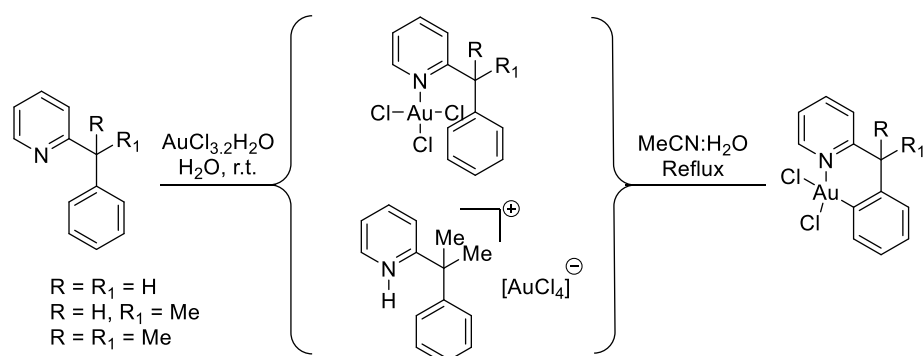
Figure 2.9: Direct auration of 2-benzyl pyridines.[26]
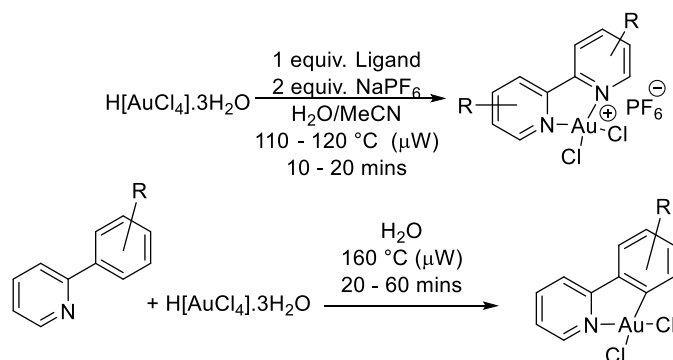
Figure 2.10: Microwave methods for direct auration.[30]

More recently, microwave methods have been investigated.[30, 31] Shaw *et al.* demonstrated that direct auration was possible for synthesis of a class of cationic and neutral gold(III) complexes of the form [AuCl$_2$(N^N)][PF$_6$] containing 2,2′-bipyridine ligands (N^N) and [AuCl$_2$(C^N)], where C^N is 2-phenylpyridine. The method (Figure 2.10) gave analytically pure products in minutes, *via* reaction of the ligand with either NaPF$_6$ and H[AuCl$_4$].H$_2$O in acetonitrile and water at 110 – 120 °C or alternately, H[AuCl$_4$].3H$_2$O and the ligand in water at 160 °C. The short reaction times (10 – 60 minutes) were notable compared to the long thermal reaction times otherwise required.[30, 31] Later work by the same group demonstrated formation of a N^C^C complex directly from Au(OAc)$_3$ and 2-(3,5-di-tert-butylphenyl)pyridine using microwave methods, with an *sp*^{3} C-H activation occurring *via* electrophilic substitution (Figure 2.11).[31] The reaction was assumed to go *via* a [Au(N^C)(OAc^F)$_2$] intermediate, although this was not observed. The product could also be formed thermally by prolonged reaction times in water at 80 °C, over 4 days using (Au(OAc^F)$_3$). DFT suggested an Au(III)$\cdots$H agostic interaction with the OAc^F anion.[31-33] Investigation of the effect of the electronic substituents on the yield indicated that

cyclometallation of N^C ligands likely takes place by an electrophilic aromatic substitution-type mechanism, with initial coordination of the gold to the nitrogen atom.[34]
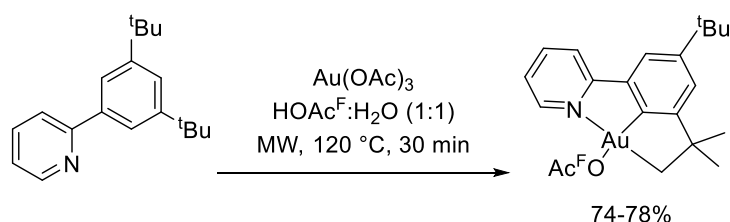
Figure 2.11: Direct auration via microwave methods.[31]

Examples of direction auration *via* oxidative addition have been reported.[35, 36] Oxidative addition of aryl-diazonium salts to a gold(I) precursor, using photoredox conditions and a [Ru(bpy)$_3$][BF$_4$]$_2$ photocatalyst, formed [Au(C^N)Cl(L)][BF$_4$] (Figure 2.12).[35] The mechanism proceeded *via* an electron transfer from the excited photocatalyst to the activated ligand. The resulting aryl radical added oxidatively to the gold(I) complex to give an open-shell gold(II) species, which was oxidised by [Ru(bpy)$_3$]$^{3+}$ to the target gold(III) complex.
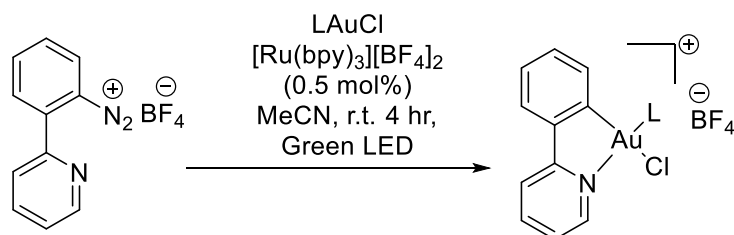
Figure 2.12: Oxidative addition of gold(I) to form gold(III) complexes.[35]

Stable gem-diaurated gold(III) complexes were formed directly from 1,3-diketone and H[AuCl$_4$] in a dichloromethane/methanol solution, in 46 – 70% yield, using 2,6-ditertbutylpyridine (DtBP) as a base (Figure 2.13). The chelating ligand was essential to stabilise the complex. It is likely that the relatively high acidity of the hydrogen atoms, due to the two carbonyl groups, combined with the presence of the coordinating nitrogen atoms facilitated direct auration.[37]
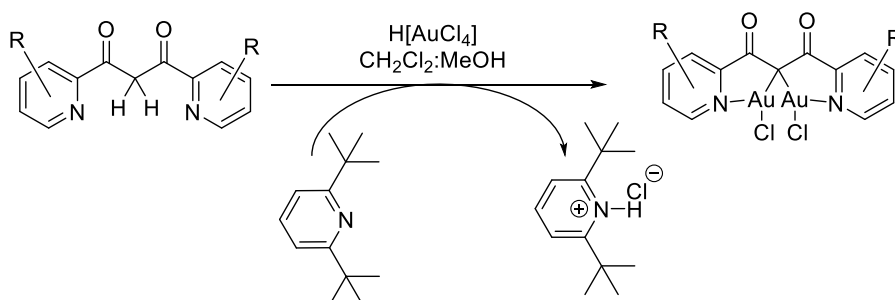
Figure 2.13: Formation of gem-diaurated gold(III) complexes.[37]

Reaction of a dilithium biphenyl derivative with [AuCl$_2$(detc)] (detc = diethyl dithiocarbamate) resulted in formation of the desired [Au(C^C)(detc)] complex in moderate yield (Figure 2.14),[38] with the chelating dithiocarbamate ligand key in stabilising the gold(III) centre to reduction to metallic gold by the organolithium species. An organotin intermediate has also been used.[39] A transmetalation reaction between a dilithium C^N^C complex and a gold(I) species, [AuCl(PCy)$_3$] was also successful.[40]
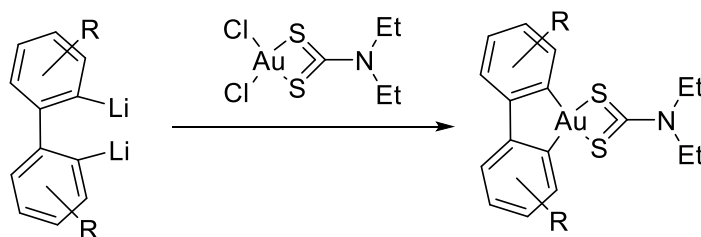
Figure 2.14: Reaction of a dilithium C^C species with [AuCl$_2$(detc)], where detc = diethyl dithiocarbamate.[38]

Most recently, a catalytic [Cp*RhCl$_2$] complex has been used to successfully aurate a wide variety of phenylpyridine ligands in good yields (>50%) (Figure 2.15).[41] The mechanism was determined to have several key steps. The first was the coordination of the ligand to [Rh] to form [Rh(C^N)(Cl)(Cp*)], which then transmetalates, in the rate limiting step, with gold(III). The gold ion then coordinates to the chloride ion coordinated to Rh. The transmetalation is thought to comprise of sequential transfer of the *C*-atom, then the *N*-atom.
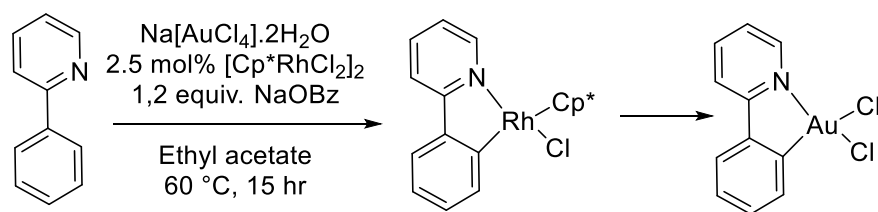
Figure 2.15: Reaction scheme for the direct auration of phenylpyridine using a rhodium catalyst.[41]

Five examples of direct auration of terdentate pincer ligands are currently known in the literature: a class of N^C^C ligands, a N^C^N ligand, a N^N^N ligand, a C^N^N ligand and most recently a C^N^C ligand. Kumar *et al.* in 2015 demonstrated that it was possible to synthesise multiple N^C^C (3,5-disubstituted phenylpyridine ligands) gold(III) complexes using microwave conditions (Figure 2.16, top).[42] It is thought that the presence of two neighbouring *C*-anion centres aids the double C-H activation, with the central aromatic ring having a strong *trans*-influence, enabling ligand exchange. A N^C^N complex was directly aurated using H[AuCl$_4$] in the presence of a base (NaHCO$_3$) to give [Au(N^C^N)Cl][AuCl$_4$] in 57% yield.[43] A C^N^N containing gold(III) complex, [Au(C^N^N-dp)Cl](X), where X = *p*-PTs or ClO$_4$, was formed using K[AuCl$_4$].1/2H$_2$O and silver *p*-toluenesulfonate (Figure 2.16, bottom).[44] Despite the use of an silver(I) salt to act as a chloride scavenger, the yield was poor (14%) and a large amount of metallic gold was formed. Reaction of 2,6-*bis*(benzimidazol-2′-yl)pyridine (N^N^N) with sodium acetate and K[AuCl$_4$] in hot methanol resulted in formation of the chlorogold complex in 90-94%.[167] More recently, functionalisation of an N^C^N ligand with a diazonium ion and reaction with [AuCl(DMS)] (where DMS is dimethyl sulfide) and blue LED light (Figure 2.17) achieved direct auration in >80% yield, with good substituent tolerance.[46]
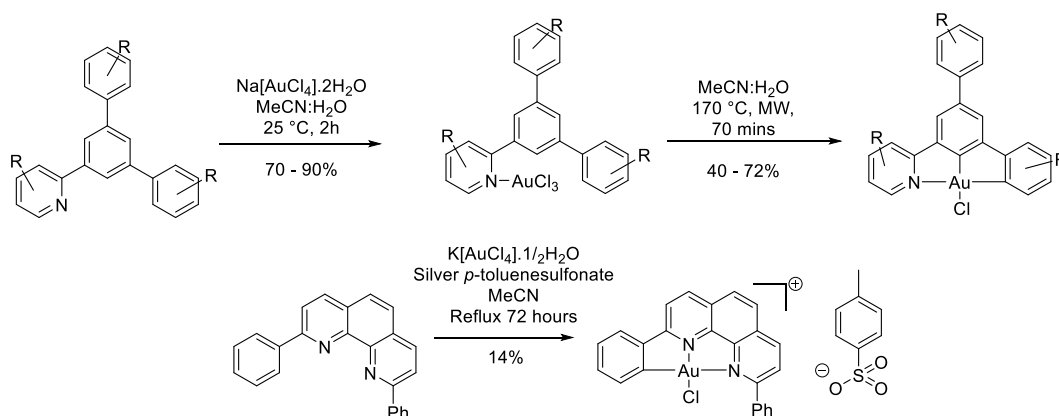
Figure 2.16: Direct auration of a N^C^C gold(III) complex (top)[42] Direct auration of a N^N^C gold(III) complex (bottom).[44]
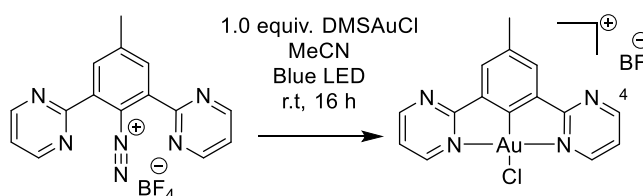
Figure 2.17: Reaction scheme for reaction of N_2^+ functionalised N^C^N ligand with [AuCl(DMS)] and blue LED light.[46]

Recently, Eppel *et al.* reported the first example of a mercury-free synthesis of a [(C^N^C)AuCl] ligand *via* an oxidative addition/C-H activation cascade reaction from the commercially available complex, [AuCl(DMS)] and the diazonium salt of a C^N^C ligand using blue LED irradiation in the presence of 2,6-di-tert-butyl-4-methylpyridine (Figure 2.18).[47] The method proved capable of producing symmetric and unsymmetrical gold(III) complexes in high yields (86%) and was functional group tolerant, with the first reported example of an alkyne-substituted C^N^C complex. Exchanging the DMS ligand on the gold(I) precursor for *N*-carbene or C_6F_5 gave the respective complexes. The proposed mechanism was an oxidative addition of gold, replacing the diazonium group, followed by a Wheland intermediate formation. Base-assisted hydrogen loss gave the desired gold(III) complex. As the first report of a mercury-free synthesis of a C^N^C gold(III) complex this is a hugely significant advance, though finding a method of direct double C-H activation is desirable to avoid the need for C^N^C ligand precursor functionalisation, which becomes highly challenging on use of more complex ligands.
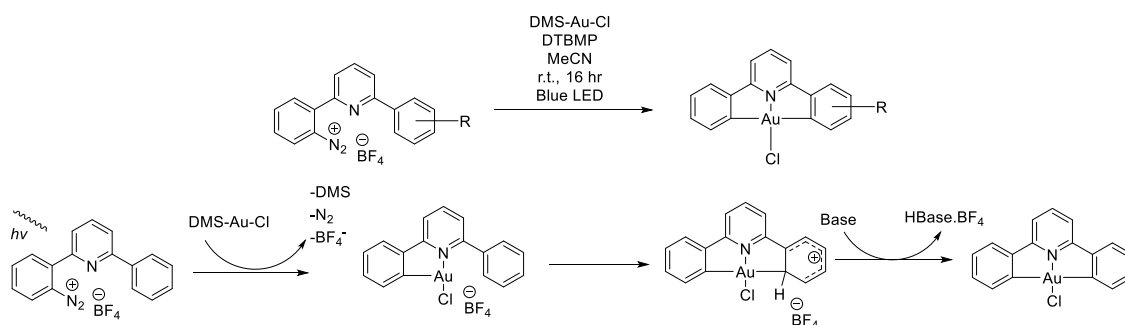
Figure 2.18: Direct auration of a C^N^C gold(III) complex.[47]

Finally, there is one very recent example of direct auration of a tetradentate C^C^N^C ligand using $Au(OAc)_3$ in TFA/H_2O using a two-step microwave synthesis (Figure 2.19), which gave the target gold(III) complex in 36% yield. While the authors did attempt to use similar methods for related tetradentate ligands from both K[$AuCl_4$] and $Au(OAc)_3$, such attempts were not successful and instead the standard mercuration/transmetalation conditions were required.[48]
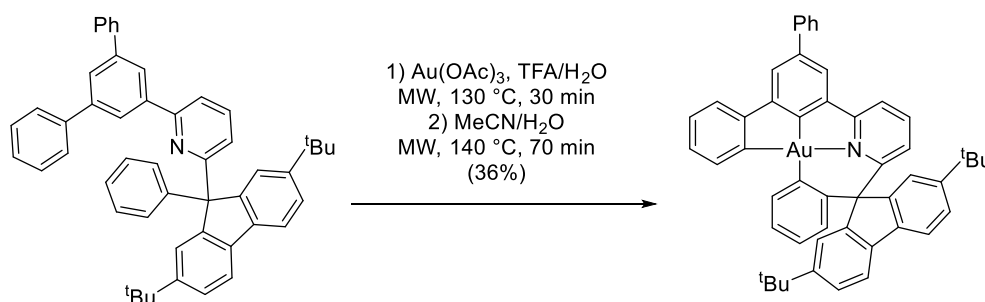
Figure 2.19: Direct auration of a tetradentate ligand using $Au(OAc)_3$ and microwave methods.[48]

In summary, easy, efficient methods of direct auration of un-activated ligands to form the respective gold(III) complexes are required and indeed, highly desirable due to the inherent toxicity of the standard method of transmetalation from organomercury complexes. Unfortunately, such methods have proved elusive. Most currently reported examples are for bidentate ligands, with very few examples for tridentate ligands, suggesting a more challenging barrier of activation for tridentate complexes, potentially due to the steric effect on addition of the third aromatic ring.

2.4   Aims of Chapter

Following on from the work by Parker on gold(III) complexes based on 2,6-*bis*(4-dodecyloxyphenyl)pyridine or 2,6-*bis*(3,4-dodecyloxyphenyl)pyridine ligands,[49-52] the decision was taken to synthesise and investigate the chloromercury(II), chlorogold(III)

and phenylacetylide complexes of the isomeric ligands to probe the effect of the change in substitution position(s) on both the chemical reactivity and the properties of the final complexes. The introduction of substituents in the 2,2′-positions is of particular interest for the future connection of these complexes to porphyrins, due to the direction of these chains away from the face of the porphyrin unit. The ^{1}H, ^{13}C{^{1}H} and, where appropriate, ^{199}Hg NMR spectra are reported and discussed. Where possible the molecular structures of the ligands, mercury(II) complexes and gold(III) complexes have been determined by XRD and discussed. Attempts towards a mercury-free direct auration method are also reported in the hope of developing a suitable method to avoid the use of highly toxic regents, intermediates and by-products.

2.5   Synthesis of C^N^C Pincer Ligands

Previous work by Parker focused on gold(III) complexes of 2,6-*bis*(4-dodecyloxyphenyl)pyridine, (two-chain) or 2,6-*bis*(3,4-dodecyloxyphenyl)pyridine (four-chain) ligands.[49-52] The syntheses developed in these studies have been applied to prepare the analogous gold(III) complexes with 2,2′-, 2,2′,3,3′-, 2,2,′4,4′-, 2,2′,5,5′-, 3,3′/5,5′- and 3,3′,5,5′- substitution patterns (Figure 2.21).

2.5.1   Synthetic Procedure
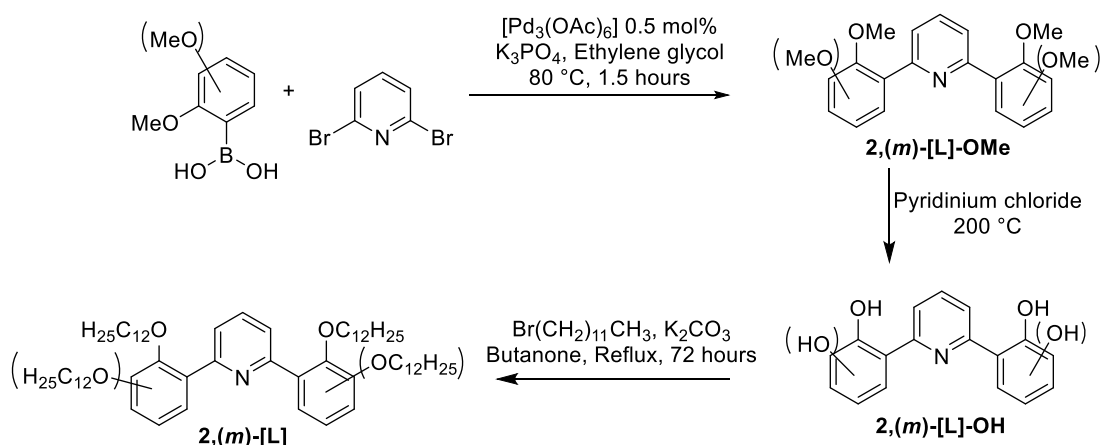
*Figure 2.20: Reaction scheme for synthesis of C^N^C pincer ligands, **n,(m)-[L]**, for ligands substituted in the 2,2′-positions of the phenyl unit.*

The diphenylpyridine framework was formed in a Suzuki-Miyaura reaction using 2,6-dibromopyridine and the appropriate (di)methoxyphenylboronic acid, with purification *via* recrystallisation from ethanol (Figure 2.20).[53] A significant increase in the yield was

obtained for the formation of 2,6-*bis*(2-methoxy)pyridine, **2-[L]-OMe**, which was 90%, compared to 52% for the isomer 2,6-*bis*(4-methoxy)pyridine, **4-[L]-OMe**, a considerable increase.[54, 55 56-59]

Deprotection using molten pyridinium chloride gave the corresponding phenols as wet solids, which proved difficult to dry and so precise yields are not known, although realistic estimations from NMR spectroscopy would suggest >90%. Yellow solids were obtained for 2,6-*bis*(4-hydroxy)pyridine, **4-[L]-OH**, 2,6-*bis*(3,4-dihydroxy)pyridine, **3,4-[L]-OH** and 2,6-*bis*(2,3-dihydroxy)pyridine, **2,3-[L]-OH**. In contrast deprotection of 2,6-*bis*(2-methoxyphenyl)pyridine (**2-[L]-OMe**) gave a beige-coloured diphenol.[60]
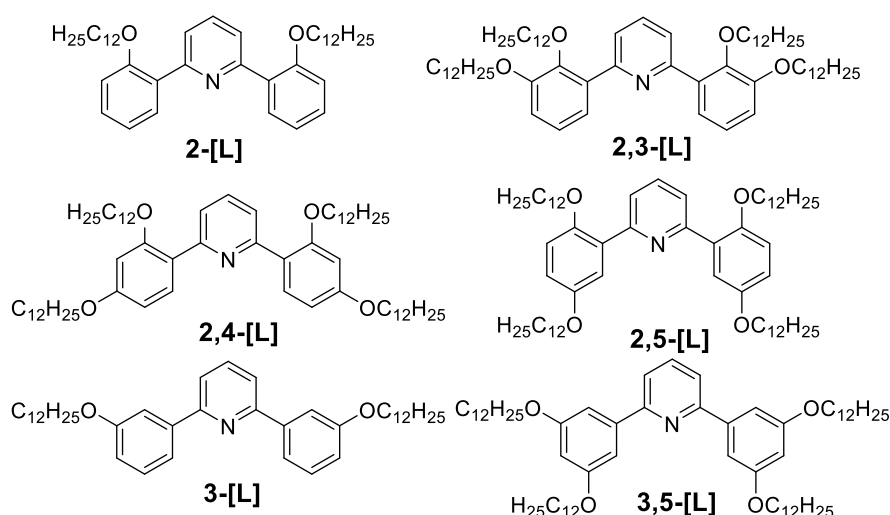
Figure 2.21: Structures of the C^N^C ligands used in this study.

Williamson alkylation was initially used to introduce dodecyloxy chains using 1-bromododecane and potassium carbonate in DMF, stirring at 90 °C overnight, for **4-[L]** and **3,4-[L]**.[61] The alkylation step to produce 2,6-*bis*(2-dodecyloxyphenyl)pyridine, **2-[L]**, however proved more troublesome, as using the conditions employed previously led only to formation of a mono-alkylated product (confirmed by APCI-MS), due to an internal hydrogen bond, the presence of which is supported by the highly deshielded -O*H* resonance at 10.03 ppm in the ^{1}H NMR spectrum and the molecular crystal structure of the related **2,3-[L]-OH**. The internal hydrogen bond resulted in the acidic hydrogen not being readily available for deprotonation *via* the basic K_2CO_3 to give the phenoxide ion for the further S_N2 reaction with 1-bromododecane to give the alkylated product. Further,

this product had a very high solubility in DMF and so its isolation was not straightforward. Therefore, the solvent was changed to butanone; the molar equivalents of K_2CO_3 per hydroxyl group increased from two to four molar equivalents and the reaction time increased to 72 hours, under which conditions an acceptable yield of **2-[L]** was achieved. **2-[L]** was purified *via* recrystallisation from methanol. **2,3-[L]** required purification *via* column chromatography (silica, petroleum ether (40 – 60 °C):ethyl acetate 95:5), followed by crystallisation from hexane and ethyl acetate. Other crystallisation solvent systems were investigated (methanol and CH_2Cl_2:MeOH), but none was effective. **3-[L]** was synthesised by the same method, through notably the methoxy- and hydroxyl-ligands proved more reluctant to crystallise, with the hydroxyl-ligand isolated as a brown oil. **3,5-[L]** was synthesised in 27% yield, with **3,5-[L]-OH** having a green colouration, turning red/orange on drying.

Synthesis of **2,4-[L]** and **2,5-[L]** proceeded smoothly for the first two steps, namely formation of the ligand framework using a Suzuki-Miyaura reaction, followed by deprotection to give the tetra-phenol. Both **2,4-[L]-OH** and **2,5-[L]-OH** were bright yellow in colour. However, synthesis of appreciable yields of **2,4-[L]** and **2,5-[L]** was challenging, with ultimately longer reaction times (~7 days), application of a protective dinitrogen atmosphere, and a 3:1 solvent mixture of 2-butanone:methanol required. It is hypothesised that addition of methanol had two effects: firstly, it increased the solubility of the K_2CO_3 base, aiding hydrogen removal and secondly, as a hydrogen-bonding solvent it helped to break up the intramolecular hydrogen bond in the ligand, aiding ligand deprotonation. **2,5-[L]** was easily isolated (56%) *via* addition of acetone due to its low solubility in that solvent. Purification of **2,4-[L]** was more challenging, with the partially substituted product proving the more crystalline and co-elution frequently occurring during purification *via* column chromatography; unfortunately co-crystallisation also occurred. Ultimately, **2,4-[L]** was isolated in 32% yield.

2.6   X-ray Structures of Ligands

Single crystals, suitable for X-ray diffraction, were grown of the novel tetramethoxy C^N^C ligands and two of the tetrahydroxy ligands. They were grown using vapour diffusion of an anti-solvent into a solution of the compound in a solvent. XRD data tables

and .cif files can be found in the data folder - see page 30. Carbon atoms are coloured grey, hydrogen turquoise, nitrogen blue and oxygen red.

2.6.1　2,6-*Bis*(2,3-dihydroxyphenyl)pyridine

2,6-*Bis*(2,3-dihydroxyphenyl)pyridine crystallised from ethyl acetate and hexane as yellow needles in the monoclinic space group ($P2_1/c$) (Figure 2.22). One of the phenyl rings is almost coplanar (8.49°) with the plane of the pyridine ring, driven by an internal hydrogen bond between one hydroxyl group and the pyridyl nitrogen (d_{N-H} = 1.616 Å). The plane of the other phenyl group makes an angle of 44.64° with that of the pyridyl ring.
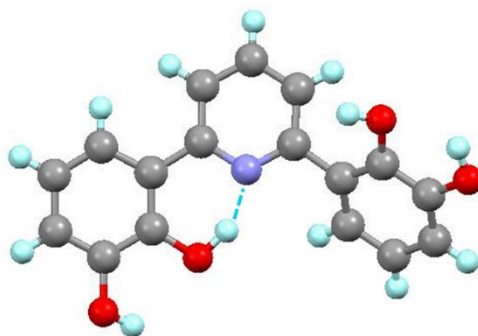
Figure 2.22: X-ray structure of 2,6-bis(2,3-hydroxyphenyl)pyridine.

2.6.2　2,6-*Bis*(2,4-dihydroxyphenyl)pyridinium hydrochloride

The hydrochloride salt of 2,6-*bis*(2,4-dihydroxyphenyl)pyridine, with two waters of crystallisation, crystallised from ethanol/hexane in triclinic space group *P*-1 (Figure 2.23). It can be assumed the chloride ion comes from the pyridinium chloride used in the deprotection reaction. The presence of two internal hydrogen bonds between the hydroxyl groups in the 2-position of the phenyl moiety and the N-H unit results in one phenyl ring being brought into the plane of the pyridyl unit, while the other is twisted at an angle of 29.98° to the plane of the other rings. Hydrogen bonding occurs between the chloride ion, the two water molecules and the hydroxyl groups.
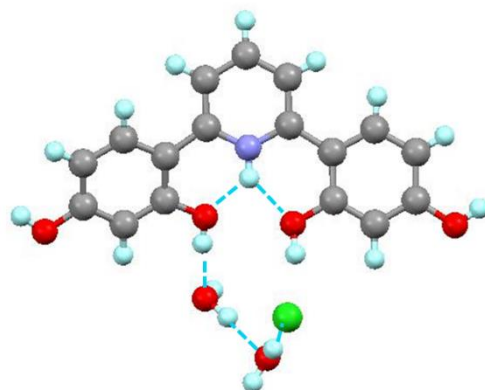
Figure 2.23: Molecular structure of the hydrochloride salt of 2,6-bis(2,4-dihydroxyphenyl)pyridine.

2.6.3   2,6-*Bis*(2,3-dimethoxyphenyl)pyridine

2,6-*Bis*(2,3-dimethoxyphenyl)pyridine crystallised from CH_2Cl_2 and ethanol in an orthorhombic space group (*Aea*2) (Figure 2.24). The phenyl rings make angles of 50.55° and 35.28° to the central pyridyl ring. The methyl unit of the 3,3′-methoxy groups are effectively in the plane of the phenyl rings, while those in the 2,2′-positions are perpendicular to the phenyl plane with the O–CH_3 bond making a dihedral angle of 79.7° to the ring, with these two methoxy groups on opposite sides of the molecule. The space-filling model shows an apparent steric barrier to rotation between the *m*-H on the pyridyl ring and the methoxy substituent in the 2,2′-positions (Figure 2.24b).
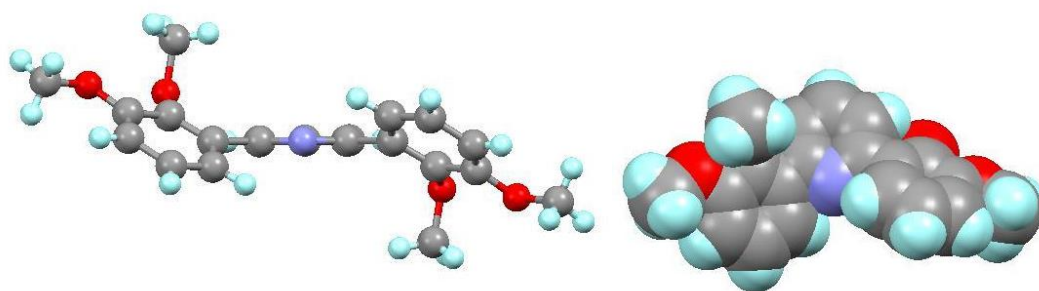
Figure 2.24: X-ray structure of 2,6-bis(2,3-methoxyphenyl)pyridine in 'ball-and-stick' view (a), 'space-fill' view (b).

2.6.4   2,6-*Bis*(2,4-dimethoxyphenyl)pyridine

2,6-*Bis*(2,4-methoxyphenyl)pyridine crystallises from both chloroform and ethanol in an orthorhombic space group ($P2_12_12_1$). Again the methoxy functional groups are coplanar with the phenyl rings, which form angles of 40.83° and 32.98° to the plane of the pyridyl ring (Figure 2.25a). Both phenyl rings are twisted in the same direction, with evidence of

a steric barrier between the *m*-H on the pyridyl ring and the methoxy substituent in the 2,2′-positions on viewing in space-filling model (Figure 2.25b), giving an achiral atropisomer.
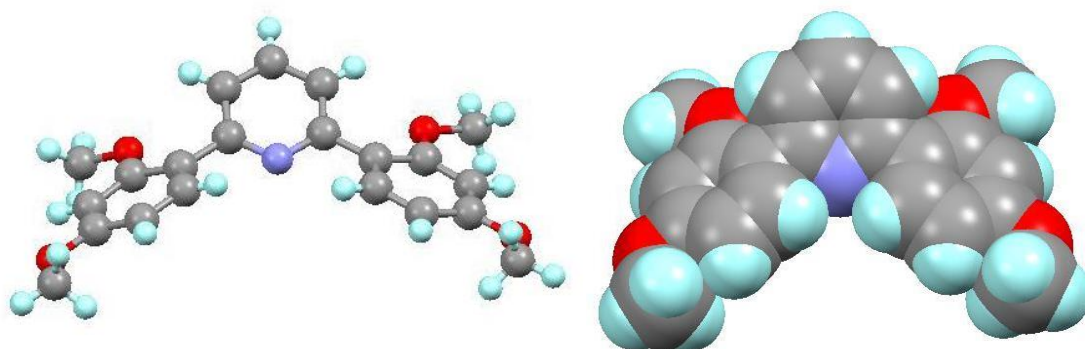
Figure 2.25: Single crystal structure of 2,6-bis(2,4-methoxyphenyl)pyridine in ball-and-stick view (a) and space-fill view (b).

2.6.5   2,6-*Bis*(2,5-dimethoxyphenyl)pyridine

2,6-*Bis*(2,5-dimethoxyphenyl)pyridine crystallises from chloroform and ethanol in orthorhombic space group (*Fdd*2). Twisting of the phenyl rings gives an angle of 40.54° to the plane of the pyridyl ring (Figure 2.26).
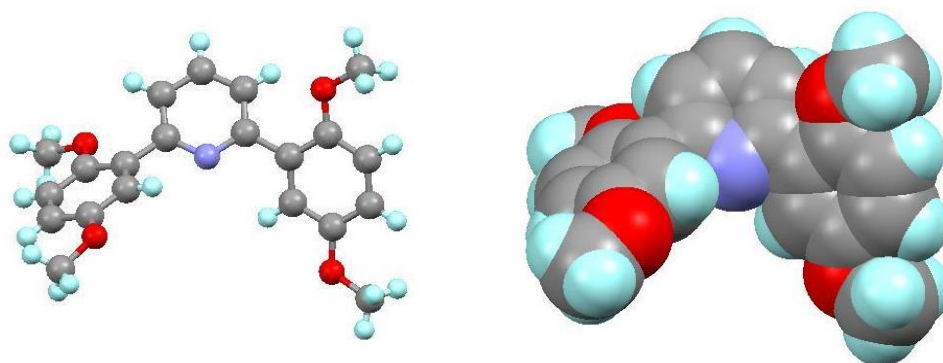
Figure 2.26: Single crystal structure of 2,6-bis(2,5-methoxyphenyl)pyridine in ball-and-stick view (a) and space-fill view (b).

2.6.6 2,6-*Bis*(3-methoxyphenyl)pyridine
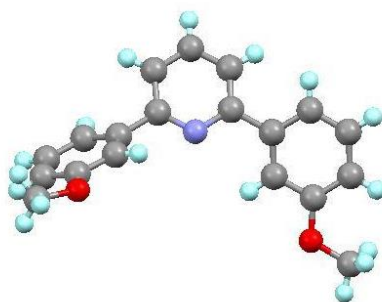
Figure 2.27: Molecular structure of one molecule of 2,6-bis(3-methoxyphenyl)pyridine.

Two solutions proved possible for the structure of 2,6-*bis*(3-methoxyphenyl)pyridine (Figure 2.27). The structure can be modelled with a cell volume of ~2200 Å^3, in the triclinic space group *P*-1, with three molecules in the asymmetric unit, one of which is completely disordered and a disordered methoxy group, with both having 50% occupancy (Figure 2.28a). Alternately, the structure can be solved with a unit cell of double volume in the same space group, with six molecules in the asymmetric unit, and no disorder (Figure 2.28b). A periodic oscillation of one molecule and one methoxy group occurs along the *a*-axis. In the bulk crystal the molecules are shown to pack in columns in a herringbone structure, with the side molecules arranged at ~90° to the central molecules.
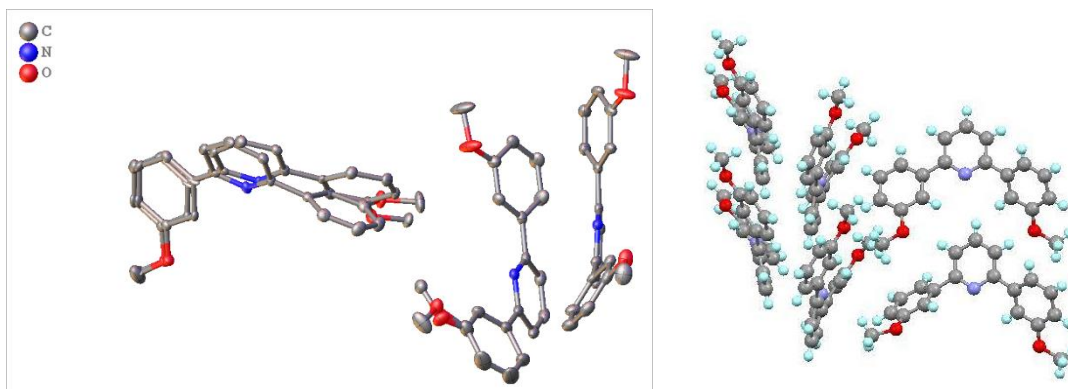
Figure 2.28: Asymmetric unit of 2,6-bis(3-methoxyphenyl)pyridine in the 'small' solution (a) and the 'large' solution (b).

2.6.7 2,6-*Bis*(3,5-dimethoxyphenyl)pyridine

2,6-*Bis*(3,5-methoxyphenyl)pyridine crystallises from chloroform and ethanol in triclinic space group *P*-1. The phenyl rings are twisted out of the pyridyl ring plane with angles of 34.1(2)° and 23.3(2)° (Figure 2.29).
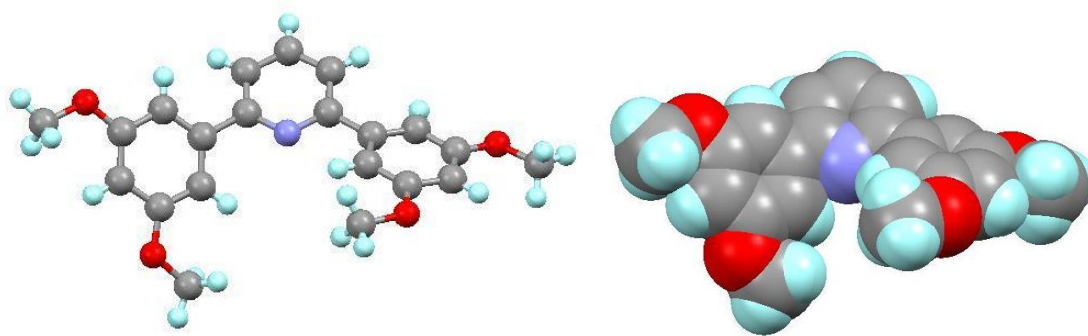
Figure 2.29: Single crystal structure of 2,6-bis(3,5-methoxyphenyl)pyridine in ball-and-stick view (a) and spacefill view (b).

2.6.8 2,6-*Bis*(4-methoxyphenyl)pyridine

2,6-*Bis*(4-methoxyphenyl)pyridine crystallised from dichloromethane and ethanol in the tetragonal space group ($P4_12_12$) (Figure 2.30). The phenyl rings make angles of 21.19° and 21.57° to the central pyridyl ring. Short contacts are observed between the oxygen atom and a methyl hydrogen atom in neighbouring methoxy groups, giving rise to anti-parallel 'zig-zag' structure. The single crystal structure of this ligand has previously been reported,[62] where the structure was resolved in the tetragonal space group ($P4_32_12$), with slightly higher unit cell dimensions (7.9181(11) *vs* 7.83812(15) Å and 24.418(5) *vs* 24.0906(8) Å), however data collection was at a higher temperature (291(2) K *vs* 110.00(10) K), which might explain the discrepancy.
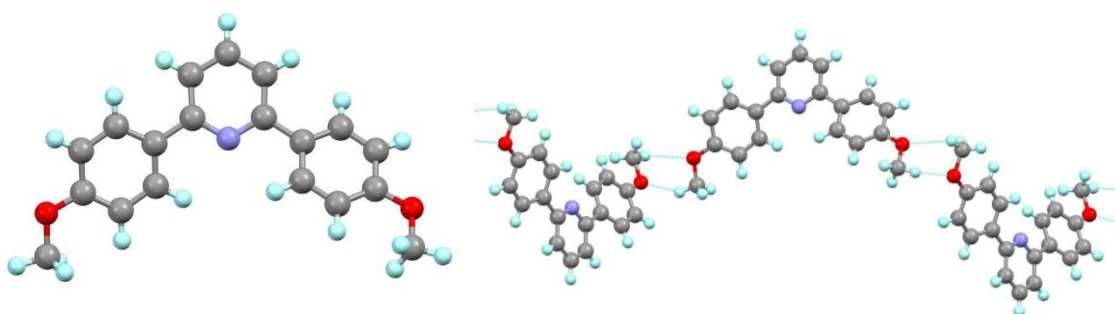
Figure 2.30: Molecular structure of 2,6-bis(4-methoxyphenyl)pyridine.

2.6.9 2,6-*Bis*(3,4-dimethoxyphenyl)pyridine

2,6-*Bis*(3,4-dimethoxyphenyl)pyridine crystallised from dichloromethane and ethanol in the monoclinic space group ($P2_1/n$) (Figure 2.31). Rotation about the pyridine-phenyl bonds led to different relative disposition of the pairs of methoxy groups.
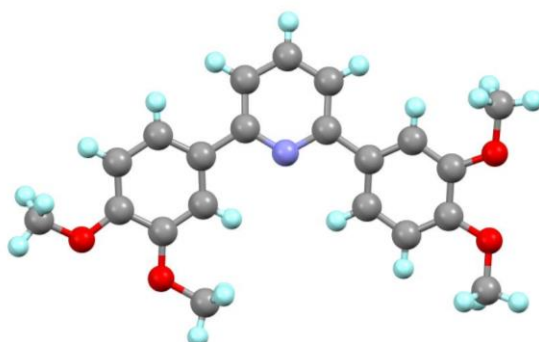
Figure 2.31: Molecular structure of 2,6-bis(3,4-dimethoxyphenyl)pyridine.

2.6.10   General Considerations for Ligands

On comparison of the torsion angels between the phenyl and pyridine rings of the ligand (Table 2.1) it can be observed that the magnitudes fall broadly into three groupings depending on the substitution pattern. Ligands with a substituent in the 2-position of the phenyl rings exhibit the greatest degree of twisting of the phenyl rings out of the plane, with torsion angles >32°. The largest is measured for **2-[L]** at an average value of 45.5°,[60] which is supported by the apparent restricted rotation observed in the ^{1}H NMR spectra (Section 2.7) and on consideration of a generated space-filled structure. The two ligands with substituents in the 3- and 5-positions (**3/5-[L]** and **3,4-[L]**) both exhibit lower average values of 28-30°. Finally, **4-[L]** and **3,4-[L]** both have significantly lower torsion angles of 21.2(3)° and 15.8(2)° respectively, with, **3,4-[L]** especially, close to planar, indicating a lack of a steric driving force for ring twisting. It is clear that the location of the substituent on the phenyl ring has a significant impact on the steric properties of the system.

Table 2.1: Ligand Torsion Angles Between the Phenyl and Pyridine Rings.

Substitution Pattern	Torsion Angle 1 / °	Torsion Angle 2 / °
2-[L][60]	48.7*	42.3*
2,3-[L]	32.5(2)	32.5(2)
2,4-[L]	38.9(3)	30.9(3)
2,5-[L]	38.7(2)	38.7(2)
4-[L]	21.2(3)	21.2(3)
3,4-[L]	18.3(2)	13.4(2)
3/5-[L]	25.2(4)	33.7(4)
3,5-[L]	34.1(2)	23.3(2)

*Esds not available in reference.

2.7　　　　　^{1}H NMR Spectra of Ligands

The main method of characterisation of the ligands was by ^{1}H NMR spectroscopy, some aspects of which deserve further comment. Taking 2,6-*bis*(2-methoxy)pyridine as an example (Figure 2.32), the four hydrogens c-f were identified both on the basis of their multiplicity and chemical shift, complemented by 2D-COSY and NOE (coupling from H_c and H_b to OMe) experiments. The highly similar values of $^3J_{ef}$, $^3J_{de}$ and $^3J_{cd}$ have the result that H_d and H_e appear as effective triplets at low spectrometer resolution, with small $^4J_{HH}$ couplings to H_f or H_c, respectively at high resolution. As drawn, the molecule appears symmetric so that a simple doublet (H_b) and triplet (H_b) would be expected for the pyridine hydrogens, forming an A_2X system, which is indeed observed for the regioisomer 2,6-*bis*(4-methoxy)pyridine and the related 2,6-*bis*(3,4-dimethoxy)pyridine. However, instead a more complex set of signals at 7.85 – 7.70 ppm is observed that could be analysed as two AB spin systems, showing strong second order effects (Figure 2.33). The two hydrogens labelled H_b must therefore in fact be chemically inequivalent. In fact, with the exception of the gold complexes, which are discussed below, all of the methoxy ligands with a substituent in the 2-position or the 3-position of the phenyl unit of the C^N^C ligand, exhibited some degree of desymmetrisation, being more marked in the former.
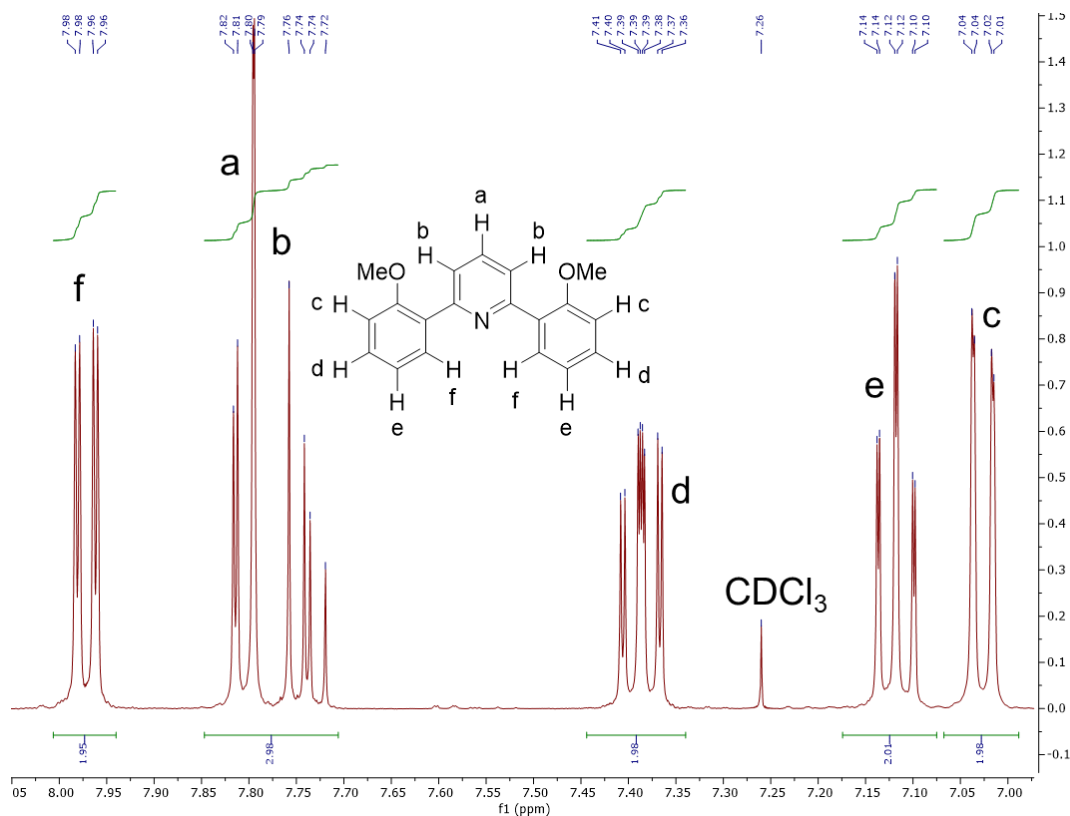
*Figure 2.32: ^{1}H NMR spectrum (400 MHz, CDCl$_3$) showing the aromatic region of 2,6-bis(2-methoxy)pyridine, **2-[L]-OMe**.*

One possible origin of the desymmetrisation is that these particular ligands can exist as one of two atropisomers, which in one case would see both methoxy groups on the same side of the pyridyl ring (*syn*) while in the other they would be on opposite sides (*anti*). When they are present on the same side in principle there would be a mirror plane bisecting the molecule passing through the nitrogen and *p*-carbon of the pyridine ring. However, when the rings are on opposite sides there would be a C_2 axis through the same two atoms of the pyridine ring, but no mirror plane, which would render the object chiral. As such, H$_b$ would then be diastereotopic, offering an explanation for the observed spectra and implying that it is the *anti*-atropisomer that is present.

Consideration of the X-ray single crystal structure shows that in the solid state such an dissymmetric arrangement is found, with the *o*-tolyl groups angled out of the pyridine ring plane in opposite directions with torsion angles of 48.8° and 42.3° respectively (Figure 2.33, insert).[60] Generation of a space-filling model suggests an apparent steric barrier to rotation between the *meta*-hydrogen atom on the pyridyl ring and the methoxy substituent, which would be consistent with the observed NMR spectrum.

86
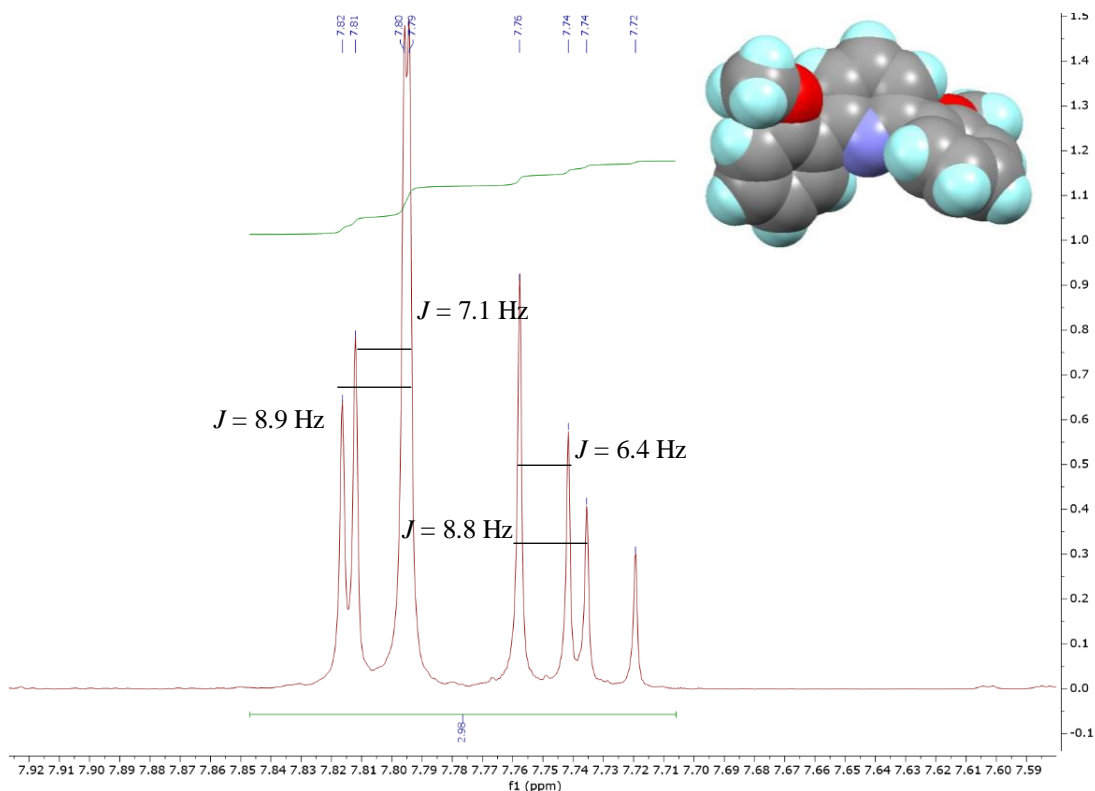
*Figure 2.33: ^1H NMR spectrum (400 MHz, CDCl$_3$) showing signals relating to the pyridine ring of 2,6-bis(2-methoxy)pyridine, **2-[L]-OMe**, and the molecular structure in space-fill view.60*

Exactly the same phenomenon was observed for 2,6-*bis*(2,3-dimethoxy)pyridine but, curiously, in the ^1H NMR spectrum of 2,6-*bis*(2,3-didodecyloxy)pyridine (Figure 2.34) the effect was damped significantly. Thus, the doublet was slightly distorted because of roofing and, H$_a$ appeared almost as a simple triplet, implying that somehow the diastereotopic nature of the *m*-pyridine hydrogens was not so strongly expressed. A clue to this comes from NOE experiments. These show a strong NOE effect between the methoxy hydrogens and H$_b$ on the pyridine ring for 2,6-*bis*(2,3-dimethoxy)pyridine and also strong coupling between H$_b$ and H$_g$ (the first methylene in the chain in the 2-position) for 2,6-*bis*(2,3-didecyloxy)pyridine. However, in addition, there is weak but finite coupling between H$_b$ and methylene groups further down the dodecyloxy chain. As such and given the length of the alkoxy chain, it is possible that it will interact with both hydrogens H$_b$ and, while strictly they remain diatereotopic, their environments may be less sensitive given that both interact with chain methylene hydrogens.

87
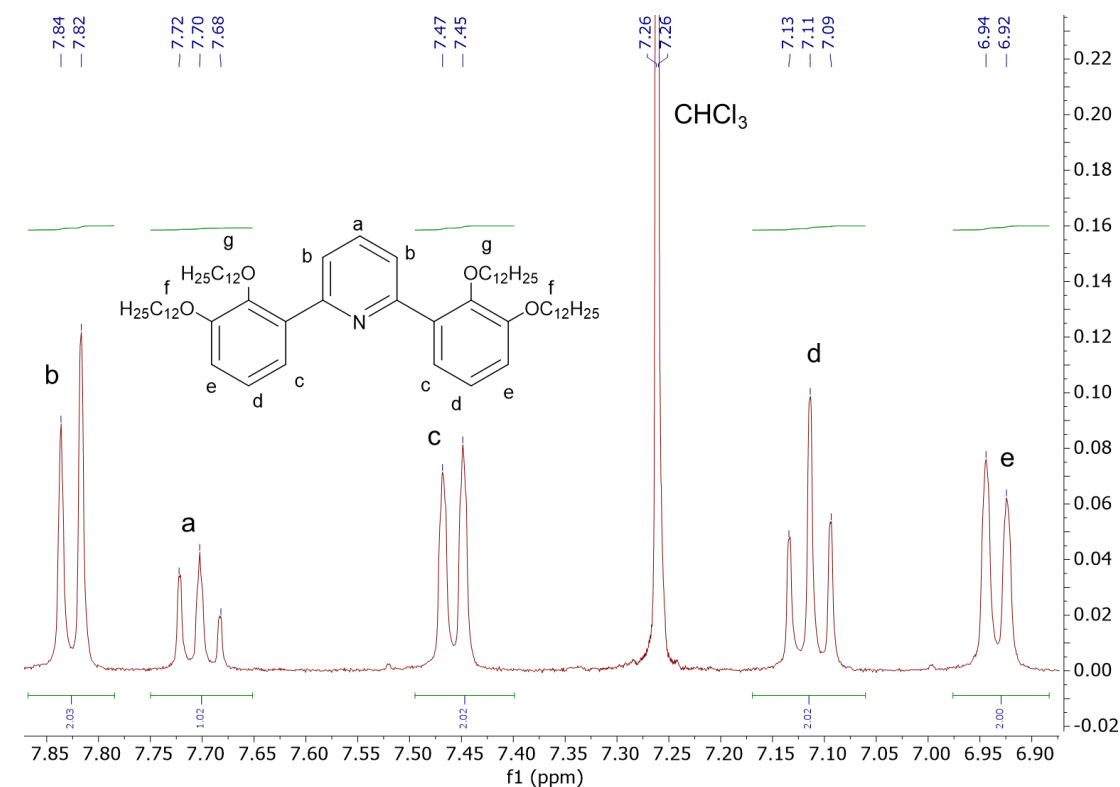
*Figure 2.34: ¹H NMR spectrum (400 MHz, CDCl₃) of compound 2,6-bis(2,3-dimethoxyphenyl)pyridine, **2,3-[L]**.*

The $^{13}C\{^1H\}$ NMR spectra were studied and fully assigned by use of HMBC and HSQC 2D-coupling NMR experiments, with HSQC giving the one-bond coupling between hydrogens and carbons and HMBC the multiple-bond coupling between hydrogens and carbons and can be found in the data folder - see page 30. It is of note that a simple first order spectrum was observed, with no evidence of atropisomers.

2.7.1   Temperature-Dependent ¹H NMR Spectroscopy

To investigate the apparent atropoisomerism present in the compounds, variable temperature ¹H NMR experiments were carried out for **2,3-[L]-OMe** and **2,3-[L]**, in chloroform-*d*, from 253.0 K to 313.0 K at 500 MHz. For **2,3-[L]-OMe** spectra were obtained between 253 – 313 K (Figure 2.35), in which range no change was observed in the peak shape. This indicated no exchange between the atropoisomers on the NMR time scale, however shifting of some of the signals was observed, the origin of which is unclear, although it could be related to temperature-dependent self-association. Spectra for **2,3-[L]** were also recorded over the same temperature range (Figures 2.36 and 2.37),

with almost identical results, indicating equivalent behaviour with longer chain substituents.
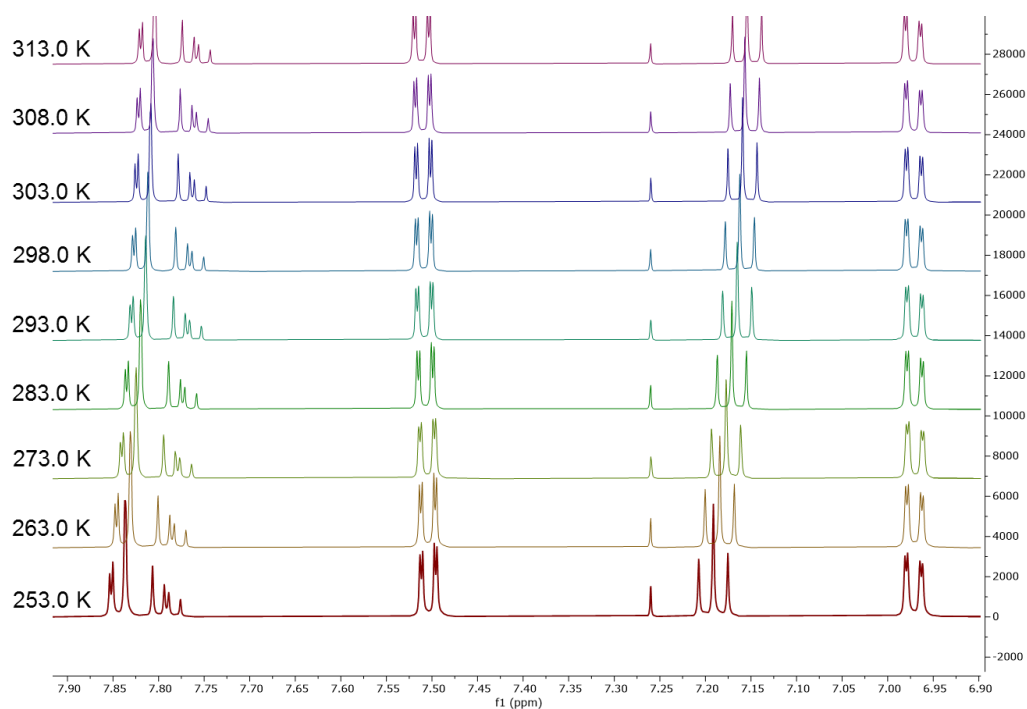
*Figure 2.35: ¹H NMR spectra for **2,3-[L]-OMe** (500 MHz, CDCl₃) from 253 – 313 K.*
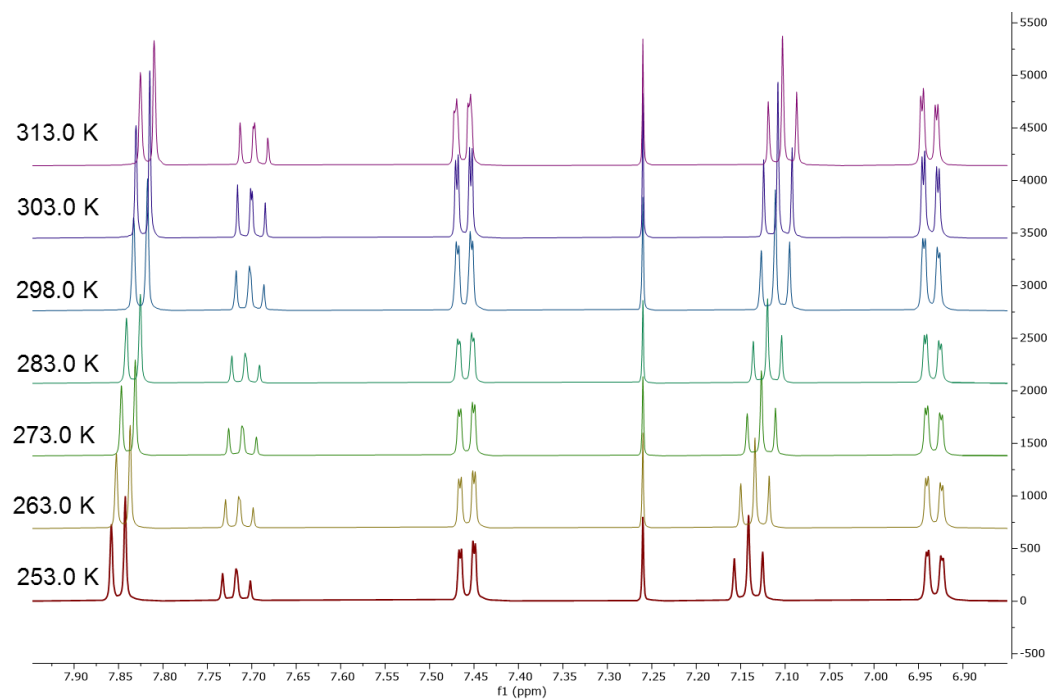
*Figure 2.36: ¹H NMR spectra (aromatic region) for **2,3-[L]** (500 MHz, CDCl₃) from 253 – 313 K.*
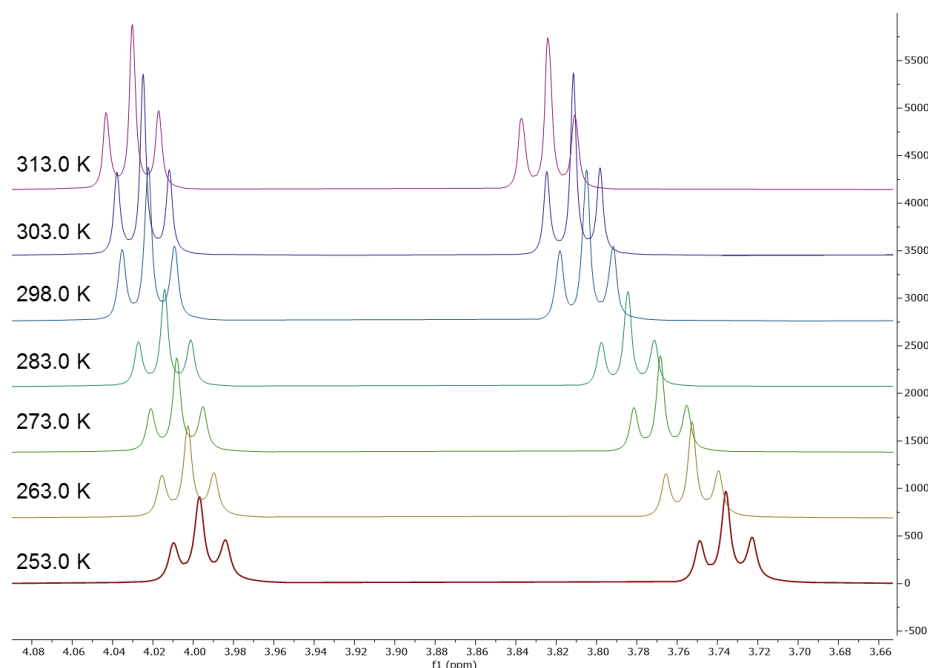
*Figure 2.37: ¹H NMR spectra (alkoxy region) for **2,3-[L]** (500 MHz, CDCl₃) from 253 – 313 K.*

2.8   Synthesis of Substituted Phenyl Alkynes

Phenylacetylene ligands, substituted with one, two and three dodecyloxy chains were prepared as shown below.[50, 62, 63]
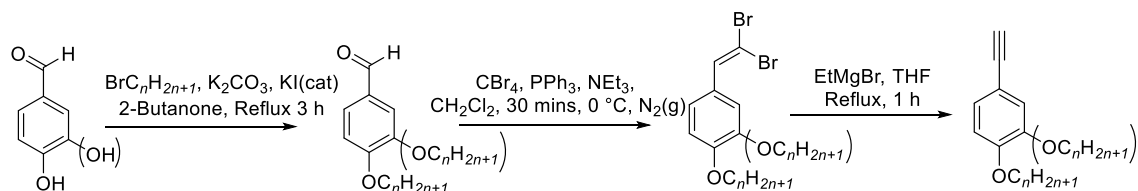
Figure 2.38: Reaction scheme for the synthesis of one and two-chain alkoxy phenyl alkynyl ligands.

Mono- and di-alkoxyphenyl acetylenes were synthesised[*] by alkylation of the precursor mono- or di-hydroxybenzaldehye, followed by a two-step Corey-Fuchs reaction to yield the terminal acetylene (Figure 2.38). For the trialkoxyphenyl acetylenes, the high cost of 3,4,5-trihydroxybenzaldehye led to a different route starting from methyl 3,4,5-trihydroxybenzoate, which was alkylated as in Figure 2.40. Reduction to the primary alcohol using LiAlH₄ and oxidation using MnO₂ gave the aldehyde, allowing conversion to the terminal alkyne, again in a Corey-Fuchs reaction (Figure 2.39).

---

[*] Previously synthesised by R. R. Parker and L. Curtis.
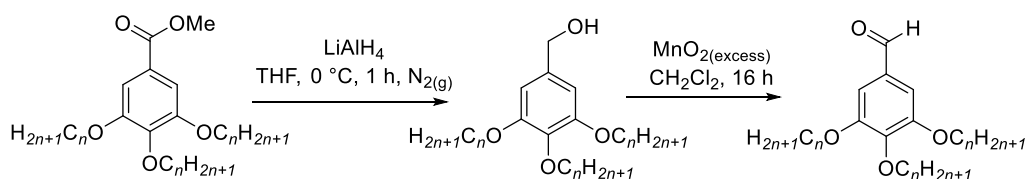
Figure 2.39: Reaction scheme for the synthesis of three-chain alkoxy phenyl alkynyl ligands.

2.8.1   Perfluorinated Phenyl Alkynes

Phenylacetylene ligands substituted in the 4-position with a perfluorinated chain (R = $O(CH_2)_2(CF_2)_8CF_3$ and $O(CH_2)_2(CF_2)_{10}CF_3$) were synthesised using procedures from Parker (Figure 2.40).[52] The synthesis proved challenging due to solubility issues and low yields in the initial synthesis of the triflate from the perfluorinated alcohol.
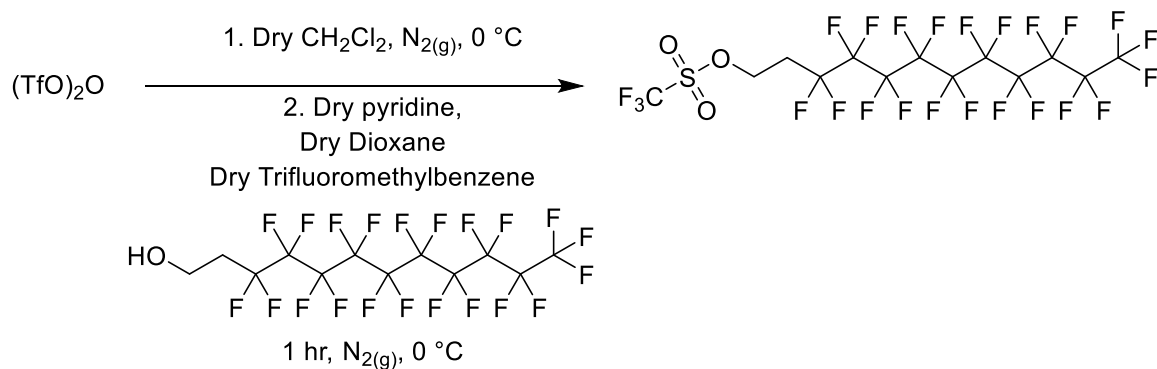
Figure 2.40: Reaction scheme for synthesis of C12 perfluorinated triflate.

Yields were low (<20%), with large amounts of starting material isolated off the silica column. This was surprising and disappointing given that yields >70% were achieved previously, with the cause still unknown.[51, 52]
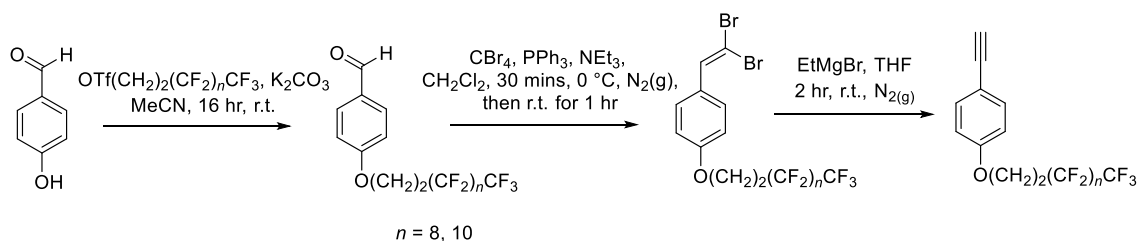
Figure 2.41: Reaction scheme for synthesis of perfluorinated phenyl alkynes.

The required perfluorinated triflate was reacted with 4-hydroxybenzaldehyde and potassium carbonate in acetonitrile at room temperature overnight. The final phenyl alkyne was formed in a two-step Corey-Fuchs reaction (Figure 2.41).

2.9 Synthesis of Mercury(II) Complexes

With direct auration of the C^N^C pincer ligand not possible (see Section 2.3), the gold(III) complexes are obtained indirectly *via* an intermediate mercury(II) complex (Figure 2.42). This is formed by the reaction of two equivalents of Hg(OAc)$_2$ to the pincer ligand in ethanol, heating under vigorous reflux overnight, and the metathesis with methanolic LiCl at 50 °C to give crude [Hg$^{(II)}$(κ^2-C^N^CH)Cl].[1,7,8] Due to the likely high toxicity of the mercury(II) complexes the thermal properties were not investigated.
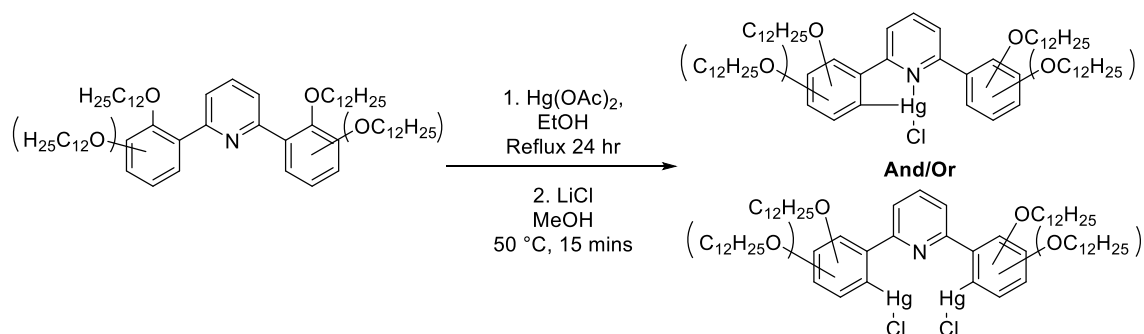
Figure 2.42: Generic reaction scheme for mercuration of ligands.

The complexes **4-[Hg]** and **3,4-[Hg]** were synthesised by previously reported methods as impure complexes in low yield.[50] On the introduction of a substituent in the 2,2′-position of the phenyl ring of the ligand (**2-[L]**) surprising behaviour was observed on mercuration, with a yellow solid/oil formed on addition of water. After washing with water and a small amount of ethanol, the solid was dissolved in boiling chloroform and filtered through Celite® to remove residual mercury salts. On reduction to dryness, a pearlescent, buttercup-yellow and very viscous oil was isolated, which was shown by ^{1}H NMR spectroscopy to obtain residual occluded chloroform and a small amount of residual ligand, but nonetheless the product was determined to be 86% [Hg$^{(II)}$(κ^2-C^N^CH)Cl], which indicates an approximate ~90% yield by mass. The identification of monomercuration can be determined by ^{1}H NMR spectroscopy as detailed below in Section 2.11. This very high conversion is unprecedented in the literature, with the previously highest reported yield being 26% of an impure complex.[49, 64, 65] Further, the complex proved to be capable of isolation in a pure form *via* column chromatography,

however due to the high toxicity the slightly impure product was generally carried forward for subsequent reactions.
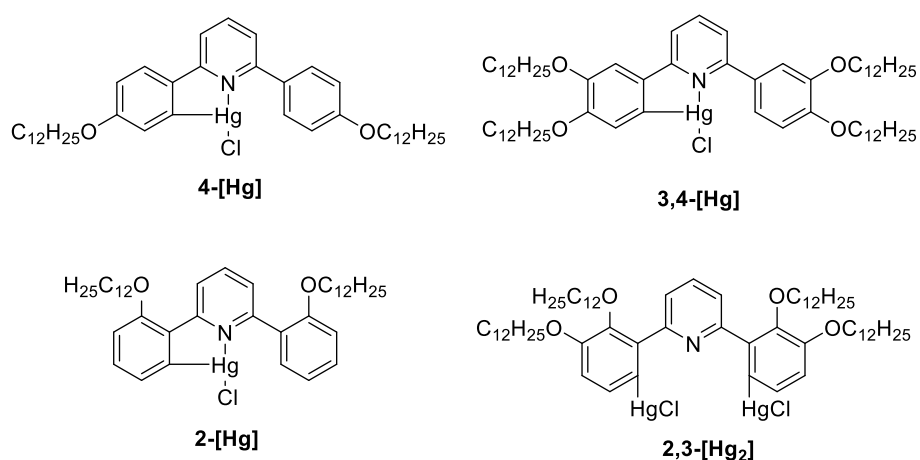
Figure 2.43: Structures of mercury(II) complexes.

Mercuration of **2,3-[L]** gave 75% of the related mercury complex, **2,3-[Hg$_2$]**, which was determined to be clean by ^{1}H NMR spectroscopy. However, consideration of the aromatic region of the ^{1}H NMR spectrum (Section 2.11.3) showed a highly symmetric pattern and one hydrogen less than anticipated in the integration. Analysis by APCI-MS (Figure 2.44) showed signals at m/z = 968.8454, 1204.7689 and 1438.7045, with those at 968.8454 and 1204.7689 corresponding to the free ligand and the monomercury complex, respectively. However, the signal at m/z = 1438.7045 matches the exact mass and predicted structure for the dimercurated complex (Figure 2.45), which is consistent with the ^{1}H NMR spectrum. Elemental analysis (CHN) confirm the production of a dimercurated complex. A higher mass signal at m/z = 2334.5929 consistent with a 2:2 dimer, is believed to be an artefact of the experiment, as no other experimental evidence for its existence was apparent.

2,6-*Bis*(2,3-dibutyloxyphenyl)pyridine was synthesised as a yellow oil and mercurated, using the standard conditions, to give a colourless solid, with ^{1}H NMR spectroscopy and elemental analysis confirming formation of the dimercuated complex, **2,3-[Hg$_2$]-4**. The product was subsequently used to grow single crystals suitable for XRD analysis from chloroform/ethanol after filtering through Celite (Section 2.10.1), unequivocally showing formation of the dimercurated product. Mercuration of 2,6-*bis*(2,3-dimethoxyphenyl)pyridine gave an unidentified product.
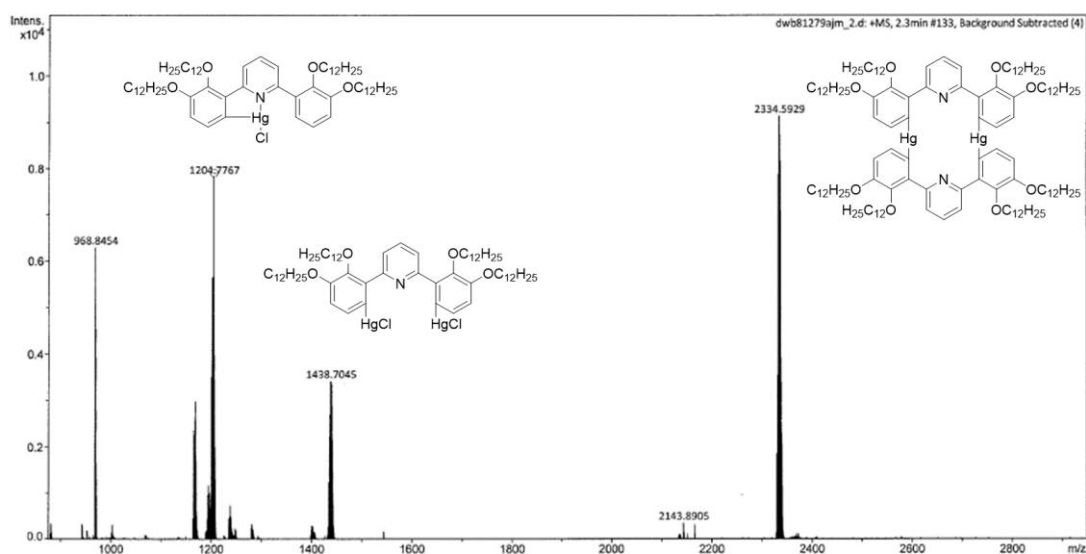
*Figure 2.44: APCI-MS spectrum of Compound **2,3-[Hg₂]**, showing the potential structures of the signals.*
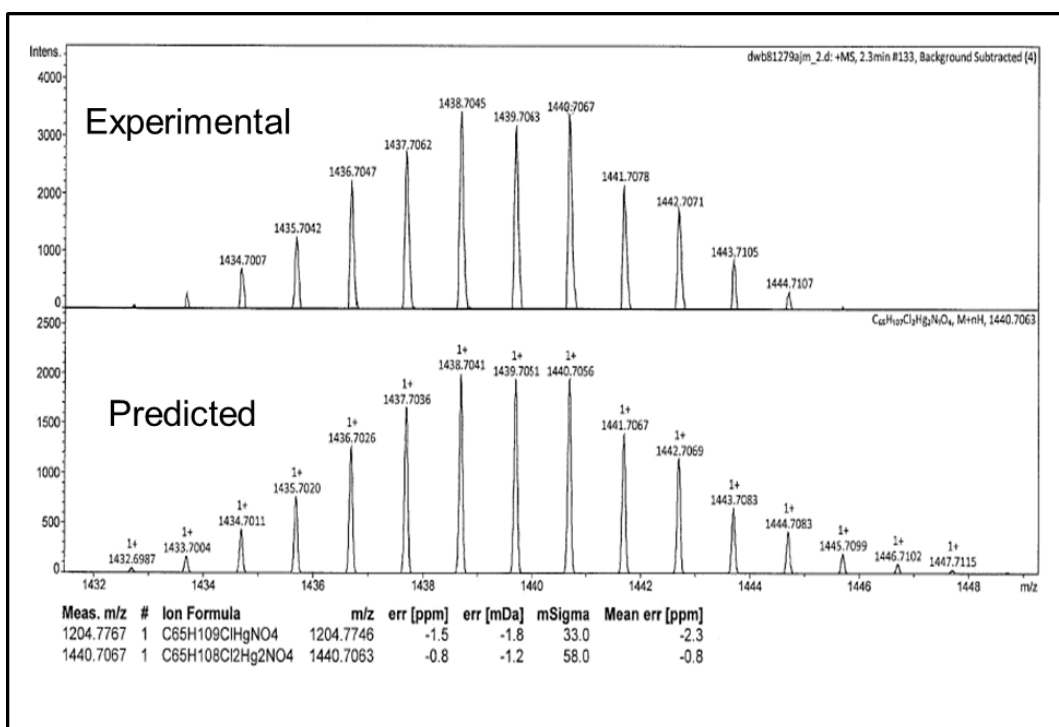
*Figure 2.45: Experimental (top) and predicted APCI-MS spectra for the signal at m/z = 1439.70 for Compound **2,3-[Hg₂]**.*

Further to this, a systematic investigation into the effect of the chain position on the pincer ligand has been carried out, with the 2,2′,4,4′-, 2,2′,5,5′- and 3,3′,5,5′-tetrasusbtituted complexes and the 3,3′- and 5,5′-disubstituted complexes synthesised (Figure 2.46). The data are summarised in Table 2.2.

94

3-[L] displayed a high yield on mercuration (57%), forming the two potential monomercury isomers, (**3-[Hg]** and **5-[Hg]**) in a 0.7:1 ratio, which were separable *via* column chromatography to give the pure monomercury complexes. **2,4-[L]** gave a ~1:1 ratio (the high level of overlapping peaks in the aromatic region of the ^{1}H NMR spectra made exact determination challenging) of the dimercurated, **2,4-[Hg$_2$]**, and monomercurated, **2,4-[Hg]**, complexes in 83% combined yield on use of two equivalents of mercury acetate. The complexes proved to be inseparable *via* column chromatography. On use of only one equivalent of mercury acetate, only the impure monomercurated product was formed in ~40% yield. **3,5-[L]** exhibited a lower yield on mercuration (15%), forming a ~1:2 ratio of the di- to monomercurated compounds. Separation to isolate pure complexes was not possible, with no separation of products observed on a TLC silica plate.
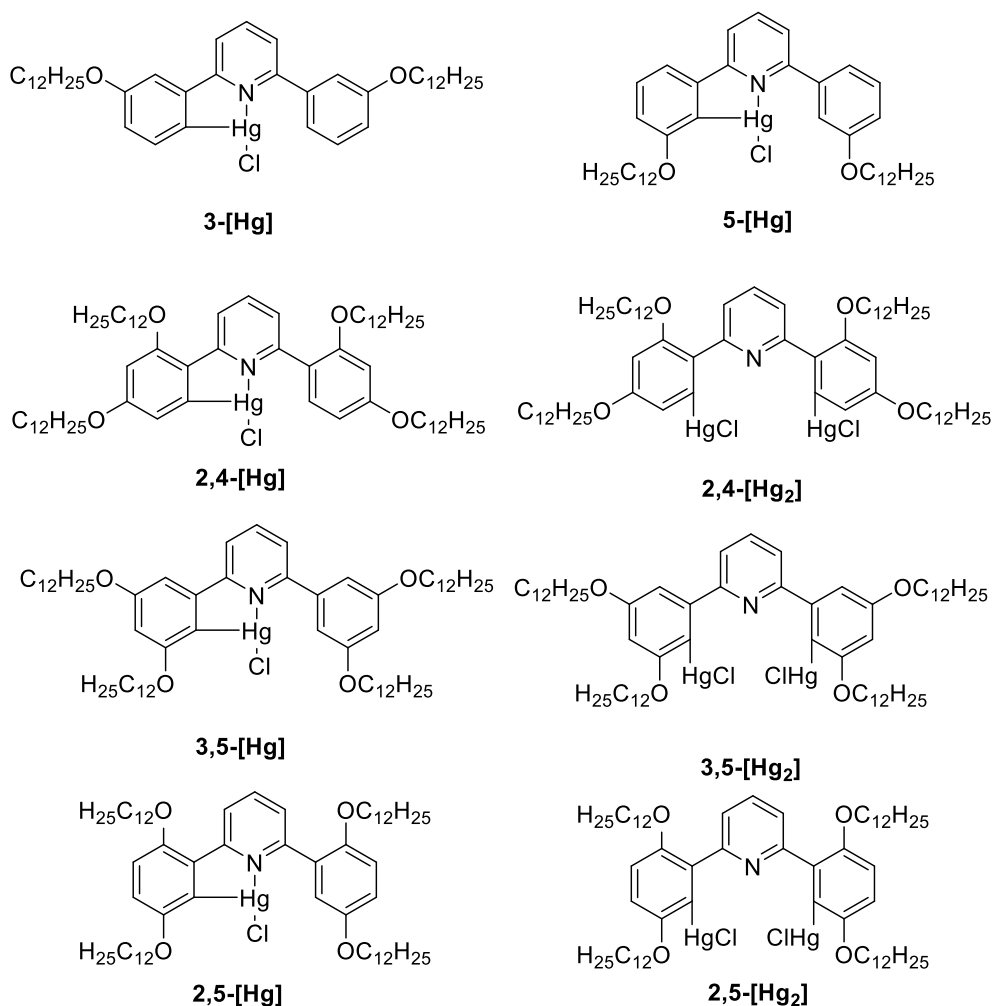
Figure 2.46: Structures of mercury(II) complexes.

2,5-[L] formed a 5:4 ratio of the monomercurated:dimercurated products (**2,5-[Hg]**: **2,5-[Hg₂]**) in good yield (>70%), however it appeared that a slightly lower temperature resulted in less favourable formation of the dimercurated complex, with the complexes instead formed in a 4:1 molar ratio, however this effect was not quantified and the overall yield was not affected.[66] Lower reagent concentrations also, not surprisingly, favoured formation of the monomercurated complex. Isolation of pure **2,5-[Hg]** and **2,5-[Hg₂]** proved challenging due to a small degree of persistent co-elution on a silica column, though conformation of the presence and identity of both complexes was achieved *via* ^{1}H NMR spectroscopy. However, mercuration of 2,6-*bis*(2,5-dibutyloxyphenyl)pyridine, **2,5-[L]-4**, led to a reaction product which, after separation by column chromatography gave firstly the pure dimercurated complex, **2,5-[Hg₂]-4** as a colourless solid and then the monomercurated complex, **2,5-[Hg]-4**, isolated as an oil, that solidified on standing.

Table 2.2: Products and yields on formation for isomers of two- and four-chain mercury(II) and gold(III) complexes.

Position of chains	Product on Mercuration	Yield on Mercuration (%)	Yield on Auration (%)
4-	Monomercury	17	48
3,4-	Monomercury	37	13[54]
2-	Monomercury	90	40
2,3-	Dimercury	75	24
2,4-	Monomercury:Dimercury ~1:1	57	5
2,5-	Monomercury:Dimercury 1.0:0.79	Mono: 33 Di: 26	17
3-/5-	Monomercury 5- and Monomercury 3-	Total: 83 5-:3- 1.0:0.72	3/5: 20
3,5-	Monomercury:Dimercury 1.0:0.5	15	0

2.10   X-Ray Single Crystal Structures of Mercury(II) Complexes

The mercury complexes substituted with dodecyloxy-chains were not suitable for growing single crystals, therefore the equivalent butoxy-complexes were synthesised and suitable crystals grown by diffusion of ethanol into a solution of the mercury complex in chloroform. XRD data tables and .cif files can be found in the data folder - see page 30. Carbon atoms are coloured grey, chlorine green, hydrogen turquoise, nitrogen blue, mercury deep pink and oxygen red.

2.10.1   2,3-[Hg₂]: [(κ²-C^N^C)(Hg^(II)Cl)₂]
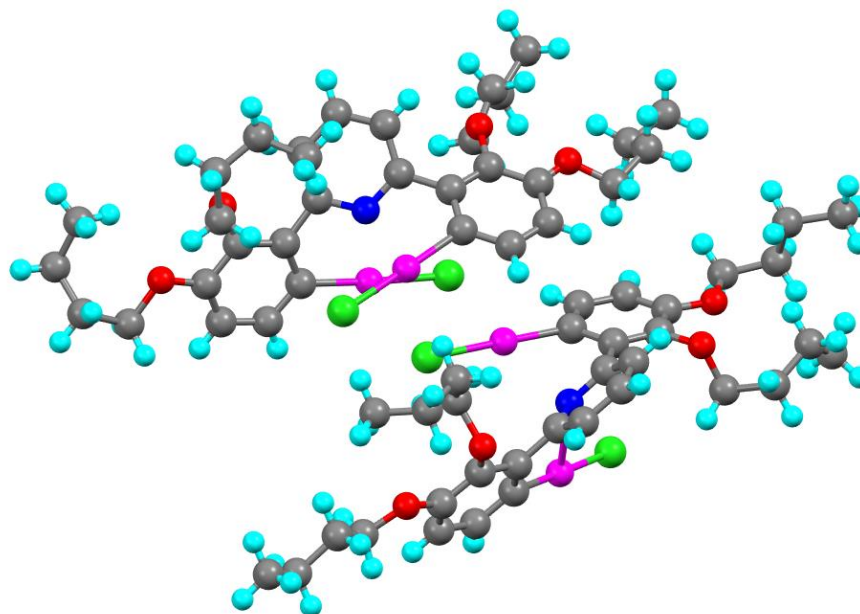
*Figure 2.47: Molecular structure of **2,3-[Hg₂]**.*

Complex **2,3-[Hg₂]** crystallised in the monoclinic space group *P*2/*c* (Figure 2.47) and significantly showed the presence of two mercury(II) ions in the complex, confirming formation of the dimercurated complex. Two complexes are present in the asymmetric unit. Each mercury is coordinated in a linear fashion to carbon and a chloride ligand, with the angles at mercury being close to perfectly linear (179.0(3)° and 179.2(4)°) . Hg–C bond lengths are found to be 2.016(12) Å, 2.027(14) Å, 2.065(17) Å and 2.062(12) Å, all of which are statistically the same and are of a magnitude very similar to those already reported. However, for the Hg–Cl distances there is a more complex story, which is not told in its entirety by the representation in Figure 2.48. Where the chloride is not bound to another atom there are short Hg–Cl distances of 2.312(4) Å and 2.309(5) Å and a second set of short distances, all at 2.336(4) Å by symmetry, where the chloride experiences a non-bonded contact to two other mercury centres. The other Hg⋯Cl distances are 3.032(3) Å, 3.091(3) Å, 3.065(3) Å and 3.112(3) Å, depending on the chloride in question. The geometric arrangement is as shown in Figure 2.48a, although the atoms are not coplanar. This extended coordination leads to four complexes being assembled through these extended Hg⋯Cl interactions, the core structure of which is indicated in Figure 2.48b.
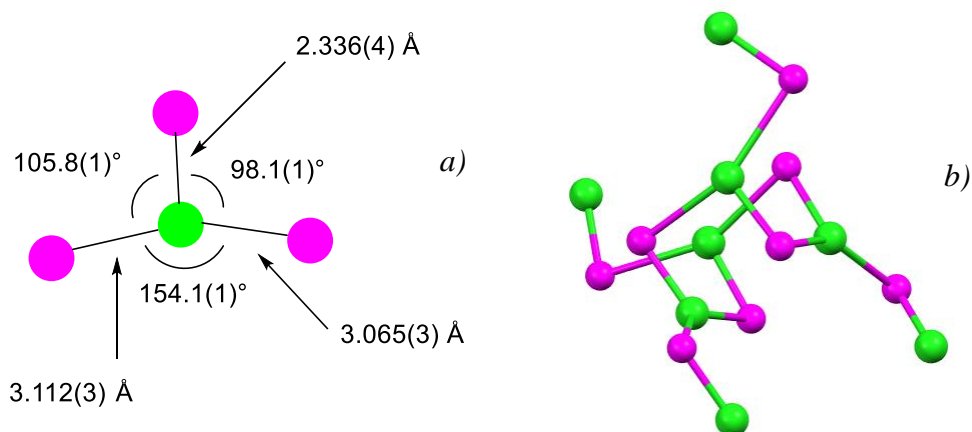
*Figure 2.48: (a) Geometric arrangement of mercury ions about a central chloride ion.(b) The core structure of the assembly of four **2,3-[Hg₂]** complexes.*

In addition, there is also a non-covalent interaction between each mercury and a pyridine nitrogen with distances of 2.75(1) Å, 2.748(9) Å, 2.767(9) Å and 2.676(9) Å, with the arrangement in each complex as exemplified in Figure 2.49. These interactions are 81-84% of the Van der Waals radius.
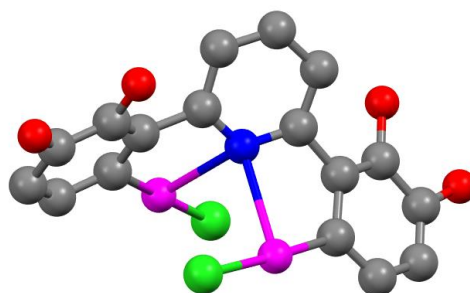
*Figure 2.49: Edited structure of the 'core' of **2,3-[Hg₂]** showing the mercury-nitrogen interactions.*

2.10.2   2,5-[Hg₂]: [(κ²-C^N^C)(Hg$^{(II)}$Cl)₂]
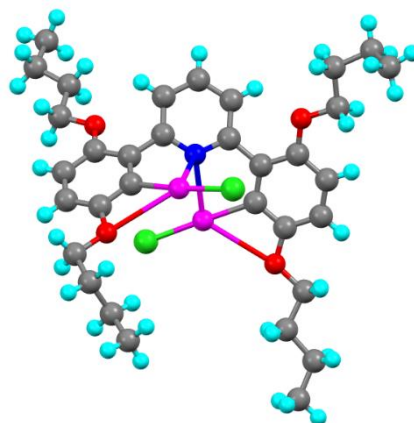
*Figure 2.50: Molecular structure of **2,5-[Hg₂]**.*

The complex **2,5-[Hg₂]** (Figure 2.50) crystallised in the triclinic space group *P*-1, with three molecules in the asymmetric unit, with one exhibiting disorder in three of the butoxy chains. The six Hg–C bond lengths are identical (2.04(1) ± 0.02 Å as are those of Hg–Cl (2.305(3) ±0.03 Å). This time there are no further short contacts from Cl to Hg. For one of the complexes in the asymmetric unit (Figure 2.50), each mercury also has short contact to both the pyridine nitrogen (2.664(8) Å and 2.763(8) Å) and to an alkoxy oxygen of the chains in the 5,5′-positions (3.037(8) Å and 3.005(6) Å). The remaining two complexes in the asymmetric unit are arranged slightly differently so that in one complex the arrangement is just as described above (Hg⋯N = 2.729(9) Å and 2.701(9) Å; Hg⋯O = 3.00(1) Å and 2.956(8) Å). However, for the other complex, while one mercury forms intramolecular coordination in likewise manor (Hg⋯N = 2.827(8) Å; Hg⋯O 2.966(5) Å), the other mercury ion forms a Hg⋯N interaction with the pyridyl nitrogen (2.767(7) Å), and a intermolecular Hg⋯O interaction (3.034(9) Å), with the oxygen being from the 5-butoxy chain of the neighbouring complex. This oxygen is also bound to a mercury ion in an intermolecular fashion (Figure 2.51).
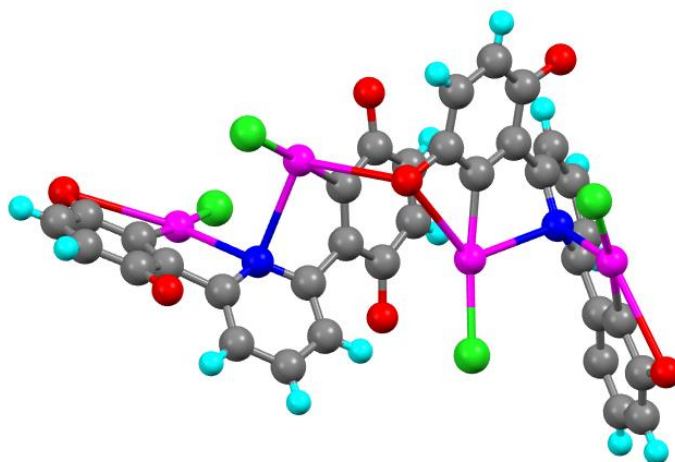
Figure 2.51: Arrangement of the two complexes linked through an intermolecular Hg⋯O interaction. Butoxy chains removed for clarity.

2.10.3 2,5-[Hg]: [Hg(κ^2-C^N^CH)Cl]
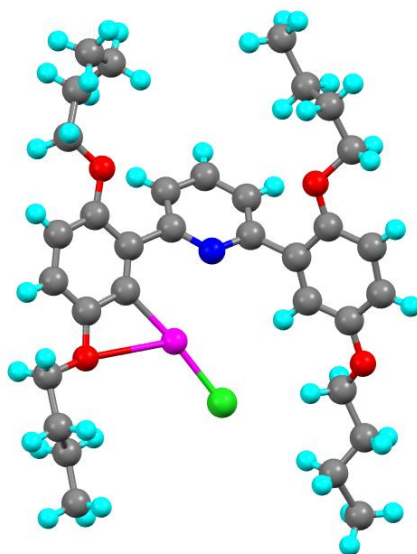
*Figure 2.52: Molecular structure of **2,5-[Hg]**.*

The complex **2,5-[Hg]** (Figure 2.52) also crystallised in the triclinic space group *P*-1. However, it exhibited severe twinning, resulting in poor resolution and an *R*-factor >12%; as such the description is not too detailed. There were three molecules in the asymmetric unit, with one exhibiting disorder about the central unit, within which the pyridine ring, mercury and chloride ions were modelled in two positions, with a refined occupancy of 0.568:0.432(3). In this disordered complex, there is a Hg⋯O distance of 2.86(2) Å and a much longer Hg⋯N distance of 3.25(2) Å. Hg⋯O distances are similar in the other two, non-disordered complexes (2.84(2) Å and 2.91(2) Å), whereas the Hg⋯N are shorter and more comparable, if slightly longer, when compared with those described above (2.85(2) Å and 2.88(2) Å). All bonds are in the standard range for organomercury complexes.[16-21]

2.11 ^{1}H NMR Spectroscopy of Mercury(II) Complexes

The ^{1}H NMR spectra of the mercury(II) complexes were recorded and discussed below. Assigned ^{13}C{^{1}H} NMR spectra can be found in the data folder - see page 30.

2.11.1   2-[Hg]: [Hg$^{(II)}$(κ^2-C^N^CH)Cl]
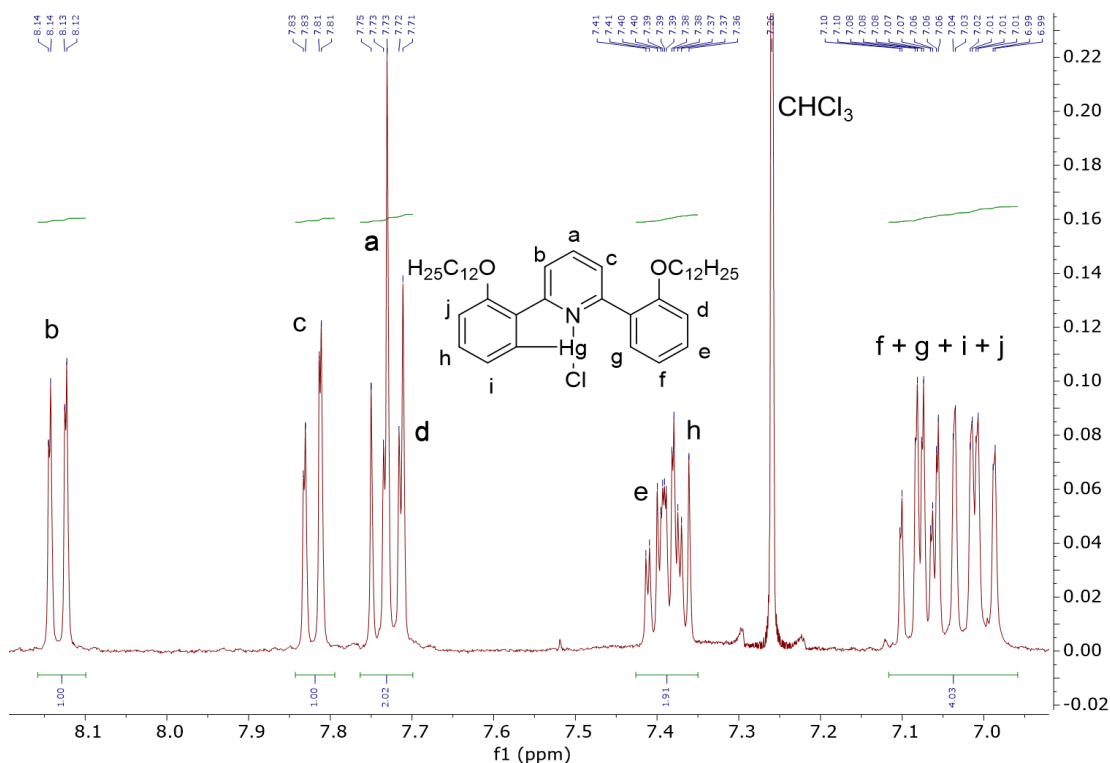
*Figure 2.53: ^{1}H NMR (400 MHz, CDCl$_3$) of Compound **2-[Hg]**, showing the aromatic region.*

Complex **2-[Hg]** can be identified as a monomercurated complex due to the unsymmetrical nature of the ^{1}H NMR spectrum (Figure 2.53) giving rise to a large number of environments in the aromatic region and two overlapping triplets at 4.06 and 4.03 ppm, each integrating to 2H, which can be assigned to the non-equivalent –OCH_2- environments. In the aromatic region a key set of signals are the doublet of doublets at 8.13 and 7.82 ppm, which consist of a ^3J-coupling of ~8.0 Hz and a mutual ^4J-coupling of ~1 Hz (which, depending on spectrometer and sample resolution, is not always observed in these systems), which are shown by COSY-NMR spectroscopy (Figure 2.54) to couple to the apparent triplet at 7.73 ppm (H$_a$). The apparent triplet is highly symmetric, indicating that the coupling constants to the signals at 8.13 and 7.82 ppm are almost identical. This system can be assigned to the three inequivalent pyridyl protons. It is thought that the signal at 8.13 ppm is assigned to H$_b$ due to the proximity of the alkoxy

oxygen. Assignment of the phenyl hydrogen environments is challenging due to extensive signal overlap and ^4J-coupling.
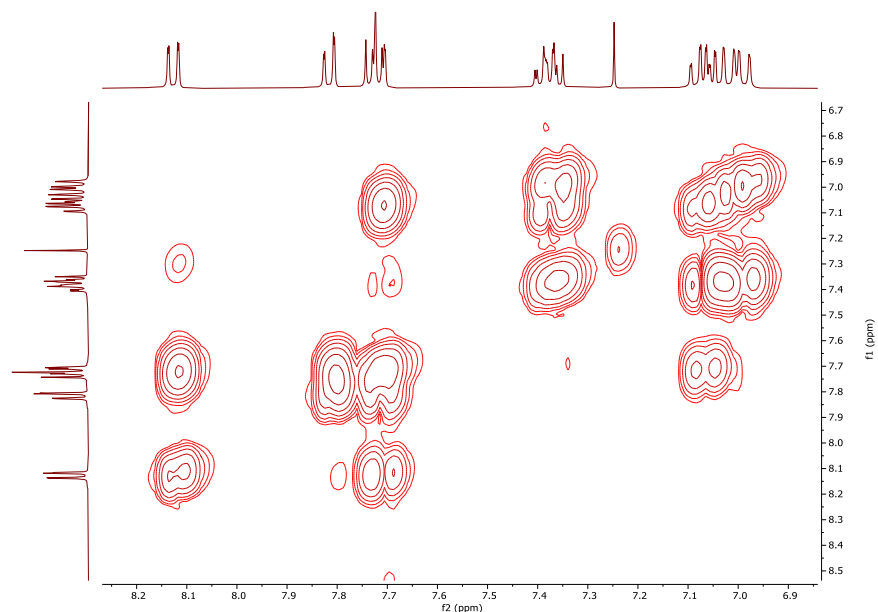
*Figure 2.54: COSY-NMR spectrum of **2-[Hg]** (400 MHz, CDCl₃) showing the aromatic region.*

2.11.2 4-[Hg]: [Hg(II)(κ^2-C^N^CH)Cl]
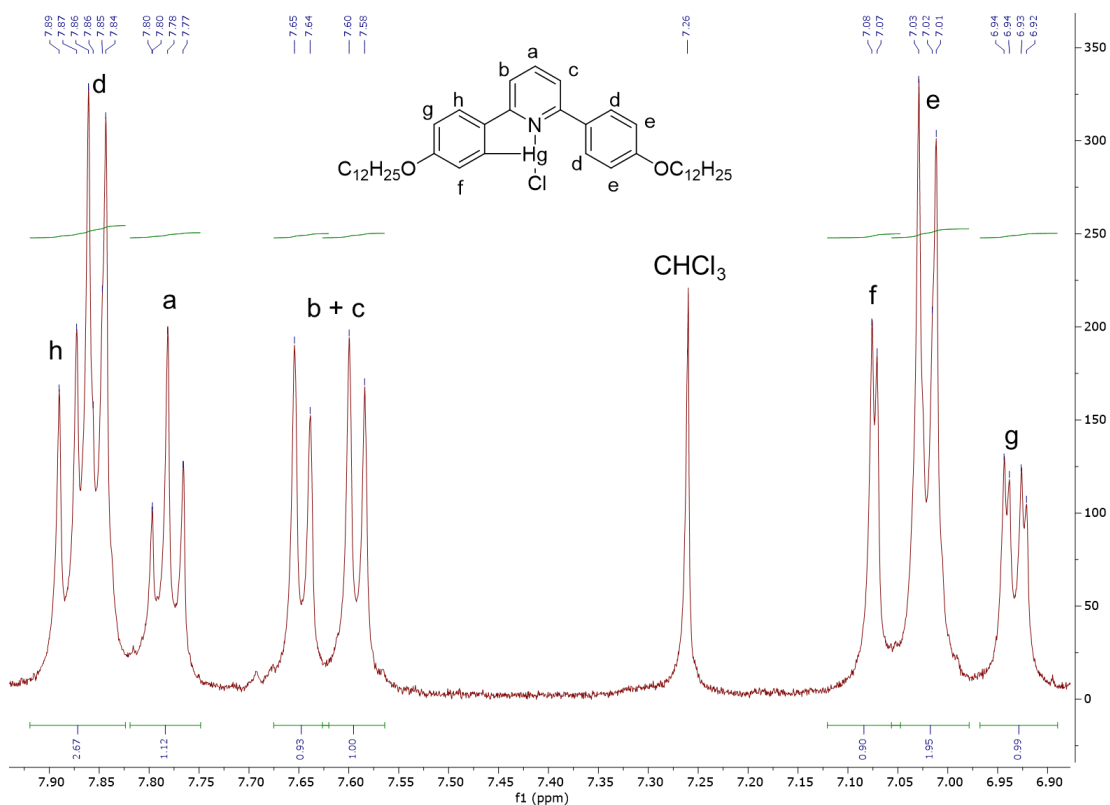
*Figure 2.55: ^{1}H NMR (400 MHz, CDCl₃) of impure Compound **4-[Hg]**, showing the aromatic region.*

4-[Hg] could not be fully purified from the residual free ligand, however by comparison of the crude ^{1}H NMR spectra with the free ligand ^{1}H NMR spectra and knowledge of the typical features of typical ^{1}H NMR spectra of purified monomercury complexes some details can be determined (Figure 2.55). The same inequivalence of the pyridyl protons is observed as in **2-[Hg]**, however H$_b$ and H$_c$ are found at a lower chemical shift (7.60 and 7.65 ppm) than H$_a$ (7.79 ppm) and with this sample $^4J_{HH}$-coupling is not observed. The higher symmetry due to the *para*-substitution of the unmetallated phenyl ring gives rise to AA′XX′ resonances at 7.02 and 7.85 ppm, with J = 8.8 Hz. A key signal is the doublet at 7.08 ppm, which due to the small ^4J-coupling is identified as being adjacent to the mercury(II) ion. It couples to the doublet of doublets at 6.93 ppm, alongside the remaining hydrogen atom on the ring, the doublet at 7.89 ppm.

2.11.3   2,3-[Hg$_2$]: [(κ^2-C^N^C)(Hg$^{(II)}$Cl)$_2$]
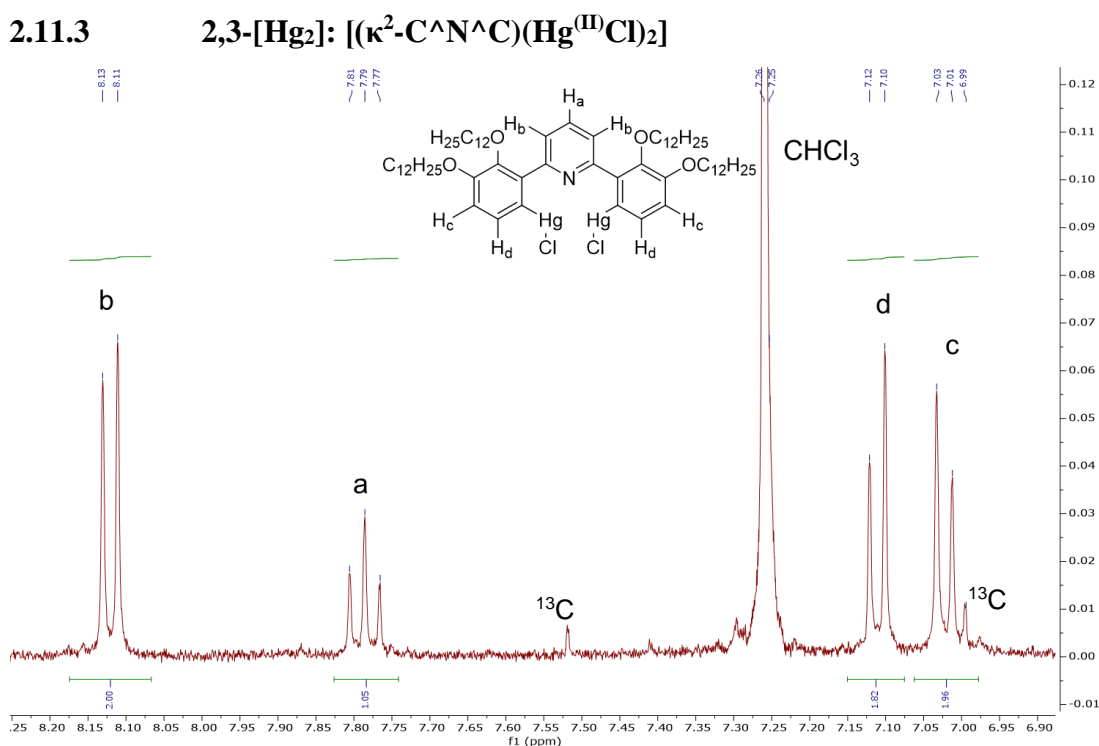
*Figure 2.56: ^{1}H NMR spectrum (400 MHz, CDCl$_3$) of compound **2,3-[Hg$_2$]**, showing the aromatic region and indicating the ^{13}C satellites of the solvent resonance.*

The ^{1}H NMR spectrum of **2,3-[Hg$_2$]** (Figure 2.56) is highly symmetric and shows four signals in the aromatic region. The doublet at 8.12 ppm (integration 2H), is shifted upfield compared to the free ligand and, with the triplet at 7.79 ppm, correspond to the pyridyl hydrogens. Two roofed doublets at 7.11 and 7.02 ppm, (integration 2H) were shown by

COSY-NMR spectroscopy to be coupled and are therefore assigned as the AB system of phenyl protons. Interestingly, broadening is observed for the alkoxy signal at 3.80 ppm, which corresponds to the O-CH_2 hydrogen of the chain in the 2,2′-positions, indicating possible fluxionality. The other alkoxy signal, at 4.05 ppm, was the expected resolved triplet (Figure 2.57). Increasing concentration caused broadening and coalescence of the signals at 7.11, 7.02 and 4.05 ppm, suggesting potential concentration-dependent aggregation.

The resonances at 4.05 and 3.80 ppm were identified using NOE experiments so that coupling was observed between H_c and the resonance at 4.05 ppm. Irradiating the signal at 3.30 ppm showed coupling to the other chain hydrogens and also to H_a, but not H_b. Sterically it would be expected that the metallated phenyl rings would be largely orthogonal to the pyridine, which would place the chains in the 2-position over the pyridyl ring. This would account for the slightly shielded chemical shift, while the unresolved nature may well arise as the O-CH_2 hydrogens will experience different local shielding fields as the phenyl ring vibrates.
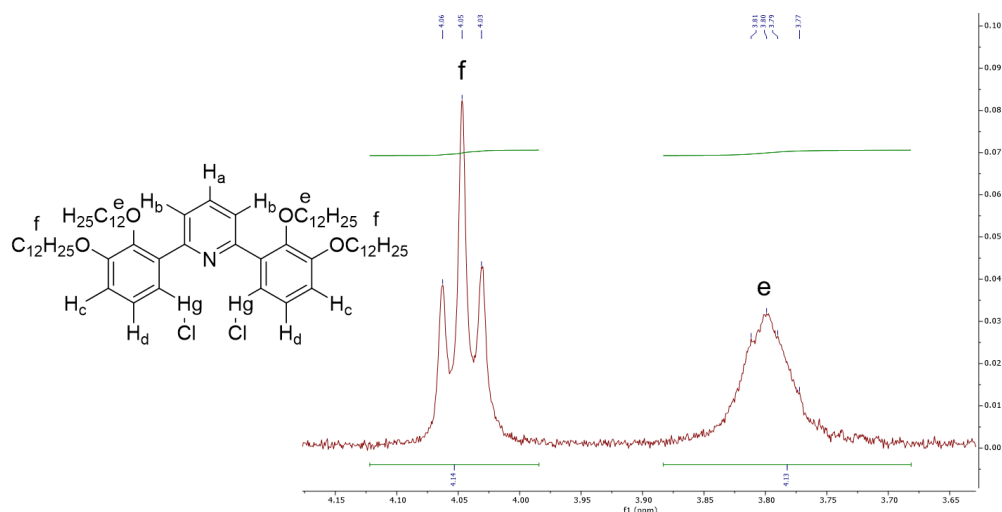
*Figure 2.57: Assignment of ^1H NMR alkoxy signals for complex **2,3-[Hg₂]** from NOE measurements.*

2.11.4   2,5-[Hg] and 2,5-[Hg₂]: [Hg$^{(II)}$(κ²-C^N^CH)Cl] and [(κ²-C^N^C)(Hg$^{(II)}$Cl)₂]

The crude ^{1}H NMR spectrum of **2,5-[Hg]** was determined to contain a mixture of two products in a 1:0.8 molar ratio. Use of COSY-NMR spectroscopy and the higher level of symmetry present in one enabled identification of formation of both monomercurated (**2,5-[Hg]**) and dimercurated (**2,5-[Hg₂]**) complexes, with the major product being the monomercurated complex, **2,5-[Hg]**.
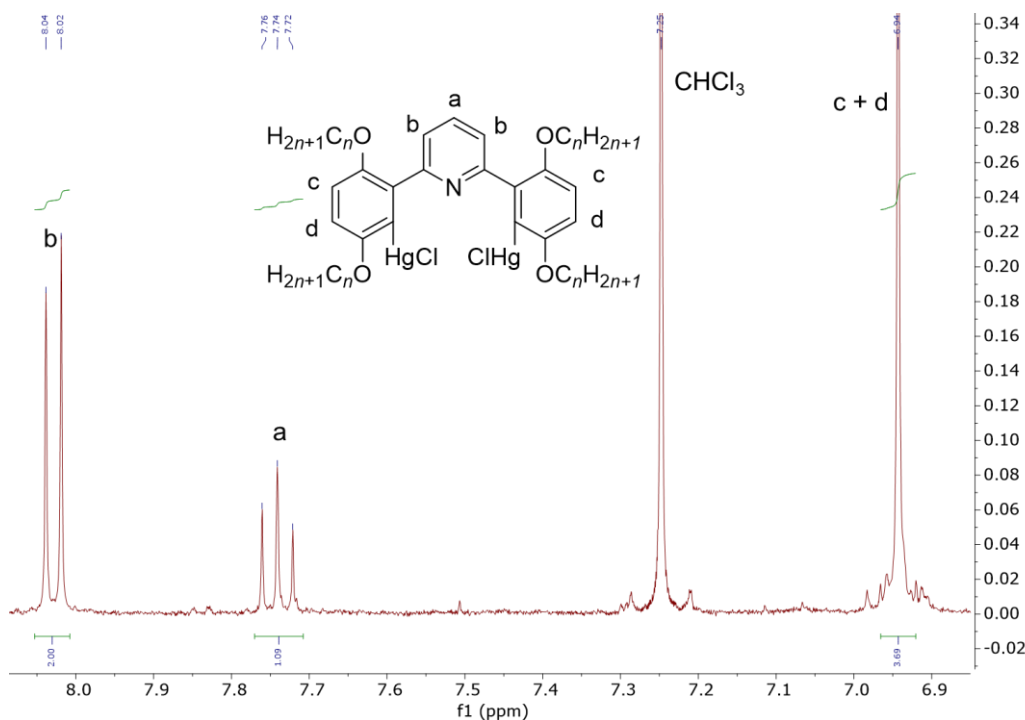
*Figure 2.58: ^{1}H NMR (400 MHz, CDCl₃) of dimercurated Compound **2,5-[Hg₂]**, showing the aromatic region.*

The dimercurated complex, **2,5-[Hg₂]**, (Figure 2.58) is highly symmetrical, with only three signals in the aromatic region: a doublet (2H) at 8.03 ppm, assigned to H$_b$, coupled to a triplet (1H) at 7.74 ppm, assigned to H$_a$, and an apparent singlet of integration 4H at 6.94 ppm, which can be assigned to the phenyl protons. The apparent equivalence of the phenyl protons indicates a high degree of second order behaviour due to the very similar chemical shifts and close inspection indicates multiple small signals close to the baseline. Two triplets of integration 4H are present at 3.93 and 3.95 ppm in the alkoxy region, confirming the symmetric nature of the complex.

The monomercurated complex, **2,5-[Hg]**, (Figure 2.59) has a higher number of aromatic hydrogen environments due to the loss of symmetry. The inequivalent pyridyl hydrogens

are assigned to two doublet of doublets at 8.11 and 7.84 ppm (^3J-coupling of ~7.5 Hz and a mutual ^4J-coupling of ~1 Hz) coupled to an apparent triplet at 7.72 ppm. Multiple overlapping triplets are present in the alkoxy region, broadly centring about both 3.94 and 3.97 ppm, with equal integration.
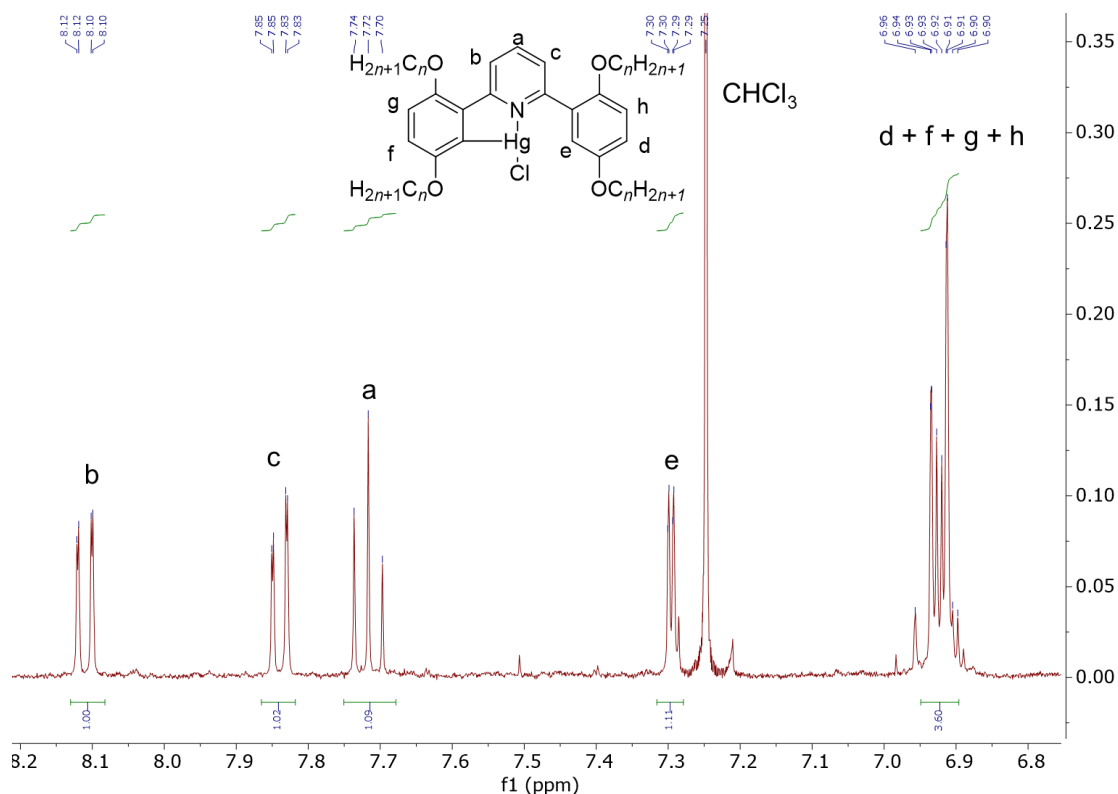
*Figure 2.59: ^1H NMR (400 MHz, CDCl₃) of monomercurated Compound **2,5-[Hg]**, showing the aromatic region.*

2.11.5   2,4-[Hg]: [Hg(κ²-C^N^CH)Cl]

It is possible to assign the ^1H NMR spectrum for the complex, **2,4-[Hg]**, (Figure 2.60), which shows a small amount of the free ligand, indicating that the reaction does not proceed purely. The pyridyl hydrogens can be assigned as the signals at ~7.7 and ~7.6 ppm. The hydrogen atoms on the phenyl ring, which is not attached to the mercury ion, can be assigned *via* coupling patterns due to its nature as an AMX spin system. The two remaining hydrogen signals show overlap with the other signals.

When both **2,4-[Hg]** and **2,4-[Hg₂]** are present the aromatic region of the ^1H NMR spectrum becomes highly complex, preventing assignment of the di-substituted NMR spectrum. On increased concentration to allow the study of nuclei with reduced NMR

sensitivity, significant signal broadening of all signals was observed, indicating a dynamic system at high concentration.
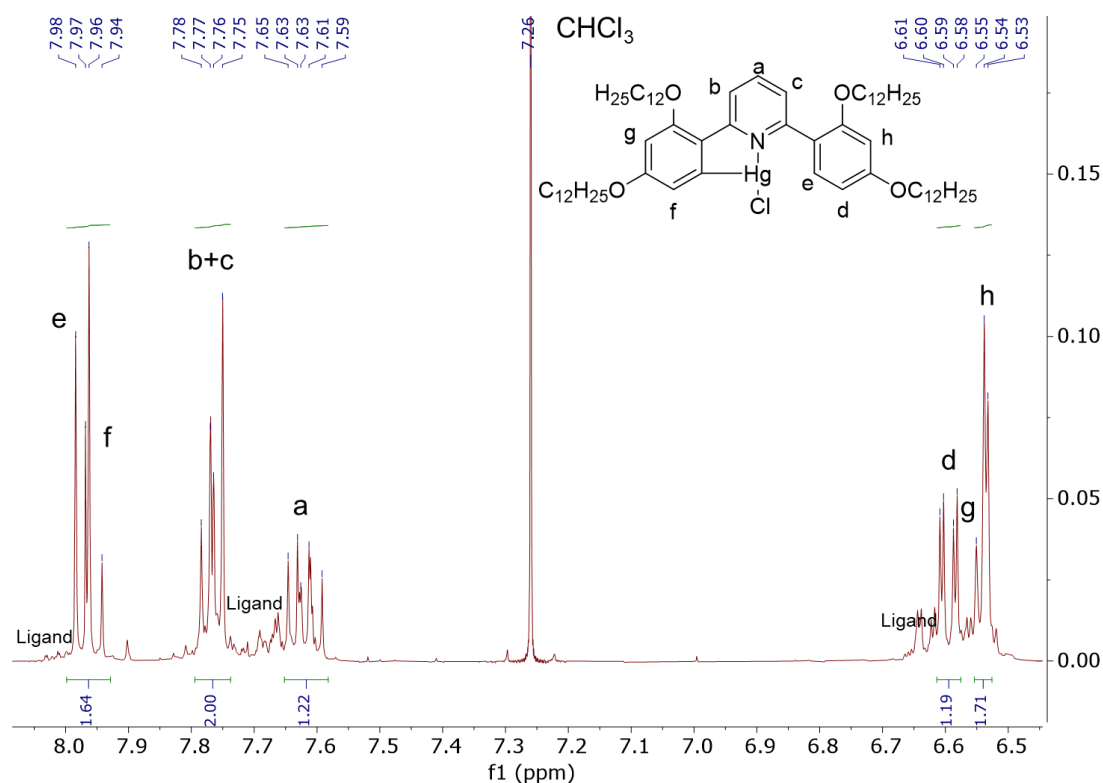
*Figure 6.60: ^1H NMR spectrum (400 MHz, CDCl₃) of **2,4-[Hg]** showing the aromatic region. The sample was not pure, with a small amount of the free ligand remaining.*

2.11.6   3-[Hg] and 5-[Hg]: [Hg^(II)(κ²-C^N^CH)Cl] Isomers

Mercuration of **3-[L]** leads to the interesting possibility that the mercury ion inserts either at the 5-position of the phenyl ring, **5-[Hg]**, (Figure 2.61) and or at the 3-position, **3-[Hg]** (Figure 2.62). ^1H NMR spectroscopy of the recovered product indicated that these were formed in a 4:3 molar ratio, with the 5-position isomer, **5-[Hg]** being the major product. As unsymmetrical monomercurated complexes with extensive ^4J-coupling, the aromatic region of the pure complexes is complex, however following separation analysis of the splitting patterns enables isomer identification.

The pyridyl hydrogens, H_b and H_c, are found at a lower chemical shift (7.7 – 7.8 ppm) than the pyridyl hydrogen, H_a (~7.87 ppm), with the spacing between the two doublets of doublets slightly larger for **5-[Hg]** than **3-[Hg]** (0.07 ppm *vs* 0.03 ppm). Both isomers

107

show both $^3J_{HH}$ and $^4J_{HH}$ couplings, the latter reflecting the unsymmetrical nature of the complexes.
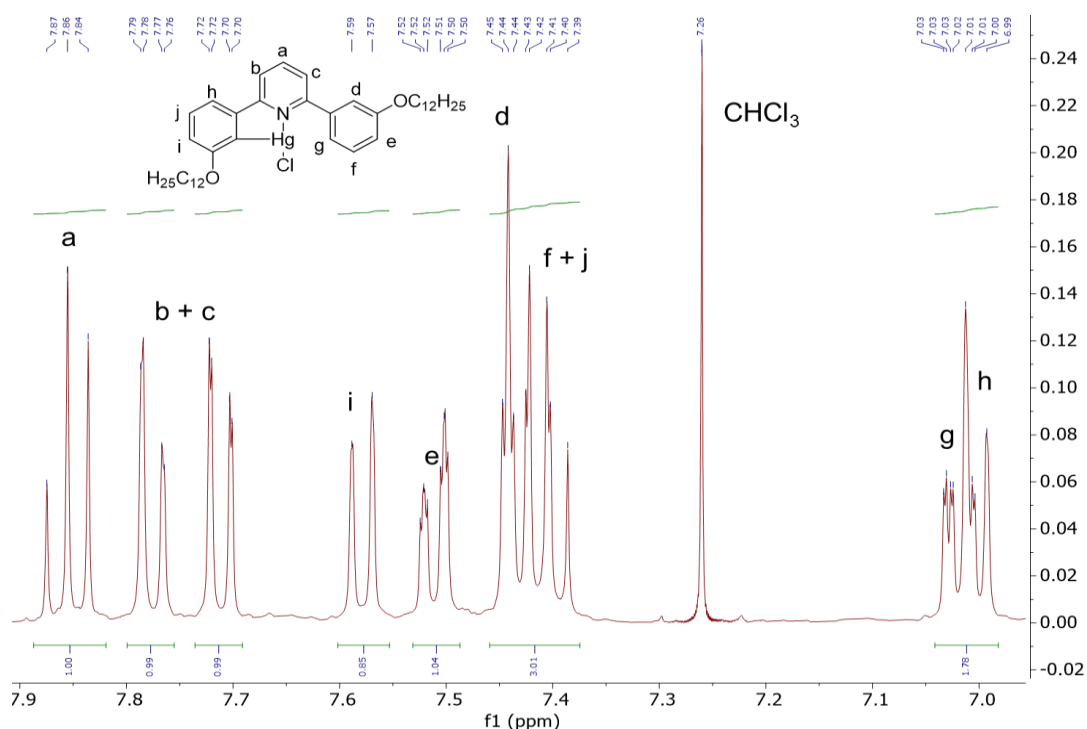
*Figure 2.61: ^{1}H NMR (400 MHz, CDCl$_3$) of the 5-position isomer of Compound **5-[Hg]**, showing the aromatic region.*

For identification of **5-[Hg]** (Figure 2.61), the key signal is the doublet of doublets at 7.44 ppm. The presence of two ^4J-couplings of 2.6 Hz indicates that it is a hydrogen in the 2-position of one of the phenyl rings and, as the only one present, indicates that this is the **5-[Hg]**; two signals of this nature are expected for **3-[Hg]**. COSY-NMR spectroscopy indicates the presence of two separate phenyl spin-systems. The signals at 7.58, 7.41 and 7.00 ppm couple (H_i, H_j, H_h), while the signals at 7.51, 7.44, 7.41 and 7.07 ppm couple in the second (H_e, H_d, H_f, H_g). The latter spin system also displays significantly more ^4J-coupling, indicating the presence of an additional hydrogen atom on the ring, signifying that this is the phenyl ring which does not have the mercury ion bound. By analysis of chemical shifts and coupling patterns the remaining phenyl protons are assigned. Two triplets, each of integration 2H, are present at 4.08 and 4.03 ppm and relate to each individual alkoxy chain.
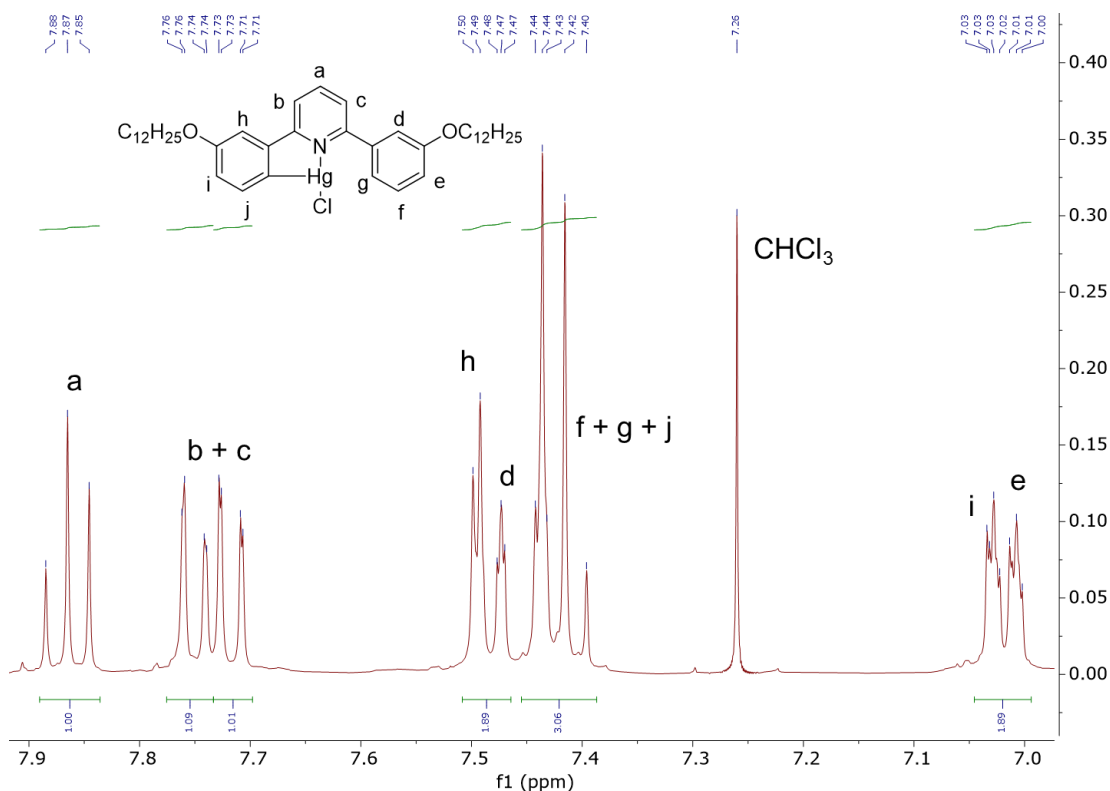
*Figure 2.62: ^1H NMR (400 MHz, CDCl$_3$) of the 3-position isomer Compound **3-[Hg]**, showing the aromatic region.*

3-[Hg] (Figure 2.62) has two hydrogens in the 2-position of the phenyl ring. One (H$_h$) has one ^4J-coupling to H$_i$, while the other has two ^4J-couplings to both H$_e$ and H$_g$. This enables assignment of the doublet at 7.49 ppm to H$_h$ and the doublet of doublets at 7.47 ppm to H$_d$. Overlap of the phenyl signals prevents exact assignment, but it is likely that H$_f$, H$_g$ and H$_j$ are found at ~7.42 ppm (several overlapping signals, integration 3H) and those of H$_i$ and H$_e$ at 7.02 ppm (several overlapping signals, integration 2H). Two triplets, each of integration 2H, are present at 4.05 and 4.07 ppm and relate to each individual alkoxy chain.

2.11.7   3,5-[Hg] and 3,5-[Hg$_2$]: [Hg$^{(II)}$(κ^2-C^N^CH)Cl] and [(κ^2-C^N^C)(Hg$^{(II)}$Cl)$_2$]

Full assignment of the ^1H NMR spectrum for **3,5-[Hg]** was not possible as the mono- and dimercury complexes were inseparable, resulting in many overlapping environments, however some information can be determined (Figure 2.63). Integration indicates they are present in a 2:1 ratio (**3,5-[Hg]**:**3,5-[Hg$_2$]**). COSY-NMR spectroscopy determined that the signals at 7.86 and 7.72 ppm coupled and 7.81 & 7.84 ppm coupled to 7.69 ppm

resulting in assignment as the dimercury and the monomercury pyridyl systems respectively. The overlapping signals around ~ 6.95 and ~7.00 ppm are assigned to both complexes, with coupling observed between the two general environments. Several overlapping triplets are observed at 4.1 – 4.0 ppm, assigned to the alkoxy groups from both complexes.
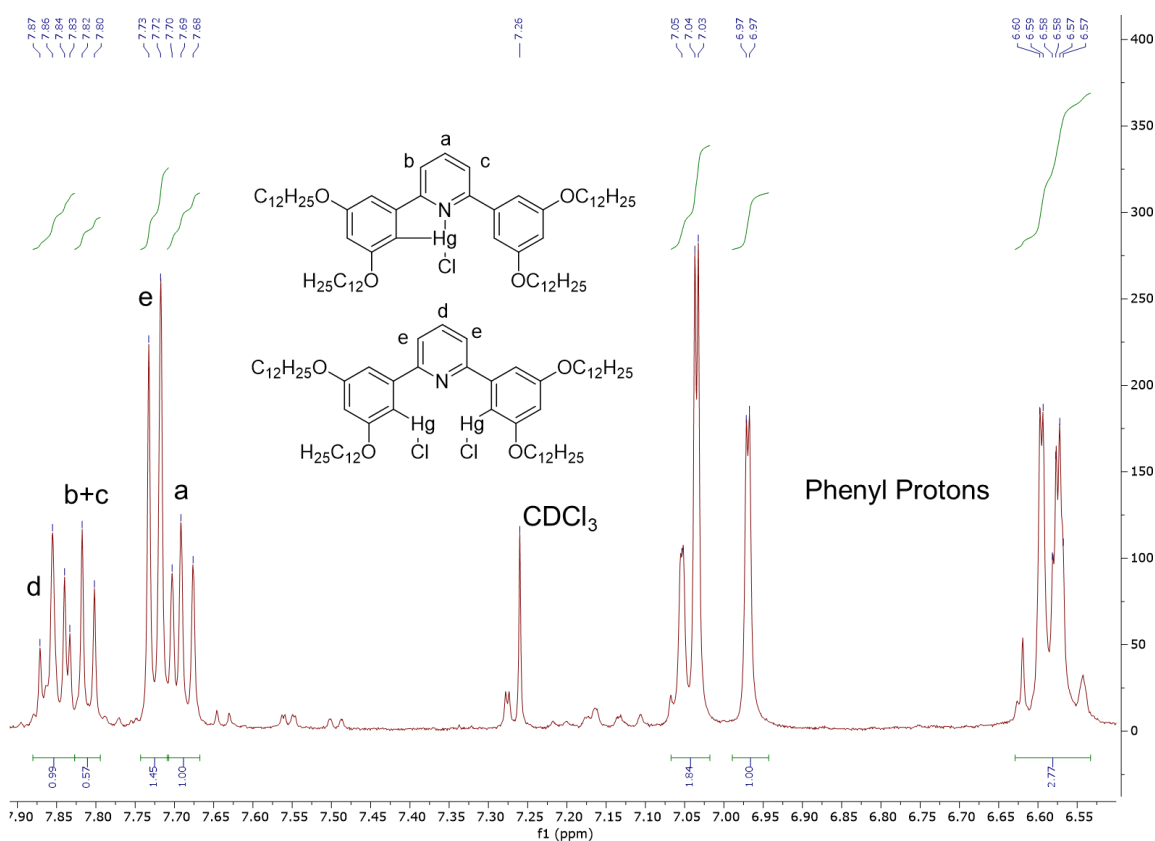
*Figure 2.63: ^1H NMR (500 MHz, CDCl₃) of the overlapping mono- and dimercury complexes (**3,5-[Hg]**), showing the aromatic region.*

2.12 ^{199}Hg NMR Spectroscopy

The ^{199}Hg and ^{199}Hg{^{1}H} NMR spectra (89.6 MHz, I = ½, 16.9% abundance) were recorded for the mercury(II) complexes in order to investigate the effect of both the different substitution patterns and mono- or di-mercuration on the ^{199}Hg chemical shift and *J*-coupling constants. All spectra were recorded at 295 K in CDCl₃ and externally referenced to Hg(OAc)₂ in D₂O (-2351.48 ppm).[67] A *zg* pulse program was used to give proton-coupled spectra and *zgpg30* pulse program to give proton-decoupled spectra. $^3J_{HHg}$-values found in the range 50 – 230 Hz are observed to be in a typical range for this type of coupling, and are given where relevant.[19, 68] Interestingly, they were not observed in the ^{1}H NMR spectrum. Likewise, no $^2J_{CHg}$ -couplings or $^1J_{CHg}$ -couplings were

observed and here it was hypothesised that this was due to fast relaxation of nuclei due to the chemical shift anisotropy mechanism (CSA), which can be significant for nuclei with large chemical shift ranges.[69, 70] Spectroscopic measurements at a lower field (300 MHz), which can sometimes be successful at resolving couplings for complexes undergoing CAS, also failed to reveal any Hg-C couplings. The model complexes Ph-Hg-Cl (δ^{Hg} = 420.4 ppm, $CDCl_3$, 278 K, referenced to aqueous $HgCl_2$, 53.673 MHz)[71] and a Hg(C^N)Cl metallacycle (-1069 ppm, $CDCl_3$)[72] were used in order to determine the spectral area of interest, due to the wide range of the [199]Hg nucleus. The NMR data are presented are Table 2.3.

Table 2.3: [199]Hg NMR Data for Mercury(II) Complexes.

Complex	[199]Hg chemical shift (multiplicity) / ppm	$^3J_{HHg}$ / Hz
4-[Hg]	-1023 (d)	234.8
2-[Hg]	-1020 (dd)	203.0, 69.9 ($^4J_{HHg}$)
3-[Hg]	-991 (d)	190.8
5-[Hg]	-993 (s)	-
2,3-[Hg₂]	-1012 (d)	154.1
2,5-[Hg₂]	-1010 (s)	-
2,5-[Hg]	-1009 (s)	-
2,4-[Hg₂]	-1042 (s)	-
2,4-[Hg]	-1011 (s)	-
3,5-[Hg₂]	-972 (s)	-
3,5-[Hg]	-954 (s)	-
3,4-[Hg]	-999 (s)	-

Typically for heavy elements, the spectra are well dispersed over a wide chemical shift range and even in this small range of related complexes, the chemical shift varies over nearly 100 ppm. Complexes with hydrogen atoms present in the 5-positions of the phenyl unit of the C^N^C ligand displayed doublet signals, due to a $^3J_{HHg}$-coupling, when proton coupling was present. 2-[Hg] also displayed a $^3J_{HHg}$-coupling of 56.5 Hz to give a doublet of doublets (Figure 2.64a). On application of proton-decoupling the multiplicity collapsed to a singlet (Figure 2.64b). Complexes with a substituent in the 5-position did not display any $^3J_{HHg}$-coupling, as would be expected. Significant signal broadening in the ^{1}H NMR spectrum was observed for 2,4-[Hg] at high concentrations, potentially explaining the lack of expected $^3J_{HHg}$-coupling in the [199]Hg NMR spectrum. The low solubility and hence, low signal-to-noise resolution of the 3,4-[Hg] complex is believed to explain the

lack of observed $^3J_{HHg}$-coupling. The variation of the ^{199}Hg NMR results on alternation of the substitution pattern are discussed in greater depth in Section 2.18.
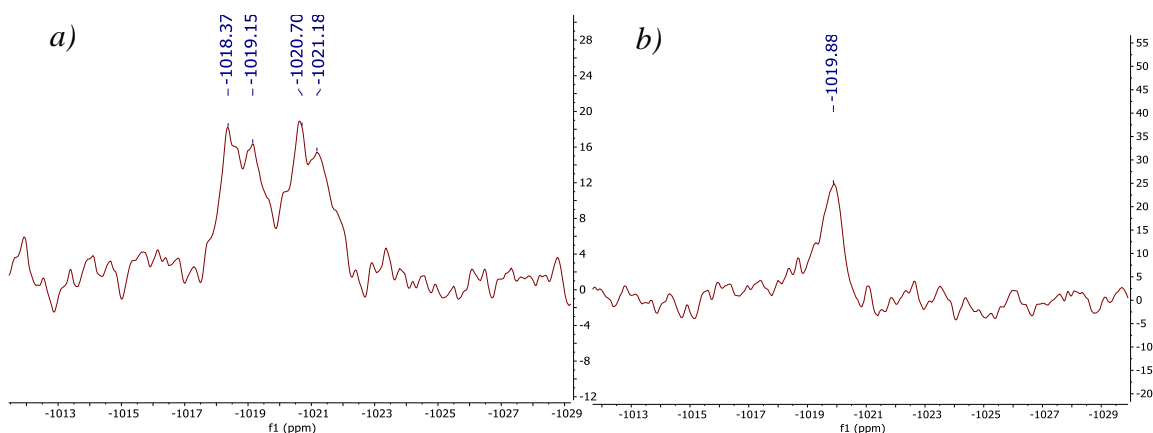
*Figure 2.64: ^{199}Hg NMR spectrum (89.6 MHz, CDCl₃) of **2-[Hg]** with proton-coupling (a) and proton-decoupling (b).*

Both the **2,4-[Hg]** and **3,5-[Hg]** complexes were inseparable, with two singlets for each observed. Two singlets were observed for **2,4-[Hg]** at -1011 and -1042 ppm, indicating the presence of two mercury species in the sample, assumed to be the di- and mono-substituted forms. The species at -1042 ppm is, on the balance of evidence, assigned as **2,4-[Hg₂]**, with this species less likely to react on auration and therefore appreciable amounts remain present on study of a sample post-auration. The chemical shifts for **3,5-[Hg]** and **3,5-[Hg₂]** (Figure 2.65), are arbitrarily assigned, based on chemical knowledge. Calculated X-ray bond lengths (Section 2.18) support this assignment.
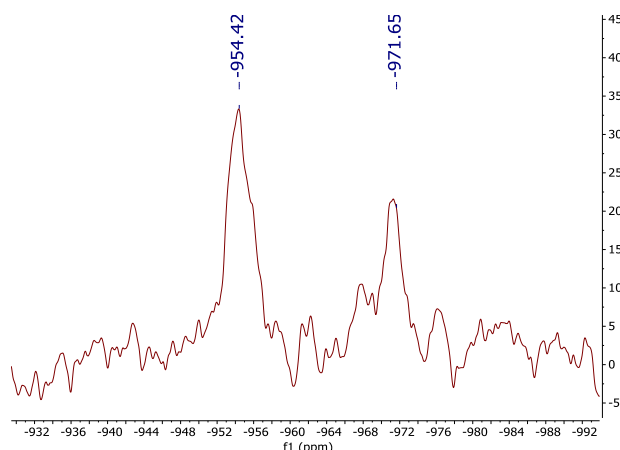
*Figure 2.65: ^{199}Hg NMR spectrum (89.6 MHz, CDCl₃) of **3,5-[Hg₂]** and **3,5-[Hg]** with proton-coupling.*

Significantly, the recorded chemical shifts strongly suggest some degree of coordination to the pyridyl nitrogen atom in solution, with values in the region around 400 ppm expected if this was not the case, based on 'model compounds' (which do not exhibit coordination to a donor atom) in the literature.[71, 72] Values in the region around -1000 ppm have been previously observed for complexes exhibiting *N*-coordination.[72] This is further supported by the single crystal structures measured for **2,3-[Hg₂]**, **2,5-[Hg]** and **2,5-[Hg₂]** (Section 2.10), which all show some degree of *N*-coordination, and possibly *O*-coordination, though the effects of crystal packing means that caution must be applied when applying data from the crystalline solid state to complexes in solution.

2.13   Synthesis of Gold(III) Complexes
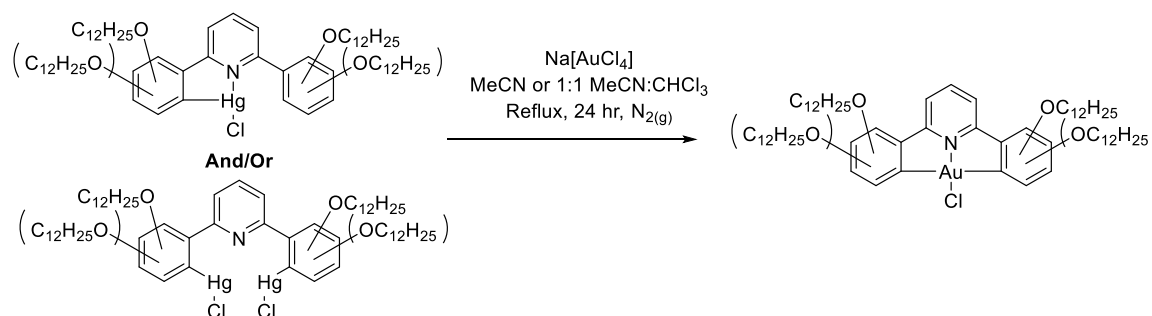
Figure 2.66: Generic reaction scheme for the transmetalation of the mercury(II) complexes to give the chlorogold(III) complex.

The mercury(II) complex is transformed to the gold(III) complex *via* a transmetalation reaction with M[AuCl₄] (M = Na or K) giving [Au$^{(III)}$(C^N^C)Cl] (Figure 2.66). Pure acetonitrile was used for the complexes substituted with two-chains, however a 1:1 mixture of chloroform:acetonitrile was required, for solubility reasons, for complexes with four-chains.[1, 7, 8, 50, 73] Where the mercury complex is isolated as an impure product (**4-[Hg]**, **3,4-[Hg]**, **2,4-[Hg]** and **3,5-[Hg]**) the mixture is reacted with [AuCl₄]⁻ without further purification and the resulting gold(III) complexes are purified by either column chromatography, followed by recrystallisation, or by serial recrystallisation, depending on the substitution pattern.
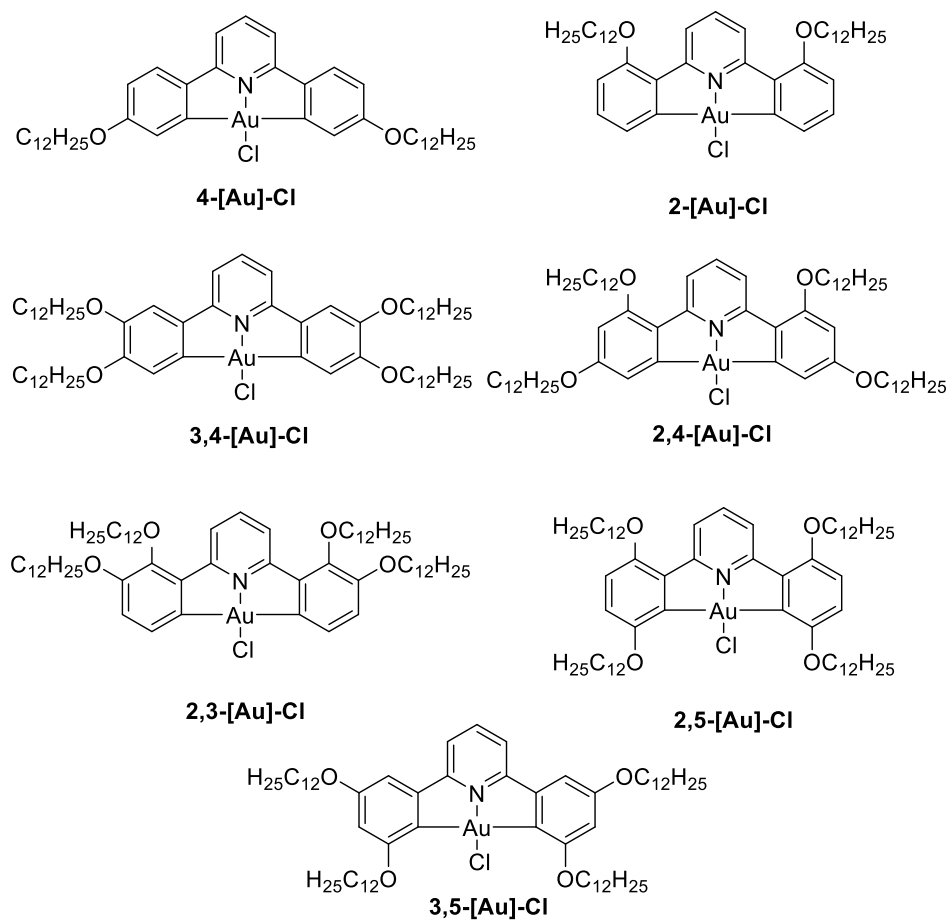
Figure 2.67: Structures of chlorogold(III) complexes synthesised in this work.

Yields were variable depending on the substitution pattern. For complexes substituted in the 2,2′-position of the phenyl ring of the C^N^C ligand there was evidence of disproportion from the appearance of a gold plate on the round-bottom flask. Use of a dinitrogen atmosphere minimised this effect, even so a lower yield was observed for **2-[Au]-Cl** (40%) compared to **4-[Au]-Cl** (50%).

Complexes which formed dimercurated complexes displayed significantly lower yields on auration (<25%), particularly **2,4-[Au]-Cl** where only ~6% yield was achieved. ^{1}H NMR spectroscopy of the crude product indicated appreciable quantities of the unreacted dimercury complex for **2,3-[Au]-Cl**, **2,5-[Au]-Cl** and **2,4-[Au]-Cl** suggesting preferential reaction of the monomercury complex. The presence of this residual dimercurated complex proved a particular issue for **2,4-[Au]-Cl**, with purification proving challenging as a result. **2,4-[Hg₂]** was unable to be removed *via* either column chromatography or recrystallisation. A pure sample of the aurated complex was gained, with difficulty on reaction from **2,4-[Hg]**, through the yield (5%) was still very low.

Three potential isomers are possible on auration of the mixture of monomercury complexes, **3-[Hg]** and **5-[Hg]**; two symmetrical, the 3,3′-position, **3-[Au]-Cl** and 5,5′-position, **5-[Au]-Cl**, and an unsymmetrical complex, **3/5-[Au]-Cl**, with one dodecyloxy chain in the 3-position of one phenyl ring and one in the 5-position of the other (Figure 2.68). On reaction of the mixed monomercury complexes, unreacted **5-[Hg]**, and the unsymmetrical gold complex, **3/5-[Au]-Cl**, (~20%) were isolated after column chromatography, with no evidence present of formation of the other two potential isomers. These isolated complexes suggests that **3-[Hg]** reacts in preference to **5-[Hg]**. Few unsymmetrical Au(C^N^C) complexes have been prepared in the literature to date, however there is evidence to suggest that only the less sterically hindered isomer is formed for some unsymmetrical complexes,[47] through the scope of the work was not large enough to determine full trends.
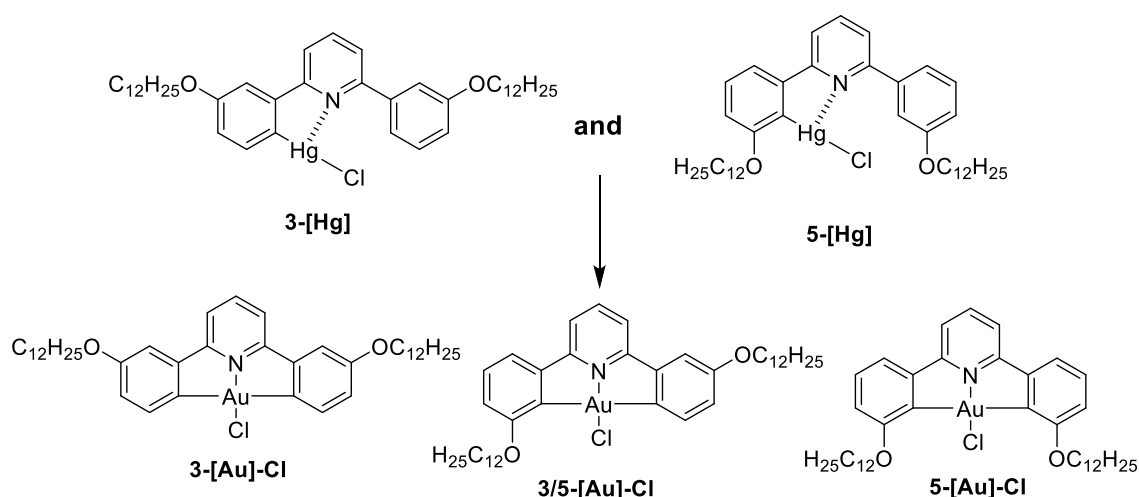
Figure 2.68: Possible chlorogold(III) complexes with substituents in the 3- and 5-positions of the phenyl unit of the C^N^C ligand. Note, only 3/5-[Au]-Cl is actually synthesised.

Surprisingly, **3,5-[Hg]** failed to transmetalate to give **3,5-[Au]-Cl**, with only the unreacted mercury complexes isolated under standard conditions. No further conditions were investigated. Complexes displaying 3,5-disubstitution of the phenyl unit of the C^N^C ligand have been rarely synthesised previously, with only two fluorine substituted examples known.[74, 75] No indication of difficulties in the synthesis was indicated, but unfortunately full synthetic procedures, including the yield, were not given, resulting in a lack of possible conclusions that can be drawn. It also has to be noted that fluorine atoms exhibit different electronic and steric properties to alkoxy-groups, which will also have an effect on the overall reactivity of the mercuration and auration steps.

2.14   Direct Auration
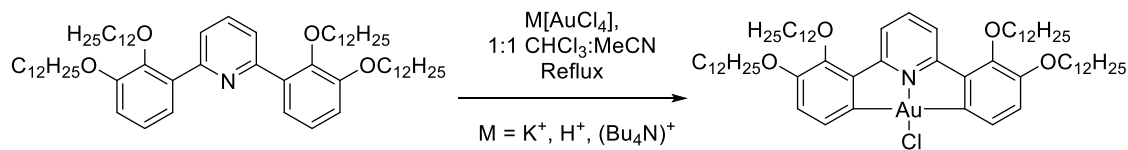
*Figure 2.69: Reaction scheme for attempted direct auration of **2,3-[L]** to give **2,3-[Au]-Cl**.*

Given the high yields obtained for preparation of intermediate mercury complexes using the 2,6-*bis*(2,3-dialkoxyphenyl)pyridine ligands, including evidence of a double C-H activation, it was speculated that the enhanced reactivity may signal an opportunity for a highly desirable direct auration. Therefore, ligand **2,3-[L]** was reacted directly with K[AuCl$_4$] under the conditions employed for transmetalation (Figure 2.69). The ^{1}H NMR spectrum of the solid obtained was dominated by unreacted ligand, although there were some small and broad peaks whose chemical shifts were similar to those of the target gold complex. Use of the more soluble starting material (NBu$_4$)[AuCl$_4$] did not change the outcome, nor did increased reaction times (5 days) for either K[AuCl$_4$], H[AuCl$_4$] or (NBu$_4$)[AuCl$_4$].
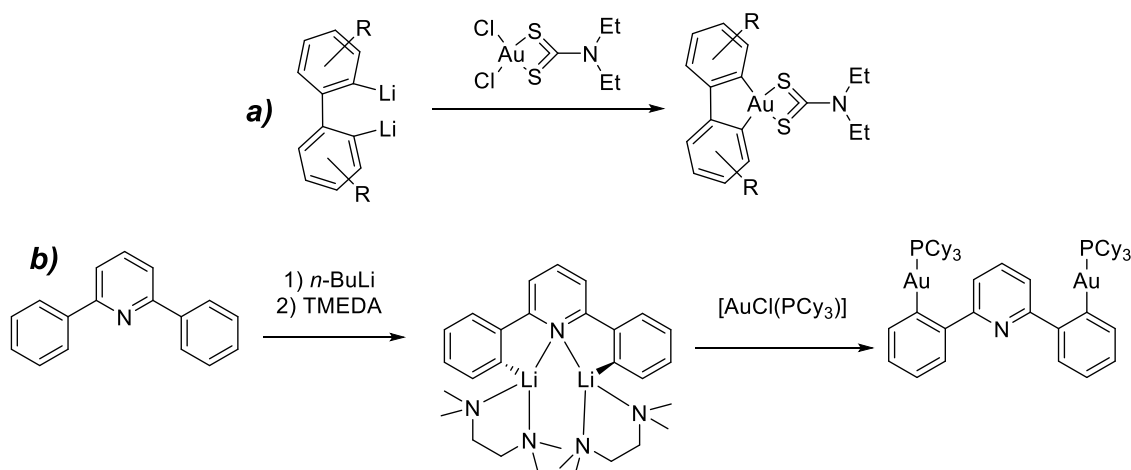
Figure 2.70: Synthesis of a C^C gold(III) complex via a dilithum complex (a)[38] and synthesis of a C^N^C gold(I) complex via a dilithum complex (b).[76]

Previously, the auration of a C^C ligand has been successfully achieved from the transmetalation of a dilithium species (Figure 2.70a),[38 39] while Au(I) species have also been successfully formed from a C^N^C ligand (Figure 2.70b).[76] It was therefore suggested that it might be possible to undertake auration of the C^N^C ligand with gold(III) *via* the dilithium complex, **2,5-[Li₂]**, as shown in Figure 2.71.[38, 39, 76-82] A modified literature procedure was used to form the dilithium species[83] *via* the addition of *n*-BuLi to **2,5-[L]**,[77] which was chosen due to the 2,2′-position alkoxy-chain providing a blocking group for one of the possible positions of auration, while the 5,5′-position alkoxy-chain could provide stabilisation for the lithium ion *via* coordination. One equivalent of Na[AuCl₄] was then added, however sadly the dilithium species reduced the Au(III) to Au(0), resulting in the isolation of unreacted free ligand and elemental gold. While, modification of the gold(III) ligands to provide additional stabilisation of the gold centre might result in successful reaction, this method was viewed as not being viable at this point in time.
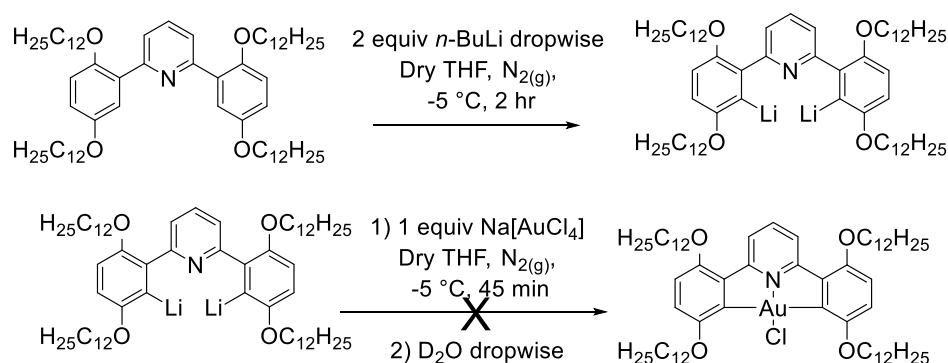
Figure 2.71: Reaction scheme for the attempted auration via a dilithium species.

2.14.1　　　Attempted Direct Auration *via* Microwave Synthesis

Attempted direct auration *via* microwave synthesis was attempted by Goult,[66] in a collaborative project, based on the previous successes reported by Tilset *et al.* with elaborate ligands (Figure 2.72). Goult's results are summarised below.[30, 31, 34, 84]
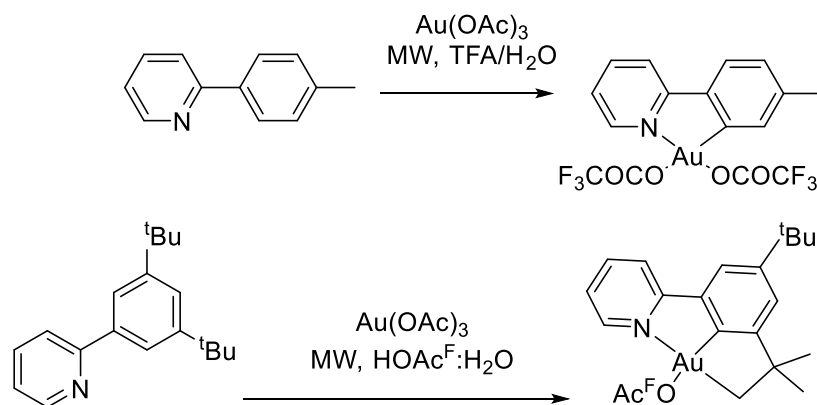
Figure 2.72: Examples of ligands used by Tilset et al. for direct auration via microwave methods.[30, 31, 34, 84]

Reacting **2,3-[L]** with Na[AuCl$_4$], under microwave conditions, in a range of solvents and at various temperatures (Table 2.4) resulted in the isolation of unreacted starting material and at high temperatures (160 °C), precipitation of Au(0) was also observed. It appeared that low solubility disfavoured reactivity. Instead the more soluble **2,3-[L]-OMe** was investigated.

Table 2.4: Microwave Reactions Tested on **2,3-[L]**, All Performed Using 0.1 mmol of Na[AuCl$_4$] and 0.1 mmol of **2,3-[L]**.[66]

Solvent	Base	T / °C	Recovered
H$_2$O	-	160	[L] + Au(0)
EtOH	-	100	[L]
MeCN	-	100	[L]
MeCN/H$_2$O	-	100	[L]
MeCN/H$_2$O	NaOAc	100	[L]
MeCN	(Bu$_4$N)(OAc)*	100	[L]
MeCN	NaOAc*	100	[L]
MeCN/H$_2$O	-	120	[L]

*2 molar equivalents

Dropwise addition of **2,3-[L]-OMe** in acetonitrile to Na[AuCl$_4$] in water resulted in a precipitate, believed to be [Au(III)(κ^2-C^N^CH)Cl$_2$]. The reaction was stirred until the solvent was dry, then the solid was re-suspended in water and microwaved at 140 °C. The resulting ^{1}H NMR spectrum showed a small doublet at ~8.2 ppm, which is a characteristic of the cyclometallated gold(III) complex, along with unreacted starting material and Au(0). This was the only evidence for any successful auration that occurred and proved not repeatable. Further conditions were investigated, which are summarised in Table 2.5.

Table 2.5: Microwave Conditions Tested Using **2,3-[L]-OMe** on 0.1 mmol scale and 2 Molar Equivalents of Base Where Required.[66]

Solvent	Base	T/ °C	Recovered
H_2O	-	140	? + Au(0)
$MeCN/H_2O$	-	0	$[Au(\kappa^2\text{-}C^\wedge N^\wedge CH)Cl_2]$
H_2O	NaOAc	120	CNC
EtOH	-	100	$[Au(\kappa^2\text{-}C^\wedge N^\wedge CH)Cl_2]$
MeCN	-	100	Unknown
H_2O	-	120	$[Au(\kappa^2\text{-}C^\wedge N^\wedge CH)Cl_2]$
H_2O	NaOAc	120	CNC + Au(0)
H_2O/TFA	-	120	$[CNCH]^+(OTf)^-$
$MeCN/H_2O$	NaOH	100	CNC + Au(0)
$H_2O/MeCN$	Lutidine	120	CNC

A further range of microwave conditions were employed in an attempt to successfully aurate the C^N^C ligand. Further, addition of TFA in water gave only the protonated ligand, while addition of base resulted in isolation of only unreacted starting material and Au(0). Use of Au(I) sources (Au(THT)Cl) to form the *N*-coordinated species, where the gold ion coordinates to solely the nitrogen ligand of the pyridine unit, then heating under microwave conditions to give the gold(III) cyclometallated product *via* oxidative addition, was considered as a possible route, however the gold(I) *N*-coordinated complexes proved unstable, readily giving gold mirrors on heating, and even in the NMR tube during analysis.

In conclusion direct auration *via* microwave techniques was not successful, however there were hopeful signs that further work on modifying conditions might succeed.

2.14.2 Direct Auration *via* Metallocycle Intermediates

It is known that cyclopalladated complexes may be transmetalated to give organomercury complexes.[23] This reaction has been studied in some detail as it has the possibility to give what can be termed a 'false positive' in the mercury drop test used to ascertain if palladium-catalysed transformations are mediated by palladium nanoparticles. Given this

reactivity, it was then of interest to see if such palladium complexes would also undergo auration (Figure 2.73).[85]
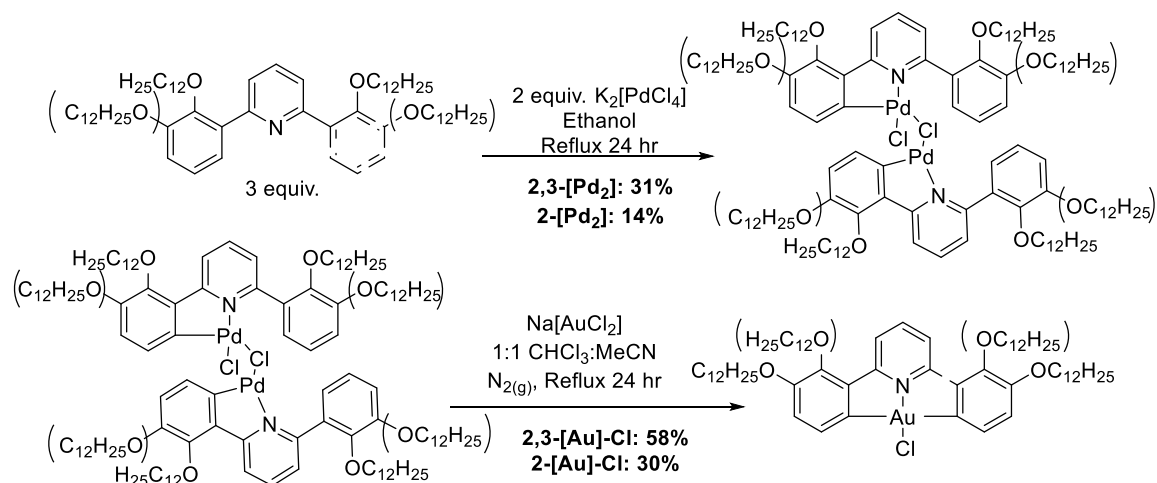
Figure 2.73: Reaction scheme for auration via a palladium complex.[85]

Cyclopalladation was achieved by heating the free ligand and $K_2[PdCl_4]$ under reflux in ethanol overnight (Figure 2.73).[86-89] The reaction was successful for **2,3-[L]** and **2-[L]**, proceeding in yields of 33% and 14% respectively. Other ligands (**2,5-[L]**, **4-[L]**, **3-[L]** and **3,4-[L]**) failed to react under the conditions used, with only the free ligand recovered. The palladium dimers were characterised by ^{1}H NMR spectroscopy (Figures 2.75-2.76), with COSY-NMR used to aid assignment, while MALDI-MS confirmed formation of a dimer (Figure 2.74). Please note that while the complex has currently been drawn in the *cis*-form, the *trans*-form is also possible and complete assignment is not possible without XRD data (Figure 2.74). These complexes were aurated by heating with $Na[AuCl_4]$ under reflux for 24 hours in 1:1 chloroform:acetonitrile with yields of 58% (**2,3-[Pd₂]**) and 30% (**2-[Pd₂]**) being achieved. The pure palladium dimer can be isolated *via* column chromatography as a golden oil, if a pure product is required at this stage, alternately the mixed complex and free ligand can be successfully aurated and the complex purified by recrystallisation, in order to avoid an additional purification step. While the lack of palladation of **2,5-[L]** could be assigned to steric hindrance due to the presence of chains in the 5,5′-positions of the phenyl unit, which would disfavour dimer formation, such an explanation would not apply to other unreactive isomers suggesting, perhaps, that some electronic factors may also be important. These studies were carried out right at the end of the lab work and so further investigation and reaction optimisation is desirable.

120
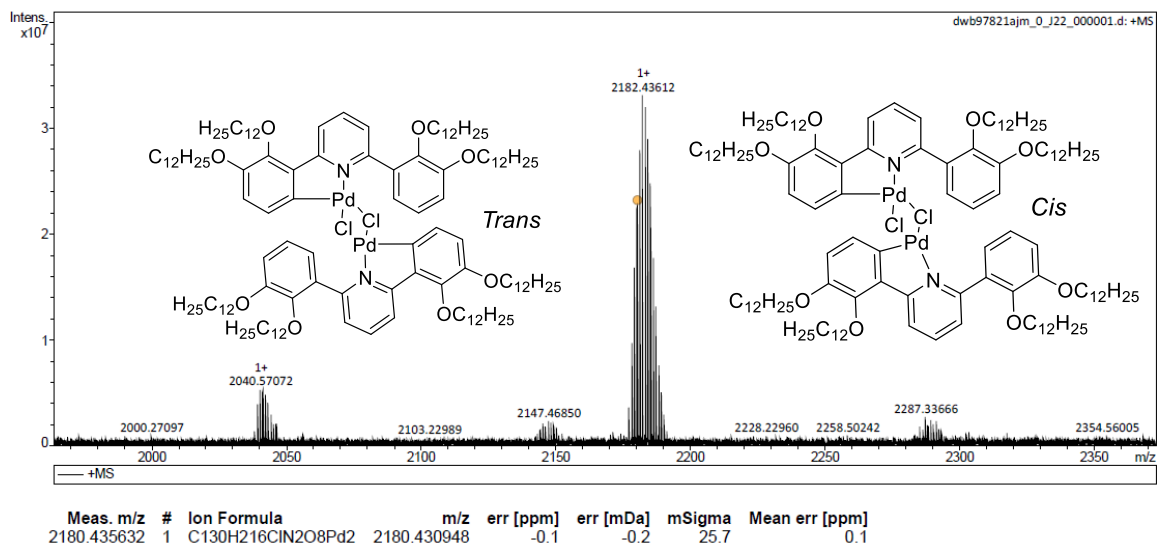
*Figure 2.74: MALDI-ms spectra of **2,3-[Pd₂]**, showing both the trans and cis forms of the dimer.*

Meas. m/z	#	Ion Formula	m/z	err [ppm]	err [mDa]	mSigma	Mean err [ppm]
2180.435632	1	C130H216ClN2O8Pd2	2180.430948	-0.1	-0.2	25.7	0.1
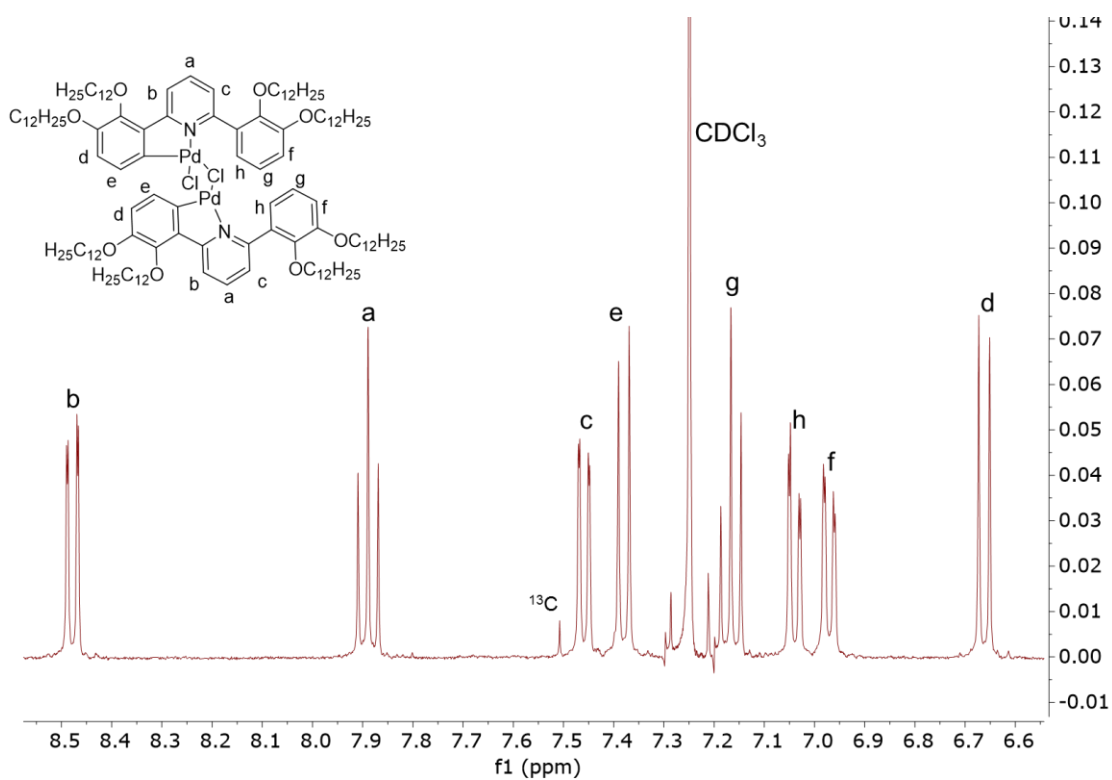
*Figure 2.75: ¹H NMR spectrum (400 MHz, CHCl₃) of **2,3-[Pd₂]** showing the aromatic region.*
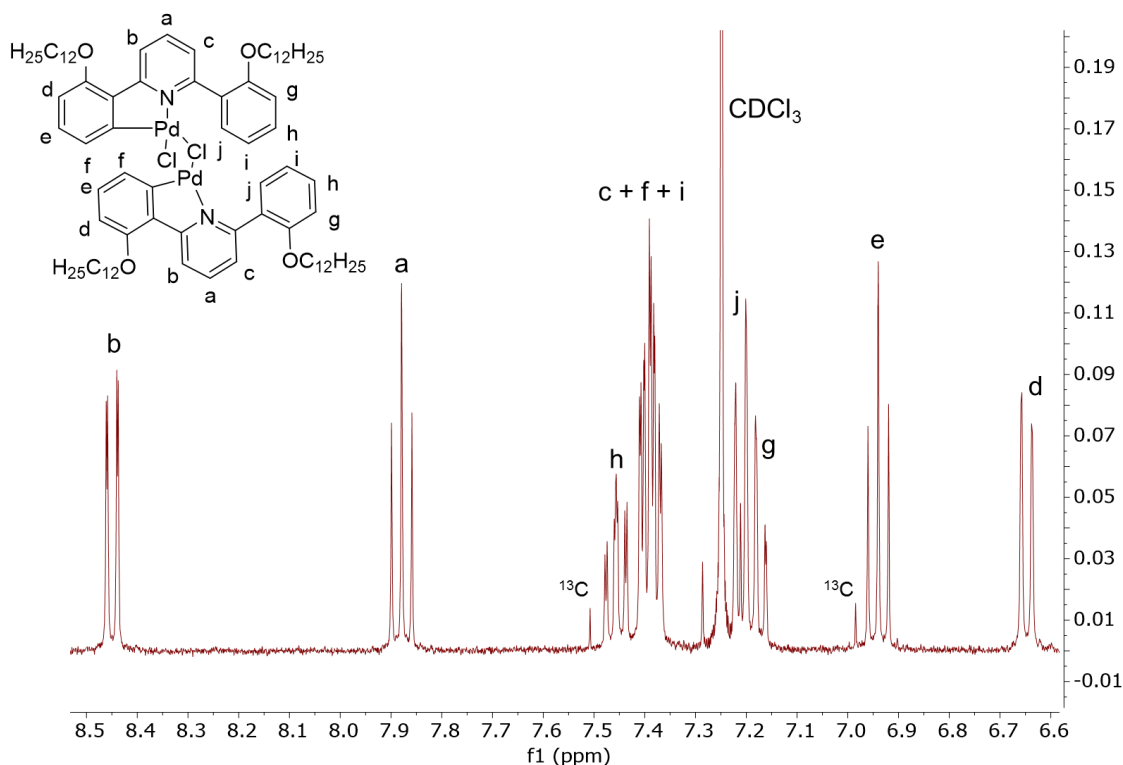
*Figure 2.76: ^1H NMR spectrum (400 MHz, CHCl$_3$) of **2-[Pd$_2$]** showing the aromatic region.*

Recently, direct auration of a range of phenylpyridine ligands has been reported using [Cp*RhCl$_2$]$_2$ as a catalyst, with the gold complexes being recovered in yields of >50%.[41] The complex [Cp*RhCl$_2$]$_2$ is known for its ability to activate C–H bonds and to cyclometallate *C^N* ligands and the study proved the intermediary of an orthorhodated intermediate. This methodology was then applied to our C^N^C ligands (Figure 2.77) and was found successfully to aurate **2,3-[L]** to give **2,3-[Au]-Cl** in 11% isolated yield.[85] Disappointingly, however, under the same conditions it did not prove possible to aurate any of the other ligands screened (**2-[L]**, **2,5-[L]**, **4-[L]**, **3-[L]** and **3,4-[L]**). This clearly requires further investigation, but what is believed to be a unique observation of the direct metalation of an unfunctionalised C^N^C ligand is nonetheless exciting.
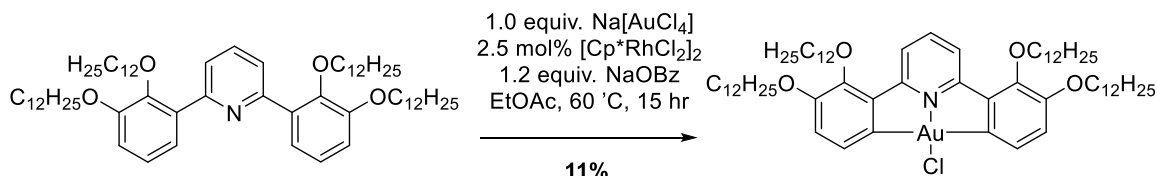
Figure 2.77: Reaction scheme for auration via rhodium catalysis.[85]

Comparison of the overall yields across the three successful methods of auration is of interest (Table 2.6). It can be observed that auration *via* a mercury(II) complex is the most versatile method, successful for all ligands, but the high inherent toxicity of the intermediate makes this reaction undesirable if it can be avoided. It is interesting to note that there is no correlation between the yield of mercuration and the yield of the subsequent transmetalation to gold, although in all but one case, the former reaction is higher yielding.

Auration *via* a palladium intermediate and using rhodium catalysis are very recent observations and there was no opportunity to optimise the conditions employed in order both to increase yields and also extend the range of substrates that can be functionalised. Nonetheless, under such unoptimised conditions, auration of **2,3-[L]** *via* its palladium complex is competitive in yield when compared to a route *via* a mercury complex. For the same ligand, direct auration yields compare reasonably well with many yields *via* mercury complexes. It is hoped that future work can optimise both mercury-free routes, which would be important for this chemistry.

Table 2.6: Summary of Auration Yields *via* Different Routes.

Complex	Mercuration / %	Auration / %	Overall Yield *via* Hg(II) / %	Palladation / %	Auration / %	Overall Yield *via* Pd(II) / %	Direct Auration / %
2,3-[M]	75*	24	18	31	48	15	11
2-[M]	90	40	36	14	30	4	0
2,5-[M]	65*	17	12	0	-	0	0
3,4-[M]	37	13[54]	5	0	-	0	0
4-[M]	17	48	8	0	-	0	0
3-[M]	83	20	17	0	-	0	0

* Dimercurated products formed.

2.15   Gold(III) alkynyl complexes
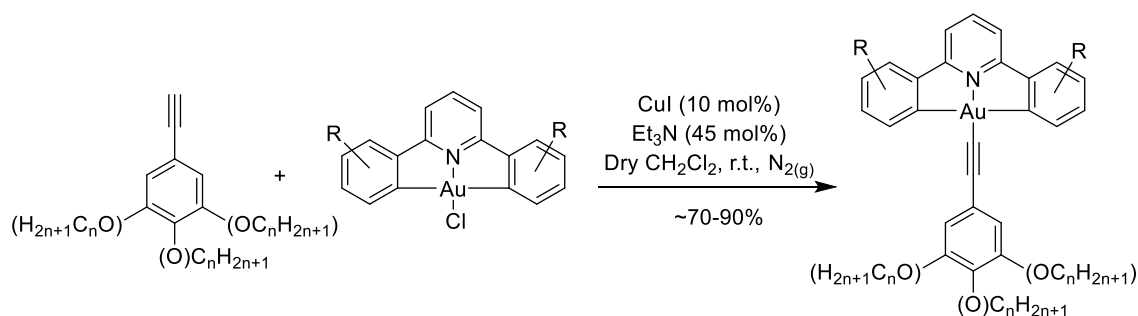
Figure 2.78: Reaction scheme for the synthesis of gold(III) alkynyl complexes.

The chlorogold(III) complexes can be coupled to substituted phenylacetylenes using a standard copper-catalysed coupling reaction (Figure 2.78).[1, 7, 8, 50] The complexes were filtered through Celite® and purified *via* column chromatography (silica) and crystallised from CH_2Cl_2/ethyl acetate to give the target complexes in $67 - 93\%$ yield, which were shown to be pure by ^1H NMR spectroscopy and CHN analysis.

2-[Au]-
5: $R_1 = R_3 = H$, $R_2 = C_5H_{11}$
8: $R_1 = R_3 = H$, $R_2 = C_8H_{17}$
1-10: $R_1 = R_3 = H$, $R_2 = OC_{10}H_{21}$
2-10: $R_1 = H$, $R_2 = R_3 = OC_{10}H_{21}$
3-10: $R_1 = R_2 = R_3 = OC_{10}H_{21}$
3-14: $R_1 = R_2 = R_3 = OC_{14}H_{29}$
F10: $R_1 = R_3 = H$, $R_2 = O(CH_2)_2(CF_2)_7CF_3$
F10: $R_1 = R_3 = H$, $R_2 = O(CH_2)_2(CF_2)_9CF_3$
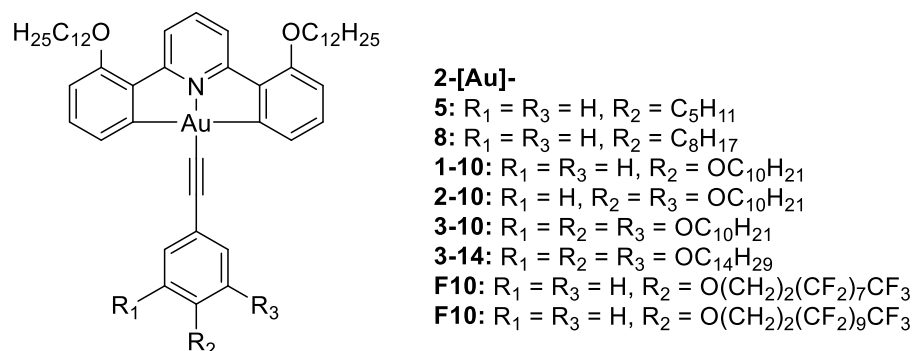
Figure 2.79: Structures of gold(III) alkynyl complexes with chains in the 2-positions of the phenyl unit of the C^N^C ligand .

Complexes based on 2,2′-, 2,2′,3,3′- and 2,2′,5,5′-substituted ligands have been used to synthesise several alkynyl complexes (Figures 2.79 and 2.80) in good yield, varying numbers of alkyl (C_nH_{2n+1}, $n = 5, 8$) and alkoxy chains (OC_nH_{2n+1}, $n = 10$) on the phenylacetylide ligand.
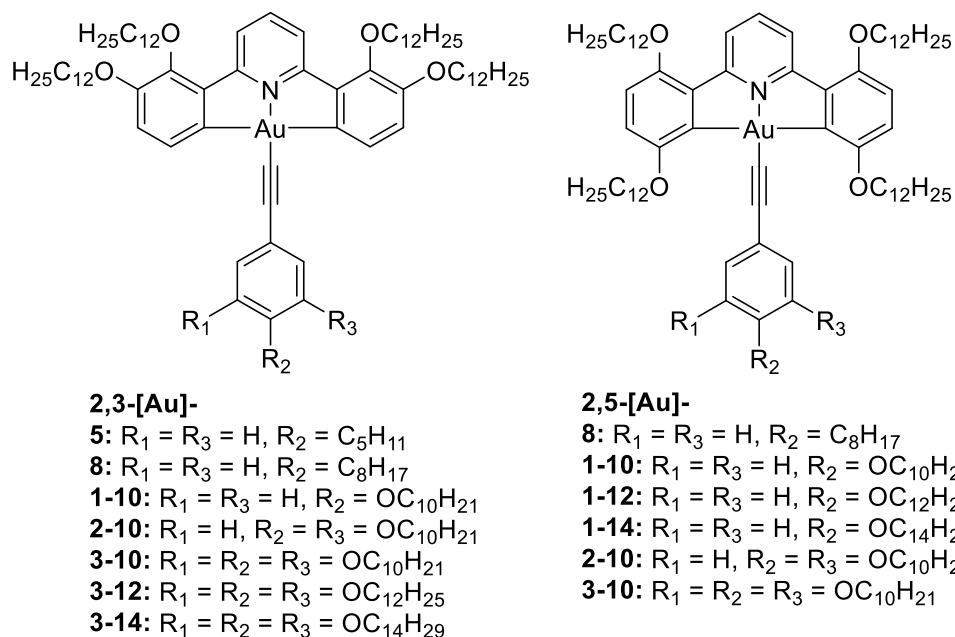
Figure 2.80: Structures of tetrasubstituted gold(III) alkynyl complexes.

2,3-[Au]-
5: $R_1 = R_3 = H$, $R_2 = C_5H_{11}$
8: $R_1 = R_3 = H$, $R_2 = C_8H_{17}$
1-10: $R_1 = R_3 = H$, $R_2 = OC_{10}H_{21}$
2-10: $R_1 = H$, $R_2 = R_3 = OC_{10}H_{21}$
3-10: $R_1 = R_2 = R_3 = OC_{10}H_{21}$
3-12: $R_1 = R_2 = R_3 = OC_{12}H_{25}$
3-14: $R_1 = R_2 = R_3 = OC_{14}H_{29}$

2,5-[Au]-
8: $R_1 = R_3 = H$, $R_2 = C_8H_{17}$
1-10: $R_1 = R_3 = H$, $R_2 = OC_{10}H_{21}$
1-12: $R_1 = R_3 = H$, $R_2 = OC_{12}H_{25}$
1-14: $R_1 = R_3 = H$, $R_2 = OC_{14}H_{29}$
2-10: $R_1 = H$, $R_2 = R_3 = OC_{10}H_{21}$
3-10: $R_1 = R_2 = R_3 = OC_{10}H_{21}$

2.16 X-ray Structures of Gold(III) Complexes

Crystals suitable for single crystal X-ray were obtained for several of the gold(III) complexes by diffusion of an anti-solvent (ethyl acetate) into a solution of the gold complex in chloroform. XRD data tables and .cif files can be found in the data folder - see page 30. Carbon atoms are coloured grey, chlorine green, gold yellow, hydrogen turquoise, nitrogen blue and oxygen red.

2.16.1 2-[Au]-Cl
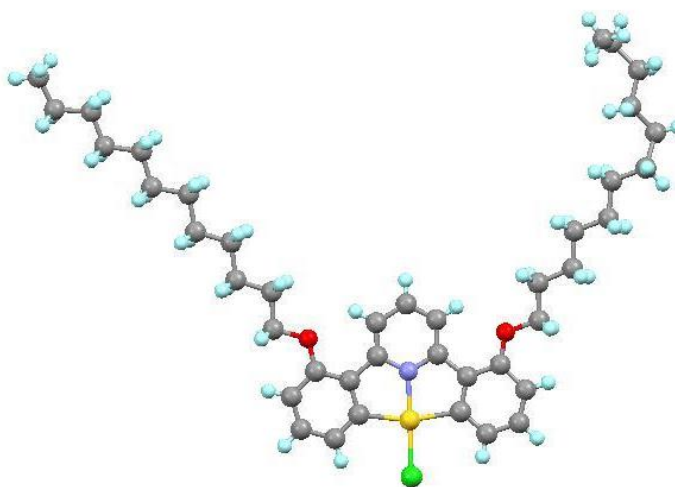
Figure 2.81: Molecular structure of compound **2-[Au]-Cl**, with disorder removed for clarity.

125

Compound **2-[Au]-Cl** (Figure 2.81) crystallised in the monoclinic crystal system in space group, *C*2/*c*. The crystal structure shows that the complex is planar, removing the twist of the phenyl rings seen in the parent ligands. The complex is highly symmetric about the gold atom, with the Au-C bond lengths being identical at 2.060(6) and 2.066(7) Å. The geometry is close to square planar, but to account for the bite-angle of the ligand the C^Au^N (82.4(2)° and 82.0(2)°) and Cl^Au^C angles (97.8(2)° and 97.8(2)°) deviate from 90°. The Au-N and Au-Cl bond lengths are 1.960(6) and 2.277(2) Å, and are of a similar magnitude with other systems known in the literature.[8, 50, 65] One of the dodecyl chains exhibited disorder from the carbon in the C8 position to the end of the chain. Both alkoxy chains are brought into planarity on complexation (Figure 2.82).
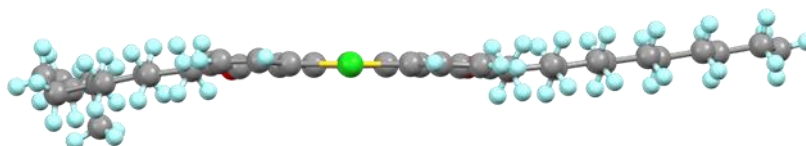
*Figure 2.82: Side view of **2-[Au]-Cl** showing the planar nature of the complex.*

In the crystal the molecules pack in 'paired' layers, which can be observed to have an 'undulating' structure when viewed from the side (Figure 2.83) and an anti-parallel arrangement of molecules in adjacent layers. The related complex **4-[Au]-Cl** exhibits a similar layered structure.[50] The rigid cores align, while the chains interpenetrate.
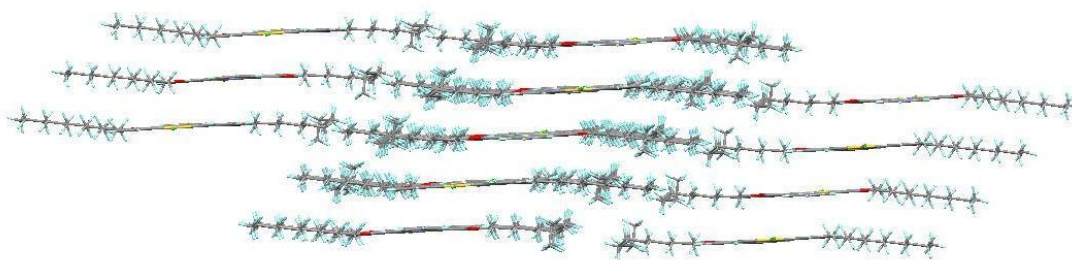
*Figure 2.83: Bulk crystal structure of **2-[Au]-Cl**, as viewed from the side.*

2.16.2   2,3-[Au]-Cl

Unfortunately crystals suitable for XRD of **2,3-[Au]-Cl** substituted with dodecyloxy chains could not be obtained, however suitable crystals were grown of the equivalent complex substituted with butoxy chains. Compound **2,3-[Au]-Cl** crystallised in the monoclinic crystal system in space group, *P*2₁/*n* (Figure 2.84a). The asymmetric unit contains two molecules in a staggered parallel arrangement (Figure 2.84b), and a distorted

square-planar geometry is observed about the gold-atom (C^Au^C angles are 81.7(1)°, 82.03(1)°, 98.90° and 97.37°). The Au-C bond lengths are measured as 2.057(3) and 2.052(3) Å. The Au-N bond length is 1.907(2) Å and Au-Cl is 2.2756(8) Å. In a notable difference to the other structures observed the butoxy-chains in the 2-position are twisted out of the plane of the molecule.
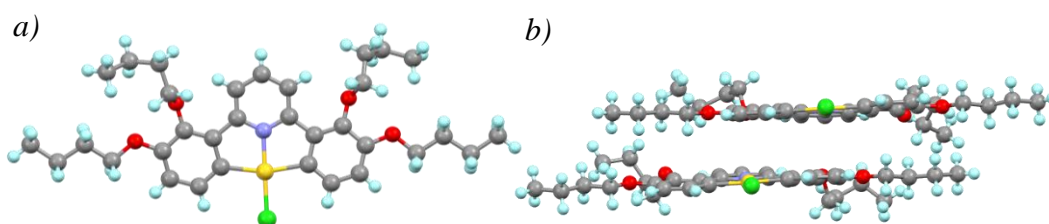
*Figure 2.84: Molecular structure of **2,3-[Au]-Cl**.*

2.16.3   2,5-[Au]-Cl
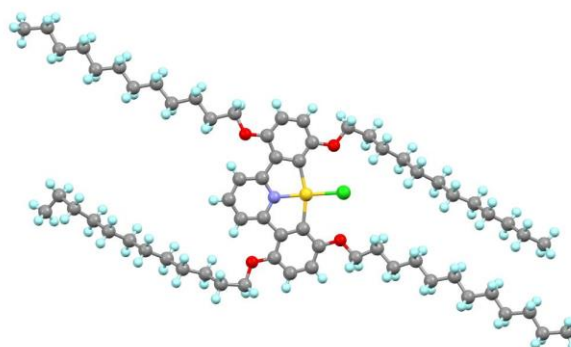
*Figure 2.85: Molecular structure of compound **2,5-[Au]-Cl**.*

2,5-[Au]-Cl crystallised in a triclinic structure in space group *P*-1 (Figure 2.85). The crystal was layered, with slippage of the layers, resulting in very broad, streaked reflections (Figure 2.86). As a result the final solution was of low quality, with an *R*-factor of 16%. A distorted square-planar geometry is observed about the gold-atom (C^Au^C angles are 80.1(5)°, 83.1(6)°, 98.4(6)° and 98.6(5)°). The Au-C bond lengths are measured as 2.09(2) and 2.07(2) Å, the Au-N bond length, 1.941(6) Å and Au-Cl, 2.286(5) Å. The complex is distorted away from planar geometry, with an angle of 11.83° between the planes formed by the atoms of each phenyl unit.
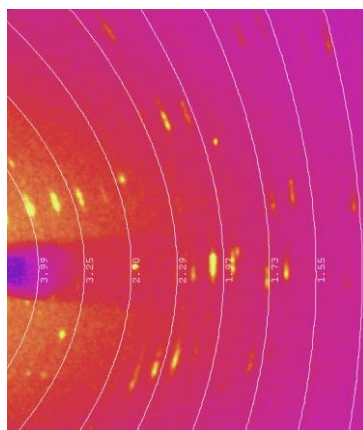
*Figure 2.86: Example of XRD diffraction for **2,5-[Au]-Cl**, showing very broad, streaked reflections due to slippage of the crystal layers.*

2.16.4   2-[Au]-5: [Au(CNC)CCPhC$_5$H$_{12}$]

Compound **2-[Au]-5** crystallised in the orthorhombic space group *Pnma* (Figure 2.87) and exhibited a high level of disorder due to a reflection about the *ac* plane, with all the atoms lying close to this plane. The data set was collected at 200 K, with a suspected phase change on cooling further, resulting in poor lower temperature datasets due to suspected fracture of the single crystal.

The geometry around the gold atom is a distorted square-planar with bond angles of 81.55(19)°, 81.4(2)°, 99.5(3)° and 97.6(2)°. The angle around the alkynyl group is also distorted slightly away from 180°, instead the measured angles about the carbon-carbon triple bond are 178.2(6)° and 171(3)°; this is not uncommon in structures of metal-alkyne complexes.
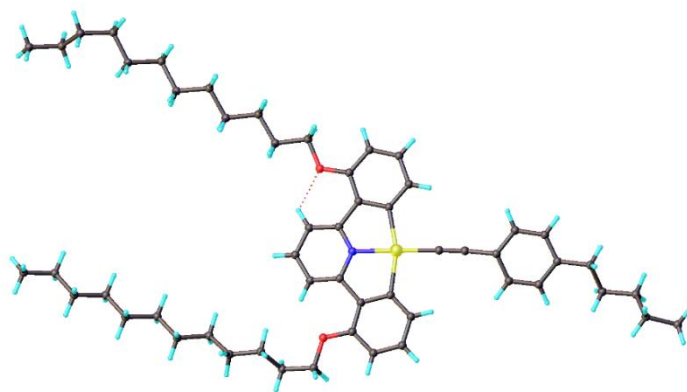
*Figure 2.87: Molecular structure of compound **2-[Au]-5**.*

2.16.5 2-[Au]-8: [Au(CNC)CCPhC$_8$H$_{17}$]
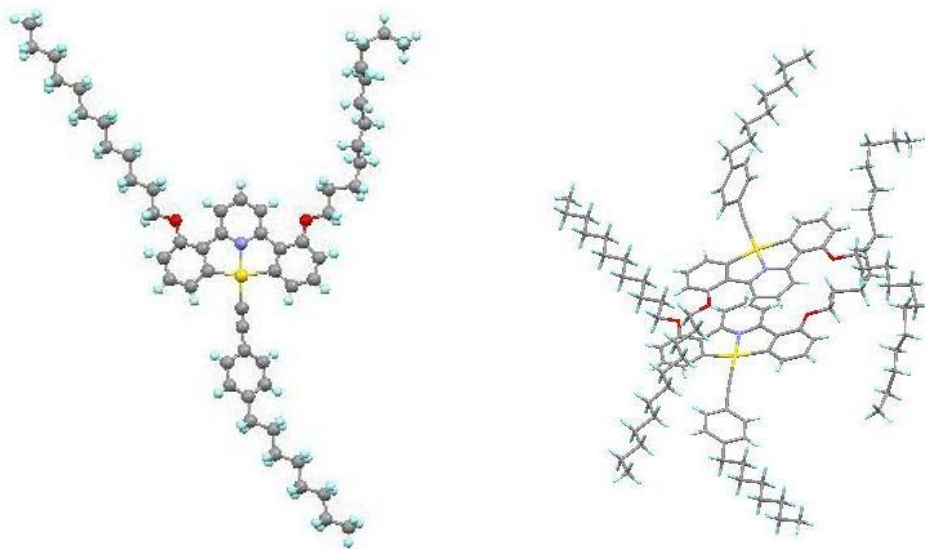
*Figure 2.88: The molecular structure of **2-[Au]-8** (left), and the asymmetric unit (right), with disorder removed for clarity.*

Compound **2-[Au]-8** crystallised in the triclinic space group *P*-1 (Figure 2.88, left), with two molecules in the asymmetric unit, paired back-to-back in an antiparallel arrangement (Figure 2.88, right). One of the dodecyloxy chains on the C^N^C ligand is curved around the side of the other molecule; disorder was also present in this chain. The angle around the alkynyl group is also distorted slightly away from 180°, this is likely to account for the presence of the phenyl group combined with the restraints about the gold atom. **2-[Au]-8** packs in layers, which when viewed from the side have no undulation present, while the curving dodecyloxy chain connects between layers (Figure 2.89). An approximate antiparallel alignment of the cores occurs, with the chains interpenetrating (Figure 2.90).
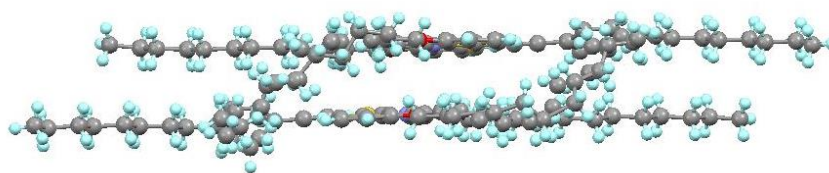
*Figure 2.89: Side view of the asymmetric unit of **2-[Au]-8**.*
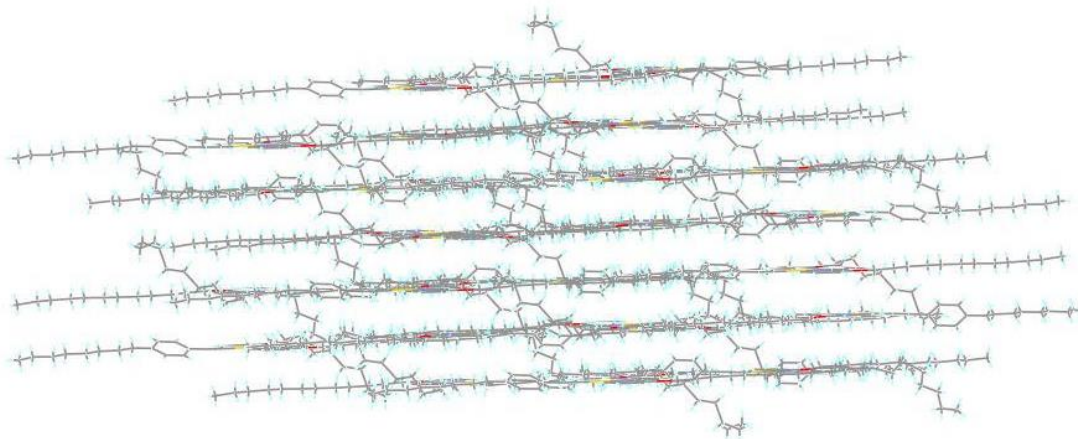
*Figure 2.90: Side view of the bulk crystal packing of **2-[Au]-8**.*

2.16.6   2-[Au]-1-10: [Au(CNC)CCPhOC$_{10}$H$_{21}$]
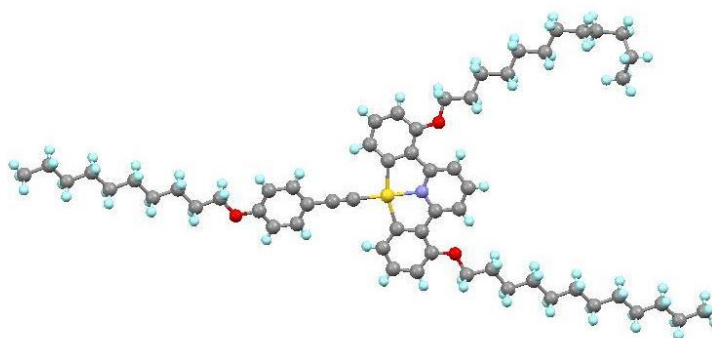
*Figure 2.91: Molecular structure of **2-[Au]-1-10**.*

2-[Au]-1-10 also crystallised in the triclinic space group *P*-1, with only one molecule in the asymmetric unit (Figure 2.91). Once again a curve is observed in one of the dodecyloxy chains, which likely arises from space-filling constraints. The complex packs in layers (Figure 2.92), with an antiparallel stacking of the cores and some undulation observed in the layers. The chains of adjacent molecules interdigitate, with the decyloxy chain on the phenylacetylene being close in space with one of the ligand dodecyloxy chains.
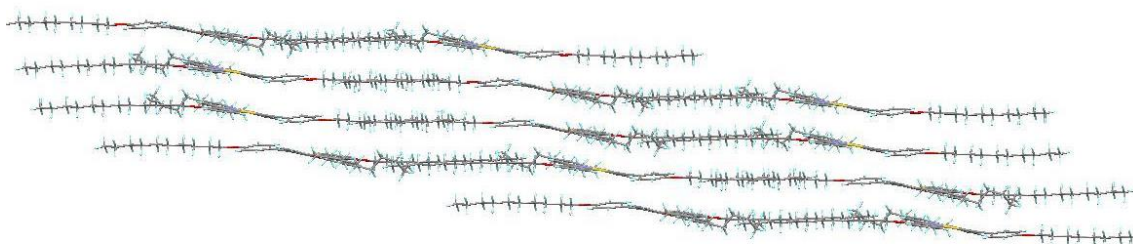
*Figure 2.92: Side view of the packing of **2-[Au]-1-10**.*

2.16.7   2-[Au]-F10: [Au(CNC)CCPh(O(CH$_2$)$_2$C$_8$F$_{17}$)]
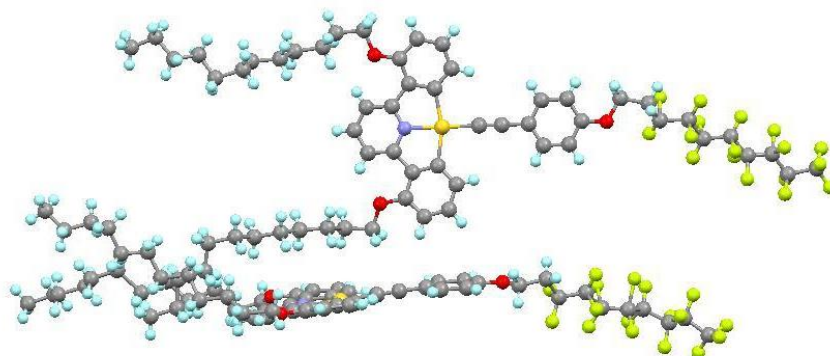
*Figure 2.93: Molecular structure of **2-[Au]-F10**, with disorder removed for clarity.*

2-[Au]-F10 crystallised in the triclinic space group *P*-1, with two molecules in the asymmetric unit. One of the dodecyloxy chains intercalates with the dodecyloxy chains of the other molecule (Figure 2.93). A large amount of disorder is observed in the chains, particularly the perfluorinated chains due to formation of a helical structure, with both helicities observed – one is shown in Figure 2.94. The molecules pack in the bulk crystal with the rigid, planar cores in columns and the perfluorinated chains pairing in an antiparallel manner to form isolated islands among the hydrocarbon chains (Figure 2.95).
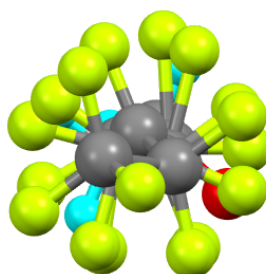
Figure 2.94: Structure of the perfluorinated chain, showing the helical nature.
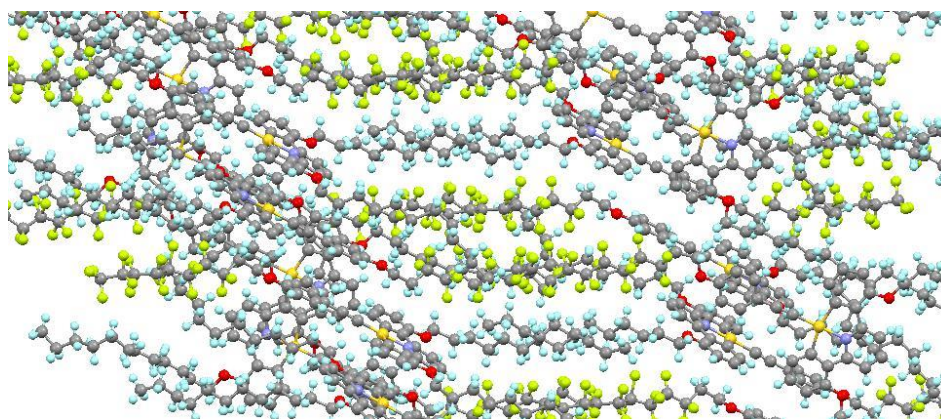
*Figure 2.95: The packing of **2-[Au]-F10**, showing the alignment of the chains.*

131

2.16.8   2-[Au]-2-10: [Au(CNC)CCPh(OC$_8$H$_{17}$)$_2$]
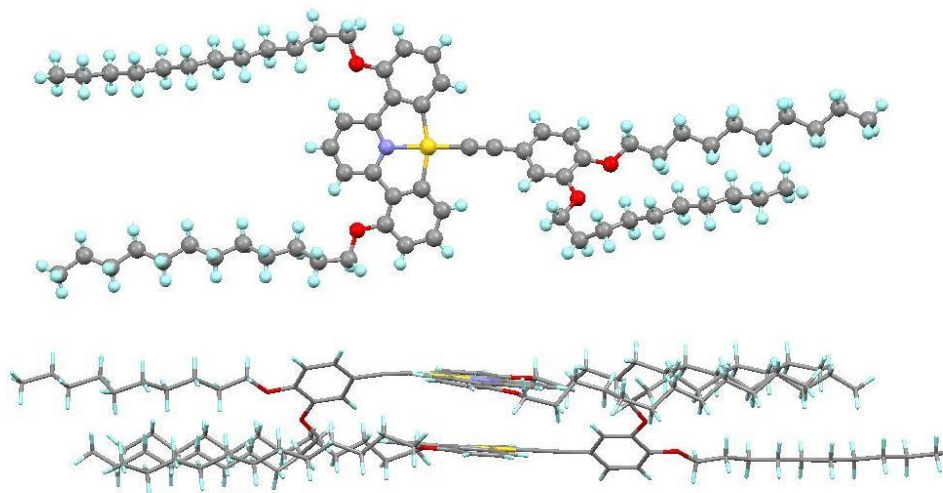
*Figure 2.96: Molecular structure of **2-[Au]-2-10** (top), and asymmetric unit from the side (bottom).*

2-[Au]-2-10 crystallised in the monoclinic space group *P*2$_1$/*c* (Figure 2.96, top), with two molecules in an antiparallel arrangement in the asymmetric unit (Figure 2.96, bottom). Interestingly the molecules are packed so that the decyloxy chain in the 3-position of the phenylacetylide is interdigitated between the C^N^C ligand dodecyloxy chains on the other molecule, with the remaining decyloxy chain below.

2.16.9   2,5-[Au]-3-10: [Au(CNC)CCPh(OC$_8$H$_{17}$)$_3$]
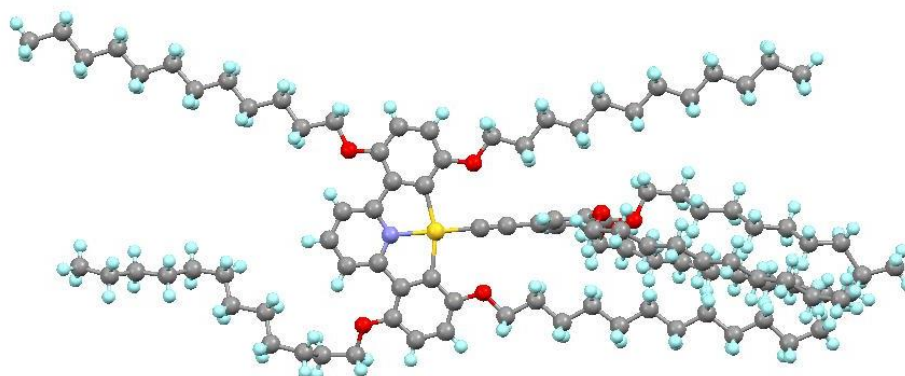
*Figure 2.97: Molecular structure of **2,5-[Au]-3-10**, with disorder removed for clarity.*

2,5-[Au]-3-10 crystallised in the triclinic space group *P*-1 (Figure 2.97). A distorted square-planar geometry is observed about the gold-atom. A slight distortion of the pincer

ligand from planarity is seen, with an angle of 9.51° between the plane of one phenyl moiety and the plane of the pyridyl and the other phenyl moieties. Notably, the phenyl acetylene ligand is rotated at 82.41° to the major plane of the pincer ligand to avoid a steric clash with the chains in the 5,5′-positions of the phenyl moiety of the pincer ligand (Figure 2.98). Extensive disorder is seen in the 4-position chain of the phenylacetylide ligand and in one of the chains in the 5-position of the phenyl-moiety of the pincer ligand.
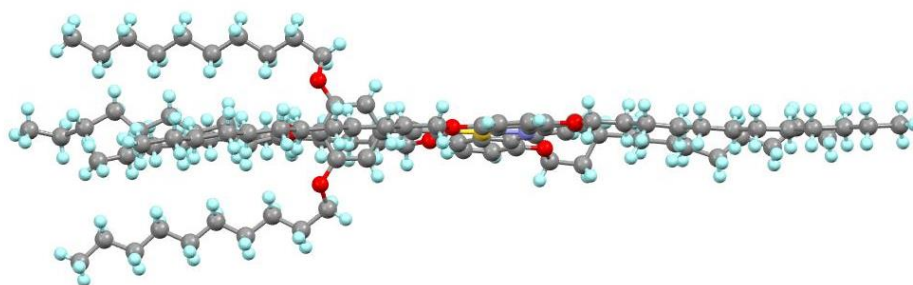
*Figure 2.98: Side view of **2,5-[Au]-Cl**, showing the rotation of the phenyl acetylene ligand.*

2.17 ^{1}H NMR Spectra of Gold(III) Complexes

The ^{1}H NMR spectra of several gold complexes are considered and are detailed below. The signals relating to the dodecyloxy chains remain fairly constant between complexes and the free ligands and therefore, with the exception of the signals relating to the –OCH_2- environments in the alkoxy region, are not discussed. Assigned ^{13}C{^{1}H} NMR spectra can be found in the data folder - see page 30.

2.17.1 2-[Au]-Cl

On complexation of **2-[L]** to gold(III) the number of hydrogen environments in the aromatic region is reduced from six to five, with also a resulting loss of some degree of $^4J_{HH}$-coupling between the phenyl hydrogen atoms. In contrast to the free ligand, a resolved triplet and doublet are observed for H_a and H_b respectively, reflecting the symmetric, planar nature of the structure. H_b is also shifted significantly upfield to 8.29 ppm. Assignment was straightforward (Figure 2.99), requiring only the observation of an NOE effect from the chain –OCH_2- hydrogens to distinguish between H_c and H_e.
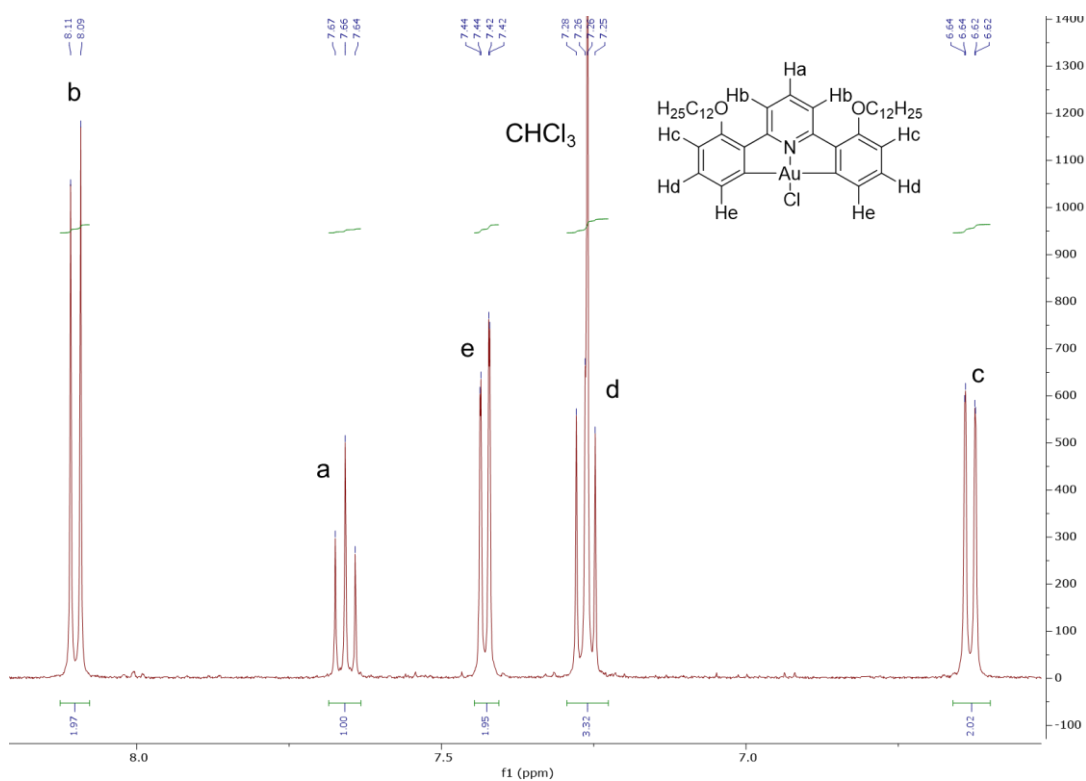
*Figure 2.99: ¹H NMR spectrum (500 MHz, CDCl₃) of complex **2-[Au]-Cl**, showing the aromatic region.*

2.17.2   2,3-[Au]-Cl and 2,5-[Au]-Cl

The ¹H NMR spectrums of **2,3-[Au]-Cl** (Figure 2.100) and **2,5-[Au]-Cl** (Figure 2.101), once again show significant shifting of the pyridyl hydrogen, H_b, upfield to >8.3 ppm compared to the free ligand. Two spin systems for both complexes are present; an A_2X-system relating to the pyridyl ring and two AB-systems relating to the phenyl rings. NOE experiments indicate assignment of the –OCH_2- hydrogen resonances as H_e at 4.09 ppm and 3.99 ppm to H_f for **2,3-[Au]-Cl**. The ordering of the –OCH_2- hydrogen resonances is altered compared to the ordering in **2,3-[L]** and **2,3-[Hg₂]**. The planar geometry on complexation results in significantly reduced electronic shielding for the hydrogen in the 2-position, H_e, while the hydrogen in the 3-position, H_f is slightly more shielded on complexation, resulting in a change in the chemical shift ordering.
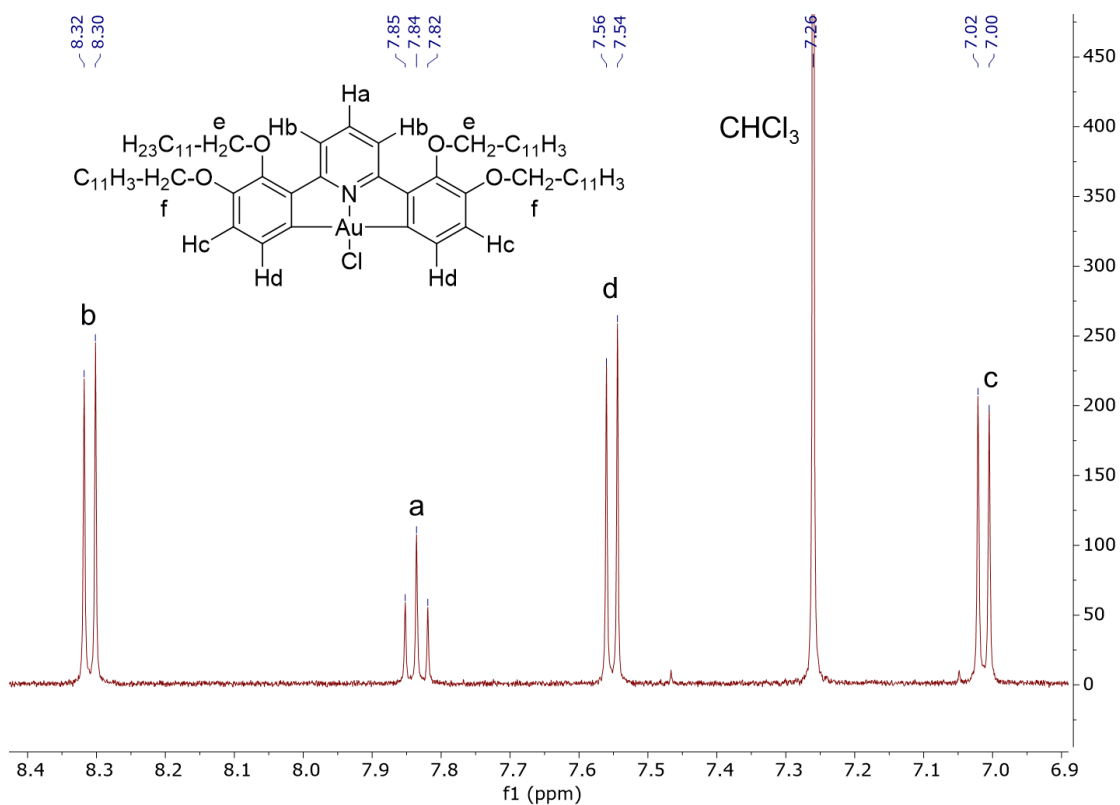
*Figure 2.100: ^1H NMR spectrum (500MHz, CDCl$_3$) of complex **2,3-[Au]-Cl**, showing the aromatic region.*
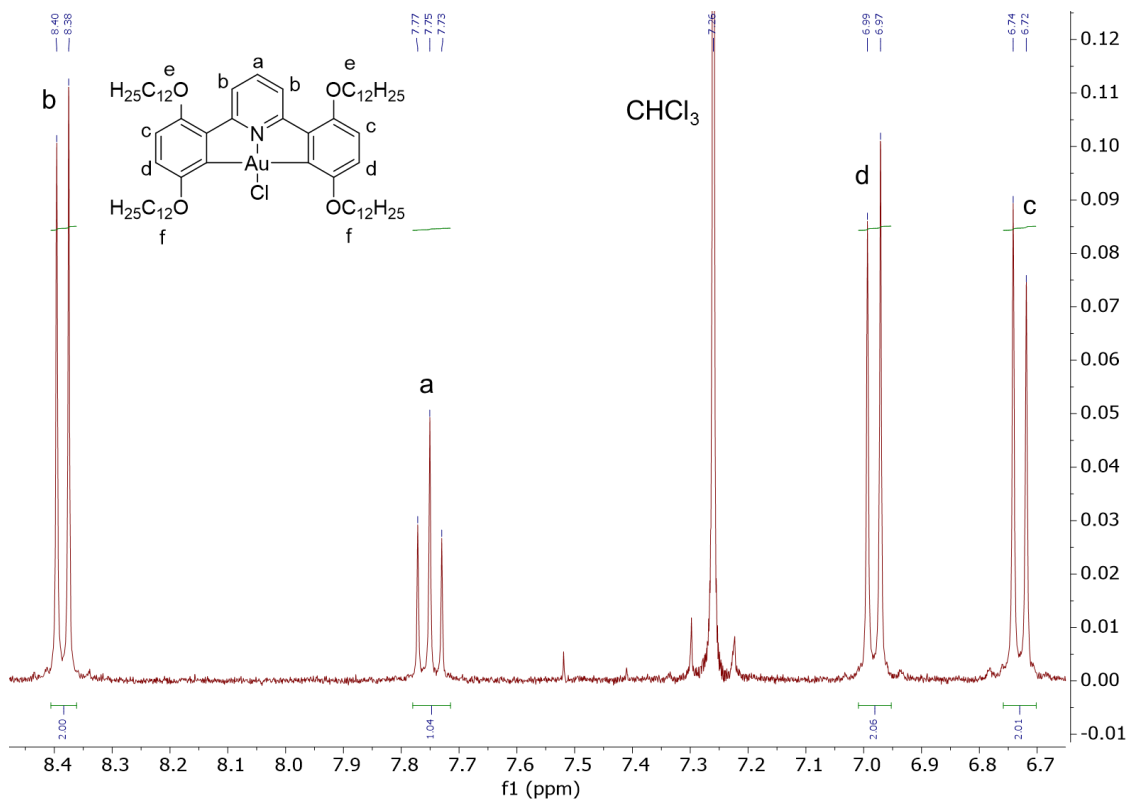
*Figure 2.101: ^1H NMR (400 MHz, CDCl$_3$) of Compound **2,5-[Au]-Cl**, showing the aromatic region.*

For **2,5-[Au]-Cl** NOE experiments result in assignment of H_f as 3.94 ppm and H_e as 4.04 ppm. The latter gave only a very weak NOE to H_b, suggesting that the chain is not spatially close to the C^N^C framework in solution. Instead it is thought that steric constants result in the chain rotating out of the plane of the molecule.

2.17.3 3/5-[Au]-Cl
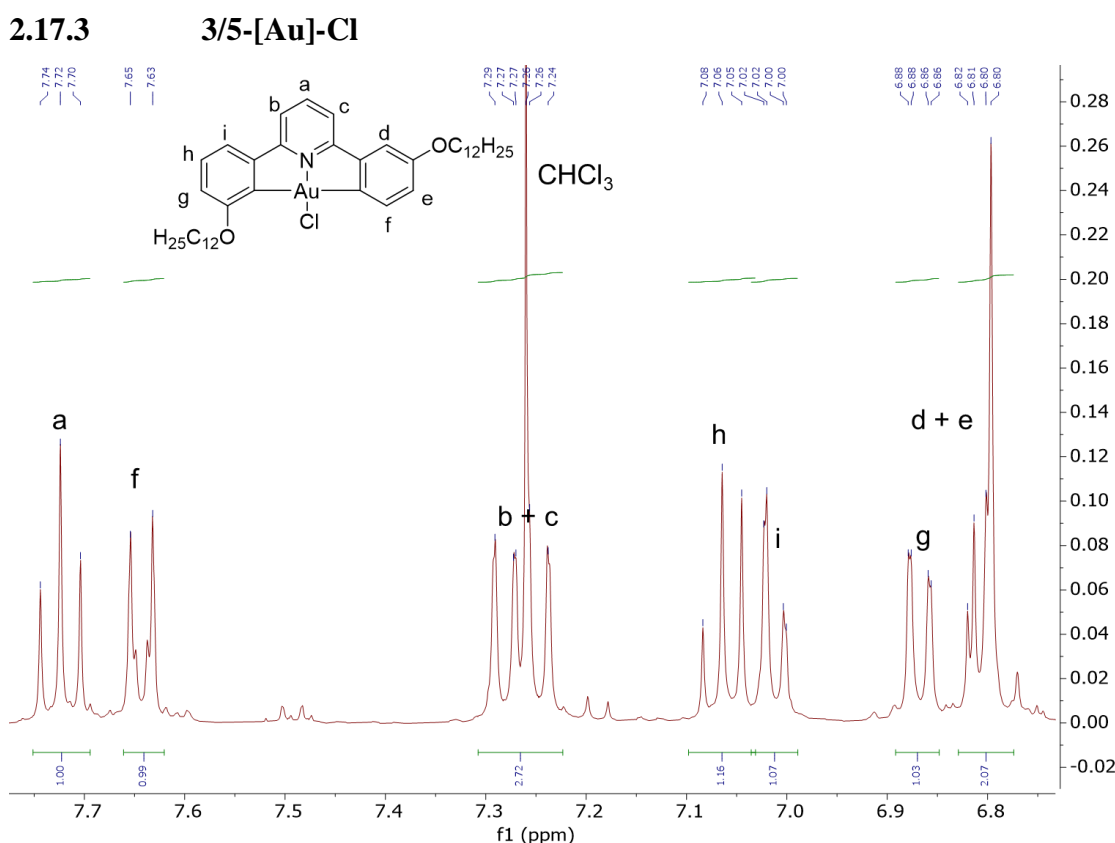
*Figure 2.102: ^1H NMR (400 MHz, CDCl₃) of Compound **3/5-[Au]-Cl**, showing the aromatic region.*

While three possible isomers can form on auration of **3/5-[Hg]** as noted earlier, ^1H NMR spectroscopy only identified formation of the unsymmetric complex, **3/5-[Au]-Cl**, as the sole gold complex isolated (Figure 2.102). The loss of symmetry results in inequivalence of the pyridyl hydrogens, H_b and H_c (7.34 and 7.29 ppm), which display a mutual ^4J-coupling and a ^3J-coupling giving an apparent triplet (H_a) at 7.76 ppm (*i.e.* $J_{HaHb} = J_{HaHc}$). On complexation to gold(III) the pyridyl signals are shifted downfield, particularly H_b and H_c, by ~0.5 ppm. Interestingly, the planarity of the complex leads to a single first-order splitting for these hydrogens different to the case, described earlier, where they were diasteotropic.

The highly deshielded nature of the doublet at 7.70 ppm indicates that this is the sole signal relating to the hydrogen adjacent to the gold(III) ion and is therefore H_f. This couples to into the signals at 6.85 ppm, which can be assigned as the overlapping resonances of H_d and H_e. The presence of ^4J-coupling in the signals at 6.90 and 7.05 ppm indicate that these are likely H_g and H_i respectively, with the remaining doublet of doublets at 7.10 ppm, H_h. Two triplets relating to the alkoxy $-O$-CH_2- hydrogens are found at 3.93 and 3.85 ppm.

2.18   Investigation of Ligands and Complexes Using Multinuclear NMR Spectroscopy

Given the unexpected formation of clean, isolated mercury complexes with some of these ligands, there was some interest to try to rationalise these observations. One possibility was that the substitution pattern of the alkoxy chains had some influence on the reactivity of the metallated carbon and so ^{13}C{^{1}H} NMR data were collected on ligands, gold complexes and where possible, mercury complexes (Table 2.7). Full spectra can be found in the data folder - see page 30.

Table 2.7: NMR Chemical Shifts for the Carbon Directly Bound to the Metal Ion in the Free Ligand, Mercury(II) Complexes and Chlorogold(III) Complex and ^{199}Hg NMR Chemical Shifts.

Ligand Substitution	NMR Chemical Shift for Carbon Directly Bound to Metal Ion / ppm						
	Free Ligand ^{13}C{^{1}H}	Free Ligand ^{1}H	[(κ^2-C^N^C)(Hg$^{(II)}$Cl)$_2$] ^{13}C{^{1}H}	[Hg$^{(II)}$(κ^2-C^N^CH)Cl] ^{13}C{^{1}H}	[Au(C^N^C)Cl] ^{13}C{^{1}H}	[Hg$^{(II)}$(κ^2-C^N^CH)Cl] ^{199}Hg{^{1}H}	[(κ^2-C^N^C)(Hg$^{(II)}$Cl)$_2$] ^{199}Hg NMR
2-	131.48	8.01	-	153.53	170.92	-1020	-
4-	128.14	8.09	-	149.83	172.24	-1023	-
3,4-	119.55	7.63	-	-	165.18	-999	-
2,4-	132.15	8.00	-	-	172.69	-1011	-1042
2,3-	122.69	7.47	148.04	-	160.51	-	-1011
2,5-	116.84	6.93	142.80	143.19	152.83	-1009	-1010
3-	118.81	7.71	-	144.72	164.08	-991	-
5-	118.81	7.71	-	144.61	163.26	-993	-
3,5-	105.55	7.29	129.76	131.39	-	-954	-972

The first data sets were recorded for the carbon that metallates. What is evident from the data is that the pattern in the ^{13}C chemical shifts is almost exactly the same, irrespective of the chemical species in which it is found (Figure 2.103). Thus, the change in chemical shift is around 40 ppm on complexation to gold(III) and around 20 ppm on complexation to mercury(II). The change in substitution gave a variation of around 10 ppm, with the one exception being when there is 3,5-disubstitution, where the change is somewhat greater. The same trend is observed in the ^{1}H NMR spectrum of this position for the free ligand (Figure 2.104).
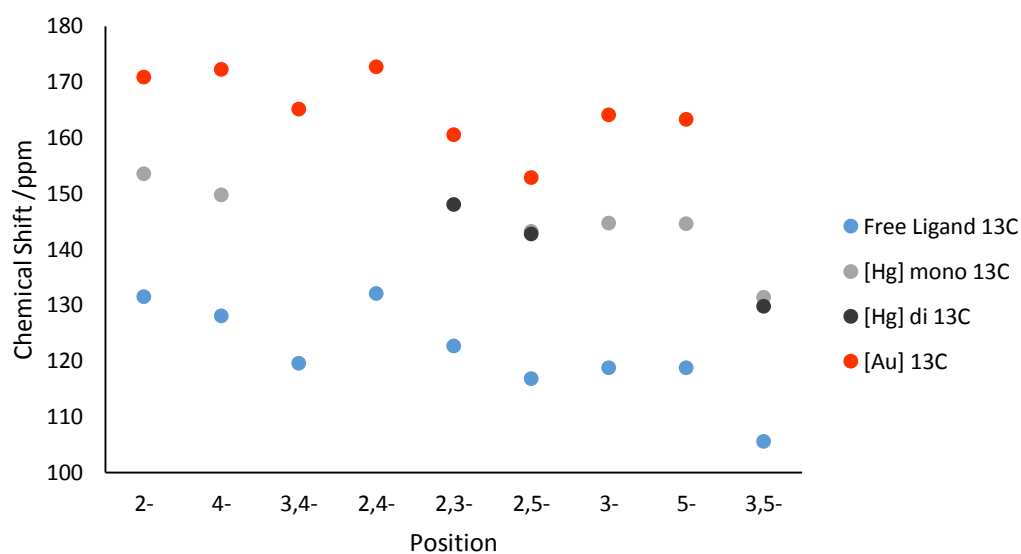
Figure 2.103: ^{13}C NMR chemical shift data in CDCl$_3$ for the free ligand, mercury(II) complexes and the chlorogold(III) complexes on alteration of the substitution pattern.
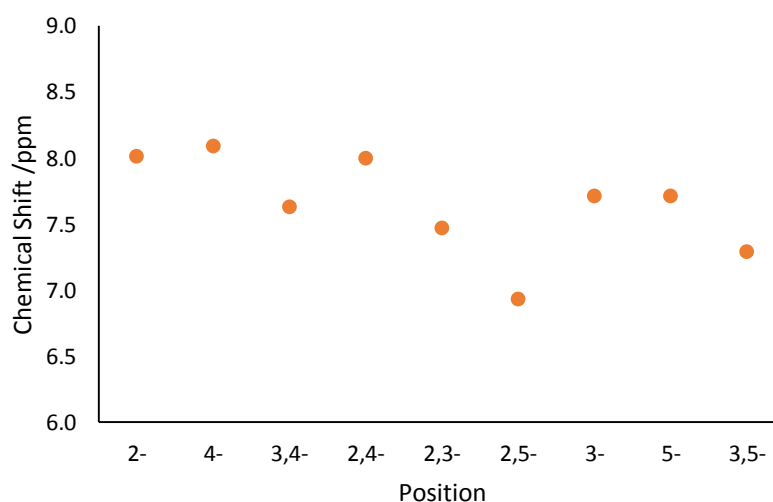
Figure 2.104: ^{1}H NMR chemical shift data in CDCl$_3$ for the free ligand on variation of the substitution pattern.

[199]Hg NMR spectroscopy in chloroform-*d* was also carried out on the mercury(II) complexes (Section 2.12). Similar chemical shifts were observed for **2-[Hg]** and **4-[Hg]** (~ -1020 ppm), **2,3-[Hg₂]**, **2,5-[Hg₂]** and **2,4-[Hg]** (~ -1010 ppm) and **3-[Hg]**, **5-[Hg]** and **3,4-[Hg]** (~ -990 ppm). The chemical shift observed for **2,4-[Hg₂]** is significantly lower at -1041 ppm, while those measured for **3,5-[Hg]** and **3,5-[Hg₂]** are significantly higher at -971 to -954 ppm, once again reflecting the strong effect that substitution in the 3,3′,5,5′-positions appears to have. A generally inverse correlation is observed with the ^{13}C NMR data, reflecting that this is the electronic effect on the metal ion centre, not on the ligand (Figure 2.105).
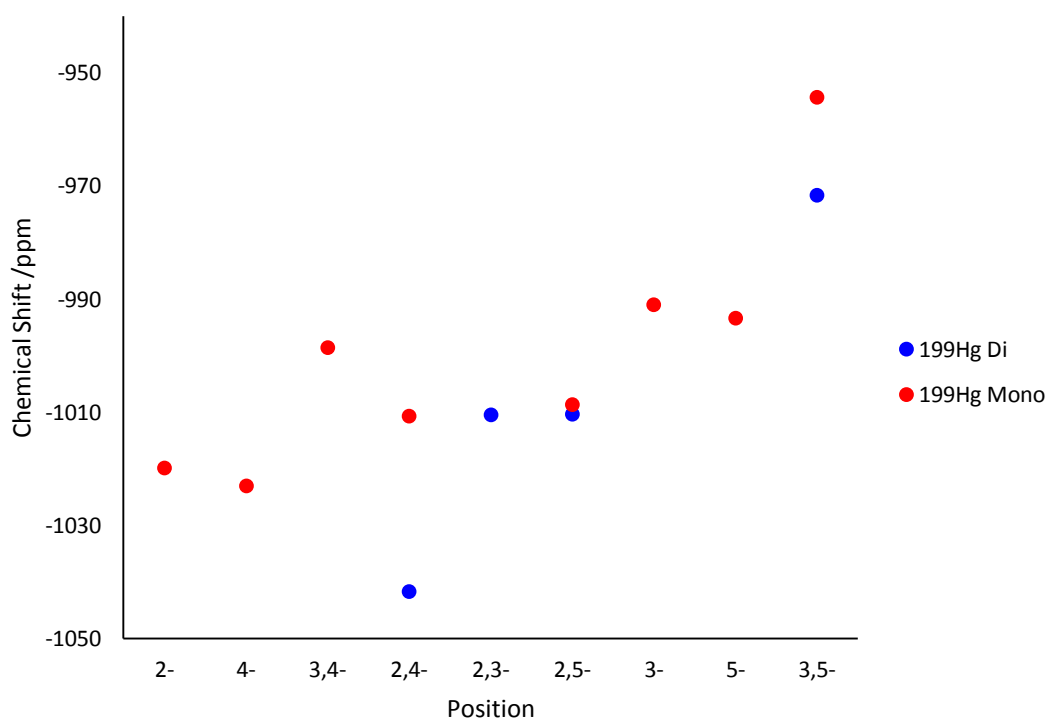
Figure 2.105: [199]Hg NMR chemical shifts in CDCl₃ for the mercury(II) complexes on alteration of the substitution pattern.

Goult[66] calculated the structures of the chlorogold(III) complexes and the mono- and di-substituted mercury complexes, including those not prepared (Table 2.8). The calculated bond lengths are generally longer than the experimental bond lengths, with this slightly outside of the region of standard deviation for the experimental results (Figures 2.106 and 2.107), however, they reproduce the experimental trends, and the difference is small. It can also be observed that the calculated bond lengths for the mono-substituted

mercury(II) complexes are longer than those for the di-substituted complexes, suggesting a potential explanation for the preferential reaction of the mono-substituted complex compared to the di-substituted complexes. Longer bonds are typically weaker and therefore less energy is required in order to break them in a reaction, potentially resulting in faster reaction rates of the mono-substituted complexes compared to the di-substituted complexes, hence the observed preference. The data, alongside the experimental data where possible, are plotted against the complex ^{13}C NMR data (Figures 2.108 and 2.109). A very weak negative correlation of Au-C bond length *vs* ^{13}C NMR chemical shifts is observed. A strong positive correlation is observed for the mono-substituted Hg-C bond lengths *vs* the ^{13}C NMR chemical shifts, with one notable outliner, **2,5-[Hg]**, which has a bond length that is significantly shorter than would be expected from the ^{13}C NMR chemical shift, based on the others in the series. The low number of data points for the di-substituted mercury complexes means that no meaningful data trends can be drawn from them.

Table 2.8: Average Experimental and Calculated C–M Bond Lengths / Å (M = Hg or Au).[†]

Position	Au-C XRD	Au-C Cal	Hg-C [(κ^2-C^N^C)(Hg$^{(II)}$Cl)$_2$] XRD	Hg-C [Hg$^{(II)}$(κ^2-C^N^CH)Cl] XRD	Hg-C [(κ^2-C^N^C)(Hg$^{(II)}$Cl)$_2$] Cal	Hg-C [Hg$^{(II)}$(κ^2-C^N^CH)Cl] Cal
2-[M]	2.063(7)	2.100	-	-	2.093	2.095
4-[M]	2.053(9)[54]	2.100	-	-	2.085	2.093
3,4-[M]	2.064(2)[54]	2.105	-	-	2.088	2.088
2,4-[M]	-	2.101	-	-	-	-
2,3-[M]	2.055(3)	2.098	2.035(17)	-	2.088	2.091
2,5-[M]	2.065(2)	2.133	2.0433(3)	2.1544(3)	2.105	2.092
3-[M]	-	2.104	-	-	2.080	2.087
5-[M]	-	2.138	-	-	2.084	-
3,5-[M]	-	2.133	-	-	2.081	2.088

[†] Calculations done by C. Goult.
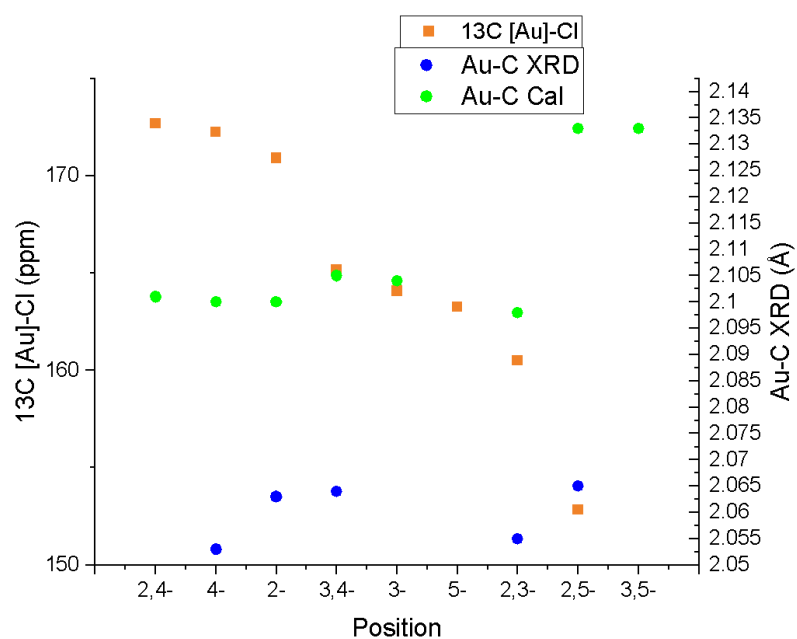
Figure 2.106: Experimental (XRD) and calculated M-C bond lengths plotted against the ^{13}C NMR chemical shifts for the gold(III) complexes based on substitution pattern.
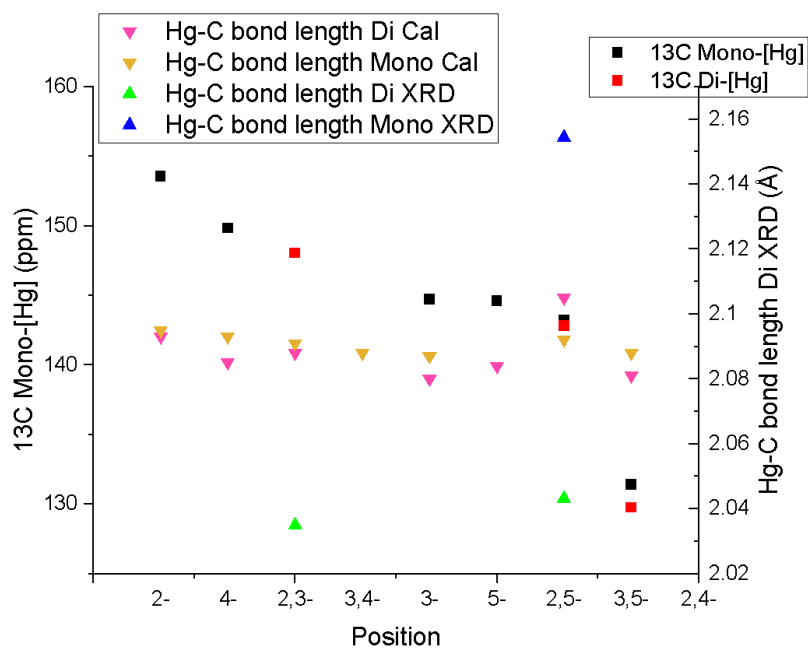
Figure 2.107: Experimental (XRD) and calculated M-C bond lengths plotted against the ^{13}C NMR chemical shifts for the mercury(II) complexes based on substitution pattern.
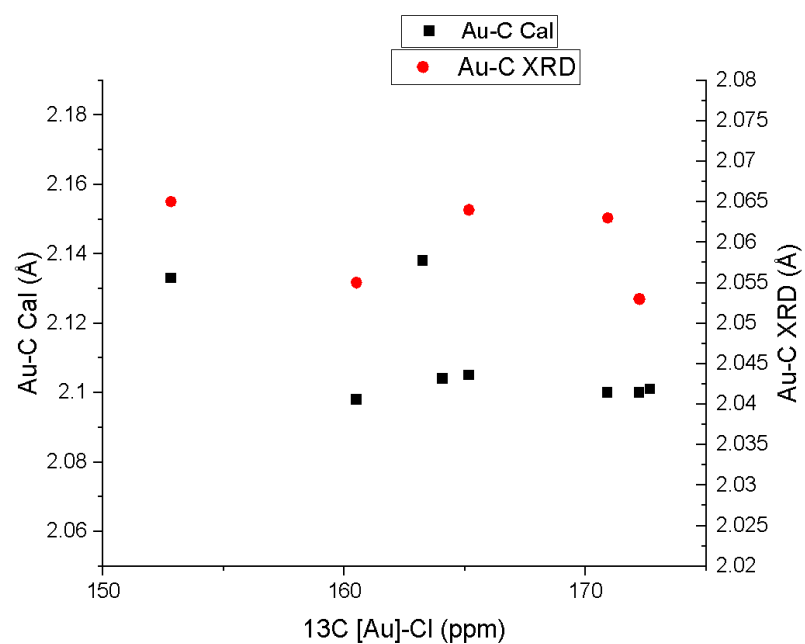
Figure 2.108: Calculated M-C bond lengths plotted against the ^{13}C NMR chemical shifts for the gold(III) complexes.
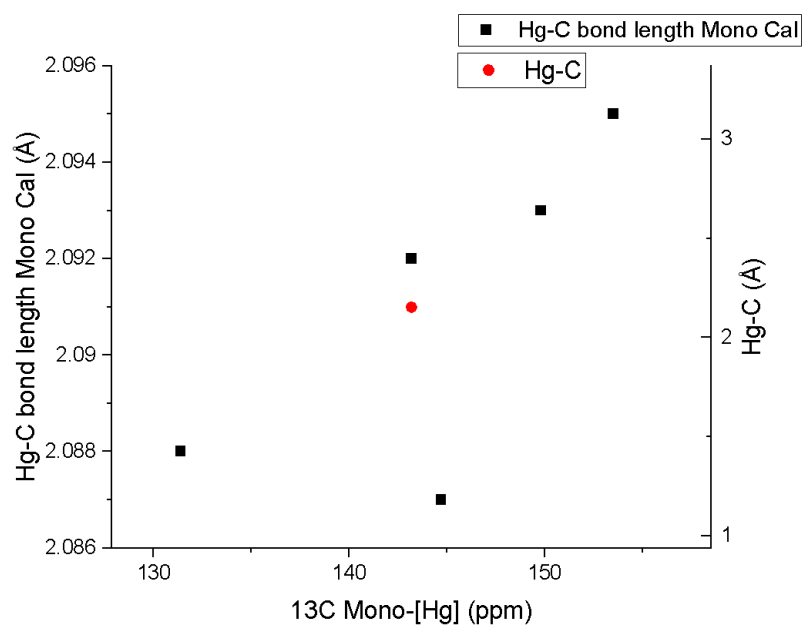
Figure 2.109: Calculated M-C bond lengths plotted against the ^{13}C NMR chemical shifts for the mercury(II) complexes .

2.18.1　　　The Shifting of the Pyridyl Protons On Changing Substitution Patterns
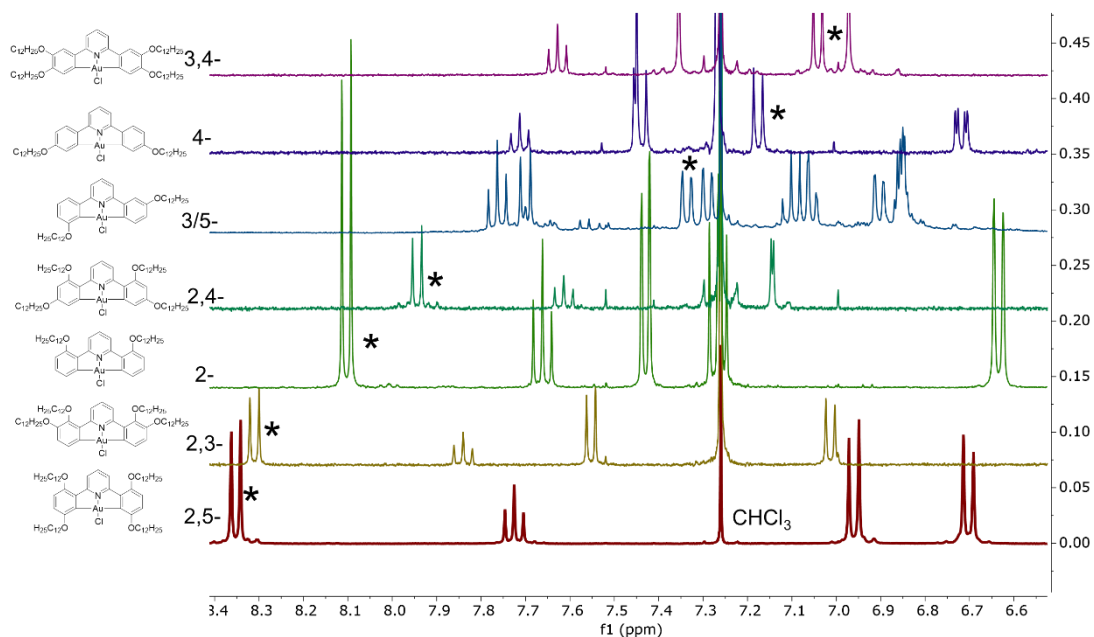
Figure 2.110: Aromatic region for all chlorogold(III) complexes in CDCl₃. The 3-pyridyl hydrogen resonance is indicated with ''.*

A significant effect on the chemical shift of the 3-pyridyl hydrogens is observed as the substitution pattern on the phenyl unit varies (Figure 2.110). Thus, while the triplet pyridyl hydrogen chemical shift lies between 7.6 – 7.9 ppm for all complexes, the chemical shift of the doublet for the *meta*-hydrogen varies from 7.04 ppm (**3,4-[Au]-Cl**) to 8.35 ppm (**2,5-[Au]-Cl**). The smallest chemical shifts are found when there is not an alkoxy chain in the 2-position, but as soon as there is a chain in that position the resonance shifts downfield. A major factor in this change will be the proximity of the alkoxy oxygen of the chain (Figure 2.111). Consideration of the single crystal structures of the chlorogold complexes, **2-Au-Cl**, **2,3-[Au]-Cl** and **2,5-[Au]-Cl**, while acknowledging that molecular packing in a crystal structure places different constraints on molecules, does indicate the presence of some degree of interaction between the oxygen of the alkoxy group and the pyridyl hydrogen, with the distance between the atoms measuring ~2.2 Å (van der Waals radii: 1.72 Å). Yet, clearly there are some substituent electronic effects, too, as the chemical shift seen for **2,3-** and **2,5-[Au]-Cl** is ~0.2 ppm higher than that for **2-[Au]-Cl**, whereas in **2,4-[Au]-Cl** the chemical shift is some 0.2 ppm lower. Similarly, the chemical shift for the hydrogen in **3,4-[Au]-Cl** is almost 0.2 ppm lower than in **4-[Au]-Cl**. In the complexes with an alkoxy chain in the 2,2′-positions, these movements could be

144

rationalised by the effect of the second alkoxy chain on the electron density at the 2,2′-oxygens and the effect this has on the interaction with the *meta*-hydrogens. However for the 3,3′-/ 3,3′,4,4′- pair, this cannot be the case, which may hint at a different mechanism altogether.

*Figure 2.111: Molecular structure of **2-[Au]-5**, showing the close contact between the pyridyl hydrogen and the oxygen from the alkoxy chain.*

2.19 Concentration-Dependent Aggregation of the Gold Complexes in Solution

Concentration-dependent shifting of NMR signals due to aggregation effects is known in the literature for some square-planar complexes, such as those of platinum(II).[90] This can be due to the availability of the axial positions and the dz^2 orbital, which can lead to intermolecular interactions, as well as intermolecular interactions from the ligand π-system. In this study, shifting of the ^{1}H NMR signals as a function of concentration was observed for gold complexes substituted in the 2,2′-positions of the phenyl ring of the C^N^C pincer ligand; such effects had also previously been observed in complexes substituted in the 4,4′-position and particularly the 3,3′,4,4′-positions,[49] as well as in other related systems.[91-94] In order to investigate the effect further ^{1}H NMR spectra (500 MHz, CDCl₃) were recorded at a range of concentrations for **2-[Au]-Cl** and the related phenylacetylide complexes, **2-[Au]-2-10** and **2,3-[Au]-2-10**. Additional measurements were carried out by Curtis, under supervision, on **2,5-[Au]-2-10**, **2-[Au]-3-14**, **3/5-[Au]-Cl**, and **2,3-[Au]-3-10**,[95] and Curtis also carried out Job plot analysis on complexes that displayed shifting using Equation 2.1:

145

Equ. 2.1
$$d_0 = \frac{(d_d - d_m)\left(1 + \left(1 - \sqrt{(8Kc+1)}\right)\right)}{4Kc} + d_m$$

where d_0 is the observed chemical shift, d_d is the estimated dimer shift, d_m is the estimated monomer shift and c is the concentration at which K is calculated at. A non-linear regression using IBM's SPSS program package was carried out.

2.19.1 Complexes Substituted in the 2,2′-Positions

Downfield shifting of all aromatic signals related to the cyclometallated ring on decreasing concentration was observed for **2-[Au]-Cl** (Figures 2.112 and 2.113), **2-[Au]-2-10** (Figures 2.116 and 2.117) and **2-[Au]-3-14**, with the effect levelling off at a concentration of 0.1 mM. The shift for **2-[Au]-Cl** was significant at ~0.12 – 0.14 ppm from a concentration of 14.2 mM to 0.5 mM. The same degree of shifting (~0.12 ppm) was observed in the alkoxy signal at ~4.00 ppm (Figure 2.114), through those relating to the –CH₂C*H*₂CH₂- resonances in the chains at <2.00 ppm were effectively concentration independent. The magnitude of this shifting is significantly larger than that previously reported for the related 3,3′,4,4′-tetrasubstituted gold(III) complexes. For a phenylacetylide ligand substituted in the 3,4,5-positions with dodecyloxy chains, **3,4-[Au]-3-12**,[50] the $\Delta\delta$ was determined to be in the range 0.07 – 0.06 ppm. Smaller chemical shifts changes were observed for the resonances assigned to the C^N^C hydrogen atoms for **2-[Au]-2-10** (0.04 -0.03 ppm) and **2-[Au]-3-14** (0.04 – 0.02 ppm). The resonances relating to the phenylacetylide ligand, however, showed no concentration-dependent shifting (Figure 2.117). The same pattern is observed in the alkoxy region, with shifting observed in the resonances related to the C^N^C ligand and no shifting observed in resonances assigned to the phenylacetylide ligand.
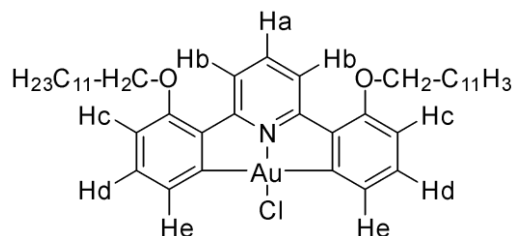
*Figure 2.112: Labelling scheme used for hydrogen atoms of **2-[Au]-Cl**.*
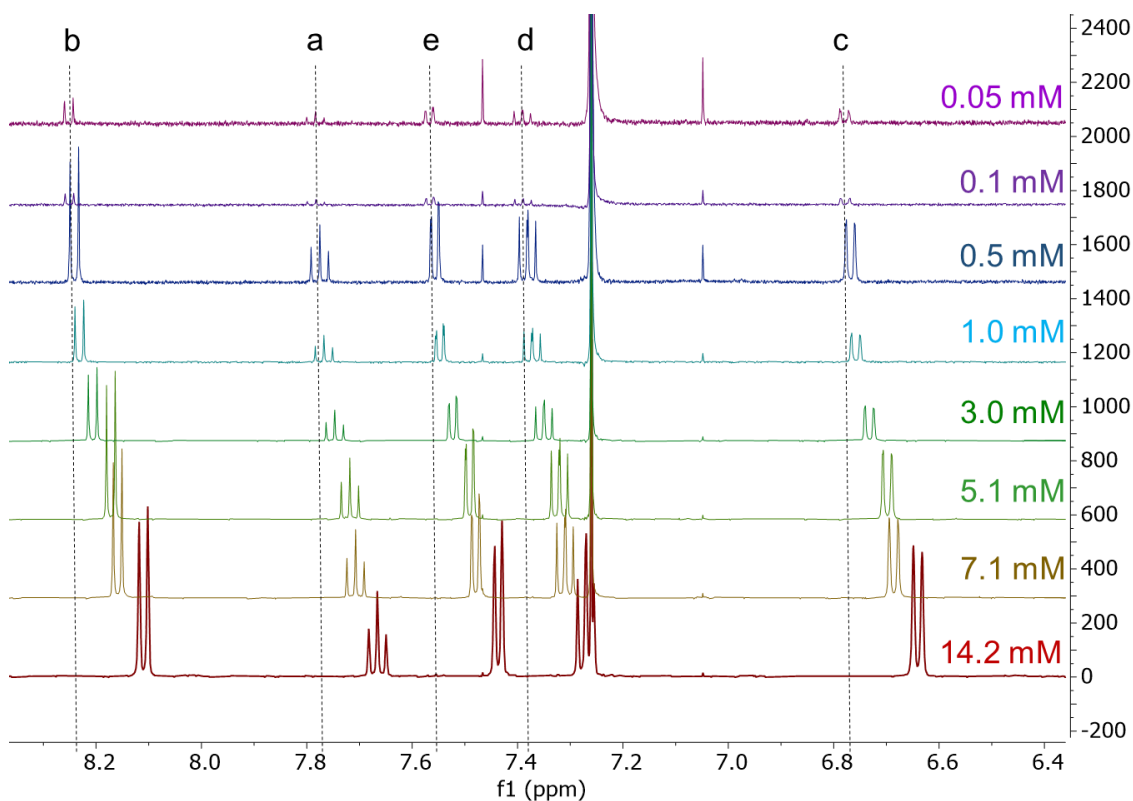
*Figure 2.113: The ${}^1H$ NMR spectra of **2-[Au]-Cl** (500 MHz, CDCl₃) at concentrations from 14.2 – 0.01 mM showing the aromatic region.*
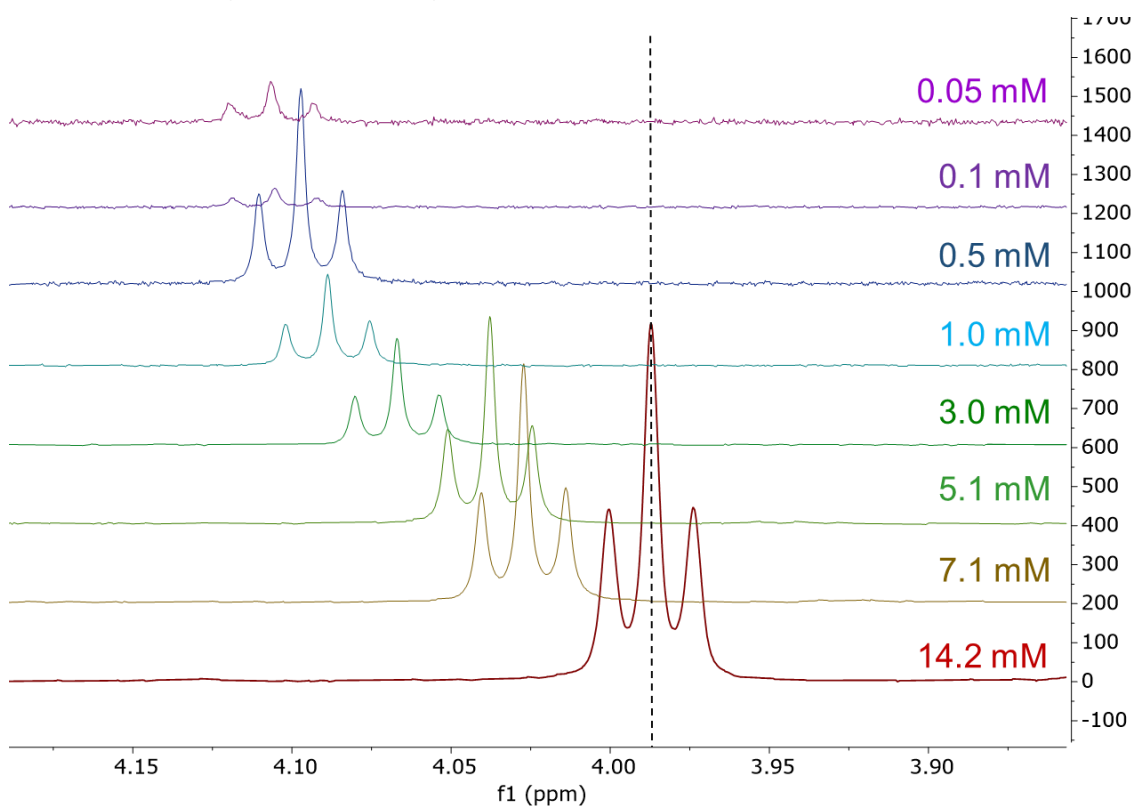
*Figure 2.114: The ${}^1H$ NMR spectra of **2-[Au]-Cl** (500 MHz, CDCl₃) at various concentrations showing the –OCH₂- region.*

These data are consistent with a ′back-to-back′ self-assembly in solution (Figure 2.115) for **2-[Au]-Cl**, **2-[Au]-2-10** and **2-[Au]-3-14**, as has been previously reported for the 4,4′- and 3,3′,4,4′-substituted isomers and related platinum(II) complexes.[50-52, 90] This is where the complexes pair in an antiparallel fashion, with the C^N^C pincer ligands associated, causing shifting of these signals in concentrated solution, hence the downfield shift, while the phenylacetylide ligands are directed away from each other and hence experience no additional interactions so the signals are independent of concentration.
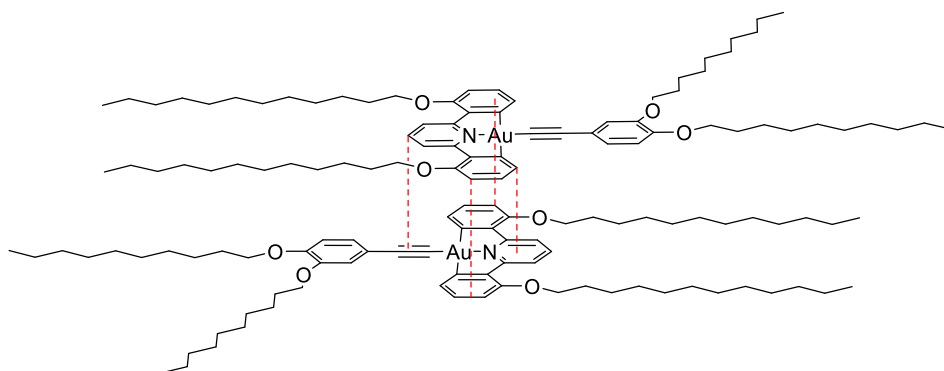
*Figure 2.115: Representative example of 'back-to-back' self-assembly in solution for **2-[Au]-2-10**.*
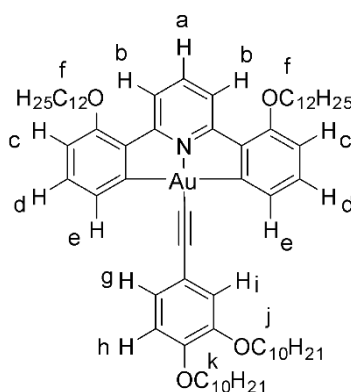
*Figure 2.116: Labelling scheme used for hydrogen atoms of **2-[Au]-2-10**.*
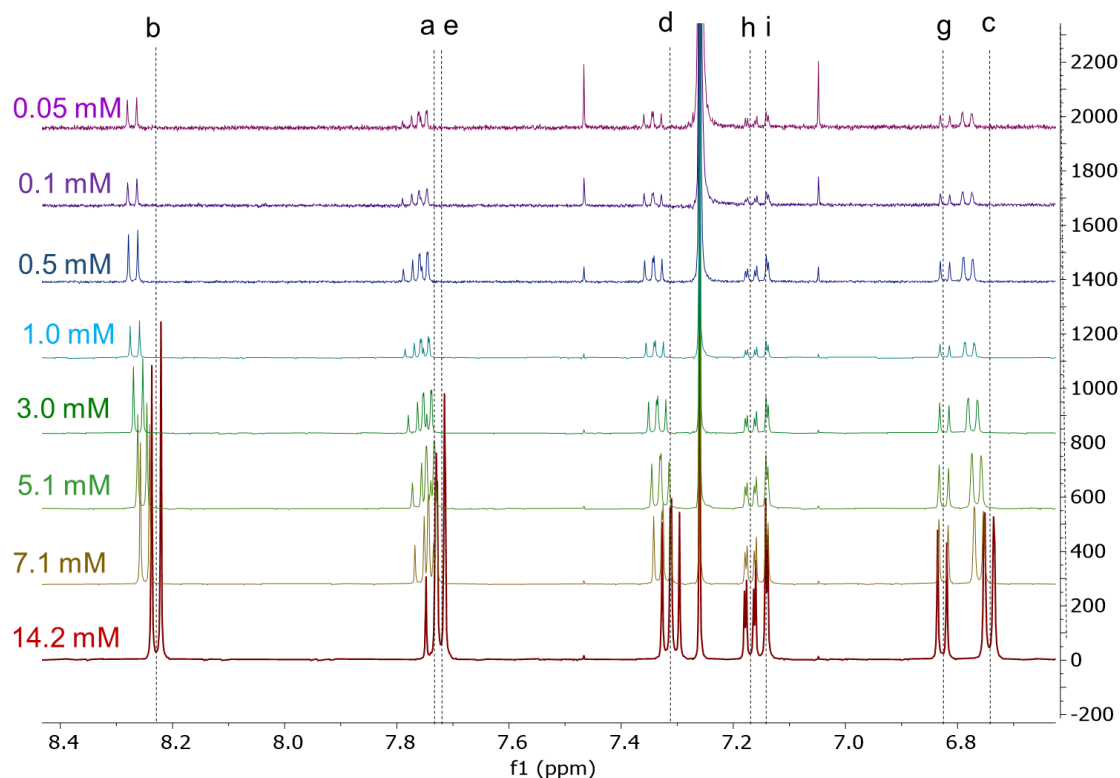
*Figure 2.117: The ^{1}H NMR spectra of **2-[Au]-2-10** (500 MHz, CDCl₃) at concentrations from 14.2 – 0.01 mM showing the aromatic region.*

Job's plot analysis was carried out on these samples by Curtis,[95] which is reported in Table 2.9. **2-[Au]-Cl** can be observed to have the highest equilibrium constant, K, with values significantly lower for complexes where the auxiliary ligand is a phenylacetylide, suggesting that the increased steric bulk of the phenylacetylide ligand disfavours intermolecular complex aggregation. A value of 25.2 dm^3 mol^{-1} was calculated for the equivalent complex, **3,4-[Au]-3-12**.[50, 95] The value is an order of magnitude larger than that calculated for **2-[Au]-3-14** indicating that the 3,3′,4,4′-substitution pattern is more favourable for induction of complex aggregation, however it is smaller than the calculated value for **2-[Au]-Cl**, reflecting the role that steric hindrance appears to play in how favourable complex aggregation is.

Table 2.9: Calculated Dimerisation Equilibrium Constants from Job's Plots.[95]

Complex	Calculated K / dm^3 mol^{-1}	% Concentration at 14.2 mM	% Concentration at 0.05 mM
2-[Au]-Cl	32.7	18.5	0.2
2-[Au]-2-10	7.2	7.2	0.03
2-[Au]-3-14	2.0	2.5	0.01
3,4-[Au]-3-12	25.2	16.3	0.1

2.19.2 Complexes with 2,2′,3,3′- and 2,2′,5,5′-Tetrasubstitution

Effectively no concentration-dependent shifting of ^{1}H NMR signals was observed for **2,3-[Au]-2-10** (Figure 2.119) in either the aromatic (Figure 2.120) or alkoxy regions. Equivalent measurements on complexes **2,3-[Au]-3-14** and **2,5-[Au]-2-10**, carried out by Curtis,[95] also displayed no shifting in either complex. It would appear that the change in substitution pattern on the C^N^C pincer ligand hinders aggregation of the complexes in solution, unlike the complexes substituted in the 2,2′-, 4,4′-, and 3,3′,4,4′- positions. A possible explanation for the behaviour in solution can be eluted on consideration of the crystal structures for **2-[Au]-Cl** and **2,3-[Au]-Cl**, through it must be noted that the behaviour in the static crystal structure is different from the more dynamic behaviour that can be observed in solution, but despite this molecular crystal structures can still be used to gain some idea of the solution behaviour. It can be observed that on viewing from the side (Figure 2.118) the presence of substituents in the 2,2′- and 3,3′-positions for **2,3-[Au]-Cl** results in steric hindrance forcing the chains in the 2,2′-positions to twist out of the plane of the molecule, while they lie in the plane of the molecule for **2-[Au]-Cl**. This would almost certainly disfavour aggregation for the former. While this behaviour is not observed for **2,5-[Au]-Cl** it is possible that the twisting by ~90° of the phenylacetylide ligand in **2,5-[Au]-R** to avoid a steric clash with the chains in the 5,5′-positions, would also disfavour aggregation in solution.
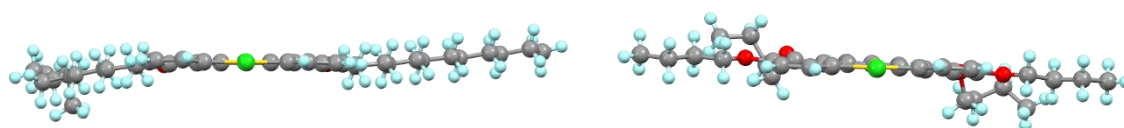
*Figure 2.118: The side-view for the molecular structures of **2-[Au]-Cl** (left) and **2,3-[Au]-Cl** (left).*
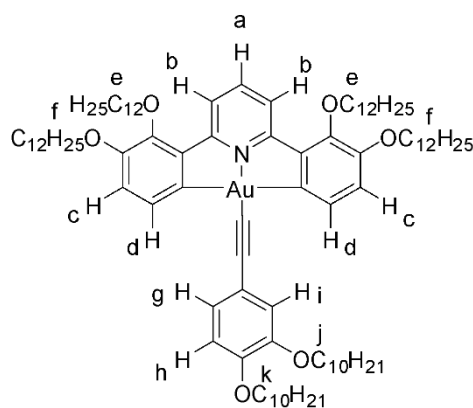
*Figure 2.119: Labelling scheme used for hydrogen atoms of **2,3-[Au]-2-10**.*

150
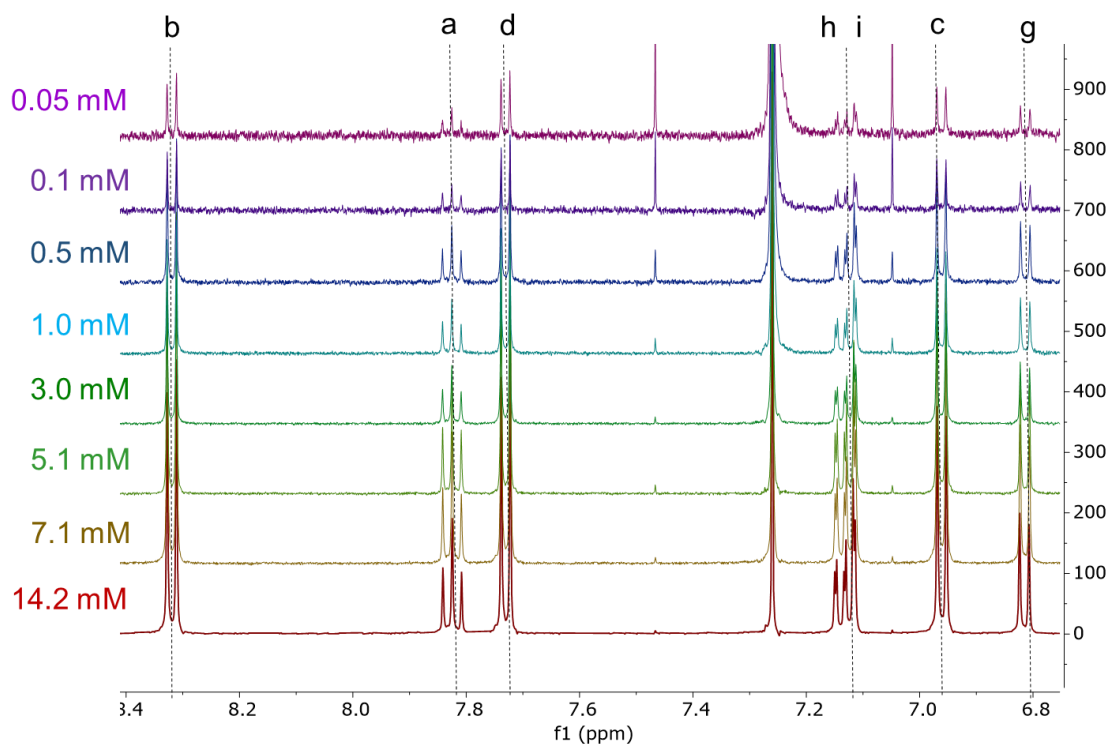
*Figure 2.120: The ¹H NMR spectra of **2,3-[Au]-2-10** (500 MHz, CDCl₃) at concentrations from 14.2 – 0.01 mM showing the aromatic region.*

2.20   Summary and Conclusions

A systematic investigation into the mercuration and auration of 2,6-*bis*(phenyl)pyridine ligands substituted with dodecyloxy chains on the phenyl ring has been undertaken. Introduction of an alkoxy substituent in the 2,2′-positions of the phenyl unit has been shown to have a striking impact. Sterically this prevents planarisation of the free ligand, introducing a barrier to free rotation and leading to atropisomerism, which is apparent through the desymmetrisation of pyridine ring hydrogens in NMR spectra. Interestingly, X-ray single crystal structures show that, on complexation to gold(III), square-planar complexes are formed and, under these conditions, the ligands do planarise.

Remarkably high yields of the pure monomercury(II) complexes (>80%) for **2-[Hg]**, **3-[Hg]** and **5-[Hg]** were realised from their parent ligands, comparing very favourably to the previously reported low yields of impure **4-[Hg]** and **3,4-[Hg]**.[50] The pure dimercurated complex, **2,3-[Hg₂]**, was isolated in >70% yield from the corresponding tetrasubstituted ligand and, using a butoxy-substituted ligands, it was possible to obtain single crystals from which an X-ray structure could be acquired. Mercuration of the 2,2′,5,5′-tetrasubstituted ligand gave a separable mixture of mono- and di-mercurated

151

complexes and again, use of the butoxy-substituted homologue allowed characterisation by single crystal X-ray diffraction. Inseparable mixtures of the mono- and dimercurated complexes were formed for 2,2′,4,4′- and 3,3′,5,5′-tetrasubstituted ligands in lower yields. It is clear from consideration of the data that the presence of a substituent in such a position as to cause twisting away from planarity of the parent ligand is required in order to achieve high yields of mercuration. In comparison, the lower yielding **4-[L]** and **3,4-[L]** have nearly planar ligands. The exception to this is **3,5-[L]** which shows a higher degree of loss of ligand planarity, but has low yields of mixed **3,5-[Hg]** and **3,5-[Hg₂]**, indicating that electronic effects evidently also play a role in at least some systems.

On reference to the literature it can be noted that while high yields (80-90%) of pure mercury(II) complexes are typical on the use of cyclometallating C^N ligands,[19-21, 23] such yields are not reproduced on use of cyclometallating C^N^C ligands, with 26% being the maximum reported yield for both unsubstituted 2,6-diphenylpyridine and 2,6-*bis*(4-*tert*-butylphenyl) pyridine.[49, 64, 65] On use of the related 1,3-bis(1-hexyl-2′-benzimidazoyl)-benzene ligand the monomercurated product was formed in 27% yield.[96] There is no doubt as to the nature of the product formed for these systems as purification was achieved *via* column chromatography, with ¹H NMR spectroscopy and elemental analysis carried out.[64, 65, 96] Most mercury complexes in the literature are used without further purification, however details are not given to indicate if this was merely to avoid the additional risk on additional handling of toxic mercury complexes or due to a lack of ability to purify. Overall, the lack of detailed synthetic procedures given in the vast majority of papers is frustrating, meaning that a full, systematic consideration of literature yields cannot be undertaken, with most authors content to merely report that the complexes were synthesised using previously reported methods, which while in itself is suggestive that yields continued to be low, cannot be taken as confirmation. It is particularly disappointing in consideration of some of the more highly functionalised ligands used, though it is notable that none exhibited substitution in the 2,2′-positions.
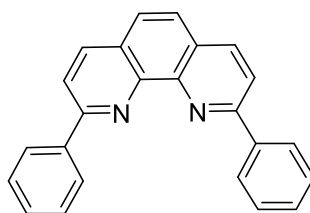
Figure 2.121: Structure of [2-(9-phenyl-1,10-phenanthrolinyl-2)phenyl].

No dimercurated systems have previously been reported in the literature, even on use of [2-(9-phenyl-1,10-phenanthrolinyl-2)phenyl] (C^N^N^C, Figure 2.121), which easily offers the possibility of two sites of C-H activation. Instead the monomercury complex is isolated in 60% yield.[15] Double mercuration is also not observed in any of the disubstituted pincer ligands studied, with it appearing that the presence of four substituents in total is required for this to occur. However, previous work showed **3,4-[L]** only undergoes monomercuration despite the presence of four substituents[50] and this study has found that **3,5-[L]** also behaves differently. This would suggest not only that four alkoxy groups are required for dimercuration, but that the electronics of the phenyl ring also matter and that, in particular, substitution in the 2,2′-positions is key. That being said, while **2,3-[L]** only forms the dimercurated complex, complexes that readily form both show a preference for formation of the monomercury complex on use of lower concentrations, lower reaction temperatures and use of one equivalent of mercury acetate, indicating that there is a delicate balancing of several factors that lead to dimercuration. The difference in behaviour of the 2,2′,3,3′- and 2,2′,5,5′-tetrasubstituted systems is likely to be due to a steric effect from the chains in the 5,5′-positions disfavouring dimercuration, since NMR studies suggest similar electronic properties for both systems and ligand torsion angles are similar.

There is evidence from the literature that initial coordination of the mercury(II) ion to the nitrogen atom in the ligand is of importance to form the *N*-coordinated complex in the mechanistic study of the mercuration of neutral mono-substituted triazoles by Lin *et al.*[23] Use of the acetate ligand was key in enabling a concerted metalation-deprotonation to occur to give the C^N complex. Mechanistic studies carried out by Goult on the mercuration of the C^N^C ligand[66] also suggest a similar mechanism, with the presence of the pyridine nitrogen atom key. Further, successful methods of direct auration with phenylpyridine ligands have also sometimes demonstrated the initial formation of the *N*-coordinated [AuCl$_3$(HL)], with subsequent formation of [AuLCl$_2$]. The non-bonding interaction between the ligand heteroatoms and gold was key in reaction success.[24, 25] On consideration of this, and the reported experimental data, it would suggest that the result of the loss of ligand planarity for ligands with a substituent in the 2,2′-positions is to make the pyridine nitrogen atom less sterically hindered due to one phenyl ring being twisted

away from the pyridine ring plane, enabling an easier approach for coordination of the metal ion to said heteroatom, initialising the mechanistic pathway.

Subsequent transmetalation from these mercury complexes gave lower conversion to the target gold complexes where mercuration yields were high, particularly for dimercurated complexes, with appreciable quantities of dimercurated complexes still present after reaction. However, the high initial yield on mercuration meant that the overall yield still remained higher than when **4-[Au]-Cl** and, in particular, **3,4-[Au]-Cl**, were used. Auration of a mixture of **3-[Hg]** and **5-[Hg]** gave selective mercuration of **3-[Hg]** to give only an unsymmetric complex, **3/5-[Au]-Cl**, while surprisingly **3,5-[Hg]** failed to aurate. **2,4-[Au]-Cl** proved challenging to purify due to the remaining presence of **2,4-[Hg₂]**, with yields <6%.

^{199}Hg NMR studies were undertaken for all mercury(II) complexes, with chemical shift range, depending on substituent positions, of over nearly 100 ppm, with the magnitude of the chemical shift (lying in the region -950 to -1020 ppm) indicating the presence of secondary bonds to electronegative atoms in solution. The X-ray structures indicate that such bonds are to both nitrogen and oxygen atoms. These data, in conjunction with ^{1}H and ^{13}C{^{1}H} NMR data, were used to consider the effect of substitution pattern variation on the molecular electronic properties. Chemical shift patterns were reproduced across the free ligand, mercury(II) and gold(III) complexes, with higher chemical shifts being observed with increasing electropositivity of the metal. **2-[M]**, **4-[M]** and **2,4-[M]** gave the highest ^{1}H and ^{13}C{^{1}H} NMR chemical shifts for the carbon that metallates (for the free ligand these are in the region 128-132 ppm), reflecting the positive directing effect of these positions of substitution on the position of interest. On changing the additional substituent position from the 4,4′- to 3,3′- and then to 5,5′-positions, the chemical shift sequentially decreases (132 ppm to 122 ppm to 117 ppm). **3,4-[M]**, **3-[M]**, **5-[M]** and **2,5-[M]** all had similar chemical shifts (~119 ppm), whereas **3,5-[M]** was quite different (106 ppm), reflecting the electronic presence of two *meta*-position groups on this position. This is likely to relate to the behaviour on metalation for the 3,3′,5,5′-tetrasubstituted ligand. On consideration of the other positions the lack of corresponding correlation with yield and reaction product indicates that the primary factor behind the differing behaviour on mercuration is likely steric in nature, relating to the degree of loss of planarity observed in the free ligand. For example **2-[M]** and **4-[M]** display very similar chemical shifts, yet

4-[L] gives low yields on mercuration and **2-[L]** high, however the degree of distortion from planarity for **2-[L]** is significantly larger.

Preparation of a palladium(II) dimer species, with subsequent transmetalation to form the chlorogold complex, proved successful, leading to **2-[Au]-Cl** and **2,3-[Au]-Cl** in 4% and 15% yield respectively.[85] Further, rhodium(III) catalysed auration was successful, giving **2,3-[Au]-Cl** in 11% yield. Both routes for **2,3-[Au]-Cl** were competitive with the route *via* a mercury complex. However, unfortunately neither reaction using the present conditions was successful for ligands with other substitution patterns nor, coming at the very end of lab work, has there been any opportunity to investigate optimisation or widening the reaction scope. This is of importance as if the range of substrates can be increased then the method can readily replace the intermediacy of mercury complexes. Currently, the requirement of toxic mercury intermediates for synthesis of cyclometallated gold(III) complexes, will impede any attempt to commercialise this class of compounds, with industry refusing absolutely to consider such a route. Therefore, despite the current limitations, this is a significant discovery as the first reported mercury-free synthesis of un-activated C^N^C ligands and it is hoped that future work can optimise both mercury-free routes, which would be important for taking this chemistry forward for successful, practical applications.

2-[Au]-Cl, **2,3-[Au]-Cl** and **2,5-[Au]-Cl** were connected in good yields (70 – 90%) to phenylacetylide ligands substituted with various lengths and numbers of alkoxy, alkyl and perfluoro chains. X-ray single crystal structures were obtained for several derivatives.

^{1}H NMR spectra were recorded for **2-[Au]-Cl** and **2-[Au]-2-10** at different concentrations (up to 15 mmol dm^{-3}) and showed the occurrence of concentration-dependent aggregation. Only hydrogens on the pincer backbone of the complexes were affected, suggesting a 'back-to-back' arrangement with the pincer sections lying above/below one another in an antiparallel fashion. Such behaviour has been previously observed in complexes substituted in the 3,3′,4,4′-positions.[50-52] Similar studies of **2,3-[Au]-2-10** and **2,5-[Au]-2-10** did not show evidence of self-assembly. For **2,3-[Au]-2-10** this is most likely because, as indicated in single crystal structure determinations, the presence of the 2,2′-chains in the plane of the complex forces the 3,3′-chains to 'escape' out of the plane so suppressing aggregation. For **2,5-[Au]-2-10**, however, the position of the 5,5′-chains

155

leads to a steric clash with the alkoxy chains at the 3,5-positions of the phenylacetylide. Crystallographic evidence suggests that this leads to the phenyl ring twisting out of plane taking the 3- and 5-alkoxy groups with it, once more suppressing self-association.

2.21 References

1. V. W.-W. Yam, S. W.-K. Choi, T.-F. Lai and W.-K. Lee, *J. Chem. Soc., Dalton Trans.*, 1993, 1001–1002.
2. A. Vogler and H. Kunkely, *Coord. Chem. Rev.*, 2001, **219-221**, 489-507.
3. M. C. Tang, M. Y. Chan and V. W. Yam, *Chem. Rev.*, 2021, **121**, 7249-7279.
4. C. Bronner and O. S. Wenger, *Dalton Trans.*, 2011, **40**, 12409-12420.
5. R. Kumar and C. Nevado, *Angew. Chem. Int. Ed.*, 2017, **56**, 1994-2015.
6. H. G. Raubenheimer and H. Schmidbaur, *J. Chem. Educ.*, 2014, **91**, 2024-2036.
7. K. M. Wong, X. Zhu, L. L. Hung, N. Zhu, V. W. Yam and H. S. Kwok, *Chem. Commun.*, 2005, 2906-2908.
8. V. W. Yam, K. M. Wong, L. L. Hung and N. Zhu, *Angew. Chem. Int. Ed.*, 2005, **44**, 3107-3110.
9. D. A. Rosca, D. A. Smith and M. Bochmann, *Chem. Commun.*, 2012, **48**, 7247-7249.
10. F. Cima, *Organometallic Compounds in the Environment*, John Wiley & Sons Ltd, Chichester, 2 edn., 2003.
11. R. C. Larock, *Angew. Chem. Int. Ed.*, 1978, **17**, 27-37.
12. P.-A. Bonnardel and R. V. Parish, *J. Organomet. Chem.*, 1996, **515**, 221-232.
13. O. Dimroth, *Ber. Dtsch. Chem. Ges.*, 1898, **31**, 2154-2156.
14. O. Dimroth, *Ber. Dtsch. Chem. Ges.*, 1899, **32**, 758-765.
15. O. Dimroth, *Ber. Dtsch. Chem. Ges.*, 1902, **35**, 2032-2045.
16. L. G. Kuźmina and Y. T. Struchkov, *CCACAA*, 1984, **57**, 701-724.
17. X. L. Cui, Y. J. Wu, C. X. Du, L. R. Yang and Y. Zhu, *J. Organomet. Chem.*, 1999, **10**, 1255-1262.
18. Y. Wu, S. Huo, J. Gong, X. Cui, L. Ding, K. Ding, C. Du, Y. Liu and M. Song, *J. Organomet. Chem.*, 2001, **637-639**, 27-46.
19. O. N. Gorunova, I. M. Novitskiy, Y. K. Grishin, I. P. Gloriozov, V. A. Roznyatovsky, V. N. Khrustalev, K. A. Kochetkov and V. V. Dunina, *Organometallics*, 2018, **37**, 2842-2858.
20. O. Bumbu, C. Silvestru, M. Concepción Gimeno and A. Laguna, *J. Organomet. Chem.*, 2004, **689**, 1172-1179.
21. S. Attar, J. H. Nelson and J. Fischer, *Organometallics*, 1995, **14**, 4776-4780.
22. A. F. M. J. Van Der Ploeg, C. E. M. Van Der Kolk and G. Van Koten, *J. Organomet. Chem.*, 1981, **212**, 283-290.
23. N.-C. Lin, H. J. H. Syu, A. R. Naziruddin, F.-C. Liu and I. J. B. Lin, *RSC Advances*, 2017, **7**, 11652-11656.
24. E. C. Constable and T. A. Leese, *J. Organomet. Chem.*, 1989, **363**, 419-424.
25. E. C. Constable, R. P. G. Penney and T. A. Leese, *J. Organomet. Chem.*, 1989, **361**, 277-282.
26. M. A. Cinellu, A. Zucca, S. Stoccoro, G. Minghetti, M. Manassero and M. Sansoni, *J. Chem. Soc., Dalton Trans.*, 1995, 2865-2872.
27. M. A. Ivanov and M. V. Puzyk, *Russ. J. Gen. Chem.*, 2001, **71**, 1660-1661.

28. R. V. Parish, J. P. Wright and R. G. Pritchard, *J. Organomet. Chem.*, 2000, **596**, 165-176.

29. M. Nonoyama, K. Nakajima and K. Nonoyama, *Polyhedron*, 1997, **16**, 4039-3044.

30. A. P. Shaw, M. Tilset, R. H. Heyn and S. Jakobsen, *J. Coord. Chem.*, 2010, **64**, 38-47.

31. M. S. M. Holmsen, A. Nova, K. Hylland, D. S. Wragg, S. Oien-Odegaard, R. H. Heyn and M. Tilset, *Chem. Commun.,* 2018, **54**, 11104-11107.

32. F. Rekhroukh, L. Estevez, C. Bijani, K. Miqueu, A. Amgoune and D. Bourissou, *Angew. Chem. Int. Ed.*, 2016, **55**, 3414-3418.

33. J. Serra, P. Font, E. D. Sosa Carrizo, S. Mallet-Ladeira, S. Massou, T. Parella, K. Miqueu, A. Amgoune, X. Ribas and D. Bourissou, *Chem. Sci.*, 2018, **9**, 3932-3940.

34. K. T. Hylland, I. L. Schmidtke, D. S. Wragg, A. Nova and M. Tilset, *Dalton Trans.*, 2022, **51**, 5082-5097.

35. A. Tlahuext-Aca, M. N. Hopkinson, C. G. Daniliuc and F. Glorius, *Chem. Eur. J.*, 2016, **22**, 11587-11592.

36. C. Y. Wu, T. Horibe, C. B. Jacobsen and F. D. Toste, *Nature*, 2015, **517**, 449-454.

37. J. F. Wunsch, L. Eberle, J. P. Mullen, F. Rominger, M. Rudolph and A. S. K. Hashmi, *Inorg. Chem.*, 2022, **61**, 3508-3515.

38. L. Nilakantan, D. R. McMillin and P. R. Sharp, *Organometallics*, 2016, **35**, 2339-2347.

39. B. David, U. Monkowius, J. Rust, C. W. Lehmann, L. Hyzak and F. Mohr, *Dalton Trans.*, 2014, **43**, 11059-11066.

40. S. C. Kui, J. S. Huang, R. W. Sun, N. Zhu and C. M. Che, *Angew. Chem. Int. Ed.*, 2006, **45**, 4663-4666.

41. J. Martin, E. Gomez-Bengoa, A. Genoux and C. Nevado, *Angew. Chem. Int. Ed.*, 2022, **61**, e202116755.

42. R. Kumar, A. Linden and C. Nevado, *Angew. Chem. Int. Ed.*, 2015, **54**, 14287-14290.

43. S. Stoccoro, G. Alesso, M. A. Cinellu, G. Minghetti, A. Zucca, M. Manassero and C. Manassero, *Dalton. Trans.*, 2009, 3467-3477.

44. O.-W. Chan, W.-T. Wong and C.-M. Che, *Inorg. Chem.*, 1994, **33**, 1266-1272.

45. K. C. Yim, E. S. Lam, K. M. Wong, V. K. Au, C. C. Ko, W. H. Lam and V. W. Yam, *Chem. Eur. J.*, 2014, **20**, 9930-9939.

46. D. Eppel, P. Penert, J. Stemmer, C. Bauer, M. Rudolph, M. Bruckner, F. Rominger and A. S. K. Hashmi, *Chem. Eur. J.*, 2021, **27**, 8673-8677.

47. D. Eppel, M. Rudolph, F. Rominger and A. S. K. Hashmi, *ChemSusChem*, 2020, **13**, 1986-1990.

48. D. Zhou, W. P. To, G. S. M. Tong, G. Cheng, L. Du, D. L. Phillips and C. M. Che, *Angew. Chem. Int. Ed.*, 2020, **59**, 6375-6382.

49. R. R. Parker, PhD Thesis, University of York, 2019.

50. R. R. Parker, D. Liu, X. Yu, A. C. Whitwood, W. Zhu, J. A. G. Williams, Y. Wang, J. M. Lynam and D. W. Bruce, *J. Mater. Chem. C*, 2021, **9**, 1287-1302.

51. R. R. Parker, A. J. McEllin, X. Zeng, J. M. Lynam and D. W. Bruce, *Liq. Cryst.*, 2021, **49**, 1162-1173.

52. R. R. Parker, R. F. Stracey, A. J. McEllin, X. Chen, Y. Wang, J. A. G. Williams, J. M. Lynam and D. W. Bruce, *ACS Omega*, 2022, **7**, 24903-24917.

53. C. Liu, N. Han, X. Song and J. Qiu, *Eur. J. Org. Chem.*, 2010, **2010**, 5548-5551.

54. F. Zhang, S. Zhang and X.-F. Duan, *Org. Lett.*, 2012, **14**, 5618-5620.

55. Y. Liu and H. Du, *J. Am. Chem. Soc.*, 2013, **135**, 12968-12971.

56. J. Leblond, H. Gao, A. Petitjean and J.-C. Leroux, *J. Am. Chem. Soc.*, 2010, **132**, 8544–8545.

57. B. M. Suijkerbuijk, D. M. Tooke, M. Lutz, A. L. Spek, L. W. Jenneskens, G. van Koten and R. J. Klein Gebbink, *J. Org. Chem.*, 2010, **75**, 1534-1549.

58. A. M. S. Silva, L. M. P. M. Almeida and J. A. S. Cavaleiro, *Tetrahedron*, 1997, **53**, 11645-11658.

59. Z. Ma, H. Liu, C. Zhang, X. Zheng, M. Yuan, H. Fu, R. Li and H. Chen, *Adv. Synth. Catal.*, 2015, **357**, 1143-1148.

60. A. Klein, K. Butsch and J. Neudörfl, *Inorg. Chim. Acta*, 2010, **363**, 3282-3290.

61. A. Santoro, A. C. Whitwood, J. A. G. Williams, V. N. Kozhevnikov and D. W. Bruce, *Chem. Mater.*, 2009, **21**, 3871-3882.

62. A. L. Isfahani, I. Mohammadpoor-Baltork, V. Mirkhani, A. R. Khosropour, M. Moghadam, S. Tangestaninejad and R. Kia, *Adv. Synth. Catal.*, 2013, **355**, 957-972.

63. T. Cardinaels, J. Ramaekers, P. Nockemann, K. Driesen, K. Van Hecke, L. Van Meervelt, G. Wang, S. De Feyter, E. F. Iglesias, D. Guillon, B. Donnio, K. Binnemans and D. W. Bruce, *Soft Matter*, 2008, **4**, 2172.

64. Z. T. Yu, X. L. Liu, Y. J. Yuan, Y. H. Li, G. H. Chen and Z. G. Zou, *Dalton Trans.*, 2016, **45**, 17223-17232.

65. K. M.-C. Wong, L.-L. Hung, W. H. Lam, N. Zhu and V. W.-W. Yam, *J. Am. Chem. Soc.*, 2007, **29**, 4350-4365.

66. C. Goult, unpublished work.

67. G. B. Deacon and G. N. Stretton, *Aust. J. Chem.*, 1985, **38**, 419-428.

68. R. K. Harris and B. E. Mann, *NMR and the Periodic Table*, Academic Press, London, 1 edn., 1978.

69. J.-Y. Lallemand, J. Oulie and J.-C. Hottard, *J. Chem. Soc., Chem. Commun.*, 1980, 436-438.

70. J. P. Sarju, PhD Thesis, University of York, 2016.

71. W. R. McWhinnie, Z. Monsef-Mirzai, M. C. Perry, N. Shaikh and T. A. Hamor, *Polyhedron*, 1993, **12**, 1193-1199.

72. D. S. C. Black, G. B. Deacon, G. L. Edwards and B. M. Gatehouse, *Aust. J. Chem.*, 1993, **46**, 1323-1336.

73. K.-H. Wong, K.-K. Cheung, M. C.-W. Chan and C.-M. Che, *Organometallics*, 1998, **17**, 3505-3511.

74. W. P. To, G. S. M. Tong, C. W. Cheung, C. Yang, D. Zhou and C. M. Che, *Inorg. Chem.*, 2017, **56**, 5046-5059.

75. W. P. To, D. Zhou, G. S. M. Tong, G. Cheng, C. Yang and C. M. Che, *Angew. Chem. Int. Ed.*, 2017, **56**, 14036-14041.

76. S. C. F. Kui, J.-S. Huang, R. W.-Y. Sun, N. Zhu and C.-M. Che, *Angew. Chem. Int. Ed.*, 2006, **45**, 4663-4666.

77. C. Cornioley-Deuschel, T. Ward and A. v. Zelewsky, *Helv. Chim. Acta*, 1988, **71**, 130-133.

78. I. A. Pocock, A. M. Alotaibi, K. Jagdev, C. Prior, G. R. Burgess, L. Male and R. S. Grainger, *Chem. Commun.*, 2021, **57**, 7252-7255.

79. V. Bonifácio, J. Morgado and U. Scherf, *Synlett*, 2010, **2010**, 1333-1336.

80. H. A. van Kalkeren, S. H. Leenders, C. R. Hommersom, F. P. Rutjes and F. L. van Delft, *Chem. Eur. J.*, 2011, **17**, 11290-11295.

81. R. L. Letsinger, J. A. Gilpin and W. J. Vullo, *J. Org. Chem.*, 1962, **27**, 627-674.

82. M. Ito, H. Kubo, I. Itani, K. Morimoto, T. Dohi and Y. Kita, *J. Am. Chem. Soc.*, 2013, **135**, 14078-14081.
83. A. Y. Fedorov and J.-P. Finet, *J. Chem. Soc., Perkin Trans. 1*, 2000, 3775-3778.
84. E. Langseth, PhD Thesis, University of Oslo, 2014.
85. A. J. McEllin, A. C. Whitwood, J. M. Lynam and D. W. Bruce, *Dalton Trans*, 2023, DOI: 10.1039/d2dt04114f
86. E. C. Constable, A. M. W. C. Thompson, T. A. Leese, D. G. F. Reese and D. A. Tocher, *Inorg. Chim. Acta*, 1991, **32**, 93-100.
87. D. Niedzielska, T. Pawlak, A. Wojtczak, L. Pazderski and E. Szlyk, *Polyhedron*, 2015, **92**, 41-51.
88. K. Kasahara, *Bull. Chem. Soc. Jpn.*, 1968, **41**, 1272.
89. C. A. Craig and R. J. Watts, *Inorg. Chem.*, 1989, **28**, 309-313.
90. A. F. Suleymanova, O. S. Eltsov, D. N. Kozhevnikov, A. O. Lantushenko, M. P. Evstigneev and V. N. Kozhevnikov, *ChemistrySelect*, 2017, **2**, 3353-3355.
91. S. K.-L. Siu, C. Y.-S. Chung and V. W.-W. Yam, *J. Organomet. Chem.*, 2017, **845**, 177-188.
92. K. C. Yim, V. K. Au, L. L. Hung, K. M. Wong and V. W. Yam, *Chem. Eur. J.*, 2016, **22**, 16258-16270.
93. K. C. Yim, V. K. Au, K. M. Wong and V. W. Yam, *Chem. Eur. J.*, 2017, **23**, 5772-5786.
94. S. K.-L. Siu, C. Po, K.-C. Yim, V. K.-M. Au and V. W.-W. Yam, *CrystEngComm*, 2015, **17**, 8153-8162.
95. L. J. Curtis, MChem Thesis, University of York, 2021.
96. A. Herbst, C. Bronner, P. Dechambenoit and O. S. Wenger, *Organometallics*, 2013, **32**, 1807-1814.

Chapter 3: The Thermal and Photophysical Properties of Phenylacetylide Gold(III) C^N^C Complexes

3.1   Emissive Gold(III) C^N^C Complexes

Gold exhibits two common oxidation states: +1 and +3. Photoactive gold(I) complexes have been widely reported in the literature, however it was only relatively recently that the photophysics of gold(III) complexes has also been studied in detail.[1-4]

Gold(III) is isoelectronic with platinum(II), which is well known for its photophysical properties, particularly when complexed with cyclometallating ligands.[2] As a result cyclometallated gold(III) complexes have become of interest as possible triplet emitters for electroluminescent devices or OLEDs as they are neutral, thermally stable, non-toxic and environmentally benign, and have potentially high brightness and efficiency.[2, 5, 6]
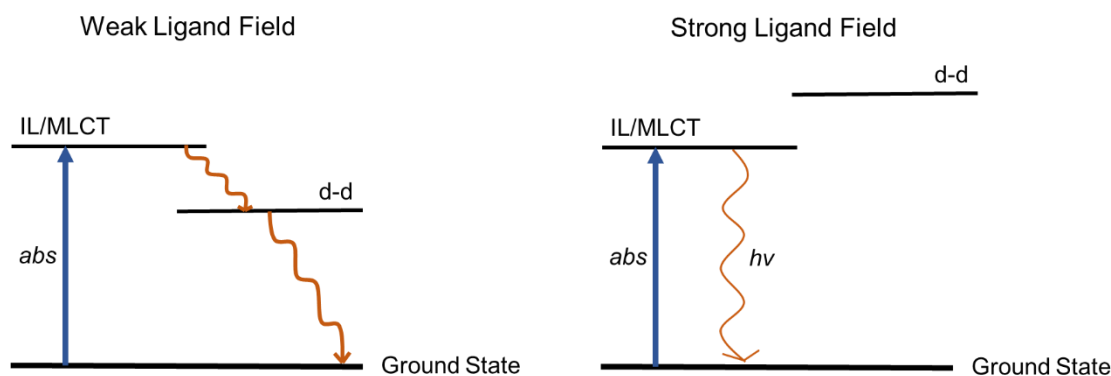
Figure 3.1: Energy level diagram for a gold(III) complex (a) in a weak ligand field situation and a strong ligand field situation (b).

A majority of gold(III) complexes rarely emit outside of the solid state or low-temperature glasses due to deactivation of excited states because of low-lying *d-d* states leading to quenching *via* thermal equilibration or energy transfer (Figure 3.1a).[7] $[AuCl_2(bipy)]^+$ for example emits in the solid form, but not in solution.[1, 2]

In 1993, the first gold(III) complex to be emissive at room temperature was reported by Yam *et. al.*[8] This was achieved by the introduction of mesityl (mes) or (trimethylsilyl)methylene (Me$_3$SiCH$_2$-) groups as a σ-donating ligand, with chelating bipyridine or phenanthroline C^C co-ligands (Figure 3.2a).[8] Then, in 1994, Che *et al* reported a cyclometallated C^N^N gold(III) complex, [Au(C^N^N-dp)Cl](X), where X = *p*-OTs or ClO$_4$ (Figure 3.2b), that was weakly emissive in solution, with an emission quantum yield of ~10^{-4}.[9] The emissive state was defined as a metal-perturbed intraligand state. Related luminescent complexes have been reported.[10, 11]
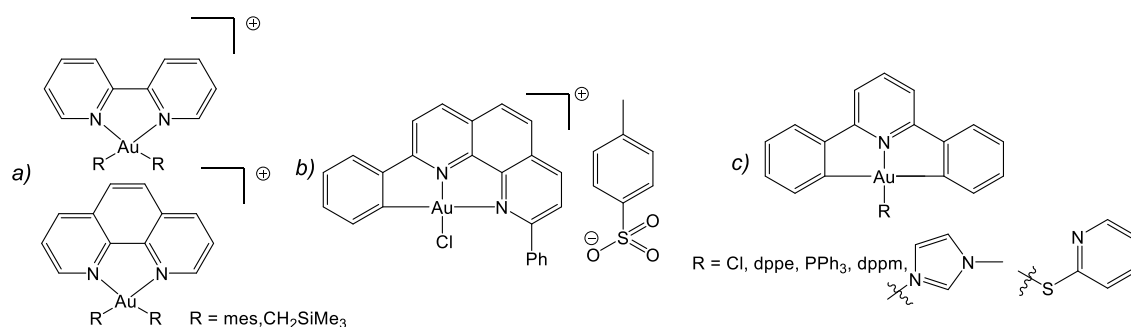
Figure 3.2: Structures of the earliest examples of luminescent gold(III) complexes, where (a)^{124} is the 1st reported example of an emissive gold(III) complex, (b)^9 is the 1st reported example of a emissive C^N^N gold(III) complex and (c)^{12} the first reported example of a room temperature, solution emissive C^N^C gold(III) complex.

The first example of a luminescent C^N^C complex (where C^N^C is 2,6-diphenylpyridine) was reported by Che *et al.* in 1998, who prepared [Au(C^N^C)Cl] and found it to be weakly emitting in a glass at 77 K.[12] Conversion to complexes with nitrogen-, phosphorus- or sulfur-donating ligands also gave complexes that were only luminescent in the solid state or at low temperature (Figure 3.2c).

Yam *et al.* later determined that the incorporation of rigid, cyclometallating ligands and strongly σ-donating ligands (alkynyl or carbenes), gave complexes of the general form [Au(RC^N^CR)(C≡C-R')] (where C^N^C is a modified 2,6-diphenylpyridine and C≡C-R a σ-donor alkynyl ligand),[5, 13] that were emissive in solution at room temperature. Indeed these were the first examples of room-temperature, solution-emissive gold complexes, opening the possibility for use in many applications.[2, 6] The presence of the strong σ-donating ligand increased the energy of the metal *d-d* state, making them thermally inaccessible at room temperature in various media (Figure 3.1b).[6, 14]

3.2   Gold(III) Complexes with Alkynyl Ligands

a

R_1= H, R = C_6H_5, C_6H_3-Cl-*p*,
$C_6H_4OCH_3$-*p*,
C_6H_4-NH_2-*p*

R_1 = *t*Bu, R = C_6H_5

b

R_1 = R_2 = H, R = C_6H_5, C_6H_4-Cl-*p*, C_6H_4-NO_2-*p*,
C_6H_4-OCH_3-*p*, C_6H_4-C_6H_{13}-*p*, C_6H_{13}

R_1 = H, R_2 = *t*Bu, R = C_6H_5

R_1 = C_6H_4-CH_3-p, R_2 = H, R = C_6H_4-C_6H_{13}-*p*
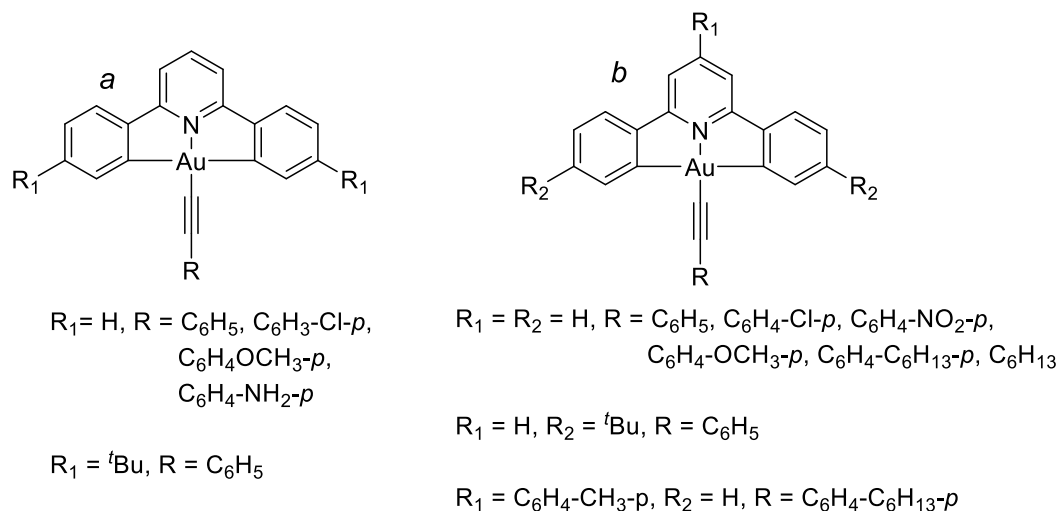
Figure 3.3: Representative examples of structures of some gold(III) C^N^C alkynyl complexes.[5-7]

Since this work by Yam,[5, 15] the most common strong σ-donor ligand used to create emissive gold(III) complexes is an alkynyl moiety (R-C≡C-) (Figure 3.3), with many early papers undertaking a systematic study of the effect of substituents on the photophysical properties.[5-7, 13, 16, 17]

Such complexes typically have vibronically structured absorption bands at ~300 – 400 nm, which are assigned,[5, 13] through DFT calculations, as a metal-perturbed, intraligand π-π* transition of the C^N^C ligand consisting of some degree of charge transfer from the phenyl to the pyridyl unit.[5] Vibrational progression spacing of 1310-1380 cm^{-1} corresponds to the C^N^C ligand skeleton vibration, indicating that this absorption is insensitive to the nature of the alkynyl ligand.[13] All complexes were strongly luminescent in solution in the range 468 - 611 nm, assigned as a metal-perturbed inter-ligand $^3[\pi\pi^*]$ transition on the C^N^C ligand.[5, 13] When R = phenyl (Figure 3.3b) an additional structureless lower-energy band at 620 nm was tentatively assigned as ^{3}LLCT ((π(C≡C-R) → π*(C^N^ C)).[5]

Introduction of electron-donating substituents on the C^N^C ligand, *e.g.* a *t*-butyl *para*-substituent on the phenyl ring of the C^N^C ligand to give [Au(*t*BuC^N^C*t*Bu)(C≡C-C_6H_5)] and the pyridyl ring to give [Au(C^N(*t*Bu)^C)(C≡C-C_6H_4-C_6H_{13}–*p*)] narrows the HOMO-LUMO gap, due to destabilisation of the HOMO π-orbital, resulting in

redshifting.[6, 7, 13] Introduction of electron-withdrawing groups[16, 17] on the phenyl units of the C^N^C ligand (-COOCH$_2$CH$_3$, CN, F, CF$_3$, OCF$_3$) increases the HOMO-LUMO gap due to HOMO stabilisation, allowing production of a sky-blue colour (λ_{max} falling in the range 466-492 nm).[16] Increasing numbers of electron withdrawing groups increases the HOMO stabilisation, resulting in increased hypsochromic emission shift.
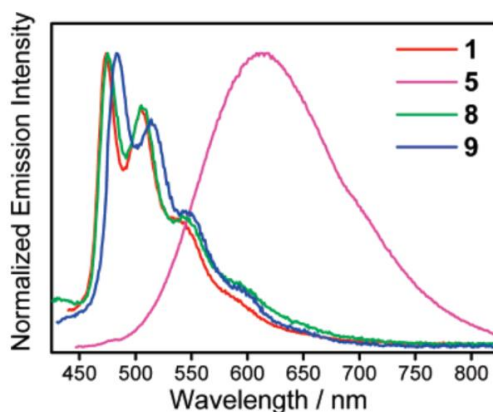
Figure 3.4: Emission of gold(III) complexes showing vibronically structured emission at 470-611 nm for all complexes ([Au(III)(C^N^C)(C$_6$H$_5$)](1), [Au(^{t}BuC ^N^C^{t}Bu)(C$_6$H$_5$)] (8) and [Au(C ^Ntol^C)(C$_6$H$_4$-C$_6$H$_{13}$-p)] (9)) apart from [Au(III)(C^N^C)(C$_6$H$_4$-NH$_2$-p)] (5), which shows a broad, structureless emission band at ~610 nm. Figure reproduced from Reference 7.[7]

Generally the photophysical properties appear to be dominated by the C^N^C ligand states, with tuning of emission colour possible by varying substituents to give emission λ_{max} over a range of 476 – 669 nm.[18] However, occasionally, on the introduction of certain strongly electron-donating or withdrawing substituents (*e.g.* –NH$_2$) on the phenyl alkynyl ligand, a change in the excited state nature from $^3[\pi\pi^*]$ to a low-lying alkynyl-to-pincer ligand-to-ligand charge-transfer absorption band ^{3}LLCT [π(C≡CC$_6$H$_4$R) → π^*(C^N^C)], results in a change in emission wavelength (Figure 3.4).[7]
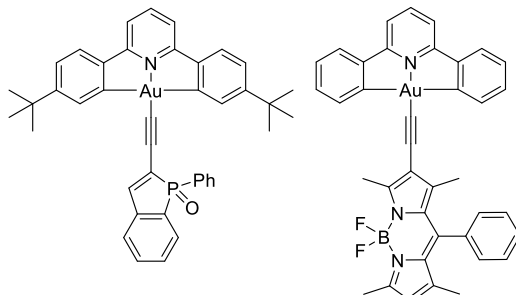
Figure 3.5: Structures of gold(III) C^N^C alkynyl complexes, containing heteroatoms in the alkynyl ligand.[19, 20]

A couple of complexes in which heteroatoms are present (a phosphole moiety[19] and a BODIPY moiety[20]) gave unusual singlet emission (Figure 3.5). No explanation was given for the change in emission origin in the phosphole complex,[19] while the change in the BODIPY complex emission was assigned as being due to the narrow HOMO-LUMO gap of the BODIPY ligand resulting in a large energy-gap between the S_1 and T_1 states (>1000 cm^{-1}).[20]

3.2.1   Mulifunctional Gold(III) Complexes

While the emissive behaviour of gold(III) C^N^C complexes is of interest, the introduction of other desirable properties, such as gelation, self-assembly and liquid-crystalline behaviour to form multifunctional materials, has become of interest in several studies.
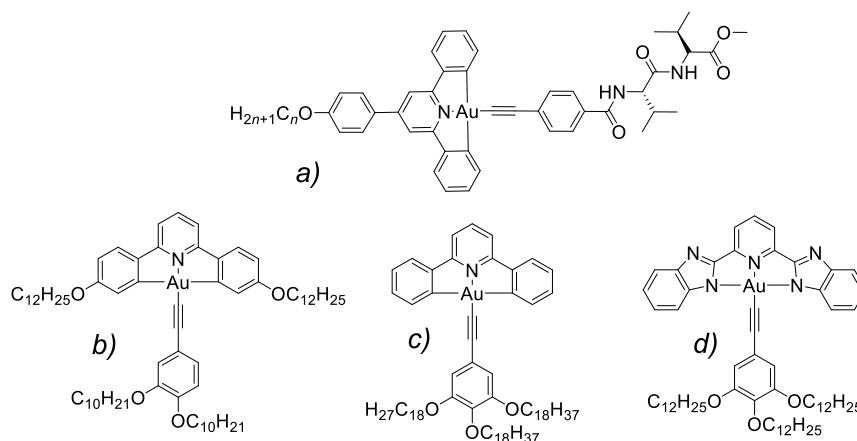
Figure 3.6: Some examples of gold(III) complexes which exhibit metallogels. Complex a) forms gels in DMSO when n = 6, 12, 18,[21] complex b) forms gels in 95:5 petroleum ether (40 – 60 °C):ethyl acetate;[22] complex c) forms gels in hexane and cyclohexane[23] and complex d) forms gels in chloroform.[24]

Gelation is reported in some gold(III) complexes due to hydrogen-bonding, π-π stacking, and hydrophilic-hydrophobic interactions, summarised in a 2018 review (Figure 3.6).[21-25] Compounds containing polar L-valine units formed gels in DMSO (Figure 3.6a),[21] while compounds substituted with long hydrophobic chains (Figure 3.6b,c)[22, 23] formed gels in non-polar solvents (*n*-hexane and cyclohexane). Gelation has been reported in some semifluorinated complexes, although the gels were not fully characterised.[22] The presence of long chains appears to be key in the formation of gels, with the chain nature determining the solvents in which gelation occurs. Complex aggregation and self-

assembly to form various structures are reported in several complexes.[26-28] Complexes that show some degree of self-assembly all contain long chains and frequently some degree of extended π-structure.

3.2.2 Liquid Crystallinity in Gold(III) Complexes
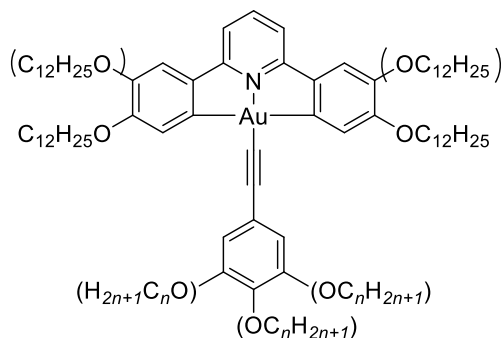
Figure 3.7: General structure for the formation of gold(III) alkynyl complexes, which were shown to form liquid crystalline phases.

Of great interest here is the work carried out on liquid-crystalline gold(III) alkynyl complexes by Parker *et al.* (Figure 3.7).[22, 29-31] It was determined that introduction of dodecyloxy-chains in the 4,4′- or the 3,3′,4,4′-positions of the C^N^C ligand, when a phenylacetylide ligand was present, induced columnar phase formation, with the phase stability and identity tuned by the number (one to three) and length of alkyl- and alkoxy-chains (n = 8, 10, 12, 14) present on the phenylacetylide ligand.[29] Phase formation appeared to be reliant on effective space-filling resulting in formation of 'disc-like' molecular geometries. The 3,3,′4,4′-tetrasubstituted complexes consistently gave hexagonal columnar phases, the complexes having an inherit 'disc-like' shape, however the 4,4′- disubstituted complexes, having a 'half-disc' shape, assembled with a back-to-back pairing, resulting in reduced mesophase stability. Introduction of perfluorinated chains destabilised mesophase formation, particularly for the 4,4′-disubstituted complexes.[30, 31]

The complexes with a 4,4′-disubstituted pincer ligand emitted at ~502 nm, in the green region, with vibronic coupling observed at room temperature (Figure 3.8a) and with a PLQY of 1-2%. The complexes with a 3,3′,4,4′-tetrasubstituted pincer ligand emitted in the yellow region at ~552 nm, with broad, poorly defined bands, indicating increased excited state mixing (Figure 3.8b). PLQY values were, however, much higher being reported up to 34%. The increase in the PLQY was assigned to the two additional

electron-donating alkoxy-substituents reducing the energy of the triplet excited state and increasing the gap to the *d-d* states. Excited state lifetimes were in the microsecond region, showing some dependency on the number of alkoxy chains on the phenylacetylide ligand, as did the emission quantum yields. The emission wavelength was observed to be independent of the alkynyl ligand identity and instead was dependant on the substitution pattern on the C^N^C pincer ligand. Several complexes were fabricated into OLEDs (5 wt% in PVK:OXD-7), with the best-performing device having an EQE of 7.14%.[22]
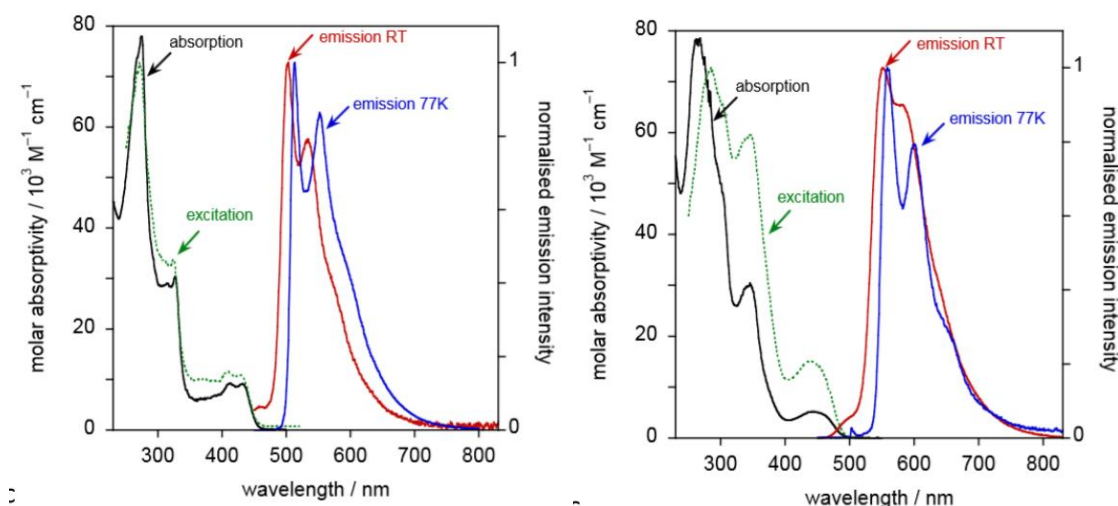
Figure 3.8: Example spectra of 2-chain gold(III) complex (a) and 4-chain gold(III) complex, reproduced from Reference 22.[22]

3.2.3 Use in OLEDs

There is great interest in use of gold(III) complexes in OLEDs and, over the past decade, there have been many papers published investigating use and how structure modification can affect OLED performance.[16, 18, 29, 32, 33] One compound has also been used in a memory device[34] and another investigated as a possible photosensitiser in production of hydrogen gas,[6] indicating further uses of interest for this class of complex. The use of gold(III) complexes in OLEDs has been reviewed previously.[33, 35, 36]

Several complexes have been used as *p*-dopants in OLEDs, with the nature of the pincer ligand substitution being the major control of emission colour. The introduction of fluorine atoms onto the phenyl unit of the pincer ligand gave sky-blue emission, with moderate EQEs of up to 5.5% and 11.3% (Figure 3.9a).[16, 18] Compound *b* (Figure 3.9) gives rise to green, OLEDs,[37] with vibronically structured absorption bands at 390 – 410 nm and an absorption tail at 475 – 500 nm. The OLED was optimised at 4 wt% dopant in

poly(methyl methacrylate) (PMMA) film to give a moderate 11.5% EQE at current efficiency of 37.4 cd A^{-1} and power efficiency of 26.2 lm W^{-1}. Compound *c* (Figure 3.9) also gave green solution-processable OLEDs,[38] emitting at 572 nm, with a good current efficiency of 56.4 cd A^{-1} and good EQE of 16.2%.

R$_1$ = F, R$_2$ = H, R$_3$ = F
R$_1$ = H, R$_2$ = OCF$_3$, R$_3$ = H
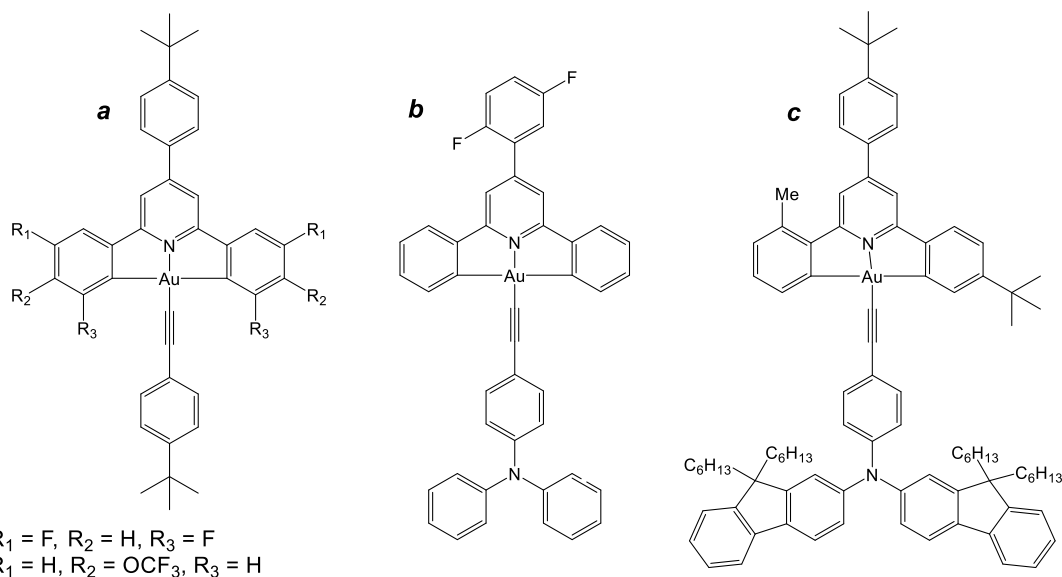
Figure 3.9: Structure of gold(III) complexes used as p-hole dopants to give a sky-blue colour (a),[16, 18] and green OLEDs (b)[37] and (c).[38]

R$_1$ = Et, R$_2$ = H, R$_3$ = ——≡—C$_6$H$_5$

R$_1$ = ^{n}Bu, R$_2$ = H, R$_3$ = ——≡—C$_6$H$_5$

R$_1$ = n-Hex, R$_2$ = H, R$_3$ = ——≡—C$_6$H$_5$

R$_1$ n-Hex, R$_2$ = 3,5-(^{t}Bu)$_2$, R$_3$ = ——≡—C$_6$H$_5$

R$_1$ n-Hex, R$_2$ = 3,5-(^{t}Bu)$_2$, R$_3$ = ——≡—p-(OMe)C$_6$H$_4$

R$_1$ = n-Oct, R$_2$ = H, R$_3$ = ——≡—C$_6$H$_5$
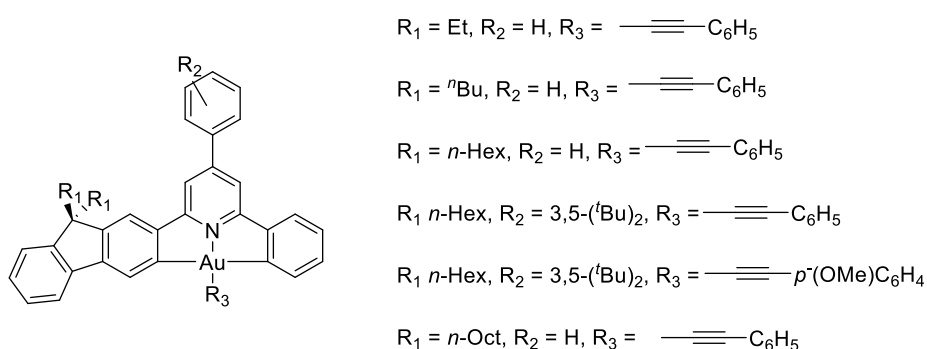
Figure 3.10: Structures of gold(III) complexes, containing a fluorene moiety.[22]

Replacement of one of the phenyl units of the C^N^C ligand with a fluorene moiety (Figure 3.10) gave yellow emission at 538 – 546 nm; a more than 100-fold increase in the emission quantum yield in the solid state up to 58% and a lifetime up to 200 μs in solution at room temperature, due to a change in the lowest triplet excited state from LLCT to ligand-centred $^3\pi\pi^*$.[39] Combination with a blue-emitting phosphorescent iridium(III) complex gave a colour-tuneable OLED.[40] White OLEDs (WOLEDs - CIE coordinates of (0.38,0.39) and (0.40,0.47)) were formed from use of yellow-emitting C^N^C gold(III) *p*-dopants combined with a blue-emitting iridium(III) complex (Figure 3.11), with moderate EQEs of 11.0% and 10.5%.[41] High PLQYs up to 86%, lifetimes of 1 μs and

broad bandwidths of 107 nm were reported. The introduction of dendrimers on the alkynyl ligand has also been investigated.[42-44]
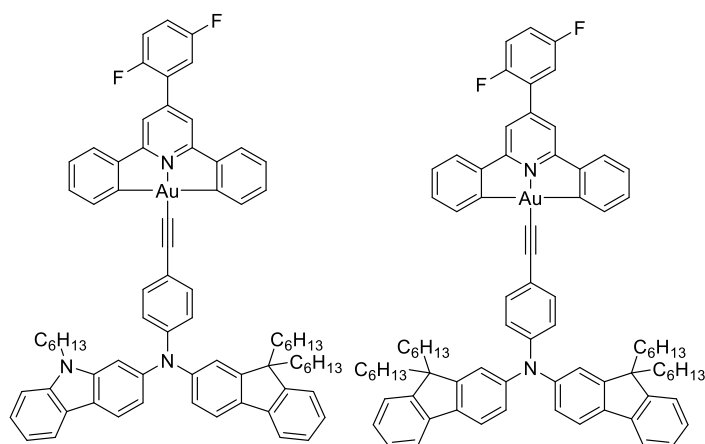
Figure 3.11: Yellow-emitting gold(III) p-dopants used with blue-emitting iridium(III) complex in white OLEDs.[41]

Bipolar gold(III) complexes, which contain both electron-rich and electron-poor moieties in the same molecule, are of interest due to the ability to tune the colour *via* alteration of the structure of two functional units and the possibility of improving hole and electron-transport properties of the emissive layer due to the presence of both in the same molecule. One example was synthesised by incorporation of both triphenylamine and an electron-accepting benzimidazole (Figure 3.12).[45] Increased methyl substitution on the central phenyl unit increased structural rigidity, decreasing the non-radiative decay to give a high PLQY of 75% in the solid state. A moderate EQE of 10.0% was achieved. Another bipolar complex was synthesised by introduction of an electron-transporting phosphine oxide moiety and a triarylamine hole-transporting auxiliary ligand, which gave a high PLQY of 70% in 1,3-*bis*(*N*-carbazolyl)benzene thin films (20 wt%), a lifetime of <3.9 μs and a moderately high EQE of 15.3%.[46] The PLQYs were determined to be 22-48% in solution.
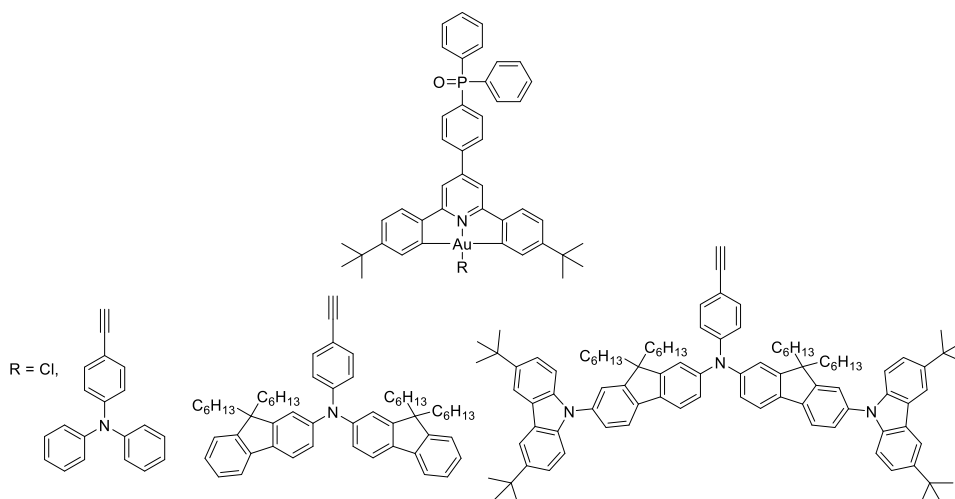
Figure 3.12: Structure of bipolar gold(III) complex containing phosphine oxide electron-transporting moiety and a triarylamine hole-transporting axillary ligand.[45]

3.3 Other Auxiliary Ligands

While the primary focus of the majority of investigation into gold C^N^C complexes has been on the use of alkynyl ligands as a strong σ-donating ligand, other ligands have been investigated, with generally no photophysics reported for weak σ-donor ligands.[12, 47-54] Photophysics for alternate strong σ-donor ligands (detailed below) has been reported. The interaction between different chromophores is frequently of interest. There are a few examples in the literature of molecules containing luminescent gold(IIII) complexes.[55-58]

3.3.1 Carbene ligands
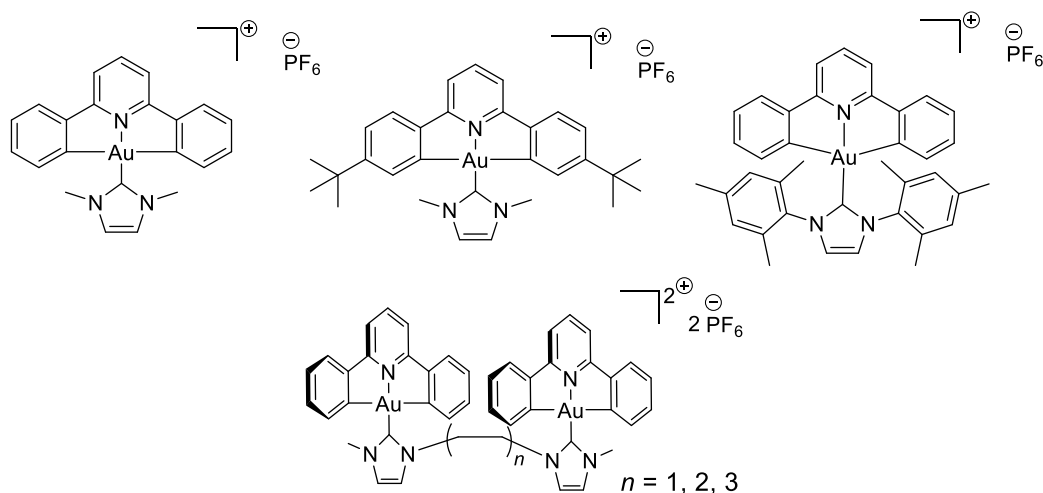
Figure 3.13: Structures of gold(III) complexes, containing a N-heterocyclic carbene auxiliary ligand.[59]

169

N-Heterocyclic carbenes (NHC) have been used as a strong σ-donor ligand to give luminescent C^N^C complexes.[59, 60] Absorption occurred at ~310 nm and 370 – 410 nm, which was insensitive to the NHC-ligand identity (Figure 3.13).[59] Emission properties in dichloromethane solution at room temperature were also typical of gold(III) complexes, occurring in the range 471 – 563 nm, with binuclear complexes typically emitting at longer wavelength. Encapsulating gold(III) carbene complexes in MOFs (Figure 3.14) increased emission intensity and lifetimes to levels equivalent to degassed solvent, giving a remarkable example of triplet emission in aerated conditions, and PLQYs up to 1%.[61]
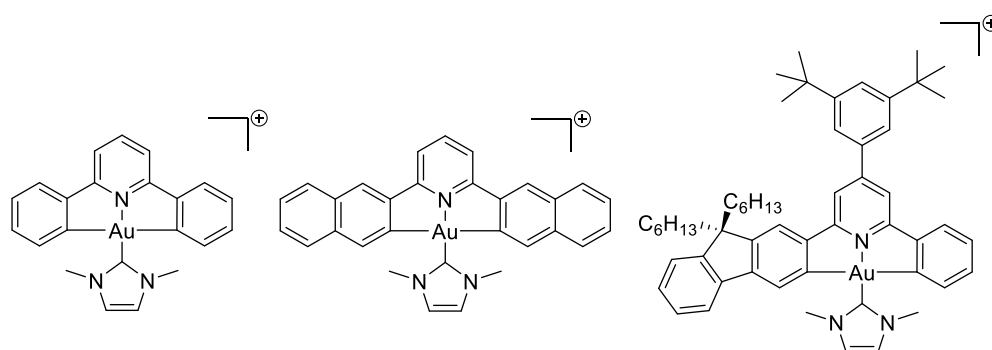
Figure 3.14: Structure of gold(III) complexes, containing a N-heterocyclic carbene, used for encapsulation in MOFs.[61]

3.3.2 Isonitrile and Allenylidene Ligands
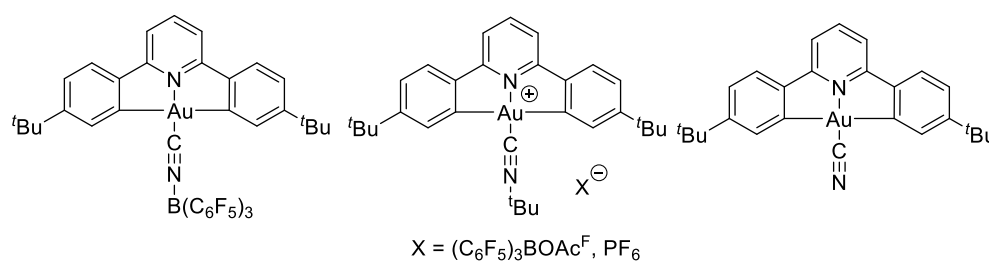
Figure 3.15: Structure of isonitrile ligand containing gold(III) complex and that of decomposition products.

There have been a few examples of introduction of a isonitrile ligand (C≡N-^{t}Bu) into a gold(III) C^N^C complex, with the resulting complexes being unstable in solution over several days (Figure 3.15).[39, 40, 62] As a cyanide ligand is a strong σ-donor, all three complexes were emissive in the yellow-green region, with the complex with the nitrile (CN) ligand an order of magnitude more intense (PLQY = 30.4%). This was assigned to the order of σ-donor strength (CN > CN-B(C$_6$F$_5$)$_3$ > CN-^{t}Bu), resulting in increased

LUMO stabilisation.[62] Replacement of one of the phenyl units of the C^N^C ligand with a fluorene moiety (auxiliary ligand = C≡N) gave PLQYs in the region of 40 – 44%.[39, 40]

An allenylidene ligand gave emissive gold(III) C^N^C complexes (Figure 3.16). When R = H the complex was weakly emissive in solution, however it gave intense, yellow emission (540 nm) in the solid state at 298 K, with lifetime 5.8 μs (no PLQY was reported).[63] In comparison, on addition of R = CH=CH-CH=CH on the C^N^C ligand dual emission occurred with weak emission at 450 nm (^{1}LLCT) and intense emission at 525 nm in dichloromethane solution at room temperature, with the later assigned as ^{3}LLCT, with PLQY of 3.3% and lifetime of 111 μs.
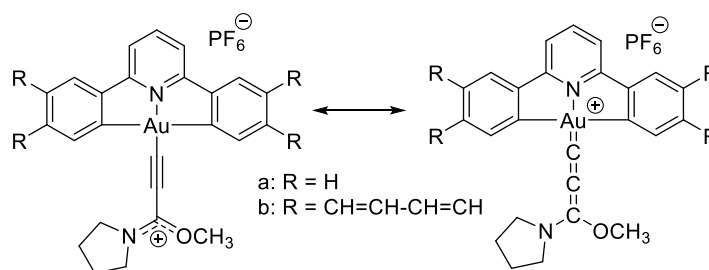
Figure 3.16: Structure of gold(III) complex, with allenylidene ligand.[63]

3.3.3 Alkyl and Aryl Ligands
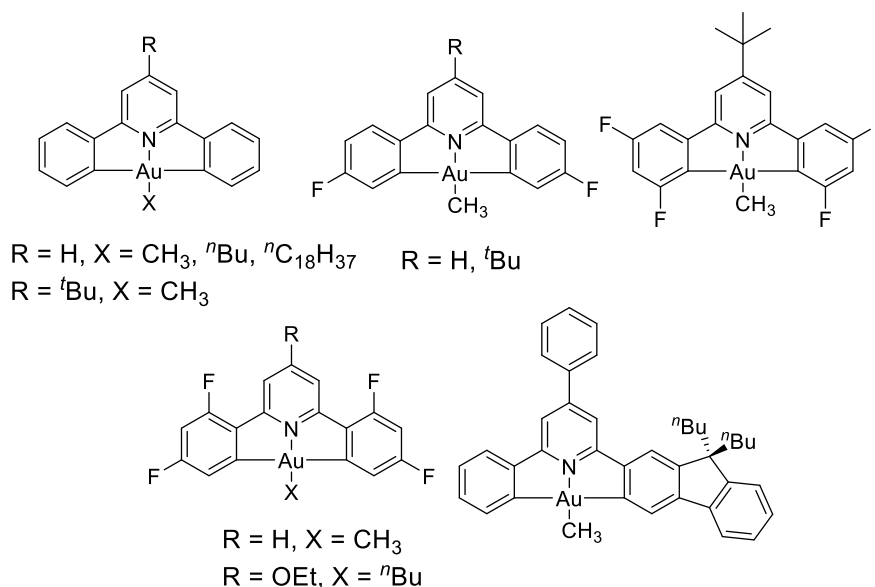
Figure 3.17: Structure of gold(III) alkyl ligand complexes.[64]

Addition of a strong σ-donating alkyl ligand to a gold(III) C^N^C complex (Figure 3.17) gave luminescent complexes.[64] A hypsochromic shift of ~12 nm compared to the

equivalent alkynyl complexes was observed in the absorption spectra, due to LUMO stabilisation. The PLQY increased to 40% and the lifetime to 180 μs in solution at room temperature due to decreased low-lying ^{3}LLCT states, which can provide a non-radiative deactivation pathway. The triplet emission was tuneable from yellow to sky-blue (443 – 465 nm and 472- 499 nm) by variation of C^N^C ligand substituents.
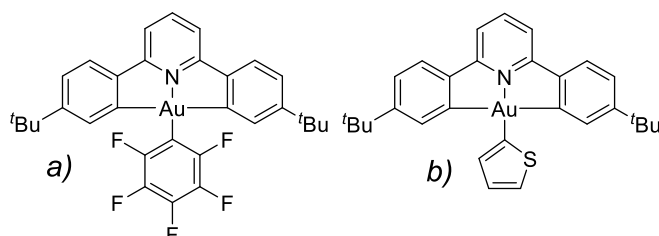
Figure 3.18: Structures of [Au(C^N^C)R] complexes where R = -C$_6$F$_5$ (a) and R = 2-thienyl (b).[52]

The synthesis and photophysics of [Au(C^N^C)(OH)] has been reported, with ligand exchange giving C-H and N-H compounds, aryl boronic acids, perfluoroaryl, *N*-heterocycle and alkynyl complexes.[52] Strong *σ*-donating aryl ligands gave strong emission, while weak *σ*-donors (*e.g.* OH) gave little or no emission. Two compounds of note are the -C$_6$F$_5$ complex (emits at 446 nm, yellow) and the 2-thienyl complex (emits 529 nm, blue) (Figure 3.18), indicating that unlike a majority of other known gold(III) complexes, emission can be tuned by the auxiliary ligand in certain cases, with C^N^C ligand substitution variation not required.
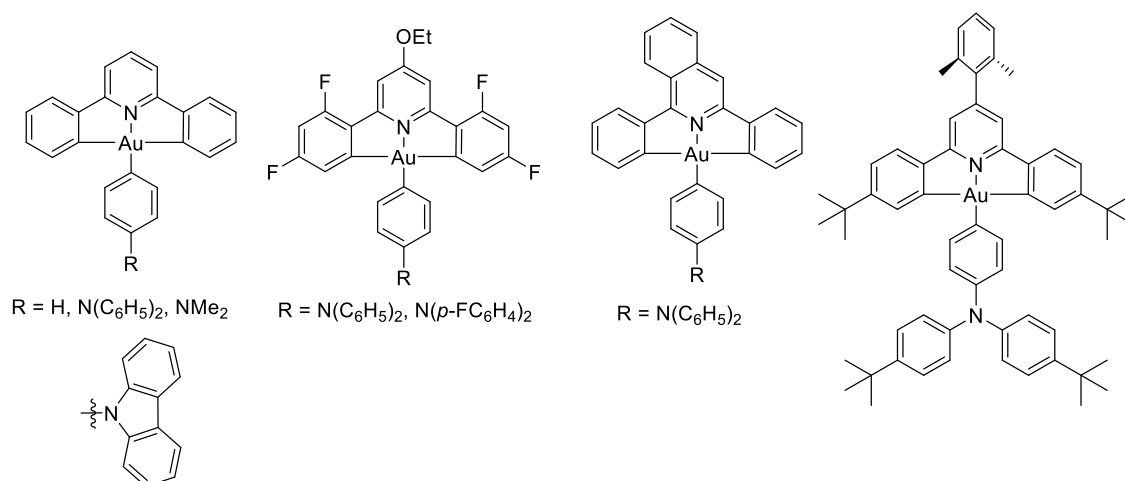
Figure 3.19: Structures of gold(III) aryl complexes.[65]

Aryl ligands have been shown to give complexes (Figure 3.19) with a PLQY of 79% in solution and 84% in thin films (PMMA, 4 wt%) at room temperature, with complexes

containing an amino-substituent displaying TADF emission.[65] The complexes gave sky-blue to green emission in solution-processed OLEDs, with high EQEs up to 23.8%. Replacement of one of the phenyl units of the C^N^C ligand in a related complex with a fluorene moiety, and use of phenyl auxiliary ligand, gave a PLQY of 55%.[40]

3.4   Other Pincer Ligand Frameworks

Generally there are fewer examples of alternate terdentate pincer ligand frameworks due to the increased synthetic challenges, however there are a few reported, including some of the earliest examples of luminescent gold(III) complexes (Section 3.1).[9, 10] Replacement of the pyridyl ring with other heteroaromatic rings is also known.[53, 54, 66-69]
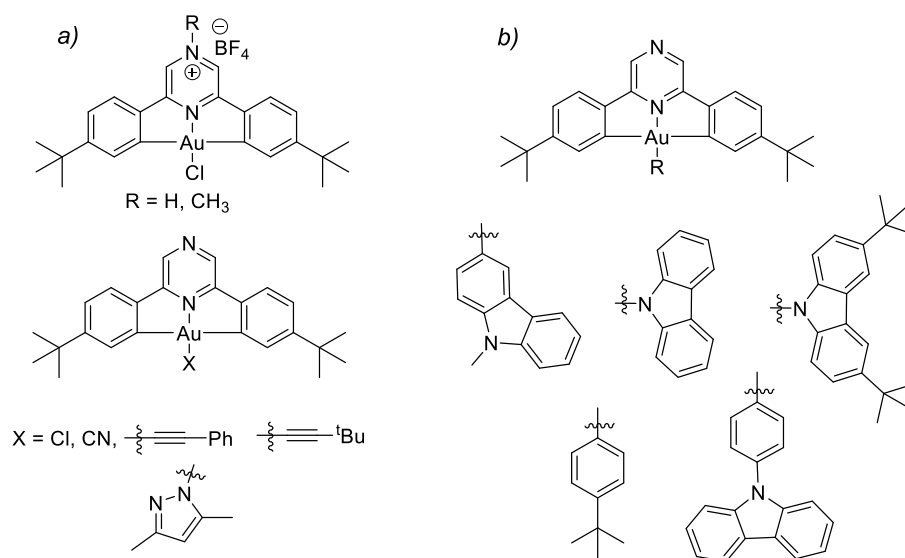
Figure 3.20: Structures of gold(III) complexes, where the central ring of the C^N^C ligand has been replaced by pyrazine.[66, 69]

Replacement of the phenyl ring in the C^N^C ligand by pyrazine (Figure 3.20a) had a strong effect on the complex photophysics, with the resulting materials displaying intense yellow-green emission in solution and the solid state; red-shifted compared to the pyridine equivalent by $40 - 50$ nm.[66] Thermally activated delayed fluorescence (TADF) caused a shift in emission colour from red at 77 K to blue at 298 K. Notably, unlike the pyridine equivalent, complexes were emissive even when the auxiliary ligand was a weak σ-donor, due to the lower π^* level in pyrazine relative to pyridine (~0.95 eV lower), increasing the π-acceptor ability.[67] Complexation to carbazole-containing ligands (Figure 3.20b) gave thermally stimulated delayed phosphorescence (TSDP).[69] Unusually, the emission colour

was sensitive to the carbazole ligand connection, such that connection through carbon gave green emission at 576 nm, while connection through nitrogen gave red emission at 727 nm. Aggregation-enhanced emission was reported in complexes containing thiolate ligands, with both red and yellow polymorphs present, due to supramolecular head-to-head π-stacking of the pyrazine ring giving a deep-red emission in solution.[67] Replacement of the central phenyl ring with triazine introduced low-lying triplet states resulting in TSDP emission (Figure 3.21).[68]
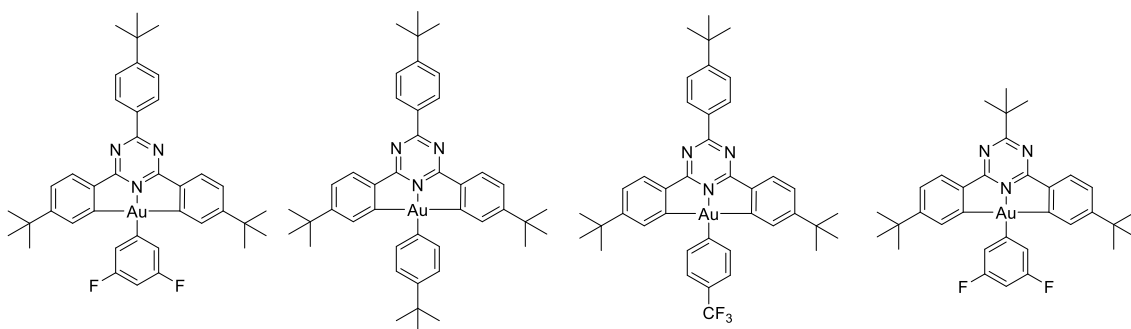
Figure 3.21: Structures of gold(III) complexes, where the central ring of the C^N^C ligand has been replaced by triazine.[68]
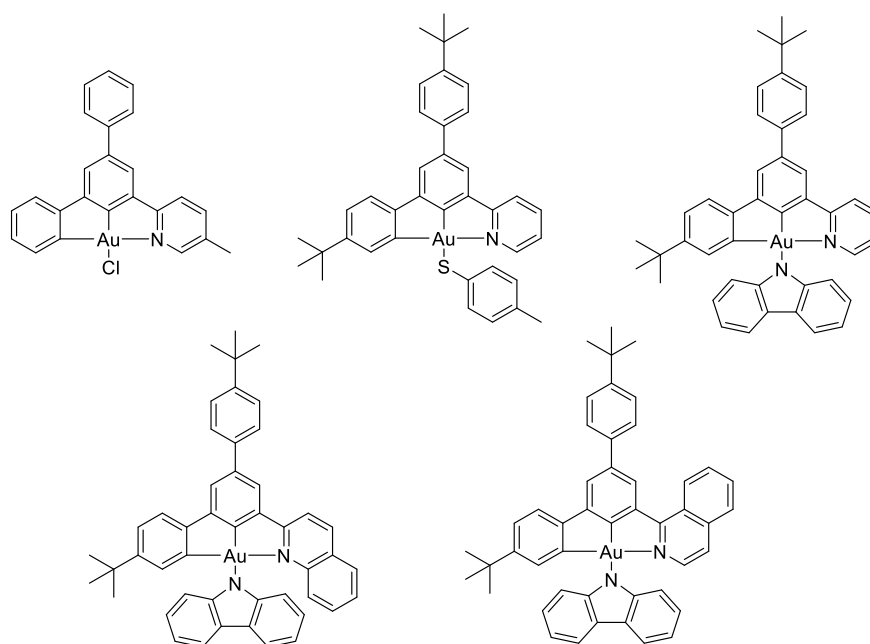
Figure 3.22: Structure of gold(III) C^C^N complexes, with various auxiliary ligands.[32]

Use of C^C^N pincer ligand (Figure 3.22) gave emission primarily from an ³LLCT state,[32] with charge-transfer from the alkynyl ligand to the C^C^N ligand (PLQY: <80%, τ <0.5 μs); however, unusually, the chloro-complex emitted from a metal perturbed ³IL π-π* [C^C^N(py)] state, with increased lifetime (τ = 9.4 μs), as did the fluorogold

complex (489 - 497 nm) (Figure 3.23).[70] Examples of cationic C^N^N ligands are known[9-11, 71, 72] and N^C^N ligands,[24, 73-75] though the synthesis of the latter has been challenging resulting in few literature examples and luminescent properties are not always reported. A change in the pincer ligand results in HOMO-LUMO gap variation.[76]

R = F, Cl
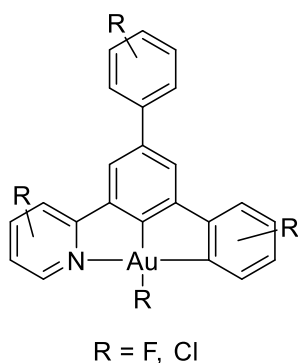
Figure 3.23: Structure of gold(III) complexes with N^C^C pincer ligands.[70]

3.5   Gold(III) Complexes Of Tetradentate Ligands

Few examples of tetradentate gold(III) complexes have been reported to date due to synthetic challenges, however there are increasing examples due to the increased molecular rigidity improving lifetimes and quantum yields due to reduced non-radiative decay.[77] The increased thermal stability of such complexes also enables the use of vacuum deposition to fabricate OLEDs. Synthesis typically requires post-synthetic modification to connect a pincer ligand and an auxiliary ligand to form the tetradentate ligand.[77-79]

In the first described example of a tetradentate gold(III) complex (Figure 3.24) a dramatic increase of the PLQY up to 40% in solution and 78% in doped thin-films at room temperature was reported.[77] The complexes were used in OLEDs giving red to yellow emission, with moderate EQE of 11.1%. A more recent example (Figure 3.25) containing an   oxygen   bridge,   gave   TADF   emission   due   to   the   presence   of phenoxazine/diphenylamine - the first reported example for a tetradentate gold(III) complex.[78] Blue-green to red emission was observed, with quantum yields up to 94% and a lifetime of 0.64 μs in deoxygenated toluene. Use in OLEDs gave a high EQE of 25%.

Figure 3.24: First reported tetradentate C^N^C^C gold(III) complex.[77]

R₁ = 4-tolyl, R₂ = H, R₃ = tert-butyl
R₁ = 4-tolyl, R₂ = R₃ = tert-butyl
R₁ = 4-tolyl, R₂ = tert-butyl, R₃ = CF₃
R₁ = 9,9-dihexyl-fluorene-2-yl, R₂ = tert-butyl, R₃ = CF₃

Figure 3.25: Structures of tetradentate gold(III) complexes, containing an oxygen bridge.[78]

Formation of regioisomers is possible (Figure 3.26) as connection can either be C^C^N^C (*a*) or N^C^N^C (*b*).[79] The complexes emitted at ~548 – 733 nm, with a structureless Gaussian-shaped band. On changing the connecting ligand from *N* to *C* there was a blue-shift of ~3143 cm⁻¹ in the emission, due to a larger structural distortion at the gold centre for the *N*-connection. A C^C^N^N ligand, gave high PLQY of 70% in solid state thin-

films, with emission in the green region, assigned as charge transfer, ^{3}ILCT [$\pi \to \pi^*$ C^C^N^N]. Use in OLEDs gave an EQE of ~20.6% (Figure 3.26c).[80]
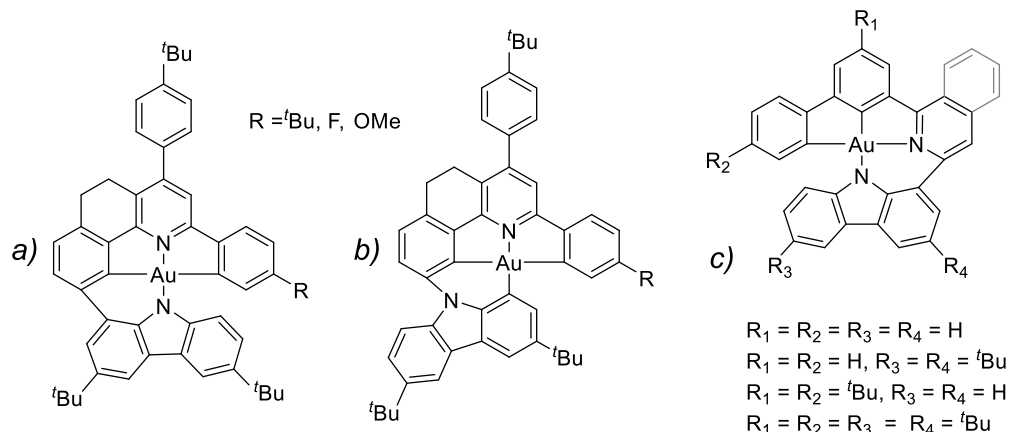
Figure 3.26: The two regioisomers formed for a tetradentate gold(III) complex, depending on the nature of the connecting atom (a and b)[79] and the structure of a tetradentate C^C^N^N complex (c).[80]

3.6　　　Aims of Chapter

In this chapter the thermal and photophysical properties of the gold(III) phenylacetylide complexes are investigated and compared to those of their previously reported 4,4′-disubstituted and 3,3′,4,4′-tetrasubstituted isomers, which have displayed favourable formation of columnar liquid crystal phases and high quantum yields up to 34%.[22, 29, 31] It was hoped that similar favourable properties, particularly maintaining the high quantum yields, would be reported for the isomeric complexes with alkoxy chains in the 2,2′-positions. The formation, or lack of, and nature of the mesophases is rationalised based on the molecular shape of the complexes. The absorption and emission properties of the complexes are discussed and theoretical computational DFT and TD-DFT calculations are undertaken to investigate the origin of the excited states in greater depth.

3.7　　　Thermal Properties of Gold(III) Complexes

The thermal properties of the **2-[Au]-**, **2,3-[Au]-** and **2,5-[Au]-**complexes, as well as the related chlorogold complexes, were investigated using polarising optical microscopy (POM), differential scanning calorimetry (DSC) and small-angle X-ray diffraction (SAXS), where required. None of the chlorogold complexes was found to be mesomorphic (Table 3.1).

None of the complexes substituted only in the 2,2′-positions of the phenyl unit of the C^N^C ligand was liquid crystalline, with the exception of **2-[Au]-3-14**, which displayed a monotropic mesophase (Table 3.1). However the number and length of the chains on the phenylacetylide ligand had an effect on the melting point. For example, an increase in the number of decyloxy-chains from one to two to three, resulted in lowering of the melting point from 122.5 to 103.3 to 94.2 °C, respectively.

Table 3.1: Thermal Transition Temperatures for the Complexes in the **2-[Au]** Series and the 3,5′- and 2,2′,4,4′-Chlorogold Complexes.

Compound	Transition	T / °C	ΔH / kJ mol^{-1}
2-[Au]-Cl	Cr-Iso	124.0	37.1
2-[Au]-5	Cr-Iso	127.3	14.2
2-[Au]-8	Cr-Iso	124.7	16.3
2-[Au]-1-10	Cr-Iso	121.1	49.7
2-[Au]-2-10	Cr-Iso	102.0	68.3
2-[Au]-3-10	Cr-Iso	92.6	44.7
2-[Au]-3-10	Cr-Iso	84.7	42.7
	(Col – Iso)	(72.6)	(1.4)
3/5-[Au]-Cl	Cr-Iso	121.9	6.9
2,4-[Au]-Cl	Cr-Iso	91.0	28.9

To investigate the monotropic behaviour of **2-[Au]-3-14** further mixtures with **2,3-[Au]-3-14** (3:1, 1.5:1, 1:1 and 1:3) were prepared and the evolution of the melting and clearing points was followed. In an ideal mixture, where two components of a very similar shape are mixed, the observed clearing point is a linear function of composition, which can allow a latent monotropic phase to be predicted by extrapolation. From the plot obtained (Figure 3.27) it is clear that mixing is not ideal as extrapolation predicts an endiotropic phase, however, the results were encouraging enough to prompt reinvestigation by microscopy. There it was found that very rapid cooling led to the observation of a monotropic mesophase at 60 °C, which cleared on reheating at 72 °C. This matches DSC data well, which showed the transition at 72.6 °C. Unfortunately, the texture of the phase formed under POM was poor and the strongly monotropic nature of the phase precluded acquisition of SAXS data, but it is most likely given that the complex is substituted by five alkoxy chains that the phase is columnar in nature.
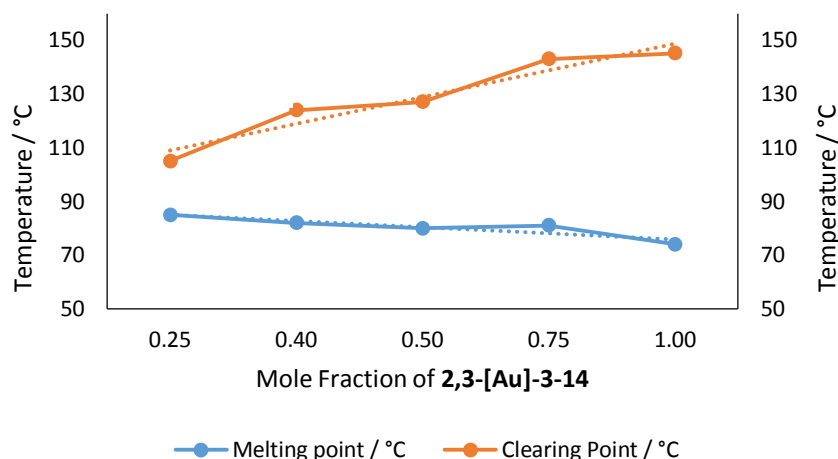
*Figure 3.27: Plot of thermal transition temperatures for mixture studies of **2-[Au]-3-14** and **2,3-[Au]-3-14** showing extrapolated data.*

On introduction of perfluorinated chains (1*H*,1*H*,2*H*,2*H*-perfluorodecyl- and 1*H*,1*H*,2*H*,2*H*-perfluorododecyl-), to the 4-position of the phenyl alkynyl ligand, to give complexes **2-[Au]-F10** and **2-[Au]-F12**, a smectic A phase was observed (Table 3.2). It is hypothesised that the induction of mesophase behaviour on the introduction of perfluorinated chains is due to formation of a bilayer structure (Figure 3.28), caused by nanophase separation due to the fluorophobic effect (a known effect due to the highly electronegative nature of perfluorinated chains compared to alkyl chains and increased stiffness due to the larger size of fluorine atoms compared to hydrogen atoms), in effect forming an amphiphile.[81-96]
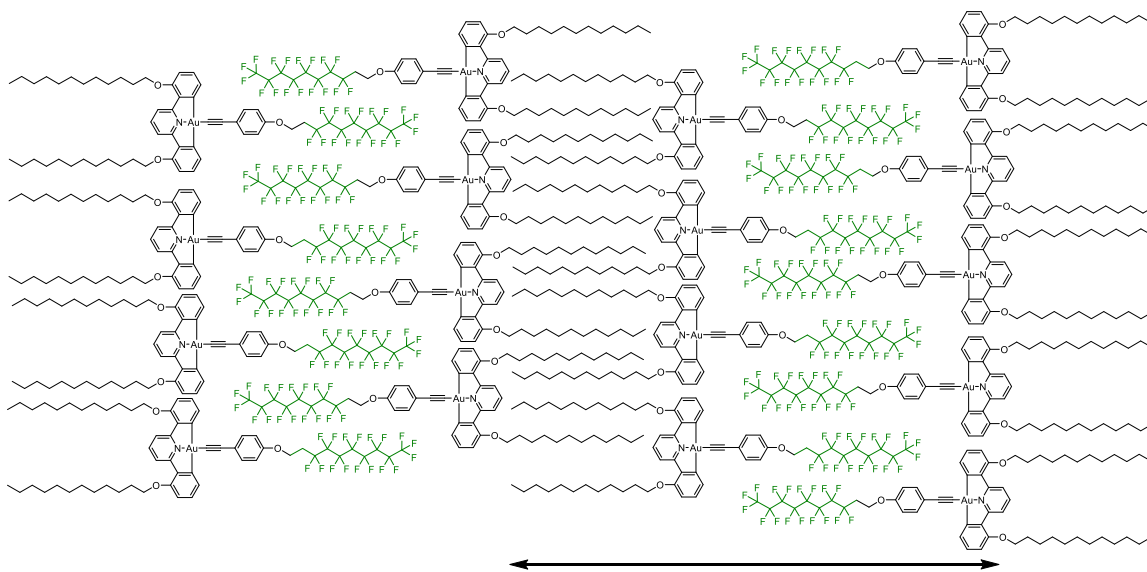
Figure 3.28: Hypothesised bilayer structure for semi-perfluorinated gold(III) complexes.
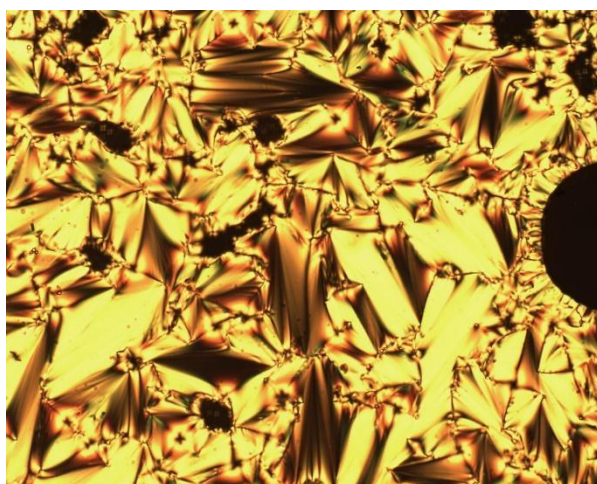
*Figure 3.29: Textures formed under POM on cooling for **2-[Au]-F10** at 195 °C.*

Table 3.2: Thermal Transition Temperatures for the Perfluorinated Complexes in the 2-[Au] Series.

Compound	Transition	T / °C	ΔH / kJ mol^{-1}
2-[Au]-F10	Cr-SmA	136.9	5.8
	SmA-Iso	200.4	5.5
2-[Au]-F12	Cr-SmA*	143.4	0.4
	SmA-Iso	216.5	4.6

*2nd heat

2-[Au]-F10 displayed a SmA phase (Figure 3.29) from 138 – 202 °C and SAXS data showed three reflections at (001), (002) and (003) (Figure 3.30), which corresponds roughly to a layer spacing of one molecule. **2-[Au]-F12** displayed a SmA phase from 146 – 218 °C and here SAXS data showed two reflections at (001) and (002), again roughly one molecular length. The SAXS data (Table 3.3) are consistent with the observation of a lamella phase and, combined with the focal conic texture observed under POM, enables identification as a smectic A phase. Notably, the (002) reflection is of a greater intensity than the (001) reflection, which is known for some perfluorinated compounds,[97, 98] due to the more electron-rich nature of the perfluorinated chains compared to hydrocarbon chains, leading to greater scattering. No reflection was observed that corresponded to twice the molecular length (~35 Å) in either complex (length obtained from single crystal data) indicating either a high level of interdigitation in the phase or coiling of the chains, nevertheless the evidence suggests formation of a bilayer phase, with this behaviour previously observed in other systems.[95, 98-101]
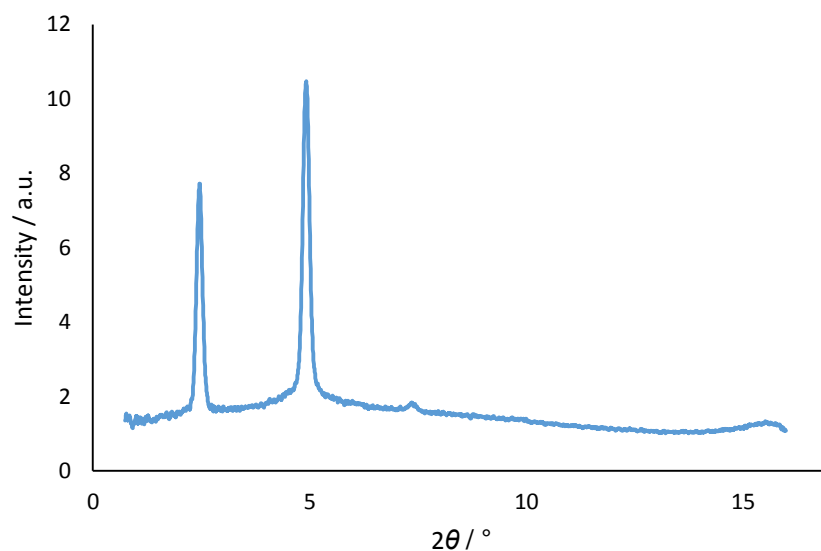
*Figure 3.30: SAXS data for **2-[Au]-F10**.*

Table 3.3: SAXS Data Table for the Perfluorinated Complexes in the **2-[Au]** Series.

Complex	Phase	2θ / °	d_{obs} / Å	d_{cal} / Å	*hkl*
2-[Au]-F10	SmA 160 °C	2.44	35.9	35.9	*001*
		4.91	17.9	17.9	*002*
		7.29	12.0	12.0	*003*
2-[Au]-F12	SmA 190 °C	2.49	35.5	*35.5*	*001*
		5.01	17.7	17.7	*002*

Complexes substituted in the 2,2′,3,3′-positions of the C^N^C ligand (**2,3-[Au]-R**), with an alkyl-chain (either pentyl or octyl) in the 4-position of the phenylacetylide ligand (**2,3-[Au]-5**, **2,3-[Au]-8)** or alkoxy-chains ($-OC_{10}H_{21}$) in the 4- or 3,4-positions of the phenylacetylide ligand (**2,3-[Au]-1-10** and **2,3-[Au]-2-10**) were not mesomorphic (Table 3.4).

However, on introduction of a third alkoxy chain, giving a total of seven chains, formation of hexagonal columnar phases was observed. When $n = 10$, a monotropic phase formed and was assumed to have hexagonal symmetry from the assignment of the phases for the longer-chain members of the series. However, the phase was transient, not observed by DSC and appeared almost simultaneously with crystallisation. The crystalline phase was strongly stabilised relative to the other compounds in the series, with a melting point temperature of 143 °C *vs* <60 °C for **2,3-[Au]-1-10** and **2,3-[Au]-2-10**. An increase in the

181

chain length to $n = 12$ and $14^{\ddagger}$ resulted in formation of wide-range columnar phases, exhibiting both focal conic and straight-line defects under POM (Figure 3.31). SAXS measurements (Figure 3.32) gave a $1:\sqrt{3}:\sqrt{4}:\sqrt{7}$ peak spacing ratio (Table 3.5), enabling assignment of the phase as hexagonal columnar. The unit cell parameter, a, is calculated as 26.1 and 27.1 Å respectively, with a slight increase with increasing chain length, and hence, complex size.
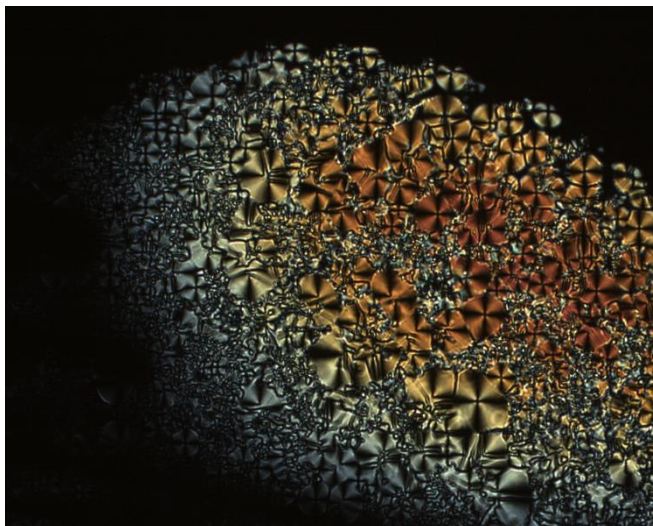
*Figure 3.31: Texture on cooling for **2,3-[Au]-3-12** at 144 °C.*

Table 3.4: Thermal Transition Temperatures for the Complexes in the **2,3-[Au]** Series.

Compound	Transition	T / °C	ΔH / kJ mol^{-1}
2,3-[Au]-Cl	Cr-Iso	129.5	63.2
2,3-[Au]-5	Cr-Iso	69.1	7.3
2,3-[Au]-8	Cr-Iso	71.3	26.7
2,3-[Au]-1-10	Cr-Iso	58.8	83.7
2,3-[Au]-2-10	Cr-Iso	73.2	123.7
2,3-[Au]-3-10	Cr-Iso	142.7	41.1
2,3-[Au]-3-12	$g - Col_h$	~92*	-
	Col_h - Iso	146.0	43.7
2,3-[Au]-3-14	Cr-Col_h	74*	-
	Col_h-Iso	144.6	27.9

*Determined from POM
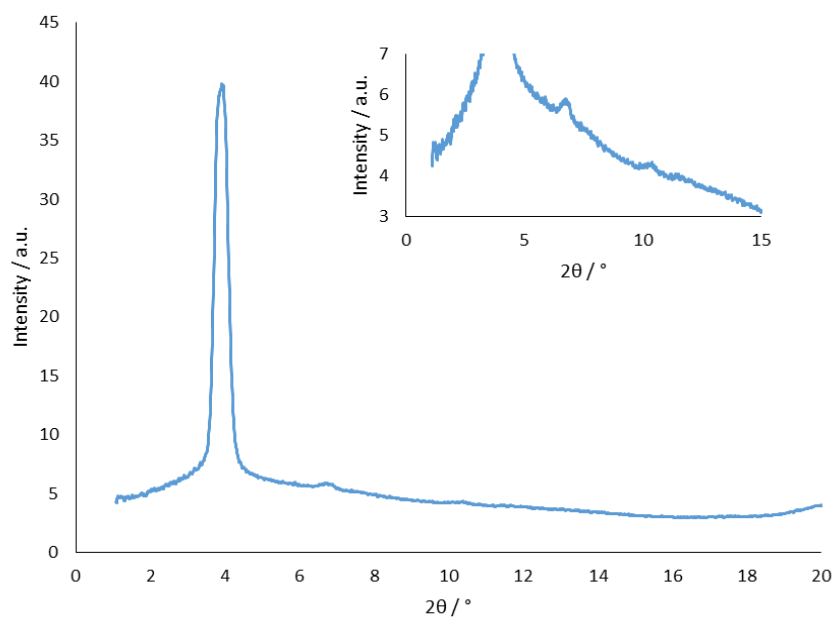
*Figure 3.32: SAXS measurements for **2,3-[Au]-3-12** at 120 °C.*

Table 3.5: SAXS Data Table for the Complexes in the **2,3-[Au]** Series.

Complex	Phase	2θ / °	d_{obs} / Å	d_{cal} / Å	hk	a / Å
2,3-[Au]-3-12	Col_h 120 °C	3.92	22.6	22.6	*10*	26.1
		6.82	13.0	13.0	*11*	
		7.61	11.6	11.3	*20*	
		10.4	8.5	8.5	*21*	
2,3-[Au]-3-14	Col_h 120 °C	3.77	23.5	23.5	*10*	27.1
		5.33	13.5	13.6	*11*	
		7.55	11.7	11.8	*20*	
		9.95	8.9	8.9	*21*	

A destabilisation of the melting point temperatures was observed with increasing chain length, though the clearing temperature remained effectively constant, resulting in a broadening of the phase range with increasing chain length (Figure 3.33).
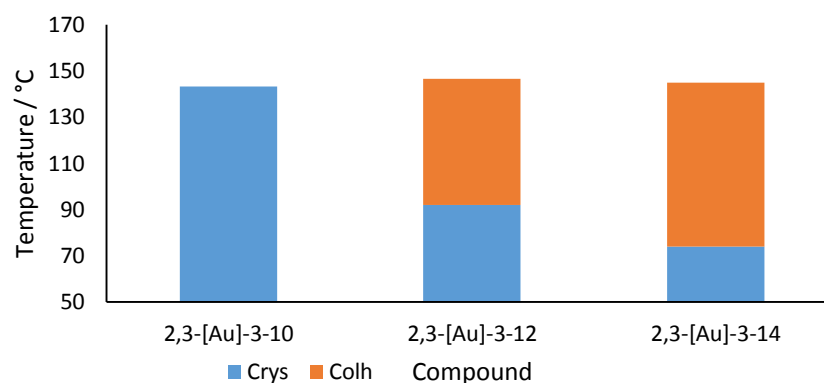
*Figure 3.33: Transition temperatures and phases shown for compounds **2,3-[Au]-3-10**, **2,3-[Au]-3-12** and **2,3-[Au]-3-14** on heating, with the crystalline solid shown in blue and hexagonal columnar phase in orange.*

Table 3.6: Thermal Transition Temperatures for the Complexes in the **2,5-[Au]** Series.

Compound	Transition	T / °C	ΔH / kJ mol^{-1}
2,5-[Au]-Cl	Cr-Iso	151.8	31.1
2,5-[Au]-8	Cr-SmA	118.5	46.3
	SmA-Iso	123.4	8.4
2,5-[Au]-1-10	Cr-SmA	111.5	44.7
	SmA-Iso	119.6	8.9
2,5-[Au]-1-12	Cr-SmA	108.8	44.5
	SmA-iso	115.5	8.4
2,5-[Au]-1-14	Cr-Iso	109.9	57.2
	(Iso-SmA)	108.0	-8.4
2,5-[Au]-2-10	Cr-Iso	102.7	80.5
	(Iso-Col)	~88-85*	-60.6
2,5-[Au]-3-10	Cr-Iso	65.2	56.4
	(Iso -Col)	45.2	-2.0

*Determined using POM

For complexes with 2,2′,5,5′-tetrasubstitution of the C^N^C pincer ligand (**2,5-[Au]-**), all of the phenylacetylide complexes are mesomorphic (Table 3.6). **2,5-[Au]-8** displayed a narrow-range enantiotropic mesophase from 120 – 124 °C, which is identified as SmA, from the focal conic phase texture. Assignment is supported by the presence of two reflections in SAXS (Table 3.7), the (*001*) reflection at 30.1 Å and the weaker (*002*) reflection at 15.0 Å. This is diagnostic of a monolayer smectic phase. As the chain length on the phenylacetylide ligand increased in length (**2,5-[Au]-8** and **2,5-[Au]-1-*n***, where *n* = 10, 12, 14)[§] it can be seen that the clearing temperature decreases. The melting point

---

[§] *n* = 12, 14 were synthesised and characterised by Liam Curtis under supervision.

similarly also decreases, resulting in a widening of the phase (Figure 3.35). However, the clearing point falls more quickly than the melting point so that for **2,5-[Au]-1-14**, the SmA phase is now monotropic. A focal conic texture was recorded for all complexes (Figure 3.34), which combined with SAXS measurements (Figure 3.36), leads to assignment of the mesophase as SmA. The interlayer spacing (30 – 33 Å) is slightly smaller than the molecular length measured from single crystal structures (~35 – 36 Å) suggesting a small amount of chain interdigitation or folding in the layers.
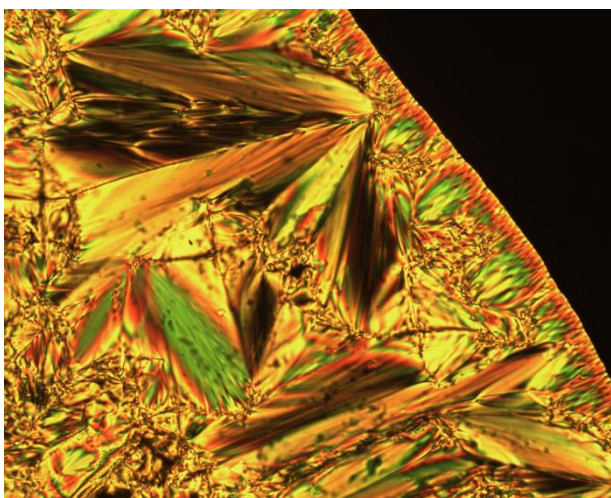
*Figure 3.34: Textures on cooling under POM for **2,5-[Au]-1-10** at 121 °C.*
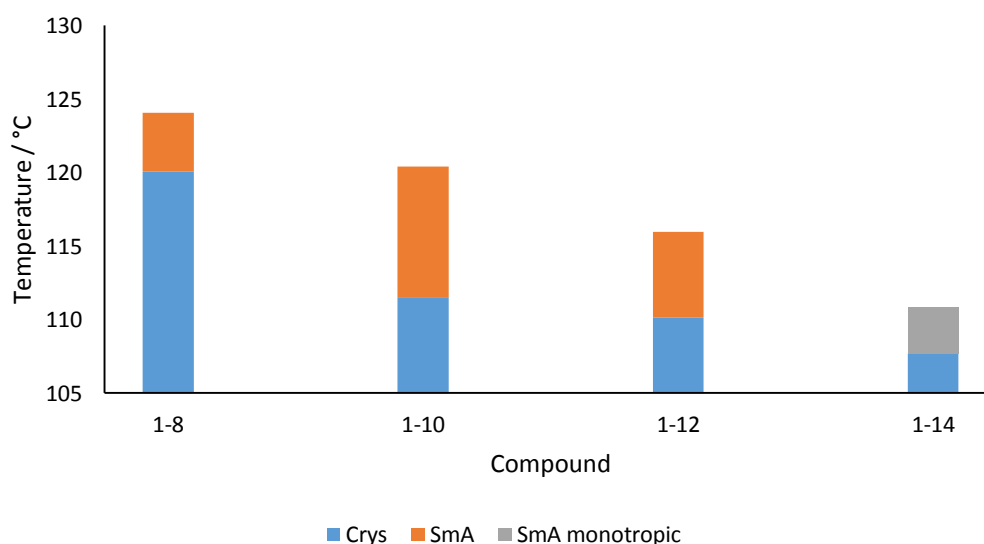
*Figure 3.35: Transition temperatures and phases shown for compounds **2,5-[Au]-8**, **2,5-[Au]-1-10**, **2,5-[Au]-1-12** and **2,5-[Au]-1-14** on heating, with the crystalline solid shown in blue, SmA phase in orange and monotropic SmA phase in grey.*
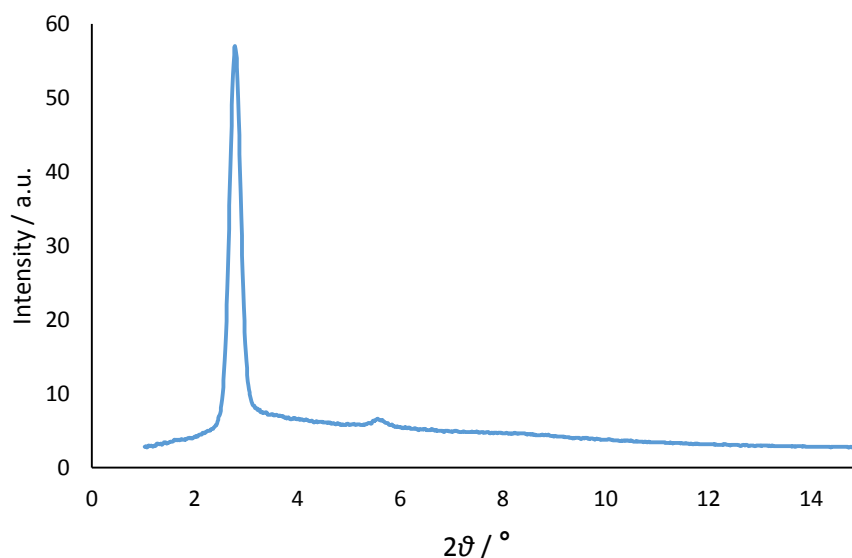
*Figure 3.36: SAXS measurements for **2,5-[Au]-1-10** at 123 °C.*

Table 3.7: SAXS Data Table for the Complexes in the **2,5-[Au]** Series.

Complex	Phase	2θ / °	d_{obs} / Å	d_{cal} / Å	hk
2,5-[Au]-8	SmA	2.96	30.1	30.1	*001*
	123 °C	5.85	15.0	15.0	*002*
2,5-[Au]-1-10	SmA	2.79	31.7	31.7	*001*
	117 °C	5.65	15.9	15.9	*002*
2,5-[Au]-1-12	SmA	2.72	32.3	32.3	*001*
	112 °C	5.45	16.2	16.2	*002*
2,5-[Au]-1-14	SmA	2.72	32.9	32.9	*001*
	111 °C				

2,5-[Au]-2-10 and **2,5-[Au]-3-10** both displayed monotropic phases, which persisted only briefly before crystallisation. This made study of the texture highly challenging, and made identification of the phase symmetry *via* SAXS impossible. However, the nature of the texture and its viscosity are more representative of columnar than smectic phases, which would not be inconsistent with the number of chains.

Overall, it was observed that with increasing chain number on the phenylacetylide ligand there is a reduction in phase stability (Figure 3.37), with the one-chain complexes displaying enantiotropic SmA phases (**2,5-[Au]-8** and **2,5-[Au]-1-*n***), while the two-chain (**2,5-[Au]-2-10**) and three-chain (**2,5-[Au]-3-10**) display monotropic columnar phases. This is discussed in greater depth below.
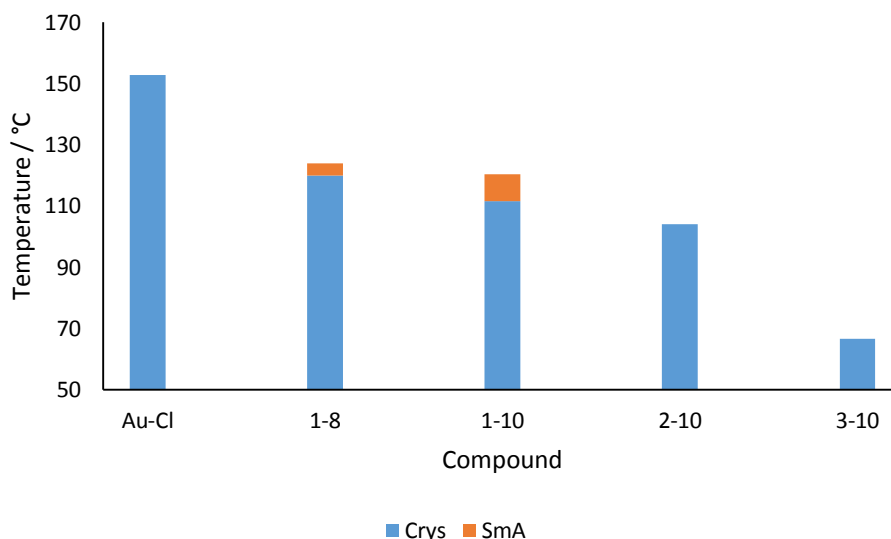
*Figure 3.37: Transition temperatures and phases shown for compounds **2,5-[Au]-Cl**, **2,5-[Au]-8**, **2,5-[Au]-1-10**, **2,5-[Au]-2-10** and **2,5-[Au]31-10** on heating, with the crystalline solid shown in blue and, SmA phase in orange.*

3.7.1   Discussion

The lack of mesophase behaviour in the series where the phenyl unit of the C^N^C ligand is substituted in the 2,2′-positions displays a striking contrast with the isomeric complexes substituted in the 4,4′-positions, which displayed both rectangular and hexagonal columnar phases.[29] In this previous study, it was determined that in order to gain effective space filling to form the required 'disc-like' shape for formation of a columnar phase, the 4,4′-disubstituted complexes are thought to pair in an anti-parallel 'back-to-back' fashion. It is thought that the change in substitution pattern results in a lack of effective space-filling for formation of a disc-like shape, with only **2-[Au]-3-14** having a large enough chain volume to form something of a 'disc-shape', disfavouring mesophase formation.

In contrast to the lack of mesophase in the complexes substituted with entirely hydrocarbon chains, on introduction of a semi-perfluorinated chain into the 4-position of the phenylacetylide ligand to create an amphiphilic molecule, a smectic phase is induced. An amphiphilic molecule is formed as perfluorinated chains, due to the high electronegativity of fluorine atoms resulting in low intermolecular forces, are hydrophobic, lipophobic and non-polar.[97] Additionally, the greater size of the fluorine atom compared to the hydrogen atom results in stiffer chains compared to hydrocarbons. Overall, this results in hydrocarbon and longer perfluorinated chains ($n > 8$), being

187

immiscible - the origin of the fluorophobic effect – with the presence of both functional units juxtaposed in one molecule giving rise to an amphiphile and the associated molecular self- assembly.[81-96] In the isomeric 4,4′- and 3,3′,4,4′-complexes microphase separation due to fluorous behaviour started to be observed when $n > 8$, suggesting similar behaviour in these complexes.[22, 30, 31] SAXS data shows the formation of a bilayer structure due to nanophase separation caused by the aforementioned fluorophobic effect.[95] The disfavouring of the two-unit mixing results in an antiparallel pairing of the molecules, with a band of perfluorinated chains sandwiched between the C^N^C ligands and the hydrocarbon chains.[95, 101]

On comparing the semi-perfluorinated complexes with **2-[Au]-1-10**, the equivalent alkylated complex, it can be seen that the melting points are similar (Figure 3.38), although, the clearing point increases for **2-[Au]-F10** compared to **2-[Au]-F12**. The increase in the transition temperatures compared to the purely alkylated equivalents is due to the increased rigidity of the perfluorinated chains, as is common with other systems, including the 4,4′-disubstituted isomers.[30, 31, 95, 102, 103]
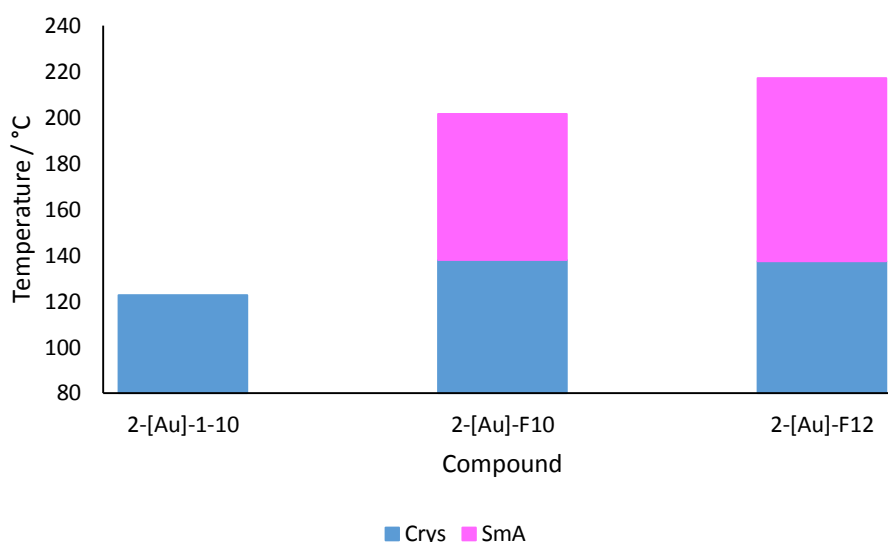
*Figure 3.38: Transition temperatures and phases shown for compounds **2-[Au]-1-10**, **2-[Au]-F10** and **2-[Au]-F12** on heating, with the crystalline solid shown in blue and SmA phase in pink.*

The induction of smectic phases in the **2-[Au]**-series stands in contrast to the 4,4′- and 3,3′,4,4′-series, which on fluorination displayed disruption of the, previously strongly favoured, columnar phases.[22, 30, 31] Greater destabilisation of mesophase formation was

observed in this series of complexes on increased levels of fluorination ($n > 8$), due to increased disruption to the columnar packing. In comparison, the more linear nature of the **2-[Au]-**series enables formation of the resulting bilayer smectic structure due to the hydrocarbon and the semi-perfluorinated chains being on juxtaposed sides of the complex. Comparison of this behaviour emphasises the importance of molecular shape in the resulting mesophase(s).

A lack of effective space-filling to form a 'disc-like' shape is once again believed to be the explanation for why the **2,3-[Au]-** complexes with only one or two chains on the phenylacetylide ligand did not display any mesophase behaviour. Only on the introduction of the additional third chain do hexagonal columnar phases form. This stands in strong comparison to the isomeric 3,3′,4,4′-series, which displayed wide range columnar phases on account of their molecular 'disc-like' shape.[29]

The importance of molecular shape on the nature of the mesophase formation is further emphasised on consideration of the **2,5-[Au]**-series. The chains in the 2,2′-positions of the phenyl unit of the C^N^C pincer ligand are directed back from the complex centre, while the chains in the 5,5′-positions are directed forwards, resulting in formation of a 'H-shaped' complex, **2,5-[Au]-Cl**.[104-106] The introduction of a 4-position substituted phenylacetylide ligand creates a rod-shaped molecule resulting in formation of a smectic phase. On the introduction of additional chains in the 3- and, also 5-positions, the planarity of the complex is reduced as the 5,5′-chains cause the phenyl ring to twist out of the plane of the gold-C^N^C unit. This results in the chains in the 3- and 5-position of the phenyl group being orientated out of the plane of the complex, significantly reducing the anisotropy. This is readily seen in the single crystal structure of **2,5-[Au]-3-10** (Figure 3.39). The loss of anisotropy reduces the phase stability, with only monotropic mesophases formed, indicating that mesophase formation is now under kinetic, not thermodynamic, control. Further, the reduction in molecular anisotropy and hence, change in molecular shape, appears to result in the formation of columnar, not smectic, phases. This change over in behaviour is known in other metallomesogen systems.[107, 108]
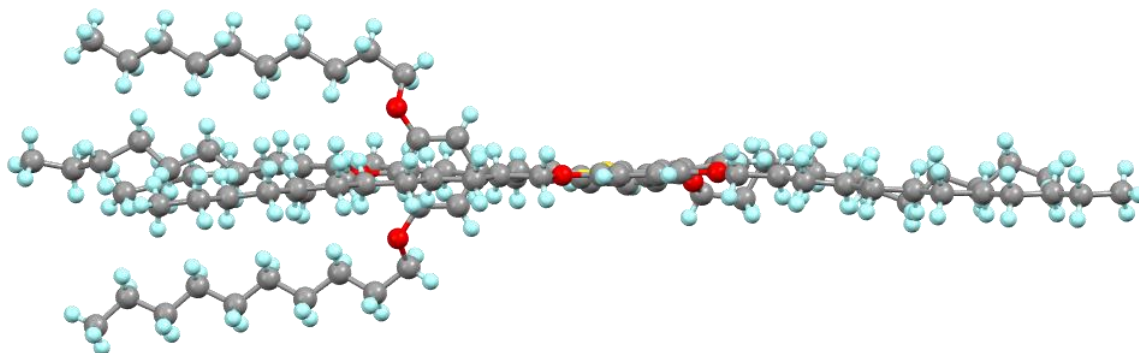
*Figure 3.39: Side-view of the molecular structure for **2,5-[Au]-3-10**.*

Overall it can be observed from the collated data that the position of the alkoxy chain substitution on the C^N^C ligand has a significant impact on whether a mesophase is formed and also the nature of the phase formed. Molecules which form effective 'disc-like' shapes form wide-range columnar phases (**3,4-[Au]-**, **4-[Au]-**), while reduced molecular space-filling of the chains on the C^N^C unit, requires longer and more chains in order to induce mesophase formation (**2-[Au]-** and **2,3-[Au]-**). Formation of more linear molecules, whether by inherent molecular shape (**2,5-[Au]-1-*n***) or microphase segregation (**2-[Au]-F*n***) gives rise to smectic phases. This control of the mesophase nature *via* alteration of the molecular shape of the complex on variation of substitution pattern is hardly surprising given it is a well-known phenomenon.

3.8   Photophysics of Gold(III) Complexes

3.8.1   Absorption Spectra

The absorption and emission properties of the 2,2′-disubstituted and 2,2′,3,3′- & 2,2′,5,5′-tetrasubstituted gold(III) complexes in dichloromethane solution were studied (Table 3.9) and one chain length from each series was chosen (1-ethynyl-4-octylbenzene), as it is assumed that the photophysical behaviour is independent of chain length; details are given below. The photophysical properties of the free ligands (Table 3.10), were also studied as a comparison.

The free ligands (Table 3.10) showed strong absorption bands below 380 nm, relating to π-π* transitions of the C^N^C rings, and a broad featureless band, with maxima ranging from 290 – 330 nm (Figure 3.40), determined by TD-DFT calculations to be ILCT in origin. The wavelength maxima depended on the nature of the ligand substitution

position. On complexation, a red-shifting of the charge-transfer band occurs, which is discussed in greater depth below.
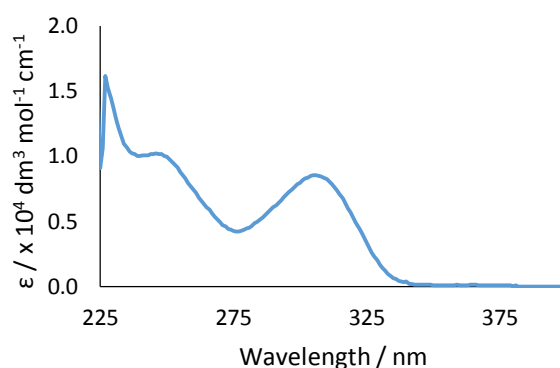
*Figure 3.40: Absorption spectrum in dichloromethane solution for **2-[L]**, taken as an exemplar for the free ligands.*

All of the complexes showed absorptions in three main areas, with the precise absorption maximum depending on the substitution pattern on the C^N^C pincer ligand, with no difference between adsorption spectra for different chain numbers on the phenylacetylide ligand being observed. Therefore, there were strong absorption bands in the range 220-270 nm with molar absorptivity in the range 4-11 x 10^4 dm^3 mol^{-1} cm^{-1}. There is then a long-wavelength shoulder between 270-320 nm and finally weaker absorptions in the range 370-450 nm. TD-DFT calculations indicate that the high energy transitions (200 – 300 nm) are due to π-π* transitions of the C^N^C pincer ligand and the lower energy band at ~300 – 450 nm is a mixture of ILCT transitions, (where energy is transferred from the phenyl unit to the pyridine unit of the C^N^C ligand) and LLCT transitions (where energy is transferred from the phenylacetylide ligand to the C^N^C ligand). This is in line with previous studies.[7, 29, 56] DFT calculations are discussed further in Section 3.9.

Little difference is observed between **2-[Au]-Cl**, **2,3-[Au]-Cl** and the phenylacetylide complexes (discussed below), with the exception of the shoulder at 290 nm becoming more marked to the extent that can be resolved as a true band for the chlorogold complexes. **2,5-[Au]-Cl** shows one intense band at 229 nm and a weaker band at 290 nm. On the change to the phenylacetylide ligand a new, intense band at 370 nm appears. Only the chloroaurate complexes for the **2,4-[Au]** and **3/5-[Au]**-series were isolated (Table 3.8). **2,4-[Au]-Cl** displayed a moderately intense band at ~380 – 480 nm, which displayed

191

vibronic coupling resulting in peak doubling (Figure 3.41a). The presence of vibronic coupling is unusual for the tetrasubstituted complexes, with no other examples displaying this.[29] This band is also red-shifted compared to the other complexes, displaying the highest λ_{max}. **3/5-[Au]-Cl** displayed three broad bands, an intense band at 246 nm, and moderately intense bands at 264 and 345 nm (Figure 3.41b). The λ_{max} was blue-shifted compared to the other chlorogold complexes. The lack of vibronic coupling for this complex stands in contrast to **2-[Au]-Cl** and **4-[Au]-Cl**, which both display vibronic coupling resulting in peak doubling.[29] This is possibly due to the unsymmetrical nature of the complex.
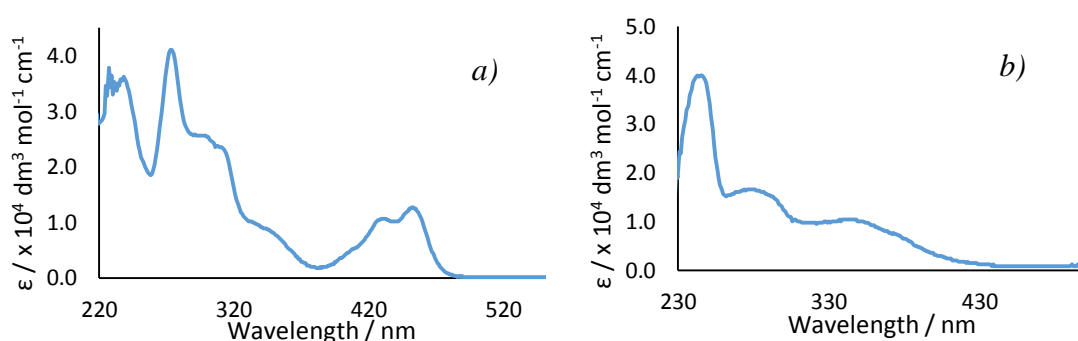
*Figure 3.41: Absorption spectra for **2,4-[Au]-Cl** in dichloromethane solution (a) and for **3/5-[Au]-Cl** in dichloromethane solution (b).*

Table 3.8: Absorbance Data for Chlorogold Complexes in Dichloromethane Solution.

Complex	Absorbance (ε / x 10^3 dm^3 mol^{-1} cm^{-1}) / nm
2-[Au]-Cl	230 (18), 256 (16), 290 (7.7), 359 (3.6), 377 (3.4), 399 (4.5), 420 (0.47)
2-[Au]-F10	232 (44), 252 (47), 357 (9.9), 374 (9.3), 349 (10), 414 (9.1)
2,3-[Au]-Cl	252 (52), 285 (20), 370 (15)
2,5-[Au]-Cl	229 (61), 290 (14), 339 (9.0), 427 (15)
2,4-[Au]-Cl	227 (68), 239 (36), 274 (41), 300 (25), 313 (23), 431 (11), 453 (13)
3/5-[Au]-Cl	246 (40), 274 (17), 345 (10)

For **2-[Au]-R** the band at 310 – 425 nm displayed vibronic coupling (Figure 3.52a). No difference in the absorption spectra was observed for the perfluorinated complex, **2-[Au]-F10**, (Figure 3.42b) which is not unexpected given that the electronic properties appear to be independent of the chain nature on the phenylacetylide ligand. Such behaviour has previously been reported for the isomeric complexes.[22, 31] For **2,3-[Au]-R** this band is slightly blue-shifted to 302-420 nm (Figure 3.43a), with no vibronic coupling observed. **2,5-[Au]-R** is red-shifted compared to the other series (Figure 3.43b), with the broad, structureless band at 350 – 450 nm.[29] Previous investigations for the 4,4′-and 3,3′,4,4′-complexes, showed that only the former displayed vibronic coupling, with the lack in the 3,3′,4,4′-complexes assigned to more effective state mixing, offering a likely explanation for the behaviour in these complexes.[29]
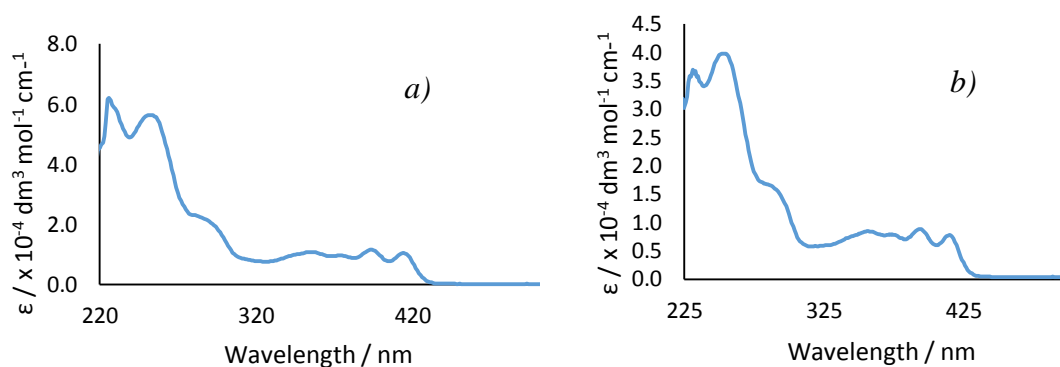
*Figure 3.42: Absorption spectra for **2-[Au]-8** in dichloromethane solution (a) and for **2-[Au]-F10** in dichloromethane solution (b).*
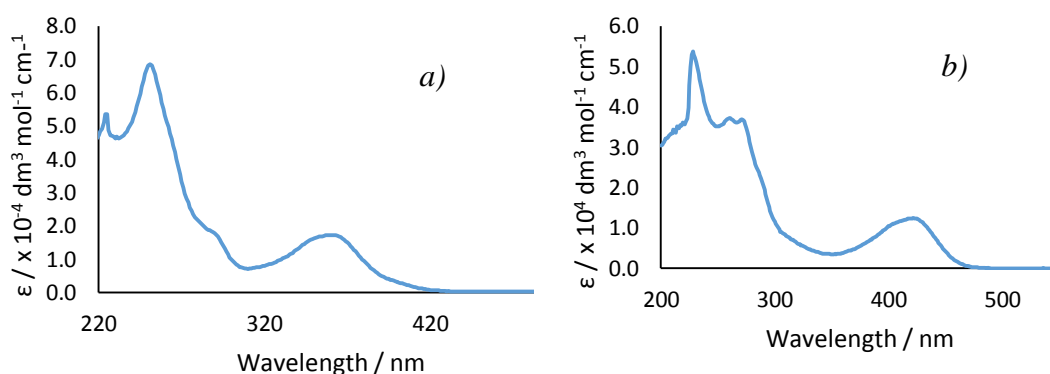
*Figure 3.43: Absorption spectra for **2,3-[Au]-8** (a) and **2,5-[Au]-8** (b) in dichloromethane solution.*

3.8.2 Emission Spectra

To provide a comparison with the emission properties of the complexes, the pincer ligands were first studied. All exhibited broad, structureless fluorescence emission bands in the UV-Vis region (350 – 380 nm, Table 3.10), with lifetimes in the region 1 - 3 ns. Quantum yields were measured with reference to $[Ru(bipy)_3]Cl_2$ in aerated water as a standard[109] and calculated using Equation 1:

Eqn. 1
$$\Phi_a = \left(\frac{I_a}{I_b}\right)\left(\frac{A_b}{A_a}\right)\left(\frac{n_a}{n_b}\right)^2 \Phi_b$$

Where *a* refers to the sample and *b* to the standard; I is the integrated spectra intensity; A is the absorbance at λ_{ex}; *n* is the refractive index of the solvent; Φ_a is the quantum yield of the sample and Φ_b the quantum yield of the standard, $[Ru(bip)_3]Cl_2$, which is 0.04.[109]

The radiative rate constant, k_r, was calculated using Equation 2:

Eqn. 2
$$k_r = \frac{\Phi}{\tau}$$

Where τ is the lifetime of the compound. The combined non-radiative rate constant, Σk_{nr}, was calculated using Equation 3:

Eqn. 3
$$\sum k_{nr} = \frac{1 - \Phi}{\tau}$$

The emission properties of the complexes were studied in oxygen-free dichloromethane solutions, exciting the 2,2′- and 2,2′,3,3′-complexes at 380 nm and the 2,2′,5,5′-complexes at 420 nm. The chlorogold complexes, **2-[Au]-Cl**, **2,3-[Au]-Cl**, **2,5-[Au]-Cl**, **3/5-[Au]-Cl**, and **2,4-[Au]-Cl** were not emissive in solution at room temperature, in line with literature precedent.[5, 12, 13] However, a vitrified solution of **2-[Au]-Cl**[**] in diethyl ether/isopentane/ethanol (EPA) (2:2:1 v/v) at 77 K showed emission at 502, 539, 574 and 631 nm and an excited state lifetime time of 80 μs, in line with literature precedent.[5, 12, 13]

[**] Measurement kindly made by Professor Gareth Williams, Durham University.

All of the [Au(C^N^C)(C≡C-R)] complexes displayed very weak triplet emission, assigned as such due to the large Stokes shift, although interestingly the weak nature of the emission meant that little difference was observed on the introduction of oxygen. The excited state lifetimes were remarkably short for triplet emission being in the region of 10 – 100s of nanoseconds instead of the usual microsecond region. Photoluminescence quantum yields (PLQYs) were very low, with correspondingly high non-radiative decay rate constants ($\sim 10^6$ s^{-1}), while radiative rate constants are three orders of magnitude lower ($\sim 10^3$ s^{-1}).

2-[Au]-R and **2,3-[Au]-R** both emitted in the green region of the spectrum and **2,5-[Au]-R** in the yellow region. The first two displayed vibronically structured emission bands, although the degree of vibronic coupling was reduced in **2,3-[Au]-R** compared to **2-[Au]-R**, indicating more effective excited state mixing. The (0,0) band for **2-[Au]-R** was present at ~488 nm, the smaller (0,1) at ~523 nm and the (0,2) at ~556 nm (Figure 3.44), while for **2,3-[Au]-R** the (0,0) band was slightly red-shifted to ~500 nm while the weaker (0,1) band at ~527 nm changed little (Figure 3.45). **2,5-[Au]-R** displayed no vibronic coupling and instead a very broad band was observed from ~580 – 590 nm (Figure 3.46); the low emission intensity and broad, featureless emission band results in a wide variation on determination of the peak maximum. The emission wavelengths for this series are significantly red-shifted compared to the **2-[Au]**-series and **2,3-[Au]**-series. While the significant red-shifting of the emission compared to the **2-[Au]**-series is not surprising given the additional two electron-donating groups present on the C^N^C pincer ligand, the red-shifting compared to the **2,3-[Au]**-complexes, which also has four electron-donating substituents on the C^N^C pincer ligand, indicates the importance of the position of the substituent on the electronic properties. It is possible, given that the molecular structure for **2,3-[Au]-Cl** shows that, due to steric constraints, the chains in the 2,2′-positions are twisted out of the molecular plane, that the ability of the oxygen atoms to donate into the aromatic π-system could be partially compromised due to reduced or ineffective orbital overlap between the aromatic π-system and the *p*-orbital of the oxygen atom.

It should be noted that due to the low intensity of the emission, uncertainty in the quantum yields is high, and exact spectral integration was challenging. As such, strong conclusions

cannot be drawn from minor variation in values, although information can still be gained by consideration of the relative magnitudes. **2,3-[Au]-R** displayed the largest PLQYs of ~0.1-0.8%, and the longest lifetimes of 75 - 110 ns. Lifetimes for **2-[Au]-R** were shorter, in the region of 25 – 28 ns, with very low PLQYs in the range ~0.01 - 0.09. The lifetimes measured for the **2,5-[Au]-**series were 2 – 4 ns, normally associated with singlet emission, but the strong Stokes shift (~170 nm) indicates that the origin of this emission is triplet in nature. Precedent comes from reports of similar triplet lifetimes.[6] Due to the very weak nature of the emission for this series no quantum yields could be recorded due to the high level of uncertainty in the measurement, hence the radiative and non-radiative rate constant uncertainty would be too high for the values to be meaningful. Interestingly, the values for **2-[Au]-3-10** and **2,3-[Au]-3-10** are both of the order of a factor of two higher than the others in the series. In previous studies on the isomeric 4,4′-disubstituted and 3,3′,4,4′-tetrasubstituted systems, it was postulated that increased protection of the emissive core occurred on addition of additional chains, due to a shielding effect.[22] This resulted in a reduction of external deactivation pathways (*e.g. via* the solvent), potentially offering an explanation for the higher PLQYs observed when three chains are present on the phenylacetylide ligand. It is possible that similar arguments may also be deployed here.
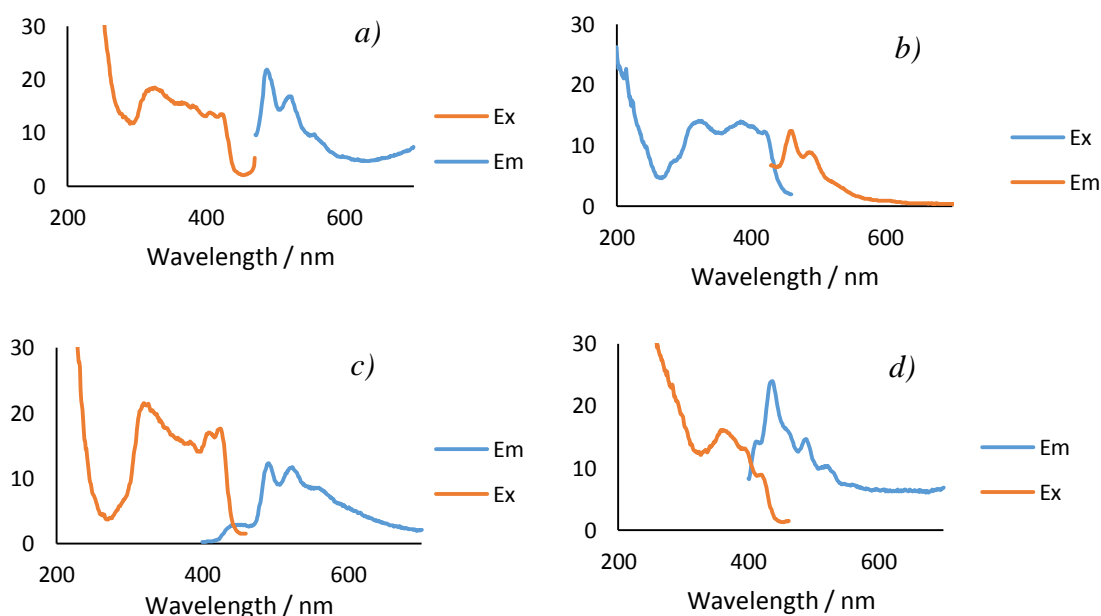
*Figure 3.44: Emission and excitation spectra for the **2-[Au]** complexes in degassed, dichloromethane solution. **2-[Au]-8** (a), **2-[Au]-1-10** (b), **2-[Au]-2-10** (c) and **2-[Au]-3-10** (d).*
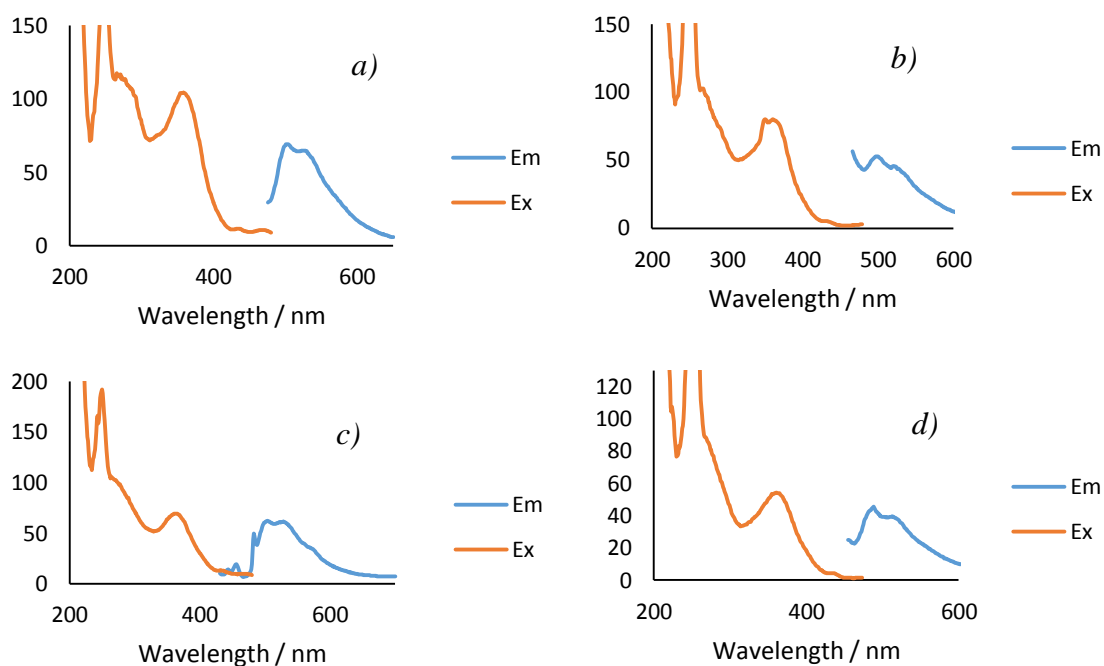
Figure 3.45: Emission and excitation spectra for the 2,3-[Au] complexes in degassed, dichloromethane solution. 2,3-[Au]-8 (a), 2,3-[Au]-1-10 (b), 2,3-[Au]-2-10 (c) and 2,3-[Au]-3-10 (d).
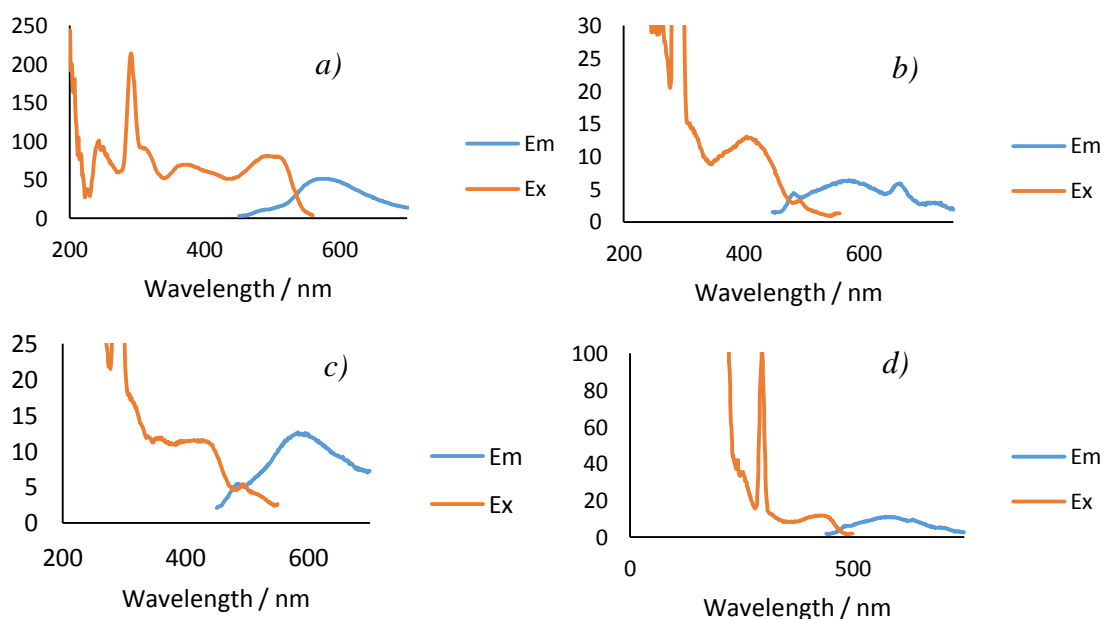
Figure 3.46: Emission and excitation spectra for the 2,5-[Au] complexes in degassed, dichloromethane solution. 2,5-[Au]-8 (a), 2,5-[Au]-1-10 (b), 2,5-[Au]-2-10 (c) and 2,5-[Au]-3-10 (d).

While the PLQYs and lifetimes are low they are comparable to several of the earlier examples in the literature,[6, 7, 13, 26, 28, 44, 45, 68] which have lifetimes 10-100 ns and quantum yields <1%. Comparison of these data with those found for the previously reported isomeric complexes, **4-[Au]-** and **3,4-[Au]-**, is of interest.[29] Thus, on consideration first of the disubstituted pincers, the **4-[Au]-**complexes emit at 502 and ~533 nm, with lifetimes in the range of 7 – 14 μs and quantum yields of 1-3%, a full order of magnitude larger than those of <0.1% reported for **2-[Au]**. The emission wavelength for **2-[Au]** is blue-shifted by ~10 nm compared to that of the **4-[Au]-**complexes, reflecting the blue-shift in the **2-[Au]** absorption spectra. Turning to the tetrasubstituted complexes, the wavelength of emission varies as **2,3-[Au]** < **3,4-[Au]** < **2,5-[Au]** complexes emit at ~500 nm, ~552 nm and ~580 nm respectively. **3,4-[Au]** displays excited state lifetimes of 60 – 120 μs and while the PLQYs (up to 34%) are considerably higher than those reported for the **2,3-[Au]-** (<1%) and **2,5-[Au]-** (too small to be measured) complexes. This indicates that radiative emission is considerably more favourable in isomers which do not have a substituent in the 2-position of the phenyl ring of the C^N^C pincer ligand. Currently the reason is unknown – further discussion will follow the section on computational studies below.

Table 3.9: Photophysical Data for Gold Complexes in Anaerobic Dichloromethane Solution at Room Temperature.

Compound	Absorbance (ε / x 10^3 dm^3 mol^{-1} cm^{-1}) / nm	Excitation / nm	Emission / nm	Lifetime [Aerobic lifetime] / ns	Quantum Yield / 10^{-4}	k_r / x 10^3 s^{-1}	Σk_{nr} / x 10^6 s^{-1}
2-[Au]-8	226 (62), 252 (56), 355 (11), 373 (9.7), 393 (11), 414 (10)	332, 423	488.0, 523.0, ~556	27 [25]	3.2	12	37
2-[Au]-1-10	254 (52), 357 (11), 373 (10), 394 (11), 415 (9.5)	250, 288sh, 319, 327.8, 385.2, 424	489.6, 519.6	25 [20]	6.1	25	40
2-[Au]-2-10	225 (77), 254 (42), 357 (9.7), 393 (11), 414 (8.7).	262, 297sh, 306, 375, 387.4, 408.6, 419	489.6, 523.4, 558	28 [28]	1.1	4	36
2-[Au]-3-10	255 (54), 360 (12), 373 (12), 394 (13), 414 (11)	216, 225.0, 280, 361.2, 390, 420	487.8, 520	28 [25]	13	47	36
2,3-[Au]-8	225 (54), 251 (68), 359 (17).	249.8, 290. 358.0	502.2, 527.2	105 [101]	58	55	9.4
2,3-[Au]-1-10	251 (88), 363 (26)	233.8, 272, 360	500, 527	90 [85]	59	65	11
2,3-[Au]-2-10	225 (72), 251 (7.5), 363 (21).	249.4, ~270, 365.8	503.4, 528.2, ~557	74 [68]	30	41	13
2,3-[Au]-3-10	251 (54), 362 (16)	212.6, 234.8, 260, 360.8	503.0, ~530	100 [65]	76	50	9.9
2,5-[Au]-8	228 (54), 260 (37), 271 (37), 422 (12)	242.6, 305, 373.4	577.8	4.8 [4.7]	-	-	-
2,5-[Au]-1-10	229 (67), 262 (44), 273 (43), 412 (15)	265.0, 315, 405.4	578.2	3.1 [3.1]	-	-	-
2,5-[Au]-2-10	229 (11), 262 (50), 274 (50), 420 (17)	252, 435.2	590.0	2.2 [2.2]	-	-	-
2,5-[Au]-3-10	229 (66), 266 (37), 276 (39), 420 (13)	242.4, 250.4, 423.8	588.4	1.6 [1.6]	-	-	-

Table 3.10: Photophysical Data for C^N^C Pincer Ligands in Dichloromethane Solution at Room Temperature.

Ligand	Absorbance (ε / x 10^3 dm^3 mol^{-1} cm^{-1}) / nm	Excitation / nm	Emission / nm	Lifetime / ns
4-[L]	277 (29), 317 (13)	280.0, 317.0	362.8	2.7
3,4-[L]	231 (25), 276 (18), 320 (15)	245.6, 279.0, 290.0, 323.6	376.0	3.1
2-[L]	228 (21), 246 (18), 304 (15)	308.4, 354	353.6	0.8
2,3-[L]	228 (32), 290 (13)	255.4, 294.4	378.4	1.5
2,5-[L]	228 (29), 324 (10)	244, 257.0, 327.2	389.6	1.8
3/5-[L]-OMe	226 (38), 306 (14)	253.0, 310.6	345.6	1.0
3,5-[L]-OMe	228 (30), 258 (18), 304 (12)	262.3, 304.0	363.8	2.8
2,4-[L]-OMe	263 (18), 311 (13)	268.2, 311.4	367.8, 423.2	2.2

3.9 Computational Studies

3.9.1 Ground State Calculations

Calculations using density function theory (DFT), followed by time-dependent density functional theory (TD-DFT) were carried out on the gold complexes, including a representative example for the **4-[Au]** and **3,4-[Au]** complexes, and the free ligands for comparison. The calculations used Gaussian16[110, 111] on the University of York Viking Computing Cluster to investigate the electronic transitions. The structures of the complexes were optimised, and the IR frequencies calculated, at the bp86/def2-SV(P) level of theory,[112-114] with the lack of negative frequencies in the calculated infrared spectra used to confirm optimisation to a minimum on the potential energy surface.[22, 29] To save on computational time and power, methoxy and ethyl groups were used in the model structures to replace alkoxy and alkyl chains respectively, as chain length is known to have little impact on the electronic properties.[22, 29] Modified single crystal structures were used as the input geometries and solvation was modelled using PCM dichloromethane solvent mask.[115-118] A superfine grid was used for **2,3-[Au]-1-OMe** in order to gain convergence within 48 hours.

TD-DFT calculations were carried out at the pbe0/def2-TZVPP level of theory,[119, 120] with only the five lowest energy transitions calculated for most complexes, as these have previously been shown to be those involved in the photophysical behaviour.[22, 29] However, for a representative complex from each series, with two methoxy-groups on the phenylacetylide ligand, the 20 lowest energy transitions were calculated in order to view a larger portion of the calculated UV-Vis spectrum, produced in GuassView with peaks assuming a Gaussian band shape, with standard deviation 0.4 eV applied to give the peak width. The calculated UV-Vis spectra were compared to the experimental data to confirm the validity of the method (Figure 3.58). The zero-point energy of each complex was calculated by optimising the structure at the pbe0/def2-SV(P) level of theory,[119,114] with an ultrafine grid applied, and then the energy calculated at the pbe0/def2-TZVPP level of theory, again with, an ultrafine grid.[119, 120]

The calculated structures showed a slightly distorted square-planar structure about the gold(III) ion (C^Au^N ~ 80° and C^Au^C ~99°), which is observed in the molecular

crystal structures (Section 2.16). Calculated bond lengths are very similar to those measured experimentally (Table 3.11), though the calculated bond lengths tend to be slightly longer. Thus in general calculation matched experiment well with the exception of positioning of the phenylacetylide ligand for the **2,5-[Au]-R** complexes, where the angles about the C≡C bond are significantly distorted away from 180°, which is not observed in the XRD structure for **2,5-[Au]-3-10**. This likely reflects the difference between the molecule in solution, which is used for the calculations, compared with the experimental measurements in the solid state.

Table 3.11: Comparison of Calculated and Experimental Bond Lengths for Key Bonds.

Bond Type / Å	Experimental Bond Length / Å	Calculated Bond Length / Å
Au-C	2.01 – 2.09	2.10 – 2.13
Au-N	1.91 – 2.01	2.02 – 2.06
Au-C	1.96 – 1.97	1.98 – 2.05
Au-Cl	2.28 – 2.29	2.35
C≡C	1.19 – 1.20	1.24
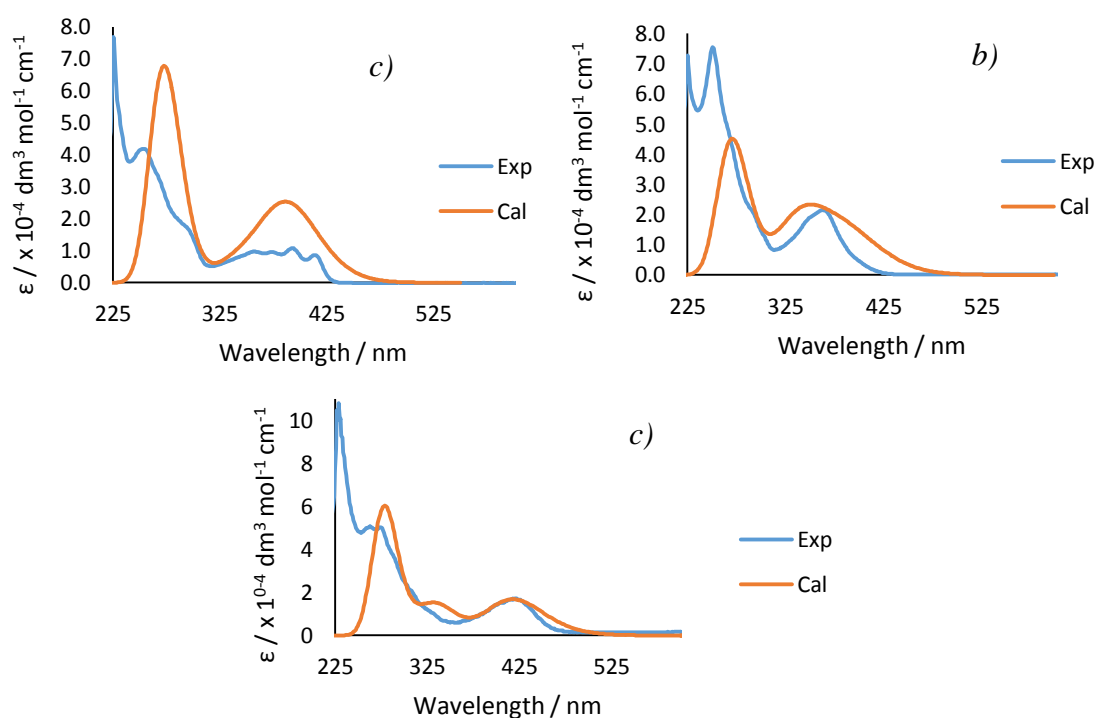
Figure 3.48: Calculated and experimental UV-Vis absorption spectra in dichloromethane solution for (a) 2-[Au]-2-n, (b) 2,3-[Au]-2-n and (c) 2,5-[Au]-2-n, where n = 10 for the experimental spectra and OMe for the calculated spectra.

Comparison of the calculated and experimental UV-Vis spectra shows that generally there is a good match, though it becomes poorer at higher energy (Figure 3.48). For the 2,2′-disubstituted series a systematic red-shift of ~20 nm is observed in the λ_{max} (~385 nm to ~405 nm) for the lower energy band and the calculated spectra do not quite reflect all of the spectral fine detail in this band. For the 2,2′3,3′-tetrasubstituted complexes a systematic blue-shift of ~10-20 nm (~350 nm to ~360-365 nm) is observed in the λ_{max} for the related band. Little difference is observed between the λ_{max} of the calculated and experimental bands (~420 nm) for the 2,2′5,5′-tetrasubstituted complexes. Overall the agreement is good in the area of interest, which gives some confidence in the results from subsequent calculations.

On comparison of the calculated MO energies (Figure 3.49), little difference is observed in the LUMO energy values across the series, bar a slight increase on the change from the chlorogold to alkyne complex. Similarly, varying the substitution pattern on the phenylacetylide ligand has a minor effect on the energy of the HOMO, with only a general increase observed reflecting the effect of increased number of electron-donating substituents on the ligand. On complexation of the free ligand a significant stabilisation of the LUMO orbitals is observed. There is, however, little change in the HOMO energies, indicating a greater influence of the gold(III) ion on the LUMOs, which are shown, below, to contain a greater degree of metal-influence. For the free ligands the LUMOs are very similar and are a π^*-antibonding orbital.
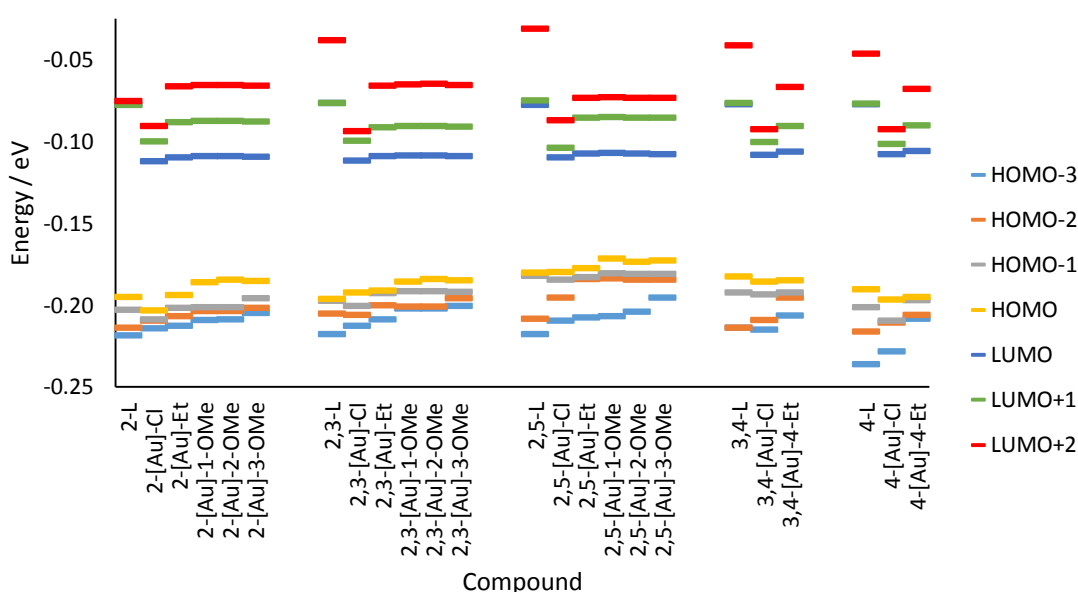
Figure 3.49: Calculated energy levels of the frontier molecular orbitals.

The orbitals for three of the free ligands are considered in more depth (using an isosurface value of 0.02). The HOMO-1 orbital for **2-[L]** is calculated to be a π-bonding orbital based on the phenyl rings (Figure 3.50, top) and the HOMO orbital a π-bonding orbital across all three rings. The HOMO-1 and HOMO orbitals for **2,3-[L]** and **2,5-[L]** are very similar, primarily the π-bonding orbital based on the phenyl rings, with some electron-density placed on the pyridyl ring for the HOMO-orbital (Figure 3.50). Notably, for the HOMO orbital of **2,3-[L]** there is a strong contribution from the nitrogen-based orbitals.
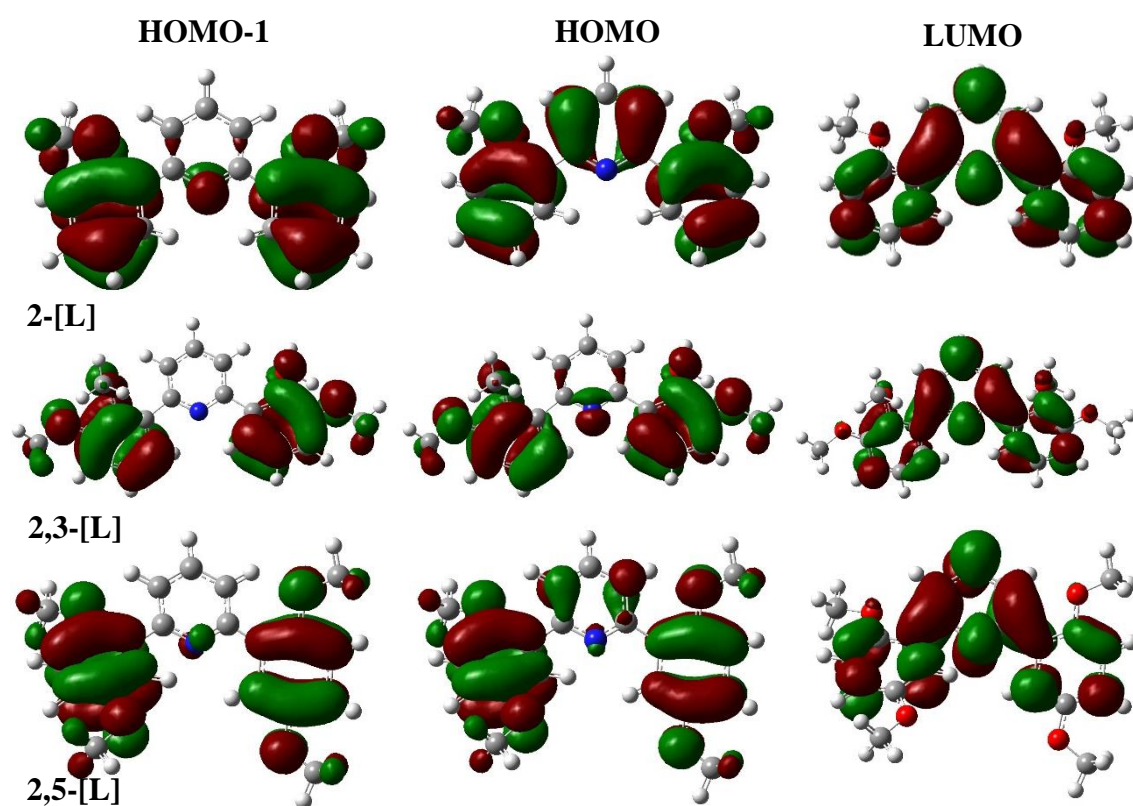
*Figure 3.50: From left to right, the calculated HOMO-1, HOMO and LUMO orbitals for **2-[L]**, top, **2,3-[L]**, middle and **2,5-[L]**, bottom.*

On consideration of the gold complexes, the LUMOs are very similar across all the series, based primarily on the pyridyl unit of the pincer ligand and can be identified as a metal-perturbed π^*-orbital of the C^N^C ligand (Figure 3.51, top).

For **2-[Au]-Cl** the HOMO is a π-bonding orbital of the C^N^C ligand, while the HOMO-1 is primarily the π^*-orbital of the Au-C and Au-Cl bonds. For **2,3-[Au]-Cl** and **2,5-[Au]-**

Cl complexes the HOMO and the HOMO-1 orbitals are very similar and are π-bonding orbitals of the phenyl rings (Figure 3.51).
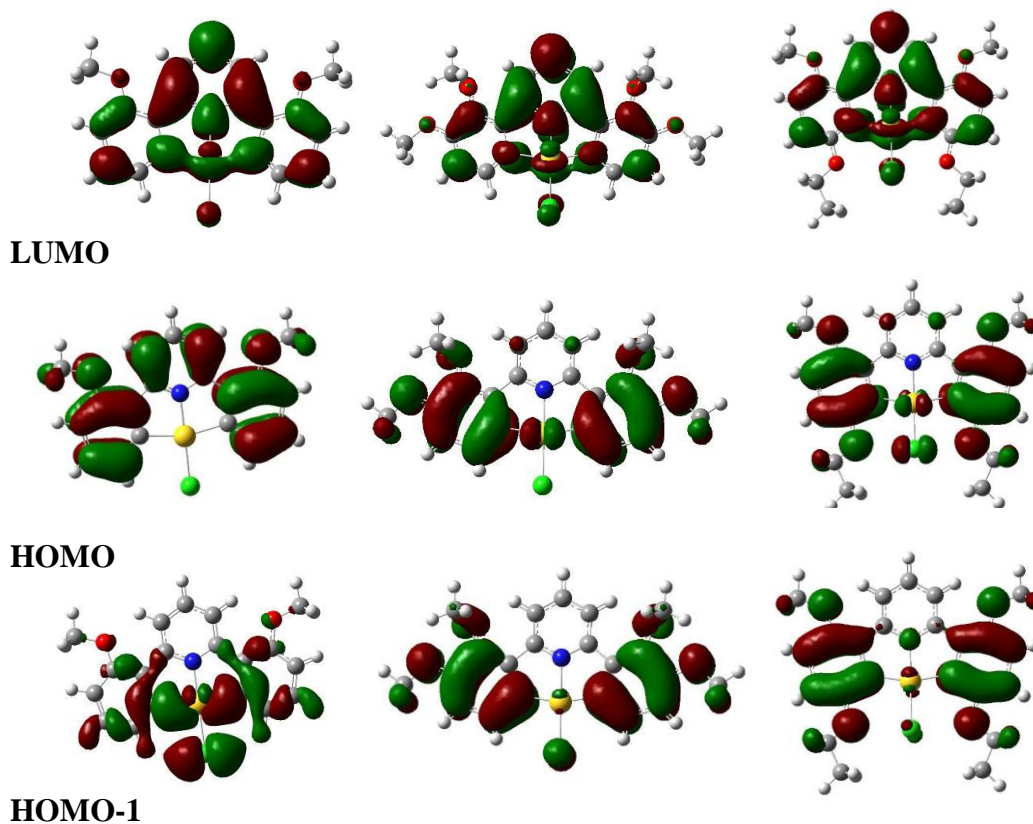
LUMO

HOMO

HOMO-1

*Figure 3.51: Calculated LUMO orbitals (top), HOMO orbitals (middle) and HOMO-1 orbitals (bottom) for, left to right, **2-[Au]-Cl**, **2,3-[Au]-Cl** and **2,5-[Au]-Cl**.*

For complexes **2-[Au]-Et**, **2-[Au]-1-OMe** and **2-[Au]-2-OMe** the HOMO-1 orbital is a π-bonding orbital of the C^N^C ligand (Figure 3.52, top), with electron density concentrated on the phenyl units and a small amount of metal influence. The HOMO orbital is a π-bonding orbital based on the phenylacetylide ligand, with some metal influence. On changing to three methoxy-substituents, **2-[Au]-3-OMe**, the HOMO orbital remains unchanged, however the HOMO-1 orbital becomes the π-orbitals of the phenyl unit of the phenylacetylide ligand (Figure 3.52, middle). This is similar to the calculated MOs reported for the **4-[Au]-*n*** series[22, 29] and related complexes, which is not unexpected given the similar electronic natures of the substituents.[7]

HOMO-1   **HOMO**   **LUMO**

2-[Au]-2-OMe
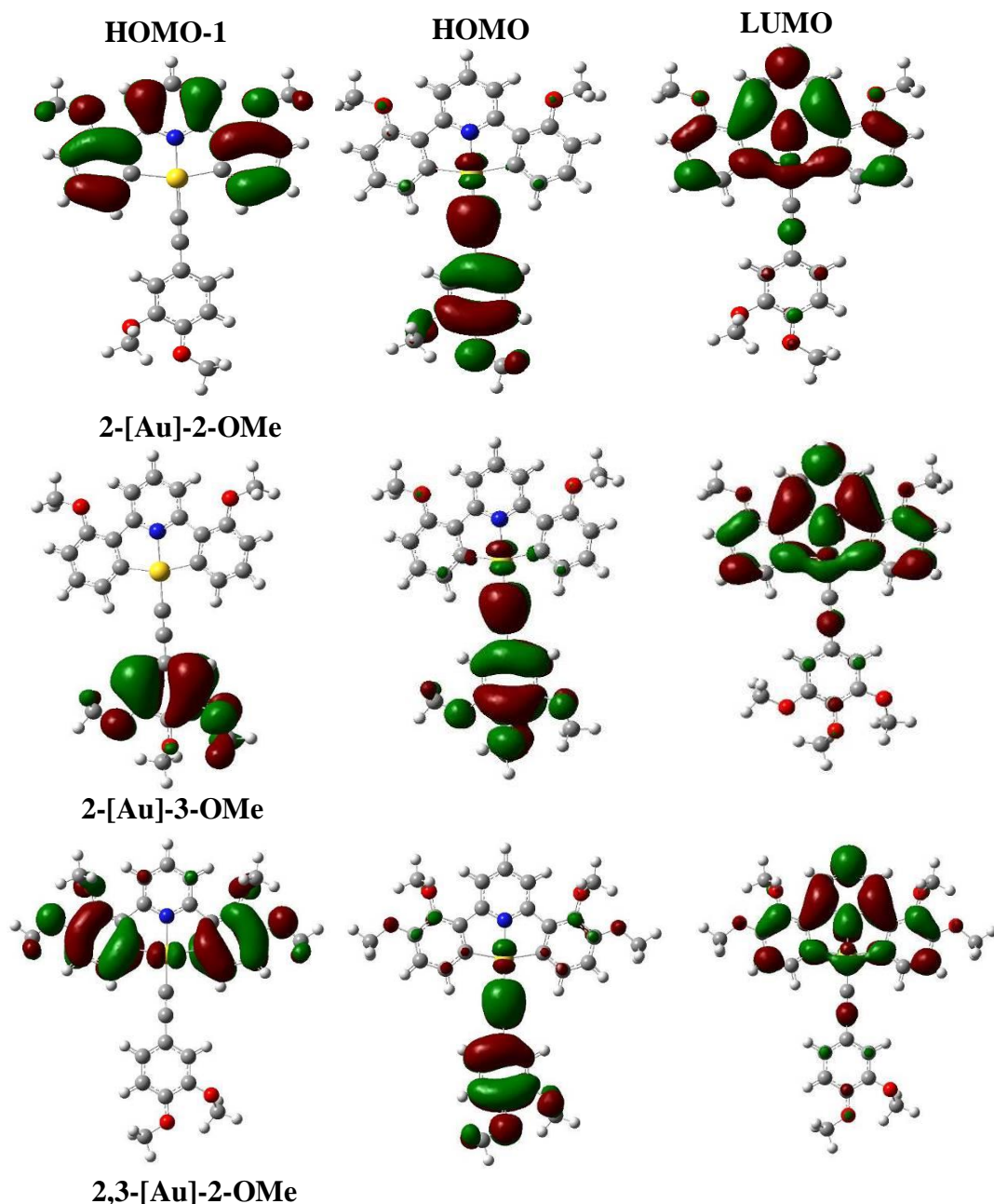
2-[Au]-3-OMe

2,3-[Au]-2-OMe

*Figure 3.52: From left to right, the calculated HOMO-1, HOMO and LUMO orbitals for **2-[Au]-2-OMe** (top), **2-[Au]-3-OMe** (middle) and **2,3-[Au]-2-OMe** (bottom).*

For the **2,3-[Au]-*n*** complexes the HOMO-1 orbital is the metal-perturbed π-bonding orbitals of the phenyl units for the C^N^C ligand, while the HOMO orbital is the metal-perturbed π-bonding orbitals of the phenylacetylide ligand (Figure 3.52, bottom). This is similar to the calculated MOs reported for the **3,4-[Au]-*n*** complexes, however less electron density is placed on the pyridyl ring in the HOMO-1 for **2,3-[Au]**.[22, 29] For **2,5-[Au]-Et** the HOMO and the HOMO-1 orbitals are the π-bonding orbitals of the phenylacetylide and the phenyl rings of the C^N^C ligand, with some metal influence,

and little difference is observed between the two (Figure 3.53, top). On introduction of methoxy substituents on the phenylacetylide ligand, electron-density on the ligand is reduced for the HOMO-1 orbital, while the electron-density on the phenyl units of the C^N^C ligand is reduced for the HOMO orbital (Figure 3.53, bottom).

HOMO-1   **HOMO**   **LUMO**
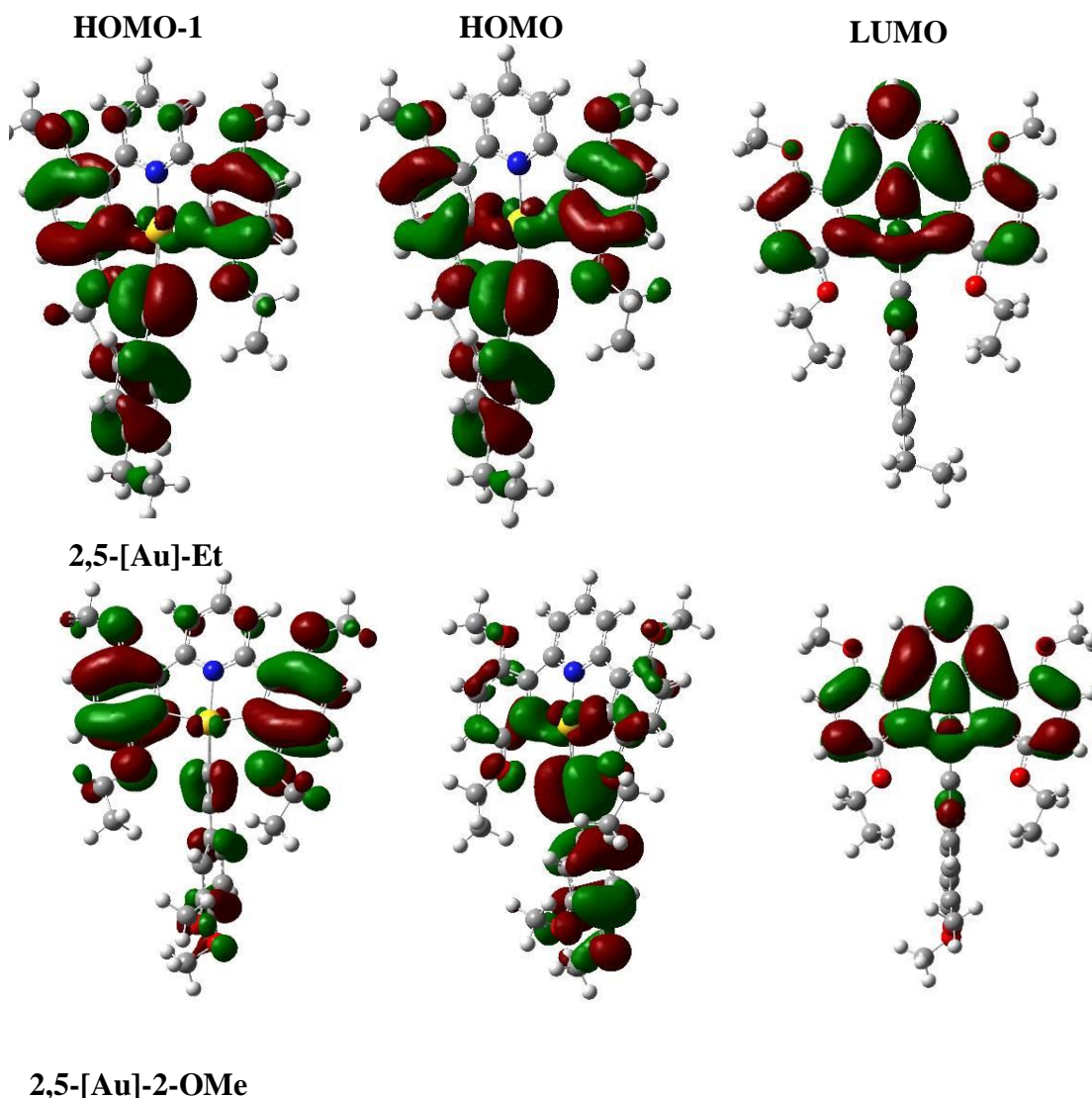
2,5-[Au]-Et

2,5-[Au]-2-OMe

Figure 3.53: From left to right, the calculated HOMO-1, HOMO and LUMO orbitals for ***2,5-[Au]-Et*** *(top) and* ***2,5-[Au]-2-OMe*** *(bottom).*

Since the HOMO is based on the phenylacetylide ligand for all complexes it is not surprising that a minor destabilisation of the energy is observed on addition of electron-donating substituents to this ligand (Figure 3.49). Equally, it is not surprising that the pincer ligand-based LUMO energy remains effectively unchanged. It is clear that for **2-[Au]** and **2,3-[Au]** the additional electron-donating substituent results in a reduction in electron-density based on the pyridyl ring in the HOMO-1, but little difference in the

phenylacetylide based HOMO. On changing the additional substituent position to the 5,5′-positions significantly more delocalisation of the electron density is observed in the HOMO and HOMO-1, particularly for **2,5-[Au]-Et**.

3.9.2 Calculated Electronic Transitions

The calculated transitions for the gold complexes (**2-[Au]-R**, **2,3-[Au]-R** and **2,5-[Au]-R**) have been studied to try to identify their nature; they are summarised in Table 3.15. The **2-[Au]-R** complexes (Table 3.12) displayed a mixture of LLCT and ILCT transitions in the frontier transitions, while **2,3-[Au]-R** (Table 3.13) displayed mainly LLCT transitions and **2,5-[Au]-R** (Table 3.14) a mix of LLCT and ILCT transitions. Where ILCT occurs electron density is transferred from the phenyl unit of the pincer ligand to the pyridyl unit. Whereas with LLCT electron density is transferred from the phenylacetylide to the pincer. These classes of transitions have been reported previously for other complexes of this type.[7, 11, 54, 56, 121, 122] The free ligands show ILCT, with electron transfer from the phenyl units to the pyridyl unit.

Table 3.12: Summary of TD-DFT predicted transitions for complexes in the **2-[Au]**-series. Only transitions with an oscillator strength >0.001 and orbital contributions >10% are listed.

Complex	Transition Energy / nm	Oscillator Strength	Occupied Orbital	Virtual Orbital	Orbital Contribution / %	Transition
2-[L]	307	0.5091	77	78	94.6	HOMO - LUMO
	284	0.0800	76	78	24.7	HOMO-1 - LUMO
			77	79	57.7	HOMO – LUMO+1
2-[Au]-Cl	388	0.1966	94	95	82.3	HOMO – LUMO
	349	0.1886	92	95	79.7	HOMO-2 - LUMO
			94	95	12.2	HOMO - LUMO
2-[Au]-Et	390	0.0904	120	121	87.3	HOMO – LUMO
	382	0.2484	119	121	89.0	HOMO–1 - LUMO
2-[Au]-1-OMe	395	0.2410	129	121	98.2	HOMO-LUMO
	382	0.2454	119	121	89.0	HOMO-1 - LUMO
2-[Au]-2-OMe	398	0.2129	128	129	95.7	HOMO - LUMO
	382	0.2458	127	129	89.0	HOMO-1 - LUMO
2-[Au]-3-OMe	391	0.1720	136	137	91.1	HOMO - LUMO
	383	0.2455	135	137	89.0	HOMO-1 - LUMO

Table 3.13: Summary of TD-DFT predicted transitions for complexes in the **2,3-[Au]**-series. Only transitions with an oscillator strength >0.001 and orbital contributions >10% are listed.

Complex	Transition Energy / nm	Oscillator Strength	Occupied Orbital	Virtual Orbital	Orbital Contribution / %	Transition
2,3-[L]	289	0.0264	92	94	22.3	HOMO-1 - LUMO
			93	95	56.1	HOMO – LUMO+1
	288	0.4136	91	95	61.3	HOMO-2 – LUMO+1
			93	95	25.0	HOMO – LUMO+1
2,3-[Au]-Cl	407	0.0029	110	111	89.8	HOMO - LUMO
	374	0.0054	110	112	85.9	HOMO – LUMO+1
2,3-[Au]-Et	399	0.0040	135	137	83.3	HOMO - LUMO
			136	137	10.4	HOMO - LUMO
	392	0.0715	136	137	79.5	HOMO - LUMO
2,3-[Au]-1-OMe	398	0.0025	135	137	93.1	HOMO-1 - LUMO
	392	0.2493	136	137	97.0	HOMO - LUMO
2,3-[Au]-2-OMe	399	0.0024	143	145	93.2	HOMO-1 - LUMO
	393	0.2518	144	145	97.8	HOMO - LUMO
2,3-[Au]-3-OMe	399	0.0028	151	153	92.9	HOMO-1 - LUMO
	390	0.1744	152	153	89.1	HOMO - LUMO

Table 3.14: Summary of TD-DFT predicted transitions for complexes in the **2,5-[Au]**-series. Only transitions with an oscillator strength >0.001 and orbital contributions >10% are listed.

Complex	Transition Energy / nm	Oscillator Strength	Occupied Orbital	Virtual Orbital	Orbital Contribution / %	Transition
2,5-[L]	328	0.3906	93	94	94.3	HOMO - LUMO
	315	0.0054	92	94	80.5	HOMO-1 - LUMO
			93	95	13.5	HOMO – LUMO+1
2,5-[Au]-Cl	433	0.2011	118	119	82.1	HOMO - LUMO
			118	120	15.5	HOMO – LUMO+1
	422	0.0837	118	119	15.6	HOMO - LUMO
			118	120	78.2	HOMO – LUMO+1
2,5-[Au]-Et	445	0.0427	144	145	95.2	HOMO - LUMO
	416	0.2681	143	145	95.3	HOMO-1 - LUMO
2,5-[Au]-1-OMe	464	0.0112	144	145	97	HOMO - LUMO
	419	0.2921	143	145	97.9	HOMO-1 - LUMO
2,5-[Au]-2-OMe	453	0.0214	152	153	96.4	HOMO - LUMO
	418	0.2860	151	153	97.6	HOMO-1 - LUMO
2,5-[Au]-3-OMe	506	0.0019	160	161	97.1	HOMO - LUMO
	420	0.1840	159	161	97.1	HOMO-1 - LUMO

Table 3.15: Summary of Primary Transition Nature and Origin for Complexes.

Complex	Nature of Primary Transition(s)	Origin
2-[Au]-Cl	ILCT	HOMO - LUMO and HOMO-3 - LUMO
2-[Au]-*n*	LLCT ILCT	HOMO – LUMO HOMO-1 – LUMO
2,3-[Au]-Cl	ILCT	HOMO - LUMO and HOMO-3-LUMO
2,3-[Au]-*n*	LLCT	HOMO – LUMO
2,5-[Au]-Cl	ILCT and MLCT	HOMO - LUMO
2,5-[Au]-*n*	LLCT ILCT	HOMO-LUMO HOMO-1 – LUMO HOMO-2-LUMO

3.9.2.1 *Natural Transition Orbitals*

Natural Transition Orbitals (NTOs)[123] offer a more qualitative description of electronic transitions treating the system as a hole-particle excitation. Frequently, electronic excitations involve several individual orbitals, as in this case, with varying degrees of contribution, which can be challenging to interpret. In NTOs all orbitals involved in the transition are combined into two representative orbitals, offering a simpler representation and leading to a more chemically intuitive description for relevant transitions.

NTOs for the complexes were calculated at the pbe0/def2-TZVPP[119, 120] level of theory. In all cases the unoccupied NTO corresponds primarily to the canonical LUMO and was unchanged across the series, except for **2,3-[Au]-Cl** and **2,5-[Au]-Cl**, with the former showing a highly complex Lowest Unoccupied NTO (LUNTO), while the **2,5-[Au]-Cl** complex shows more influence from the metal-chloride bond (Figure 3.54). The chlorogold complexes NTOs indicate that the primary transition is the π-π* transition of the C^N^C ligand.
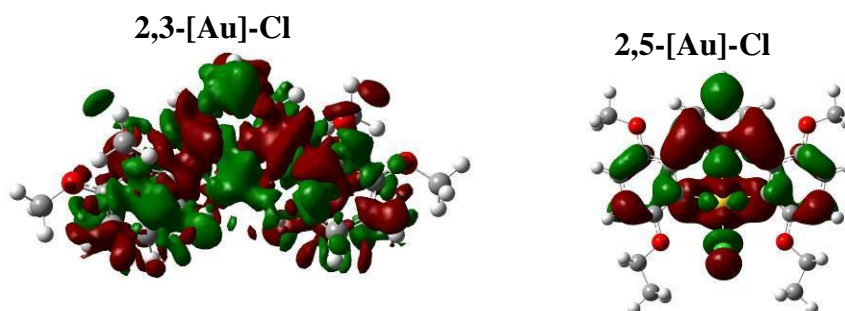
2,3-[Au]-Cl   **2,5-[Au]-Cl**

*Figure 3.54: Calculated LUNTOs for **2,3-[Au]-Cl** (left) and **2,5-[Au]-Cl** (right).*
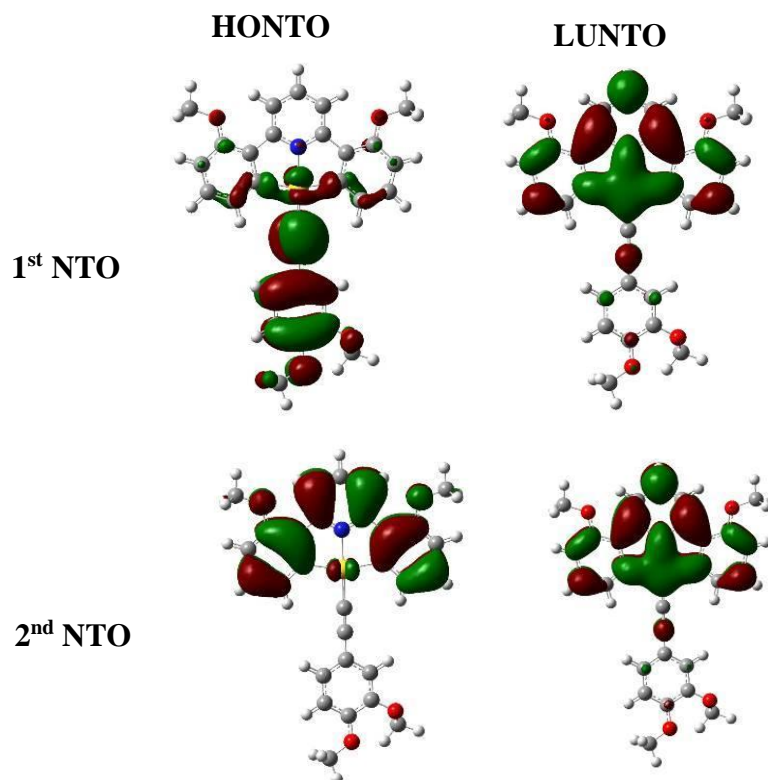
*Figure 3.55: The calculated first NTO (top) and second NTO (bottom) for **2-[Au]-2-OMe**.*

For **2-[Au]-R** the first NTO transition is shown to be primarily the HOMO-LUMO LLCT transition, with an electronic transition from the phenylacetylide ligand to the C^N^C ligand (Figure 3.55, top). The second NTO, which is relatively close in energy to the first NTO (<0.1 eV), with an even greater oscillator strength, is primarily the HOMO-1 – LUMO transition - the π-π* transition of the C^N^C ligand, with some degree of ILCT from the phenyl unit to the pyridyl unit (Figure 3.55, bottom). **2,5-[Au]-R** complexes display the same general pattern, although there is calculated to be a greater degree of electron density present on the phenyl units of both ligands in the Highest Occupied NTO (HONTO), particularly for **2,5-[Au]-Et** (Figure 3.56).

HONTO   LUNTO
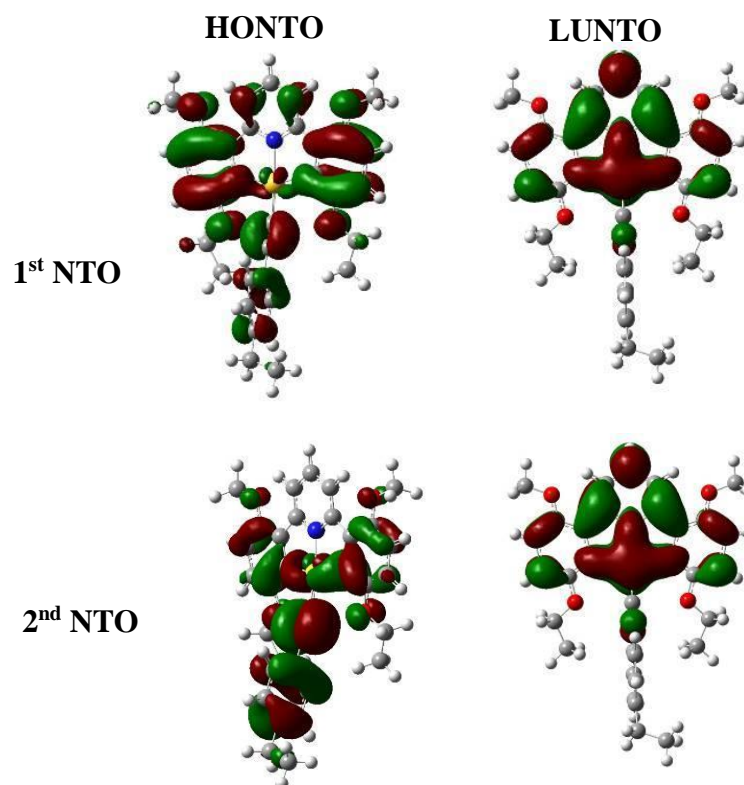
1st NTO

2nd NTO

*Figure 3. 56: The calculated first NTO (top) and second NTO (bottom) for **2,5-[Au]-2-Et**.*

For **2,3-[Au]-R** the lowest energy NTO with the highest oscillator strength is the second NTO (Figure 3.57), the HOMO – LUMO transition, which is primarily a LLCT transition, with electronic transition from the phenylacetylide ligand to the C^N^C ligand.

HONTO   LUNTO
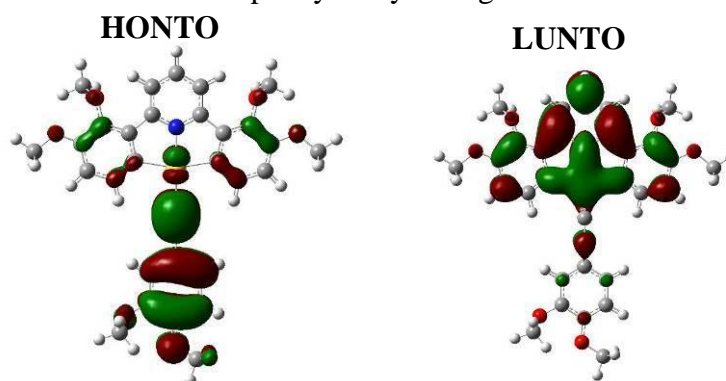
*Figure 3.57: The calculated second NTO for **2,3-[Au]-2-OMe**.*

Calculation of the NTOs supports the conclusions drawn from consideration of the component MOs of the complexes, with frequently the 'particle' and 'hole' arising predominately from one of the frontier orbitals. However calculation of the NTOs enables consideration of the influences of the minor contributions from other orbitals involved in the transitions. Notably, in the 2nd NTO for **2-[Au]-2-10** it can be seen that despite the

HONTO being predominantly composed of the HOMO-1 which displays no metal influence, the minor mixing of other MOs results in the calculated HONTO having a small metal influence, important in the behaviour of the transition.

3.9.3   Calculated Excited States

The first singlet excited state structure was calculated at the pbe0/def2-TZVPP level of theory.[119, 120]

2-[Au]-Cl   **2,3-[Au]-Cl**   **2,5-[Au]-Cl**
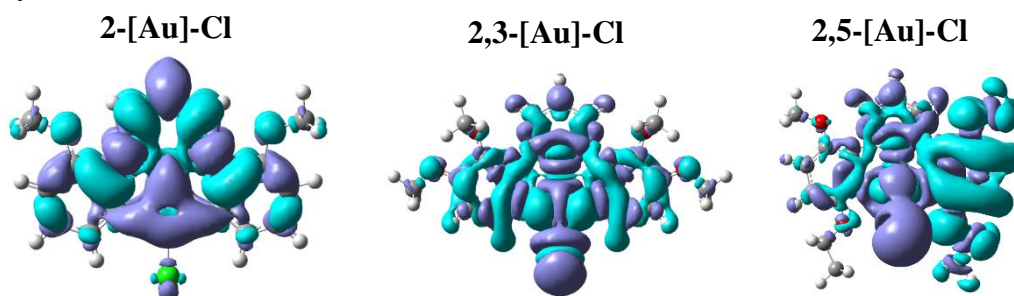
*Figure 3.58: Calculated S$_1$ state, showing the electron difference map for the S$_1$ state compared to the ground state for, left to right, **2-[Au]-Cl**, **2,3-[Au]-Cl** and **2,5-[Au]-Cl**. Turquoise shows loss of electron density and purple gain of electron density.*

2-[Au]-2-OMe   **2,3-[Au]-2-OMe**   **2,5-[Au]-2-OMe**
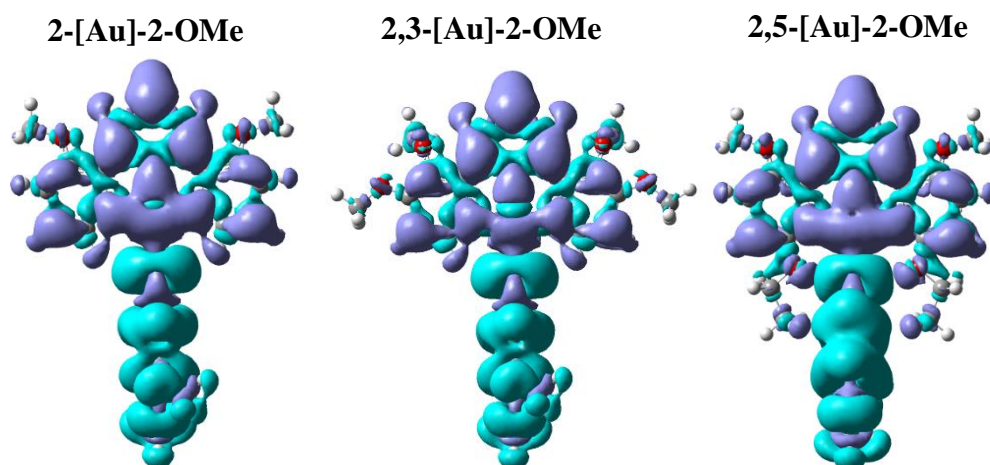
*Figure 3.59: Calculated S$_1$ state, showing the electron difference map for the S$_1$ state compared to the ground state, left to right, for **2-[Au]-2-OMe**, **2,3-[Au]-2-OMe** and **2,5-[Au]-2-OMe**. Turquoise shows loss of electron density and purple gain of electron density.*

No major structural distortion to the aromatic framework was observed in the S$_1$ state, although the plane of the phenylacetylide ligand is twisted ~90° relative to the plane of the pincer ligand, which is only observed in the **2,5-[Au]-**series in the ground state. Minor negative IR frequencies were observed for **2-[Au]-Et** and **2-[Au]-2-OMe** falling in the range of -10 to -150 cm^{-1}, indicating that optimisation has failed to find the true energy

minimum, however the small magnitude of the frequencies indicates that this is unlikely to have a significant impact on the overall energies. Complexes **2-[Au]-3-OMe**, **2,3-[Au]-Et**, **2,3-[Au]-1-OMe**, **2,3-[Au]-3-OMe** and **2,5-[Au]-3-OMe** failed to converge to a solution within 30 days, therefore were deemed too computationally expensive to calculate.

Electron difference maps between the S_1 excited state and the S_0 ground state were calculated and for the chlorogold complexes it is found that electron density is transferred primarily from the phenyl units to the pyridyl unit and the gold centre (Figure 3.58). For the alkynyl gold(III) complexes, for all series, almost identical electron difference maps are calculated, where electron density is transferred from the phenylacetylide ligand to the C^N^C ligand (Figure 3.59). However, when the S_1 states for the previously reported complexes, **4-[Au]-Et**, **3,4-[Au]-Et** and **3,4-[Au]-2-OMe**,[22, 29] were calculated the electron difference maps showed a significant difference (Figure 3.60). Therefore, electron density is transferred primarily from the phenyl units to the pyridyl unit of the C^N^C and the gold, with no significant electron density transfer from the phenylacetylide ligand being observed. Planarity of the phenylacetylide ligand with respect to the plane of the C^N^C ligand was also maintained. It appears that there is a change in the primary transition type from ILCT for the **4-[Au]-** and the **3,4-[Au]-**series to LLCT for the **2-[Au]-**, **2,3-[Au]-** and **2,5-[Au]-**series for formation of the first excited singlet state, potentially offering a hint as to the difference in the PLQYs between the complexes.
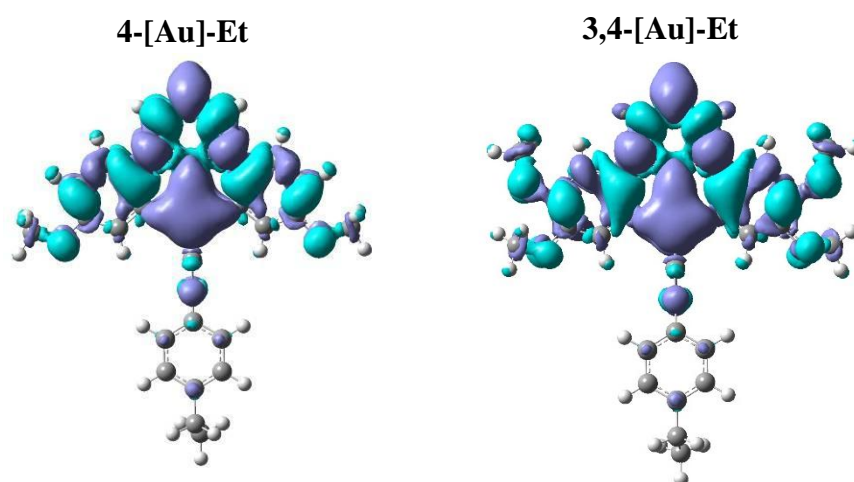
4-[Au]-Et   **3,4-[Au]-Et**

*Figure 3.60: Calculated S_1 state, showing the electron difference map for the S_0 state compared to the ground state, left to right, for **4-[Au]-Et**, and **3,4-[Au]-Et**. Turquoise shows loss of electron density and purple gain of electron density.*

The geometry of the lowest-energy triplet state structure was calculated at the pbe0/def2-SV(P) level of theory,[119, 114] and then the single point energy calculated at the pbe0/def2-TZVPP level of theory,[119, 120] with the optimised singlet excited state used as the input geometry. The triplet spin states for complexes **2-[Au]-1-OMe** and **2,3-[Au]-1-OMe** failed to converge using this method.

2-[Au]-2-OMe   **2,3-[Au]-2-OMe**   **2,5-[Au]-2-OMe**
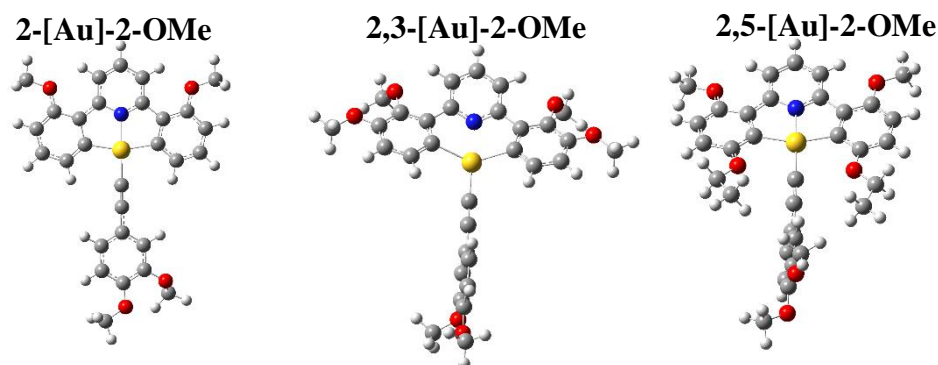
*Figure 3.61: Calculated T$_1$ excited states, left to right, for **2-[Au]-2-OMe**, **2,3-[Au]-2-OMe** and **2,5-[Au]-2-OMe**.*

The degree of distortion in the square-planar geometry about the gold ion is increased in the excited triplet state (Figure 3.61), resulting in a change in the bond angles for C^Au^C from ~99° to ~110° and for C^Au^N from ~80° to ~74°. As a result the Au-N bond length increases from ~2.0-2.05 Å to ~2.2 Å and the two Au-C bond lengths from ~2.1 Å to ~2.2 Å. Only the remaining Au-C bond length remains unchanged at ~1.98 Å. Twisting of the plane of the phenylacetylide ligand by ~90° to the plane of the C^N^C ligand was observed in **2-[Au]-4-Et**, **2,3-[Au]-2-OMe** and **2,3-[Au]-3-OMe**. A very small energy gap between the T$_1$ and S$_1$ state is calculated for all complexes (~0.02 eV).

The singlet and triplet emission energies were calculated by taking the difference between the calculated excited state energies and the ground state energy (Figure 3.62), where possible, and are reported in Table 3.16. Generally, they show a good match with the experimental values, with the **2,5-[Au]-** complexes calculated to emit at longer wavelengths than the **2-[Au]-** and **2,3-[Au]**-complexes. The calculated values for **2-[Au]-** and **2,3-[Au]**-complexes were very similar, with those for the **2,3-[Au]**-complexes being slightly longer. Again, this is replicated in the experimental results, though the experimental values gives a larger average difference between the emission wavelengths (10 nm *vs* 2-10 nm). The calculations would suggest more influence of the number of

substituents on the phenylacetylide ligand on the emission wavelength that is observed experimentally (variation in experimental values is within the instrument variation), however this could be due to state mixing that is not replicated in the calculations. The experimental values are red-shifted 15 nm compared to those calculated for the **2-[Au]-**complexes, 13-25 nm for the **2,3-[Au]-**complexes and 30-50 nm for the **2,5-[Au]-**complexes[††]. While the absolute values are not replicated the trend in the emission energies is.

Table 3.16: Calculated Singlet and Triplet Emission Wavelengths Compared to Experimental

Complex	Calculated Singlet Emission Wavelength / nm	Calculated Triplet Emission Wavelength / nm	Experimental Triplet Emission Wavelength / nm
2-[Au]-Cl	418	495	-
2-[Au]-8	441	475	488
2-[Au]-1-10	470	-	490
2-[Au]-2-10	472	474	490
2-[Au]-3-10	-	475	488
2,3-[Au]-Cl	477	571	-
2,3-[Au]-8	-	490	502
2,3-[Au]-1-10	-	-	500
2,3-[Au]-2-10	474	477	503
2,3-[Au]-3-10	-	477	503
2,5-[Au]-Cl	566	684	-
2,5-[Au]-8	500	549	578
2,5-[Au]-1-10	531	555	579
2,5-[Au]-2-10	534	542	590
2,5-[Au]-3-10	-	542	588
3/5-[Au]-Cl	429	495	-
2,4-[Au]-Cl	445	496	-

[††] Please note the low emission intensity and broad, featureless emission band results in a wide variation on determination of the peak maximum.
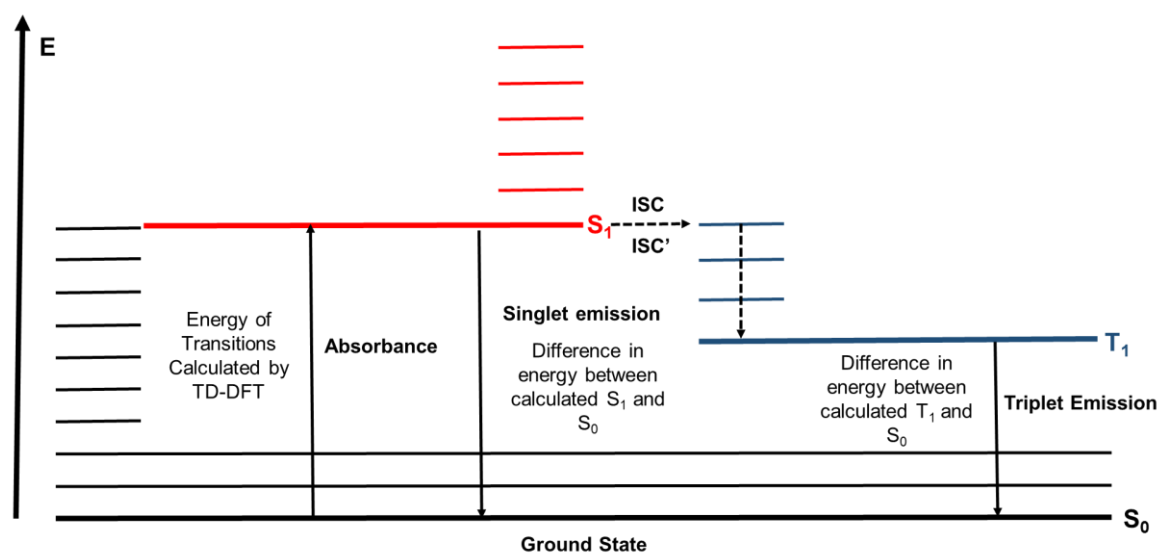
Figure 3.62: Simple Jabłoński diagram demonstrating the method of calculation of the singlet and triplet energies from the calculated energies of the ground and excited states.

3.9.4 Discussion

A series of 2,2′-disubstituted, 2,2′,3,3′- and 2,2′,5,5′-tetrasubstituted gold(III) complexes have been synthesised that are structurally similar to the previously reported 4,4′-disubstituted and 3,3′,4,4′-tetrasubstituted gold(III) complexes,[22, 29] however they exhibit significantly lower PLQYs. Therefore computational calculations have been undertaken to further investigate their photophysical behaviour.

For all complexes the LUMO is primarily concentrated on the pyridyl unit of the pincer ligand and is identifiable as a metal-perturbed π*-orbital of the C^N^C ligand. For the **2-[Au]-R** and **2,3-[Au]-R** phenylacetylide complexes, the HOMO is predominately based on the phenylacetylide ligand, while the HOMO-1 is primarily based on the C^N^C pincer ligand. This is similar to the calculated MOs reported for the **4-[Au]-*n*** series[22, 29] and related complexes.[7] For the **2,5-[Au]-R** complexes the HOMO and HOMO-1 orbitals are both based on the phenylacetylide ligand and the phenyl rings of the pincer ligand. Due to the location of the orbitals on the complexes, little change in the pincer ligand based HOMO-1 energies is observed within individual series of complexes, although a change is observed between the series. Thus, on the introduction of two additional electron-donating substituents (*i.e.* the 2,2′,3,3′-tetrasubstituted complexes) there is a slight destabilisation of the orbital energies compared to the 2,2′-disubstituted analogues.

217

For the phenylacetylide-based HOMO, there is a slight increase in orbital energies on the introduction of additional electron-donating substituents. A similar relationship is observed in the isomeric 4,4′-disubstituted and 3,3′,4,4′-tetrasubstituted series.[22] The electronic transitions can be identified as a mix of HOMO → LUMO and HOMO-1 → to LUMO, which can be assigned as LLCT and IL, with some ILCT, respectively, with the latter generally having the greater oscillator strength. For the 2,2′,5,5′-tetrasubstituted complexes, the change in orbital nature results in both the HOMO and the HOMO-1 being at higher energies than the other two series, with the result that the electronic transition is inherently a mix of ILCT and LLCT, which is not unknown in similar literature.[27] The state mixing might account for the lack of vibronically structured emission for this system.

Where the pincer ligand has substituents in the 4,4′- or 3,3′,4,4′-positions, the S_1 excited state arises from a ^{1}IL transition within the pincer ligand itself. However, where the pincer ligand has substituents in the 2,2′-positions, then the transition is ^{1}LLCT in nature with electron transfer from the phenylacetylide to the pincer. This indicates a change in the relative ordering of these two singlet excited states on the change in the substitution pattern.[7] However, what is not entirely clear is the extent to which these Franck-Condon transitions contribute to populating the emissive states as evidently there are several transitions of similar energy and the calculations quickly become very expensive as more are accommodated into the model. As such, while these differences can be identified, it is not clear that they would account for such a huge change in PLQY in the new complexes and so an alternative explanation is required.

Previously, the higher quantum yields for **3,4-[Au]-R** has been assigned to the additional two electron-donating substituents reducing the triplet excited state energy, resulting in a greater energy gap with the deactivating *d-d* states therefore non-radiative decay became less efficient,[22, 29] however given that the triplet excited state is lower in energy for **2,3-[Au]-R** and **2,5-[Au]-R** compared to **4-[Au]-R**, and the **2,5-[Au]-R** triplet state is lower than that for **3,4-[Au]-R**, yet quantum yields are considerably lower it would suggest that this does not provide the explanation for these complexes. Previously, it has been shown in studies that the presence of low-lying non-emissive states close in energy to the triplet state result in effect non-radiative emission, and this likely offers a possible explanation for the high non-radiative rate constants,[38, 122,124] through such 'dark' states are extremely

challenging to calculate computationally. In particular it must be noted that previously it has been showed that low-lying ^{3}LLCT states which 'have a large out-of-plane torsional motion between the planes of the C^N^C and arylacetylide ligands'[122] are shown to increase k_{nr}, giving a 690-1500-fold increase, compared to the k_{nr} rate constant for the higher energy ^{3}IL state.

As shown in Table 3.9 and in ref. 22, the values of the radiative decay constant, k_r, obtained from the emission data for both the new complexes (1-5 x 10^3 s^{-1}) and those studied previously (6-70 x 10^3 s^{-1}) are not dissimilar. As such, the differing values of the PLQYs are determined by the efficiency of the non-radiative processes as expressed by k_{nr} and it is here that significant variations are observed. Thus, in **4-[Au]-R and 3,4-[Au]-R**, k_{nr} is on the order of 5-10 x 10^3 s^{-1} for the more emissive tetrasubstituted complexes and *ca* 100-140 x 10^3 s^{-1} for the less emissive disubstituted materials. However, for **2-[Au]-R and 2,3-[Au]-R**, k_{nr} is on the order of 10-40 x 10^6 s^{-1} – some two orders of magnitude greater. The emission for **2,5-[Au]-R** was too low to give measurable PLQYs and, therefore, reliable calculated values of k_{nr}, but it can be assumed that the actual values are higher than those for calculated for **2,3-[Au]-R** on consideration of the fact that the measured emission was too low for values to be obtained.

Therefore, the lower quantum yields exhibited by complexes with substituents in the 2,2′-positions may be due to the greater efficiency of deactivation for these complexes compared to their isomers. Potentially, this is due to either the aforementioned possible low-lying 'dark' state(s) or alternately the presence of the steric clash between the 2,2′-position substituents and the pyridyl hydrogens. This is evidenced by the twisted configuration present in the free ligand compared with the enforced co-planarity in the gold complexes where a steric clash ensues, demonstrated by the shifting of the pyridyl hydrogen signals significantly downfield (see Sections 2.7, 2.16 and 2.18.1). This steric clash can possibly result in more motion and distortion in the excited states resulting in deactivation through vibrations and rotations and less emissive decay. Further investigation of this *via* computational calculations would be challenging and beyond the scope of this work.

3.10   Summary and Conclusions

The mesophase and photophysical properties of [Au(III)(C^N^C)(C≡C-R)] complexes, where R is a phenyl ring substituted with alkyl, alkoxy and perfluoro chains, were investigated. For the 2,2′-disubstituted series, where the substituents are hydrocarbon chains, only **2-[Au]-3-14** displayed a monotropic columnar mesophase, with a lack of effective space-filling by the chains preventing formation of columnar mesophases for the other complexes in the series. However, on introduction of perfluorinated chains to give **2-[Au]-F10** and **2-[Au]-F12**, microphase segregation due to the perfluorinated effect resulted in formation of a bilayer SmA mesophase.[95, 101] An antiparallel pairing of the molecules, due to the amphiphilic nature of the complex, is believed to occur to give a rod-shape, which can then arrange in the lamella SmA mesophase. This behaviour of mesophase induction on introduction of perfluorinated chains stands in contrast with that observed in the isomeric 4,4′-disubstituted series where induction of perfluorinated chains results in destabilisation of the mesophase.[30, 31]

Most of the **2,3-[Au]-R** complexes did not show mesophases, again thought to be due to a lack of effective space-filling by the chains to form a disc-like shape, however compounds substituted with three alkoxy chains on the phenylacetylide ligand displayed hexagonal columnar mesophases. **2,3-[Au]-3-10** displayed a monotropic columnar phase, however on increasing chain length to give **2,3-[Au]-3-12** and **2,3-[Au]-3-14** fully endiotropic hexagonal columnar phases were formed. The clearing point temperature remained stable with increasing chain length, however the melting point temperature decreased, resulting in a widening of the phase range.

The more rod-shaped nature of complexes that were substituted in the 2,2′,5,5′-positions of the C^N^C ligand resulted in formation of smectic A phases when there was only one chain in the *para*-position of the phenylacetylide ligand (**2,5-[Au]-8** and **2,5-[Au]-1-***n* (where *n* = 10, 12, 14)).[104-106] On increasing change length both the clearing temperature and the melting point decreased, initially resulting in a widening of the phase. However, the clearing point falls more quickly than the melting point so that for **2,5-[Au]-1-14**, the SmA phase becomes monotropic. The smectic A mesophases are lost on introduction of additional chains with **2,5-[Au]-2-10** and **2,5-[Au]-3-10** both displaying monotropic columnar phases. The additional molecular width due to the addition of lateral chains

results in a loss of molecular anisotropy lengthways destabilising mesophase formation. This, combined with the change in molecular shape, resulted in formation of monotropic columnar phases, which is known of in other metallomesogen systems.[107, 108] The narrowness of the phase meant that further characterisation by SAXS to determine the symmetry of the mesophase could not be undertaken. Overall, it can be observed that, unsurprisingly, molecular shape with these complexes is highly important in the nature of the phase formed.

The photophysics of the complexes proved to be surprising due to the unusually short lifetimes for triplet emission (<100 ns) and very low PLQYs (<0.1%), particularly for the **2,5-[Au]**-series, driven by high non-radiative rate constants (k_{nr} ~10^6 s^{-1}). Given that the isomeric 4,4′-disubstituted and 3,3′,4,4′-tetrasubstituted complexes display considerably higher PLQYs,[29] particularly the latter, this is disappointing, though it must be noted that these results are not entirely unexpected for this type of complex, with many complexes in the literature displaying this behaviour.[6, 7, 13, 26, 28, 44, 45, 68] The 2,2′-disubstituted series emitted in the green region at 490 nm, with a vibronically structured band, lifetimes of 25 – 28 ns and low PLQYs of ~0.01 - 0.09%. The 2,2′,3,3′-disubstituted series emitted in the green region at 500 nm, with a vibronically structured band, with longer lifetimes of 75 - 110 ns and higher PLQYs of ~0.1-0.8%. Finally, the 2,2′,5,5′-disubstituted series emitted in the yellow region with a broad band at 570 – 590 nm. The very low intensity of the emission meant that PLQYs could not be determined. TD-DFT calculations indicated that the emission type was primarily LLCT, where electron density is transferred from the phenylacetylide ligand to the C^N^C ligand, with some mixed IL/ILCT, where electron density is transferred from the phenyl rings to the pyridine ring. This is in line with calculations for related systems.[7, 29, 56] The S_1 excited state was calculated and determined to be [1]LLCT, with electron transfer from the phenylacetylide ligand to the C^N^C ligand. This marks a change from the calculated S_1 excited state for the 4,4′-disubstituted and 3,3′,4,4′-tetrasubstituted systems, which are shown to be [1]IL. Calculated triplet emission energies show a good match with the experimental data giving good confidence for the validity of the calculations. Higher non-radiative decay constants for complexes with substituents in the 2,2′-positions compared to their isomeric complexes, which results in the considerably lower quantum yields, is possibly due to low-lying dark state(s) or alternating the presence of a steric clash between the substituents in the 2,2′-positions and the pyridyl hydrogen resulting in more distortion and motion in the excited states resulting

in more deactivation *via* vibrational energy pathways. Further investigation of this would be challenging and beyond the scope of this work.

3.11 References

1. A. Vogler and H. Kunkely, *Coord. Chem. Rev.*, 2001, **219-221**, 489-507.
2. C. Bronner and O. S. Wenger, *Dalton Trans.*, 2011, **40**, 12409-12420.
3. R. Kumar and C. Nevado, *Angew. Chem. Int. Ed.*, 2017, **56**, 1994-2015.
4. V. W.-W. Yam and A. S.-Y. Law, *Coord. Chem. Rev.*, 2020, **414**.
5. K. M. Wong, X. Zhu, L. L. Hung, N. Zhu, V. W. Yam and H. S. Kwok, *Chem. Commun.*, 2005, 2906-2908.
6. Z. T. Yu, X. L. Liu, Y. J. Yuan, Y. H. Li, G. H. Chen and Z. G. Zou, *Dalton Trans.*, 2016, **45**, 17223-17232.
7. K. M.-C. Wong, L.-L. Hung, W. H. Lam, N. Zhu and V. W.-W. Yam, *J. Am. Chem. Soc.*, 2007, **29**, 4350-4365.
8. V. W.-W. Yam, S. W.-K. Choi, T.-F. Lai and W.-K. Lee, *J. Chem. Soc., Dalton Trans.*, 1993, 1001–1002.
9. O.-W. Chan, W.-T. Wong and C.-M. Che, *Inorg. Chem.*, 1994, **33**, 1266-1272.
10. H.-Q.-Liu, T.-C. Cheung, S.-M. Peng and C.-M. Che, *J. Chem. Soc., Chem. Commum.*, 1995, 1787-1788.
11. V. K. Au, W. H. Lam, W. T. Wong and V. W. Yam, *Inorg. Chem.*, 2012, **51**, 7537-7545.
12. K.-H. Wong, K.-K. Cheung, M. C.-W. Chan and C.-M. Che, *Organometallics*, 1998, **17**, 3505-3511.
13. V. W. Yam, K. M. Wong, L. L. Hung and N. Zhu, *Angew. Chem. Int. Ed.*, 2005, **44**, 3107-3110.
14. M. S. M. Holmsen, A. Nova, K. Hylland, D. S. Wragg, S. Oien-Odegaard, R. H. Heyn and M. Tilset, *Chem. Commun.,* 2018, **54**, 11104-11107.
15. V. W. Yam, K. H. Chan, K. M. Wong and N. Zhu, *Chem. Eur. J.*, 2005, **11**, 4535-4543.
16. M. C. Tang, W. K. Kwok, S. L. Lai, W. L. Cheung, M. Y. Chan and V. Wing-Wah Yam, *Chem. Sci.*, 2019, **10**, 594-605.
17. V. K.-M. Au, D. P.-K. Tsang, Y.-C. Wong, M.-Y. Chan and V. W.-W. Yam, *J. Organomet. Chem.*, 2015, **792**, 109-116.
18. V. K. Au, D. P. Tsang, K. M. Wong, M. Y. Chan, N. Zhu and V. W. Yam, *Inorg. Chem.*, 2013, **52**, 12713-12725.
19. E. Y. Hong, C. T. Poon and V. W. Yam, *J. Am. Chem. Soc.*, 2016, **138**, 6368-6371.
20. K. T. Chan, G. S. M. Tong, W. P. To, C. Yang, L. Du, D. L. Phillips and C. M. Che, *Chem. Sci.*, 2017, **8**, 2352-2364.
21. S. K.-L. Siu, C. Po, K.-C. Yim, V. K.-M. Au and V. W.-W. Yam, *CrystEngComm*, 2015, **17**, 8153-8162.
22. R. R. Parker, PhD Thesis, University of York, 2019.
23. V. K. Au, N. Zhu and V. W. Yam, *Inorg. Chem.*, 2013, **52**, 558-567.
24. K. C. Yim, E. S. Lam, K. M. Wong, V. K. Au, C. C. Ko, W. H. Lam and V. W. Yam, *Chem. Eur. J.*, 2014, **20**, 9930-9939.
25. H. L.-K. Fu and V. W.-W. Yam, *Chem. Lett.*, 2018, **47**, 605-610.
26. S. K.-L. Siu, C. Y.-S. Chung and V. W.-W. Yam, *J. Organomet. Chem.*, 2017, **845**, 177-188.

27.	K. C. Yim, V. K. Au, L. L. Hung, K. M. Wong and V. W. Yam, *Chem. Eur. J.*, 2016, **22**, 16258-16270.

28.	K. C. Yim, V. K. Au, K. M. Wong and V. W. Yam, *Chem. Eur. J.*, 2017, **23**, 5772-5786.

29.	R. R. Parker, D. Liu, X. Yu, A. C. Whitwood, W. Zhu, J. A. G. Williams, Y. Wang, J. M. Lynam and D. W. Bruce, *J. Mater. Chem. C*, 2021, **9**, 1287-1302.

30.	R. R. Parker, A. J. McEllin, X. Zeng, J. M. Lynam and D. W. Bruce, *Liq. Cryst.*, 2021, **49**, 1162-1173.

31.	R. R. Parker, R. F. Stracey, A. J. McEllin, X. Chen, Y. Wang, J. A. G. Williams, J. M. Lynam and D. W. Bruce, *ACS Omega*, 2022, **7**, 24903-24917.

32.	L.-K. Li, M.-C. Tang, S.-L. Lai, M. Ng, W.-K. Kwok, M.-Y. Chan and V. W.-W. Yam, *Nat. Photonics*, 2019, **13**, 185-191.

33.	M. C. Tang, M. Y. Chan and V. W. Yam, *Chem. Rev.*, 2021, **121**, 7249-7279.

34.	V. K. Au, D. Wu and V. W. Yam, *J. Am. Chem. Soc.*, 2015, **137**, 4654-4657.

35.	X. Li, Y. Xie and Z. Li, *Chem Asian J*, 2021, **16**, 2817-2829.

36.	J. Bauri, R. B. Choudhary and G. Mandal, *J. Mater. Sci.*, 2021, **56**, 18837–18866.

37.	V. K.-M. Au, K. M.-C. Wong, F. P.-K. Tsang, M.-Y. Chan, N. Zhu and V. W.-W. Yam, *J. Am. Chem. Soc.*, 2010, **132**, 14273-14278.

38.	H. Beucher, S. Kumar, E. Merino, W.-H. Hu, G. Stemmler, S. Cuesta-Galisteo, J. A. González, J. Jagielski, C.-J. Shih and C. Nevado, *Chem. Mater.*, 2020, **32**, 1605-1611.

39.	W. P. To, K. T. Chan, G. S. Tong, C. Ma, W. M. Kwok, X. Guan, K. H. Low and C. M. Che, *Angew. Chem. Int. Ed.*, 2013, **52**, 6648-6652.

40.	G. Cheng, K. T. Chan, W. P. To and C. M. Che, *Adv. Mater.*, 2014, **26**, 2540-2546.

41.	W.-L. Cheung, S.-L. Lai, W.-K. Kwok, M.-C. Tang, C.-H. Lee, M.-Y. Chan and V. W.-W. Yam, *J. Mater. Sci.*, 2020, **55**, 9686-9694.

42.	M. C. Tang, C. K. Chan, D. P. Tsang, Y. C. Wong, M. M. Chan, K. M. Wong and V. W. Yam, *Chem. Eur. J.*, 2014, **20**, 15233-15241.

43.	C. H. Lee, M. C. Tang, Y. C. Wong, M. Y. Chan and V. W. Yam, *J. Am. Chem. Soc.*, 2017, **139**, 10539-10550.

44.	M.-C. Tang, D. P.-K. Tsang, M.-Y. Chan, K. M.-C. Wong and V. W.-W. Yam, *Mater. Chem. Front.*, 2017, **1**, 2559-2568.

45.	M. C. Tang, D. P. Tsang, Y. C. Wong, M. Y. Chan, K. M. Wong and V. W. Yam, *J. Am. Chem. Soc.*, 2014, **136**, 17861-17868.

46.	C. H. Lee, M. C. Tang, W. L. Cheung, S. L. Lai, M. Y. Chan and V. W. Yam, *Chem. Sci.*, 2018, **9**, 6228-6232.

47.	N. Savjani, D. A. Rosca, M. Schormann and M. Bochmann, *Angew. Chem. Int. Ed.*, 2013, **52**, 874-877.

48.	L. Rocchigiani, J. Fernandez-Cestau, G. Agonigi, I. Chambrier, P. H. M. Budzelaar and M. Bochmann, *Angew. Chem. Int. Ed.*, 2017, **56**, 13861-13865.

49.	D.-A. Roşca, J. Fernandez-Cestau, J. Morris, J. A. Wright and M. Bochmann, *Sci. Adv.*, 2015, **1**.

50.	D. A. Rosca, J. A. Wright and M. Bochmann, *Dalton Trans.*, 2015, **44**, 20785-20807.

51.	L. Currie, L. Rocchigiani, D. L. Hughes and M. Bochmann, *Dalton Trans.*, 2018, **47**, 6333-6343.

52.	D. A. Rosca, D. A. Smith and M. Bochmann, *Chem. Commun.*, 2012, **48**, 7247-7249.

53. L. Rocchigiani, J. Fernandez-Cestau, I. Chambrier, P. Hrobarik and M. Bochmann, *J. Am. Chem. Soc.*, 2018, **140**, 8287-8302.

54. J. Fernandez-Cestau, B. t. Bertrand, A. Pintus and M. Bochmann, *Organometallics*, 2017, **36**, 3304-3312.

55. X. Lv, Y. Han, Z. Yang, Z. Li, Z. Gao and F. Wang, *Tetrahedron Lett.*, 2016, **57**, 1971-1975.

56. L.-L. Hung, W. H. Lam, K. M.-C. Wong, E. C.-C. Cheng, N. Zhu and V. W.-W. Yam, *Inorg. Chem. Front.*, 2015, **2**, 453-466.

57. R. Munoz-Rodriguez, E. Bunuel, N. Fuentes, J. A. Williams and D. J. Cardenas, *Dalton Trans.*, 2015, **44**, 8394-8405.

58. R. Munoz-Rodriguez, E. Bunuel, J. A. Williams and D. J. Cardenas, *Chem. Commun.* , 2012, **48**, 5980-5982.

59. V. K.-M. Au, K. M.-C. Wong, N. Zhu and V. W.-W. Yam, *J. Am. Chem. Soc.*, 2009, **131**, 9076-9085.

60. M. Williams, A. I. Green, J. Fernandez-Cestau, D. L. Hughes, M. A. O'Connell, M. Searcey, B. Bertrand and M. Bochmann, *Dalton Trans.*, 2017, **46**, 13397-13408.

61. C. Y. Sun, W. P. To, X. L. Wang, K. T. Chan, Z. M. Su and C. M. Che, *Chem. Sci.*, 2015, **6**, 7105-7111.

62. D.-A. Roşca, J. Fernandez-Cestau, A. S. Romanov and M. Bochmann, *J. Organomet. Chem.*, 2015, **792**, 117-122.

63. X. S. Xiao, W. L. Kwong, X. Guan, C. Yang, W. Lu and C. M. Che, *Chem. Eur. J.*, 2013, **19**, 9457-9462.

64. W. P. To, G. S. M. Tong, C. W. Cheung, C. Yang, D. Zhou and C. M. Che, *Inorg. Chem.*, 2017, **56**, 5046-5059.

65. W. P. To, D. Zhou, G. S. M. Tong, G. Cheng, C. Yang and C. M. Che, *Angew. Chem. Int. Ed.*, 2017, **56**, 14036-14041.

66. J. Fernandez-Cestau, B. Bertrand, M. Blaya, G. A. Jones, T. J. Penfold and M. Bochmann, *Chem. Commun.,* 2015, **51**, 16629-16632.

67. L. Currie, J. Fernandez-Cestau, L. Rocchigiani, B. Bertrand, S. J. Lancaster, D. L. Hughes, H. Duckworth, S. T. Jones, D. Credgington, T. J. Penfold and M. Bochmann, *Chem. Eur. J.*, 2017, **23**, 105-113.

68. M. C. Tang, M. Y. Leung, S. L. Lai, M. Ng, M. Y. Chan and V. Wing-Wah Yam, *J. Am. Chem. Soc.*, 2018, **140**, 13115-13124.

69. M. Y. Leung, M. C. Tang, W. L. Cheung, S. L. Lai, M. Ng, M. Y. Chan and V. Wing-Wah Yam, *J. Am. Chem. Soc.*, 2020, **142**, 2448-2459.

70. R. Kumar, A. Linden and C. Nevado, *Angew. Chem. Int. Ed.*, 2015, **54**, 14287-14290.

71. W. Lu, K. T. Chan, S.-X. Wu, Y. Chen and C.-M. Che, *Chem. Sci.*, 2012, **3**, 752-755.

72. L. K. Li, C. C. Au-Yeung, M. C. Tang, S. L. Lai, W. L. Cheung, M. Ng, M. Y. Chan and V. W. Yam, *Mater Horiz*, 2022, **9**, 281-293.

73. G. Alesso, M. A. Cinellu, S. Stoccoro, A. Zucca, G. Minghetti, C. Manassero, S. Rizzato, O. Swang and M. K. Ghosh, *Dalton Trans.*, 2010, **39**, 10293-10304.

74. A. Herbst, C. Bronner, P. Dechambenoit and O. S. Wenger, *Organometallics*, 2013, **32**, 1807-1814.

75. S. Stoccoro, G. Alesso, M. A. Cinellu, G. Minghetti, A. Zucca, M. Manassero and C. Manassero, *Dalton. Trans.*, 2009, 3467-3477.

76. B.-Z. Yang, X. Zhou, T. Liu, F.-Q. Bai and H.-X. Zhang, *J. Phys. Chem. A*, 2009, **113**, 9396-9403.

77. B. Y. Wong, H. L. Wong, Y. C. Wong, M. Y. Chan and V. W. Yam, *Angew. Chem. Int. Ed.*, 2017, **56**, 302-305.

78. D. Zhou, W. P. To, G. S. M. Tong, G. Cheng, L. Du, D. L. Phillips and C. M. Che, *Angew. Chem. Int. Ed.*, 2020, **59**, 6375-6382.

79. C. H. Lee, M. C. Tang, F. K. Kong, W. L. Cheung, M. Ng, M. Y. Chan and V. W. Yam, *J. Am. Chem. Soc.*, 2020, **142**, 520-529.

80. M. C. Tang, L. K. Li, S. L. Lai, W. L. Cheung, M. Ng, C. Y. Wong, M. Y. Chan and V. W. Yam, *Angew. Chem. Int. Ed..*, 2020, **59**, 21023-21031.

81. M. Prehm, S. Diele, M. K. Das and C. Tschierske, *J. Am. Chem. Soc.*, 2003, **125**, 614-615.

82. M. Prehm, X. H. Cheng, S. Diele, M. K. Das and C. Tschierske, *J. Am. Chem. Soc.*, 2002, **124**, 12072-12073.

83. X. Cheng, M. Prehm, M. K. Das, J. Kain, U. Baumeister, S. Diele, D. Leine, A. Blume and C. Tschierske, *J. Am. Chem. Soc.*, 2003, **125**, 10977-10996.

84. M. Prehm, F. Liu, U. Baumeister, X. Zeng, G. Ungar and C. Tschierske, *Angew. Chem. Int. Ed.*, 2007, **46**, 7972-7975.

85. M. Prehm, F. Liu, X. Zeng, G. Ungar and C. Tschierske, *J. Am. Chem. Soc.*, 2008, **130**, 14922–14923.

86. R. Kieffer, M. Prehm, B. Glettner, K. Pelz, U. Baumeister, F. Liu, X. Zeng, G. Ungar and C. Tschierske, *Chem. Commun.*, 2008, 3861-3863.

87. B. Glettner, F. Liu, X. Zeng, M. Prehm, U. Baumeister, M. Walker, M. A. Bates, P. Boesecke, G. Ungar and C. Tschierske, *Angew. Chem. Int. Ed.*, 2008, **47**, 9063-9066.

88. G. Ungar, F. Liu, X. B. Zeng, B. Glettner, M. Prehm, R. Kieffer and C. Tschierske, *J. Phys.: Conf. Ser.*, 2010, **247**.

89. M. Prehm, F. Liu, X. Zeng, G. Ungar and C. Tschierske, *J. Am. Chem. Soc.*, 2011, **133**, 4906-4916.

90. V. Percec, M. Glodde, G. Johansson, V. S. K. Balagurusamy and P. A. Heiney, *Angew. Chem.*, 2003, **115**, 4474-4478.

91. V. Percec, M. R. Imam, T. K. Bera, V. S. Balagurusamy, M. Peterca and P. A. Heiney, *Angew. Chem. Int. Ed.*, 2005, **44**, 4739-4745.

92. B. Glettner, F. Liu, X. Zeng, M. Prehm, U. Baumeister, G. Ungar and C. Tschierske, *Angew. Chem. Int. Ed.*, 2008, **47**, 6080-6083.

93. M. Lehmann, *Chem. Eur. J.*, 2009, **15**, 3638-3651.

94. L. de Campo, M. J. Moghaddam, T. Varslot, N. Kirby, R. Mittelbach, T. Sawkins and S. T. Hyde, *Chem. Mater.*, 2015, **27**, 857-866.

95. A. Martin, C. Mügge, D. L. Gin, B. Donnio and W. Weigand, *Eur. J. Inorg. Chem.*, 2014, **2014**, 5609-5617.

96. A. Gainar, M.-C. Tzeng, B. Heinrich, B. Donnio and D. W. Bruce, *J. Phys. Chem. B*, 2017, **121**, 8817-8828.

97. B. I. Ostrovskii, in *Structure and Bonding, Liquid Crystals I*, ed. D. M. P. Mingos, Springer, New York/Heidelberg, 1999, p. 199.

98. W. H. d. Jeu, B. I. Ostrovskii and A. N. Shalaginov, *Rev. Mod. Phys.*, 2003, **75**, 181-235.

99. V. Molinier, P. H. Kouwer, Y. Queneau, J. Fitremann, G. Mackenzie and J. W. Goodby, *Chem. Commun.,* 2003, 2860-2861.

100. P. Gyawali, R. Saha, G. P. Smith, M. Salamonczyk, P. Kharel, S. Basu, R. Li, M. Fukuto, J. T. Gleeson, N. A. Clark, A. Jakli, H. Balci and S. Sprunt, *Proc. Natl. Acad. Sci. USA*, 2021, **118**.

101. J. C. Haenle, Y. Stöckl, R. Forschner, E. Haenle and S. Laschat, *ChemPhysChem*, 2018, **19**, 2758-2767.

102. A. Pegenau, X. Hong Cheng, C. Tschierske, P. Göring and S. Diele, *New J. Chem.*, 1999, **23**, 465-467.

103. X. H. Cheng, S. Diele and C. Tschierske, *Angew. Chem. Int. Ed.*, 2000, **39**, 592-595.

104. M. A. J. S. Baena, P. Espinet, M. A. B. Ros, J. L. Serrano and A. Ezcurra, *Angew. Chem. Int. Ed..*, 1993, **32**, 1203-1205.

105. M. J. Baena, J. Buey, P. Espinet, H.-S. Kitzerow and G. Heppke, *Angew. Chem. Int. Ed.*, 1993, **32**, 1201-1203.

106. M. J. Baena, J. Barberfi, P. Espinet, A. Ezcurra, M. B. Ros and J. L. Serrano, *J. Am. Chem. Soc.*, 1994, **116**, 1899-1906.

107. C. Damm, G. Israel, T. Hegmann and C. Tschierske, *J. Mater. Chem.*, 2006, **16**, 1808.

108. T. Hegmann, J. Kain, S. Diele, B. Schubert, H. Bögel and C. Tschierske, *J. Mater. Chem.*, 2003, **13**, 991-1003.

109. K. Suzuki, A. Kobayashi, S. Kaneko, K. Takehira, T. Yoshihara, H. Ishida, Y. Shiina, S. Oishi and S. Tobita, *Phys. Chem. Chem. Phys.*, 2009, **11**, 9850-9860.

110. M. J. Frisch, G. W. Trucks, H. B. Schlegel, G. E. Scuseria, M. A. Robb, J. R. Cheeseman, G. Scalmani, V. Barone, G. A. Petersson, H. Nakatsuji, M. C. X. Li, A. V. Marenich, J. Bloino, B. G. Janesko, R. Gomperts, B. Mennucci, H. P. Hratchian, J. V. Ortiz, A. F. Izmaylov, J. L. Sonnenberg, D. Williams-Young, F. Ding, F. Lipparini, F. Egidi, J. Goings, B. Peng, A. Petrone, T. Henderson, D. Ranasinghe, V. G. Zakrzewski, N. R. J. Gao, G. Zheng, W. Liang, M. Hada, M. Ehara, K. Toyota, R. Fukuda, J. Hasegawa, M. Ishida, T. Nakajima, Y. Honda, O. Kitao, H. Nakai, T. Vreven, K. Throssell, J. J. A. Montgomery, J. E. Peralta, F. Ogliaro, M. J. Bearpark, J. J. Heyd, E. N. Brothers, K. N. Kudin, V. N. Staroverov, T. A. Keith, R. Kobayashi, J. Normand, K. Raghavachari, A. P. Rendell, J. C. Burant, S. S. Iyengar, J. Tomasi, M. Cossi, J. M. Millam, M. Klene, C. Adamo, R. Cammi, J. W. Ochterski, R. L. Martin, K. Morokuma, O. Farkas, J. B. Foresman and D. J. Fox, GAUSSIAN 16 (Revision G16W), Gaussian, Inc., Wallingford CT, 2016.

111. R. Dennington, T. A. Keith and J. M. Millam, GAUSSVIEW 6.0, Semichem Inc., Shawnee Mission, KS, 2016.

112. J. P. Perdew, *Phys. Rev. B Condens. Matter.*, 1986, **33**, 8822-8824.

113. A. D. Becke, *Phys. Rev. A Gen. Phys.*, 1988, **38**, 3098-3100.

114. F. Weigend and R. Ahlrichs, *Phys. Chem. Chem. Phys.*, 2005, **7**, 3297-3305.

115. S. Miertus, E. Scrocco and J. Tomasi, *Chem. Phys.*, 1981, **55**, 117-129.

116. S. Miertus and J. Tomasi, *Chem. Phys.*, 1982, **65**, 239-245.

117. J. L. Pascual-Ahuir, E. Silla and I. Tunon, *J. Comput. Chem.*, 1994, **15**, 1127-1138.

118. J. Tomasi, B. Mennucci and R. Cammi, *Chem. Rev.*, 2005, **105**, 2999−3093.

119. A. D. Becke, *J. Chem. Phys.*, 1993, **98**, 5648-5652.

120. F. Weigend, *Phys. Chem. Chem. Phys.*, 2006, **8**, 1057-1065.

121. C. C. Au-Yeung, L. K. Li, M. C. Tang, S. L. Lai, W. L. Cheung, M. Ng, M. Y. Chan and V. W. Yam, *Chem. Sci.*, 2021, **12**, 9516-9527.

122. G. S. Ming Tong, K. T. Chan, X. Chang and C. M. Che, *Chem. Sci.*, 2015, **6**, 3026-3037.

123. R. L. Martin, *J. Chem. Phys.*, 2003, **118**, 4775-4777.

124. E. S. Lam, W. H. Lam and V. W. Yam, *Inorg. Chem.*, 2015, **54**, 3624-3630.

Chapter 4: Synthesis of Gold-Porphyrin Dyads and Their Thermal and Photophysical Properties

4.1 What are Porphyrins?

Porphyrins are heterocyclic, macrocycle organic compounds composed of four pyrrole subunits connected at the *α*-carbon *via* methine bridges (=CH-) and are widely found in nature (Figure 4.1), the parent compound being the rarely observed porphine. The name porphyrin comes from the Greek *porphyra,* 'purple', due to the typical intense purple colour in the solid state. The porphyrin macrocycle core has a total of twenty-two π-electrons, of which 18 are viewed as forming a planar, delocalised cycle,[1, 2] resulting in porphyrins being considered aromatic. The presence of four pyrrolic nitrogen atoms results in porphyrins being capable of binding metals (normally in the +2, +3 and +4 oxidation states) as a tetradentate ligand, with possible axial ligands present. Due to their photophysical properties, metalloporphyrins are of interest in several different areas including solar cells, OLEDs and photo-medicine.[3-6]
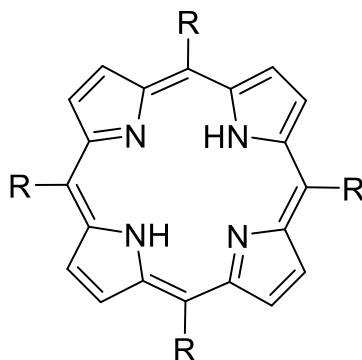
Figure 4.1: General structure of a free-base meso-tetrasubstituted porphyrin.

4.2 Absorption Spectra of Porphyrins

4.2.1 Free-Base Porphyrin Absorption Spectra

Porphyrins exhibit very typical absorption spectra (Figure 4. 2).[7, 8] In the free-base (non-complexed) porphyrin the highest symmetry possible is D_{2h} and the absorption spectra displays five main bands: the Soret or B-band and the four Q-bands (Figure 4.3a). The Soret band is very intense and found at ~380-420 nm, which has an origin of the second

excited singlet state, B(0,0) and a typical molar absorption coefficient of $2 - 4$ x 10^5 dm^3 mol^{-1} cm^{-1}. The four Q-bands fall between $500 - 600$ nm giving raise to the characteristic porphyrin colouration: purple in the solid form and claret-red in solution. The two lower energy bands $Q_x(0,0)$ and $Q_y(0,0)$, are derived from the lowest energy excited singlet state; while the two higher energy bands $Q_x(1,0)$ and $Q_y(1,0)$, include one mode of vibrational excitement. The origin of all the bands are (π,π^*) transitions, with the Q and Soret bands typically shifting together on occurrence of red-shifting.
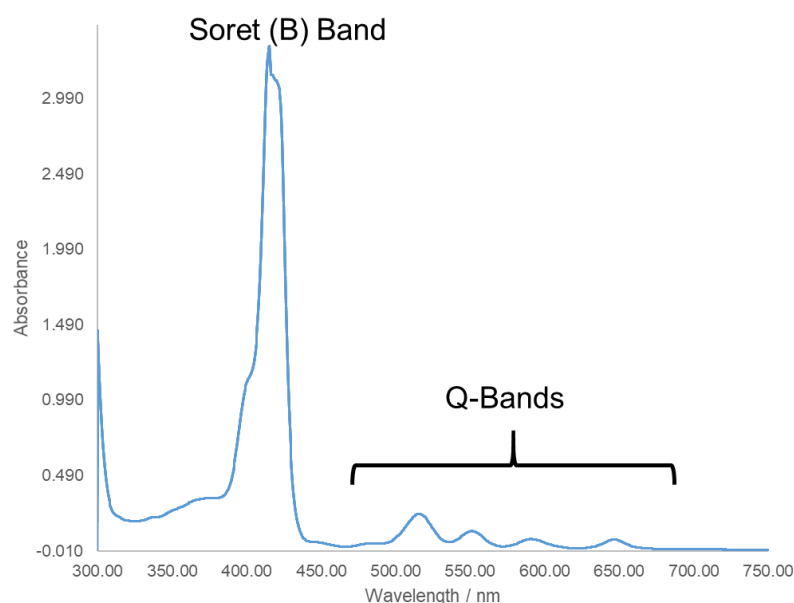
Figure 4.2: UV-Vis spectrum of 5,10,15,20-tetrakis(p-tolyl)porphyrin, a typical porphyrin.

On metalloporphyrin formation, the symmetry normally increases to D_{4h} and hence, the number of bands in the UV-Vis spectrum decreases to three (Figure 4.3b), so that while the Soret band remains largely unchanged, metalloporphyrins show only two Q-bands. Interactions between the metal atom and solvent or other donor atoms can result in spectral shifting.[9-20]
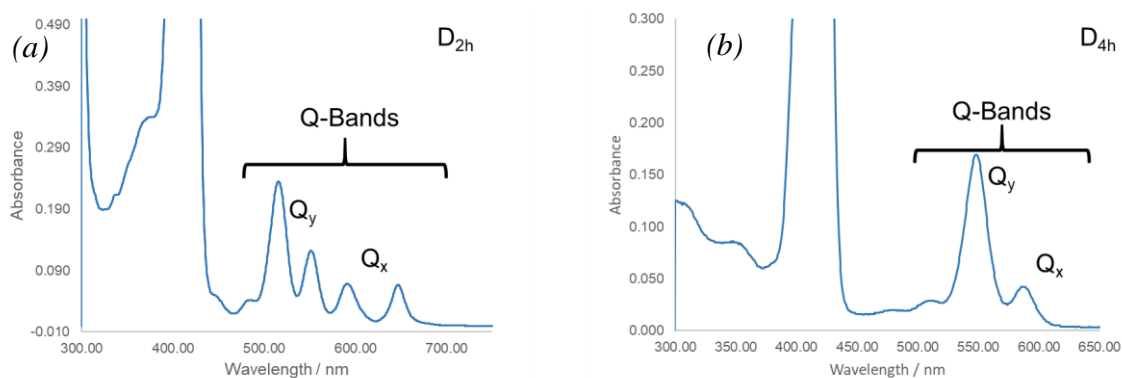
Figure 4.3: Typical UV-Vis spectra in dichloromethane solution at room temperature (a) for a D_{2h} porphyrin (5,10,15,20-tetrakis(p-tolyl)porphyrin), showing the four Q-bands and (b) a D_{4h} metalloporphyrin (zinc 5,10,15,20-tetrakis(p-tolyl)porphyrin) showing two Q-bands.
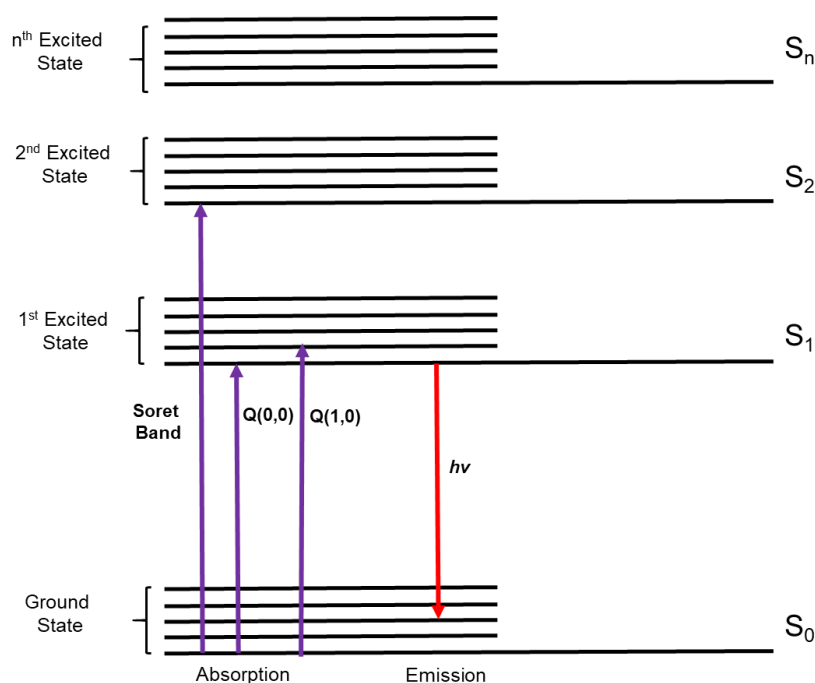
Figure 4.4: Simplified energy diagram for porphyrin absorption and emission.

4.2.2 Bonding Models in Porphyrins

The most commonly used bonding model to explain the typical porphyrin absorption spectra is Gouterman's Theory, also known as the Four-Orbital Model, though other simpler models have been used in the past (Figure 4.5).[21, 22] Gouterman's Theory considers the two highest HOMOs (labelled a_{1u} and a_{2u}) and the two lowest LUMOs (e_g orbitals), derived from Hückel Theory. Orbital mixing accounts for the Q-band multiplicity and relative molar absorption coefficients, with molecular vibration in the macrocycle making the Q-bands weakly allowed.
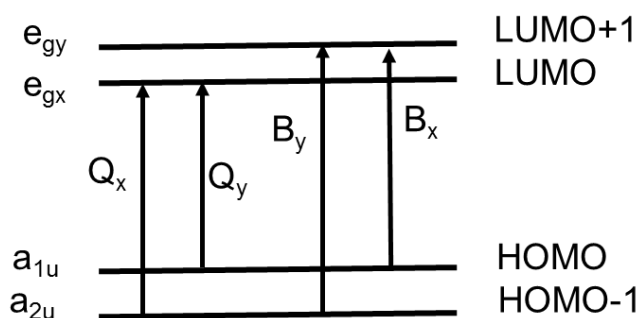
Figure 4.5: Molecular orbital diagram of Gouterman's Theory or the Four-Orbital Model.

A more detailed look determines that the Soret band is defined as $^1A_{1g} \rightarrow \,^1E'_u$, an allowed transition (Figure 4.6). On substitution E'_u is split into B'_{2u} and B'_{3u}, however due to the very similar energies these are rarely resolved. Bands I ($^1A_{1g} \rightarrow \,^1B_{3u}$) and III ($^1A_{1g} \rightarrow \,^1B_{2u}$) are quasi-forbidden, with increasing symmetry on metalation resulting in combination to form E_u and one visible band. Bands I ($^1A_{1g} \rightarrow \,^1B''_{3u}$) and III ($^1A_{1g} \rightarrow \,^1B''_{2u}$) are quasi-forbidden; combining to form E_u'' on increasing symmetry. Therefore in the metalloporphyrin the α-band is $^1A_{1g} \rightarrow \,^1E_u$ and the β-band $^1A_{1g} \rightarrow \,^1E_u''$.
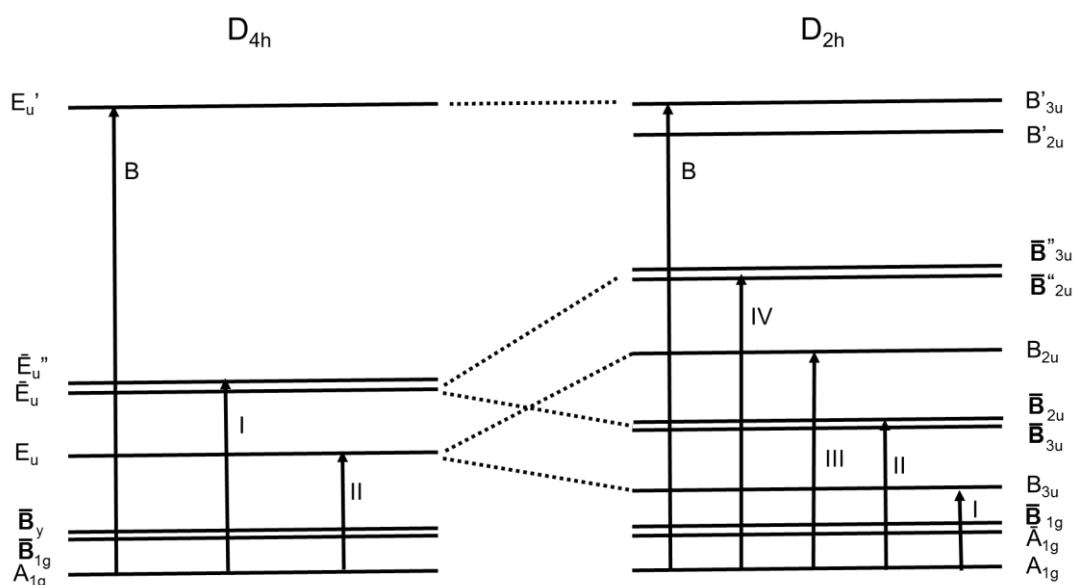
Figure 4.6: Energy levels for a metalloporphyrin (left) and free-base porphyrin (right).

4.2.3 Porphyrin Emission

On fluorescence, the Q-bands are mirror images of the absorption spectra,[7] while in phosphorescence spectra, strong T(0,0) and weaker T(0,1) bands are seen. For metalloporphyrins the quantum yield for phosphorescence is typically between $10^{-4} - 0.2$,

with heavy metal atoms enhancing it due to increased spin-orbit coupling. In free-base porphyrins there is strong fluorescence, but very little phosphorescence, due to the lack of heavy metal atoms. On excitation into the Soret band (S_2) in tetraphenylporphyrin, emission occurs from the Q-bands, in line with Kasha's Rule, due to very fast multiple electronic and vibrational relaxation processes on the timescale of 10^2 fs to 10^1 ps.[23-28] On excitation into the Q-band (S_1) emission occurs directly from there on the nanosecond timescale.[24] Emission is slowed in zinc(II) tetraphenylporphyrin due to the wider energy gap.[27]

4.2.4   5,10,15,20-Tetraalkynylporphryins

5,10,15,20-Tetraalkynylporphryins (Figure 4.7), which introduce a carbon-carbon triple bond between the porphyrin core and substituents, were first reported in 1992 by Anderson,[29] and the extended conjugation results in extensive red-shifting of the absorption bands up to 100 nm.[29-33] The resulting brilliant green colour in solution gives the trivial name of chlorophyrin[30] and several examples have been reported.[30, 32, 34-40]
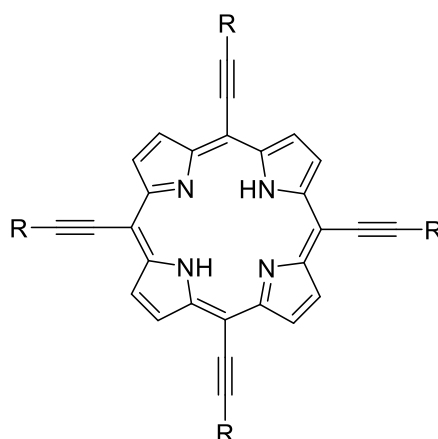
Figure 4.7: General structure of a 5,10,15,20-tetraalkynylporphryin.

4.3   Synthesis of Porphyrins

4.3.1   Rothemund Reaction

The first synthetic method for porphyrins was developed in 1935 by Rothemund and involved the reaction of pyrrole with either gaseous acetaldehyde or formaldehyde in methanol in a sealed container.[41] However yields were low; for example synthesis of tetraphenylporphryin (TPP) at 220 °C under nitrogen for 48 hours gave a yield of less than 5% and was contaminated with chlorin.[42] Later work used acetaldehyde, propionaldehyde, n-butyraldehyde, benzaldehyde and α-furaldehyde.[43] The Rothemund

reaction is now rarely used owing to the harsh conditions required, low yields and limited range of aldehydes to which it can be applied, however more modern synthetic reaction methods have been developed based on this earlier method.

4.3.2   Adler-Longo Reaction

Adler and Longo developed the Rothemund synthesis further by heating pyrrole and the corresponding aldehyde together under reflux conditions in propionic acid, using atmospheric oxygen as an oxidant (Figure 4.8).[42, 44] However this development of porphyrin synthesis is incompatible to some degree with acid-sensitive functional groups, limiting reaction scope.[45, 46]
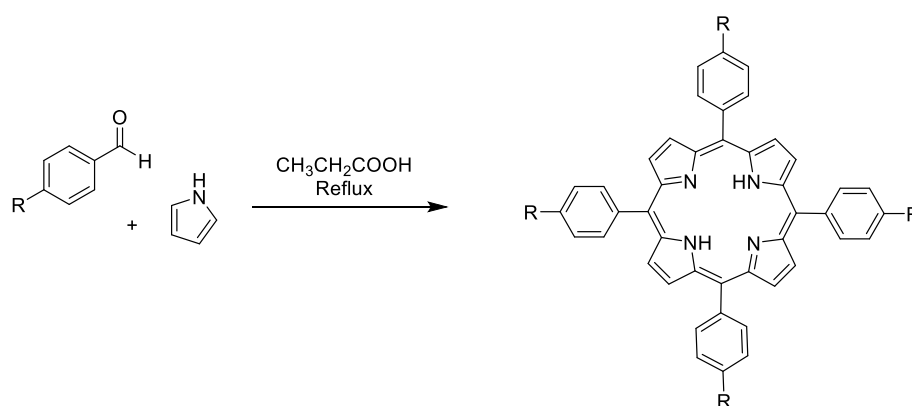
Figure 4.8: Generic reaction scheme for the Alder-Longo reaction.

4.3.3   Lindsey Reaction

The next advance in porphyrin synthetic methods, and now the most commonly used variation, was developed by Lindsey as a one-pot, two-step synthesis and is based on increased mechanistic understanding (Figure 4.9).[45-47] The first step is an oxygen-free cyclisation using Brønstred or Lewis acids, such as BF_3, $BF_3.OEt_2$ or TFA.[46] The use of anaerobic conditions and high dilution (10^{-2} M is optimal) allows equilibrium to be reached over several hours (typically 1-2 hours are required) maximising the macrocycle formation (porphyrinogen). Subsequent addition of an oxidant (*p*-chloranil or DDQ) oxidises the porphyrinogen to the corresponding porphyrin. The commonly used oxidants are interchangeable; the milder *p*-chloranil requires heating under reflux for an hour for full oxidation, while DDQ reacts almost instantly at room temperature, although it has been noted that *p*-chloranil often gives cleaner products and higher yields than DDQ.[46]
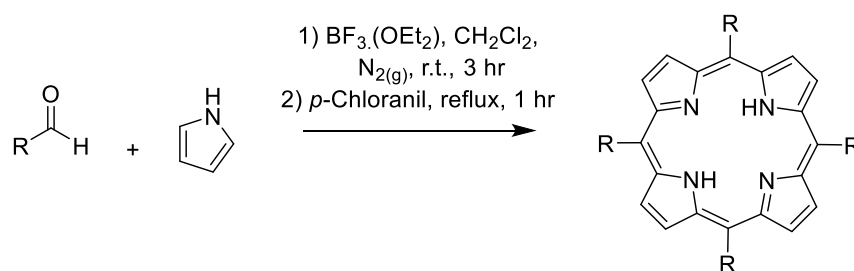
Figure 4.9: Generic reaction scheme for a Lindsey reaction.

The low reaction temperatures and mild conditions means the Lindsey synthesis can be applied to a much wider range of functional groups and yields of 30-40% (scaling linearly from 25 mL to 1 L) are typical for optimised reactions;[46, 48] purification is also typically easier. A disadvantage however is that the high dilution required makes scaling up challenging. Continuous flow systems have been used more recently to enable high amounts of porphyrin to be produced without requiring multiple batches, however each system requires tuning for the desired system and specialised equipment, while the lack of familiarity of many chemists with continuous-flow chemistry means that this has yet to gain wide-spread use.[49]

4.3.4   Synthesis of Dipyrromethane

5,15-Mesosubstituted porphyrins can be formed from a 1:1 mixture of the respective dipyrromethane and aldehyde,[50] using the Lindsey and Adler-Longo reactions.[51] Several methods, detailed below, have been developed over time to synthesise unsubstituted dipyrromethane, the most challenging of the dipyrromethanes to synthesise.

The initial synthesis of dipyrromethane was reported in 1969 by Clezy *et al.*, consisting of a three-step synthesis, in 40% yield (Figure 4.10). Thiophosgene and pyrrole were reacted together to form a thioketone, which was oxidised using 5% H_2O_2/KOH to give the ketone, after which reduction using $NaBH_4$ gave dipyrromethane.[52] While this method allows synthesis of dipyrromethane at scale, it is not a desirable method due to the toxicity of thiophosgene.
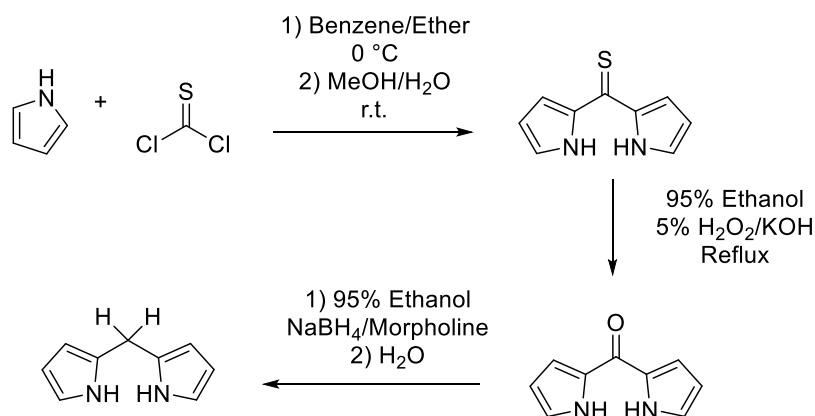
Figure 4.10: Reaction scheme for Clezy's method for synthesis of dipyrromethane.[52]

Based on Lindsey's one-step procedure for the generic synthesis of substituted dipyrromethanes, it was determined that using an excess of pyrrole prevented formation of higher polypyrroles, with the respective aldehyde and a TFA catalyst used in the ratio 40:1:0.1.[53, 54] Wang and Bruce developed a method for the synthesis of dipyrromethane where the solubility of paraformaldehyde was increased by the addition of a small amount of methanol (1-2 cm^3) and there was a change in acid catalyst from TFA to acetic acid (Figure 4.11).[55] While this method proved capable of producing a high purity of dipyrromethane it could not be scaled up, requiring multiple parallel batches to achieve sufficient quantity for further reactions.
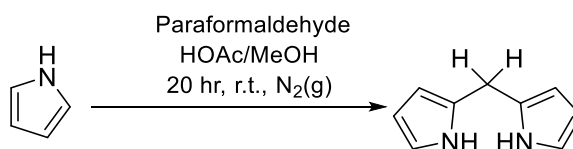
Figure 4.11: Reaction scheme for Wang's method for synthesis of dipyrromethane.

More recent methods byLindsey[56, 57] and by Anderson[58] have produced formaldehyde by cracking paraformaldehyde at elevated temperatures. Lindsey's method cracks the paraformaldehyde *in situ* before addition of the acid catalyst (either TFA or InCl$_3$),[56, 57] while Anderson's method passes the produced formaldehyde gas into a vessel containing pyrrole and TFA catalyst (Figure 4.12).[58] Both methods produce high-purity dipyrromethane on a gram scale, though Lindsey's method allows easier recovery of excess pyrrole for recycling. Ka *et al.* determined that the sequence of reagent addition determines the major product. On mixing of the aldehyde and pyrrole before addition of acid catalyst, dipyrromethane is given as the major product, whereas pre-mixing of

234

catalyst and aldehyde followed by addition of pyrrole gives tripyrromethane as the major product.[59]
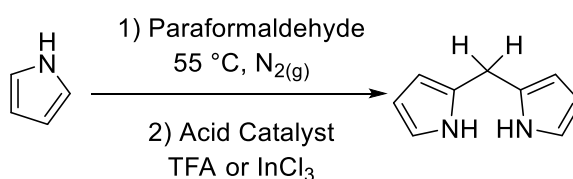
Figure 4.12: Reaction scheme for Lindsey's method for synthesis of dipyrromethane.[56, 57]

4.3.5 Formation of Metalloporphyrins

It is possible to form a metalloporphyrin with many different metal ions, with the procedure used dependent on the identity of the metal ion.[60] The process of metal ion insertion is known as metalation and the reverse as demetalation.

$$H_2P + MX_2 \underset{\text{Demetalation}}{\overset{\text{Metalation}}{\rightleftharpoons}} M(P) + 2HX$$
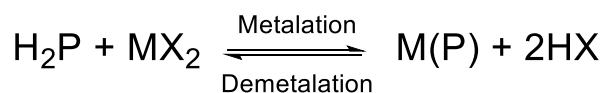
Figure 4.13: Formation of metalloporphyrins.

The most commonly used and preferred method of synthesis is the acetate method, where the metal acetate is reacted with the free-base porphyrin in acetic acid under reflux or alternately at room temperature in solvent mixture of methanol and dichloromethane/chloroform to solubilise both the metal salt and porphyrin. Sodium acetate is sometimes added as a buffer and to aid deprotonation of the porphyrin. Zinc(II) is a popular choice of metal ion due to ease of addition by the zinc acetate method under mild conditions to form a highly stable neutral metalloporphyrin. Zinc(II) can be readily removed by addition of mild aqueous acid.[61, 62]

For more acid-labile metalloporphyrins, the basic solvent pyridine is used, however higher-charged complexes can form complexes with the solvent. Metal acetylacetones are readily available for the lanthanides and early transition metals and their good stability, ease of manipulation and liberation of a weak acid are highly desirable, however some of the highly charged and small radii metal ions prove to require additional conditions in order to liberate the metal ion for reaction. Where early transition metal complexes do not form acetylacetonate complexes metal oxides or chlorides might be used in boiling phenol. This method is also used to liberate more highly stable acetylacetonate complexes.

The benzonitrile method, where a metal chloride is reacted with the porphyrin in benzonitrile is preferred for several transition metals, including Pt(II), due to the good solubility, weak coordination and basic nature of the benzonitrile solvent. Further the very high temperatures required assist in cracking the high molecular aggregates of some metal chlorides, which are otherwise insoluble and unreactive. An overview of common, more complex methods can be found in Volume 1 of the Handbook of Porphyrins.[60]

4.4   Liquid Crystal Porphyrins

Several porphyrin compounds have been shown to display liquid crystal phases, with columnar phases dominating, due to the planar, disc-shaped macrocycle core. In 1980 Goodby *et al.* reported the first example of a liquid-crystalline porphyrin, showing that uro-porphyrin I octa-*N*-dodecyl ester displayed a monotropic columnar phase over ~5 °C.[63] Shimizu *et al.* reported the first example of a liquid-crystalline meso-substituted porphyrin in 1986, determining 5,10,15,20-tetrakis(4-alkylphenyl)porphyrin derivatives displayed discotic lamellar-phases.[64]

4.4.1   *β*-Substituted Liquid Crystalline Porphyrins

a: M = H_2
b: M = Zn

1: R = CO_2H (M = H_2 only)
2: R = $CO_2(CH_2)_3Me$
3: R = $CO_2(CH_2)_5Me$
4: R = $CO_2(CH_2)_7Me$
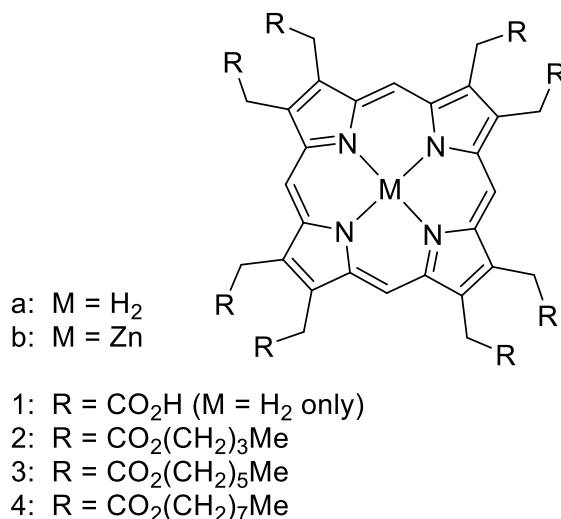
Figure 4.14: Structure of octakis(β-hydroxyethyl)porphyrins studied by Bard et. al.[65]

β-Substituted porphyrins are capable of forming liquid crystal phases.[63, 65-75] Octakis(*β*-hydroxyethyl)porphyrins (Figure 4.14) were shown by Gregg *et al.* to have two broad liquid-crystalline phases initially assigned as highly ordered, though unidentified,

phases.[65] However in 1999, the lower temperature phase, was re-identified as a crystal phase transition, with the higher temperature phase assigned as rectangular columnar ($C2/m$).[69] Several metal complexes (Zn, Pt, Cu, Cd, Ni, Pd and Pb) were studied, with almost all forming enantiotropic rectangular columnar phases.[67, 69-71] A high level of substitution on both the eight β-positions and also various *meso*-positions failed to give mesophases, thought to be due to a strong porphyrin core distortion.[76, 77]

Since β-substituted porphyrins are not investigated in this work they will not be considered in further depth.

4.4.2 Meso-Substituted Liquid Crystalline Porphyrins
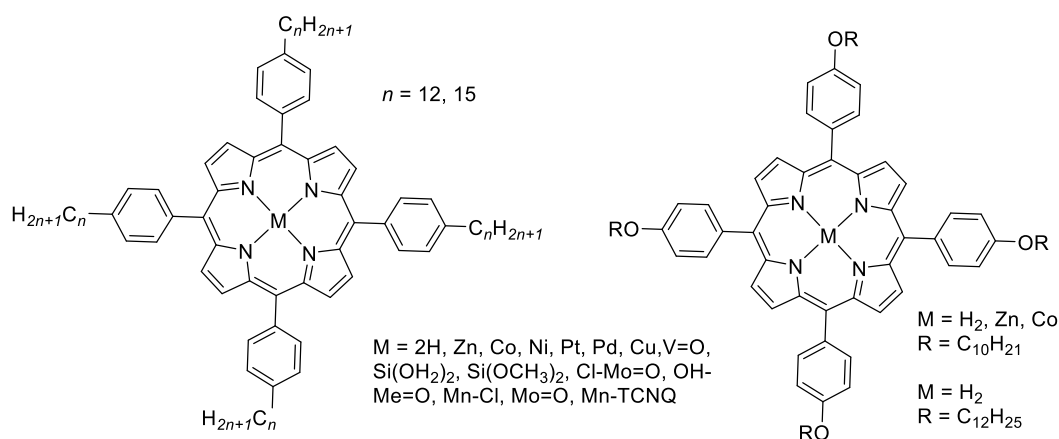
Figure 4.15: Structures of 5,10,15,20-tetrakis(4-alkylphenyl)porphyrins and 5,10,15,20-tetrakis(4-alkyloxyphenyl)porphyrins which display mesophases.

Porphyrins substituted in the *meso*-positions can also display liquid-crystalline phases.[78-80] The first reported examples were 5,10,15,20-tetrakis(4-dodecylphenyl)porphyrin ($C_{12}TPP$)[81] and 5,10,15,20-tetrakis(4-pentadecylphenyl)porphyrin ($C_{15}TPP$) (Figure 4.15),[64, 82] which were determined to display two unidentified enantiotropic mesophases, with phase transition temperatures increasing with chain length. X-ray results for $n = 12$ suggested a lamellar phase, thought to be discotic. Various metal ions, with axial ligands as needed, have been inserted into the porphyrin and the resulting mesophase properties investigated, with M = SiX$_2$ ((X = OH or OCH$_3$), Cl-Mo=O, Co, Ni, Cu, Zn, Pd, Pt, V=O, Al(OH), M=O(OH), Mn-TCNQ all shown to give mesophases.[83-90]

An amide linkage between the chain and the phenyl group (Figure 4.16),[91] where R = C_nH_{2n+1} (n = 8, 10, 12, 14, 16, 18) gave broad, high-temperature, enantiotropic liquid

crystal phase(s) for the free-base porphyrin when $n > 12$. The zincated complexes were not liquid crystalline, thought to be due to core non-co-planarity disfavouring packing. A diphenylacrylonitrile-porphyrin derivative, continuing multiple polyglycol chains formed a hexagonal columnar mesophase from $70 - 120\ °C$.[92]
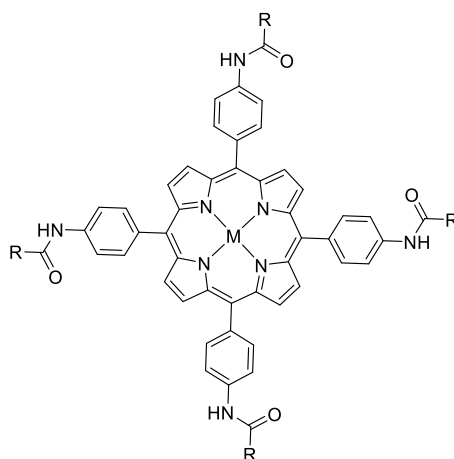
Figure 4.14: Structures of meso-tetra-(4-alkylamidophenyl) porphyrin derivatives.[91]
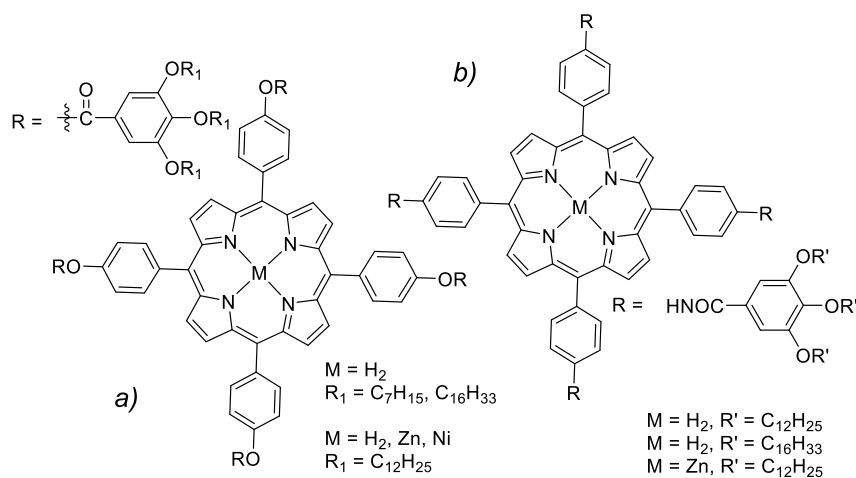
Figure 4.16: Structure of discotic meso-tetra[4-(3,4,5-trialkoxybenzoate)phenyl]porphyrins (a)[93] and meso-tetra(3,4,5-n-trialkoxybenzoylaminophenyl)porphyrins (b).[94]

An increase in steric bulk on the phenyl rings by introduction of three alkoxy chains in to the 3,4,5-positions (Figure 4.16a)[6, 93, 95, 96] resulted in all complexes forming rectangular columnar phases, with the range of the phase increasing with n. The presence of the twelve chains gave the porphyrins a disc-like shape, making formation of columnar phases unsurprising. Introduction of Zn(II) and Ni(II) decreased the mesophase range. Changing to an amide linkage (Figure 4.16b)[94] also gave rectangular columnar phases and pseudohexagonal columnar phases, however there was a small increase in the phase

transition temperatures compared to the ester linkage. Introduction of a partly fluorinated chain caused self-assembly into nanostructures and stabilised the hexagonal columnar phase.[97] A second phase with higher viscosity was seen at room temperature, with an unchanged texture. Substitution with alkoxy-chains gave lamellar mesophases.[98] Substituents with higher steric bulk are also still capable of mesophase formation.[99-103]
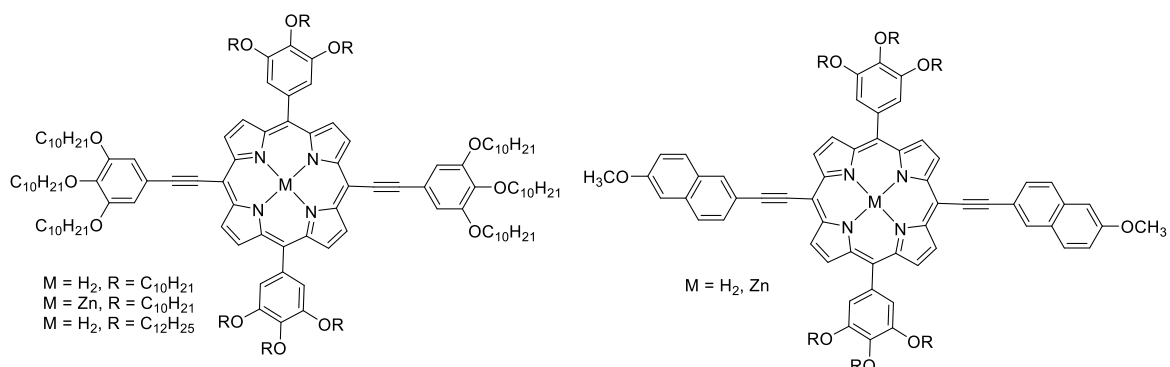
Figure 4.17: Structures of porphyrins and their metallo-derivatives, with laterally extended π-conjugation system.[104]

Extending the π-conjugation system laterally by addition of four *meso*-trialkoxyphenyl meso-substituents (Figure 4.17) gave room-temperature rectangular and oblique columnar liquid crystal phases.[104] Introduction of a naphthalene unit increased molecular anisotropy and also increased the melting and clearing temperatures, giving a biaxial smectic phase. Extension of the π-conjugation system to form zinc 5,10,15,20-tetraarylethynylporphyrins (R_1, R_2, R_3 = OC_nH_{2n+1} or H) (Figure 4.18) gave hexagonal columnar phases. The increased core molecular planarity, due to ethylene group introduction, increased effective molecular packing.[77]

R$_1$ = R$_2$ = R$_3$ = OC$_n$H$_{2n+1}$ or H
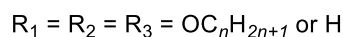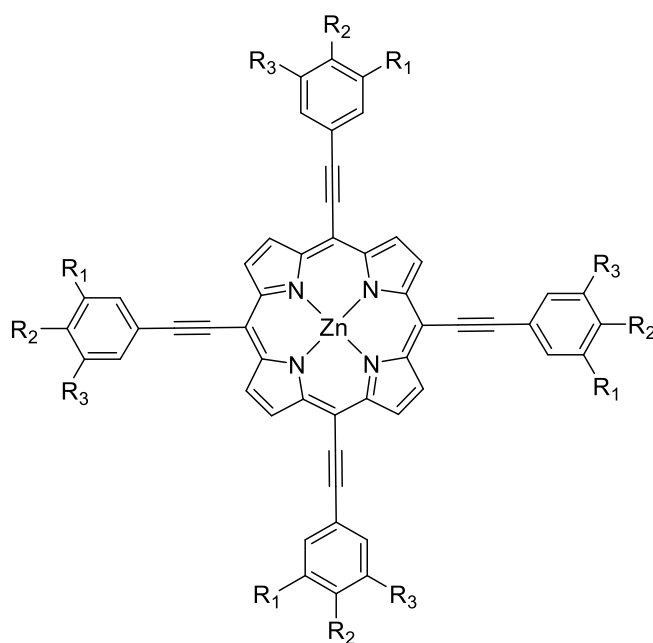
Figure 4.18: Structure of zinc 5,10,15,20-(ethynyl(3,4,5-trialkoxyphenyl))porphyrin.[77]

Extensive functionalisation in the 5,15-positions of the porphyrin increases the system anisotropy and results in formation of sematic phases – a change of a normally discotic system to a calamitic system (Figure 4.19).[103, 105-110] Fused copper porphyrin dimers have also been determined to give liquid crystalline porphyrins, with the fluorophobic effect encouraging mesophase formation.[111, 112]

R = C$_n$H$_{2n+1}$, *n* = 8, 10, 12, 14, 16,
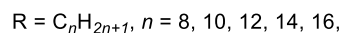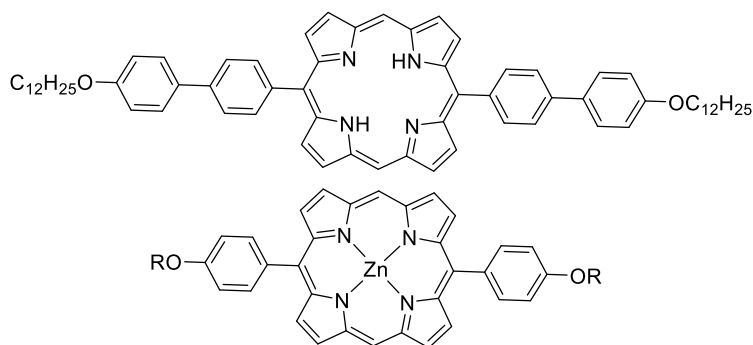
Figure 4.19: Structures of 5,15-disubstituted porphyrins, which give rise to smectic phases.[106]

4.5   Metalloporphyrins Functionalised with Other Metal Complexes

Porphyrins are both redox and photophysically active, as are many metal complexes. On combination in the same molecule, this can in principle result in both electronic and photophysical interactions between the porphyrin and the other chromophore. For example, photoexcitation, electronic energy transfer (a radiationless transfer between two 'local' electronically excited states of a system) and photoinduced electron transfer are possible.

$$*D\text{-}B\text{-}A \rightarrow D\text{-}B\text{-}A*$$
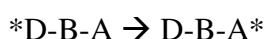
Figure 4.20: Electronic energy transfer between a donor unit 'D' and an acceptor unit 'A', connected with a linker 'B'.

Columbic energy transfer, also known as Förster-type energy transfer, is long range and requires no physical interaction. In contrast, exchange energy transfer, also known as Dexter type energy transfer, is short-range in nature, and requires orbital overlap and therefore physical contact, hence it is linker sensitive (Figure 4.20).

$$D*\text{-}B\text{-}A \rightarrow D^+\text{-}B\text{-}A^-$$
$$D^+\text{-}B\text{-}A^- \rightarrow D\text{-}B\text{-}A$$
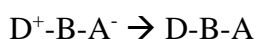
Figure 4.21: Photoinduced electron transfer on excitation of donor 'D', resulting in formation of a charge separated species, with recombines to give the group species.

Photoinduced electron transfer (Figure 4.21) occurs when the excited state transfers an electron to an acceptor molecule forming an ionic species. In the absence of subsequent chemical reactions the ground state is regenerated by back electron transfer. The forward process is referred to as charge separation (cs) and the back process as charge recombination (cr).

Due to the immense interest in the photophysical properties of porphyrin, the effects of connection to other chromophores has been investigated and some representative examples are now described.

4.5.1 Porphyrins Connected to Platinum(II) Complexes
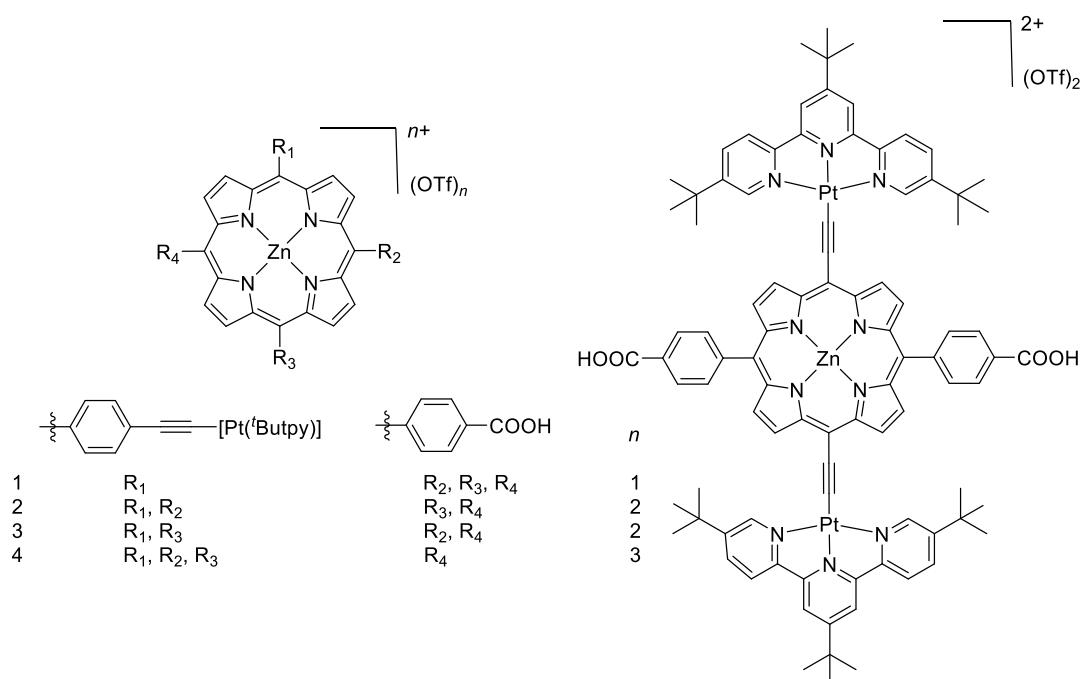
Figure 4.22: Structure of zinc porphyrin connected to varying numbers of alkynylplatinum(II) terpyridine units.[113]

Several studies have been carried out investigating the photophysical interaction between a zinc porphyrin and a platinum complex,[113-128] with platinum metallopolyyne polymers of the form *trans*-[-Pt(L)$_2$-C≡C-R-C≡C-]$_n$, where L = PR$_3$ and R is an aromatic spacer unit, investigated for use in solar cells.[114-118, 122, 125, 126, 128] Connection of one, two or three alkynylplatinum(II) terpyridine units to a zinc porphyrin (Figure 4.22) allowed investigation of charge-transfer properties, with platinum(II) terpyridine capable of long-lived, charge-separated state formation post-photoexcitation and the porphyrin capable of acting as an electron acceptor.[113] Nanosecond transient absorption spectroscopy showed formation of a charge-separated species, by rapid electron transfer from the alkynylplatinum(II) unit to the porphyrin, placing a positive charge on the platinum complex and a negative charge on the porphyrin. The platinum ^{3}MLCT state is efficiently quenched by this mechanism, resulting in no platinum-based emission. Porphyrin fluorescence (~620 – 675 nm) occurred in both the solid and glassy states. Alternately, connection of a zinc(II) or magnesium(II) porphyrin to an alkynylplatinum (II) terpyridine complex (Figure 4.23) resulted in very rapid electronic transfer from the porphyrin to the platinum unit (τ = 2 – 20 ps), with no formation of a charge-separated

species, indicating rapid charge recombination.[119] This indicates the importance of the unit nature on the result of photoexcitation.

R = PO$_3$Et, M = Zn
R = H, M = Zn
R = OC$_7$H$_{15}$, M = Zn
R = PO$_3$Et$_3$, M = Mg
R = H, M = Mg
R = OC$_7$H$_{15}$, M = Mg
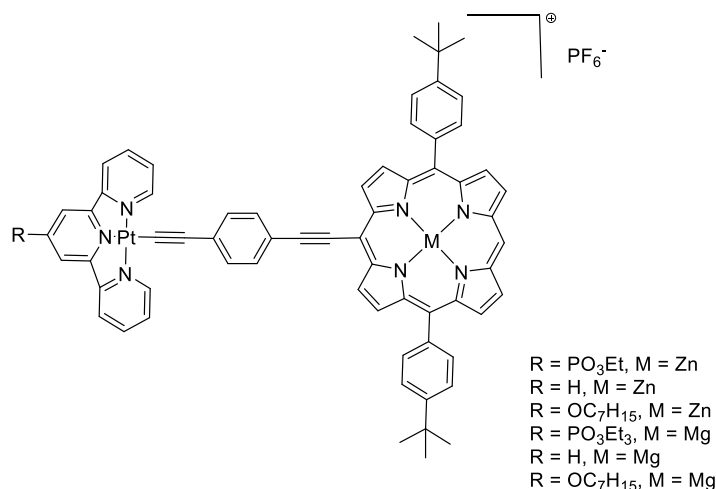
Figure 4.23: Structures of zinc(II) or magnesium(II) porphyrins, connected to alkynylplatinum(II) *terpyridine.*[119]

4.5.2   Connection of Ruthenium(II) and Iridium(III) Complexes

There has been a high level of interest in the connection of ruthenium(II) complexes to porphyrins,[129-148] particularly since the determination by Steiger and Anson that connection of [Ru^{II}Cl(bipy)$_2$]$^+$ or [Ru^{II}(NH)$_5$]$^{2+}$ to cobalt *meso*-tetra(4-pyridyl)porphyrin (Figure 4.24) and its derivatives were capable of the four-electron reduction of dioxygen to water.[149] Backbonding from ruthenium(II) to porphyrin is thought to be of importance in the electron transfer from a ruthenium(II) complex to dioxygen bonded to cobalt(II).[129, 150] Connection of the same complex(es) to zinc(II) *meso*-tetra(4-pyridyl)porphyrin gave florescence centred on the porphyrin unit, with the ruthenium units acting as antenna for electron transfer.[134] Connection to a TiO$_2$ surface, provided seven-fold enhanced photoconversion efficiency enhancement in a dye for use in dye-sensitised solar cells.[135] Work in ruthenium(II) terpyridyl-porphryin dyads and triads[137] has led to an interest in the attachment of iridium(II) complexes.[151]
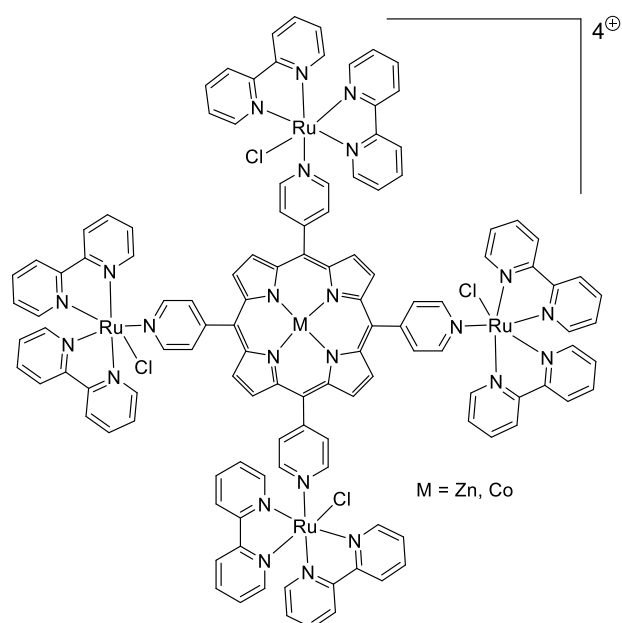
Figure 4.24: Structure of 5,10,15,20-tetrapyridylporphyrin connected to [Ru^{II}(bipy)$_2$Cl].
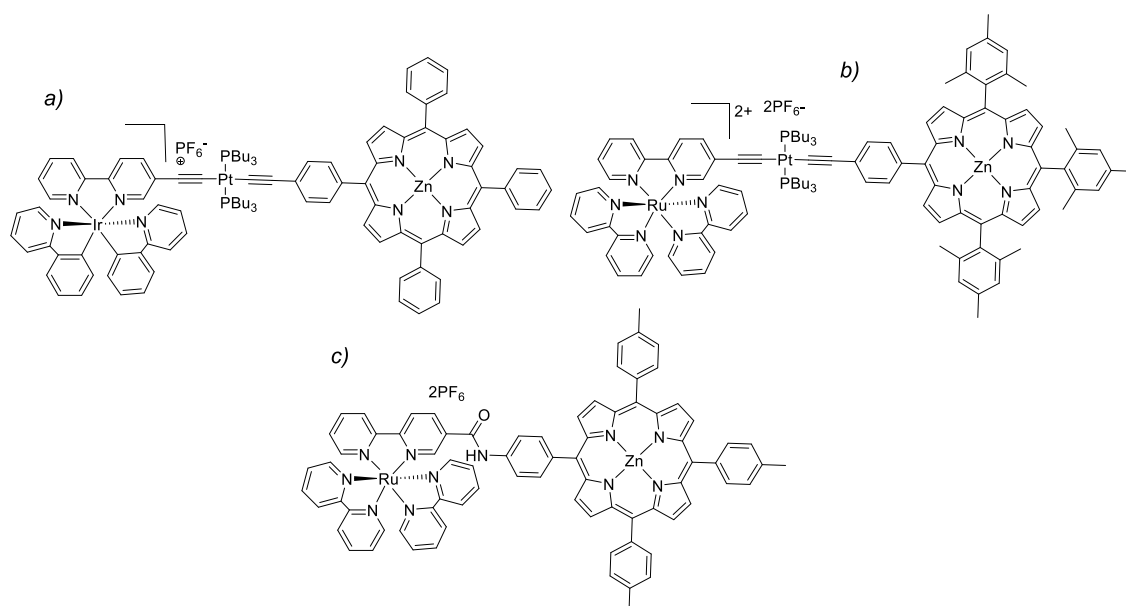
Figure 4.25: Connection of bis(phenylpyridinate)-(bipyridine)metal complexes to metalloporphyrins.[145, 146, 152]

Bis(phenylpyridinate)(bipyridine)iridium(III) is capable of acting as a donor, however connection to zinc(II) tetraphenylporphyrin by *trans*-C≡C-Pt(Bu$_3$)$_2$-C≡C- (Figure 4.25a) gave essentially no triplet energy-transfer to the zinc porphyrin states indicating weak electronic communication.[152] Connection of a very similar zinc(II) porphyrin to ruthenium(II) tri(2,2'-bipyridyl) (Figure 4.25b) gave fast singlet to triplet energy transfer, deactivating the first excited porphyrin singlet state to give a ruthenium triplet state,

which converts to the porphyrin triplet state.[145] A change to an amide bond linkage (Figure 4.25c) gave electron transfer ($k = 6 \times 10^{11}$ s^{-1}) from an excited state, populated through Soret band excitation ($\tau = 0.8$ ps).[146] Introduction of electron-withdrawing COOEt groups on the bipyridine ligands also gave efficient fluorescence quenching, through the nature of the mechanism (electron transfer or energy transfer) was not determined.[131]
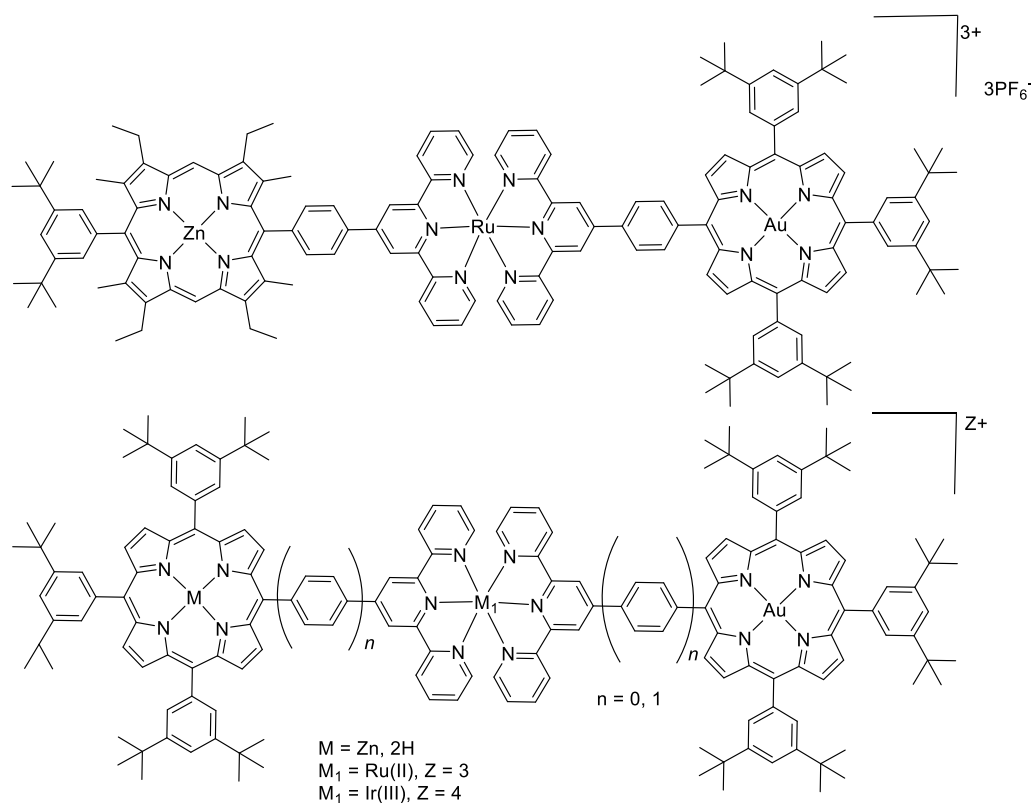
Figure 4.26: Structure of MP-[M₁]-AuP dyads, M = 2H or Zn and M₁ is Ru(II) or Ir(III).

Several papers investigating the connection of a gold(III) complex to either a free-base or zinc(II) porphyrin by a ruthenium(II) terpyridyl complex, or in later work an iridium(III) terpyridyl complex, have been investigated by Sauvage et al. (Figure 4.26).[137, 153-162] It has been demonstrated that the relative energy levels of the units was important on the fate of excited states in a related system where zinc(II) and gold(III) porphyrins are connected by a linking unit, with energy transfer from the zinc porphyrin to gold porphyrin.[144, 163-167] Similar relationships in this system are observed, with photoexcitation of the zinc porphyrin giving sequential electron transfer to the ruthenium complex, then to the gold(III) porphyrin.[153] Photoexcitation of the gold(III) porphyrin gave an unreactive triplet state, while ruthenium complex excitation gave rapid electron transfer to the porphyrin.[154] Formation of a charge separated state over 30 Å was possible

at 77 K. Replacement of ruthenium(II) with iridium(III)[137, 157-160, 162] increased electron donation to the gold porphyrin, due to reduced formation of ^{3}MLCT states.[157, 158]

4.5.3   Connection of Other Metal Complexes

There has been a body of work investigating connection of [rhenium (bipyridine)(tricarbonyl)(ligand)] complexes to porphyrin and the subsequent photophysical and redox properties.[168-175] In one example porphyrin photoexcitation sensitised a [Re(bipy)(CO)$_3$L] unit to photoreduction by electron transfer,[170] becoming capable of CO_2 reduction, with other examples of photocatalytic reduction of CO_2 to CO now known.[171-173] The porphyrin acts as a photosensitiser, transferring electrons to the rhenium unit (Figure 4.27). *Bis*(terpyridine)rhodium(III) proved capable of triplet electron transfer to either a free-base or zinc(II) porphyrin, providing efficient fluorescence quenching.[176, 177]
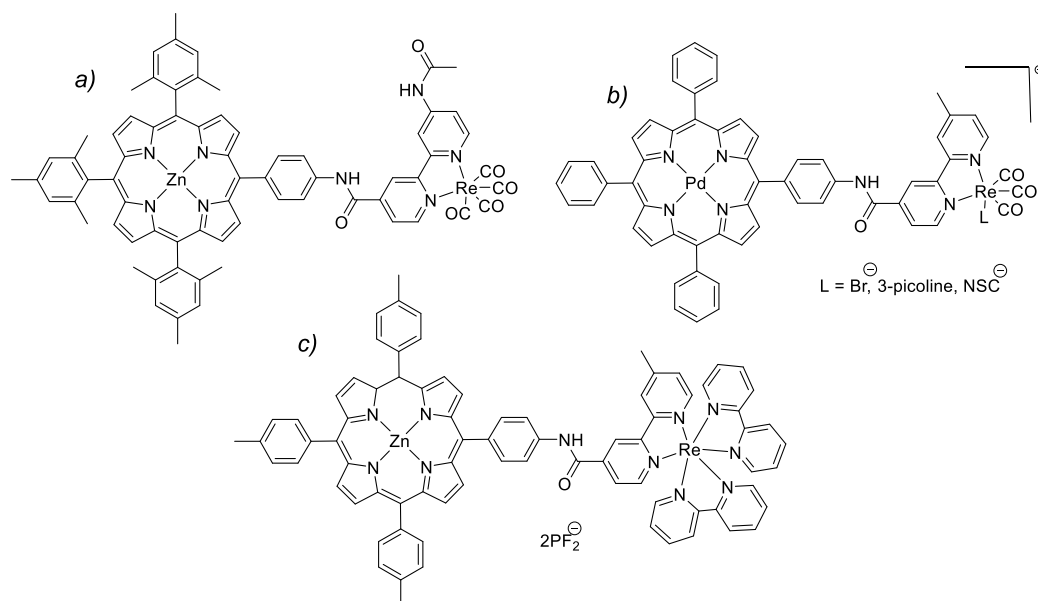
Figure 4.27: Structures of metalloporphyrins connected to rhenium complexes, where fac-Re(bpy)(CO)$_3$Cl, M = Zn (a), [Re(CO)$_3$(Pic)Bpy][PF$_6$], M = Pd (b) and Re(II) tris-bipyridine, M = Zn (c)

The first report of pincer complexes connected to a porphyrin was by Huck *et al* in 1998 where metallodendrimers, containing Pd(II), were connected to up to twelve porphyrins.[178] Since then there have been several other reports of pincer complexes[179] connected to metalloporphyrins with the pincer ligand in the meso-positions (Figure 4.28a)[180-183] or through a direct porphyrin-meso carbon-metal σ-bond (Figure 4.28b), with

246

such connections causing significant porphyrin structural distortion and hence changes in the electronic absorption spectrum.[184-187] The palladium-containing members of the former class are of interest as catalysts in the Heck Reaction.[181, 183] There are frequently electronic interactions between the porphyrin and the pincer complex causing bathochromic shifts and occurrence of electron-donation from Pd(II) and Pt(II) complexes to the porphyrin.[181, 182] One system (M_1 = Pd(II) and M = 2H) proved to give 74% fluorescence quenching due to promotion of $S_1 \rightarrow T_1$ ISC.[180] Pincer platinum(II) complexes have also been introduced axially on to a tin(IV) porphyrin (Figure 4.28c), with small electronic interactions between the units.[188] Linkage of nickel porphyrins to form a *meso-meso* linked dimer *via* Pt(L^L) is known, with intramolecular coupling causing spectral red-shifting.[189]

E = NMe$_2$, PPH$_2$, SR
M = 2H, Cu, Mg, Ni, Zn, Co, MnCl
M$_1$ = Pd, Pt, Ru
X = Halide
Ar = Aryl or princer aryl subsitutent

E = Pyridyl, 1-methylimidazolyl, PPh$_3$
M = 2H, Ni, Cu, Zn
N$_1$ = Ni, Pd, Pt, Ir
Ar = Aryl subsitutent
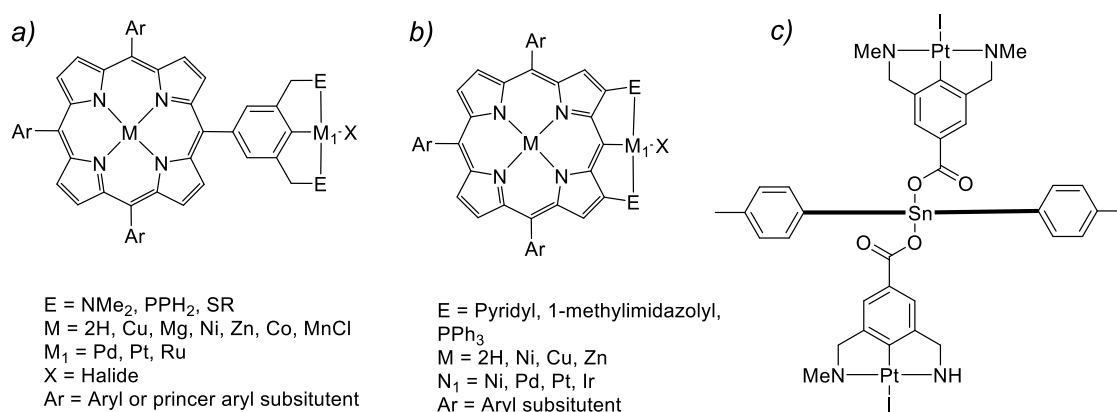
Figure 4.28: Generic structures of porphyrins containing pincer ligands in the meso-positions (a), through a direct porphyrin-meso carbon-metal σ-bond (b) or axially in a tin(IV) porphyrin (c).

4.6   Aims of Chapter

In this chapter the synthesis of several types of disubstituted and tetrasubstituted *meso-*porphyrins will be investigated, followed by their connection to various gold(III) C^N^C complexes to give gold(III)-porphyrin dyads. The liquid crystalline properties of the gold(III)-porphyrin dyads will be investigated in the hope that connection of the gold(III) C^N^C complexes introduces mesophase behaviour, with protential columnar mesophases a high possibility and, for the disubstituted porphyrins, protentially smectic mesophases due to the change in molecular shape. The photophysics of the porphyrins and the gold(III)-porphyrin dyads will also be investigated in the hope that the presence of two photophysically active units in one molecule results in electronic interaction

between the two. Further, it is hoped to investigate the influence of a driect carbon-carbon triplet bond between the two active units and the introduction of a platinum(II) ion into the centre of the porphyrin, which is well known to introduce triplet emission into porphryins.

4.7 The Building Blocks of Porphyrins

A porphyrin macrocycle ring can be formed from an aldehyde and a pyrrole, with dipyrromethane used in place of pyrrole for formation of a 5,15-disubstituted porphyrin. The aldehydes used in this work and dipyrromethane required synthesis as detailed below.

4.7.1 4-[(Trimethylsilyl)ethynyl)]benzaldehyde
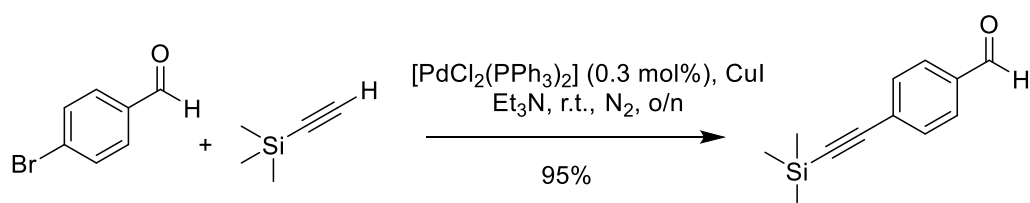
Figure 4.29: Reaction scheme for synthesis of 4-[(trimethylsilyl)ethynyl)]benzaldehyde.

4-[(Trimethylsilyl)ethynyl)]benzaldehyde was synthesised, in an adapted literature procedure, from 4-bromobenzaldehyde and 4-iodobenzaldehyde in a Sonogashira reaction with trimethylsilylacetylene, [PdCl$_2$(PPh$_3$)$_2$], CuI and triethylamine/THF solvent under a nitrogen atmosphere (Figure 4.29).[190] The liquid components were degassed by bubbling with dinitrogen.

Initial use of 4-bromobenzaldehyde in triethylamine gave the product in 49% yield, with ^{1}H NMR spectroscopy showing significant residual starting material. Separation *via* column chromatography proved challenging, although serial recrystallisation from a polar solvent, such as acetone, proved capable of removing residual starting material. An increase in both catalyst loading and the molar equivalence of trimethylsilylacetylene proved unsuccessful strategies for increasing the reaction yield, as did the use of a more rigorous freeze-thaw degassing. Use of the more reactive 4-iodobenzaldehyde, combined with solubility tests, indicated that marginal solubility in triethylamine was the potential issue and addition of dry THF to the reaction solvent gave a near quantitative yield within ten minutes. Substituting 4-bromobenzaldehyde gave a successful reaction overnight.

4.7.2   Synthesis of Protected 2-Propynals
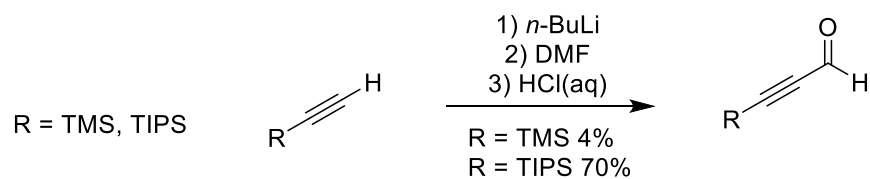
Figure 4.30: Reaction scheme for synthesis of protected 2-propynals.

3-(Trimethylsilyl)-2-propynal was synthesised by addition of *n*-BuLi to trimethylsilylacetylene, followed by addition of DMF to form the aldehyde in 4% yield (Figure 4.30).[191, 192]

The very low yield is thought to be due to the high product volatility (boiling point 52 °C), which made removal of residual THF and DMF challenging. Ultimately the product was isolated as a 10% solution in hexane and used as such. Due to these difficulties a triisopropylsilyl (TIPS) protecting group was substituted, under the same conditions (Figure 4.30). The increased molecular weight results in isolation of a yellow oil in 70% yield, which was pure by ^{1}H NMR spectroscopy.[33]

4.7.3   Dipyrromethane

Dipyrromethanes are required for the synthesis of 5,15-disubstituted porphyrins and are obtained from pyrrole and the relevant aldehyde in the presence of an appropriate catalyst (Figure 4.31).[50] In the case of unsubstituted dipyrromethane, pyrrole is used as the solvent, which suppresses formation of higher-order polypyrroles. Due to the challenges and risks of handling toxic formaldehyde it was formed *in situ via* the cracking of paraformaldehyde at 55 °C in pyrrole, before subsequent addition of a catalyst to the resulting reaction mixture.[56, 57]

1) Paraformaldehyde
55 °C, 15 mins N$_{2(g)}$

2) TFA, 5 minutes r.t.
or
InCl$_3$, 2.5 hr 55 °C

TFA: 8%
InCl$_3$: 60%
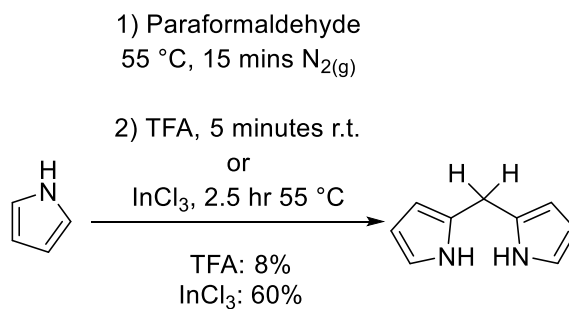
Figure 4.31: Reaction scheme for synthesis of dipyrromethane using TFA catalyst.

Initially CF$_3$CO$_2$H (TFA, 0.1 equiv., catalyst) was used, requiring a very short reaction time (~5 minutes, due the initial fast formation of dipyrromethane), before quenching with aqueous NaOH.[56] Due to the photosensitive nature of dipyrromethane, reactions were carried out in the dark and anhydrous pyrrole, which had been dried over CaH$_2$ and distilled under vacuum, was required due to the water-sensitive nature of the condensation reaction. Use of a TFA catalyst gave low yields (<10.5% compared to >40% in the literature)[56] and challenging purification, ultimately achieved by column chromatography (silica, 100:1 CH$_2$Cl$_2$:Et$_3$N, addition of triethylamine to the mobile phase to neutralise the acidic silica).[55] Subsequent crystallisation was also not always successful, sometimes leading to decomposition.

However, use of the milder Lewis acid catalyst InCl$_3$ was successful[‡‡] and, while longer reaction times were required (2.5 hours compared to 5 minutes), purer dipyrromethane was obtained in 60% yield.[57] Thus, comparison of the crude ^{1}H NMR spectra demonstrated formation of fewer side products. Trituration of the crude product with hexane removed residual pyrrole aiding crystallisation, although recrystallisation still proved challenging. Fortunately, use of the InCl$_3$ catalyst gave a relatively pure product that could be taken forward to porphyrin formation at which stage the other impurities were readily removed.

The ^{1}H NMR spectrum of dipyrromethane (Figure 4.32) shows a broad signal at 7.93 ppm from N-H, with multiplets at 6.68, 6.15 and 6.04 ppm being assigned to the pyrrole protons and the singlet at 4.00 ppm to the bridging CH$_2$ protons.

[‡‡] We thank Professor Jonathan Lindsey for his helpful correspondence and suggestion.
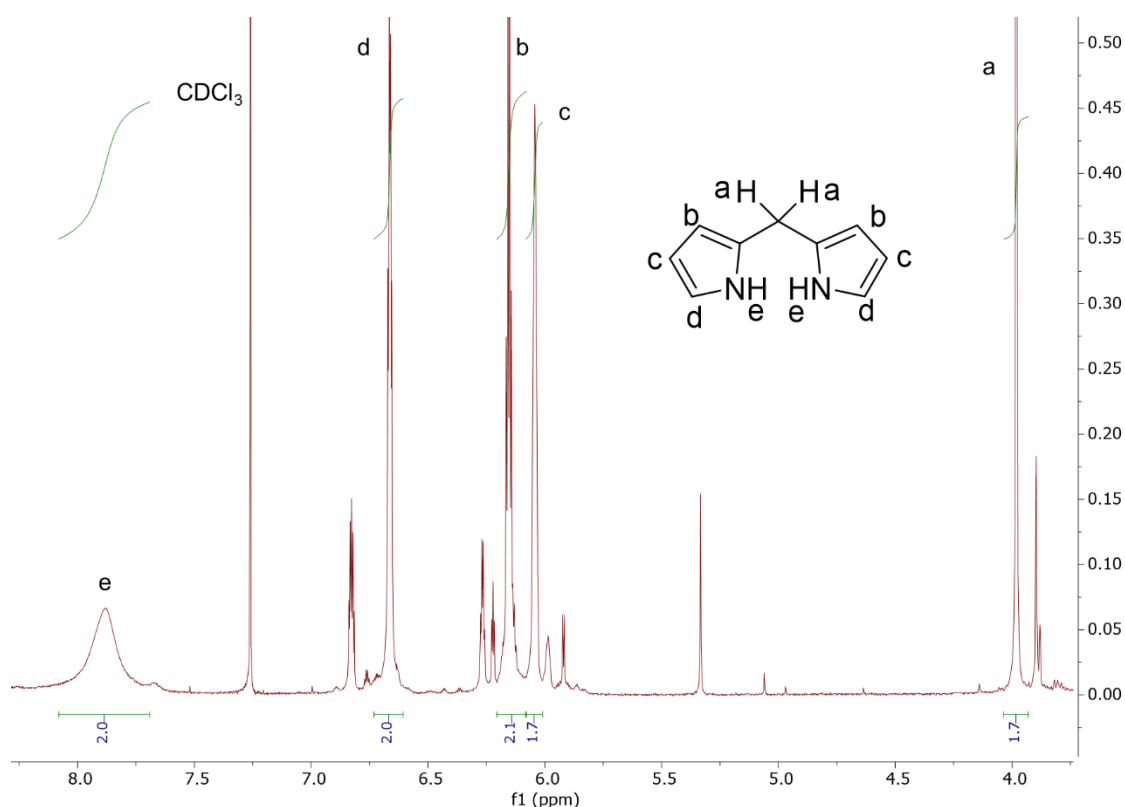
Figure 4.32: ¹H NMR spectrum (400 MHz, CDCl₃) for dipyrromethane.

4.7.3.1 *Dipyrromethanes with iso-Propyl and tert-Butyl Substituents*
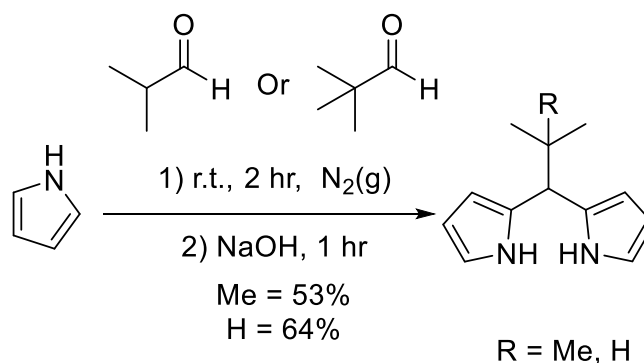
Figure 4.33: Reaction scheme for synthesis of 5-(1,1-dimethylethyl)dipyrromethane and 5-(1-methylethyl)dipyrromethane.

Introduction of a bulky substituent into the bridging methylene position of the dipyrromethane was of interest. 5-(1,1-Dimethylethyl)dipyrromethane, the ᵗbutyl-substituted dipyrromethane, was synthesised by addition of pivaldehyde and a TFA catalyst to dry pyrrole, in high dilution, and stirring at room temperature for two hours under nitrogen, before quenching by addition of solid NaOH, following a literature procedure (Figure 4.33).[193] After filtration, removal of pyrrole under reduced pressure

and aqueous workup, the product was purified by recrystallisation from CH_2Cl_2/hexane to give colourless needle-like crystals, which displayed a higher general stability to light than dipyrromethane.

The *iso*-propyl substituted analogue was synthesised by the same method (Figure 4.33),[193] however trituration with hexanes was required to remove trace pyrrole and induce crystallisation. The major remaining impurities were removed by dissolution in the minimum hexane and isolation of the insoluble solid.

4.8 Synthesis of Tetra-Substituted Porphyrins
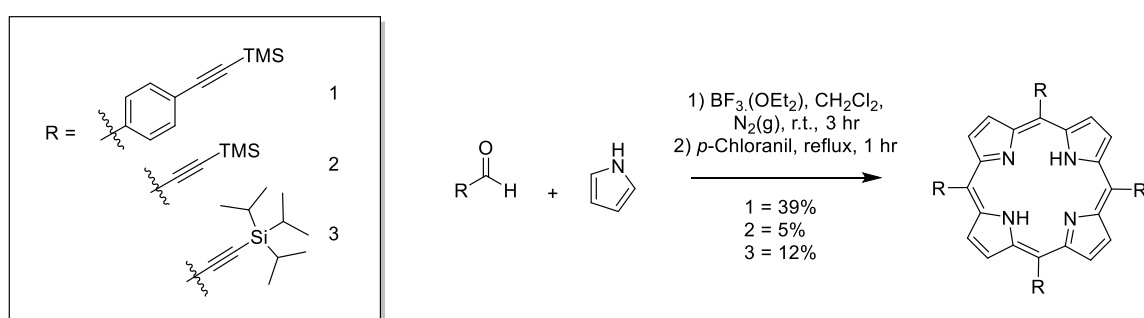
Figure 4.34: Reaction scheme for synthesis of 5,10,15,20-tetra-substituted porphyrins.

Tetrasubstituted porphyrins were synthesised using the two-step, one-pot Lindsey reaction (Figure 4.34).[194] Thus, pyrrole and the respective aldehyde were reacted together under mild conditions (dry CH_2Cl_2, under nitrogen at room temperature) for around three hours in the presence of $BF_3.OEt_2$ as catalyst, to allow equilibration of the forming macrocycle, hence the need for anhydrous and airless conditions. An oxidant, *p*-chloranil, was then added and the mixture heated under reflux to give the crude product. Purification *via* column chromatography, followed by recrystallisation from CH_2Cl_2/MeOH gave the pure target product as evidenced by ^{1}H NMR spectroscopy.

4.8.1   5,10,15,20-Tetrakis[4-(ethynyl)phenyl)]porphyrin
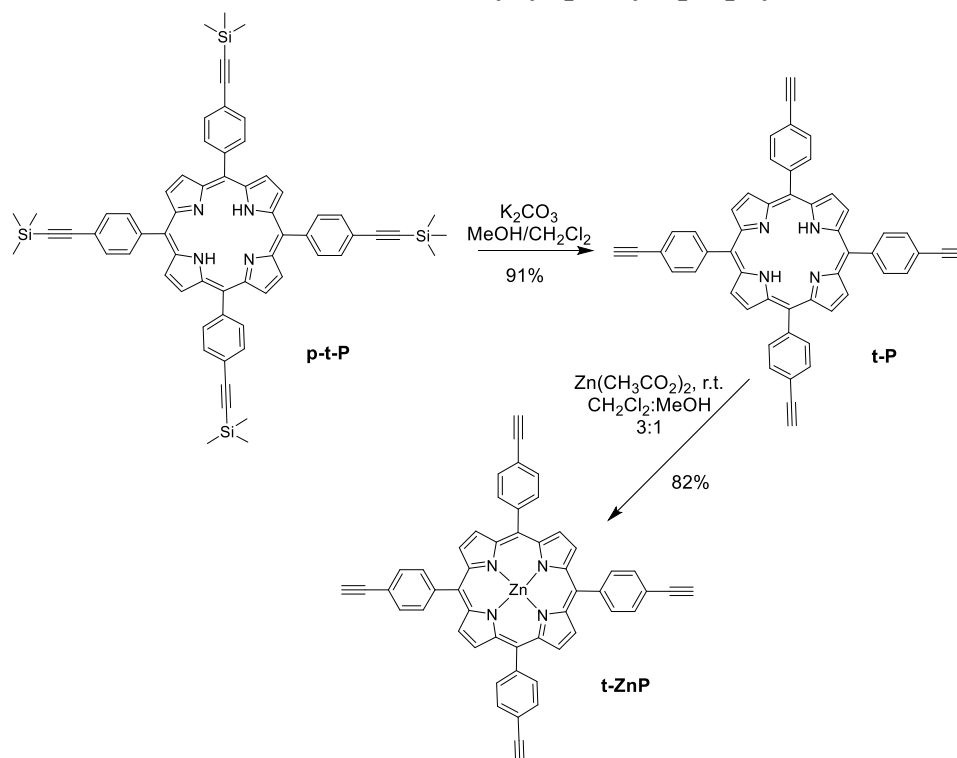
Figure 4.35: Reaction scheme for synthesis of 5,10,15,20-tetrakis[4-(ethynyl)phenyl)]porphyrin.

4-[(Trimethylsilyl)ethynyl)]benzaldehyde and pyrrole were used to form 5,10,15,20-tetrakis[4-{(trimethylsilyl)ethynyl}phenyl)]porphyrin, under Lindsey conditions, as purple crystals in 30-40% yield, equivalent to those reported in the literature (Figure 4.35).[194] ^{1}H NMR spectroscopy (Figure 4.36) shows a typical porphyrin spectrum, with the signal from the *β*-pyrrole hydrogens found as a singlet at 8.82 ppm and the H-N signal as a broad singlet at -2.86 ppm. The phenyl resonances from the *meso*-substituent are present as an AA'XX' system at 8.14 and 7.87 ppm. The singlet at 0.38 ppm is associated with -SiMe$_3$ and shows [29]Si satellites ($^2J_{Si-H} = 120.2$ Hz).

The porphyrin was deprotected to give the free alkyne in >90% yield *via* base hydrolysis using K$_2$CO$_3$ in CH$_2$Cl$_2$:MeOH 3:1 (Figure 4.35).[194] Loss of the intense singlet at 0.38 ppm in the ^{1}H NMR spectrum (Si(CH$_3$)$_3$) and the appearance of a singlet at 3.33 ppm, integrating as four hydrogens (C≡C-*H*) indicated successful deprotection.
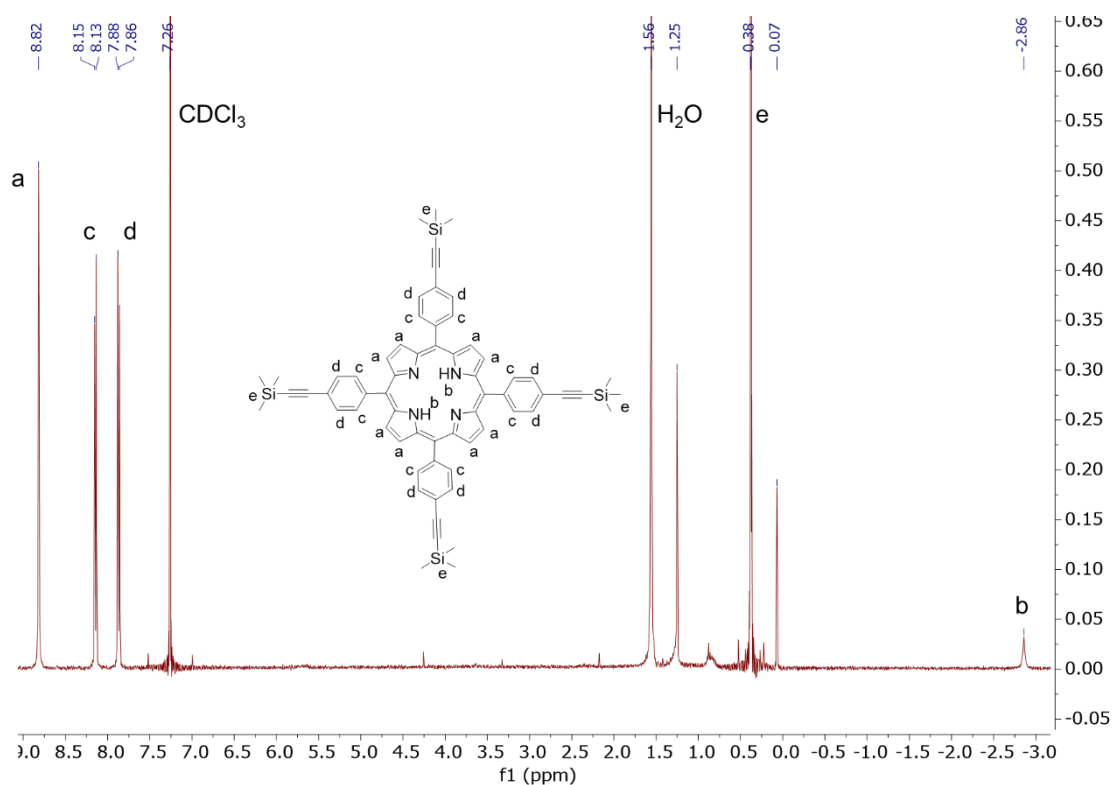
Figure 4.36: *¹H NMR spectrum (400 MHz, CDCl₃) of 5,10,15,20-tetrakis[4-{(trimethylsilyl)ethynyl}phenyl)]porphyrin.*

Insertion of zinc to form the zincated porphyrin, was achieved using excess Zn(OAc)$_2$ in 3:1 CH$_2$Cl$_2$:MeOH at room temperature, giving a bright purple crystalline solid (Figure 4.35).[194] The reaction proceeded effectively in >80% yield, although low solubility due to aggregation made the work-up challenging, with large volumes of solvent (CH$_2$Cl$_2$) required. It was noted that addition of a small amount of a coordinating solvent, such as methanol, aided solubility, likely due to coordination to the zinc ion, though in large amounts methanol is a good anti-solvent. Successful reaction is confirmed by the loss of the NH signal at -2.83 ppm and a small downfield shift of the β-hydrogen resonance by ~0.9 ppm.

Combustion analysis has proved challenging for porphyrins and the protected porphyrin has failed to pass CHN by a significant margin of 20% low on carbon, even after filtering through celite, serial recrystallisation and addition of a combustion aid at a higher temperature in the analysis. It is suspected that the high carbon and silicon content is hindering combustion.[195, 196] Nonetheless, APCI-MS, UV-vis and ¹H NMR spectroscopy all support the structural assignment and the absence of impurities. Likewise the deprotected porphyrin and the zincated porphyrin have also proved to be challenging to

analyse by CHN, frequently being low on hydrogen, nitrogen and particularly carbon (~1-6%). This resulted in the decision being taken not to analyse the porphyrin cores by CHN.

4.8.2   5,10,15,20-Tetrakis(trimethylsilylethynyl)porphyrin and 5,10,15,20-tetrakis(triisopropylsilylethynyl)porphyrin
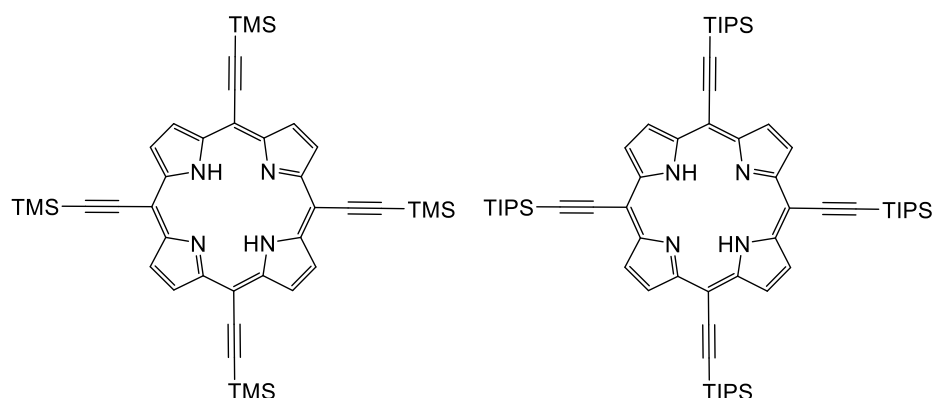
Figure 4.37: Structures of 5,10,15,20-tetrakis(trimethylsilylethynyl)porphyrin (left) and 5,10,15,20-tetrakis(triisopropylsilylethynyl)porphyrin (right).

Porphyrins with a direct carbon-carbon triple bond connected to the macrocycle ring (Figure 4.37) were synthesised using Lindsey conditions from protected 2-propynals, using a $BF_3.OEt_2$ catalyst (Figure 4.34).

Initially, 3-(trimethylsilyl)-2-propynal was used to form 5,10,15,20-tetrakis(trimethylsilylethynyl)porphyrin in 5% yield,[29, 39, 197] however the decision was taken to change the protecting group from TMS to TIPS. Thus, 3-(triisopropylsilyl)-2-propynal was used to form 5,10,15,20-tetrakis(triisopropylsilylethynyl)porphyrin which was recovered in 11.5% yield in an initial trial reaction, appearing as a metallic purple solid, which was a deep green in solution. A slight modification to the general method was required, with the first step carried out at −20 °C, before warming to room temperature.[33, 198, 199] Owing to the difficulty encountered later attaching four gold complexes to tetraphenylalkynyl-substituted porphyrin, this synthesis was not developed further.

4.9   5,15-Disubstituted Porphyrins
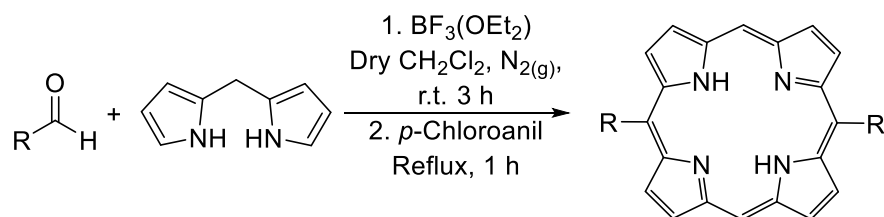
Figure 4.38: Generic reaction scheme for the synthesis of 5,15-disubstituted porphyrins.

The 5,15-disubstituted porphyrins in this work were synthesised using the one-pot, two-step Lindsey reaction (Figure 4.38) from dipyrromethane and the aldehyde of interest under the conditions detailed above to give the product, which appeared pure by ^{1}H NMR spectroscopy.[51, 200-202]

4.9.1   5,15-*Bis*((4-ethynyl)phenyl)porphyrin
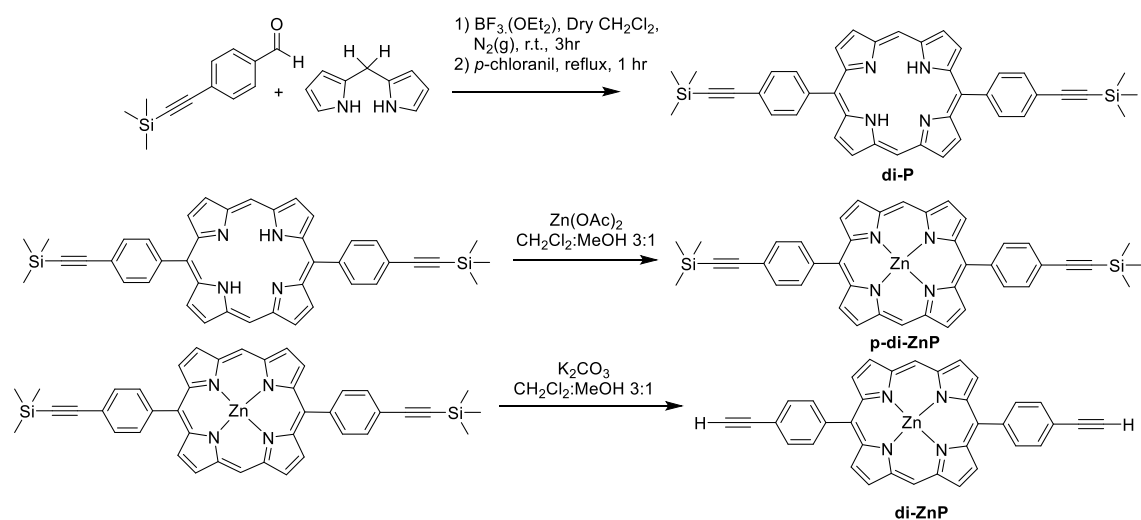
Figure 4.39: Reaction scheme for synthesis of zinc 5,15-bisphenyl(4-ethynyl)porphyrin.

5,15-*Bis*(4-[(trimethylsilyl)ethynyl)]phenyl)porphyrin (Figure 4.39) was synthesised using the Lindsey synthesis from dipyrromethane and 4-[(trimethylsilyl)ethynyl)]benzaldehyde with BF$_3$.OEt$_2$ catalyst in up to 36% yeild.[194]

On the reduction in symmetry from the *meso*-tetrasubstituted system to the *meso*-di-substituted system, the aromatic region of the ^{1}H NMR spectrum becomes more complex (Figure 4.40). Significantly a new signal from the hydrogens in the 10- and 20-positions is present at 10.34 ppm and an AB system is seen for the β-hydrogens, which are shifted downfield from 8.82 ppm to 9.41 and 9.05 ppm; the small AB-coupling of ~4.5 Hz

reflects the bond angle of 108° present in a five-membered ring, which reduces orbital overlap between hydrogen atoms on adjacent carbons. The N*H* signal is shifted upfield to -3.14 ppm from -2.86 ppm. Combined with the downfield shift of the *β*-hydrogen signals, this suggests the ring current is increased compared to the tetra-substituted analogue.
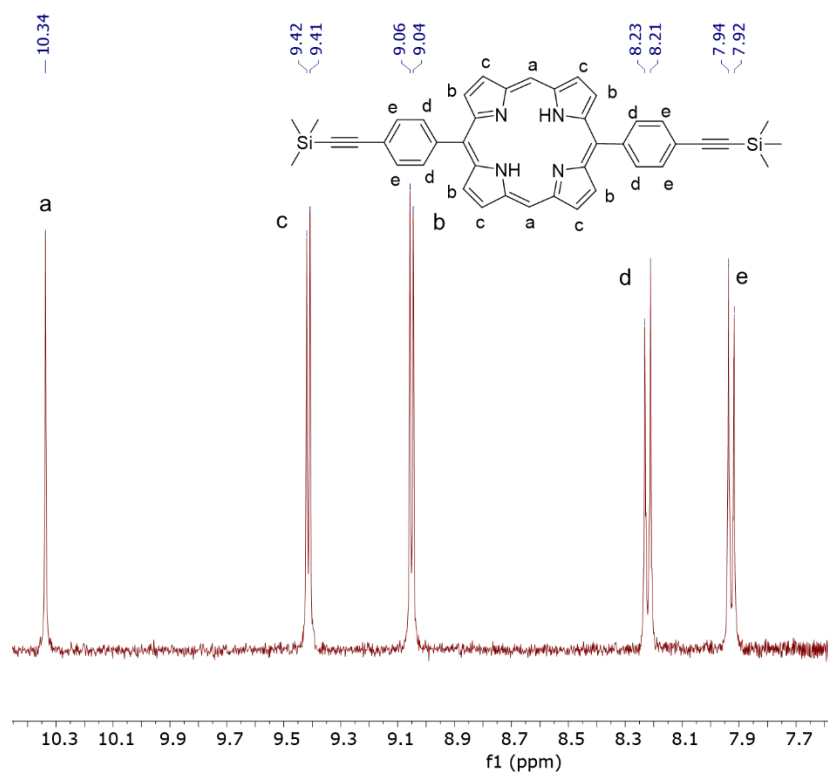
Figure 4.40: Aromatic region of the ^{1}H NMR spectrum (400 MHz, CDCl$_3$) of 5,15-bis(4-[(trimethylsilyl)ethynyl)phenyl])porphyrin.

The trimethylsilyl-protected porphyrin was zincated using Zn(OAc)$_2$ in 4:1 CH$_2$Cl$_2$:MeOH, after which the trimethylsilyl group was removed using K$_2$CO$_3$ in 4:1 CH$_2$Cl$_2$:MeOH (Figure 4.39) to give the unprotected acetylene. The reactions were carried out in this sequence following literature precedent, which suggests that this increases the ease of synthesis due to compound solubility.[51, 200-202]

4.9.1.1 *Porphyrins with Bulky Groups in the 10- and 20-Positions*

iPr-ZnP
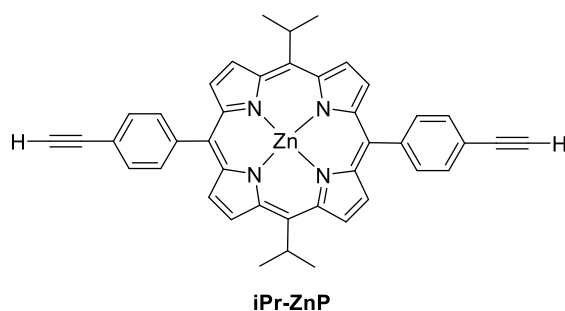
Figure 4.41: Structure of zinc 5,15-bis(4-(ethynyl)phenyl)-10,20-isopropyl-porphyrin.

As will become apparent, it became desirable to investigate the effect of introduction of a bulky substituent in the 10,20-positions of the porphyrin. Initially a *tert*-butyl group was used, however yields on porphyrin formation proved low (~6%) and McDonald scrambling led to an inseparable mixture of porphyrins. Reduction of the solubility by either zincation or deprotection also failed to facilitate purification therefore the decision was taken to investigate use of an *iso*-propyl substituent (Figure 4.41). This proved to give reasonable yields (~12%) and allowed the product to be purified. Zincation and deprotection were carried out by the standard procedures detailed above.[194, 200-202]

4.9.2 5,15-*Bis*(ethynyl)porphyrin
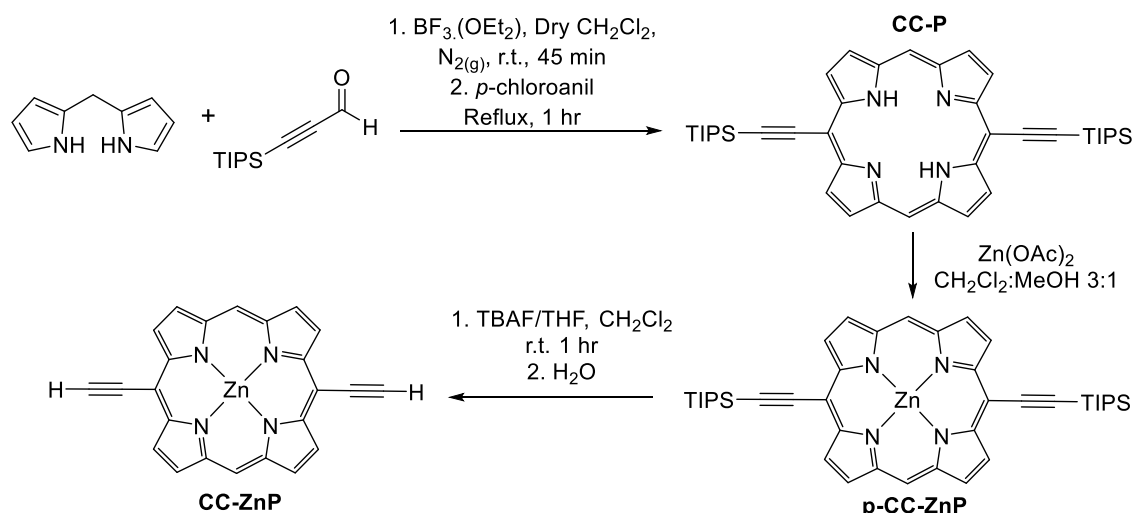
Figure 4.42: Reaction scheme for synthesis of 5,15-bis((triisopropylsilyl)ethynyl)porphyrin.

5,15-*Bis*((triisopropylsilyl)ethynyl)porphyrin (Figure 4.42) was synthesised, in up to 45% yield, as a greenish-purple, crystalline solid using the Lindsey synthesis from dipyrromethane and 3-(triisopropylsilyl)-2-propynal with $BF_3.OEt_2$ catalyst.[58] The

reaction time of the first stage was reduced to 45 minutes compared with the standard reaction procedure, where the reaction time is 3 hours.[58] Only signals relating to the porphyrin macrocycle ring (10.12 – 9.30 ppm and N-*H* at -2.70 ppm) and the TIPS-protecting group (1.53 – 1.49 ppm) were present in the ^{1}H NMR spectrum.

The free-base porphyrin was zincated using the standard procedure to give zinc 5,15-*bis(*(triisopropylsilyl)ethynyl)porphyrin in 92% yield as an olive-green crystalline solid, which was a cyan to deep emerald green colour in solution. Successful reaction was confirmed by loss of the N-*H* signal at -2.70 ppm in the ^{1}H NMR spectrum. The porphyrin was subsequently deprotected using a TBAF solution in THF (1 mol dm^{-3}).[198, 199, 203] Addition of water and removal of volatile organics enabled isolation of the pure porphyrin as a dark purple solid *via* filtration. Successful deprotection was confirmed by loss of the TIPS-proton resonances and gain of a new resonance at 5.27 ppm in the ^{1}H NMR spectrum. A large reduction in solubility in halogenated solvents (dichloromethane and chloroform) was observed on deprotection, while solubility in polar solvents (methanol and DMSO) increased. This is likely due to the increased aggregation possible with the more planar zinc porphyrin core. Deprotection was carried out immediately prior to coupling to prevent any Glazer coupling occurring, which can be a major issue with (ethynyl)porphyrin systems.[29, 102]

4.10   Attempted Synthesis of Platinum(II) Porphyrins

Platinum(II) porphyrins are well known to give an intense red phosphorescence in deaerated solutions due to the strong spin-orbit coupling effect of platinum as a heavy metal atom. Not only are platinum(II) porphyrins triplet emitters, but their square-planar, neutral nature is desirable compared to other potential heavy metal atoms. It was therefore of interest to attempt to synthesise platinum(II) porphyrins, with the ultimate aim of investigating their connection to gold(III) C^N^C complexes.
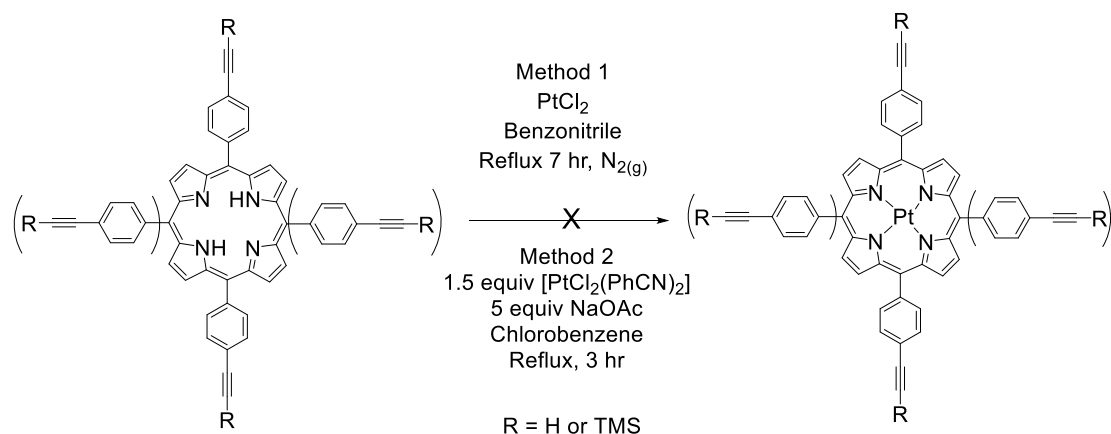
Figure 4.43: Reaction scheme for attempted insertion of platinum(II).

The standard method of platinum(II) insertion into porphyrins is *via* heating under reflux ($T = 190$ °C) the respective free-base porphyrin and $PtCl_2$ in benzonitrile over several hours,[204-210] with small variations involving the use of microwave irradiation[211] or addition of the preformed complex $[PtCl_2(PhCN)_2]$.[209, 212] Unfortunately, such harsh conditions, required in order to gain solubilisation of $PtCl_2$ in benzonitrile in order to form the more labile complex $[PtCl_2(PhCN)_2]$ *in situ* and to insert into the porphyrin core, can prove incompatible with some porphyrins, particularly those containing halogen substituents.[213] It is, also notable that there is only one reported example of platination of a porphyrin containing alkyne functional groups.[208] This method, under a nitrogen atmosphere, was used to attempt to platinate the protected tetra-substituted porphyrin (Figure 4.43, Method 1), however an insoluble black product was isolated, which could not be characterised.[206]

Suspecting an unwanted side-reaction between the platinum complex and the functional groups of the porphyrin, facilitated by the high reaction temperatures, use of milder reaction conditions was investigated.[213, 214] $[PtCl_2(PhCN)_2]$ was synthesised by the addition of $PtCl_2$ to benzonitrile, with the mixture being stirred at room temperature overnight.[212] Addition of hexane resulted in the formation of the yellow precipitate of the product, which could be isolated by filtration. 1.5 molar equivalents of $[PtCl_2(PhCN)_2]$ and five molar equivalents of sodium acetate (the latter to aid in the deprotonation of the free-base porphyrin and to neutralise HCl produced during the course of the reaction) in chlorobenzene were heated under reflux for three hours and proved a milder method for

260

the insertion of platinum(II) into 5,10,15,20-*p*-tolyporphyrin.[213] The workup procedure was considerably eased by the use of chlorobenzene, which, unlike benzonitrile, can be removed on a standard rotary evaporator. Unfortunately, again only an insoluble, unidentifiable black solid was isolated, for both the protected and deprotected tetra-substituted and di-substituted porphyrins (Figure 4.43, Method 2).
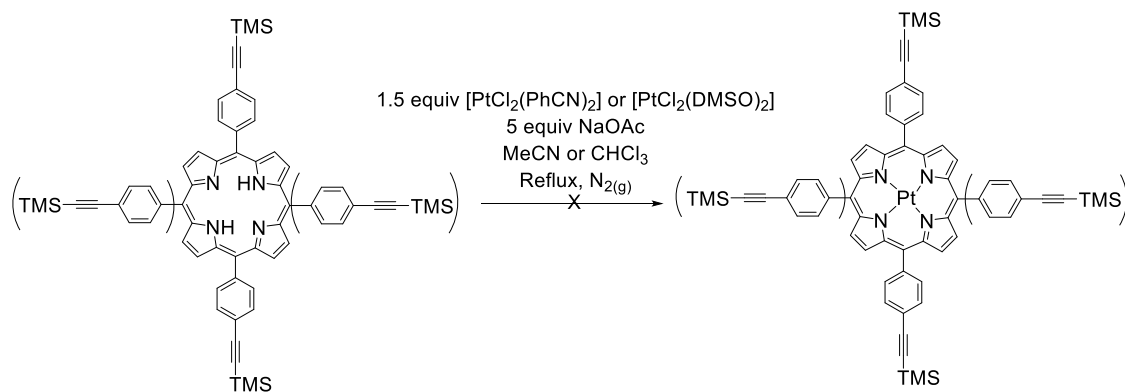
Figure 4.44: Attempted insertion of platinum(II) using milder conditions.

Use of either [PtCl$_2$(PhCN)$_2$] or [PtCl$_2$(DMSO)$_2$],[215] with five molar equivalents of sodium acetate in either acetonitrile or chloroform heated under reflux (Figure 4.44), gave only recovered starting material, with no evidence for insertion occurring. Sadly, it has therefore been concluded that, for the present time, insertion of platinum(II) into the porphyrin cores is incompatible with the alkyne functionally and therefore this work has not been pursued further.

4.11　　　X-ray Single Crystal Structures of Porphyrins

Some of the synthesised porphyrins were characterised structurally by X-ray methods, results of which are reported here. XRD data tables and .cif files can be found in the data folder - see page 30. Carbon atoms are coloured grey, chlorine green, hydrogen turquoise, nitrogen blue, oxygen red, silicon pale yellow, and zinc pink.

4.11.1 5,15-*Bis*(4-[(trimethylsilyl)ethynyl)]phenyl)porphyrin
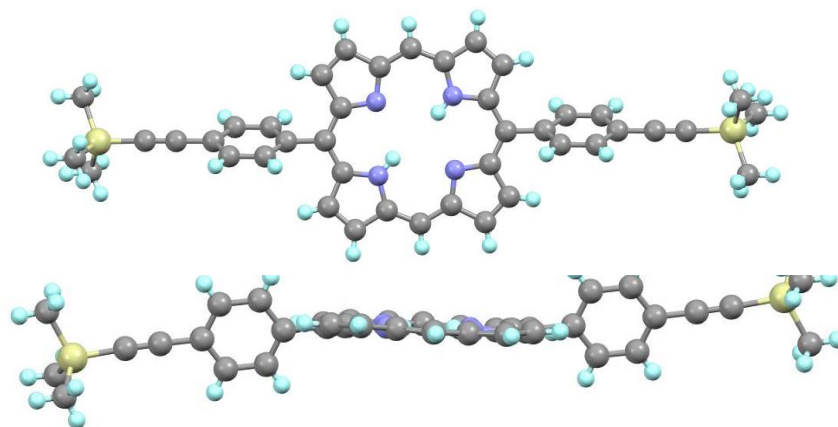
Figure 4.45: Molecular structure of 5,15-bis(4-[(trimethylsilyl)ethynyl)]phenyl)porphyrin (top) and side view (bottom).

Single crystals of 5,15-*bis*(4-[(trimethylsilyl)ethynyl)]phenyl)porphyrin (Figure 4.45) were obtained by the slow diffusion of ethyl acetate into CH_2Cl_2. The compound crystallised in the monoclinic space group $I2/a$. The aromatic porphyrin core is planar with the phenyl groups twisted at an angle of 69.92° to the plane (Figure 4.45, bottom). The C≡C bond angles are slightly distorted away from 180° with C^C^C = 178.8(2)° and C^C^Si = 177.0(2)°. The molecules pack in slanted columns, with the molecular orientation alternating between layers, so that each molecule is oriented at an angle of 75.72° to those in the neighbouring layers (Figure 4.46).
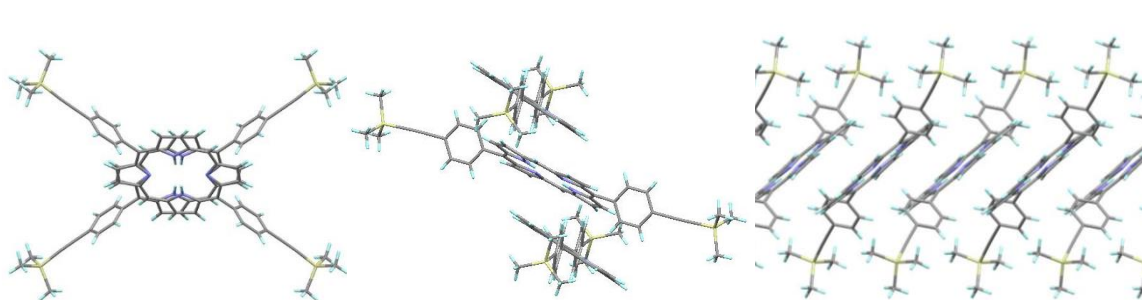
Figure 4.46: Packing of 5,15-bis(4-[(trimethylsilyl)ethynyl)]phenyl)porphyrin viewed down crystallographic axis a (left, from the side (middle) and down crystallographic axis b (left).

4.11.2　Zinc 5,15-*bis*(4-(ethynyl)phenyl)porphyrin
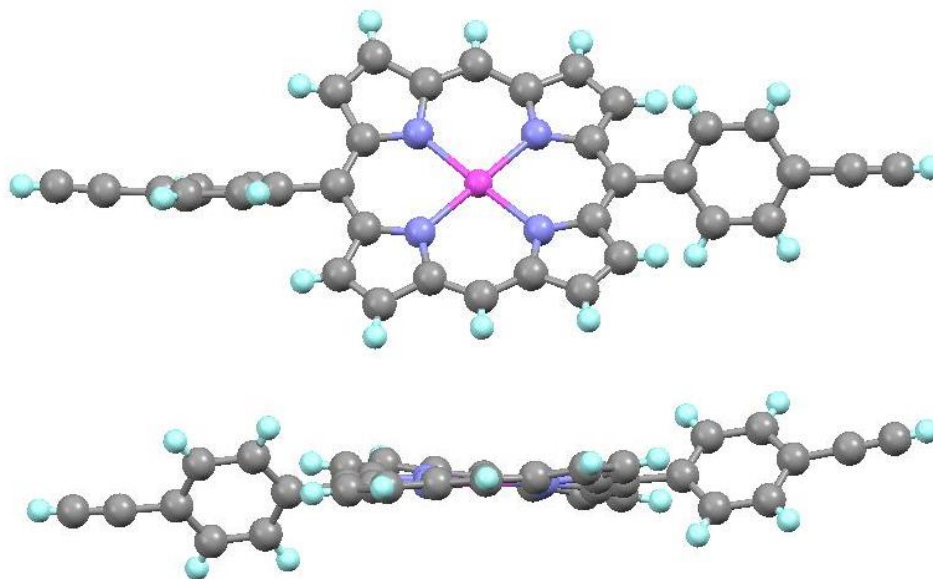
Figure 4.47: Molecular structure of zinc 5,15-bis(4-(ethynyl)phenyl)porphyrin (top) and side view (bottom).

Single crystals of zinc 5,15-*bis*(4-(ethynyl)phenyl)porphyrin (Figure 4.47) were obtained by the slow diffusion of methanol into chloroform. The compound crystallised in the monoclinic space group $P2_1/c$. The porphyrin core is distorted from planar on the introduction of the zinc ion, with a slightly distorted square plane geometry about the zinc ion (N^Zn^N angles are measured as 91.42(7)° and 88.58(7)° respectively). The phenylacetylene units are rotated at 78.02° and 58.41° from the porphyrin plane and the molecules pack in columns with a distance of 4.436 Å between adjacent layers (Figure 4.48).
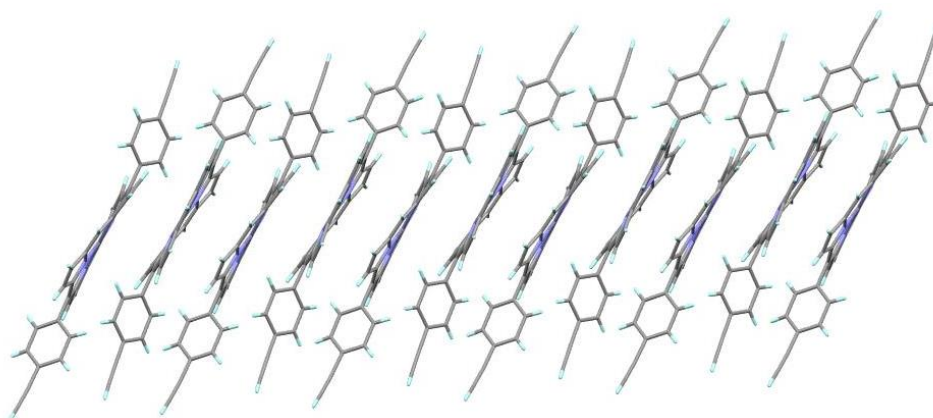
Figure 4.48: Packing of zinc 5,15-bis(4-(ethynyl)phenyl)porphyrin.

4.11.3   5,15-*Bis*(4-(triisopropylsilyl)ethynyl)porphyrin
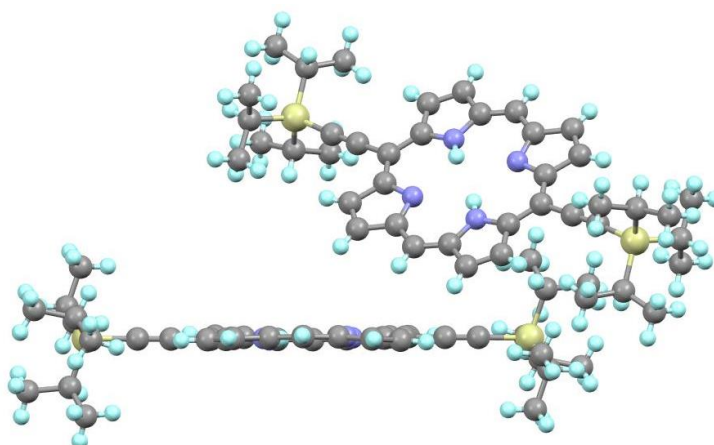
Figure 4.49: Molecular structure of 5,15-bis(4-(triisopropylsilyl)ethynyl)porphyrin.

Single crystals of 5,15-*bis*(4-(triisopropylsilyl)ethynyl)porphyrin (Figure 4.49) were obtained by the slow diffusion of methanol into chloroform. The compound crystallised in the triclinic space group *P*-1, with two molecules in the asymmetric unit. On the introduction of the ethylene substituent the porphyrin core becomes completely planar, with bulky TIPS-groups at the sides. 5,15-*Bis*(4-(triisopropylsilyl)ethynyl)porphyrin packs in slanted columns (Figure 4.50).
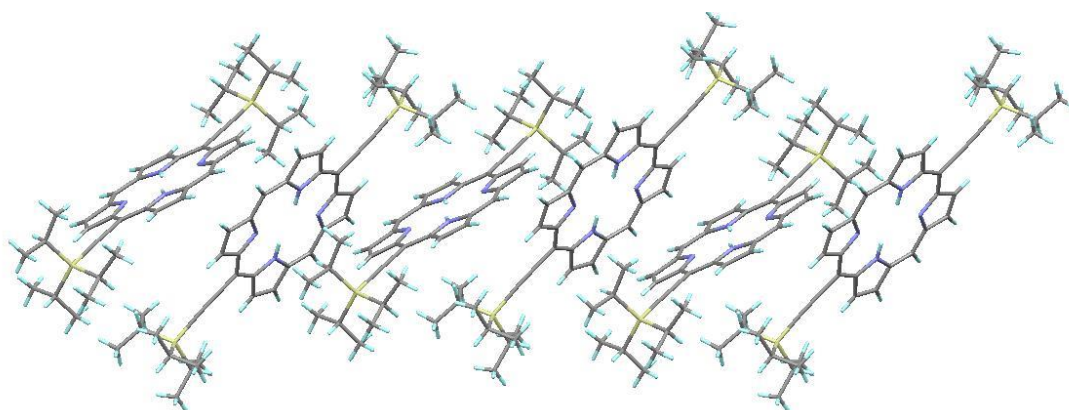
Figure 4.50: Packing of 5,15-bis(4-(triisopropylsilyl)ethynyl)porphyrin in the crystal.

4.11.4   Zinc 5,15-*bis*(4-(triisopropylsilyl)ethynyl)porphyrin
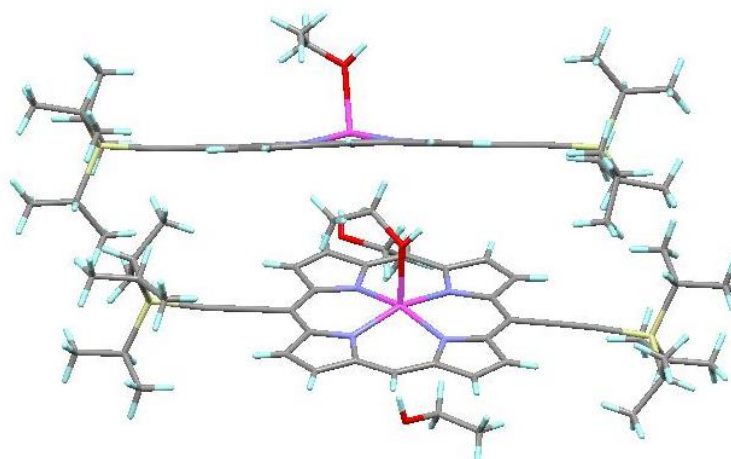
Figure 4.51: Molecular structure of zinc 5,15-bis(4-(triisopropylsilyl)ethynyl)porphyrin.

Single crystals of zinc 5,15-*bis*(4-(triisopropylsilyl)ethynyl)porphyrin (Figure 4.51) were obtained by the slow diffusion of ethanol into chloroform. The compound crystallised in the triclinic space group *P*-1. Two compounds are present in the asymmetric unit, which are angled towards each other at an angle of 31.08°. Three molecules of ethanol are present in the asymmetric unit, one of which displays coordination to the zinc ion. The zinc ion itself is slightly displaced out of the plane of the porphyrin core, with a very slight distortion from square-planar geometry with N^Zn^N angles of 90.4(2)°, 87.5(2)°, 89.0(2)° and 87.6(2)°. The porphyrin core is planar, with bulky TIPS-groups on either side; the C≡C bond is slightly distorted from linearity with the C^C^Si angle measuring 177.2(6)°.
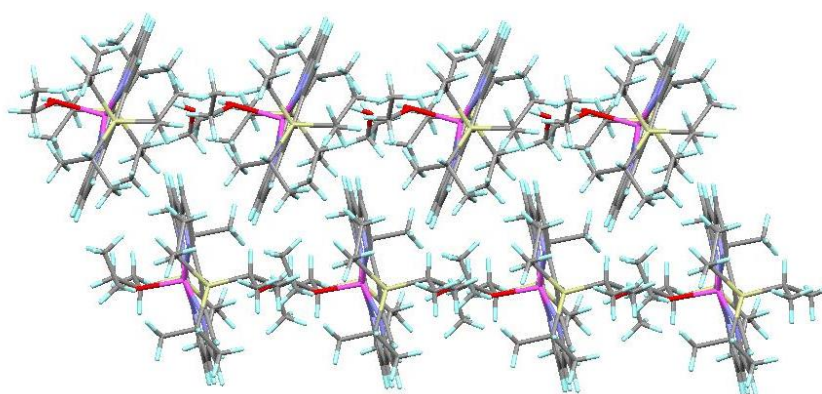
Figure 4.52: Packing of zinc 5,15-bis(4-(triisopropylsilyl)ethynyl)porphyrin in the crystal.

The compounds pack in columns (Figure 4.52), where the porphyrin cores stack parallel on top of each other in planes at a distance of 7.041 Å, with two ethanol molecules

between. The cores in adjacent columns are set at a distance of 3.302 Å from the neighbouring porphyrin cores.

4.12 Linking Gold(III) Complexes to the Porphyrins

4.12.1 Tetrasubstituted Porphyrins
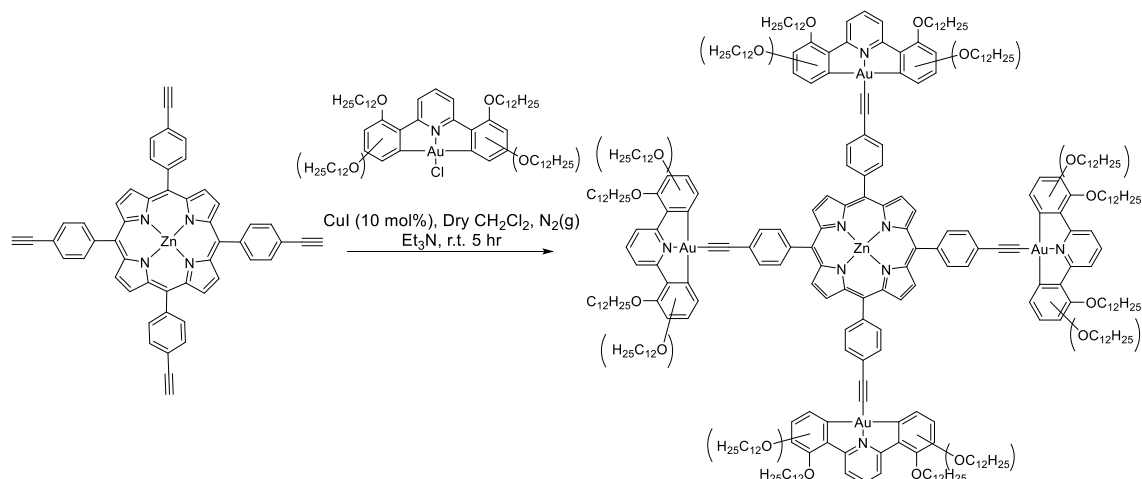
Figure 4.53: Reaction scheme for connection of gold complexes to tetra-substituted porphyrin core.

Attempts were made to connect each of the two-chain gold complexes, substituted in the 4,4′-positions (**4-[Au]-Cl**) or the 2,2′-positions (**2-[Au]-Cl**), to the porphyrin core using a modified standard literature procedure (Figure 4.53).[216, 217] The stoichiometry of the gold(III) complexes in the reaction was increased from the 1 molar equivalent used in the generic method, to account for the attempted connection to four alkyne groups in one molecule.[218] However, use of 4.1 molar equivalents of **4-[Au]-Cl**, and 6 molar equivalents of **2-[Au]-Cl**, respectively, to form the tetra-substituted porphyrin led to inseparable mixtures of tri-, di- and mono-substituted porphyrins. Significant was the remaining presence of the alkyne signal at 3.33 ppm in the ^{1}H NMR spectra in these mixtures, indicating incomplete substitution. Further, it was observed on use of the free-base porphyrin that the copper used to facilitate coupling had been inserted into the porphyrin,[34] so that subsequent reactions used the zinc porphyrin precursor. Several variations were employed in which catalyst loading and regent ratios were varied. These are detailed in the Experimental in Chapter 6; none were successful.

An alternative route to the target porphyrin is to add the functionality during the synthesis of the porphyrin itself, employing a suitably substituted aldehyde. Successful synthesis of highly sterically hindered porphyrins in good yield (>40%) is known.[219] Such an approach is outlined in Figure 4.54.
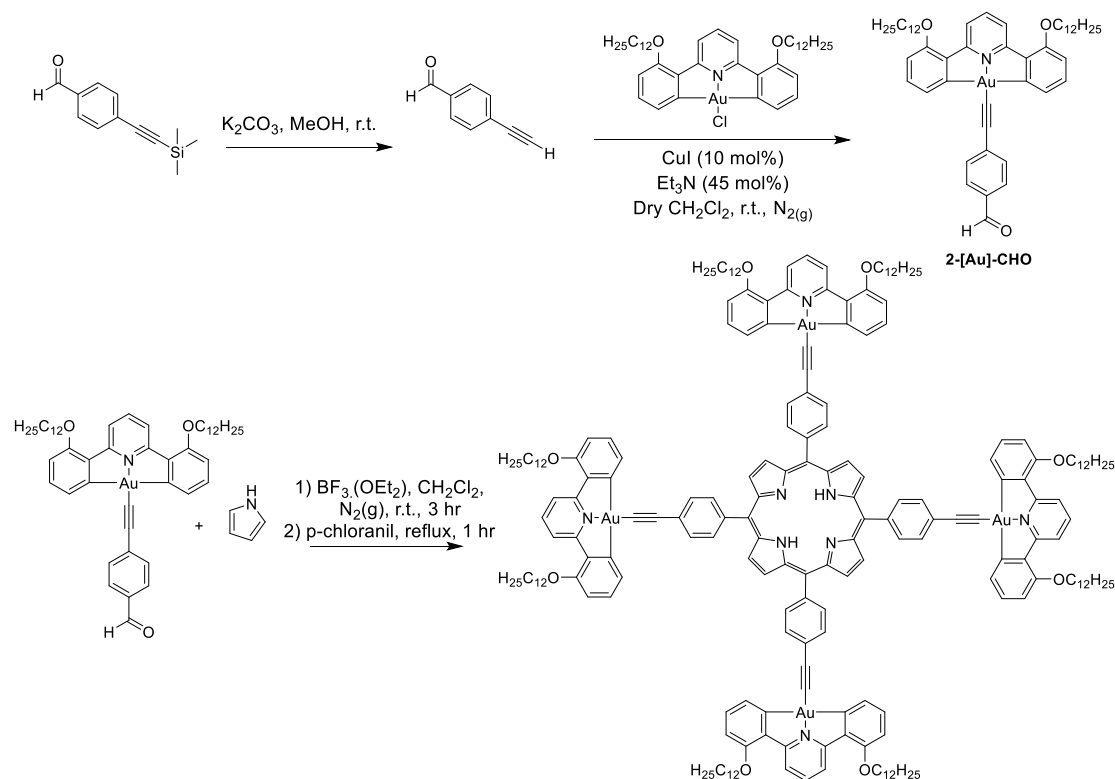
Figure 4.54: Reaction scheme for synthesis for formation of the tetra-substituted porphyrin directly.

Thus, the starting aldehyde was formed by deprotection of 4-[(trimethylsilyl)ethynyl)]benzaldehyde using K_2CO_3 in MeOH to give the terminal alkyne (Figure 4.54, top).[220] This was coupled to **2-[Au]-Cl,** using standard conditions, to give **2-[Au]-CHO** in 79% yield. **2-[Au]-CHO** was used in the standard Lindsey reaction (Figure 4.54, bottom), however only tar and a yellow crystalline solid were isolated. ^{1}H NMR spectroscopy showed only signals relating to the starting gold complex, **2-[Au]-Cl**, with characteristic porphyrin signals absent; APCI-MS indicated the reformation of the chlorogold complex.

However, using a 2,2′,3,3′-tetrasubstituted gold complex, coupling using the approach in Figure 4.53, and with the benefit of experience gained in preparing 5,15-disubstituted systems (Section 4.12.2), **2,3-[Au]-t-ZnP** (Figure 5.55) was synthesised in an exceptional yield of 72%. Replacement of dodecyloxy chains with butoxy chains gave the analogue,

2,3-[Au]-t-ZnP-C4, which was synthesised in the hope that it would prove capable of producing crystals suitable for single crystal diffraction. Unfortunately, good quality crystals were not obtained. The yield of this porphyrin was significantly lower (37%), with noticeable amounts of Glazer-coupled products formed.
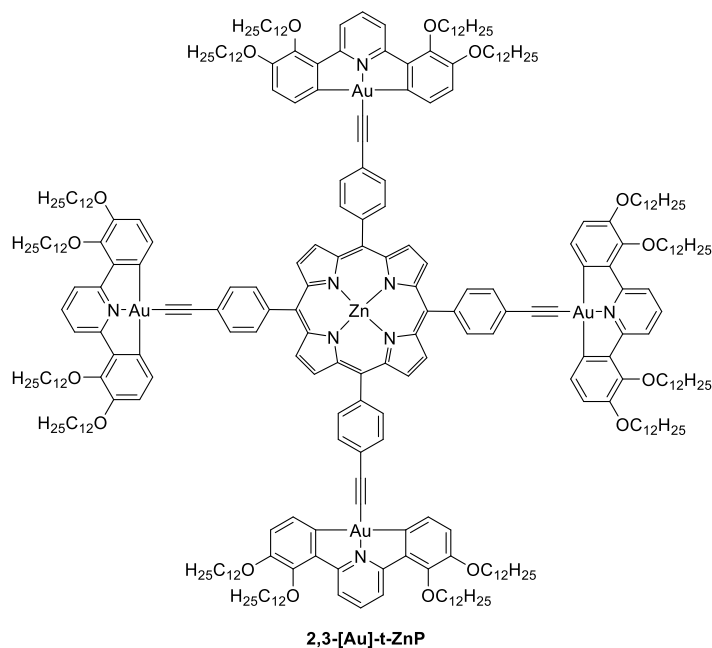
*Figure 4.55: Structure of tetrasubstituted porphyrin with **2,3-[Au]** complexes.*

The ^{1}H NMR spectrum (Figure 4.56) was highly symmetric with the porphyrin and the gold complex signals present in a 1:4 ratio. Loss of the acetylene C-*H* singlet at 3.33 ppm confirmed successful reaction. The singlet relating to the *β*-hydrogen of the porphyrin is shifted 0.15 ppm downfield to 9.08 ppm and one of the signals relating to the phenyl ring is shifted 0.10 ppm downfield to 8.00 ppm; this is likely to be the hydrogen closer to the connection site, as the other is barely shifted (0.02 ppm). Three of the signals relating to the gold complex are shifted slightly downfield (<0.08 ppm), while the other is shifted significantly downfield by 0.4 ppm to 7.95 ppm. Both the −OCH$_2$ signals were shifted ~0.04 ppm downfield.
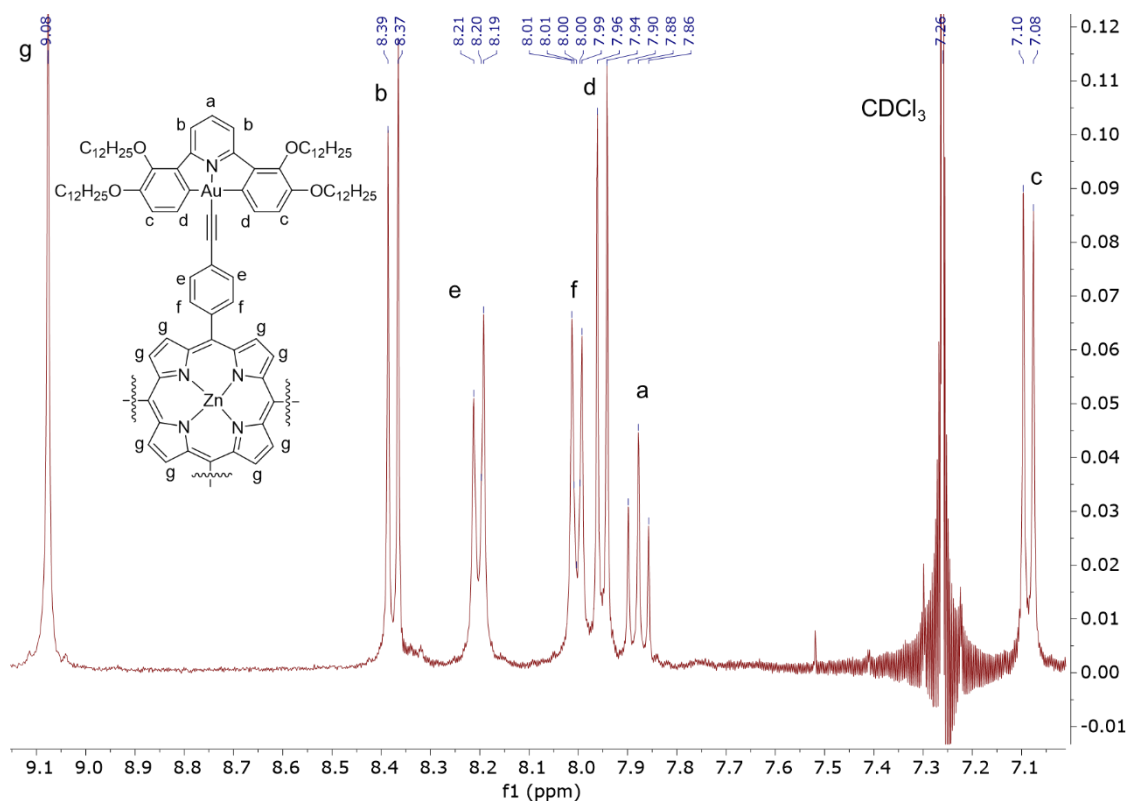
*Figure 4.56: Aromatic region of the ^{1}H NMR spectra (400 MHz, CDCl$_3$) for **2,3-[Au]-t-ZnP**.*

A tetrafunctionalised porphyrin was also obtained using **2,5-[Au]-Cl**, with a yield of 68%, through the ^{1}H NMR spectrum showed the presence of a small amount of inseparable tri-substituted porphyrin due to the presence of a small alkyne C-*H* signal at 3.31 ppm. The reduced yield and the presence of a small amount of tri-substituted porphyrin compared to the 2,2′,3,3′-system is not surprising given the highly sterically congested nature of the complex, with eight chains found across the porphyrin core. The presence of these chains results in a loss of equivalence of the pyrrolic hydrogen signals and those relating to the phenyl linking group, leading to increased complexity in the aromatic region. The chemical shift of the alkoxy chains in the 5,5′- positions, which are directed over the porphyrin core, were found to be shifted to lower field owing to the porphyrin ring current providing increased shielding.

4.12.2   5,15-Disubstituted Porphyrins

4.12.2.1   2H in the 10,20-Positions of the Porphyrin
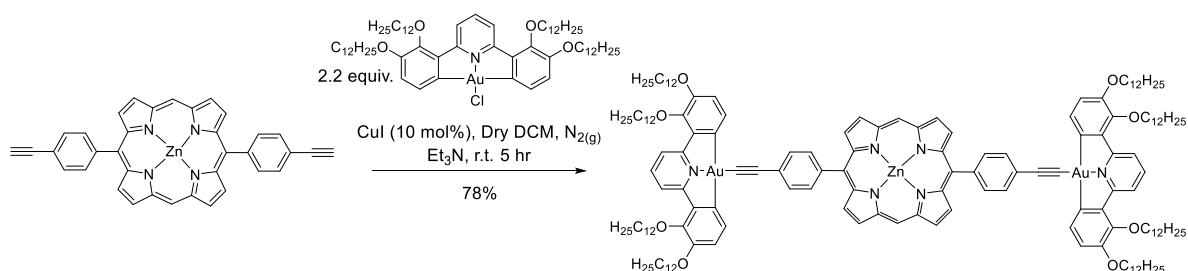
Figure 4.57: Reaction scheme for final connection of 2,2',3,3'- tetrasubstituted gold(III) complex to 5,15-disubstituted zinc porphyrin.

The gold(III) complex, **2,3-[Au]-Cl** was connected to **di-ZnP** using 1 equiv. of **di-ZnP**, 2.2 equiv. of **2,3-[Au]-Cl**, CuI (20 mol%) and triethylamine (90 mol%) in dry CH_2Cl_2 under nitrogen at room temperature (Figure 4.57).[216, 221] Monitoring by TLC (silica, 7:3 CH_2Cl_2:petroleum ether (40-60 °C)) indicated formation of a new broad spot with $R_f =$ 0.28. On purification *via* column chromatography, a reddish-purple solid was isolated, identified by ^{1}H NMR spectroscopy as the target product. The C4 equivalent, **2,3-[Au]-di-ZnP-C4** was also synthesised giving crystals suitable for characterisation by diffraction methods (Section 4.15).

The ^{1}H NMR spectrum of the product (Figure 4.58) showed the same component resonances as the starting units, with small changes in chemical shift and, of course, the loss of the acetylene hydrogen signal at 3.33 ppm. There was a consistent 1:2 ratio of porphyrin to gold complex signal integration.
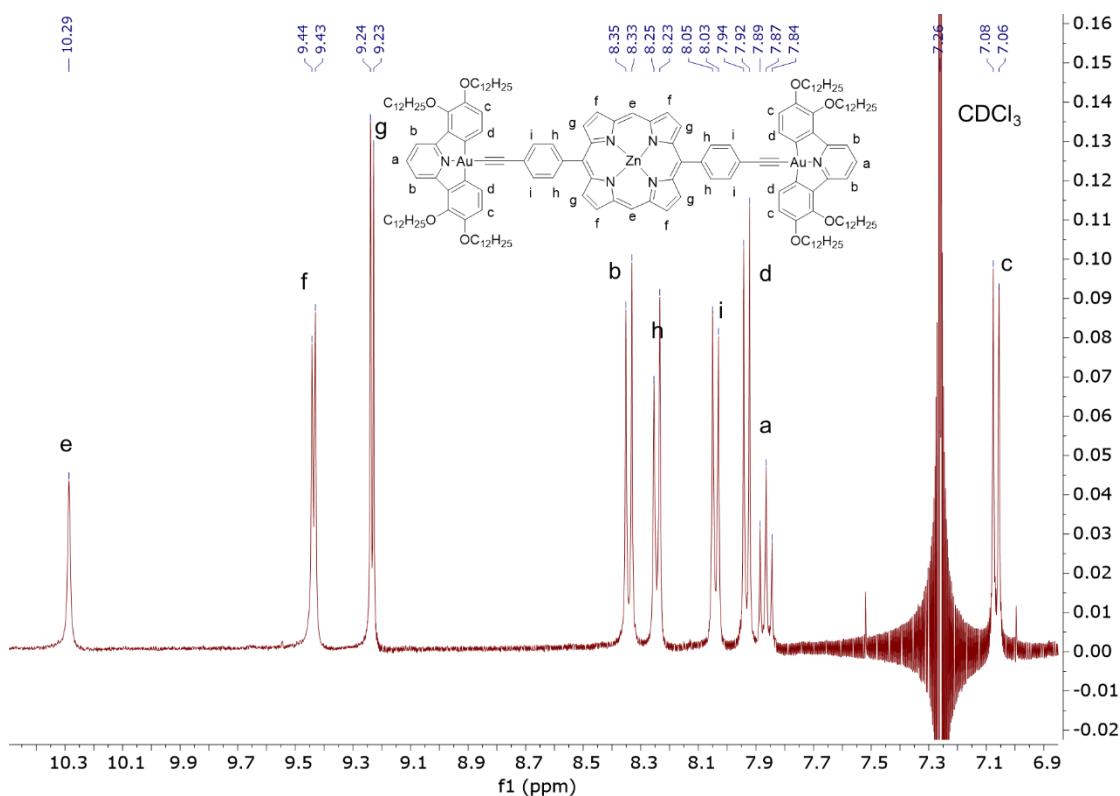
Figure 4.58: ¹H NMR spectrum of Compound **2,3-[Au]-di-ZnP** *(400 MHz, CDCl₃) showing the aromatic region.*
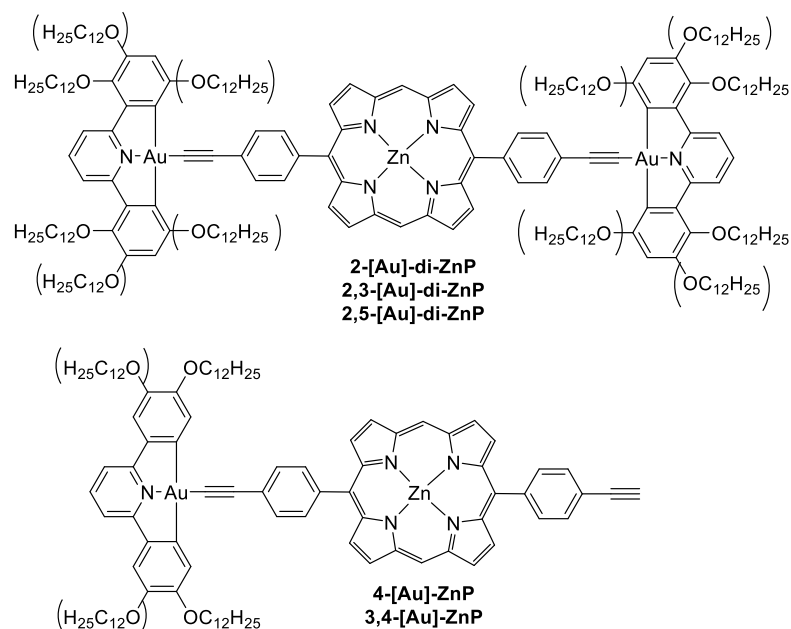
Figure 4.59: Structures of di- and mono-substituted phenylacetylene porphyrins connected to gold(III) complexes.

Connection of **2,5-[Au]-Cl** to **di-ZnP** formed **2,5-[Au]-di-ZnP** in 74% yield, and this time a more polar solvent (5% methanol in CH₂Cl₂) was required in order to gain elution

from a silica column. The ^{1}H NMR spectrum shows the expected signals, however the alkoxy chains in the 5,5′-position, which are directed over the porphyrin core, displayed increased shielding due to the porphyrin ring current, with the effect most marked for hydrogens at the end of the chain. Thus, one of the methyl (-CH$_3$) signals was shifted from 0.89 ppm to 0.60 ppm (Figure 4.60).
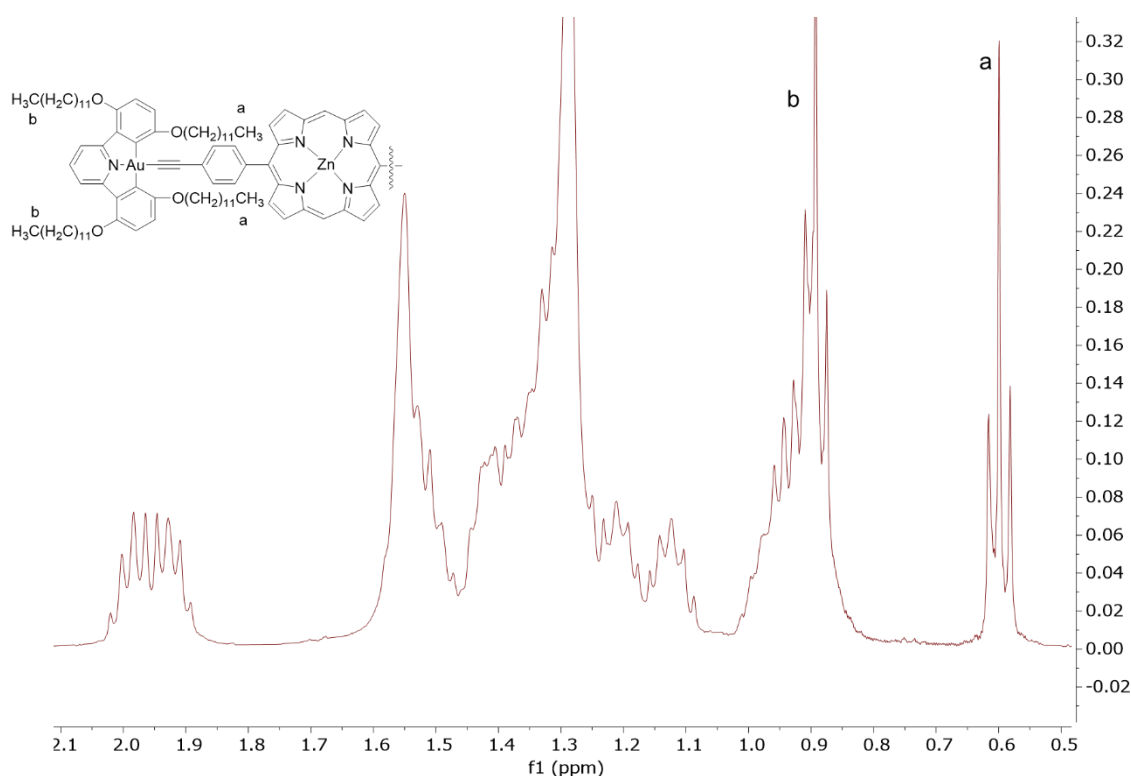
Figure 4.60: Alkyl region of 2,5-[Au]-di-ZnP showing the shifting of the alkyl and methyl signals of the chain in the 5,5'-position due to the ring current of the porphyrin core (^{1}H NMR, 400 MHz, CDCl$_3$).

While both **2,3-[Au]-Cl** and **2,5-[Au]-Cl** proved to connect easily to the porphyrin core, differing outcomes were observed for gold complexes with other substitution patterns (Figure 4.59). Using **2-[Au]-Cl** led to a considerably lower yield (19%) and competing Glazer coupling proved to be an issue, most likely as the coupled product had low solubility, with formation of the dialkyne a successful competing reaction. This hypothesis is supported by a lower yield also found for **2,3-[Au]-t-ZnP-C4** which, due to the shorter chain, exhibits lower solubility and also formed Glazer coupled side products, reducing the yield compared to **2,3-[Au]-t-ZnP**.

In comparison, **4-[Au]-Cl** and **3,4-[Au]-Cl** selectively formed the mono-substituted porphyrin in yields of 19% and 70%, respectively, with no evidence of formation of the disubstituted product, as evidenced by the reduced symmetry in the aromatic region of the ^{1}H NMR spectrum and the spectra integration.

4.12.2.2　10,20-Diiospropylporphyrins

2,3-[Au]-iPr-ZnP

2,5-[Au]-iPr-ZnP
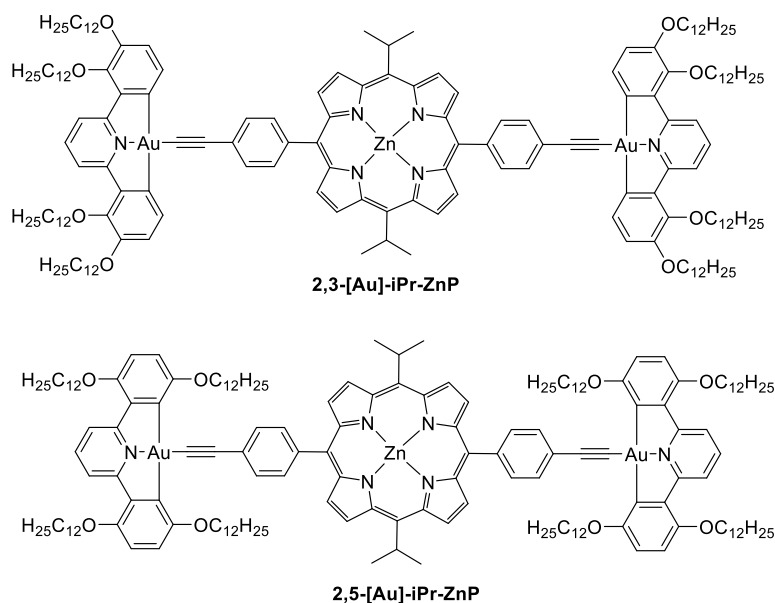
Figure 4.61: Structures of gold(III) complexes attached to di-substituted porphyrins, with an iso-propyl substituent in the 10,20-positions.

These porphyrins were prepared by reacting **2,3-[Au]-Cl** and **2,5-[Au]-Cl** to a 5,15-disubstituted 4-ethynylphenylpophryin, containing an *iso*-propyl group in the 10,20-positions. Using the standard method, they were obtained in 40-45% yield as burgundy or dark-purple crystalline solids, respectively.[216, 221]

4.12.2.3　*Attempted Preparation of Porphyrins with Direct Acetylide Linkers*

Attempts were made to connect the gold complexes to zinc 5,15-*bis*(ethynyl)porphyrin directly *via* an alkyne link to investigate the effect of removal of the phenyl spacer unit and hence, the effect of having potential direct conjugation from the porphyrin core to the appended gold complex. Initial attempts to connect **2-[Au]-Cl**, **2,3-[Au]-Cl** and **3,4-[Au]-Cl** complexes were unsuccessful (Figure 4.62), with high recovery of the starting chlorogold complex and isolation of an insoluble and un-characterisable green solid, suggesting that the Glazer coupling appeared to be a successful competing reaction. Further attempts using **2,3-[Au]-Cl** were successful, giving the product in 5% yield, along

with a high amount of unreacted chlorogold complex. However the small amount of product recovered (<10 mg) made purification and use of the complex highly challenging and reluctantly it was concluded that this approach was unviable.
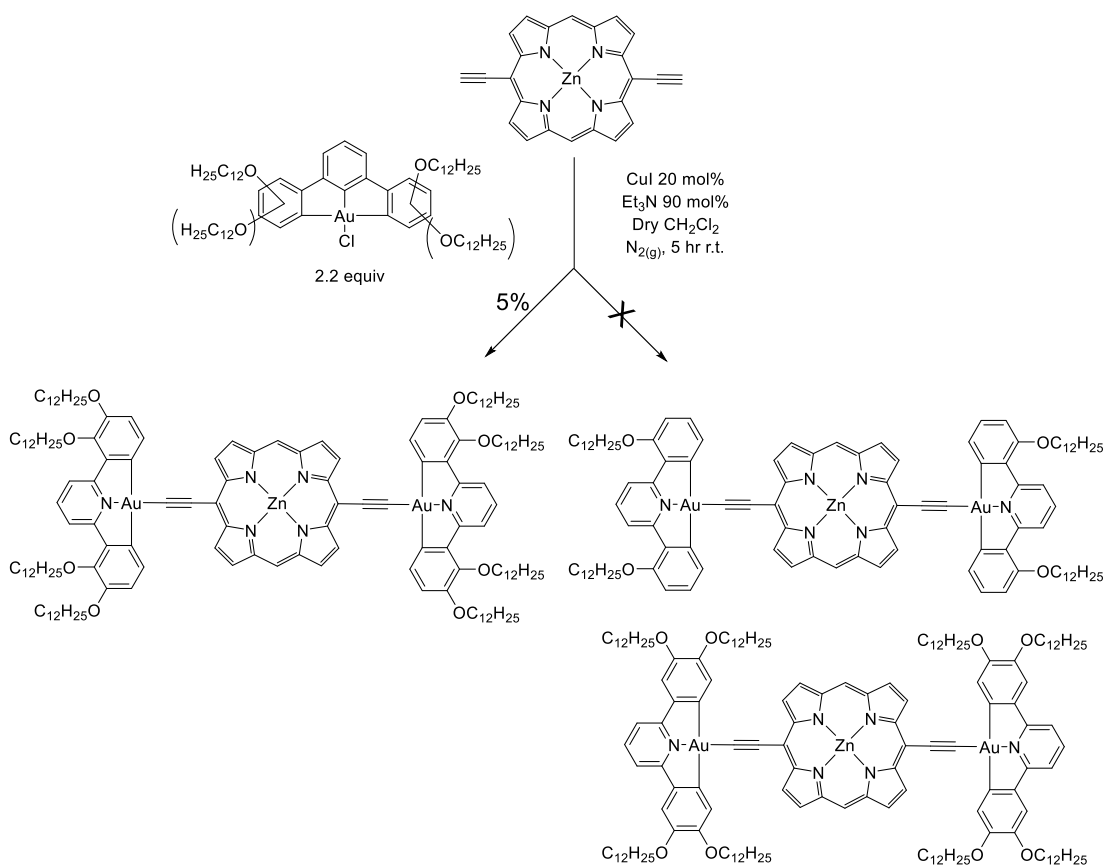
Figure 4.62: Reaction scheme for attempted connection of gold(III) C^N^C complexes to zinc 5,15-bis(ethynyl)porphyrin.

4.13 Porphyrin Demetallation

Removal of the zinc(II) ion was of interest to investigate the effect on both the liquid-crystalline properties and the photophysics. As metalation/demetallation is an equilibrium, demetallation can be easily achieved for zinc(II) porphyrins by the addition of an acid.[61, 62, 222, 223] An adapted literature synthesis was used where nine equivalents of TFA in CH_2Cl_2 was added, and after stirring for 1 hour, the remaining acid was quenched by the addition of excess triethylamine, followed by an aqueous work-up and recrystallisation (Figure 4.63).[222] The same method was used for both di- and tetra-substituted porphyrins. The success of reaction could be confirmed by the reappearance of the broad, N-*H* signal in the ^{1}H NMR spectrum below 0 ppm; the presence of four Q-bands in the UV-Vis spectrum and *via* the change in R_F value in TLC. A visible colour change was also noticeable on reaction, with a green colour observed on addition of TFA,

followed by a change from the initial pink red of the starting zinc porphyrin to the deeper red of the free-base porphyrin on reaction quenching.
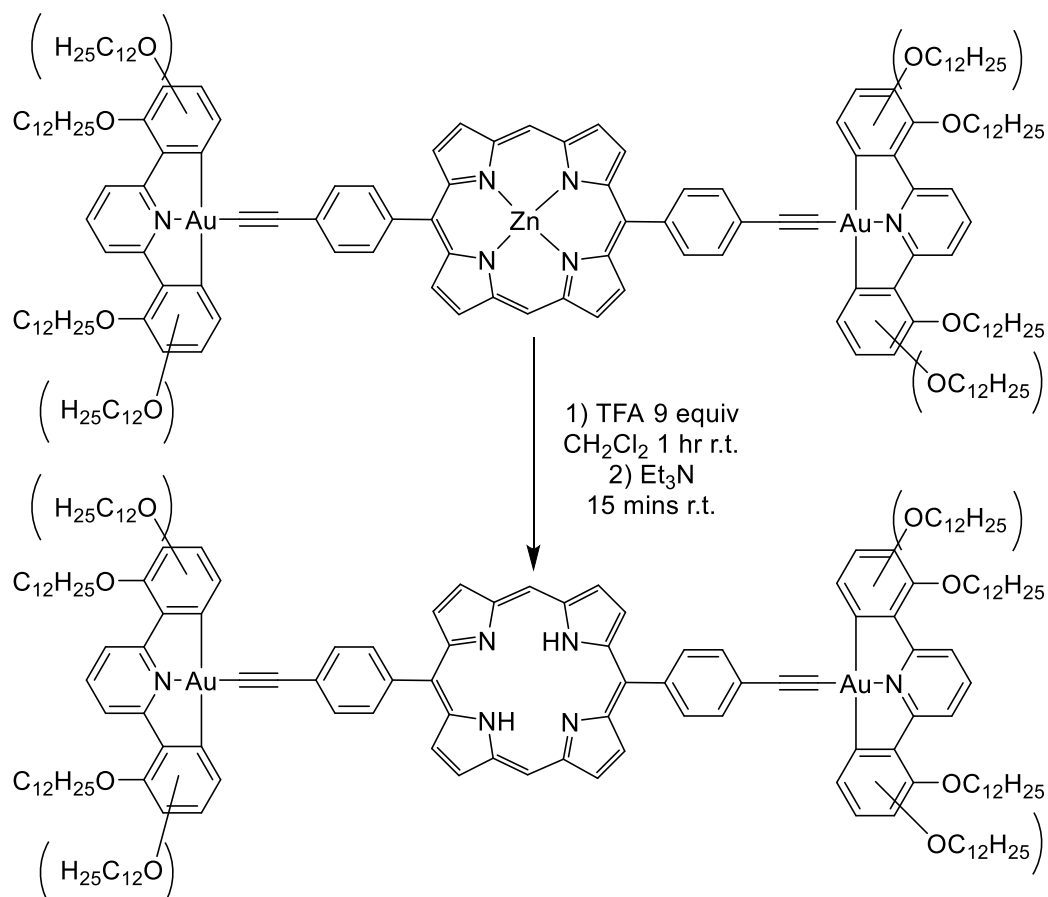
Figure 4.63: Reaction scheme for removal of zinc(II) from gold porphyrins to give the free-base porphyrin.

On removal of the zinc ion from **2,5-[Au]-di-ZnP** to give **2,5-[Au]-di-P** the ^{1}H NMR spectrum became extremely messy, resulting in an inability to identify signals. Extensive attempts to purify the compound by column chromatography and recrystallisation to gain a clean ^{1}H NMR spectrum were not successful. The origin of this effect is not clear, but pure, demetallated porphyrins could not be obtained. A similar issue was observed with **2,3-[Au]-iPr-P** and **2,5-[Au]-iPr-P**.

4.14   Summary of Synthesis of Gold-Porphyrin Dyads

In this work connection of several gold alkynyl complexes to both zincated 5,15-disubstituted and 5,1,0,15,20-tetrasubstituted porphyrins was successful in yields that for

some were >70%. Of particular note was the synthesis of the pure tetrasubstituted **2,3-[Au]-t-ZnP** in 75% yeild, which indicates the highly favourable nature of linkage of **2,3-[Au]-**complexes to this class of porphyrin molecules. However, connection of the isomeric complex, **2,5-[Au]-** was less successful, giving an inseparable mixture of the tri- and tetrasubstituted porphyrins, likely due to steric hindrance from the presence of chains across the porphyrin face disfavouring full substitution.

The synthesis of 5,15-disubstituted porphyrins was attempted using a range of gold units and, perhaps unsurprisingly, was found to be quite dependent on the nature of that unit. A range of complexes linked in good yields (>70%, **2,3-[Au]-di-ZnP**, **2,5-[Au]-di-ZnP**), while other complexes gave lower yields (**2-[Au]**) or only monosubstitution (**4-[Au]** and **3,4-[Au]**). Steric properties were evidently significant in determining yield, as was product solubility, the latter illustrated by the lower yields on use of gold complexes with butoxy chains. The central zinc ion could be easily removed in high yield (>90%) by addition of TFA, but sadly, platinum(II) porphyrins could not be synthesised. Likewise, connection of gold complexes to zinc 5,15-*bis*(ethynyl)porphyrin proved unfavourable, with only low yields (<5%) achieved with **2,3-[Au]-Cl**.

Determination of purity of the gold-porphyrin dyads proved to be rather challenging due to the challenges of undertaking CHN combustion analysis on porphyrins.[195, 196] As such, a product was defined as ′pure′ if the ^{1}H NMR spectrum was clean and if there was one spot on the TLC plate. By this measure **2,3-[Au]-di-ZnP**, **2,5-[Au]-di-ZnP**, **2,3-[Au]-di-P**, **2,3-[Au]-t-ZnP**, **2,3-[Au]-t-P** and **2-[Au]-di-ZnP** are defined as 'pure'. **2,3-[Au]-iPr-ZnP**, **2,5-[Au]-iPr-ZnP**, **4-[Au]-ZnP** and **3,4-[Au]-ZnP** showed small peaks at the baseline of the aromatic region, suggesting the presence of a low amount of impurities. **2,5-[Au]-t-ZnP** is known from ^{1}H NMR spectroscopy to be isolated as an impure mixture of the tri- and tetrasubstituted porphyrins, while three complexes - **2,5-[Au]-di-P**, **2,3-[Au]-iPr-P** and **2,5-[Au]-iPr-P** - displayed highly 'messy' ^{1}H NMR spectra.

4.15   Molecular Structures of Gold(III) Porphyrin Dyads

By use of *n*-butoxy-chains in the gold(III) complex units, it was possible to produce samples of **2,3-[Au]-di-ZnP** and **2,3-[Au]-di-P** that were sufficiently crystalline for structural determination. Unfortunately, the tetrasubstituted equivalents did not give

suitably crystalline material, likely due to the high number of chains disfavouring crystal packing. Data tables and .cif files can be found in the data folder - see page 30.

A low-resolution structure of **2,3-[Au]-di-ZnP** (R-factor ~12%) was determined by X-ray single-crystal analysis, however very small single crystals prevented data collection for any other members of the series. Therefore the relatively new technique of microcrystal electron diffraction (microED), which works with very small crystals, was used to determine the crystal and molecular structures of **2,3-[Au]-di-ZnP** and **2,3-[Au]-di-P**. MicroED uses a transmission cryo-electron microscope (cryo-TEM) in diffraction mode and because electrons interact with materials more strongly than X-rays, very small crystals can be used; those being used here were around 2 μm long (Figure 4.64). The first reported use of MircoED for the solution of a crystal structure was in 2013 when Shi *et al.* determined the structure of lysozyme.[224]
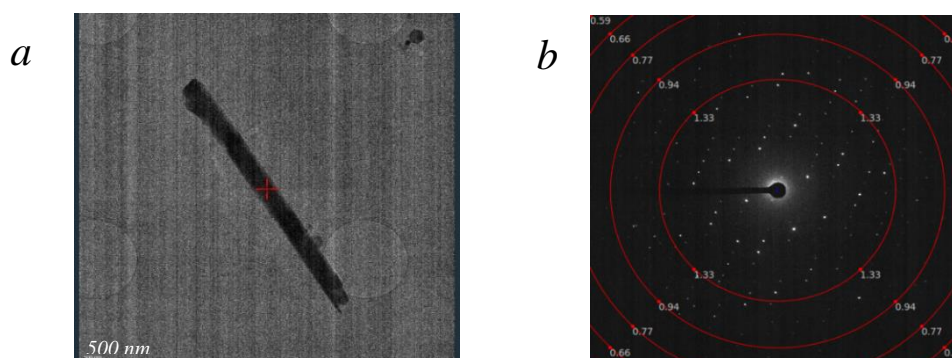
*Figure 4.64: a) View of the crystals of **2,3-[Au]-di-ZnP** under transmission cryo-electron microscope. b) Electron diffraction pattern formed for **2,3-[Au]-di-ZnP**. Data was collected by E. Thompson.*

It is worth noting that in microED, the recorded datasets are refined against a merged dataset from multiple crystals and the 'best' unit cell parameters are defined based on fitting calculated structures to the observed 2θ values for the strong reflections from all datasets. As such, parameters are an average of the merged datasets and therefore may not be reflective of any one single crystal.

4.15.1 2,3-[Au]-di-ZnP (XRD)

Purple, needle-like crystals of **2,3-[Au]-di-ZnP** (Figure 4.65) were grown by the slow diffusion of methanol into a solution of CH_2Cl_2. The quality of the single crystals, due to the large molecular size, proved to be poor for XRD, with weak diffraction and rather

smeared reflections, characteristic of a structure in which layer slipping is occurring. This resulted in the very large and elongated atomic displacement parameters (ADP) of all atoms (Figure 4.65, bottom). Data collection was achieved to 0.95 Å resolution. Some disorder was observed in the position of the phenyl linker groups. The poor resolution of the data resulted in an apparent distortion of the alkyne group from linearity. This is believed to be an artefact of the poor data quality, not a real effect. Carbon atoms are coloured grey, gold yellow, hydrogen turquoise, nitrogen blue, oxygen red, and zinc pink.
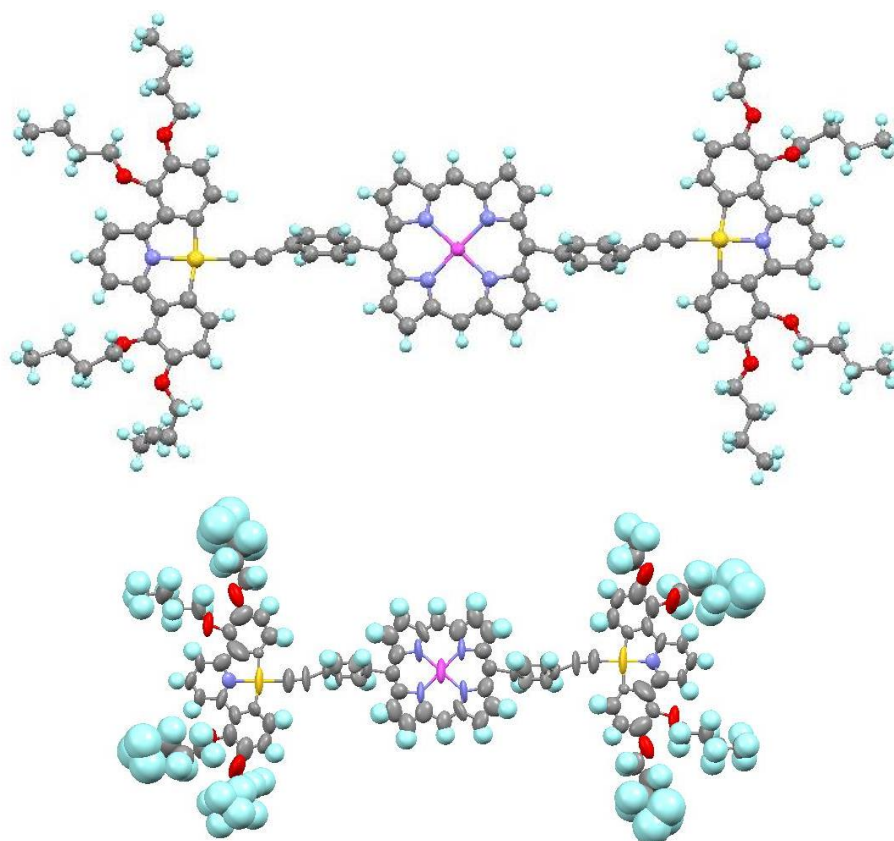
*Figure 4.65: Molecular structure of **2,3-[Au]-di-ZnP**, with disorder removed for clarity (top) and showing thermal ellipsoids (bottom).*

Despite the poor data quality some information could be determined and basic atomic positions found. The compound crystallised in the monoclinic $P2_1/c$ space group. The zinc(II) porphyrin core was planar, with the phenyl linker groups forming an angle of ~64° to the plane. The gold(III) complexes were almost co-planar with the zinc(II) porphyrin core (~5 – 7°) (Figure 4.66).
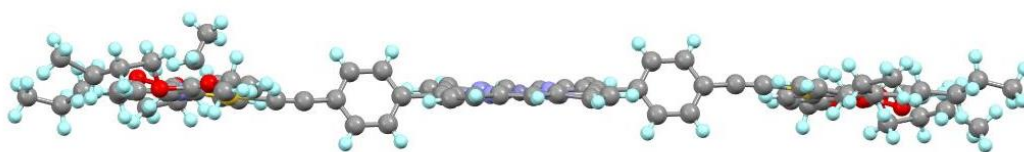
*Figure 4.66: Side view of the molecular structure of **2,3-[Au]-di-ZnP**.*

4.15.2　　2,3-[Au]-di-ZnP (microED)

Crystals suitable for microED were achieved by layering methanol over a concentrated solution of **2,3-[Au]-di-ZnP** in dichloromethane and allowing diffusion to form a solvent/anti-solvent mixture. The isolated microcrystals were finely ground. The compound crystallised in the triclinic *P*-1 space group (Figure 4.67). This is a different space group to that determined *via* XRD, though it should be noted that crystals suitable for each method were formed by alternate crystallisation methods therefore potentially resulting in different crystal packing. It is also of note that the atomic positions are more defined *via* this method than they were previously *via* XRD, as can be observed by consideration of thermal ellipsoids (Figure 4.68), resulting in more information that can be determined from the structure. The asymmetric unit was half of the molecule.
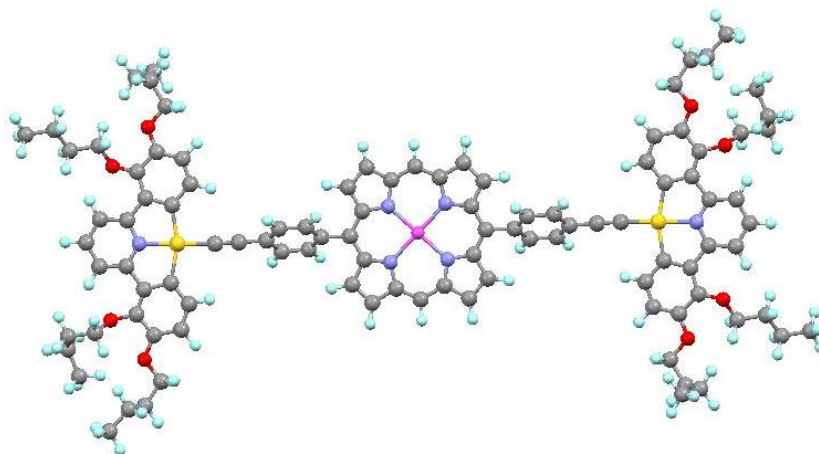
*Figure 4.67: Molecular structure of **2,3-[Au]-di-ZnP** determined by MicroED.*
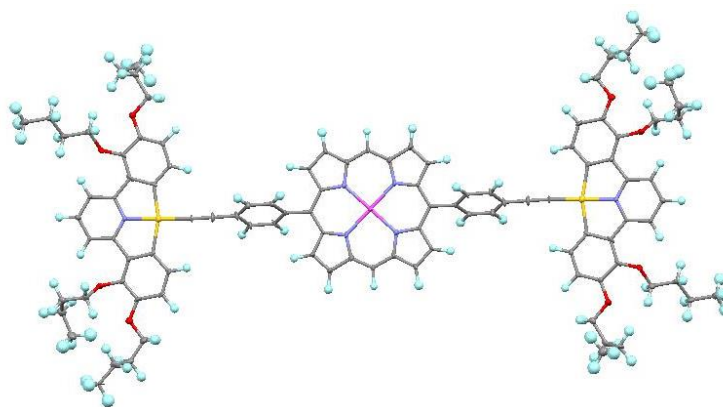
*Figure 4.68: Molecular structure of **2,3-[Au]-di-ZnP** showing small thermal ellipsoids.*

The zinc porphyrin core was planar, with the gold complexes almost coplanar - the respective planes make an angle of 2.41°. The phenyl linker was rotated 59.52° relative to the porphyrin core. Distortion away from linearity was observed about the carbon-carbon triple bond (C^C^C and C^C^Au angles measured as 176(1)° and 177(1)°). The bond measurements about the gold centre were comparable to those measured in **2,3-[Au]-Cl**, indicating that there is little change in the complex structure on linkage to the porphyrin. The geometry about the zinc(II) centre was distorted square planar (N^Zn^N: 88.6° and 91.4° and Zn-N: 2.08 and 2.053 Å), though, unlike in the XRD structure for **di-ZnP**, no distortion of the porphyrin core from planarity was observed. The molecules are packed in layers, with two gold complex units between each zinc porphyrin core (Figure 4.69). A porphyrin – porphyrin distance of 10.3 Å was measured and a gold complex – gold complex distance of 4.3 Å.
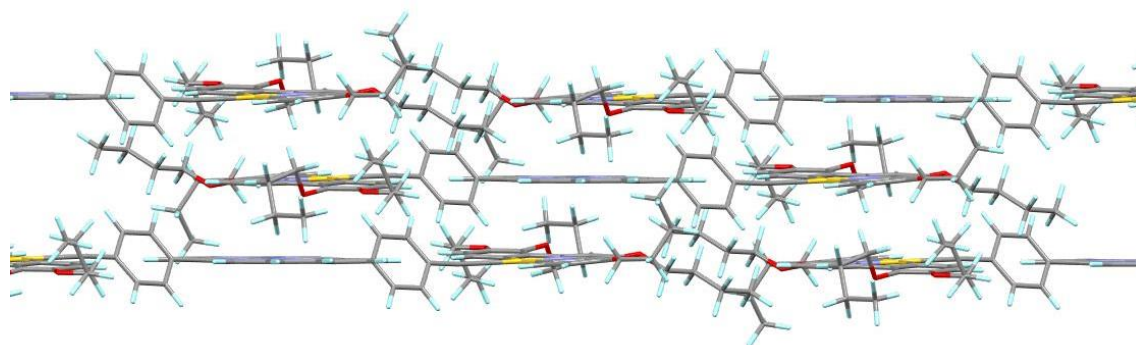
*Figure 4.69: Packing of **2,3-[Au]-di-ZnP** viewed along c-crystallographic axis.*

4.15.3   2,3-[Au]-di-P (MicroED)

Crystals suitable for mircoED resulted from layering methanol over a concentrated solution of **2,3-[Au]-di-P** in dichloromethane and allowing diffusion to form a

solvent/anti-solvent mixture. The isolated microcrystals were finely ground. The compounds crystallised in the triclinic *P*-1 space group and the asymmetric unit was half of the molecule (Figure 4.70).
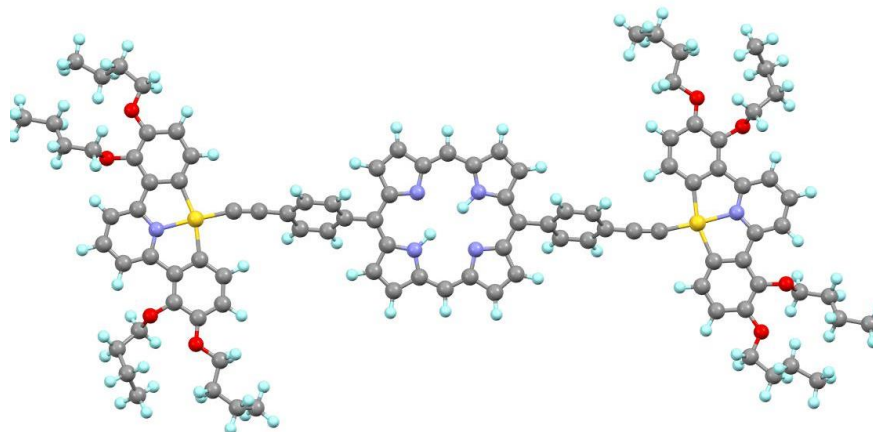
*Figure 4.70: Molecular structure of **2,3-[Au]-di-P** determined by MicroED*

The porphyrin core was slightly distorted away from planarity for one of the pyrrole units, with the gold complexes almost co-planar with the porphyrin core (9.87°). The plane of the phenyl linker made an angle of 51.03° relative to the porphyrin core. Strong distortion away from linearity was again observed about the carbon-carbon triple bond (C^C^C and C^C^Au angles measured as 176(1)° and 168(1)°). A high level of resolution was observed with this structure, with electron density relating to several hydrogen atoms, including one of the N-*H* atoms in the porphyrin ring, observed (Figure 4.71).
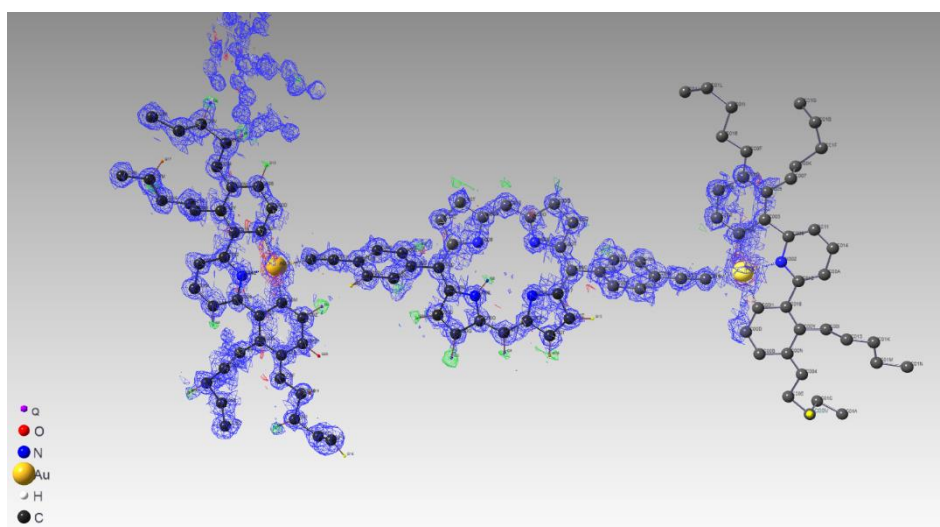
Figure 4.71: Map of electrostatic potential map (blue) and the F_{obs}-F_{calc} map (green) after initial Refinement. The F_{obs} map is contoured to 0.22 e/Å and the F_{obs}-F_{calc} map to 0.12e/Å.

4.16 Photophysics of the Porphyrins

4.16.1 Photophysics of Porphyrin Cores

Porphyrins exhibit a highly characteristic UV-Vis absorption spectrum (Section 4.2), hence UV-Vis spectroscopy provides a vital characterisation tool for determining porphyrin formation and metalation. Porphyrins are also strongly emissive. The photophysical data for the porphyrin cores are reported in Table 4.1.

4.16.1.1 Tetrasubstituted Porphyrins

The UV-Vis absorption spectra in CH_2Cl_2 for 5,10,15,20-tetrakis[4-(ethynyl)phenyl)]porphyrin[225, 226] are determined by the aromatic π-system of the porphyrin, and so little difference is observed between the protected and deprotected porphyrins (Figure 4.72a). On insertion of zinc(II) the expected change from the four Q-band spectrum to the two Q-band spectra of a metalloporphyrin occurs (Figure 4.72b), accompanied by a noticeable colour change in the solid state from dark to bright purple. 5,10,15,20-Tetrakis[4-(ethynyl)phenyl)]porphyrin emits strongly in the red region at 655 and 719 nm in CH_2Cl_2 on excitation into either the Soret or the Q-bands. A blueshift in the emission colour of ~50 nm occurs for the zincated porphyrin, emitting at 603 and 650 nm.
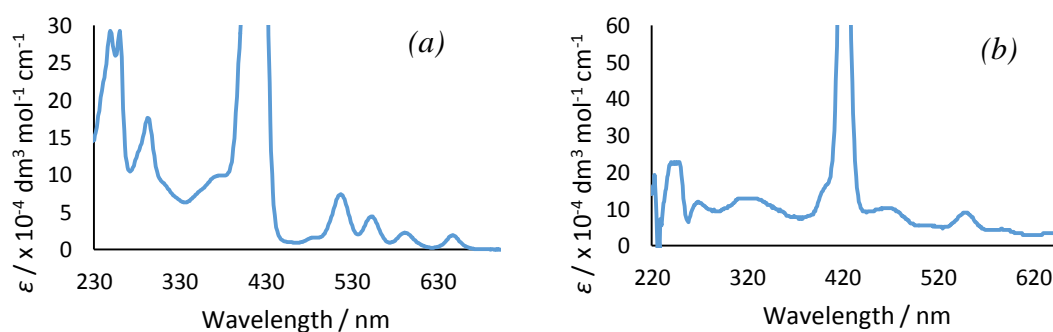
Figure 4.72: UV-Vis absorption spectra for 5,10,15,20-tetrakis[4-{(trimethylsilyl)ethynyl}phenyl)]porphyrin, (a), and zinc 5,10,15,20-tetrakis[4-((ethynyl)phenyl)]porphyrin, (b) in CH_2Cl_2.

UV-Vis absorption spectra for 5,10,15,20-tetrakis(trimethylsilylethynyl)porphyrin in CH$_2$Cl$_2$ showed a significant red-shift of ~50 nm compared to 5,10,15,20-tetrakis[4-(ethynyl)phenyl)]porphyrin, resulting in a green colour in solution (Figure 4.73). This is due to the extended π-conjugation in **TMS-CC-t-P** compared to **t-P** due to the effect of the introduction of four directly conjugated alkynyl groups.[29-33, 227] Emission data was not recorded as derivatives of these compounds were not studied further.
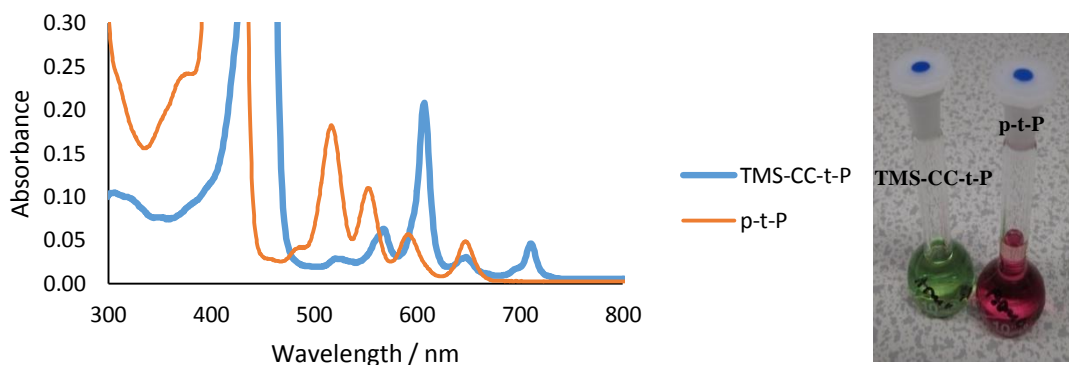
*Figure 4.73: UV-Vis absorption spectrum for tetra-substituted porphyrins **TMS-CC-t-P** and **p-t-P** (left) and colour in solution (right).*

4.16.1.2   5,15-Disubstituted Porphyrins

5,15-*Bis*[4-((trimethylsilylethynyl)phenyl)]porphyrin[228] (Figure 4.74a) shows the expected four Q-band UV-Vis absorption spectrum in CH$_2$Cl$_2$, with a very intense Soret band. A 14 nm redshift occurs relative to the equivalent tetra-substituted porphyrin. On zincation, as expected, the number of Q-bands reduces to two, with no observed difference between the protected and deprotected zincated porphyrin[228] (Figure 4.74b). The free-base porphyrin emits at 637 and 700 nm and the zincated porphyrin at a blueshifted 584 and 624 nm. Emission is redshifted compared to the tetrasubstituted porphyrins by ~20 nm. On the introduction of *meso-iso*-propyl substituents there is a redshift of 12 nm in the free-base porphyrin and a redshift of 15 nm in the zincated porphyrin. The emission is redshifted to 659 and 724 nm and to 606 and 651 nm, respectively (Figure 4.75).
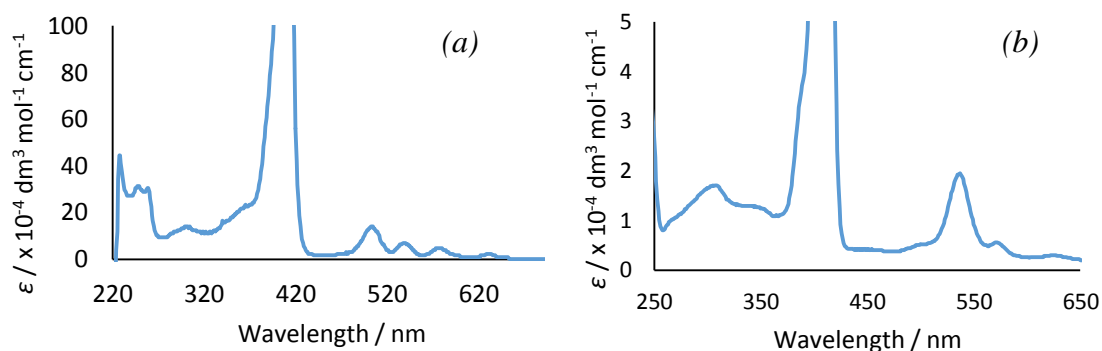
Figure 4.74: UV-Vis absorption spectra of 5,15-bis[4-((trimethylsilylethynyl)phenyl)]porphyrin (a) and zinc 5,15-bis[4-(ethynylphenyl)]porphyrin (b) in dichloromethane.
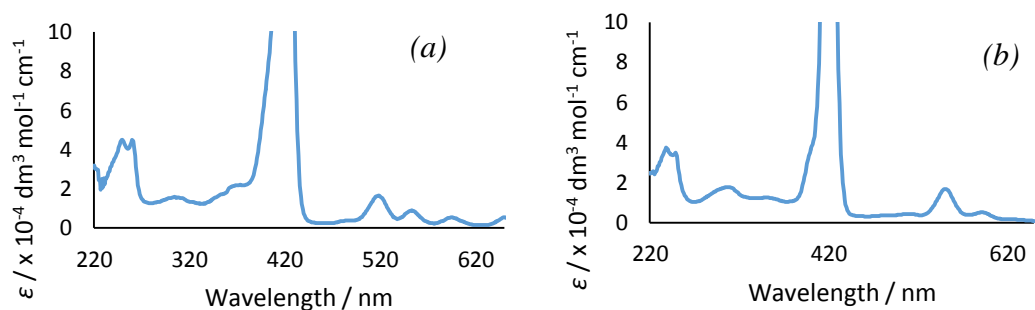
Figure 4.75: UV-Vis absorption spectra of 5,15-bis[4-((trimethylsilylethynyl)phenyl)]-10,20-(iso-propyl)porphyrin (left) and zinc 5,15-bis[4-(ethynylphenyl)] -10,20-(iso-propyl)porphyrin (right) in dichloromethane.

The absorption maximum of 5,15-*bis*((triisopropylsilyl)ethynyl)porphyrin[229] (Figure 4.76) displayed a redshift of 30 nm compared to 5,15-*bis*[4-((trimethylsilylethynyl)phenyl)]porphyrin due to the increased molecular conjugation. This resulted in a deep purple colour in solution, inclining towards green in lower concentrations and in the solid state, though the typical four Q-band spectrum of a free-base porphyrin, with an intense Soret band, was retained. Compared to 5,10,15,20-tetrakis(triisopropylsilylethynyl)porphyrin, the magnitude of red-shifting is reduced (50 nm *vs* 30 nm) due to the reduced molecular conjugation with only two carbon-carbon triple bonds instead of four. On zincation, the number of Q-bands is reduced to the expected two, giving a cyan-to-deep-emerald-green colouration in solution.
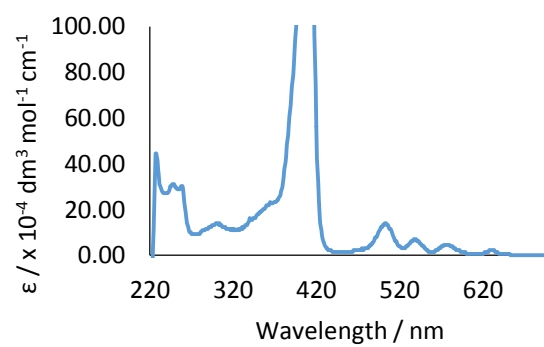
Figure 4.76: UV-Vis absorption spectra of 5,15-bis((triisopropylsilyl)ethynyl)porphyrin in dichloromethane.

Table 4.1: Photophysics for Porphyrin Precursors in Dichloromethane Solution at Room Temperature.

Porphyrin	Absorbance (ε / x 10^3 dm^3 mol^{-1} cm^{-1}) / nm	Excitation / nm	Emission / nm	Lifetime / ns	PLQY / %
di-ZnP[228]	238 (34), 248 (33), 307 (17), 409 (350), 537 (20), 572 (5.7)	412, 538, 572	584, 624	2.2	7
p-di-ZnP	220 (74), 250 (97), 259 (100), 292 (56), 341 (33), 410 (500), 537 (28), 572 (5.7)	-	-	-	-
di-P[228]	248 (33), 258 (32), 302 (14), 408 (310), 503 (14), 539 (6.8), 577 (4.6), 631 (2.2)	256, 305, 399, 417.8, 505, 540, 631.0	638, 700	8.2	6
t-ZnP[225, 226]	249 (3.1), 268 (1.6), 321 (1.8), 422 (220), 468 (1.4), 549 (1.2), 586 (0.6)	326, 424, 551, 600	603, 650	2.1	4
t-P	249 (62), 260 (63), 307 (19), 421 (130), 517 (16), 553 (9.5), 591 (5.0), 647 (4.3)	249, 306, 411, 431.4, 457, 519, 554, 593, 652	655, 719	8.4	17
p-t-P[225, 226]	220 (20), 249 (29), 260 (29), 293 (18), 421 (130), 517 (7.4), 553 (4.5), 520 (2.3), 647 (2.0)	-	-	-	-
iPr-ZnP	252 (130), 359 (45), 424 (250), 479 (8.7), 552 (15), 593 (6.6)	220, 248, 423, 553	607, 651	1.8	2
iPr-P	250 (45), 260 (45), 305 (16), 422 (317), 518 (17), 553 (9.0), 595 (5.3), 650 (5.3)	258, 310, 368, 423, 520, 554, 596, 651	659, 724	7.6	10
p-CC-P[229]	292 (42), 422 (120), 529 (3.0), 569 (1.8), 607 (1.9), 661 (6.2).	-	-	-	-
p-CC-ZnP	292 (18), 426 (330), 603 (21), 564 (7.3)	-	-	-	-
CC-ZnP	205 (8.3), 325 (3.0), 417 (220), 557 (9.0), 591 (1.2)	-	-	-	-
TIPS-CC-t-P[227]	229 (54), 325 (25), 453 (420), 524 (9.0), 571 (71), 611 (65), 649 (8.5), 713 (15)	-	-	-	-

4.16.2   Photophysics of Gold-Porphyrin complexes

The photophysics of the porphyrins connected to the gold complexes were investigated (Table 4.2), in the hope that the presence of two photophysically active groups in one molecule would result in interaction between the two units. The properties of the gold-porphyrin dyads are therefore compared relative to the individual units. Note, by the measure of purity applied (one spot on the TLC plate, clean ^{1}H NMR spectrum) **2,3-[Au]-di-ZnP**, **2,5-[Au]-di-ZnP**, **2,3-[Au]-di-P**, **2,3-[Au]-t-ZnP**, **2,3-[Au]-t-P** and **2-[Au]-di-ZnP** can be defined as 'pure' and therefore reported properties can be viewed with confidence. **2,3-[Au]-iPr-ZnP**, **2,5-[Au]-iPr-ZnP**, **4-[Au]-ZnP** and **3,4-[Au]-ZnP** display a low level of impurities. **2,5-[Au]-t-ZnP** is known to be isolated as an impure mixture. Three complexes are potentially highly impure, **2,5-[Au]-di-P**, **2,3-[Au]-iPr-P** and **2,5-[Au]-iPr-P**.

The UV-Vis absorption spectra show three regions of signals: broad signals below 400 nm relating to the gold complex unit, with the intensity reflecting the number of attached complexes and two areas of signals relating to the porphyrin unit. These are a very intense Soret band in the region 419 – 430 nm and weak Q-bands above 500 nm, with two present for zincated porphyrins and four present for free-base porphyrins (Figure 4.77). There is no evidence of any major band shifting of either the gold peaks or the porphyrin peaks.
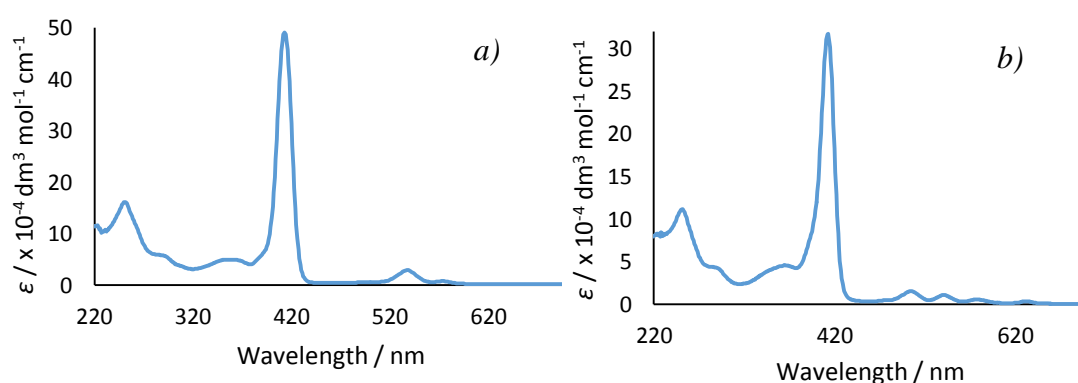
*Figure 4.77: Absorption spectra for **2,3-[Au]-di-ZnP** (a) and **2,3-[Au]-di-P** (b) showing the change in the number of Q-bands on zinc(II) removal.*

Compounds with two gold complexes appended to the disubstituted porphyrin core exhibited molar absorption coefficients for the peaks relating to the gold complex that were approximately twice the value of the free complex (taking account of the

287

contribution of small porphyrin peaks in this region), while the molar absorption coefficients for the peaks relating to the porphyrin core are of the same magnitude to those in the unsubstituted porphyrin. For **4-[Au]-ZnP** the molar absorption coefficient for the gold peaks is approximately equivalent to that of the free gold complex, supporting the assignment of monosubstitution. The same proportionality arguments could also be deployed successfully for **2,3-[Au]-t-ZnP** (Figure 4.78a) and, interestingly, for what is known to be the impure **2,5-[Au]-t-ZnP**, (Figure 4.78b) - the magnitude of the peaks below 400 nm are approximately ~2.8 times the value of the free complex, consistent with the incomplete substitution determined from NMR spectroscopy.
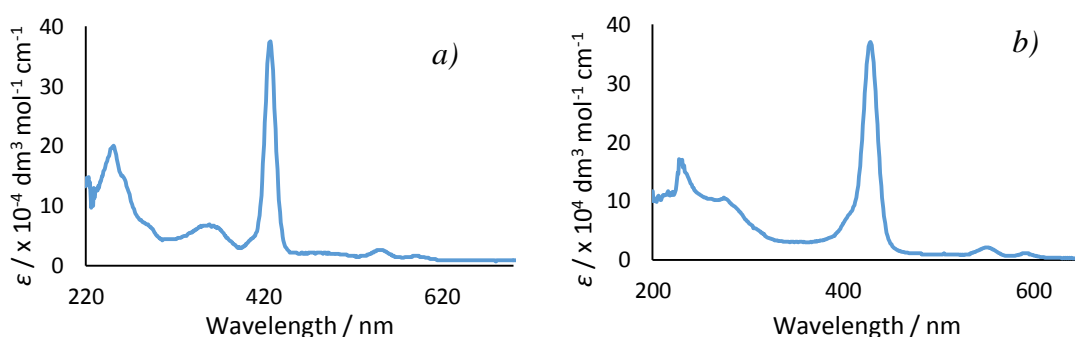
*Figure 4.78: Absorption spectra for **2,3-[Au]-t-ZnP** (a) and **2,5-[Au]-t-ZnP** (b).*
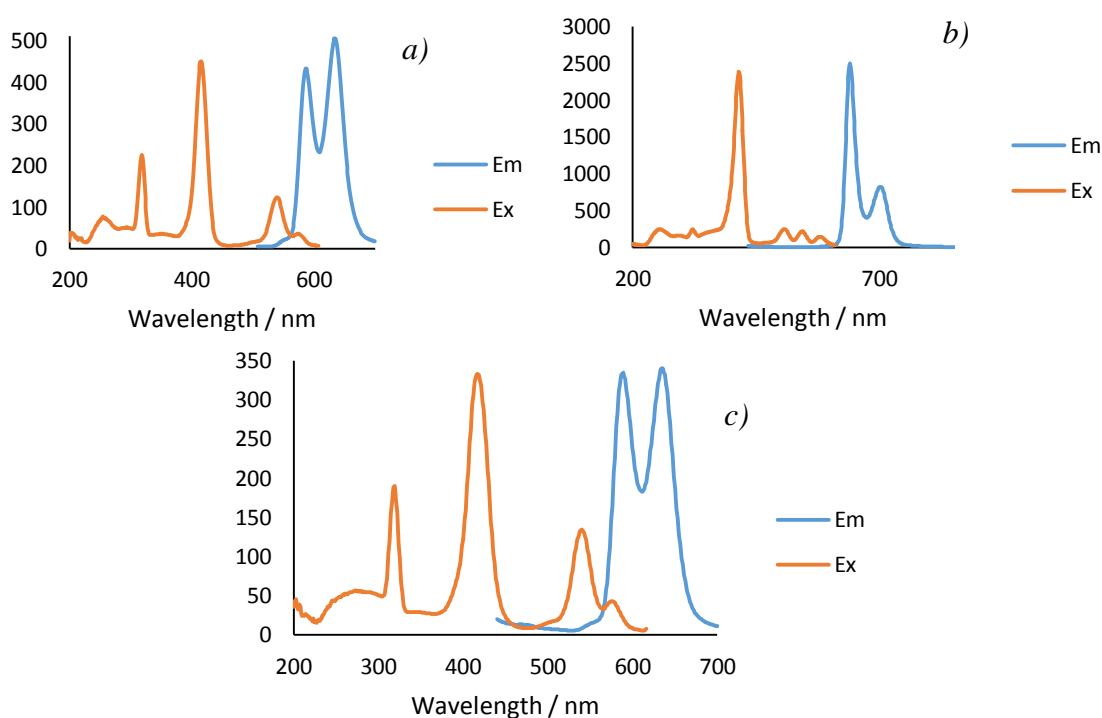
*Figure 4.79: Emission and excitation spectra for **2,3-[Au]-di-ZnP** (a), **2,3-[Au]-di-P** (b) and **2,5-[Au]-di-ZnP** (c) on excitation into the Soret band.*

The emission spectra were investigated in solution in both degassed and aerated dichloromethane (Table 4.2). The porphyrin units were excited into either the Soret or Q-band (all radiative emission occurs from the latter) and emitted at two bands in the red region at the same wavelengths as that of the unsubstituted porphyrins (Figures 4.79 – 4.82).
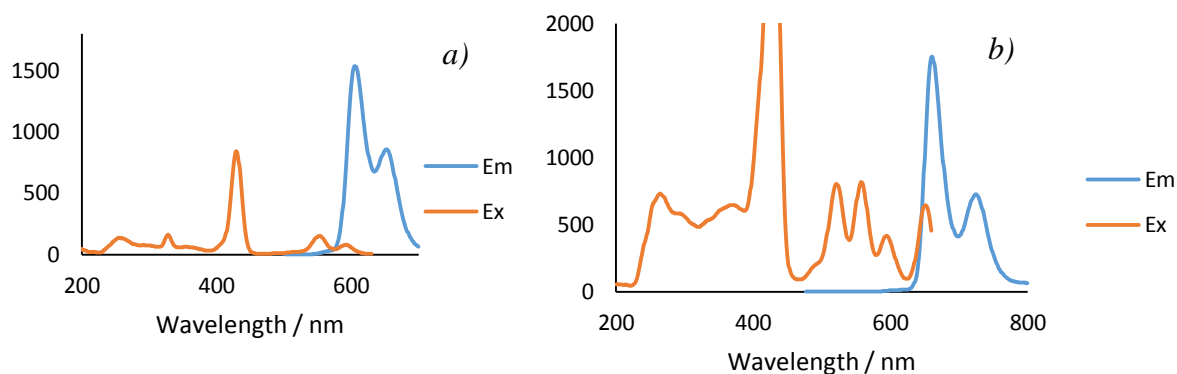
*Figure 4.80: Emission and excitation spectra for **2,3-[Au]-t-ZnP** (a) and **2,3-[Au]-t-P** (b) on excitation into the Soret band.*

The lifetimes remained equivalent to those of the free porphyrin core, with generally longer lifetimes (7 – 8 ns) for the free-base porphyrins compared to the zincated equivalents (2 – 3 ns). PLQYs are generally measured in the range of ~10 – 50%, indicating that these dyads are efficient emitters. This is also higher than for the parent porphyrin complexes. The lack of difference in the spectrum on the introduction of oxygen into the system, a small Stokes shift from the Q-band and lifetimes on the ns region, indicates that emission is fluorescent in nature.
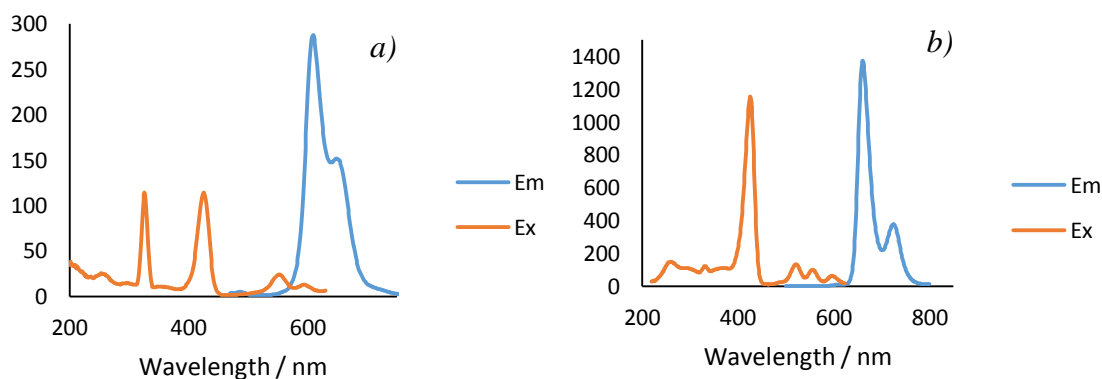
*Figure 4.81: Emission and excitation spectra for **2,3-[Au]-iPr-ZnP** (a) and **2,3-[Au]-iPr-P** (b) on excitation into the Soret band.*

The gold complex units were excited at 380 nm (**2-[Au]-**, **2,3-[Au]-**, **2,5-[Au]-**), 410 nm (**4-[Au]-**), and 450 nm (**3,4-[Au]-**). Only emission in the red region, which was at the same wavelengths as the porphyrin emission, was observed for almost all dyads, with no emission present in the yellow or green regions, where the gold complexes typically emit. The exception was **3,4-[Au]-ZnP**, which showed emission at 556, 587 and 629 nm on excitation at 450 nm, which can be assigned as dual emission of the gold complex and the porphyrin (Figure 4.82), with two lifetimes measured. The lifetime at 556 nm was 90 µs, which is indicative of triplet emission and a reduction in emission intensity was observed on the introduction of oxygen into the system. The lifetime at 587 nm was 2.4 ns, indicative of porphyrin-based fluorescence. The measured PLQY for the gold emission was a factor of magnitude lower than is typical for the complexes substituted in the 3,3′,4,4′-positions of the phenyl ring of the pincer ligand, even accounting for the inaccuracies due to the presence of overlapping emission from the porphyrin.
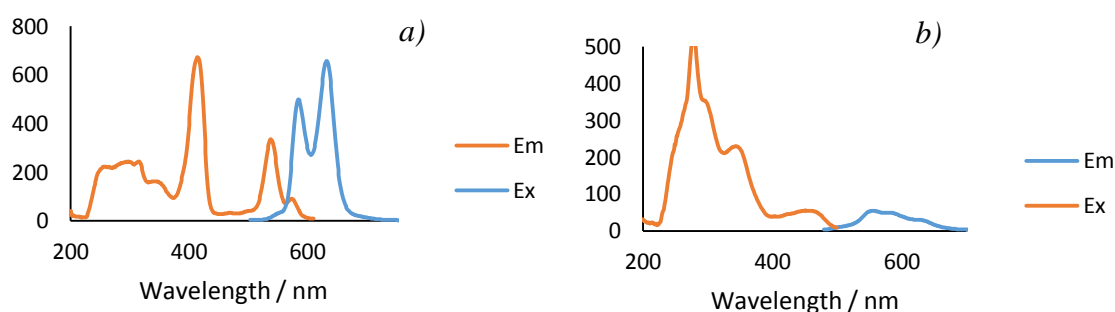
*Figure 4.82: Emission and excitation spectra for **3,4-[Au]-ZnP** on excitation into the Soret Band (a) and on excitation at 450 nm (b).*

The lack of gold based emission for the majority of the gold-porphyrin dyads suggests that the emission is being quenched in some manner. With the exception of **3,4-[Au]-** PLQYs are very low for the majority of the gold complexes used in this study, particularly for **2,5-[Au]-**.[217, 230] It must also be noted that it is challenging to avoid exciting the very intense Soret band, therefore independent excitation of the gold complex units is unlikely to be achieved. Therefore, it is likely that the intense porphyrin emission is overwhelming the much weaker gold(III) emission for the majority of complexes. However, some form of energy-transfer from the gold complex to the porphyrin unit, which is known in some examples of connection of the isoelectric platinum(II) complexes to porphyrins,[113, 115, 120, 127] cannot be entirely ruled out by current methods, but would appear unlikely.

Table 4.2: Photophysical Data for the Gold(III)-Porphyrin Dyads in Room Temperature Dichloromethane Solution.

Porphyrin	Absorbance (ε / x 10^3 dm^3 mol^{-1} cm^{-1}) / nm	Excitation / nm	Emission / nm	Lifetime / ns	PLQY %
2-[Au]-di-ZnP	249 (44), 291 (23), 354 (13), 414 (150), 539 (8.7), 573 (2.3)	256, 302, 317, 346, 418, 539, 574	586, 634.0	2.3	2
4-[Au]-ZnP	261 (11), 275 (11), 310 (6.6), 325 (6.0), 412 (48), 537 (2.8), 572 (0.8)	256, 318, 414, 539, 547	587, 633	2.5	5
3,4-[Au]-ZnP	250 (44), 259 (48), 286 (40), 341 (21), 412 (180), 537 (13), 573 (6.5)	556: 278, 342, 452 632: 262, 298, 315, 344, 414, 470, 538, 573	[Au] 556 P: 585, 632	[Au]: 90,000 P: 2.4	[Au]: 2 P: 0.4
2,3-[Au]-di-ZnP	251 (160), 357 (49), 413 (490), 537 (2.9), 573 (7.7)	253, 292, 319, 353, 416, 539, 575, 499	586, 634	2.6	54
2,5-[Au]-di-ZnP	233 (120), 272 (64), 415 (310), 540 (22), 573 (5.6)	277,319, 418, 575, 540	588,635	2.7	22
2,3-[Au]-di-P	213 (320), 251 (110), 289 (44), 365 (47), 505 (17), 540 (11), 577 (5.9), 633 (3.5)	256, 282, 291, 322, 415, 500, 543, 580	640, 702	7.8	30
2,5-[Au]-di-P	229 (60), 412 (180), 505 (12), 542 (8.5), 577 (4.6), 633 (2.8)	242, 274, 353, 414, 507, 543, 580, 633	640, 703	7.8	10
2,3-[Au]-iPr-ZnP	252 (130), 359 (45), 424 (250), 479 (87), 552 (15), 593 (6.6)	209, 256, 297, 425, 554, 592	608, 649	2.0	55
2,3-[Au]-iPr-P	252 (100), 366 (39), 425 (260), 519 (13), 554 (8.4), 595 (4.2), 652 (4.8)	255, 364, 426, 463, 521, 556, 597, 655.	661, 728	7.6	10
2,5-[Au]-iPr-ZnP	228 (140), 275 (82), 426 (300), 552 (20), 594 (8.9).	213, 249, 298, 428, 557, 594	608, 649	2.7	33
2,3-[Au]-iPr-P	240 (117), 424 (390), 520 (20), 554 (12), 599 (6.2), 651 (6.7)	243, 300, 365, 423, 457, 522, 599, 655	608, 660, 724	7.5	9
2,3-[Au]-t-ZnP	251 (200), 365 (67), 427 (370), 550 (26), 592 (16)	256, 295,328,430,520, 552, 632	606, 653	2.1	45
2,3-[Au]-t-P	252 (250), 289 (88), 365 (85), 426 (530), 519 (21), 519 (21), 556 (18), 593 (8.1), 650 (8.1).	263, 295, 334, 370, 430, 521, 558, 549	661, 725	8.6	17
2,5-[Au]-t-ZnP	230 (170), 275 (98), 429 (370), 511 (8.8), 552 (20), 592 (9.9)	277, 328, 430, 554, 593	607, 653	2.6	10

4.17   Thermal Properties of the Gold-Porphyrin Conjugates

Unfortunately, only one of these complexes displayed a mesophase (Table 4.3) and the analytical data show it to be an impure mixture of porphyrins of differing degree of gold complex substitution. For completeness, the phase observed appeared to be nematic by polarised optical microscopy, but the appearance of two fairly sharp reflections in the SAXS pattern (not seen for nematic phases) and not in any simple ratio, precludes any formal assignment.

While the other gold-porphyrin dyads did not give any mesophases it is of interest to examine the effect of the differing substitution patterns about the gold complex and the presence and removal of zinc(II) (Figure 4.83).

Connection of the 2,2′,3,3′-tetrasubstituted gold complex, **2,3-[Au]-Cl**, with zinc 5,15-*bis*(4-ethynylphenyl)porphyrin (**2,3-[Au]-di-ZnP**) resulted in a high melting point of ~295 °C, with the complex entering the isotropic liquid with decomposition. It is hypothesised that the central zinc ion increased molecular rigidity and the vacant fifth-coordination positions of zinc, favoured molecular aggregation, and hence porphyrin core stacking, resulting in the high melting temperature. To mitigate this several strategies were investigated: removal of the zinc ion; introduction of a shielding chain across the face of the porphyrin and introduction of a bulky substituent in the 10,20-positions of the porphyrin.

On removal of the zinc ion to form the free-base (**2,3-[Au]-di-P**), a significant lowering of the melting temperature to 240 °C was observed, due to decreased molecular rigidity.[91, 94, 104] Introduction of a chain across the face of the porphyrin was achieved by connection of a 2,2′,5,5′-tetrasubstituted gold complex, **2,5-[Au]-Cl**, to the porphyrin (**2,5-[Au]-di-ZnP**). Again, a significant reduction in the clearing temperature to 230 °C was observed. The additional lateral chains prevents intermolecular π-π interactions and hence, aggregation, which has previously been shown to be an effective method in lowering phase transitions in porphyrins.[109, 110]

Introduction of a bulky substituent in the 10,20-positions of the porphyrin by means of an *iso*-propyl group again resulted in a lowering of the melting temperature.[108] The magnitude of which was more substantial for **2,3-[Au]-iPr-ZnP** compared to **2,5-[Au]-iPr-ZnP** as the latter already has increased steric bulk due to the chains in the 5,5′-position of the gold complex pincer ligand.

Table 4.3: Thermal Transitions of Porphyrin-Gold(III) Dyads.

Porphyrin	Transition	T / °C	ΔH / kJ mol^{-1}
2,3-[Au]-di-ZnP	Cr-Iso	294.5*	-
2,5-[Au]-di-ZnP	Cr-Iso	230.2	27.60
2,3-[Au]-di-P	Cr-Iso	239.6	16.70
2,3-[Au]-iPr-ZnP	Cr-Iso	155.1	8.83
2,5-[Au]-iPr-ZnP	Cr-Iso	167.0	17.42
2,3-[Au]-t-ZnP	Cr-Iso	210.4	25.12
2,3-[Au]-t-P	Cr-Iso	185.4	11.78

*With decomposition. Observed from POM.
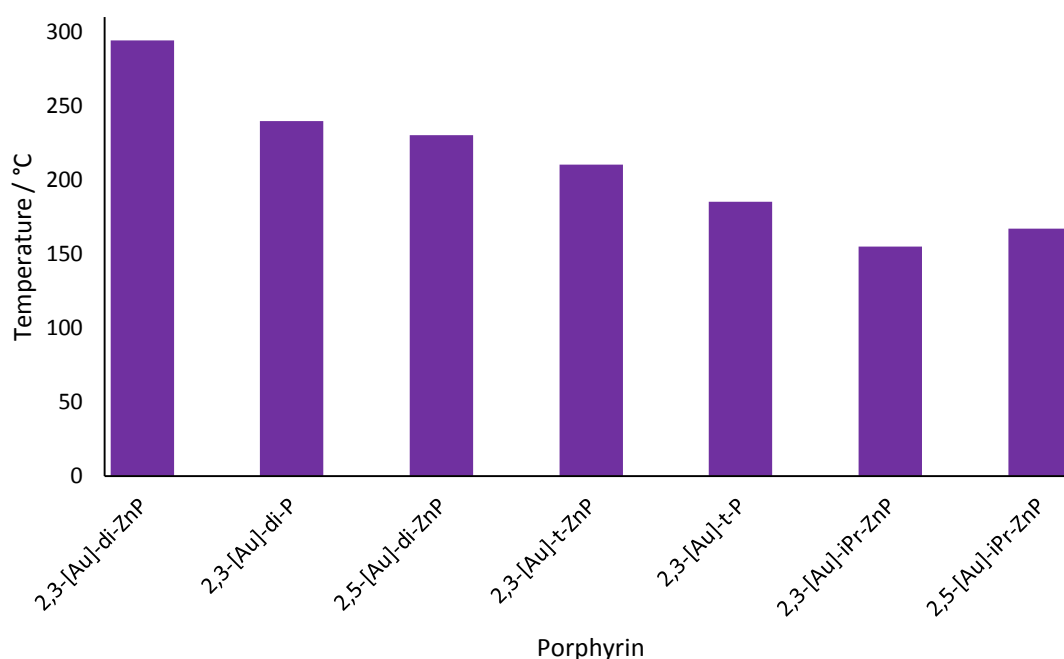
Figure 4.83: Comparison of melting temperatures for gold(III)-porphyrin dyads.

The tetra-substituted porphyrins, with chains in the 2,2′3,3′-positions of the pincer ligand, **2,3-[Au]-t-ZnP** and **2,3-[Au]-t-P**, were also investigated and, despite the presence of sixteen chains, did not give mesophases. In similar systems this has sometimes been

assigned to a distortion of the porphyrin core.[76, 77] The melting temperatures were both lowered compared to the disubstituted analogues due to the increased chain number.

4.18 Summary of Gold-Porphyrin Dyads

Several free-base and zinc 5,10,15,20-tetrasubstituted and 5,15-disubstituted porphyrins, including some with bulky *iso*-propyl substituents in the 10,20-positions, were successfully synthesised and used to link to several gold(III) C^N^C complexes to form a range of gold-porphyrin dyads, sometimes in yields in excess of 70%. The compound yield was determined to be dependent on the solubility of the final product, with lower solubility generally translating to a lower yield.

Establishing the purity of the final products turned out to be an issue as it was found, in common with several previous studies,[195, 196] that CHN combustion analysis was unreliable owing to the stability of porphyrins. As such, the criteria for purity were to have *both* a clean NMR spectrum *and* a single spot by TLC. Support for this approach came from the observation that, as the electronic systems of the porphyrins and the gold appeared isolated from one another, then the ratio of attached gold units per porphyrin could be evaluated by considering the relative molar absorptivities of the component units referenced against the newly formed material. As indicated above, steric factors and issues of solubility, combined with the inevitable challenge of multiple functionalisation of the same unit, further limited the porphyrins available for study as using the adopted criteria, not all prepared materials could be considered pure. That said, these are challenging materials to prepare and some of the very high yields realised represent a significant achievement.

The photophysical properties were investigated in the hope that the presence of two photophysically active groups in the molecule would result in interesting interactions between them. The absorption spectra for the gold-porphyrin dyads proved to give a superposition of the absorption peaks for the individual units, with the magnitude of the molar absorption coefficient for the peaks relating to the gold complexes dependent on the number appended. The emission spectra showed only fluorescence from the porphyrin at the same wavelengths as those of the porphyrin cores, with one exception, that of **3,4-[Au]-ZnP**, which displayed dual emission from the individual units.

The reason for the lack of gold-based emission for most dyads is believed to be the very low quantum yields determined for the majority of the gold complexes used (Section 3.8.2). However it is notable that the emission quantum yields for **3,4-[Au]-R**, prepared earlier by Parker,[217, 230] are several orders of magnitude greater and the only dyad (**3,4-[Au]-ZnP**) prepared using this gold unit was therefore unique in exhibiting measureable triplet emission. However, given that emission from the porphyrin was observed on excitation at the wavelengths for the gold complex, it is possible that some degree of energy transfer from the gold complexes to the porphyrin occurs. While precedent for this comes from the linking to porphyrins of some platinum(II) complexes,[115, 120, 127, 231] it is recognised as challenging to avoid exciting the porphyrin unit *via* the edge of the intense Soret band and confirmation would require more detailed studies beyond the scope of this project.

The other property envisaged for these new dyads was liquid crystallinity, but unfortunately none of the pure materials showed any interesting thermal behaviour beyond simple melting. Some evidence of mesomorphism was seen for one sample 9**2,5-[Au]-t-ZnP**), but it was known to be an impure mixture and, furthermore, the optical and SAXS data were not self-consistent, meaning that nothing can be learnt from this isolated observation. The melting point of the new dyads varied hugely from near room temperature to close to 300 °C, with the existence of chains that extended across the face of the porphyrin and the presence or absence of metalating zinc being the major factors in determining what that temperature was. Likewise, *iso*propyl groups in the 10- and 20-positions also destabilised the crystal phase.

In conclusion, while excitingly a range of gold-porphyrin dyads has been successfully synthesised demonstrating that the standard method for linkage of gold(III) C^N^C complexes is valid when applied to porphyrins, the compound properties proved disappointing. No mesophases formed and only porphyrin-based emission was observed in almost every case owing to the very weak phosphorescence of the gold complexes prepared.

4.19   References

1. E. Steiner and P. W. Fowler, *J. Phys. Chem. A*, 2001, **105**, 9553-9562.
2. E. Steiner and P. W. Fowler, *ChemPhysChem*, 2002, **1**, 114-116.
3. O. Birel, S. Nadeem and H. Duman, *J. Fluoresc.*, 2017, **27**, 1075-1085.
4. L.-L. Li and E. W.-G. Diau, *Chem. Soc. Rev.*, 2013, 291-304.
5. M. Imran, M. Ramzan, A. K. Qureshi, M. A. Khan and M. Tariq, *Biosensors (Basel)*, 2018, **8**.
6. L. Li, S. W. Kang, J. Harden, Q. Sun, X. Zhou, L. Dai, A. Jakli, S. Kumar and Q. Li, *Liq. Cryst.*, 2008, **35**, 233-239.
7. M. Gouterman, ed. D. Dolphin, Academic Press, New York, 1 edn., 1978, vol. 3, ch. 1, pp. 1-165.
8. B. F. Kim and J. Bohandy, *Johns Hopkins APL Tech. Dig.*, 1981, **2**, 153-163.
9. O. W. Rolling, *Inorg. Chem.*, 1979, **18**, 1175-1176.
10. M. Nappa and J. S. Valentine, *J. Am. Chem. Soc.*, 1978, **100**, 5075-5080.
11. S. M. Pinto, M. A. Lourenco, M. J. Calvete, A. R. Abreu, M. T. Rosado, H. D. Burrows and M. M. Pereira, *Inorg. Chem.*, 2011, **50**, 7916-7918.
12. T. Carofiglio, E. Lubian, I. Menegazzo, G. Saielli and A. Varotto, *J. Org. Chem.*, 2009, **74**, 9034-9043.
13. L. Elisa, F. Baldini, A. Giannetti, C. Trono and T. Carofiglio, *Chem. Commun.*, 2010, **46**, 3678-3680.
14. K. S. Suslick, N. A. Rakow and A. Sen, *Tetrahedron*, 2004, **60**, 11133-11138.
15. N. A. Rakow, A. Sen, M. C. Janzen, J. B. Ponder and K. S. Suslick, *Angew. Chem. Int. Ed.*, 2005, **44**, 4528-4532.
16. A. Alimelli, G. Pennazza, M. Santonico, R. Paolesse, D. Filippini, A. D'Amico, I. Lundstrom and C. Di Natale, *Anal. Chim. Acta*, 2007, **582**, 320-328.
17. Z. Zhou, C. Cao, Q. Liu and R. Jiang, *Org. Lett.*, 2010, **12**, 1780-1783.
18. J. A. Shelnutt, X.-Z. Song, J.-G. Ma, S.-L. Jia, W. Jentzen and C. J. Medforth, *Chem. Soc. Rev.*, 1998, **27**, 31-41.
19. R. E. Haddad, S. Gazeau, J. Pécaut, J.-C. Marchon, C. J. Medforth and J. A. Shelnutt, *J. Am. Chem. Soc.*, 2003, **125**, 1253-1268.
20. P. C. Heier, PhD Thesis, Institut für Anorganische und Analytische Chemie der Johannes Gutenberg-Universität, 2014.
21. S. S. Vijayendra, S. Shetti and G. Hegde, *New J. Chem.*, 2018, **42**, 12328-12348.
22. L. R. Milgorm, *The Colours of Life; An Introduction to the Chemistry of Porphyrins and Related Compounds*, Oxford University Press, Oxford, 1997.
23. G. G. Gurzadyan, T. H. Tran-Thi and T. Gustavsson, *J. Chem. Phys.*, 1998, **108**, 385-388.
24. H.-Z. Yu, J. S. Baskin and A. H. Zewail, *J. Phys. Chem. A*, 2002, **106**, 9845-9854.
25. J. S. Baskin, H.-Z. Yu and A. H. Zewail, *J. Phys. Chem. A*, 2002, **106**, 9837-9844.
26. S. Akimoto, T. Yamazaki, I. Yamazaki and A. Osuka, *Chem. Phys. Lett.*, 1999, **309**, 177–182.
27. A. Marcelli, P. Foggi, L. Moroni, C.Gellini and P. R. Salvi, *J. Phys. Chem. A*, 2002, **106**, 9837-9844.
28. A. Marcelli, P. Foggi, L. Moroni, C. Gellini and P. R. Salvi, *J. Phys. Chem. A*, 2008, **112**, 1864-1872.
29. H. L. Anderson, *Tetrahedron Lett.*, 1992, **33**, 1101-1104.
30. X. Zhang and C. O. Paul-Roth, *J. Porphyrins Phthalocyanines*, 2019, **23**, 185-195.
31. L. R. Milgrom and G. Yahioglu, *Tetrahedron Lett.*, 1995, **36**, 9061-9064.
32. L. R. Milgrom and G. Yahioglu, *Tetrahedron Lett.*, 1996, **36**, 4069-4072.
33. M. J. Plater, S. Aiken and G. Bourhill, *Tetrahedron*, 2002, **58**, 2415-2422.

34. A. Nowak-Krol, B. Koszarna, S. Y. Yoo, J. Chrominski, M. K. Weclawski, C. H. Lee and D. T. Gryko, *J. Org. Chem.*, 2011, **76**, 2627-2634.
35. Y. Matsuo, J. Hatano and T. Nakagawa, *J. Phys. Org. Chem.*, 2014, **27**, 87-93.
36. W.-N. Yen, S.-S. Lo, M.-C. Kuo, C.-L. Mai, G.-H. Lee, S.-M. Peng and C.-Y. Yeh, *Org. Lett.*, 2006, **8**, 4239-4242.
37. M. C. Kuo, L. A. Li, W. N. Yen, S. S. Lo, C. W. Lee and C. Y. Yeh, *Dalton Trans.*, 2007, 1433-1439.
38. U.-H. Lee, W. T. Hadmojo, J. Kim, S. H. Eom, S. C. Yoon, S.-Y. Jang and I. H. Jung, *Front. Chem.*, 2006, **6**, 1-8.
39. H. L. Anderson, A. P. Wylie and K. Prout, *J. Chem. Soc., Perkin Trans. 1*, 1998, **38**, 4905-4908.
40. A. Krivokapic, H. L. Anderson, G. Bourhill, R. Ives, S. Clark and K. J. McEwan, *Adv. Mater.*, 2001, **13**, 652-656.
41. P. Rothemund, *J. Am. Chem. Soc.*, 1935, **57**, 2010-2011.
42. J. B. Kim, A. D. Adler and F. R. Longo, in *The Porphyrins, Structure and Synthesis, Part A*, ed. D. Dolphin, Academic Press, New York, 1 edn., 1978, vol. 1, ch. 3, pp. 85-100.
43. P. Rothemund, *J. Am. Chem. Soc.*, 1936, **58**, 625-627.
44. A. D. Adler, F. R. Longo and J. D. Finarelli, *J. Org. Chem.*, 1967, **32**, 476.
45. J. S. Lindsey, H. C. Hsu and I. C. Schreiman, *Tetrahedron Lett.*, 1986, **27**, 4969-4970.
46. J. S. Lindsey, I. C. Schreiman, H. C. Hsu, P. C. Kearney and A. M. Margueretta, *J. Org. Chem.*, 1987, **52**, 827-836.
47. R. W. Wagner, D. S. Lawrence and J. S. Lindsey, *Tetrahedron Lett.*, 1987, **28**, 3069-3070.
48. J. S. Lindsey and R. W. Wagner, *J. Org. Chem.*, 1989, **54**, 828-836.
49. P. B. Momo, B. S. Bellete, T. J. Brocksom, R. O. M. A. de Souzab and K. T. de Oliveira, *RSC Adv.*, 2015, **5**, 84350–84355.
50. J. B. Paine, in *The Porphyrins, Structure and Synthesis, Part A*, ed. D. Dolphin, Academic Press, New York, 1 edn., 1978, vol. 1, ch. 4, pp. 101-234.
51. J. S. Manka and D. S. Lawrence, *Tetrahedron Lett.*, 1989, **30**, 6989-6992.
52. P. S. Clezy and G. A. Smythe, *Aust. J. Chem.*, 1969, **22**, 239 – 249.
53. C.-H. Lee, F. Li, K. Iwamoto, J. Dadok, A. A. Bothner-By and J. S. Lindsey, *Tetrahedron*, 1995, **51**, 11645-11672.
54. J. S. Lindsey, *Acc. Chem. Res.*, 2010, **43**, 300-311.
55. J. J. Hunt, PhD Thesis, University of Exeter,, 2000.
56. B. J. Littler, M. A. Miller, C.-H. Hung, R. W. Wagner, D. F. O'Shea, P. D. Boyle and J. S. Lindsey, *J. Org. Chem.*, 1999, **64**, 1391-1396.
57. J. K. Laha, S. Dhanalekshmi, M. Taniguchi, A. Ambroise and J. S. Lindsey, *Org. Process Res. Dev.*, 2003, **7**, 799-812.
58. T. E. O. Screen, K. B. Lawton, G. S. Wilson, N. Dolney, R. Ispasoiu, T. Goodson Iii, S. J. Martin, D. D. C. Bradley and H. L. Anderson, *J. Mater. Chem.*, 2001, **11**, 312-320.
59. J.-W. Ka and C.-H. Lee, *Tetrahedron Lett.*, 2000, **41**, 4609-4613.
60. J. W. Buchler, in *The Porphyrins, Structure and Synthesis, Part A*, ed. D. Dolphin, Academic Press, New York, 1 edn., 1978, vol. 1, ch. 10, pp. 389-483.
61. P. Hambright and E. B. Fleischer, *Inorg. Chem.*, 1970, **9**, 1757-1761.
62. T. P. Stein and R. A. Plane, *J. Am. Chem. Soc.*, 1969, **91**, 607-610.
63. J. W. Goodby, P. S. Robinson, B.-K. Teo and P. E. Cladi, *Mol. Cryst. Liq. Cryst.*, 1980, **56**, 303-309.

64. Y. Shimizu, A. Ishikawa and S. Kusabayashi, *Chem. Lett.*, 1986, 1041-1044.
65. B. A. Gregg, M. A. Fox and A. J. Bard, *J. Chem. Soc. Chem. Commun.*, 1987, 1134-1135.
66. B. A. Gregg, M. A. Fox and A. J. Bard, *J. Am. Chem. Soc.*, 1989, **111**, 3024-3029.
67. B. A. Gregg, M. A. Fox and A. J. Bard, *J. Phys. Chem.*, 1989, **93**, 4227-4234.
68. B. A. Gregg, M. A. Fox and A. J. Bard, *J. Phys. Chem.*, 1990, **94**, 1586-1598.
69. V. Paganuzzia, P. Guatteri, P. Riccardi, T. Sacchelli, J. Barberá, M. Costa and E. Dalcanale, *Eur. J. Org. Chem.*, 1999, 1527-1539.
70. E. Satori, M. P. Fontana, M. Costa, E. Dalcanale and V. Paganuzzi, *Thin Solid Films*, 1996, **284-285**, 204-207.
71. E. Dalcanale, M. Costa and T. Sacchelli, *Langmuir*, 2000, **16**, 7726-7730.
72. C.-Y. Liu, H.-L. Pan, M. A. Fox and A. J. Bard, *Science*, 1993, **261**, 897-899.
73. P. G. Schouten, J. M. Warman, M. P. d. Haas, M. A. Fox and H.-L.Pan, *Nature*, 1991, **383**, 736-734.
74. C.-Y. Liu, H.-L. Pan, H. Tang, M. A. Fox and A. J. Bard, *J. Phys. Chem.*, 1995, **99**, 7632-7636.
75. M. Castella, F. López-Calahorra, D. Velasco and H. Finkelmann, *Liq. Cryst.*, 2002, **29**, 559-565.
76. E. J. R. Sudholter, M. v. Dijk, C. J. Teunis, G. M. Sanders, S. Harkema, G. M. H. v. d. Velde, P. G. Schoutend and J. M. Warmand, *J. Mater. Chem.*, 1996, **6**, 357-363.
77. T. K. Khan, M. Bröring, S. Mathur and M. Ravikanth, *Coord. Chem. Rev.*, 2013, **257**, 2348-2387.
78. N. Usol'tseva, V. Bykova, N. Zharnikova, A. Alexandrov, A. Semeikin and A. Kazak, *Mol. Cryst. Liq. Cryst.*, 2010, **525**, 184-193.
79. K. Ohta, N. Ando and I. Yamamoto, *Liq. Cryst.*, 1999, **26**, 663-668.
80. S.-I. Kugimiya and M. Takemura, *Tetrahedron Lett.*, 1990, **31**, 3157-3160.
81. Y. Shimizu, M. Miya, A. Nagata, K. Ohta, A. Matsumura, I. Yamamoto and S. Kusabayashi, *Chem. Lett.*, 1991, 25-28.
82. Y. Shimizua, T. Higashiyamaa and T. Fuchita, *Thin Solid Films*, 1998, **331**, 279-284.
83. H. Monobe, Y. Miyagawa, S. Mima, T. Sugino, K. Uchida and Y. Shimizu, *Thin Solid Films*, 2001, **393**, 217-224.
84. T. Sugino, J. Santiago, Y. Shimizu, B. Heinrich and D. Guillon, *Mol. Cryst. Liq. Cryst.*, 1999, **330**.
85. A. Nagata, Y. Shimizu, H. Nagamoto and M. Miya, *Inorg. Chim. Acta*, 1995, **238**, 169-171.
86. Y. Shimizu, *Mol. Cryst. Liq. Cryst.*, 2001, **370**, 83-91.
87. Y. Shimizu, M. Miya, A. Nagata, K. Ohta, I. Yamamoto and S. Kusabayashi, *Liq. Crys.*, 1993, **14**, 795-805.
88. H. Monobe, S. Mima, T. Sugino and Y. Shimizu, *J. Mater. Chem.*, 2001, **11**, 1383-1392.
89. J. Hill, T. Sugino and Y. Shimizu, *Mol. Cryst. Liq. Cryst. Sci. Technol., Sect. A*, 1999, **332**, 119-125.
90. K. Griesar, M. A. Athanassopoulou, E. A. S. Bustamante, Z. Tomkowicz, A. J. Zaleski and W. Haase, *Adv. Mater.*, 1997, **9**, 45-48.
91. E. Sun, Z. Sun, M. Yuan, D. Wang and T. Shi, *Dyes Pigm.*, 2009, **81**, 124-130.
92. H. Guo, S. Zheng, S. Chen, C. Han and F. Yang, *Soft Matter*, 2019, **15**, 8329-8337.
93. J. Li, T. Tang, F. Li and M. Li, *Dyes Pigm.*, 2008, **77**, 395-401.

94. J. Li, H. Xin and M. Li, *Liq. Cryst.*, 2006, **33**, 913-919.
95. Q. Sun, L. Dai, X. Zhou, L. Li and Q. Li, *Appl. Phys. Lett.*, 2007, **91**.
96. E. J. Sun, G. J. Sun, X. Y. Bai, H. J. Zhai, X. Y. Yang and S. W. Lin, *Russ. J. Gen. Chem.*, 2019, **89**, 1667-1672.
97. X. Zhou, S.-W. Kang, S. Kumar and Q. Li, *Liq. Cryst.*, 2009, **36**, 269-274.
98. Y. Haketa, Y. Bando, Y. Sasano, H. Tanaka, N. Yasuda, I. Hisaki and H. Maeda, *iScience*, 2019, **14**, 241-256.
99. B. R. Patel and K. S. Suslick, *J. Am. Chem. Soc.*, 1998, **120**, 11802-11803.
100. C. Arunkumar, P. Bhyrappa and B. Varghese, *Tetrahedron Lett.*, 2006, **47**, 8033-8037.
101. R. Wang, S. Chen, Q. Chen, H. Guo and F. Yang, *Dyes Pigm.*, 2021, **190**.
102. U. H. Lee, W. T. Hadmojo, J. Kim, S. H. Eom, S. C. Yoon, S. Y. Jang and I. H. Jung, *Front. Chem.*, 2018, **6**, 473.
103. K. Ohta, N. Yamaguchi and I. Yamamoto, *J. Mater. Chem.*, 1998, **8**, 2637–2650.
104. M. Salamonczyk, D. Pociecha, A. Nowak-Krol, D. Koszelewski, D. T. Gryko and E. Gorecka, *Chem. Eur. J.*, 2015, **21**, 7384-7388.
105. C. J. Wilson, D. A. Wilson, R. W. Boyle and G. H. Mehl, *J. Mater. Chem. C*, 2013, **1**, 144-150.
106. D. W. Bruce, D. A. Dunmur, L. S. Santa and M. A. Wali, *J. Mater. Chem.*, 1992, **2**, 363–364.
107. D. W. Bruce, M. A. Wali and Q. M. Wang, *J. Chem. Soc. Chem. Commun.*, 1994, 2089-2090.
108. Q. M. Wang and D. W. Bruce, *Tetrahedron Lett.*, 1996, **37**, 7641-7644.
109. Q. M. Wang and D. W. Bruce, *Chem. Commun.*, 1996, 2505-2506.
110. Q. M. Wang and D. W. Bruce, *Angew. Chem. Int. Ed.*, 1997, **36**, 150-152.
111. T. Sakurai, K. Shi, H. Sato, K. Tashiro, A. Osuka, A. Saeki, S. Seki, S. Tagawa, S. Sasaki, H. Masunaga, K. Osaka, M. Takata and T. Aida, *J. Am. Chem. Soc.*, 2008, **130**, 13812–13813.
112. T. Sakurai, K. Tashiro, Y. Honsho, A. Saeki, S. Seki, A. Osuka, A. Muranaka, M. Uchiyama, J. Kim, S. Ha, K. Kato, M. Takata and T. Aida, *J. Am. Chem. Soc.*, 2011, **133**, 6537-6540.
113. E. C. Kwok, M. Y. Chan, K. M. Wong and V. W. Yam, *Chem. Eur. J.*, 2014, **20**, 3142-3153.
114. L. Liu, D. Fortin and P. D. Harvey, *Inorg. Chem.*, 2009, **48**, 5891-5900.
115. D. Bellows, T. Goudreault, S. M. Aly, D. Fortin, C. P. Gros, J.-M. Barbe and P. D. Harvey, *Organometallics*, 2009, **29**, 317-325.
116. D. Bellows, S. M. Aly, C. P. Gros, M. El Ojaimi, J. M. Barbe, R. Guilard and P. D. Harvey, *Inorg. Chem.*, 2009, **48**, 7613-7629.
117. A. Ferri, G. Polzonetti, S. Licoccia, R. Paolesse, D. Favretto, P. Traldi and M. V. Russo, *J. Chem. Soc., Dalton Trans.*, 1998, 4063–4069.
118. G. Polzonetti, V. Carravetta, G. Iucci, A. Ferri, G. Paolucci, A. Goldoni, P. Parent, C. Laffon and M. V. Russo, *Chem. Phys.*, 2004, **296**, 87-100.
119. C. Monnereau, J. Gomez, E. Blart and F. Odobel, *Inorg. Chem.*, 2005, **44**, 4806-4817.
120. A. Jana, L. McKenzie, A. B. Wragg, M. Ishida, J. P. Hill, J. A. Weinstein, E. Baggaley and M. D. Ward, *Chem. Eur. J.*, 2016, **22**, 4164-4174.
121. E. Goransson, J. Boixel, C. Monnereau, E. Blart, Y. Pellegrin, H. C. Becker, L. Hammarstrom and F. Odobel, *Inorg. Chem.*, 2010, **49**, 9823-9832.
122. S.-X. Zhang, Z.-R. Gu, F.-B. Li, L. Liu, Q.-M. Fu, S.-Z. Liu, Z.-L. Du and W.-Y. Wong, *J. Inorg. Organomet. Polym.*, 2013, **23**, 95-103.

123. V. A. Oliveira, B. A. Iglesias, B. L. Auras, A. Neves and H. Terenzi, *Dalton Trans.*, 2017, **46**, 1660-1669.
124. T. T. Tasso, T. M. Tsubone, M. S. Baptista, L. M. Mattiazzi, T. V. Acunha and B. A. Iglesias, *Dalton Trans.*, 2017, **46**, 11037-11045.
125. H. Zhan, S. Lamare, A. Ng, T. Kenny, H. Guernon, W.-K. Chan, A. B. Djurišić, P. D. Harvey and W.-Y. Wong, *Macromolecules*, 2011, **44**, 5155-5167.
126. L. Liu, L. Hu, H. Fu, Q.-M. Fu, S.-Z. Liu, Z.-L. Du, W.-Y. Wong and P. D. Harvey, *J. Organomet. Chem.*, 2011, **696**, 1319-1324.
127. B. Du and P. D. Harvey, *Chem. Commun.*, 2012, **48**, 2671-2673.
128. G. Langlois, S. M. Aly, C. P. Gros, J.-M. Barbe and P. D. Harvey, *New J. Chem.*, 2011, **35**.
129. H. E. Toma and K. Araki, *Coord. Chem. Rev.*, 2000, **196**, 307-329.
130. K. Araki, P. Losco, F. M. Engelmann, H. Winnischofer and H. E. Toma, *J. Photochem. Photobiol., A*, 2001, **142**, 25–30.
131. X. Liu, J. Liu, K. Jin, X. Yang, Q. Peng and L. Sun, *Tetrahedron*, 2005, **61**, 5655-5662.
132. L. Flamigni, J.-P. Collin and J.-P. Sauvage, *Acc. Chem. Res.*, 2008, **41**, 857-871.
133. B. Steiger and F. C. Anson, *Inorg. Chem.*, 1995, **34**, 3355-3357.
134. K. Araki and H. E. Toma, *J. Photochem. Photobiol. A: Chem.*, 1994, **83**, 245-250.
135. A. L. Parussulo, B. A. Iglesias, H. E. Toma and K. Araki, *Chem. Commun.,* 2012, **48**, 6939-6941.
136. L. Flamigni, N. Armaroli, F. Barigelletti, V. Balzani, J.-P. Collin, J.-O. Dalbavie, V. Heitz and J.-P. Sauvage, *J. Phys. Chem. B*, 1997, **101**, 5936-5943.
137. L. Flamigni, F. Barigelletti, N. Armaroli, J.-P. Collin, I. M. Dixon, J.-P. Sauvage and J. A. G. Williams, *Coord. Chem. Rev.*, 1999, **190-192**, 671–682.
138. K. Mishiba, M. Ono, Y. Tanaka and M. Akita, *Chem. Eur. J.*, 2017, **23**, 2067-2076.
139. E. J. Shin and D. Kim, *J. Photochem. Photobiol. A: Chem.*, 2002, **152**, 25-31.
140. A. D. Hamilton, H.-D. Rubin and A. B. Bocarsly, *J. Am. Chem. Soc.*, 1984, **106**, 7255-7257.
141. A. Prodi, M. T. Indelli, C. J. Kleverlaan, F. Scandola, E. Alessio, T. Gianferrara and L. G. Marzilli, *Chem . Eur. J.*, 1999, **5**, 2668-2679.
142. J.-P. CoIlin, V. Heitz and J.-P. Sauvage, *Tetrahedron Lett.*, 1992, **42**, 5977-5980.
143. M. de Torres, S. Semin, I. Razdolski, J. Xu, J. A. Elemans, T. Rasing, A. E. Rowan and R. J. Nolte, *Chem. Commun.,* 2015, **51**, 2855-2858.
144. A. Harriman, V. Heitz and J.-P. Sauvage, *J. Phys. Chem.*, 1993, **97**, 5940-5946.
145. A. Harriman, M. Hissler, O. Trompette and R. Ziessel, *J. Am. Chem. Soc.*, 1999, **121**, 2516-2525.
146. D. LeGourriérec, M. Andersson, J. Davidsson, E. Mukhtar, L. Sun and L. Hammarström, *J. Phys. Chem. A*, 1999, **103**, 557-559.
147. I. M. Dixon and J.-P. Collin, *J. Porphyrins Phthalocyanines*, 2001, **5**, 600–607.
148. J. L. Sessler, V. L. Capuano and A. K. Burrell, *Inorg. Chim. Acta*, 1993, **204**, 93-101.
149. F. C. A. B. Steiger, *Inorg. Chem.*, 1994, **33**, 5767-5779.
150. B. Steiger and F. C. Anson, *Inorg. Chem.*, 1995, **34**, 3355-3357.
151. D. Rota Martir, G. J. Hedley, D. B. Cordes, A. M. Slawin, D. Escudero, D. Jacquemin, T. Kosikova, D. Philp, D. M. Dawson, S. E. Ashbrook, I. D. Samuel and E. Zysman-Colman, *Dalton Trans.*, 2016, **45**, 17195-17205.
152. A. M. Soliman, M. Abdelhameed, E. Zysman-Colman and P. D. Harvey, *Chem. Commun.,* 2013, **49**, 5544-5546.

153. A. Harriman, *J. Am. Chem. Soc.*, 1994, **116**, 5481-5482.

154. A. Harriman, F. Odobel and J.-P. Sauvage, *J. Am. Chem. Soc.*, 1995, **117**, 9461-9472.

155. L. Flamigni, F. Barigelletti, N. Armaroli, J.-P. Collin, J.-P. Sauvage and J. A. G. Williams, *Chem. Eur. J.*, 1998, **4**, 1744-1754.

156. L. Flamigni, F. Barigelletti, N. Armaroli, B. Ventura, J.-P. Collin, J.-P. Sauvage and J. A. G. Williams, *Inorg. Chem.*, 1999, **38**, 661-667.

157. L. Flamigni, I. M. Dixon, J.-P. Collin Jean and P. Sauvage, *Chem. Commun.*, 2000, 2479-2480.

158. I. M. Dixon, J.-P. Collin, J.-P. Sauvage, F. Barigelletti and L. Flamigni, *Angew. Chem.*, 2000, **112**, 1348-1351.

159. I. M. Dixon, J.-P. Collin, J.-P. Sauvage and L. Flamigni, *Inorg. Chem.*, 2001, **40**, 5507-5517.

160. L. Flamigni, G. Marconi, I. M. Dixon, J.-P. Collin and J.-P. Sauvage, *J. Phys. Chem. B*, 2002, **106**, 6663-6671.

161. E. Baranoff, J. P. Collin, L. Flamigni and J. P. Sauvage, *Chem. Soc. Rev.*, 2004, **33**, 147-155.

162. L. Flamigni, J.-P. Collin and J.-P. Sauvage, *Acc. Chem. Res.*, 2008, **41**, 857-871.

163. J. Fortage, J. Boixel, E. Blart, H. C. Becker and F. Odobel, *Inorg. Chem.*, 2009, **48**, 518-526.

164. J. Fortage, J. Boixel, E. Blart, L. Hammarstrom, H. C. Becker and F. Odobel, *Chem. Eur. J.*, 2008, **14**, 3467-3480.

165. J.-C. Chambron, A. Harriman, V. Heitz and J.-P. Sauvage, *J. Am. Chem. Soc.*, 1993, **115**, 6109-6114.

166. J.-C. Chambron, A. Harriman, V. Heitz and J.-P. Sauvage, *J. Am. Chem. Soc.*, 1993, **115**, 7419-7425.

167. A. M. Brun, A. Harriman, V. Heitz and J.-P. Sauvage, *J. Am. Chem. Soc.*, 1991, **113**, 8657-8663.

168. A. Gabrielsson, F. Hartl, H. Zhang, J. R. L. Smith, M. Towrie, A. V. Jr. and R. N. Perutz, *J. Am. Chem. Soc.*, 2006, **128**, 4253-4266.

169. C. J. Aspley, J. R. L. Smith and R. N. Perutz, *J. Chem. Soc., Dalton Trans.*, 1999, 2269–2271.

170. A. Gabrielsson, F. Hartl, J. R. Smith and R. N. Perutz, *Chem. Commun.,* 2002, 950-951.

171. C. D. Windle, M. W. George, R. N. Perutz, P. A. Summers, X. Z. Sun and A. C. Whitwood, *Chem. Sci.*, 2015, **6**, 6847-6864.

172. J. Schneider, K. Q. Vuong, J. A. Calladine, X. Z. Sun, A. C. Whitwood, M. W. George and R. N. Perutz, *Inorg. Chem.*, 2011, **50**, 11877-11889.

173. K. Kiyosawa, N. Shiraishi, T. Shimada, D. Masui, H.Tachibana, S. Takagi, O. Ishitani, D. A. Tryk and H. Inoue, *J. Phys. Chem. C*, 2009, **113**, 11667–11673.

174. D. LeGourriérec, M. Andersson, J. Davidsson, E. Mukhtar, L. Sun and L. Hammarström, *J. Phys. Chem. A*, 1999, **103**, 557-559.

175. M. Casanova, E. Zangrando, E. Iengo, E. Alessio, M. T. Indelli, F. Scandola and M. Orlandi, *Inorg. Chem.*, 2008, **47**, 10407-10418.

176. J.-P. Collin, A. Harriman, V. Heitz, F. Odobel and J.-P. Sauvage, *J. Am. Chem. Soc.*, 1994, **116**, 5679-5690.

177. F. Odobel, J.-P. Sauvage and A. Harriman, *Tetrahedron Lett.*, 1993, **34**, 8113-8116.

178. W. T. S. Huck, A. Rohrer, A. T. Anilkumar, R. H. Fokkens, N. M. M. Nibbering, F. C. J. M. v. Veggel and D. N. Reinhoudt, *New J. Chem.*, 1998, 165-168.

179. G. S. Ananthnag and V. S. Shetti, *Dalton Trans.*, 2017, **46**, 14062-14082.
180. B. M. J. M. Suijkerbuijk, M. Lutz, A. L. Spek, G. v. Koten and R. J. M. K. Gebbink, *Org. Lett.*, 2004, **6**, 3023-3026.
181. B. M. J. M. Suijkerbuijk, S. D. H. Martínez, G. v. Koten and R. J. M. K. Gebbink, *Organometallics*, 2008, **27**, 534–542.
182. B. M. Suijkerbuijk, D. M. Tooke, M. Lutz, A. L. Spek, L. W. Jenneskens, G. van Koten and R. J. Klein Gebbink, *J. Org. Chem.*, 2010, **75**, 1534-1549.
183. B. M. Suijkerbuijk, D. J. Schamhart, H. Kooijman, A. L. Spek, G. van Koten and R. J. Klein Gebbink, *Dalton Trans.*, 2010, **39**, 6198-6216.
184. K. Yoshida, S. Yamaguchi, A. Osuka and H. Shinokubo, *Organometallics*, 2010, **29**, 3997-4000.
185. K. Fujimoto, T. Yoneda, H. Yorimitsu and A. Osuka, *Angew. Chem. Int. Ed.*, 2014, **53**, 1127-1130.
186. S. Anabuki, H. Shinokubo, N. Aratani and A. Osuka, *Angew. Chem. Int. Ed.*, 2012, **51**, 3174-3177.
187. S. Yamaguchi, T. Katoh, H. Shinokubo and A. Osuka, *J. Am. Chem. Soc.*, 2007, **129**, 6392-6393.
188. B. M. J. M. Suijkerbuijk, D. M. Tooke, A. L. Spek, G. van Koten and R. J. M. Klein Gebbink, *Z. Anorg. Allg. Chem.*, 2007, **633**, 2649-2653.
189. N. Fukui, H.-W. Jiang and A. Osuka, *Org. Chem. Front.*, 2017, **4**, 767-772.
190. O. Dumele, B. Schreib, U. Warzok, N. Trapp, C. A. Schalley and F. Diederich, *Angew. Chem. Int. Ed.*, 2017, **56**, 1152 –1157.
191. H. Yamada, K. Kushibe, T. Okujima, H. Unob and N. Ono, *Chem. Commun.*, 2006, 383–385.
192. R. Chauvin, *Tetrahedron Lett.*, 1995, **36**, 401-404.
193. M. H. Beyzavi, D. Lentz, H.-U. Reissig and A. Wiehe, *Eur. J. Org. Chem.*, 2013, **2013**, 269-282.
194. S. Drouet, A. Merhi, D. Yao, M. P. Cifuentes, M. G. Humphrey, M. Wielgus, J. Olesiak-Banska, K. Matczyszyn, M. Samoc, F. Paul and C. O. Paul-Roth, *Tetrahedron*, 2012, **68**, 10351-10359.
195. V. P. Fadeeva, V. D. Tikhova and O. N. Nikulicheva, *J. Anal. Chem.*, 2008, **63**, 1094-1106.
196. R. F. Culmo, *The Elemental Analysis of Various Classes of Chemical Compounds Using CHN*, PerkinElmer, Inc., Shelton, 2013.
197. L. R. Milgrom, R. D. Rees and G. Yahioglu, *Tetrahedron Lett.*, 1997, **38**, 4905-4908.
198. H. Jia, Z. Sun, D. Jiang and P. Du, *Chem. Mater.*, 2015, **27**, 4586-4593.
199. S. Matsunaga, N. Endo and W. Mori, *Eur. J. Inorg. Chem.*, 2011, **2011**, 4550-4557.
200. D. Gao, S. M. Aly, P. L. Karsenti, G. Brisard and P. D. Harvey, *Phys. Chem. Chem. Phys.*, 2017, **19**, 2926-2939.
201. K.-Y. Tomizaki, L. Yu, L. Wei, D. F. Bocian and J. S. Lindsey, *J. Org. Chem.*, 2003, **86**, 8199-8207.
202. B. J. Littler, Y. Ciringh and J. S. Lindsey, *J. Org. Chem.*, 1999, **64**, 2864-2872.
203. O. Robles and F. E. McDonald, *Org. Lett.*, 2008, **10**, 1811-1814.
204. L. M. Mink, M. L. Neitzel, L. M. Bellomy, R. E. Falvo, R. K. Boggess, B. T. Trainum and P. Yeaman, *Polyhedron*, 1997, **16**, 2809-2817.
205. W. Wu, W. Wu, S. Ji, H. Guo, X. Wang and J. Zhao, *Dyes Pigm.*, 2011, **89**, 199-211.

206. C. He, Q. He, C. Deng, L. Shi, D. Zhu, Y. Fu, H. Cao and J. Cheng, *Chem. Commun.*, 2010, **46**, 7536–7538.
207. W. P. To, Y. Liu, T. C. Lau and C. M. Che, *Chem. Eur. J.*, 2013, **19**, 5654-5664.
208. W. Bian, H. Lian, Y. Zhang, F. Tai, H. Wang, Q. Dong, B. Yu, X. Wei and Q. Zhao, *J. Organomet. Chem.*, 2017, **835**, 25-30.
209. S. M. Borisov and I. Klimant, *Dyes Pigm.*, 2009, **83**, 312-316.
210. C. He, Q. He, C. Deng, L. Shi, D. Zhu, Y. Fu, H. Cao and J. Cheng, *Chem. Commun.*, 2010, **46**, 7536-7538.
211. N. A. Pereira, M. Laranjo, J. Casalta-Lopes, A. C. Serra, M. Pineiro, J. Pina, J. S. Seixas de Melo, M. O. Senge, M. F. Botelho, L. Martelo, H. D. Burrows and E. M. T. M. Pinho, *ACS Med Chem Lett*, 2017, **8**, 310-315.
212. U. Toshihiko, T. Yoshio, N. Yukio, M. Toshio and K. Shinichi, *Bull. Chem. Soc. Japan*, 1981, **54**, 181-185.
213. K.-i. Yamashita, N. Katsumata, S. Tomita, M. Fuwa, K. Fujimaki, T. Yoda, D. Hirano and K.-i. Sugiura, *Chem. Lett.*, 2015, **44**, 492-494.
214. S. Ito, D. Makihata, Y. Ishii, Y. Saito and T. Oba, *Tetrahedron Lett.*, 2015, **56**, 7043-7045.
215. V. Y. Kukushkin, A. J. L. Pombeiro, C. M. P. Serreira and L. I. Elding, *Inorg. Synth.*, 2002, **33**, 189-196.
216. K. M. Wong, X. Zhu, L. L. Hung, N. Zhu, V. W. Yam and H. S. Kwok, *Chem. Commun.*, 2005, 2906-2908.
217. R. R. Parker, D. Liu, X. Yu, A. C. Whitwood, W. Zhu, J. A. G. Williams, Y. Wang, J. M. Lynam and D. W. Bruce, *J. Mater. Chem. C*, 2021, **9**, 1287-1302.
218. K. C. Yim, V. K. Au, K. M. Wong and V. W. Yam, *Chem. Eur. J.*, 2017, **23**, 5772-5786.
219. D. Lungerich, J. F. Hitzenberger, F. Hampel, T. Drewello and N. Jux, *Chem . Eur. J.*, 2018, **24**, 15818 – 15824.
220. J. Lu, X. Xu, K. Cao, J. Cui, Y. Zhang, Y. Shen, X. Shi, L. Liao, Y. Cheng and M. Wang, *J. Mater. Chem. A*, 2013, **1**, 10008-10015.
221. V. W. Yam, K. M. Wong, L. L. Hung and N. Zhu, *Angew. Chem. Int. Ed.*, 2005, **44**, 3107-3110.
222. D. K. Dogutan, M. Ptaszek and J. S. Lindsey, *J. Org. Chem.*, 2007, **72**, 5008-5011.
223. S. J. Webb and J. K. M. Sanders, *Inorg. Chem.*, 2000, **39**, 5912-5919.
224. D. Shi, B. L. Nannenga, M. G. Iadanza and T. Gonen, *Elife*, 2013, **2**, e01345.
225. A. R. McDonald, N. Franssen, G. P. M. van Klink and G. van Koten, *J. Organomet. Chem.*, 2009, **694**, 2153-2162.
226. K. Wu, J. Guo and C. Wang, *Chem. Commu.*, 2014, **50**, 695-697.
227. M. Drobizhev, A. Karotki, M. Kruk, A. Krivokapic, H. L. Anderson and A. Rebane, *Chem. Phys. Lett.*, 2003, **370**, 690-699.
228. K.-y. Tomizaki, L. Yu, L. Wei, D. F. Bocian and J. S. Lindsey, *J. Org. Chem.*, 2003, **68**, 8199-8207.
229. P. Zwick, C. Hsu, M. El Abbassi, O. Fuhr, D. Fenske, D. Dulic, H. S. J. van der Zant and M. Mayor, *J. Org. Chem.*, 2020, **85**, 15072-15081.
230. R. R. Parker, PhD Thesis, University of York, 2019.
231. E. C. Kwok, M. Y. Chan, K. M. Wong, W. H. Lam and V. W. Yam, *Chem. Eur. J.*, 2010, **16**, 12244-12254.

Chapter 5: Summary, Conclusions and Future Work

5.1   Synthesis of Target Complexes
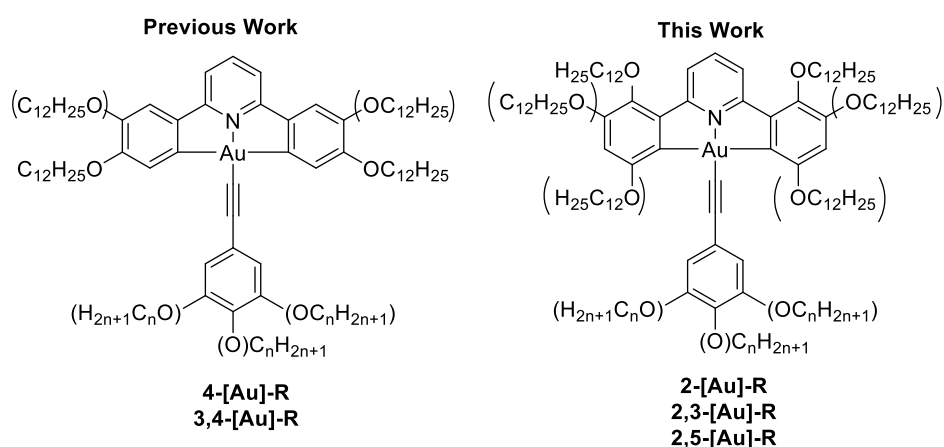
Figure 5.1: Structures of previously synthesised cyclometallated gold(III) phenylacetyelide complexes and the structure of complexes synthesised in this work.[1]

Previously, gold(III) C^N^C complexes where the pincer ligand is substituted in the 4,4′- or the 3,3′,4,4′-positions of the phenyl unit (Figure 5.1), have been investigated and shown to display strong phosphorescence in the yellow and green regions respectively and to process columnar mesophases over a wide temperature range.[1] Several of the complexes were fabricated into OLEDs, with the best-performing device having a measured EQE of 7.14%.

The potential linking of these complexes to porphyrins was of interest due to the potential effects of introducing an additional photophysically active unit and the possibility of cooperativity. However, chains bound to the 4,4'-positions of the pincer ligand are likely to be sterically unfavourable (Figure 5.2) and so related gold complexes substituted in the 2,2′-positions and 2,2′,3,3′-positions were chosen for study.
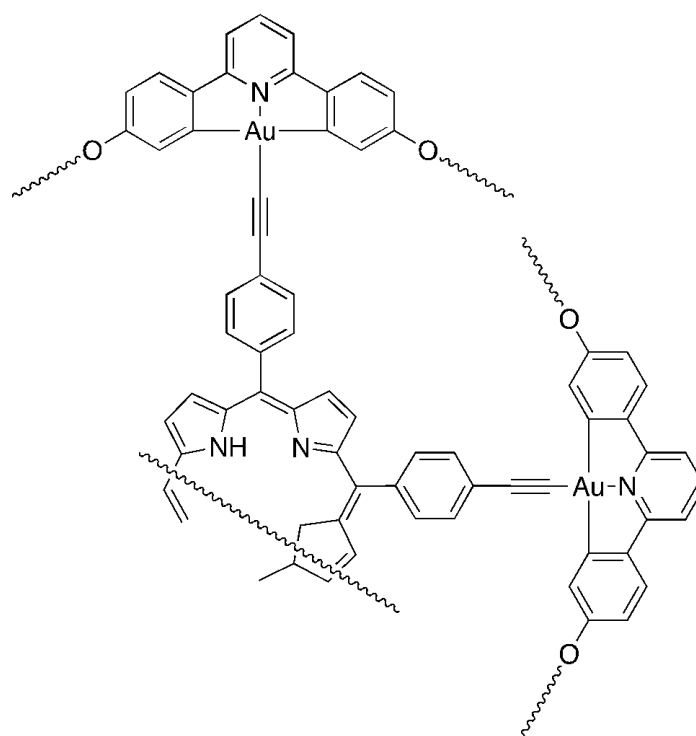
Figure 5.2: Schematic to show potential steric clash of chains in the 4,4'-positions of the pincer ligand.

While the introduction of alkoxy chains in the 2,2′-positions caused the ligands to be non-planar as evidenced both from X-ray single crystal structures (torsion angles of $30° − 50°$ measured in XRD structures)[2] and from solution ^{1}H NMR spectroscopy, the corresponding gold complexes were planar. Thus, the free ligands containing chains in the 2,2′-positions of the phenyl ring, show a desymmetrisation of the ^{1}H NMR resonances relating to the pyridyl signals. The origin of this effect is the existence of atropoisomers due to the steric barrier to rotation caused by the interaction between the *meta*-hydrogen atoms on the pyridine ring and the alkoxy substituents. This resulted in the *meta*-hydrogens being diastereotopic, leading to a more complex set of resonances for these hydrogens.
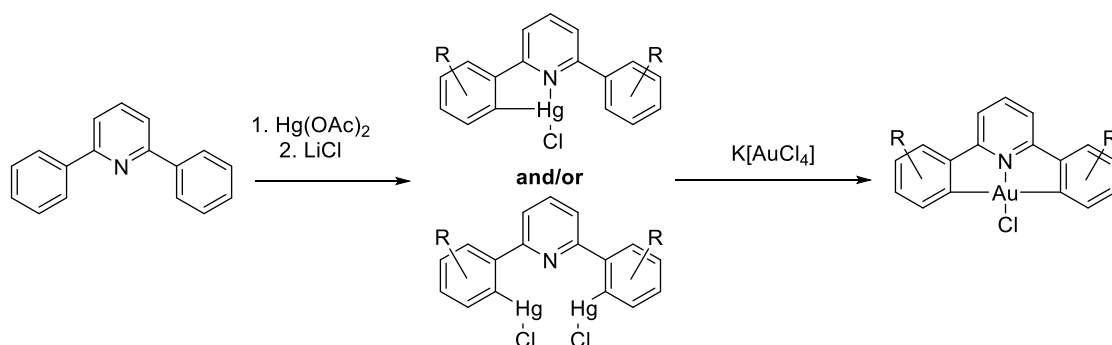
Figure 5.3: Reaction scheme for synthesis of cyclometallated gold(III) complexes.

Gold complexes of C^N^C pincer ligands cannot be prepared directly by reaction with a gold salt, and are therefore obtained by first preparing a mercury(II) complex as an intermediate from which the gold complex is obtained *via* transmetalation (Figure 5.3). In the previous studies with the 4,4′- and 3,3′,4,4′-substituted ligands, the intermediate mercury complex was obtained in low yield as a grey solid that was resistant to purification.[1] However, on reaction of the 2,2′-disubstituted ligand with mercury(II) acetate followed by a ligand metathesis using LiCl in methanol, a pure monomercurated ligand was obtained in >90% yield.

When the ligand was substituted in the 2,2′,3,3′-positions, a pure dimercurated complex was isolated in >70% yield, characterised by X-ray single crystal diffraction, while with the 2,2′,5,5′-tetrasubstituted ligand, pure mono- and di-mercurated complexes could be obtained, also characterised with X-ray single crystal diffraction. Employing a 3,3′-disubstituted ligand gave a separable mixture of the two possible isomers, **3-[Hg]** and **5-[Hg]** in ~1:1 ratio, whereas inseparable mixtures of the mono- and dimercurated complexes were formed for the 2,2′,4,4′- and 3,3′,5,5′-tetrasubstituted ligands in lower yields. Where mixtures of the dimercurated and the monomercurated complexes were formed, the monomercurated complex was the major product. All of the complexes were characterised by ^{1}H, ^{13}C$\{^1$H$\}$ and ^{199}Hg NMR spectroscopy.

Synthesis of high yields of pure monomercury complexes of C^N^C ligands is unprecedented in the literature,[3-5] while there is no previous report of dimercuration of ligands, even on use of [2-(9-phenyl-1,10-phenanthrolinyl-2)phenyl] (C^N^N^C), which also has two possible sites of C-H activation and for which a monomercurated complex is obtained in 60% yield.[6] While low yields of mercuration are typical for C^N^C ligands

(for reference the maximum reported yield for unsubstituted 2,6-bis(phenyl)pyridine and 2,6-*bis*(4-*tert*-butylphenyl)pyridine is 26%,[3-5] while for 1,3-bis(1-hexyl-2′-benzimidazoyl)-benzene it is 27%[7]), high yields are typical on mercuration of cyclometallating C^N ligands.[6, 8-10] Evidently, in previously reported terdentate systems the presence of the additional ring hinders high yields on mercuration. Unfortunately however, most experimentalists fail to report full procedures, and in particular yields, for this type of synthesis, with most content to merely report that previously reported methods were used. While suggestive of continuing low yields, given the sometimes exotic ligands used in latter studies it is disappointing on consideration of structure-activity relationships related to this mechanism. However, notably no other C^N^C ligands used in the literature have exhibited substitution in the 2,2′-postions of the phenyl ring. Additionally, it would appear that four alkoxy chains, one of which is in the 2,2′-positions of the phenyl ring, is required for double mercuration (**3,4-[L]** only undergoes monomercuration). The notable exception is **3,5-[L]**, which forms a mixture of **3,5-[Hg]** and **3,5-[Hg2]**, however NMR studies indicates that this substitution pattern exhibits decidedly different electronic properties to the others.

With the aforementioned exception of the 3,3′,5,5′-tetrasubstituted ligand, ^{1}H, ^{13}C{^{1}H} and ^{199}Hg NMR studies suggest relativity similar electronic properties, on consideration of the chemical shifts, at the position that metallates for all other ligands. Only relatively minor changes in chemical shift are shown on alteration of the substitution pattern and no strong correlation to the yield and product on mercuration is observed. For example **2-[M]** and **4-[M]** display very similar chemical shifts (128-132 ppm in the ^{13}C{^{1}H} NMR spectra for the free ligand), yet **4-[L]** gives low yields on mercuration and **2-[L]** high yields. What is however noticeable is that the degree of distortion from planarity for **2-[L]** is significantly larger in the molecular structure than for **4-[L]**, with the desymmetrisation of the ^{1}H NMR resonances for the pyridyl signals for **2-[L]** suggesting this is maintained to some degree in solution. This correlation, combined with the difference in yields on consideration of mercuration of C^N and C^N^C ligands,[6, 8-10 3-5] would suggest that the presence of atropisomerism in the free ligand, due to the twisting of the rings due to the aforementioned steric barrier, is the major force in the unprecedented yields and products in these systems.

On the basis of the studies carried out as part of this work, it is not straightforward to assign a definitive reason for the observation of the isolation of mono- and di-mercurated complexes clean and in high yield. Certainly the substitution pattern of alkoxy chain(s) has an effect, but at least on the basis of data from ^{13}C{^{1}H} and ^{199}Hg chemical shifts, there is no obvious electronic effect driving the chemistry. Another potential factor is the steric effect when there are alkoxy chains in the 2,2'-positions of the phenyl ring. Previously, initial coordination of the metal ion (both for mercury(II)[9, 11] and gold(III)[12, 13]) has been shown to be a key initial step in metalation of C^N ligands, with use of the acetate ligand also key in enabling a concerted metalation-deprotonation to mercurate a C^N complex.[9] It is clear from solution NMR spectra that the existence of the alkoxy chains in the 2,2'-positions suppresses free rotation of the phenyl rings about the phenyl-pyridine bond. It is conceivable that this may somehow facilitate the mercuration reaction and because the preferred rotamers reduce steric crowding close to the pyridine nitrogen, they may play a role in directing the C–H bond activation step, but such a proposal for now remains unproven.

Subsequent auration gave lower yields for dimercurated complexes, with the yield on transmetalation of **2-[Hg]** being 40%, while that for **2,3-[Hg₂]** is 24%. This is perhaps unsurprising given that two C-Hg bonds must be broken, however the high initial yield of mercuration meant that the overall yield (18%) still remained higher than for the 4,4′-disubstituted (8%) and 3,3′,4,4′-tetrasubstituted complexes (5%). Auration of a mixture of **3-[Hg]** and **5-[Hg]** gave selective mercuration of **3-[Hg]** to give an unsymmetric complex, **3/5-[Au]-Cl** (Figure 5.4), while surprisingly **3,5-[Hg]** failed to aurate.
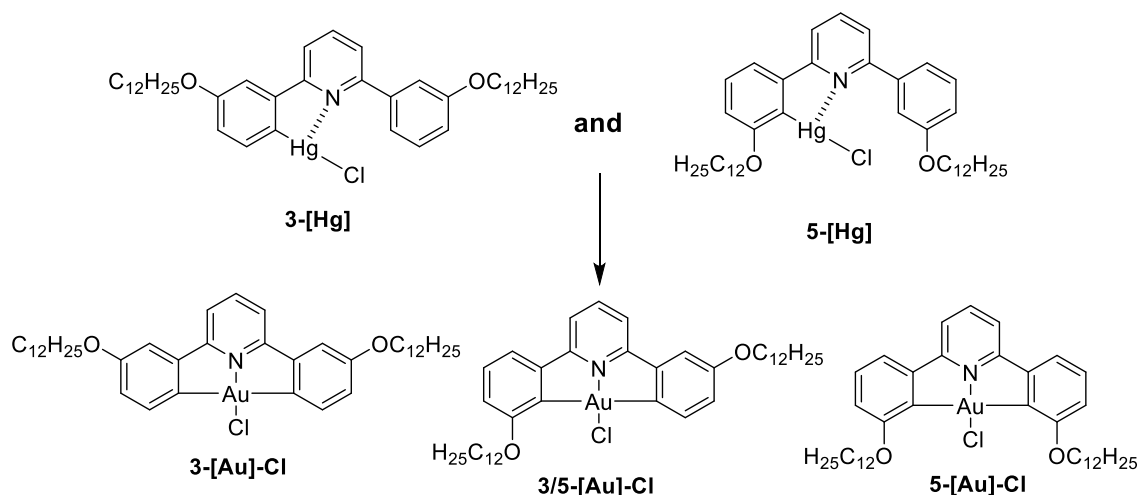
*Figure 5.4: Possible chlorogold(III) complexes that can be synthesised from a mixture of **3-[Hg]** and **5-[Hg]**. Note, only **3/5-[Au]-Cl** is actually synthesised.*

The enhanced reactivity of these new C^N^C ligands towards mercury raised the question of whether they may also be susceptible to direct auration, thus avoiding the current requirement for toxic intermediates. Unfortunately, extensive calculations plus an investigation of microwave-promoted reactions failed to provide any clues as to productive approaches.[11] However, it was noted that in a separate study by Gorunova *et al.* in 2018 that there had been interest in palladium-to-mercury transmetalation reactions in understanding aspects of the mercury drop test to screen for possible palladium nanoparticle catalysis.[10] This prompted the suggestion that, given the propensity for *ortho*-metalation by palladium, perhaps a palladium intermediate could replace the mercury equivalent with subsequent transmetallation to the target gold complex. This approach was successful for **2-[Au]-Cl** and **2,3-[Au]-Cl**, giving yields comparable to those gained *via* use of a mercury intermediate, revealing for the first time an approach to aurated C^N^C ligands that required neither prefunctionalisation of the ligand nor a toxic intermediate.[14]

Then, in mid-2022, a report appeared of the direct auration of a series of 2-phenylpyridine derivatives catalysed by [Cp*RhCl₂]₂, in which an *ortho*-rhodated intermediate reacts to form the gold product.[15] Deploying the same conditions with a 2,2′,3,3′-tetrasubstituted C^N^C ligand also led to direct auration of **2,3-[L]**.[14]

Both the rhodium-catalysed and palladium-mediated pathways were discovered very late in the project and both require work to optimise the conditions to increase both the yields

and reaction range. Nonetheless, both observations are without precedent and indicate potentially viable approaches to chelated gold complexes of this ligand type while avoiding the intermediacy of mercury compounds.

2-[Au]-
5: $R_1 = R_3 = H$, $R_2 = C_5H_{11}$
8: $R_1 = R_3 = H$, $R_2 = C_8H_{17}$
1-10: $R_1 = R_3 = H$, $R_2 = OC_{10}H_{21}$
2-10: $R_1 = H$, $R_2 = R_3 = OC_{10}H_{21}$
3-10: $R_1 = R_2 = R_3 = OC_{10}H_{21}$
3-14: $R_1 = R_2 = R_3 = OC_{14}H_{29}$
F10: $R_1 = R_3 = H$, $R_2 = O(CH_2)_2(CF_2)_7CF_3$
F10: $R_1 = R_3 = H$, $R_2 = O(CH_2)_2(CF_2)_9CF_3$
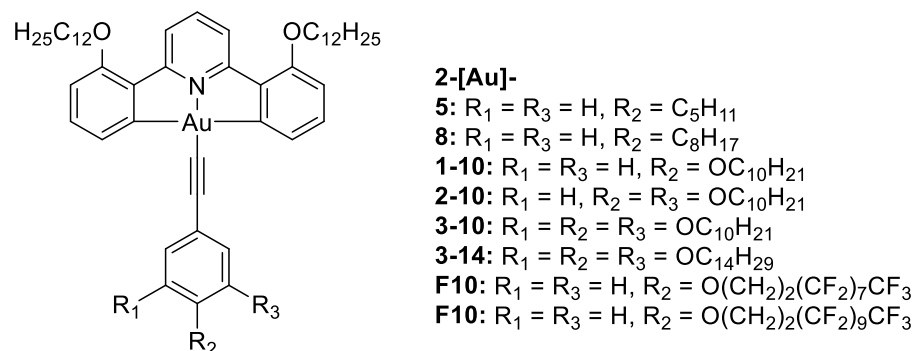
Figure 5.5: Structures of gold(III) phenylacetylide complexes substituted in the 2,2'-positions.

Finally in terms of synthesis, chlorogold complexes substituted in the 2,2'-, 2,2',3,3'- and 2,2',5,5'-positions (Figures 5.5 and 5.6) were attached to alkyl- and alkoxy-substituted phenylacetylide ligands and X-ray single crystal structures of several examples were solved. The possibility of concentration-dependent self-assembly in solution was investigated by looking for shifting of some of the resonances in their ^{1}H NMR spectra over concentrations from $0.05 – 14.2$ mmol dm^{-3}. Three series of complexes were studied and those with pincer ligands substituted in the 2,2'-positions did show concentration-dependent shifting of resonances, consistent with 'back-to-back' self-assembly in solution. Those substituted in the 2,2',3,3'- and 2,2',5,5'-positions, however, did not and the lack of self-assembly in these latter complexes was ascribed to unfavourable steric interactions from the ligand chains in the 3,3'- or 5,5'-positions.

2,3-[Au]-
5: R$_1$ = R$_3$ = H, R$_2$ = C$_5$H$_{11}$
8: R$_1$ = R$_3$ = H, R$_2$ = C$_8$H$_{17}$
1-10: R$_1$ = R$_3$ = H, R$_2$ = OC$_{10}$H$_{21}$
2-10: R$_1$ = H, R$_2$ = R$_3$ = OC$_{10}$H$_{21}$
3-10: R$_1$ = R$_2$ = R$_3$ = OC$_{10}$H$_{21}$
3-12: R$_1$ = R$_2$ = R$_3$ = OC$_{12}$H$_{25}$
3-14: R$_1$ = R$_2$ = R$_3$ = OC$_{14}$H$_{29}$

2,5-[Au]-
8: R$_1$ = R$_3$ = H, R$_2$ = C$_8$H$_{17}$
1-10: R$_1$ = R$_3$ = H, R$_2$ = OC$_{10}$H$_{21}$
1-12: R$_1$ = R$_3$ = H, R$_2$ = OC$_{12}$H$_{25}$
1-14: R$_1$ = R$_3$ = H, R$_2$ = OC$_{14}$H$_{29}$
2-10: R$_1$ = H, R$_2$ = R$_3$ = OC$_{10}$H$_{21}$
3-10: R$_1$ = R$_2$ = R$_3$ = OC$_{10}$H$_{21}$
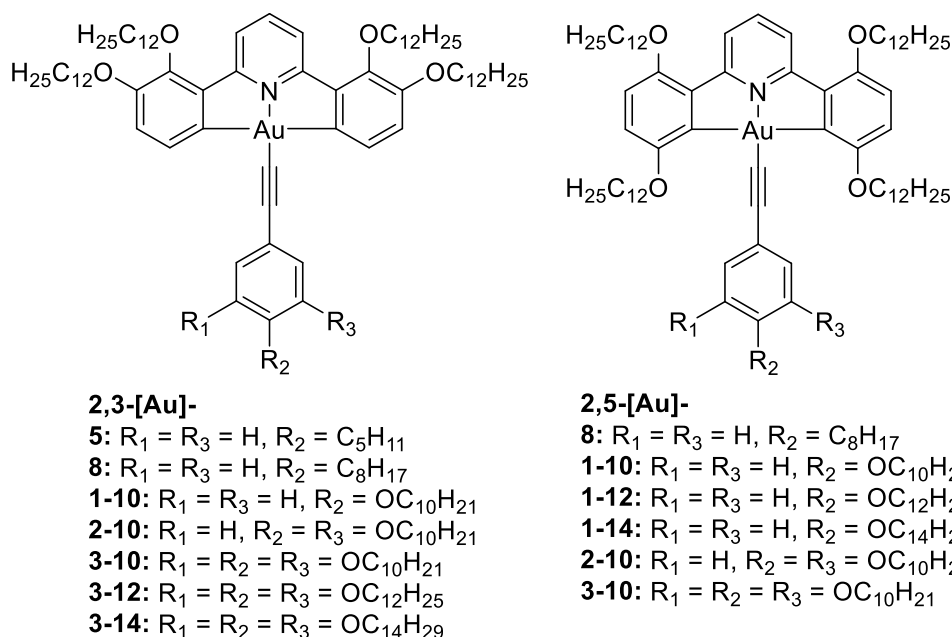
Figure 5.6: Structures of gold(III) phenylacetylide complexes substituted in the 2,2'3,3'-positions and 2,2',5,5'-positions.

5.1.1 Areas of Further Work

There are several areas where future work remains of interest in the synthesis of gold(III) complexes. Firstly, further work is required on the mercury-free auration methods. While formation of a palladium dimer and subsequent transmetalation to give the chlorogold(III) complexes was successful, as was rhodium(III)-catalysed auration for particular examples, the ligand scope was limited. Further work on optimising conditions for both methods is required to maximise yields and hopefully develop methods for auration of other ligands, particularly those substituted in the 4,4'- and 3,3',4,4'-positions, due to the higher quantum yields possible for these complexes.[1] Further, replacement of palladium with a cheaper metal would be desirable. Investigation of alternate conditions for auration of the 3,3',5,5'-ligand would also be of interest as transmetalation failed under standard conditions. Due to synthetic issues insufficient **3/5-[Au]-Cl** and **2,4-[Au]-Cl** to form the phenylacetylide complexes was not achieved. To do so would enable investigation of the mesophase and photophysical properties of the resulting complexes and would therefore be of interest.

311

5.2   Physical Properties of the Gold(III) Complexes

The thermal and photophysical properties of the synthesised phenylacetylide complexes were investigated. Of the 2,2′-disubstituted series only one complex substituted with alkoxy and alkyl chains gave a monotropic columnar mesophase, **2-[Au]-3-14**, with a lack of effective space-filling from the chains to form a 'disc-like' shape believed to prevent mesophase formation for the others in the series. However, on introduction of perfluorinated chains to give the complexes **2-[Au]-F10** and **2-[Au]-F12**, the fluorophobic effect resulted in microphase separation and formation of bilayer smectic A phases. Further work to investigate the effect of perfluorinated ligands on the 2,2′-disubstituted and 2,2′,3,3′-tetrasubstituted complexes would be of interest, particularly the latter, to observe if a similar effect is observed with the two additional chains in the 3,3′-positions.

For complexes substituted in the 2,2′,3,3′-positions, compounds with three alkoxy chains on the phenylacetylide ligand, **2,3-[Au]-3-n** (where n = 10, 12, 14), displayed hexagonal columnar phases, due to effective space-filling to form a 'disc-like' structure, not observed with other members of the series. The complex **2,3-[Au]-3-10** displayed a monotropic phase and on increasing the chain length, the mesophase became enantiotropic and existed over quite a wide temperature range owing to a destabilisation of the crystal phase. A glassy solid formed on cooling.

2,2′,5,5′-Tetrasubstituted complexes with only one chain on the phenylacetylide ligand, **2,5-[Au]-8** and **2,5-[Au]-1-n** (where n = 10, 12, 14), displayed a smectic A phase, due to the rod-like molecular shape. On increasing chain length both the clearing point and the melting point temperatures decrease, but not as the same rate, initially resulting in a widening of the phase range. However, the clearing point fell more quickly so that for **2,5-[Au]-1-14**, the SmA phase becomes monotropic. On the introduction of additional chains the phase stability was reduced due to the loss of molecular anisotropy along the length of the molecule, while the overall change in molecular shape to a more 'disc-like' shape, resulted in formation of monotropic columnar phases.

Overall it can be observed that the positions of the alkoxy chain(s) on the C^N^C ligand has a significant impact on whether a mesophase is formed and also on the nature of that phase, due to the resulting changes in molecular shape. Wide-range columnar phases are formed for molecules which have an effective disc-like shape (**3,4-[Au]-**, **4-[Au]-**), while reduced molecular space-filling of the chains, requires increased numbers and longer chains in order to induce mesophase formation (**2-[Au]-** and **2,3-[Au]-**). Formation of more linear, rod-shaped molecules gives rise to smectic phases.

The photophysics of the complexes proved to be surprising when compared with the isomeric **4-[Au]-R** and **3,4-[Au]-R** complexes. Thus, while all phenylacetylide complexes displayed triplet emission in the green (**2-[Au]-** and **2,3-[Au]-**) and yellow regions (**2,5-[Au]-**), emitting at 490, 500 and ~580 nm respectively, lifetimes were unusually short for triplet emission (<100 ns) and PLQYs very low (<0.1%). This precluded the possible application of these complexes as the emitters in OLEDs devices. While, these properties are not what was anticipated, particularly when compared to the favourable properties reported in the isomeric **4-[Au]-** and (in particular) **3,4-[Au]-** complexes,[1] they are comparable to those reported in early investigations of complexes of this general type.[3, 4, 16-21]

TD-DFT calculations were undertaken to investigate the excited states properties further, particularly in the hope of understanding the origin of the lower PLQYs. The results indicated that the transitions were primarily LLCT in nature, with electron density being transferred from the phenylacetylide to the C^N^C ligand, with some mixed IL/ILCT, where electron density is transferred from the phenyl rings to the pyridine ring on the pincer ligand. This is consistent with calculations for related systems[1, 4, 22] and calculated triplet emission energies were similar to those observed experimentally. The S_1 excited state was calculated and determined to be ^{1}LLCT in nature. This marks a change from the S_1 excited state calculated for the 4,4'-disubstituted and 3,3',4,4'-tetrasubstituted systems, which are shown to be ^{1}IL in nature and indicates a change in the relative ordering of these two singlet excited states on alternation in the substitution pattern.[4] On further, consideration of the data it can be observed that the radiative decay constant, k_r, obtained from the emission data for both the new complexes (1-5 x 10^3 s^{-1}) and those studied previously (6-70 x 10^3 s^{-1}) are not dissimilar. However, the non-radiative decay constants for complexes with substituents in the 2,2'-positions are considerably higher (~10-40 x

10^6 s^{-1}) compared to their isomeric complexes (~100-140 x 10^3 s^{-1}), which results in the considerably lower quantum yields, is possibly due to low-lying ′dark state(s)′[23-25] or alternately the presence of a steric clash between the substituents in the 2,2′-positions and the pyridyl hydrogen and hence more distortion and motion in the excited states resulting in more deactivation *via* vibrational energy pathways. Further, more detailed investigations of this would be challenging and beyond the scope of this work.

5.3 Preparation and Physical Properties of Gold-Porphyrin Dyads
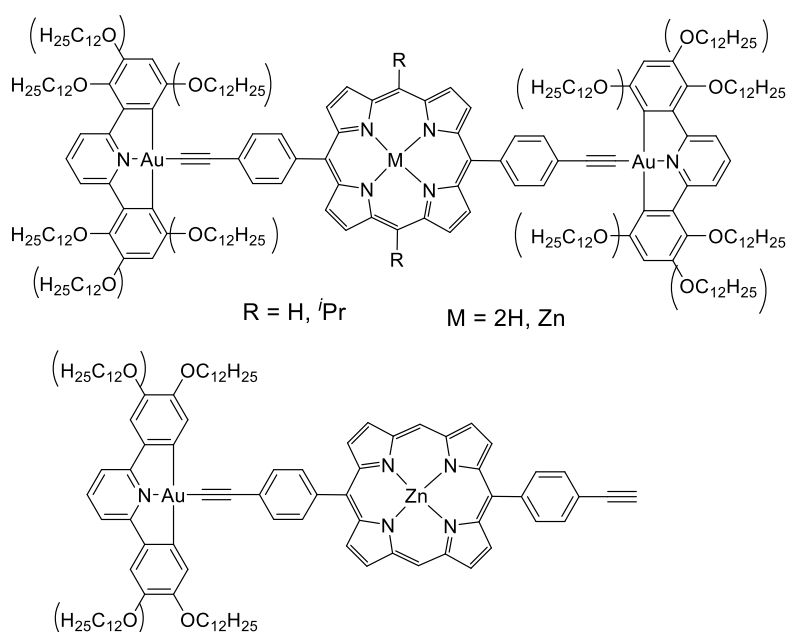
Figure 5.7: The structures of synthesised mono- and disubstituted gold-porphyrin dyads.

The gold complexes were linked to zincated 5,15-disubstituted (Figure 5.7) and 5,10,15,20-tetrasubstituted porphyrins (Figure 5.8) in varying yields and with varying degrees of success. 2,2′,3,3′- and 2,2′,5,5′-Tetrasubstituted gold complexes gave high yields (>70%) of both di- and tetrasubstituted porphyrins, though **2,5-[Au]-t-ZnP** was only isolated as part of a mixture and as such was impure; unfavourable sterics are thought to be a major reason for this observation. Use of a 2,2′-disubstituted gold complex gave lower yields (14%), while only the monosubstituted dyad was synthesised for the 4,4′-disubstituted and 3,3′,4,4′-tetrasubstituted complexes. Qualitative experimental evidence suggests that the solubility of the final product is also a major contributing factor here. Thus, higher solubility gave higher yields, while lower solubility resulted in Glazer coupling being capable of becoming a successful competing reaction. Removal of zinc

314

via addition of TFA was successful for most complexes, as was introduction of a bulky *iso*-propyl group in the 10,20-positions.

Purity issues were noted for several gold-porphyrin dyads, with a complex (due to the challenges of undertaking CHN on porphyrins[26, 27]) defined as ′pure′ if the ^{1}H NMR spectrum was clean and if there was one spot on the TLC plate. By this measure **2,3-[Au]-di-ZnP**, **2,5-[Au]-di-ZnP**, **2,3-[Au]-di-P**, **2,3-[Au]-t-ZnP**, **2,3-[Au]-t-P** and **2-[Au]-di-ZnP** were defined as ′pure′. **2,3-[Au]-iPr-ZnP**, **2,5-[Au]-iPr-ZnP**, **4-[Au]-ZnP** and **3,4-[Au]-ZnP** showed small peaks at the baseline of the aromatic region of the ^{1}H spectra, suggesting the presence of a low amount of impurities. **2,5-[Au]-t-ZnP** is known from ^{1}H NMR spectroscopy to be isolated as an impure mixture of the tri- and tetrasubstituted porphyrins. Three complexes, **2,5-[Au]-di-P**, **2,3-[Au]-iPr-P** and **2,5-[Au]-iPr-P** displayed very messy ^{1}H NMR spectra and were evidently very impure.
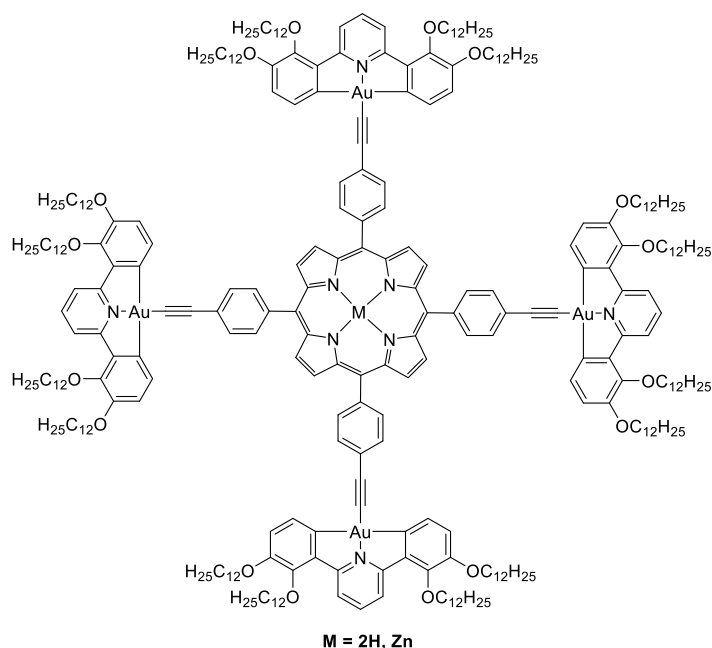
Figure 5.8: The structures of synthesised tetrasubstituted gold-porphyrin dyads.

Unfortunately, the analogous platinum(II) porphyrins could not be synthesised due to incompatibility between the insertion methods and the reactivity of alkynyl function used in the porphyrin. Further investigation, and development, of an alternate method of insertion of platinum(II) (starting materials and reaction conditions) into the porphyrins used in this study would be of interest. If successful insertion of platinum(II) into these

porphyrins could be achieved it would still be of interest to investigate the connection with gold(III) complexes and the resulting mesophase and photophysical properties. Attempts to connect gold complexes to zinc 5,15-*bis*(ethynyl)porphyrin proved unfavourable, with only low yields (<5%) achieved with **2,3-[Au]-Cl**.

By use of shorter butoxy chains, mircoED was used to gain structures for **2,3-[Au]-di-ZnP** and **2,3-[Au]-di-P**. This improved to be an excellent illustration of the ability of mircoED to solve structures for compounds that single crystals of large enough size for XRD analysis are unable to be achieved, particularly for these larger molecules.

Unfortunately, only one impure complex, **2,5-[Au]-t-ZnP**, displayed a monotropic nematic phase, with the others all having high melting points, though it was demonstrated that the melting point temperature could be tuned by several methods. For example, introduction of chains in the 5,5′-positions of the gold unit directed these chains across the porphyrin face resulting in lowering of the melting point due the prevention of intermolecular π-π interactions and hence, aggregation and crystallisation.[28, 29] Introduction of a bulky substituent in the 10,20-positions also reduced intermolecular π-π interactions due to increased steric bulk and hence, also preventing aggregation.[30] Removal of zinc(II) from the porphyrin decreased molecular rigidity and also lowered the melting point.[31-33]

The photophysical properties of the dyads also proved to be disappointing, with only fluorescence in the red region from the porphyrin unit observed for the majority of complexes unperturbed from those of the parent complexes. This is likely due to the extremely low emission quantum yields of the parent gold complexes, particularly when compared to those of the porphyrins, resulting in the porphyrin emission overwhelming any gold-based emission. Only **3,4-[Au]-ZnP** showed triplet emission from the gold complex (where the PLQY is >30%), alongside the porphyrin fluorescence. It is notable that the quantum yields for **3,4-[Au]-R** are several orders of magnitude greater than those measured for the other gold complexes, explaining this observation. However, the porphyrin-based emission observed on excitation at the wavelengths for the gold complex, raises the possibility that some degree of energy transfer from the gold complexes to the porphyrin occurs in this class of complexes. Precedent for this is set by the linkage of some platinum(II) complexes to porphyrins,[34-37] but it is known to be

challenging to avoid exciting the porphyrin unit *via* the edge of the intense Soret band and confirmation would require more detailed studies beyond the scope of this project.

5.4 References

1. R. R. Parker, D. Liu, X. Yu, A. C. Whitwood, W. Zhu, J. A. G. Williams, Y. Wang, J. M. Lynam and D. W. Bruce, *J. Mater. Chem. C*, 2021, **9**, 1287-1302.
2. A. Klein, K. Butsch and J. Neudörfl, *Inorg. Chim. Acta*, 2010, **363**, 3282-3290.
3. Z. T. Yu, X. L. Liu, Y. J. Yuan, Y. H. Li, G. H. Chen and Z. G. Zou, *Dalton Trans.*, 2016, **45**, 17223-17232.
4. K. M.-C. Wong, L.-L. Hung, W. H. Lam, N. Zhu and V. W.-W. Yam, *J. Am. Chem. Soc.*, 2007, **29**, 4350-4365.
5. R. R. Parker, PhD Thesis, University of York, 2019.
6. O. Bumbu, C. Silvestru, M. Concepción Gimeno and A. Laguna, *J. Organomet. Chem.*, 2004, **689**, 1172-1179.
7. A. Herbst, C. Bronner, P. Dechambenoit and O. S. Wenger, *Organometallics*, 2013, **32**, 1807-1814.
8. S. Attar, J. H. Nelson and J. Fischer, *Organometallics*, 1995, **14**, 4776-4780.
9. N.-C. Lin, H. J. H. Syu, A. R. Naziruddin, F.-C. Liu and I. J. B. Lin, *RSC Advances*, 2017, **7**, 11652-11656.
10. O. N. Gorunova, I. M. Novitskiy, Y. K. Grishin, I. P. Gloriozov, V. A. Roznyatovsky, V. N. Khrustalev, K. A. Kochetkov and V. V. Dunina, *Organometallics*, 2018, **37**, 2842-2858.
11. C. Goult, unpublished work.
12. E. C. Constable, R. P. G. Penney and T. A. Leese, *J. Organomet. Chem.*, 1989, **361**, 277-282.
13. E. C. Constable and T. A. Leese, *J. Organomet. Chem.*, 1989, **363**, 419-424.
14. A. J. McEllin, A. C. Whitwood, J. M. Lynam and D. W. Bruce, *Dalton Trans*, 2023, DOI: 10.1039/d2dt04114f
15. J. Martin, E. Gomez-Bengoa, A. Genoux and C. Nevado, *Angew. Chem. Int. Ed.*, 2022, **61**, e202116755.
16. S. K.-L. Siu, C. Y.-S. Chung and V. W.-W. Yam, *J. Organomet. Chem.*, 2017, **845**, 177-188.
17. V. W. Yam, K. M. Wong, L. L. Hung and N. Zhu, *Angew. Chem. Int. Ed.*, 2005, **44**, 3107-3110.
18. K. C. Yim, V. K. Au, K. M. Wong and V. W. Yam, *Chem. Eur. J.*, 2017, **23**, 5772-5786.
19. M. C. Tang, D. P. Tsang, Y. C. Wong, M. Y. Chan, K. M. Wong and V. W. Yam, *J. Am. Chem. Soc.*, 2014, **136**, 17861-17868.
20. M. C. Tang, M. Y. Leung, S. L. Lai, M. Ng, M. Y. Chan and V. Wing-Wah Yam, *J. Am. Chem. Soc.*, 2018, **140**, 13115-13124.
21. M.-C. Tang, D. P.-K. Tsang, M.-Y. Chan, K. M.-C. Wong and V. W.-W. Yam, *Mater. Chem. Front.*, 2017, **1**, 2559-2568.
22. L.-L. Hung, W. H. Lam, K. M.-C. Wong, E. C.-C. Cheng, N. Zhu and V. W.-W. Yam, *Inorg. Chem. Front.*, 2015, **2**, 453-466.
23. H. Beucher, S. Kumar, E. Merino, W.-H. Hu, G. Stemmler, S. Cuesta-Galisteo, J. A. González, J. Jagielski, C.-J. Shih and C. Nevado, *Chem. Mater.*, 2020, **32**, 1605-1611.

24. G. S. Ming Tong, K. T. Chan, X. Chang and C. M. Che, *Chem. Sci.*, 2015, **6**, 3026-3037.
25. E. S. Lam, W. H. Lam and V. W. Yam, *Inorg. Chem.*, 2015, **54**, 3624-3630.
26. V. P. Fadeeva, V. D. Tikhova and O. N. Nikulicheva, *J. Anal. Chem.*, 2008, **63**, 1094-1106.
27. R. F. Culmo, *The Elemental Analysis of Various Classes of Chemical Compounds Using CHN*, PerkinElmer, Inc., Shelton, 2013.
28. Q. M. Wang and D. W. Bruce, *Chem. Commun.*, 1996, 2505-2506.
29. Q. M. Wang and D. W. Bruce, *Angew. Chem. Int. Ed.*, 1997, **36**, 150-152.
30. Q. M. Wang and D. W. Bruce, *Tetrahedron Lett.*, 1996, **37**, 7641-7644.
31. J. Li, H. Xin and M. Li, *Liq. Cryst.*, 2006, **33**, 913-919.
32. M. Salamonczyk, D. Pociecha, A. Nowak-Krol, D. Koszelewski, D. T. Gryko and E. Gorecka, *Chem. Eur. J.*, 2015, **21**, 7384-7388.
33. E. J. Sun, G. J. Sun, X. Y. Bai, H. J. Zhai, X. Y. Yang and S. W. Lin, *Russ. J. Gen. Chem.*, 2019, **89**, 1667-1672.
34. E. C. Kwok, M. Y. Chan, K. M. Wong, W. H. Lam and V. W. Yam, *Chem. Eur. J.*, 2010, **16**, 12244-12254.
35. A. Jana, L. McKenzie, A. B. Wragg, M. Ishida, J. P. Hill, J. A. Weinstein, E. Baggaley and M. D. Ward, *Chem. Eur. J.*, 2016, **22**, 4164-4174.
36. D. Bellows, T. Goudreault, S. M. Aly, D. Fortin, C. P. Gros, J.-M. Barbe and P. D. Harvey, *Organometallics*, 2009, **29**, 317-325.
37. B. Du and P. D. Harvey, *Chem. Commun.*, 2012, **48**, 2671-2673.

Chapter 6: Experimental

6.1 General Synthetic and Instrument Methods

6.1.1 Synthetic Methods

Unless otherwise stated in the experimental, all starting materials and reagents were obtained commercially and used without further purification. All solvents were obtained from either Merck or VWR Chemicals. Dry solvents were used from an Innovative Technologies SPS-7 solvent purification system, unless otherwise specified. Pyrrole was dried over CaH_2 and distilled under vacuum. Dichloromethane used for porphyrin synthesis was dried over CaH_2 and distilled. Na[AuCl$_4$] was kindly donated by Johnson Matthey. Phenylacetylene ligands, unless given, were synthesised by R. Parker and L. Curtis using previously reported methods.[1, 2]

Thin layer chromatography, where appropriate, was done on silica coated aluminium plates (Kieselgel 60 F-254), purchased from Merck and visualised by UV light (254 nm or 365 nm) or by oxidation with potassium permanganate solution. Flash column chromatography was carried out using flash grade silica (Fluka, 70-230 mesh, 63 μm - 200 μm particle size).

6.1.2 Analytical Methods

^{1}H and ^{13}C{^{1}H} NMR spectra were recorded on a Jeol ECS400 spectrometer operating at 400 MHz, with chemical shifts referenced to appropriate residual non-deuterated solvent signal. ^{1}H and ^{13}C{^{1}H} NMR spectra, NOE measurements and temperature-dependent ^{1}H NMR spectra were recorded on a Bruker 500 AVANCE II spectrometer operating at 500 MHz. ^{199}Hg NMR spectra were recorded on a Bruker 500 AVANCE II spectrometer operating at 89.6 MHz and externally referenced to Hg(OAc$_2$) in D_2O. ^{19}F NMR spectra were recorded on a Jeol ECS400 spectrometer operating at 376.5 MHz. The chemical shifts are reported in ppm (δ). The following abbreviations are used: s = singlet, d = doublet, t = triplet, q = quartet, dd = doublet of doublets, m = multiplet, br = broad.

APCI mass spectroscopy data was collected on a Bruker compact® time of flight mass spectrometer and MALDI-TOF on a Bruker Ultraflex III mass spectrometer, using the

University of York Chemistry department MS service (Karl Heaton). Spectra were internally calibrated using sodium formate calibrant and samples were transferred to the spectrometer using an Agilent 1260 Infinity LC system.

Elemental analysis (CHN) was carried out by Dr Graeme McAllister on an Exeter Analytical Inc. CE-440 analyser with samples of between 1.6 and 1.8 mg weighed on a Sartorius SE2 analytical balance. Calibration was performed against acetanilide standards and *S*-benzyl thiouronium chloride as an internal standard. CHN was performed on the final gold complexes and mercury complexes, where required, to support product identity. It was not routinely done on all mercury complexes due to the general high toxicity. CHN was not routinely undertaken on intermediate compounds or porphyrin containing compounds, the latter due to the high stability of porphyrins causing issues with combustion analysis. As such, the criteria for purity for the gold-porphyrin dyads were to have *both* a clean NMR spectrum *and* a single spot by TLC.

Differential scanning calorimetry was recorded on a Mettler DSC 822^e calibrated using an indium standard (onset = 156.55 ± 0.2 °C, $\Delta H = 28.45 \pm 0.40$ J g^{-1}) and a scan rate of 10 °C min^{-1}, operated using Mettler STAR-E software, under an atmosphere of dry dinitrogen. Polarising light microscopy (x200 magnification) was done on a Zeiss Axioskys 40 microscope, with Mettler Toledo FP82HT hot stage controlled by a Mettler Toledo FP90 central processer. Pictures were taken with an Infinity Capture digital camera. Small-angle X-ray scattering was recorded using a Bruker D8 Discover equipped with a temperature controlled, bored graphite rod furnace, custom built at the University of York. Cu-Kα ($\lambda = 0.154056$ nm) radiation was used, generated from a 1 μS microfocus source. Diffraction patterns were recorded on a 2048 x 2048 pixel Bruker VANTEC 500 area detector set at a distance of 121 mm from the sample, allowing simultaneous collection of small angle and wide angle scattering data. Samples were measured in 1 mm capillary tubes in a magnetic field of *ca* 1 T.

Absorption spectra were measured in solution in CH_2Cl_2 in 1 cm pathlength quartz cuvettes using a Biotek Instruments XS spectrometer. Emission spectra were recorded using a Jobin Yvon Fluoromax-2 spectrometer equipped with a Hamamatsu R928 photomultiplier tube (PMT). For anaerobic measurements a 1 cm pathlength quartz curvet modified for connection to a vacuum line was used. The sample was degassed by a

minimum of three freeze-pump-thaw cycles. Luminescence lifetimes in degassed solutions were measured by multi-channel scaling following excitation into the lowest-energy absorption band using a microsecond pulsed xenon lamp or PicoBright pulsed diode laser of appropriate excitation wavelength. The emitted light was detected at 90˚ using a Peltier-cooled R928 PMT after passage through a monochromator. The lifetimes in air-equilibrated solution (< 10 μs) were measured by time-correlated single photon counting (TCSPC), following excitation at 375.6 nm with a pulsed laser diode.

Diffraction data were collected at 110 K on an Oxford Diffraction SuperNova dual-source X-ray diffractometer with MoKα radiation (λ = 0.71073 Å) and CuKα radiation (λ = 1.54184 Å) using an EOS CCD camera. The crystal was cooled with an Oxford Instruments Cryojet. Diffractometer control, data collection, initial unit cell determination, frame integration and unit-cell refinement were carried out with 'Crysalis'.[3] Face-indexed absorption corrections were applied using spherical harmonics, implemented in SCALE3 ABSPACK scaling algorithm.[4] OLEX2[5] was used for overall structure solution, refinement and preparation of computer graphics and publication data. Within OLEX2,[5] the algorithms used for structure solution were ShelXT. Refinement by full-matrix least-squares used the SHELXL-97[6] algorithm within OLEX2.[5] All non-hydrogen atoms were refined anisotropically. Hydrogen atoms were placed using a 'riding model' and included in the refinement at calculated positions. In the figures of the molecular structures carbon atoms are coloured grey, chlorine green, gold yellow, hydrogen turquoise, nitrogen blue, mercury deep pink, oxygen red, silicon pale yellow, and zinc pink.

For microED structures samples of **2,3-[Au]-di-ZnP-C4** and **2,3-[Au]-di-P-C4** were finely ground and deposited onto Quantifoil Cu R1/4 grids that were pre-assembled into autogrid cartridges. The grids were plunged into liquid nitrogen and then transferred to the cassette before loading into the TEM.

MicroED data were collected using a Thermo Fisher Glacios microscope operated at 200 kV and equipped with a Ceta-D camera. A low flux of ~0.075 e$^-$ Å^{-2} s^{-1} was achieved using the following illumination conditions: gun lens 8, spot size 11, 30 μm C2 aperture. This resulted in an illuminated area of 1.05 μm. Data were acquired using EPU-D with the following settings: 2x binning, a rotation speed of 1.33°/s and an exposure time of

0.75 s. For **2,3-[Au]-di-ZnP-C4**, datasets were collected from 14 crystals, for **2,3-[Au]-di-P-C4**, datasets were collected from 7 crystals.

All data were processed using DIALS.[7] The images recorded on the Ceta-D camera show mean negative background values at high resolution which hampers background modelling. A pedestal of 64 ADU (analog-to-digital units) was added to each individual pixel value. Initially the detector distance was fixed to 958.5 mm. This was determined by performing a camera length calibration using powder diffraction from an aluminium powder calibration grid. For **2,3-[Au]-di-ZnP-C4**, six datasets from six crystals were combined to give 94.8% complete data to 0.83 Å resolution. For **2,3-[Au]-di-P-C4**, 5 datasets from five crystals could be combined resulting in 91.7% complete data to 0.83 Å resolution. The strong reflections from each of the combined datasets were used to post-refine the detector distance and unit cell parameters of each dataset. The unit cell parameters for each of the combined datasets were then refined by fitting calculated to observed 2θ values.

The structures were solved *ab initio* using SHELXT.[8] Structure refinement was performed using SHELXL.[9] Electron scattering factors from Peng[10] were used in refinement. Anisotropic ADPs were refined for all non-hydrogen atoms and all hydrogen atoms were geometrically placed using the idealised (inter-nuclear) X-H distances used in refinement of structures against neutron diffraction data with SHELXL[11] and allowed to ride on their parent atoms. For refinement of both **2,3-[Au]-di-ZnP-C4** and **2,3-[Au]-di-P-C4**, a RIGU restraint was applied to all non-hydrogen atoms to improve the refinement. The RIGU instruction restrains the relative motion of a bonded pair of atoms to be perpendicular to the bond between them. For **2,3-[Au]-di-ZnP-C4**, additional instructions were required to prevent the ADPs of some atoms from becoming non-positive determinant during refinement. ISOR restraints were applied to carbon atoms 10 to 18 and a SIMU restraint was applied to carbon atoms 50 and 51. These restraints, together with refinement of an extinction parameter (EXTI instruction), enabled anisotropic refinement of all non-hydrogen atoms without using XNDP instructions to prevent ADPs of some atoms becoming non-positive determinant.

Accompanying data can be found at (https://bit.ly/3LpAm4d).

6.2 Synthesis and Complexation of the Pincer Ligands

4-[L]-OMe: 2,6-Bis(4-methoxyphenyl)pyridine
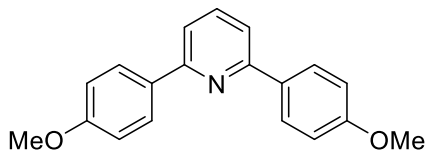
2,6-Dibromopyridine (12.21 g, 51.5 mmol) and 4-methoxyphenyl boronic acid (23.47 g, 154.5 mmol) were added to a flask containing $[Pd_3(OAc)_6]$ (65.0 mg, 0.5 mol%) and K_3PO_4 (32.80 g, 154.5 mmol). Ethylene glycol (400 mL) was added, and the reaction mixture heated to 80 °C for 1.5 hr with vigorous stirring. The reaction mixture was then cooled to room temperature and the produced solid was isolated by filtration and washed with water (200 mL), after which it was air dried. The resulting grey solid was dissolved in warm CH_2Cl_2 (~400 mL), filtered through Celite® and reduced to dryness. The solid crystalline, off-white residue was recrystallised from the minimum amount of hot ethanol to give the pure product as colourless crystals. Yield: 7.81 g (52%)

^{1}H NMR (400 MHz, CDCl$_3$) δ^H ppm: 8.11 (4H, AA'XX', J = 8.6 Hz), 7.74 (1H, t, J = 7.5 Hz), 7.57 (2H, d, J = 7.8 H), 7.02 (2H, AA'XX', J = 8.7 Hz), 3.88 (6H, s).

4-[L]-OH: 2,6-*Bis*(4-hydroxyphenyl)pyridine
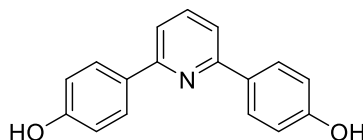
2,6-*Bis*(4-methoxyphenyl)pyridine (5.23 g, 18.0 mmol) was added to molten pyridinium chloride (26.85 g, 232.3 mmol) at 200 °C and stirred for 16 hr. The still molten mixture was added carefully to distilled water (350 mL) and the resulting yellow precipitate was isolated by filtration, air-dried and was used without further purification. Yield: 5.20 g (110%, product contaminated with water).

^{1}H NMR (400 MHz, d^6-DMSO) δ^H ppm: 9.85 (2H, s), 8.02 (4H, AA'XX', J = 8.3 Hz), 7.89 (1H, t, J = 8.8 Hz), 7.73 (2H, d, J = 7.8 H), 6.90 (4H, AA'XX', J = 8.8 Hz).

4-[L]: 2,6-Bis(4-dodecyloxyphenyl)pyridine
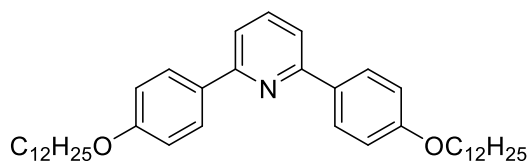
2,6-*Bis*(4-hydroxyphenyl)pyridine (5.20 g, 19.75 mmol), 1-bromododecane (11.9 mL, 12.31 g, 94.39 mmol) and K_2CO_3 (8.1783 g, 59.18 mmol) were heated to 90 °C in DMF (300 mL) for 16 hr. The reaction mixture was cooled to room temperature and the off-white solid was isolated by filtration, washed with water (300 mL) and acetone (60 mL) before being left to air dry. Yield: 7.00 g (59%)

^{1}H NMR (400 MHz, CDCl$_3$) δ^H ppm: 8.09 (4H, AA'XX', J = 9.0 Hz), 7.73 (1H, t, J = 8.2 Hz), 7.56 (2H, d, J = 7.8 H), 7.00 (2H, AA'XX', J = 8.9 Hz), 4.02 (4H, t, J = 6.0 Hz), 1.81 (4H, m), 1.46 (4H, m), 1.27 (32H, broad m), 0.88 (6H, t, $^3J_{HH}$ = 7.0 Hz).

^{13}C{^{1}H} NMR (125.8 MHz, CDCl$_3$) δ^C ppm: 160.01, 156.37, 137.22, 132.07, 128.15, 117.05, 114.57, 68.11, 31.92, 29.66, 29.63, 29.60, 29.58, 29.41, 29.35, 29.28, 26.05, 22.68, 14.11.

4-[Hg]: [Mercury(II)(2,6-*Bis*(4-dodecyloxyphenyl)pyridine)chloride]
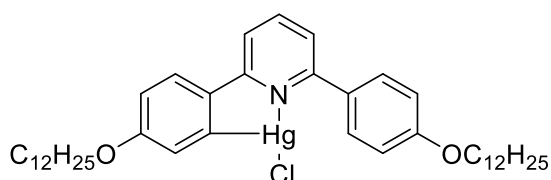
2,6-*Bis*(4-dodecyloxyphenyl)pyridine (7.00 g, 11.67 mmol) and Hg(OAc)$_2$ (7.40 g, 23.22 mmol) were added to ethanol (500 mL) and heated to vigorous reflux for 24 hr. The mixture was then cooled to 50 °C and a solution of LiCl (0.9893 g, 23.34 mmol) in methanol (50 mL) was added; the resulting mixture was allowed to stir for 15 min. Distilled water (200 mL) was added and the resulting solution cooled to room temperature, stirred overnight and filtered. The precipitate was washed with copious amounts of water and air-dried. The dried precipitate was dissolved in boiling CH$_2$Cl$_2$ (~200 mL) and filtered through Celite$^®$, after which the solvent was removed from the filtrate under reduced pressure. The solid residue was recrystallised from CHCl$_3$ and

acetone, the resulting free ligand precipitate removed *via* filtration and the filtrate concentrated *in vacuo* to give a colourless solid, which was used without further purification. (1.87 g, 77% estimated [Hg(C^N^CH)Cl]).

^{1}H NMR (500 MHz, CDCl$_3$) δ^H ppm: 7.88 (1H, d, $^3J_{HH}$ = 8.7 Hz), 7.85 (2H, AA'XX', *J* = 8.8 Hz), 7.78 (1H, dd, $^3J_{HH}$ = 7.7 Hz, $^3J_{HH}$ = 7.7 Hz), 7.64 (1H, d, $^3J_{HH}$ = 7.9 Hz), 7.59 (1H, d, $^3J_{HH}$ = 7.9 Hz), 7.07 (1H, d, $^4J_{HH}$ = 2.7 Hz), 7.02 (1H, d, $^3J_{HH}$ = 8.8 Hz), 6.93 (1H, dd, $^3J_{HH}$ = 8.7 Hz, $^4J_{HH}$ = 2.6 Hz), 4.03 (2H, t, $^3J_{HH}$ = 6.6 Hz), 4.02 (2H, t, $^3J_{HH}$ = 6.6 Hz), 1.82 (4H, m), 1.48 (4H, m), 1.4-1.2 (32H, br m), 0.89 (6H, t, $^3J_{HH}$ = 7.1 Hz), 0.89 (6H, t, $^3J_{HH}$ = 7.1 Hz).

^{13}C{^{1}H} NMR (125.8 MHz, CDCl$_3$) δ^C ppm: 160.27, 159.97, 157.66, 157.17, 149.83, 138.15, 135.65, 130.85, 129.05, 128.86, 123.23, 119.55, 118.35, 114.95, 130.85, 129.05, 128.86, 123.23, 119.55, 118.35, 114.95, 114.73, 68.29, 68.12, 31.91, 29.66, 29.63, 29.59, 29.57, 29.49, 29.38, 29.34, 29.26, 29.21, 26.05, 26.01, 22.68, 14.11.

^{199}Hg{^{1}H} NMR (89.6 MHz, CDCl$_3$) δ^{Hg} ppm: -1023.07
^{199}Hg NMR (89.6 MHz, CDCl$_3$) δ^{Hg} ppm: -1023.43 (d, $^3J_{HHg}$ = 234.8 Hz)

4-[Au]-Cl: [Gold(III)(2,6-*Bis*(4-dodecyloxyphenyl)pyridine)chloride]
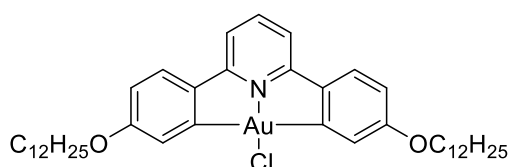
K[AuCl$_4$] (0.3930 g, 1.04 mmol) and the mixed **4-[Hg]** product (0.92 g, 84.5% estimated **4-[Hg]**) were heated in acetonitrile (400 mL) at reflux for 24 hr. The mixture was cooled to room temperature and distilled water (200 mL) was added and the resultant yellow precipitate isolated by filtration and washed with acetone (60 mL). The yellow solid was then treated with boiling hexane and the residual solid isolated by filtration, then purified further *via* column chromatography (CH$_2$Cl$_2$:petroleum ether (40-60 °C) 6:4, R_f = 0.67). The product was recrystallised from CH$_2$Cl$_2$ and ethyl acetate to give a yellow microcrystalline solid. Yield: 0.418 g (48%)

^{1}H NMR (400 MHz, CDCl$_3$) δ^H ppm: 7.70 (1H, t, $^3J_{HH}$ = 7.8 Hz), 7.44 (2H, s), 7.43 (2H, d, $^3J_{HH}$ = 8.5 Hz), 7.17 (2H, d, $^3J_{HH}$ = 8.0 Hz), 6.17 (2H, dd, $^3J_{HH}$ = 8.4 Hz, $^4J_{HH}$ = 2.7 Hz), 4.06 (4H, t, $^3J_{HH}$ = 6.6 Hz), 1.79 (4H, m), 1.47 (4H, m), 1.21 (32H, broad m), 0.88 (6H, t, $^3J_{HH}$ = 7.0 Hz).

^{13}C{^{1}H} NMR (125.8 MHz, CDCl$_3$) δ^C ppm: 172.24, 164.52, 161.75, 142.46, 139.48, 126.70, 118.42, 114.74, 113.78, 68.10, 31.92, 29.67, 29.66, 29.68, 29.65, 29.62, 29.60, 29.44, 29.36, 29.28, 26.05, 22.60, 14.12.

Elemental Analysis: Found (%): C 58.2, H 6.9, N 1.6; Calc (%) for C$_{41}$H$_{59}$AuClNO$_2$: C 59.3, H 7.2, N 1.7.

2-[L]-OMe: 2,6-*Bis*(2-methoxyphenyl)pyridine
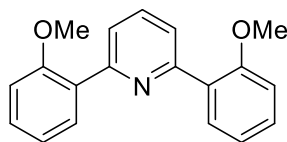
2,6-Dibromopyridine (12.20 g, 51.5 mmol) and 2-methoxyphenyl boronic acid (23.48 g, 154.5 mmol) were added to a flask containing [Pd$_3$(OAc)$_6$] (60.0 mg, 0.5 mol%) and K$_3$PO$_4$ (32.82 g, 154.5 mmol). Ethylene glycol (400 mL) was added, and the reaction mixture heated to 80 °C for 1.5 hr with vigorous stirring, then the reaction mixture was cooled to room temperature. The grey precipitated solid was recovered by filtration and washed with water (150 mL), after which it was air dried. The solid was dissolved in warm CH$_2$Cl$_2$ and filtered through Celite$^®$. The filtrate was collected and, following solvent removal, the crystalline solid, off-white residue was recrystallised from the minimum amount of hot ethanol to give the pure product as colourless needle-like crystals. Yield: 12.86 g (86%)

^{1}H NMR (400 MHz, CDCl$_3$) δ^H ppm: 7.97 (2H, dd, $^3J_{HH}$ = 7.6 Hz, $^4J_{HH}$ = 1.8 Hz), 7.77 (2H, m), 7.77 (1H, m), 7.39 (2H, ddd, $^3J_{HH}$ = 7.4 Hz, $^3J_{HH}$ = 8.3 Hz, $^4J_{HH}$ = 1.8 H), 7.12 (2H, ddd, $^3J_{HH}$ = 7.4 Hz, $^3J_{HH}$ = 8.3 Hz, $^4J_{HH}$ = 1.8 Hz), 7.03 (2H, dd, $^3J_{HH}$ = 8.3 Hz, $^4J_{HH}$ = 0.9 Hz), 3.89 (6H, s).

^{13}C{^{1}H} NMR (100.5 MHz, CDCl$_3$) δ^H ppm: 157.01, 155.32, 135.11, 131.42, 129.61, 129.46, 123.03, 120.97, 111.29, 55.54.

2-[L]-OH: 2,6-*Bis*(2-hydroxyphenyl)pyridine
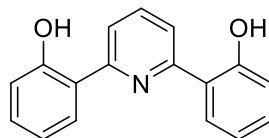
2,6-*Bis(*2-methoxyphenyl)pyridine (11.53 g, 39.57 mmol) was added to molten pyridinium chloride (64.90 g, 554.1 mmol) at 200 °C and stirred for 18 hr. The still molten mixture was carefully added to distilled water (350 mL) and the resulting beige precipitate was isolated by filtration, air-dried and was used without further purification. Yield: 10.25 g (93%)

^{1}H NMR (400 MHz, CDCl$_3$) δ^H ppm: 10.03 (2H, br s), 8.01 (1H, t, $^3J_{HH}$ = 8.3 Hz), 7.72 (2H, d, $^3J_{HH}$ = 8.3 Hz)), 7.72 (2H, d, $^3J_{HH}$ = 8.0 Hz), 7.69 (2H, dd, $^3J_{HH}$ = 7.8 Hz, $^4J_{HH}$ = 1.7 Hz), 7.36 (2H, ddd, $^3J_{HH}$ = 7.2 Hz, $^3J_{HH}$ = 8.2 Hz, $^4J_{HH}$ = 1.6 Hz), 7.03 (2H, d, $^3J_{HH}$ = 8.3 Hz, $^4J_{HH}$ = 0.8 Hz), 7.01 (2H, ddd, $^3J_{HH}$ = 8.0 Hz, $^3J_{HH}$ = 8.0 Hz, $^4J_{HH}$ = 0.8 Hz).

2-[L]: 2,6-*Bis*(2-dodecyloxyphenyl)pyridine
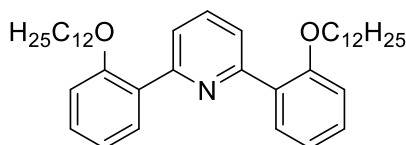
2,6-*Bis*(2-hydroxyphenyl)pyridine (10.10 g, 37.98 mmol), 1-bromododecane (17.25 mL, 23.66 g, 94.95 mmol) and K$_2$CO$_3$ (15.76 g, 113.9 mmol) were heated to reflux in 2-butanone (100 mL) for 67 hr, then filtered and reduced to dryness *in vacuo* to give an orange oil, which was crystallised from the minimum amount of hot methanol to give colourless plates. Yield: 3.47 g (64%)

^{1}H NMR (400 MHz, CDCl$_3$) δ^H ppm: 7.98 (2H, dd, $^3J_{HH}$ = 7.6 Hz, $^4J_{HH}$ = 1.8 Hz), 7.78 (2H, d, $^3J_{HH}$ = 7.6 Hz), 7.68 (1H, m), 7.33 (2H, ddd, $^3J_{HH}$ = 8.3 Hz, $^3J_{HH}$ = 7.4 Hz, $^4J_{HH}$ = 1.8 H), 7.06 (2H, ddd, $^3J_{HH}$ = 7.6 Hz, $^3J_{HH}$ = 7.6 Hz, $^4J_{HH}$ = 1.1 Hz), 6.99 (2H, dd, $^3J_{HH}$ = 8.4 Hz, $^4J_{HH}$ = 1.2 Hz), 4.03 (4H, t, $^3J_{HH}$ = 6.5 Hz), 1.79 (4H, m), 1.44 (4H, m), 1.35-1.15 (32H, br m), 0.88 (6H, t, $^3J_{HH}$ = 6.8 Hz)

^{13}C{^{1}H} NMR (100.5 MHz, CDCl$_3$) δ^{H} ppm: 156.69, 155.25, 134.82, 131.49, 129.59, 129.55, 123.02, 120.85, 112.46, 68.58, 31.91, 29.66, 29.63, 29.58, 29.56, 29.35, 29.32, 29.27, 26.13, 22.68, 14.11

ESI MS (m/z): Expected for C$_{41}$H$_{62}$NO$_2$ = 600.4775; Observed: 600.4759 [M + H]$^+$ (Error = 1.6 mDa)

2-[Hg]: [Mercury(II)(2,6-*Bis*(2-dodecyloxyphenyl)pyridine)chloride]
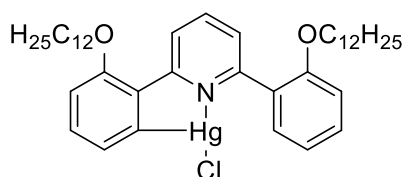
2,6-*Bis*(2-dodecyloxyphenyl)pyridine (12.39 g, 20.65 mmol) and Hg(OAc)$_2$ (13.53 g, 42.46 mmol) were added to ethanol (500 mL) and heated to vigorous reflux for 24 hr. The mixture was then cooled to 50 °C and a solution of LiCl (0.9893 g, 23.34 mmol) in methanol (50 mL) was added; the resulting mixture was allowed to stir for 15 min. Distilled water (200 mL) was added and the resulting solution cooled to room temperature and filtered. The precipitate (yellow solid/oil) was washed with copious amounts of water and a small amount of ethanol. The precipitate was dissolved in boiling CHCl$_3$ (~500 mL) and filtered through Celite®, after which the solvent was removed under reduced pressure to give the product as a very viscous pearlescent yellow oil. The residue was used without further purification. (~16 g, 86% estimated [Hg(C^N^CH)Cl]).

^{1}H NMR (400 MHz, CDCl$_3$) δ^{H} ppm: 8.13 (1H, dd, $^3J_{\mathrm{HH}}$ = 7.9 Hz, $^4J_{\mathrm{HH}}$ = 1.2 Hz), 7.82 (1H, dd, $^3J_{\mathrm{HH}}$ = 7.8 Hz, $^4J_{\mathrm{HH}}$ =1.1 Hz), 7.73 (1H, dd, $^3J_{\mathrm{HH}}$ = 7.6 Hz, $^3J_{\mathrm{HH}}$ = 7.6 Hz), 7.72 (1H, dd, $^3J_{\mathrm{HH}}$ = 7.6 Hz, $^4J_{\mathrm{HH}}$ = 2.0 Hz), 7.39 (1H, ddd, $^3J_{\mathrm{HH}}$ = 8.2 Hz, $^3J_{\mathrm{HH}}$ = 7.3 Hz, $^4J_{\mathrm{HH}}$ = 1.8 Hz), 7.38 (1H, dd, $^3J_{\mathrm{HH}}$ = 8.2 Hz, $^3J_{\mathrm{HH}}$ = 7.1 Hz), 7.04 (4H, m), 4.06 (2H, t, $^3J_{\mathrm{HH}}$ = 6.5 Hz), 4.03 (2H, t, $^3J_{\mathrm{HH}}$ = 6.5 Hz), 1.83 (2H, m), 1.74 (2H, m), 1.47 (2H, m), 1.4-1.1 (34 H, broad m), 0.88 (3H, t, $^3J_{\mathrm{HH}}$ = 7.1 Hz), 0.87 (3H, t, $^3J_{\mathrm{HH}}$ = 7.1 Hz).

^{13}C{^{1}H} NMR (125.8 MHz, CDCl$_3$) δ^{C} ppm: 158.28, 156.68, 155.83, 155.20, 153.53, 135.71, 132.22, 131.46, 130.13, 129.87, 129.55, 128.43, 124.16, 124.14, 120.86, 113.00, 112.65, 68.73, 68.56, 31.88, 29.65, 29.63, 29.61, 29.58, 29.54, 29.33, 29.28, 29.24, 29.22, 26.19, 26.17, 22.66, 14.10.

^{199}Hg NMR (89.6 MHz, CDCl$_3$) δ^{Hg} ppm: -1020 (dd, $^3J_{HHg}$ = 203.0 Hz, $^4J_{HHg}$ = 69.9 Hz).

R_f = 0.53 (CH$_2$Cl$_2$:petroleum ether (40 – 60 °C) 6:4)

2-[Au]-Cl: [Gold(III)(2,6-*Bis*(2-dodecyloxyphenyl)pyridine)chloride]
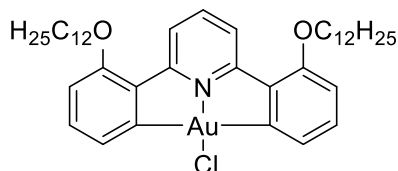
K[AuCl$_4$] (1.3211 g, 3.4971 mmol) and the mixed **2-[Hg]** product (2.92 g, 86.0% estimated **2-[Hg]**) were heated to reflux in acetonitrile (400 mL) under a dinitrogen atmosphere for 24 hr. Then the mixture was cooled to room temperature, distilled water (100 mL) added and filtered to isolate the product as a dirty yellow solid, which was purified *via* column chromatography (silica, CH$_2$Cl$_2$:petroleum ether (40 – 60 °C) 6:4, R_f = 0.71) to give a bright yellow crystalline solid, which was recrystallised from CH$_2$Cl$_2$ and ethyl acetate to give yellow, needle-like crystals. Yield: 1.1463 g (40%)

^{1}H NMR (400 MHz, CDCl$_3$) δ^H ppm: 8.19 (2H, d, $^3J_{HH}$ = 8.5 Hz), 7.74 (1H, t, $^3J_{HH}$ = 8.2 Hz), 7.51 (2H, dd, $^3J_{HH}$ = 7.2 Hz, $^4J_{HH}$ = 1.0 Hz), 7.34 (2H, dd, $^3J_{HH}$ = 8.3 Hz, $^3J_{HH}$ = 7.2 H), 6.72 (2H, dd, $^3J_{HH}$ = 8.4 Hz, $^4J_{HH}$ = 0.9 Hz), 4.05 (4H, t, $^3J_{HH}$ = 6.6 Hz), 1.90 (4H, quint, $^3J_{HH}$ = 7.1 Hz), 1.51 (4H, m), 1.30 (32H, m), 0.88 (6H, t, $^3J_{HH}$ = 6.7 Hz)

^{13}C{^{1}H} NMR (125.8 MHz, CDCl$_3$) δ^C ppm: 170.92, 164.14, 157.71, 142.42, 134.79, 132.09, 125.25, 121.62, 110.73, 68.36, 31.92, 29.67, 29.66, 29.61, 29.59, 29.40, 29.36, 29.13, 26.19, 22.69, 14.11.

APCI MS (m/z): Expected for C$_{41}$H$_{59}$AuClNO$_2$ = 830.39727; Observed: 830.400227 [M + H]$^+$ (Error = 2.9 mDa)

Elemental Analysis: Found (%): C 58.8, H 7.1, N 1.7; Calc (%) for C$_{41}$H$_{59}$AuClNO$_2$: C 59.3, H 7.2, N 1.7.

3-[L]-OMe: 2,6-*Bis*(3-methoxyphenyl)pyridine

MeO ⟶ ⟵ OMe
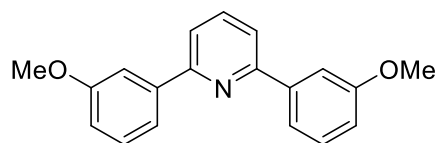
2,6-Dibromopyridine (12.20 g, 52.5 mmol) and 3-methoxyphenyl boronic acid (23.48 g, 154.5 mmol) were added to a flask containing [$Pd_2(OAc)_6$] (61.6 mg, 0.5 mol%) and K_3PO_4 (32.80 g, 154.5 mmol). Ethylene glycol (400 mL) was added, and the reaction mixture heated to 80 °C for 2 hr with vigorous stirring. The reaction mixture was cooled to room temperature and the black, tar-like solid was isolated by filtration and washed with water (150 mL), after which it was air dried. The resulting solid was dissolved in warm CH_2Cl_2 (~100 mL) and filtered through Celite®. The filtrate was collected and the solvent removed under reduced pressure to give an off-white solid, which was crystallized from the minimum amount of hot ethanol to give the pure product as white needle-like crystals. Yield = 13.29 g (89%)

^{1}H NMR (400 MHz, CDCl$_3$) δ^H ppm: 7.81 (1H, dd, $^3J_{HH}$ = 8.5 Hz, $^3J_{HH}$ = 7.2 Hz), 7.75 (2H, dd, $^4J_{HH}$ = 2.8 Hz, $^4J_{HH}$ = 1.6 Hz), 7.70 (2H, ddd, $^3J_{HH}$ = 7.8 Hz, $^4J_{HH}$ = 1.7 Hz, $^4J_{HH}$ = 0.9 Hz), 7.69 (2H, dd, J = 8.0 Hz, J = 7.6 Hz), 7.41 (2H, dd, $^3J_{HH}$ = 7.9 Hz, $^3J_{HH}$ = 7.9 Hz), 6.89 (2H, ddd, $^3J_{HH}$ = 8.3 Hz, $^4J_{HH}$ = 2.6 Hz, $^4J_{HH}$ = 0.9 Hz), 3.92 (6H, s).

^{13}C NMR (100.6 MHz, CDCl$_3$) δ^C ppm: 159.97, 1566.42, 140.88, 137.42, 129.62, 119.35, 118.87, 119.35, 114.60, 112.43, 55.29.

3-[L]-OH: 2,6-*Bis*(3-hyroxyphenyl)pyridine

HO ⟶ ⟵ OH
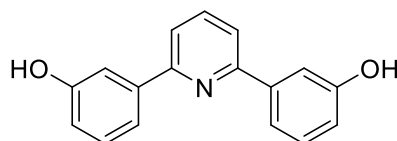
2,6-*Bis*(3-methoxyphenyl)pyridine (12.50 g, 42.90 mmol) was added to molten pyridinium chloride (62.35 g, 539.8 mmol) at 200 °C and stirred for 16 hours. The still molten mixture was added to distilled water (200 mL) and the resulting treacle-like dark brown oil was isolated by filtration and air-dried. It was used without further purification. Yield: 11.59 g (103%, product contaminated with water)

^{1}H NMR (400 MHz, DMSO-d$_6$) δ^H ppm: 9.65 (2H, br s), 7.92 (1H, dd, J = 8.5 Hz, J = 7.0 Hz), 7.82 (1H, d, J = 7.2 Hz), 7.82 (1H, d, J = 8.4 Hz), 7.63 (2H, dd, $^4J_{HH}$ = 2.5 Hz,

$^4J_{HH}$ = 1.6 Hz), 7.57 (2H, ddd, $^3J_{HH}$ = 7.8 Hz, $^4J_{HH}$ = 1.6 Hz, $^4J_{HH}$ = 1.1 Hz), 7.31 (2H, dd, $^3J_{HH}$ = 7.9 Hz, $^3J_{HH}$ = 7.9 Hz), 6.85 (2H, ddd, $^3J_{HH}$ = 8.0 Hz, $^4J_{HH}$ = 2.5 Hz, $^4J_{HH}$ = 1.2 Hz).

3-[L]: 2,6-*Bis*(3-dodecyloxyphenyl)pyridine
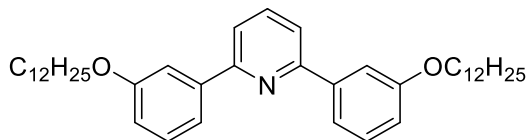
2,6-*Bis*(3-hydroxyphenyl)pyridine (11.30 g, 26.18 mmol), 1-bromododecane (48 mL, 65.28 g, 261.9 mmol) and K_2CO_3 (57.89 g, 418.9 mmol) were heated to reflux in 2-butanone (500 mL) for 21 hr, then cooled to room temperature and filtered to isolate a brown filtrate. On reduction to dryness to a brown oil was achieved, which was purified *via* column chromatography (silica, petroleum ether (40-60 °C), R_f = 0.00, then CH_2Cl_2, R_f = 0.91) to give a yellow oil, which solidified on standing. The product was recrystallised from hot ethanol to give small pale yellow needle-like crystals, which were filtered, washed with ethanol and air dried. Yield: 15.23 g (97%)

^{1}H NMR (400 MHz, CDCl$_3$) δ^H ppm: 7.80 (1H, dd, J = 8.4 Hz, J = 7.1 Hz), 7.73 (2H, dd, $^4J_{HH}$ = 2.6 Hz, $^4J_{HH}$ = 1.6 Hz), 7.69 (2H, ddd, $^3J_{HH}$ = 7.7 Hz, $^4J_{HH}$ = 1.7 Hz, $^4J_{HH}$ = 1.0 Hz), 7.68 (2H, dd, J = 7.4 Hz, J = 8.3), 7.39 (2H, dd, $^3J_{HH}$ = 8.0 Hz, $^3J_{HH}$ = 8.0 Hz), 6.87 (2H, ddd, $^3J_{HH}$ = 8.2 Hz, $^4J_{HH}$ = 2.6 Hz, $^4J_{HH}$ = 1.0 Hz), 4.07 (4H, $^3J_{HH}$ = 6.5 Hz), 1.83 (4H, m), 1.49 (4H, m), 1.4-1.2 (32H, br m), 0.88 (6H, t, $^3J_{HH}$ = 6.9 Hz).

^{13}C{^{1}H} NMR (100.6 MHz, CDCl$_3$) δ^C ppm: 159.53, 159.52, 140.84, 137.32, 129.54, 11.17, 118.79, 115.16, 113.06, 68.01, 31.89, 29.66, 29.62, 29.60, 29.59, 29.51, 29.43, 29.33, 26.07, 22.66, 14.08.

3-[Hg]: [Mercury(II)(2,6-*Bis*(3-dodecyloxyphenyl)pyridine)chloride] and 5-[Hg]: [Mercury(II)(2,6-*Bis*(5-dodecyloxyphenyl)pyridine)chloride]
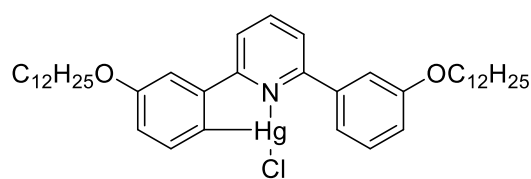
3-[Hg]
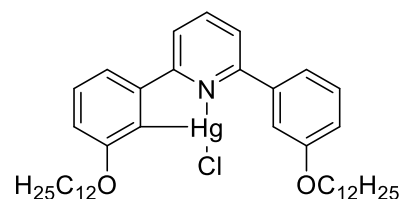
5-[Hg]

2,6-*Bis*(3-dodecyloxyphenyl)pyridine (7.00 g, 11.67 mmol) and Hg(OAc)$_2$ (7.41 g, 23.25 mmol) were added to ethanol (500 mL) and heated to a vigorous reflux for 24 hr. The reaction mixture was cooled to 50 °C and a solution of LiCl (0.9908 g, 23.37 mmol) in methanol (50 mL) was added; the resulting mixture was allowed to stir for 15 min. Distilled water (200 mL) was added and the resulting solution cooled to room temperature and filtered. The resulting sticky grey/green solid was washed with copious amounts of water, a small amount of ethanol and air-dried. Yield: 9.74 g (77% estimated [Hg(C^N^CH)Cl]) (82.8%)

The two isomers were present in a 1:0.72 ratio by ^{1}H NMR spectroscopy.

3-[Hg]:

^{1}H NMR (400 MHz, CDCl$_3$) δ^H ppm: 7.87 (1H, dd, $^3J_{HH}$ = 7.9 Hz, $^3J_{HH}$ = 7.9 Hz), 7.75 (1H, dd, $^3J_{HH}$ = 8.0 Hz, $^4J_{HH}$ = 0.9 Hz), 7.72 (1H, dd, $^3J_{HH}$ = 7.8 Hz, $^4J_{HH}$ = 1.0 Hz), 7.49 (1H, d, $^3J_{HH}$ = 2.6 Hz), 7.47 (1H, dd, $^4J_{HH}$ = 1.5 Hz, $^4J_{HH}$ = 1.5 Hz), 7.42 (3H, m), 7.02 (1H, ddd, $^3J_{HH}$ = 8.2 Hz, $^4J_{HH}$ = 2.4 Hz, $^4J_{HH}$ = 1.0 Hz), 7.02 (1H, d, $^3J_{HH}$ = 8.2 Hz), 4.07 (2H, t, $^3J_{HH}$ = 6.7 Hz), 4.05 (2H, t, $^3J_{HH}$ = 6.5 Hz), 1.802(4H, m), 1.49 (4H, m), 1.4 – 1.2 (32H, br m), 0.88 (3H, t, $^3J_{HH}$ = 6.9 Hz), 0.88 (3H, t, $^3J_{HH}$ = 6.8 Hz).

^{13}C{^{1}H} NMR (100.6 MHz, CDCl$_3$) δ^C ppm: 159.78, 159.53, 157.91, 157.49, 144.72, 140.07, 139.63, 138.39, 138.34, 129.73, 121.10, 120.01, 119.92, 115.80, 115.09, 115.06, 113.58, 68.21, 68.13, 31.91, 29.66, 29.62, 29.59, 39.57, 29.45, 29.37, 29.34, 29.24, 26.08, 26.03, 22.67, 14.11.

[199]Hg{^{1}H} NMR (89.6 MHz, CDCl$_3$) δ^{Hg} ppm: -991.09

^{199}Hg NMR (89.6 MHz, CDCl$_3$) δ^{Hg} ppm: -991.17 (d, $^3J_{HHg}$ = 190.8 Hz)

R_f = 0.44 (1:1 CH$_2$Cl$_2$:petroleum ether (40 – 60 °C)

5-[Hg]:

^{1}H NMR (400 MHz, CDCl$_3$) δ^H ppm: 7.86 (1H, dd, $^3J_{HH}$ = 7.8 Hz, $^3J_{HH}$ = 7.8 Hz), 7.78 (1H, dd, $^3J_{HH}$ = 8.0 Hz, $^4J_{HH}$ = 1.0 Hz), 7.71 (1H, dd, $^3J_{HH}$ = 7.6 Hz, $^4J_{HH}$ = 1.2 Hz), 7.58 (1H, d, $^3J_{HH}$ = 6.8 Hz), 7.51 (1H, ddd, $^3J_{HH}$ = 7.7 Hz, $^4J_{HH}$ = 1.6 Hz, $^4J_{HH}$ = 1.6 Hz), 7.44 (1H, dd, $^4J_{HH}$ = 2.6 Hz, $^4J_{HH}$ = 2.6 Hz), 7.42 (1H, dd, $^3J_{HH}$ = 7.8 Hz, $^3J_{HH}$ = 7.8 Hz), 7.41 (1H, dd, $^3J_{HH}$ = 7.8 Hz, $^3J_{HH}$ = 7.8 Hz), 7.02 (1H, ddd, $^3J_{HH}$ = 8.2 Hz, $^4J_{HH}$ = 2.8 Hz, $^4J_{HH}$ = 1.0 Hz), 7.00 (1H, dd, $^3J_{HH}$ = 7.2 Hz, $^4J_{HH}$ = 1.0Hz), 4.08 (2H, t, $^3J_{HH}$ = 6.5 Hz), 4.03 (2H, t, $^3J_{HH}$ = 6.4 Hz), 1.80 (4H, m), 1.47 (4H, m), 1.4 – 1.2 (32H, br m), 0.88 (3H, t, $^3J_{HH}$ = 6.9 Hz), 0.87 (3H, t, $^3J_{HH}$ = 6.9 Hz).

^{13}C{^{1}H} NMR (100.6 MHz, CDCl$_3$) δ^C ppm: 161.69, 159.50, 157.91, 157.13, 144.40, 139.75, 138.21, 137.95, 130.57, 129.73, 121.02, 120.28, 120.04, 119.97, 115.67, 113.82, 112.06, 68.59, 68.12, 13.91, 29.67, 29.63, 29.61, 29.56, 29.45, 29.37, 29.35, 29.25, 26.08, 22.68, 14.11.

^{199}Hg{^{1}H} NMR (89.6 MHz, CDCl$_3$) δ^{Hg} ppm: -993.39

R_f = 0.5 (4:6 CH$_2$Cl$_2$:petroleum ether (40 – 60 °C)), 0.56 (1:1 CH$_2$Cl$_2$:petroleum ether (40 – 60 °C), 0.72 (CH$_2$Cl$_2$:petroleum ether (40 – 60 °C) 6:4).

APCI MS (m/z): Expected for C$_{41}$H$_{60}$ClHgNO$_2$ = 835.40; Observed: 836.4126 [M + H]$^+$

3/5-[Au]-Cl:[Gold(III)((2-(3-dodecyloxyphenyl)-6-(5'-dodecyloxyphenyl))pyridine)chloride]
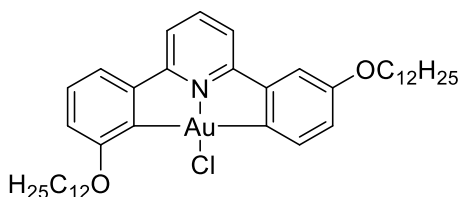
Na[AuCl$_4$] (1.1805 g, 2.9676 mmol) and the mixed **3-[Hg]** and **5-[Hg]** product (3.04 g, 77.4% estimated [Hg(C^N^CH)Cl])) were heated to reflux in acetonitrile (400 mL) under a dinitrogen atmosphere for 24 hr. The reaction mixture was cooled to room temperature and the resulting dirty yellow/white precipitate isolated by filtration and washed with ethanol. The product was dissolved in CH$_2$Cl$_2$ (74 mL) and filtered through Celite$^\circledR$ to remove solid gold(0). After reduction to dryness the crude product was purified *via* column chromatography (silica, CH$_2$Cl$_2$:petroleum ether (40 – 60 °C) 4:6, then CH$_2$Cl$_2$:petroleum ether (40 – 60 °C) 6:4) , followed by a second column to give two products: a pale yellow crystalline solid, which on recrystallisation from CH$_2$Cl$_2$/ethyl acetate gave a white crystalline solid identified as **5-[Hg]**, and a yellow crystalline solid, identified as **3/5-[Au]-Cl**.

3/5-[Au]-Cl was purified further *via* column chromatography (silica, then CH$_2$Cl$_2$:petroleum ether (40 – 60 °C) 6:4, R_f = 0.5) twice, then recrystallised from CH$_2$Cl$_2$/ethyl acetate to give a yellow microcrystalline solid. Yield: 0.4964 g (20%)

^{1}H NMR (400 MHz, CDCl$_3$) δ^H ppm: 7.76 (1H, dd, $^3J_{HH}$ = 7.9 Hz, $^3J_{HH}$ = 7.9 Hz), 7.70 (1H, d, $^3J_{HH}$ = 9.8 Hz), 7.34 (1H, dd, $^3J_{HH}$ = 8.2 Hz, $^4J_{HH}$ = 1.2 Hz), 7.29 (1H, dd, $^3J_{HH}$ = 8.1 Hz, $^4J_{HH}$ = 1.0 Hz), 7.10 (1H, dd, $^3J_{HH}$ = 7.7 Hz, $^3J_{HH}$ = 7.7 Hz), 7.05 (1H, dd, $^3J_{HH}$ = 7.8 Hz, $^4J_{HH}$ = 1.5 Hz), 6.90 (1H, dd, $^3J_{HH}$ = 7.9 Hz, $^4J_{HH}$ = 1.4 Hz), 6.85 (2H, m), 3.93 (2H, t, $^3J_{HH}$ = 6.6 Hz), 3.85 (2H, t, $^3J_{HH}$ = 6.4 Hz), 1.92 (2H, m), 1.73 (2H, m), 1.4 – 1.2 (32H, br m), 0.88 (3H, t, $^3J_{HH}$ = 6.9 Hz), 0.87 (3H, t, $^3J_{HH}$ = 4.8 Hz).

^{13}C{^{1}H} NMR (100.6 MHz, CDCl$_3$) δ^C ppm: 165.27, 164.08, 163.26, 159.25, 158.63, 158.46, 148,59, 147.71, 142.40, 132.88, 128.16, 117.93, 117.51, 117.27, 116.75, 116.26, 111.14, 69.14, 67.96, 31.93, 31.92, 29.72, 29.69, 29.65, 29.63, 29.49, 29.38, 29.36, 29.29, 29.23, 26.32, 26.02, 22.69, 14.12.

R_f = 0.07 (CH$_2$Cl$_2$:petroleum ether (40 – 60 °C) 4:6), 0.5 (6:4 CH$_2$Cl$_2$:petroleum ether (40 – 60 °C)).

APCI MS (m/z): Expected for C$_{41}$H$_{59}$AuClNO$_2$ = 830.3973; Observed: 830.3982 [M + H]$^+$ (Error = -0.9 mDa)

Elemental Analysis: Found (%): C 58.7, H 6.9, N 1.3; Calc (%) for C$_{54}$H$_{74}$AuNO$_2$: 59.3, H 7.2, N 1.7. (Carbon is 0.6% out.)

3,4-[L]-OMe: 2,6-*Bis*(3,4-dimethoxyphenyl)pyridine
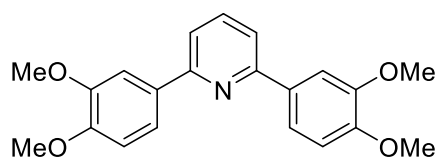
2,6-Dibromopyridine (6.75 g, 28.46 mmol) and 3,4-dimethoxyphenyl boronic acid (15.55 g, 85.37 mmol) were added to a flask containing [Pd$_3$(OAc)$_6$] (24.7 mg, 0.5 mol%) and K$_3$PO$_4$ (18.19 g, 85.37 mmol). Ethylene glycol (200 mL) was added, and the reaction mixture heated to 80 °C for 1.5 hr with vigorous stirring. The reaction mixture was cooled to room temperature, isolated by filtration and washed with water (150 mL), after which it was air dried. The resulting grey solid was dissolved in warm CH$_2$Cl$_2$ (~75 mL) and filtered through Celite®. The filtrate was collected and the solvent removed under reduced pressure. The solid, off-white residue was recrystallised from the minimum amount of hot ethanol to give the pure product as colourless needle-like crystals. Yield: 9.20 g (92%)

^{1}H NMR (400 MHz, CDCl$_3$) δ^H ppm: 8.84 (2H, d, $^4J_{HH}$ = 2.0 Hz), 7.75 (1H, t, $^3J_{HH}$ = 8.1 Hz), 7.65 (2H, dd, $^3J_{HH}$ = 8.0 Hz, $^4J_{HH}$ = 2.0 Hz), 7.60 (2H, d, $^3J_{HH}$ = 7.9 Hz), 6.98 (2H, d, $^3J_{HH}$ = 8.4 Hz), 4.01 (6H, s), 3.95 (6H, s).

3,4-[L]-OH: 2,6-*Bis*(3,4-dihydroxyphenyl)pyridine
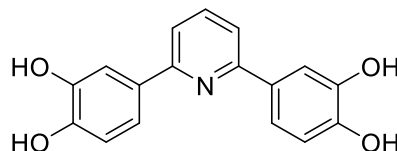
2,6-*Bis*(3,4-dimethoxyphenyl)pyridine (12.78 g, 36.37 mmol) was added to molten pyridinium chloride (53.93 g, 466.68 mmol) at 200 °C and stirred for 16 hr. The still molten mixture was carefully added to distilled water (350 mL) and the resulting bright

yellow precipitate was isolated by filtration, air-dried, and was used without further purification. Yield: ~10 g (product heavily contaminated with water).

^{1}H NMR (400 MHz, d^6-DMSO) δ^H ppm: 9.20 (4H, s), 7.82 (1H, t, $^3J_{HH}$ = 8.2 Hz), 7.64 (2H, d, $^4J_{HH}$ ~ 2.0 Hz), 7.63 (2H, d, $^3J_{HH}$ ~ 7.8 Hz), 7.55 (2H, dd, $^3J_{HH}$ = 8.2 Hz, $^4J_{HH}$ = 2.0 H), 6.85 (2H, d, $^3J_{HH}$ = 8.3 Hz).

3,4-[L]: 2,6-*Bis*(3,4-didodecyloxyphenyl)pyridine
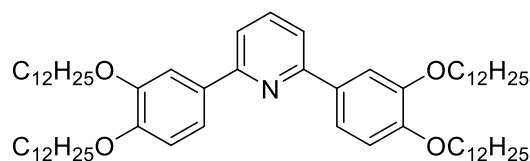
2,6-*Bis*(3,4-dihydroxyphenyl)pyridine (10 g, 4 mmol), 1-bromododecane (54.0 mL, 56.05 g, 224.9 mmol), K_2CO_3 (58.67 g, 424.5 mmol) were heated to 90 °C in DMF (400 mL) for 16 hr. The reaction mixture was cooled to room temperature and the solid precipitate isolated by filtration, washed with water (700 mL) and acetone (160 mL) and left to air dry to give a tan solid. Crude recrystallisation from hot ethanol, then filtered and washed with ethanol, distilled water (200 mL) and acetone (60 mL) to give an off-white solid. Subsequently the product was recrystallised from hot ethanol, filtered and washed with ethanol and acetone (60 mL) to give an off-white solid, then finally recrystallised from hot CH_2Cl_2 and ethanol to give small off-white needle-like crystals. Yield: 22.42 g (69%)

^{1}H NMR (400 MHz, CDCl$_3$) δ^H ppm: 7.80 (2H, d, $^4J_{HH}$ = 2.1 Hz), 7.72 (1H, t, $^3J_{HH}$ = 8.2 Hz), 7.62 (2H, dd, $^3J_{HH}$ = 8.4 Hz, $^4J_{HH}$ = 2.0 Hz), 7.56 (2H, d, $^3J_{HH}$ = 7.8 Hz), 6.97 (2H, d, $^3J_{HH}$ = 8.4 Hz), 4.12 (4H, t, $^3J_{HH}$ = 6.6 Hz), 4.06 (4H, t, $^3J_{HH}$ = 6.7 Hz), 1.85 (8H, m), 1.49 (8H, m), 1.27 (64H, broad m), 0.87 (6H, t, $^3J_{HH}$ = 7.0 Hz), 0.87 (6H, t, $^3J_{HH}$ = 7.0 Hz).

^{13}C{^{1}H} NMR (100.6 MHz, CDCl$_3$) δ^C ppm: 156.23, 150.10, 149.17, 137.18, 132.49, 119.55, 117.28, 113.38, 112.52, 69.23, 69.19, 31.91, 29.72, 29.69, 29.66, 29.63, 29.49, 29.37, 29.25, 26.11, 2602, 22.68, 14.11.

3,4-[Hg]: [Mercury(II)(2,6-*Bis*(3,4-didodecyloxyphenyl)pyridine)chloride]
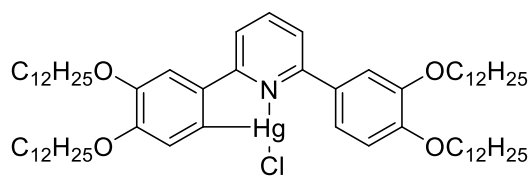
2,6-*Bis*(3,4-dodecyloxyphenyl)pyridine (0.50 g, 0.52 mmol) and $Hg(OAc)_2$ (0.60 g, 1.88 mmol) were added to ethanol (150 mL) and heated to vigorous reflux for 24 hr. The resulting solution was then cooled to 50 °C and a solution of LiCl (0.0803 g, 1.8941 mmol) in methanol (50 mL) was added. The resulting mixture was allowed to stir for 15 min. Distilled water (50 mL) was added and the resulting solution cooled to room temperature and filtered. The off-white precipitate was washed with copious amounts of water, a small amount of ethanol and air-dried. Yield: 0.46 g (37%)

^{199}Hg NMR (89.6 MHz, $CDCl_3$) δ^{Hg} ppm: -998.63

2,3-[L]-OMe: 2,6-*Bis*(2,3-dimethoxyphenyl)pyridine
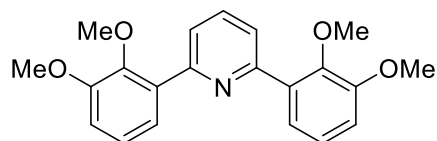
2,6-Dibromopyridine (6.74 g, 28.46 mmol) and 2,3-dimethoxyphenyl boronic acid (15.54 g, 85.37 mmol) were added to a flask containing $[Pd_2(OAc)_6]$ (22.0 mg, 0.5 mol%) and K_3PO_4 (18.12 g, 85.37 mmol). Ethylene glycol (200 mL) was added, and the reaction mixture heated to 80 °C for 2 hr with vigorous stirring. The reaction mixture was cooled to room temperature, and the solid precipitate isolated by filtration and washed with water (150 mL), after which it was air dried. The resulting grey solid was dissolved in warm CH_2Cl_2 (~50 mL) and filtered through Celite® and reduced to dryness. The cubic crystalline, off-white residue was recrystallised from the minimum amount of hot ethanol to give the pure product as white broad rectangular crystals. Yield: 8.91 g (89.1%)

^{1}H NMR (400 MHz, $CDCl_3$) δ^H ppm: 7.81 (3H, m), 7.51 (2H, dd, $^3J_{HH}$ = 7.9 Hz, $^4J_{HH}$ = 1.6 Hz), 7.17 (2H, dd, $^3J_{HH}$ = 8.0 Hz, $^3J_{HH}$ = 8.0 Hz), 6.97 (2H, d, $^3J_{HH}$ = 8.2 Hz, $^4J_{HH}$ = 1.5 Hz),), 3.92 (6H, s), 3.72 (6H, s).

^{13}C{^{1}H} NMR (100.5 MHz, $CDCl_3$) δ^H ppm: 155.23, 152.97, 147.20, 136.02, 134.59, 124.18, 123.02, 122.88, 112.46, 60.97, 55.92.

2,3-[L]-OH: 2,6-*Bis*(2,3-dihydroxyphenyl)pyridine
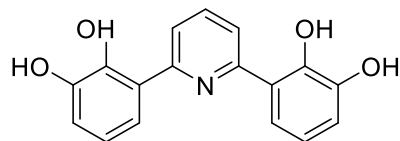
2,6-*Bis*(2,3-dimethoxyphenyl)pyridine (8.50 g, 24.19 mmol) was added to molten pyridinium chloride (38.93 g, 336.9 mmol) at 200 °C and stirred for 16 hr. The still molten mixture was added carefully to distilled water (350 mL) and the resulting mustard yellow precipitate was isolated by filtration, air-dried and used without further purification. Yield: 6.42 g (90%).

^{1}H NMR (400 MHz, CDCl$_3$) δ^H ppm: ~10.18 (2H, s br), 8.01 (1H, t, $^3J_{HH}$ = 8.2 Hz), 7.75 (2H, d, $^3J_{HH}$ = 8.0 Hz), 7.25 (2H, dd, $^3J_{HH}$ ~ 8 Hz, $^4J_{HH}$ = 1.4 Hz), 7.04 (2H, dd, $^3J_{HH}$ = 7.8 Hz, $^4J_{HH}$ = 1.4 Hz), 6.93 (2H, dd, $^3J_{HH}$ = 8.0 Hz, $^3J_{HH}$ = 7.9 Hz), 5.78 (2H, s br).

2,3-[L]: 2,6-*Bis*(2,3-didodecyloxyphenyl)pyridine
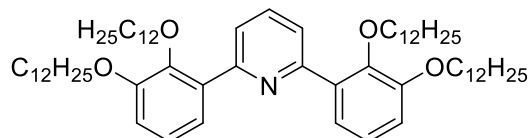
2,6-*Bis*(2,3-dihydroxyphenyl)pyridine (6.40 g, 21.33 mmol), 1-bromododecane (32.4 mL, 33.63 g, 134.9 mmol) and K$_2$CO$_3$ (47.21 g, 138.3 mmol) were heated to reflux in 2-butanone (200 mL) for 144 hr, then filtered and reduced to dryness *in vacuo* to give an orange oil, which solidified to a brown solid, which was crystallised from the minimum amount of hot methanol to give a red-brown solid. The product was purified *via* column chromatography (silica, 95:5 petroleum ether (40-60 °C):ethyl acetate, R_f = 0.35) to give an orange oil, which solidified on standing to give an off-white solid. The product was crystallised from hot hexane/ethyl acetate twice to give a white crystalline solid. Yield: 13.42 g (64%)

^{1}H NMR (400 MHz, CDCl$_3$) δ^H ppm: 7.83 (2H, d, $^3J_{HH}$ = 7.7 Hz), 7.70 (1H, m), 7.47 (2H, dd, $^3J_{HH}$ = 7.8 Hz, $^4J_{HH}$ = 1.3 Hz), 7.12 (2H, dd, $^3J_{HH}$ = 8.2 Hz, $^3J_{HH}$ = 8.2 Hz), 6.94 (2H, dd, $^3J_{HH}$ = 7.9 Hz, $^4J_{HH}$ = 1.3 Hz), 4.02 (4H, t, $^3J_{HH}$ = 6.5 Hz), 3.80 (4H, t, $^3J_{HH}$ = 6.6 Hz),

1.86 (4H, m), 1.59 (4H, m), 1.51 (4H, m), 1.27 (68H, broad m), 0.88 (6H, t, $^3J_{HH}$ = 7.2 Hz), 0.88 (6H, t, $^3J_{HH}$ = 7.0 Hz).

^{13}C{^{1}H} NMR (100.6 MHz, CDCl$_3$) δ^C ppm: 155.45, 152.59, 146.57, 135.28, 135.11, 123.93, 123.34, 122.69, 113.37, 73.77, 68.68, 31.91, 30.19, 29.71, 29.70, 26.69, 29.68, 29.66, 29.63, 29.52, 29.45, 29.36, 29.17, 26.03, 22.67, 14.10.

2,3-[Hg$_2$]: [Dimercury(II)(2,6-*Bis*(2,3-didodecyloxyphenyl)pyridine)dichloride]
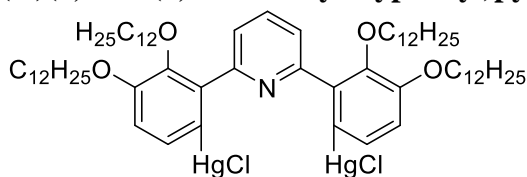
2,6-*Bis*(2,3-dodecyloxyphenyl)pyridine (4.02 g, 4.15 mmol) and Hg(OAc)$_2$ (2.92 g, 9.19 mmol) were added to ethanol (500 mL) and heated to vigorous reflux for 24 hr. The reaction mixture was cooled to 50 °C and a solution of LiCl (0.3526 g, 8.3172 mmol) in methanol (50 mL) was added; the resulting mixture was allowed to stir for 15 min. Distilled water (200 mL) was added and the resulting solution cooled to room temperature and filtered. The resulting white precipitate was filtered, washed with copious amounts of water and air-dried. Yield = 4.45 g (75%)

^{1}H NMR (400 MHz, CDCl$_3$) δ^H ppm: 8.12 (2H, d, $^3J_{HH}$ = 7.9 Hz), 7.79 (1H, t, $^3J_{HH}$ = 8.1 Hz), 7.11 (2H, d, $^3J_{HH}$ = 8.0 Hz), 7.01 (2H, m), 4.05 (4H, t, $^3J_{HH}$ = 6.3 Hz), 3.90 (4H, broad m), 1.88 (4H, m), 1.55 (4H, m), 1.42-1.18 (72H, broad m), 0.88 (6H, t, $^3J_{HH}$ = 6.4 Hz), 0.87 (6H, t, $^3J_{HH}$ = 7.3 Hz).

^{13}C{^{1}H} NMR (100.6 MHz, CDCl$_3$) δ^C ppm: 157.13, 153.19, 148.04, 137.35, 136.67, 132.38, 125.47, 113.93, 74.41, 68.60, 31.92, 31.90, 30.32, 29.71, 29.67, 29.65, 29.51, 29.43, 29.40, 29.37, 29.34, 26.18, 26.15, 22.68, 14.11.

^{199}Hg NMR (89.6 MHz, CDCl$_3$) δ^{Hg} ppm: -1012 (d, $^3J_{HHg}$ = 154.1 Hz)
ACPI MS: m/z = 968.8454 [ligand], 1204.7689 [M+H]$^+$, 1438.7045 [M+H$^+$], 2334.5929 [Dimer]

Elemental Analysis: Found (%): C 53.5, H 7.4, N 1.2; Calc (%) for $C_{65}H_{107}Cl_2Hg_2NO_4$: C 54.3, H 7.5, N 1.0. Formally impure (further purification was not undertaken), but confirms assignment as dimercurated complex.

2,3-[Au]-Cl: [Gold(III)(2,6-*Bis*(2,3-didodecyloxyphenyl)pyridine)chloride]
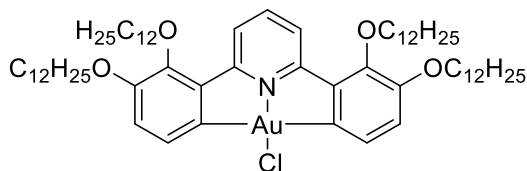
Na[AuCl$_4$] (1.4678 g, 3.6898 mmol) and **2,3-[Hg$_2$]** (4.50 g, 3.1279 mmol) were heated to reflux in 1:1 chloroform:acetonitrile (400 mL) under nitrogen for 24 hr. The reaction mixture was cooled to room temperature and reduced to dryness under reduced pressure, then extracted into acetonitrile (50 mL) and the insoluble solid isolated by filtration. The brown solid was washed sequentially with distilled water (50 mL) and ethanol (25 mL), dried *in vacuo* and crystallised from CH_2Cl_2. The resulting dirty yellow solid was isolated by filtration, washed with ethyl acetate and then redissolved in CH_2Cl_2 and a hot filtrate was done to give a yellow solid on solvent removal, which was recrystallised from chloroform/hexane to give the titular product as a microcrystalline yellow solid. Yield: 1.041 g (24%)

^{1}H NMR (400 MHz, CDCl$_3$) δ^H ppm: 8.31 (2H, d, $^3J_{HH}$ = 8.3 Hz), 7.84 (1H, t, $^3J_{HH}$ = 8.4 Hz), 7.55 (2H, d, $^3J_{HH}$ = 8.4 Hz), 7.01 (2H, d, $^3J_{HH}$ = 7.9 Hz), 4.08 (4H, t, $^3J_{HH}$ = 6.8 Hz), 3.98 (4H, t, $^3J_{HH}$ = 6.4 Hz), 1.83 (8H, m), 1.54-1.19 (72H, broad m), 0.88 (6H, t, $^3J_{HH}$ = 5.9 Hz), 0.88 (6H, t, $^3J_{HH}$ = 6.5 Hz).

^{13}C{^{1}H} NMR (125.8 MHz, CDCl$_3$) δ^C ppm: 164.45, 160.42, 151.62, 148.31, 142.72, 140.14, 128.31, 122.08, 116.53, 73.40, 68.86, 31.92, 30.37, 29.70, 29.66, 29.65, 29.55, 29.45, 29.37, 26.23, 26.10, 22.69, 14.11.

APCI MS (m/z): Expected for $C_{78}H_{122}AuNO_4$ = 1198.7627; Observed: 1198.7565 [M + H]$^+$ (Error = -5.2 mDa)

Elemental Analysis: Found (%): C 70.0, H 9.1, N 0.9; Calc (%) for $C_{78}H_{122}AuNO_4$: C 70.2, H 9.2, N 1.1.

Attempted Synthesis of [Dimercury(II)(2,6-*Bis*(2,3-dimethoxyphenyl)pyridine)dichloride]

MeO OMe / MeO OMe / N / HgCl HgCl
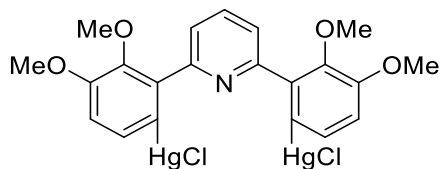
2,6-*Bis*(2,3-methoxyphenyl)pyridine (0.0853 g, 0.2427 mmol) and Hg(OAc)$_2$ (0.17 g, 0.5335 mmol) were added to ethanol (200 mL) and heated to vigorous reflux for 24 hr, then cooled to 50 °C and a solution of LiCl (0.0215 g, 0.5071 mmol) in methanol (50 mL) added. The resulting mixture was allowed to stir for 15 minutes, then distilled water (200 mL) was added and the resulting solution cooled to room temperature and filtered. The white precipitate was washed with copious amounts of water and air-dried. Yield = 0.0652 g (32.6%)

Elemental Analysis: Found (%): C 30.70, H 1.550, N 1.087; Calc (%) for C$_{21}$H$_{19}$Cl$_2$Hg$_2$NO$_4$: C 30.7, H 2.3, N 1.7.

Product unable to be identified from ^{1}H NMR or elemental analysis.

2,3-[L]-C4: 2,6-*Bis*(2,3-dibutoxyphenyl)pyridine

H$_9$C$_4$O OC$_4$H$_9$ / C$_4$H$_9$O OC$_4$H$_9$ / N
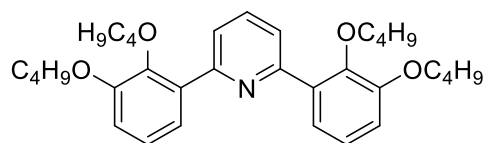
2,6-*Bis*(2,3-dihydroxyphenyl)pyridine (1.4083 g, 4.7692 mmol), 1-bromobutane (9.5 mL, 12.12 g, 88.47 mmol) and K$_2$CO$_3$ (10.23 g, 74.02 mmol) were heated to reflux in 2-butanone (100 mL) for 89 hr. Then the resulting solution was filtered, washed with acetone (50 mL) and reduced to dryness *in vacuo* to give an orange oil. The product was purified *via* column chromatography (silica, 95:5 petroleum ether (40-60 °C):ethyl acetate, R_f = 0.23) to give an orange oil, then on application of a second column to give a viscous yellow oil. Yield: 1.165 g (53%)

^{1}H NMR (400 MHz, CDCl$_3$) δ^H ppm: 7.83 (2H, m), 7.71 (1H, m), 7.46 (2H, dd, $^3J_{HH}$ = 7.9 Hz, $^4J_{HH}$ = 1.5 Hz), 7.12 (2H, dd, $^3J_{HH}$ = 7.9 Hz, $^3J_{HH}$ = 7.9 Hz), 6.94 (2H, dd, $^3J_{HH}$ = 8.1 Hz, $^3J_{HH}$ = 1.6 Hz), 4.03 (4H, t, $^3J_{HH}$ = 6.6 Hz), 3.80 (4H, t, $^3J_{HH}$ = 6.6 Hz), 1.85 (4H, m), 1.55 (8H, m), 1.30 (4H, m), 1.00 (6H, t, $^3J_{HH}$ = 7.3 Hz), 0.88 (6H, t, $^3J_{HH}$ = 7.3 Hz).

2,3-[Hg$_2$]-C4: [Dimercury(II)(2,6-*Bis*(2,3-dibutoxyphenyl)pyridine)dichloride]
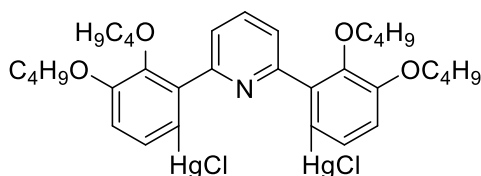
2,6-*Bis*(2,3-butoxyphenyl)pyridine (1.00 g, 1.92 mmol) and Hg(OAc)$_2$ (1.31 g, 4.11 mmol) were added to ethanol (200 mL) and heated to vigorous reflux for 24 hr. The resulting mixture was cooled to 50 °C and a solution of LiCl (0.19 g, 4.48 mmol) in methanol (50 mL) was added and the resulting mixture allowed to stir for 15 min. Distilled water (200 mL) was added and the resulting solution cooled to room temperature and filtered. The white precipitate was washed with copious amounts of water, a small amount of ethanol (<5 mL) and air-dried. Yield = 1.0443 g (55%)

^{1}H NMR (400 MHz, CDCl$_3$) δ^H ppm: 8.12 (2H, d, $^3J_{HH}$ = 7.9 Hz), 7.80 (1H, t, $^3J_{HH}$ = 7.9 Hz), 7.11 (2H, d, $^3J_{HH}$ = 8.1 Hz), 7.03 (2H, d, $^3J_{HH}$ = 8.1 Hz), 4.06 (4H, t, $^3J_{HH}$ = 6.5 Hz), .380 (4H, m), 1.87 (4H, m), 1.55 (8H, m), 1.34 (4H, m), 1.01 (6H, t, $^3J_{HH}$ = 7.3 Hz), 0.82 (6H, t, $^3J_{HH}$ = 7.3 Hz).

Elemental Analysis: Found (%): C 40.0 H 4.4, N 1.8; Calc (%) for C$_{33}$H$_{43}$Cl$_2$Hg$_2$NO$_4$: C 40.1, H 4.4, N 1.4.

2,3-[Au]-Cl-C4: [Gold(III)(2,6-*Bis*(2,3-dibutoxyphenyl)pyridine)chloride]
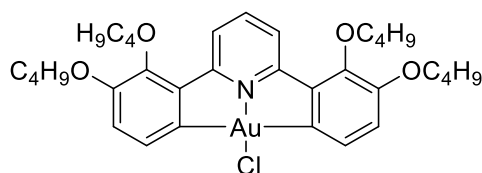
K[AuCl$_4$] (0.3433 g, 0.9085 mmol) and **2,3-[Hg$_2$]-C4** (0.90 g, 0.90 mmol) were heated to reflux in 1:1 chloroform:acetonitrile (200 mL) under a dinitrogen atmosphere for 24 hr. The reaction mixture was cooled to room temperature and reduced to dryness under reduced pressure, then extracted into acetonitrile (50 mL) and the insoluble solid isolated

by filtration. The dirty tan solid was washed sequentially with distilled water (50 mL) and ethanol (25 mL) and dried *in vacuo*. It was dissolved in CH_2Cl_2 and filtered through Celite® to remove elemental gold. The resulting clear bright yellow solution was reduced to dryness under reduced pressure and the yellow, needle-like crystals recrystallised from CH_2Cl_2/hexane. The yellow solid was purified *via* column chromatography (silica; then 6:4 CH_2Cl_2: petroleum ether (40 – 60 °C) (R_f = 0.65)) and recrystallised from CH_2Cl_2/ethyl acetate to give bright yellow, long needle-like crystals. Yield: 0.3094 g (47%)

^{1}H NMR (400 MHz, CDCl$_3$) δ^H ppm: 8.30 (2H, d, $^3J_{HH}$ = 8.2 Hz), 7.84 (1H, t, $^3J_{HH}$ = 8.2 Hz), 7.54 (2H, d, $^3J_{HH}$ = 8.0 Hz), 7.01 (2H, d, $^3J_{HH}$ = 8.2 Hz), 4.10 (4H, t, $^3J_{HH}$ = 6.9 Hz), 3.99 (4H, t, $^3J_{HH}$ = 6.4 Hz), 1.82 (8H, m), 1.00 (6H, t, $^3J_{HH}$ = 7.5 Hz), 1.00 (6H, t, $^3J_{HH}$ = 7.3 Hz).

2,4-[L]-OMe: 2,6-*Bis*(2,4-dimethoxyphenyl)pyridine
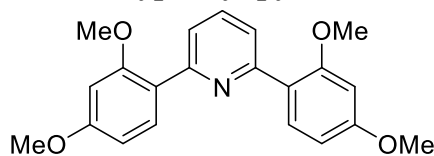
2,6-Dibromopyridine (6.74 g, 28.46 mmol) and 2,4-dimethoxyphenyl boronic acid (15.54 g, 85.37 mmol) were added to a flask containing $[Pd_2(OAc)_6]$ (24.9 mg, 0.5 mol%) and K_3PO_4 (18.44 g, 86.87 mmol). Ethylene glycol (400 mL) was added, and the reaction mixture heated to 80 °C for 1.5 hr with vigorous stirring. The reaction mixture was cooled to room temperature and the solid precipitate isolated by filtration and washed with water (150 mL), and ethanol (50 mL), after which it was air dried. The resulting grey solid was dissolved in warm CH_2Cl_2 (~125 mL) and filtered through Celite®. The filtrate was collected and the solvent removed under reduced pressure. The crystalline, off-white residue was recrystallised from the minimum amount of hot ethanol to give the pure product as white needle-like crystals. Yield = 9.10 g (91%)

^{1}H NMR (400 MHz, CDCl$_3$) δ^H ppm: 7.95 (2H, d, $^3J_{HH}$ = 8.6 Hz), 7.72 (2H, m), 7.67 (1H, m), 6.64 (2H, dd, $^3J_{HH}$ = 8.6 Hz, $^4J_{HH}$ = 2.4 Hz), 6.57 (2H, d, $^4J_{HH}$ = 2.4 Hz), 3.87 (6H, s), 3.86 (6H, s).

$^{13}C\{^1H\}$ NMR (100.6 MHz, CDCl$_3$) δ^C ppm: 161.05, 158.18, 154.91, 135.16, 132.20, 122.56, 122.12, 104.99, 98.75, 55.53, 55.38.

2,4-[L]-OH: 2,6-*Bis*(2,4-dihydroxyphenyl)pyridine
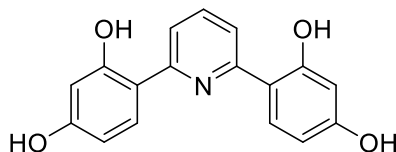
2,6-*Bis*(2,4-dimethoxyphenyl)pyridine (8.81 g, 25.07 mmol) was added to molten pyridinium chloride (37.28 g, 322.60 mmol) at 200 °C and stirred for 16 hr. The still molten mixture was carefully added to distilled water (200 mL) and the resulting bright yellow precipitate was isolated by filtration and air-dried. It was used without further purification. Yield: 10.55 g (143%, product heavily contaminated with water)

^{1}H NMR (400 MHz, DMSO-d$_6$) δ^H ppm: 10.37 (2H, br s), 8.23 (1H, t, $^3J_{HH}$ = 8.2 Hz), 7.96 (2H, d, $^3J_{HH}$ = 8.2 Hz), 7.71 (4H, d, $^3J_{HH}$ = 8.8 Hz), 6.55 (2H, d, $^4J_{HH}$ = 2.5 Hz), 6.48 (2H, dd, $^3J_{HH}$ = 7.2 Hz, $^4J_{HH}$ = 2.6 Hz).

2,4-[L]: 2,6-Bis(2,4-didodecyloxyphenyl)pyridine
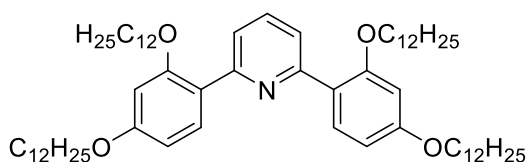
2,6-*Bis*(2,4-dihydroxyphenyl)pyridine (7.69 g, 26.04 mmol), 1-bromododecane (47.5 mL, 49.2 g, 167 mmol) and K$_2$CO$_3$ (57.66 g, 417.2 mmol) were heated to reflux in 3:1 2-butanone:methanol (500 mL) for 113 hr, then filtered and the filtrate reduced to dryness *in vacuo* to give an brown oil. The product was purified *via* column chromatography (silica, petroleum ether (40-60 °C (R_f = 0.00), then 7:3 CH$_2$Cl$_2$:petroleum ether (40-60 °C), (R_f = 0.15), then 5% ethyl acetate in petroleum ether (40-60 °C) (R_f = 0.36)) and a second column (silica, petroleum ether (40-60 °C (R_f = 0.00), then 7:3 CH$_2$Cl$_2$:petroleum ether (40-60 °C), (R_f = 0.15)), to give an orange oil, which solidified on standing to give an off-white solid. Yield: 6.64 g (26%)

^{1}H NMR (400 MHz, CDCl$_3$) δ^H ppm: 8.00 (2H, d $^3J_{HH}$ = 8.6 Hz), 7.79 (2H, d, $^3J_{HH}$ = 7.9 Hz), 7.63 (1H, t, $^3J_{HH}$ = 7.7 Hz), 7.62 (2H, dd, $^3J_{HH}$ = 8.6 Hz, $^4J_{HH}$ = 2.4 Hz), 6.55 (2H, d,

$^4J_{HH}$ = 2.4 Hz), 4.02 (4H, t, $^3J_{HH}$ = 6.5 Hz), 4.01, (4H, t $^3J_{HH}$ = 6.6 Hz), 1.81 (8H, m), 1.46 (8H, m), 1.4 – 1.2 (64H, br s), 0.90 (6H, t, $^3J_{HH}$ = 7.1 Hz), 0.90 (6H, t, $^3J_{HH}$ = 7.0 Hz).

^{13}C{^{1}H} NMR (100.6 MHz, CDCl$_3$) δ^C ppm: 160. 52, 157.79, 154.84, 134.81, 132.51, 122.42, 121.95, 105.58, 100.09, 68.47, 68.04, 31.91, 29.66, 29.63, 29.60, 29.58, 29.55, 29.46, 29.41, 29.35, 29.30, 29.28, 29.20, 26.14, 26.04, 22.67, 14.09.

2,4-[Hg]: [Mercury(II)(2,6-*Bis*(2,4-dibutyloxyphenyl)pyridine)chloride] and 2,4-[Hg₂]: [DiMercury(II)(2,6-*Bis*(2,4-dibutyloxyphenyl)pyridine)dichloride]

Using 2 molar equivalents of mercury

2,4-[Hg]   **2,4-[Hg₂]**
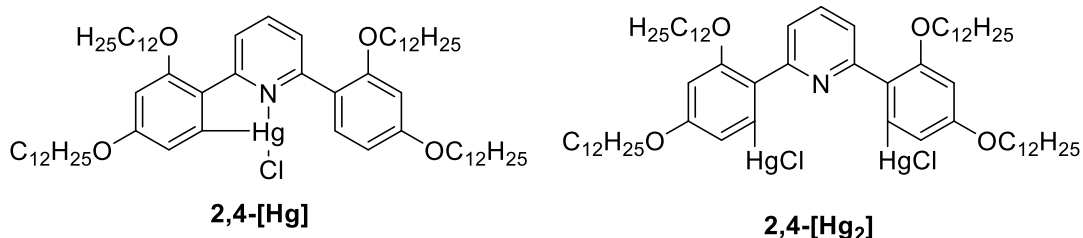
2,6-*Bis*(2,4-dodecyloxyphenyl)pyridine (1.70 g, 1.76 mmol) and Hg(OAc)$_2$ (1.18 g, 3.70 mmol) were added to ethanol (500 mL) and heated to a vigorous reflux for 24 hr. The reaction mixture was cooled to 50 °C and a solution of LiCl (0.1488 g, 3.51 mmol) in methanol (50 mL) was added; the resulting mixture was allowed to stir for 15 min. Distilled water (200 mL) was added and the resulting solution cooled to room temperature and filtered. The resulting caramel-like precipitate was washed with copious amounts of water and air-dried. Yield = 1.21 g (57%)

Highly complex ^{1}H NMR spectra. ~1:1 **2,4-[Hg]**: **2,4-[Hg₂]** estimated.

^{199}Hg NMR (89.6 MHz, CDCl$_3$) δ^{Hg} ppm: -1010.78, -1041.72

Using 1 molar equivalent of mercury
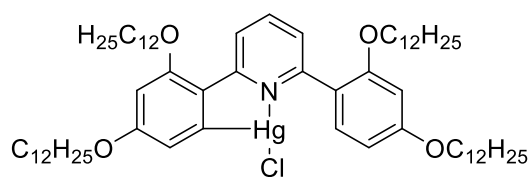
2,4-[Hg]

2,6-*Bis*(2,4-dodecyloxyphenyl)pyridine (4.19 g, 4.33 mmol) and $Hg(OAc)_2$ (1.48 g, 4.64 mmol) were added to ethanol (500 mL) and heated to a vigorous reflux for 24 hr. The reaction mixture was cooled to 50 °C and a solution of LiCl (0.3666 g, 8.65 mmol) in methanol (50 mL) was added; the resulting mixture was allowed to stir for 15 min. Distilled water (200 mL) was added and the resulting solution cooled to room temperature and filtered. The resulting caramel-like precipitate was washed with copious amounts of water and air-dried. Yield = 1.86 g (36%)

^{1}H NMR (400 MHz, CDCl$_3$) δ^H ppm: 7.97 (1H, d, $^3J_{HH}$ = 8.6 Hz), 7.96 (1H, d, $^4J_{HH}$ = 2.2 Hz), 7.77 (1H, d, $^3J_{HH}$ = 7.8 Hz), 7.76 (1H, d, $^3J_{HH}$ = 7.8 Hz), 7.63 (1H, m), 6.60 (1H, dd, $^3J_{HH}$ = 8.7 Hz, $^4J_{HH}$ = 2.3 Hz), 6.55 (1H, s), 6.53 (1H, d, $^4J_{HH}$ = 2.4 Hz), 4.00 (8H, m), 1.80 (8H, m), 1.45 (8H, m), 1.35 – 120 (52H, br m), 0.88 (12H, t, $^3J_{HH}$ = 6.8 Hz), 0.88 (12H, t, $^3J_{HH}$ = 7.1 Hz).

^{199}Hg NMR (89.6 MHz, CDCl$_3$) δ^{Hg} ppm: -1041.72

2,4-[Au]-Cl: [Gold(III)(2,6-*Bis*(2,4-didodecyloxyphenyl)pyridine)chloride
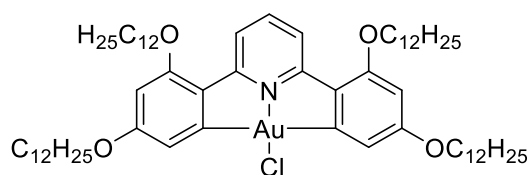
Na[AuCl$_4$] (1.2818 g, 3.2222 mmol) and the mixed **2,4-[Hg]** product (3.89 g, 3.23 mmol) were heated in 1:1 chloroform:acetonitrile (600 mL) under a dinitrogen atmosphere at reflux for 24 hr. The solution was cooled to room temperature and reduced to dryness to give a brown solid, which was extracted into acetonitrile (50 mL). The insoluble solid was isolated by filtration and extracted into CH$_2$Cl$_2$ (~50 mL), then filtered to remove insoluble Au(0) and the filtrate reduced to dryness to give a brown solid, which was purified *via* column chromatography (silica; 1:1 CH$_2$Cl$_2$: petroleum ether (40 − 60 °C) (R_f

= 0.53)) twice to give a yellow solid. The solid was recrystallised from CH_2Cl_2/ethyl acetate to give bright yellow small needles. The product was purified *via* column chromatography (silica; 4:6 CH_2Cl_2: petroleum ether (40 – 60 °C) (R_f = 0.41)) to give a yellow solid, which was recrystallised from chloroform/ethyl acetate to give bright yellow small needles. Yield: 0.0849 g (5%)

^{1}H NMR (400 MHz, $CDCl_3$) δ^H ppm: 7.93 (2H, d, $^3J_{HH}$ = 8.1 Hz), 7.60 (2H, t, $^3J_{HH}$ = 8.0 Hz), 7.13 (2H, d, $^4J_{HH}$ = 2.9 Hz), 6.24 (2H, d, $^4J_{HH}$ = 2.2 Hz), 4.07 (4H, t, $^3J_{HH}$ = 6.3 Hz), 4.01 (4H, t, $^3J_{HH}$ = 6.9 Hz), 1.88 (8H, m) 1.78 (8H, m), 1.5-1.2 (72H, br m), 0.88 (6H, t, $^3J_{HH}$ = 6.6 Hz), 0.88 (6H, t, $^3J_{HH}$ = 6.6 Hz).

$^{13}C\{^1H\}$ NMR (125.8 MHz, $CDCl_3$) δ^C ppm: 172.69, 164.05, 162.30, 159.43, 142.08, 127.40, 118.77, 110.02, 98.50, 68.40, 68.14, 31.96, 31.92, 29.79, 29.75, 29.70, 29.68, 29.66, 29.64, 29.61, 29.59, 29.48, 29.43, 29.38, 29.39, 29.08, 26.16, 26.07, 22.73, 22.69, 14.12.

APCI MS (m/z): Expected for $C_{78}H_{122}AuNO_4$ = 1198.7627; Observed: 1198.7588 [M + H]$^+$ (Error = 3.9 mDa)

2,5-[L]-OMe: 2,6-*Bis*(2,5-dimethoxyphenyl)pyridine
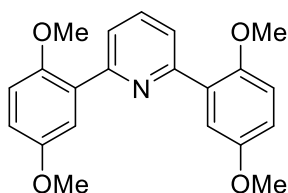
2,6-Dibromopyridine (6.74 g, 28.46 mmol) and 2,5-dimethoxyphenyl boronic acid (15.54 g, 85.37 mmol) were added to a flask containing $[Pd_2(OAc)_6]$ (24.6 mg, 0.5 mol%) and K_3PO_4 (18.12 g, 85.37 mmol). Ethylene glycol (300 mL) was added, and the reaction mixture heated to 80 °C for 2 hr with vigorous stirring. The reaction mixture was cooled to room temperature, the solid precipitate isolated by filtration and washed with water (200 mL), after which it was air dried. The resulting grey solid was dissolved in warm CH_2Cl_2 (~100 mL) and filtered through Celite®. The filtrate was collected and the solvent removed under reduced pressure. The crystalline, off-white residue was recrystallised from the minimum amount of hot ethanol to give the pure product as white needle-like crystals. Yield = 8.98 g (90%)

^{1}H NMR (400 MHz, CDCl$_3$) δ^{H} ppm: 7.81 (2H, m), 7.73 (1H, m), 7.56 (2H, d, $^4J_{\mathrm{HH}}$ = 2.4 Hz), 6.93 (4H, m), 3.84 (6H, s), 3.83 (6H, s).

^{13}C{^{1}H} NMR (100.6 MHz, CDCl$_3$) δ^{C} ppm: 155.01, 153.90, 151.48, 135.40, 130.19, 123.21, 116.30, 115.19, 113.08, 56.43, 55.78.

2,5-[L]-OH: 2,6-*Bis*(2,5-dihydroxyphenyl)pyridine
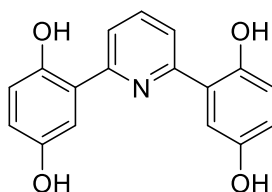
2,6-*Bis*(2,5-dimethoxyphenyl)pyridine (8.69 g, 24.73 mmol) was added to molten pyridinium chloride (30.79 g, 266.44 mmol) at 200 °C and stirred for 16 hr. The still molten mixture was carefully added to distilled water (200 mL) and the resulting bright yellow precipitate was isolated by filtration and air-dried. It was used without further purification. Yield: 8.48 g (116%, product contaminated with water)

^{1}H NMR (400 MHz, DMSO-D6) δ^{H} ppm: ~9.00 (2H, s br), 8.10 (1H, t, $^3J_{\mathrm{HH}}$ = 8.2 Hz), 7.92 (2H, d, $^3J_{\mathrm{HH}}$ = 8.0 Hz), 7.17 (2H, s), 6.83 (2H, d, $^3J_{\mathrm{HH}}$ = 8.7 Hz), 6.78 (2H, d, $^3J_{\mathrm{HH}}$ = 8.7 Hz).

2,5-[L]: 2,6-*Bis*(2,5-didodecyloxyphenyl)pyridine
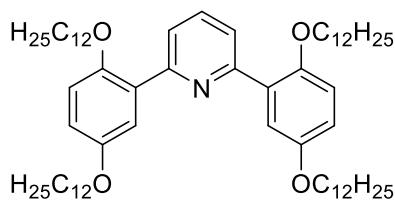
2,6-*Bis*(2,5-dihydroxyphenyl)pyridine (11.56 g, 39.15 mmol), 1-bromododecane (60.2 mL, 62.45 g, 250.56 mmol) and K$_2$CO$_3$ (86.71 g, 627.40 mmol) were heated to reflux in 2-butanone (300 mL) and methanol (100 mL) for 10 days, then cooled to room temperature and filtered. The resulting solid was washed with water (60 cm), and acetone. The remaining insoluble tan solid was recrystallised from CH$_2$Cl$_2$/acetone twice to give an off-white microcrystalline solid. The crude filtrate was collected, reduced to dryness under reduced pressure and then extracted into CH$_2$Cl$_2$ and acetone added. The resulting

solution was cooled at 5 °C, before being filtered and washed with acetone to isolate an off-white microcrystalline solid. Yield = 21.20 g (56%)

^{1}H NMR (400 MHz, CDCl$_3$) δ^H ppm: 7.86 (2H, d, $^3J_{HH}$ = 7.8 Hz), 7.67 (1H, m), 7.59 (2H, d, $^4J_{HH}$ = 3.1 Hz), 6.92 (2H, d, $^3J_{HH}$ = 8.8 Hz $^3J_{HH}$ = 8.8 Hz), 6.87 (2H, dd, $^3J_{HH}$ = 8.8 Hz, $^4J_{HH}$ = 2.3 Hz), 3.97 (4H, t, $^3J_{HH}$ = 6.5 Hz), 3.94 (4H, t, $^3J_{HH}$ = 6.6 Hz), 1.75 (8H, m), 1.42 (8H, m), 1.27 (72H, br m), 0.87 (6H, t, $^3J_{HH}$ = 6.1 Hz), 0.87 (6H, t, $^3J_{HH}$ = 6.3 Hz).

^{13}C{^{1}H} NMR (100.6 MHz, CDCl$_3$) δ^C ppm: 154.95, 153.46, 150.97, 134.99, 130.47, 123.14, 116.87, 115.92, 114.62, 69.73, 68.55, 31.91, 29.68, 29.66, 29.63. 29.61, 29.58, 29.47, 29.43, 29.35, 29.33, 26.13, 26.11, 22.67, 14.10.

2,5-[Hg]: [Mercury(II)(2,6-*Bis*(2,5-didodecyloxyphenyl)pyridine)chloride] and 2,5-[Hg$_2$]: [DiMercury(II)(2,6-*Bis*(2,5-didodecyloxyphenyl)pyridine)dichloride]
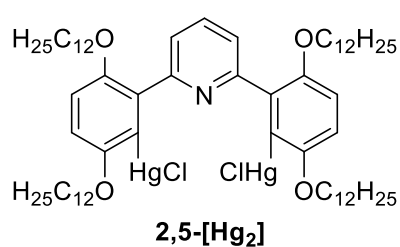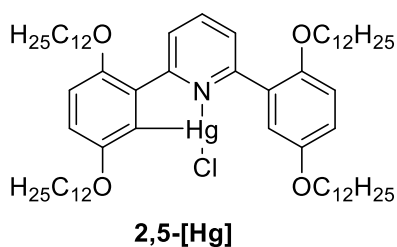
2,6-*Bis*(2,5-dodecyloxyphenyl)pyridine (3.00 g, 3.10 mmol) and Hg(OAc)$_2$ (2.06 g, 6.46 mmol) were added to ethanol (500 mL) and heated to a vigorous reflux for 24 hours. The resulting solution was cooled to 50 °C and a solution of LiCl (0.2630 g, 6.20 mmol) in methanol (50 mL) was added. The resulting mixture was allowed to stir for 15 min. Distilled water (200 mL) was added and the resulting solution cooled to room temperature and filtered. The waxy tan precipitate was washed with copious amounts of water and air-dried. Total Yield: 2.41 g

^{1}H NMR spectroscopy indicates that **2,5-[Hg]** and **2,5-[Hg$_2$]** were formed in a 5:4 ratio. Complexes can be separated *via* column chromatography (silica; 2:3 CH$_2$Cl$_2$: petroleum ether (40 – 60 °C), then 1:1 CH$_2$Cl$_2$: petroleum ether (40 – 60 °C)).

2,5-[Hg]
Yield: 1.24 g (33%)

^{1}H NMR (400 MHz, CDCl$_3$) $\delta^{\rm H}$ ppm: 8.14 (1H, d, $^3J_{\rm HH}$ = 8.0 Hz), 7.84 (1H, d, $^3J_{\rm HH}$ = 7.6 Hz), 7.71 (1H, q, $^3J_{\rm HH}$ = 8.1 Hz, $^3J_{\rm HH}$ = 8.1 Hz), 7.29 (1H, d, $^4J_{\rm HH}$ = 2.9 Hz), 6.94 (4H, s), 3.97 (8H, m), 1.75 (8H, m), 1.43 (8H, m), 1.35 – 1.15 (64H, m), 0.87 (12H, t, $^3J_{\rm HH}$ = 6.8 Hz).

^{13}C{^{1}H} NMR (100.6 MHz, CDCl$_3$) $\delta^{\rm C}$ ppm: 155.58, 155.16, 154.87, 153.60, 152.51, 150.87, 142.84, 135.67, 133.20, 129.43, 124.27, 124.05, 117.36, 116.39, 114.92, 114.77, 112.54, 69.75, 69.70, 69.15, 68.81, 31.89, 29.65, 29.61, 29.59, 29.55, 29.44, 29.41, 29.37, 29.33, 29.31, 26.20, 26.16, 26.14, 29.09, 26.04, 14.08.

R_f = 0.63 (1:1 CH$_2$Cl$_2$:petroleum ether (40 – 60 °C))

2,5-[Hg$_2$]

Yield: 1.17 g (26%)

^{1}H NMR (400 MHz, CDCl$_3$) $\delta^{\rm H}$ ppm: 8.04 (1H, d, $^3J_{\rm HH}$ = 7.9 Hz), 7.74 (1H, t, $^3J_{\rm HH}$ = 8.1 Hz), 6.95-6.90 (4H, m), 3.95 (8H, t, $^3J_{\rm HH}$ = 6.6 Hz), 1.75 (8H, m), 1.43 (8H, m), 1.35 – 1.15 (64H, m), 0.87 (12H, t, $^3J_{\rm HH}$ = 6.8 Hz).

^{13}C{^{1}H} NMR (100.6 MHz, CDCl$_3$) $\delta^{\rm C}$ ppm: 156.41, 155.31, 152.42, 143.26, 136.06, 133.33, 132.10, 132.00, 128.51, 128.39, 124.97, 116.08, 113.09, 70.46, 69.31, 31.87, 29.44, 29.41, 29.29, 29.27, 29.24, 29.28, 26.31, 14.08.

R_f = 0.69 (1:1 CH$_2$Cl$_2$:petroleum ether (40 – 60 °C))

2,5-[Au]-Cl: [Gold(III)(2,6-*bis*(2,5-didodecyloxyphenyl)pyridine)chloride]
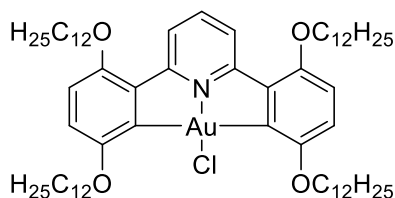
Na[AuCl$_4$] (0.7971 g, 2.00 mmol) and the mixed **2,5-[Hg]** product (2.41 g, 2.00 mmol) were heated in 1:1 chloroform:acetonitrile (200 mL) under a dinitrogen atmosphere at reflux for 24 hr. The reaction mixture was cooled to room temperature and reduced to dryness under reduced pressure, then extracted into acetonitrile (50 mL) and the insoluble

solid isolated by filtration. The brown solid was washed sequentially with distilled water (25 mL) and ethanol (25 mL), dried *in vacuo*, dissolved in CH_2Cl_2 and filtered to remove solid gold(0). The filtrate was reduced to dryness under reduced pressure and triturated with diethyl ether three times to solidify to a brown solid, which was recrystallised three times from CH_2Cl_2/ethyl acetate to give a bright yellow microcrystalline solid. Yield: 0.4071 g (17%)

^{1}H NMR (400 MHz, $CDCl_3$) δ^H ppm: 8.39 (2H, d, $^3J_{HH}$ = 82 Hz), 7.75 (2H, t, $^3J_{HH}$ = 8.4 Hz), 6.98 (2H, d, $^3J_{HH}$ = 9.1 Hz), 6.73 (2H, d, $^3J_{HH}$ = 9.2 Hz), 4.04 (4H, t, $^3J_{HH}$ = 6.6 Hz), 3.94 (4H,), 0.88 (6H, t, $^3J_{HH}$ = 7.0 Hz), t, $^3J_{HH}$ = 6.8 Hz), 1.88 (8H, m) 1.50 (8H, m), 0.88 (6H, t, $^3J_{HH}$ = 7.0 Hz).

^{13}C{^{1}H} NMR (100.6 MHz, $CDCl_3$) δ^C ppm: 164.13, 157.52, 157.08, 152.83, 141.57, 135.56, 122.04, 121.45, 112.03, 72.14, 68.19, 31.93, 31.90, 29.74, 29.69, 29.66, 29.64, 29.58, 29.56, 29.38, 29.34, 29.23, 26.29, 29.23, 22.69, 22.67, 14.11.

APCI MS (m/z): Expected for $C_{65}H_{107}AuClNO_4$ = 1198.7627; Observed: 1198.7588 [M + H]$^+$ (Error = -3.9 mDa)

Elemental Analysis: Found (%): C 64.9, H 8.9, N 0.8; Calc (%) for $C_{65}H_{107}AuClNO_4$: C 65.1, H 9.0, N 1.2.

2,5-[L]-C4: 2,6-*Bis*(2,5-butoxyphenyl)pyridine
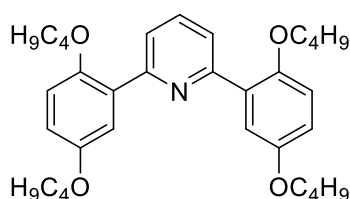
Sodium methoxide (0.95 g, 17.57 mmol) in methanol (30 mL) was added to 2,6-*Bis*(2,5-dihydroxyphenyl)pyridine (1.26 g, 4.26 mmol) and 1-bromobutane (2.9 mL, 3.70 g, 27.01 mmol) in dry THF (100 mL) and was heated to reflux for 168 hr, with a further four equivalents of NaOMe (0.92 g, 1.7068 mmol) added over this time period. The reaction was cooled to room temperature and distilled water (50 mL) added, before the resulting solution was concentrated under reduced pressure. The remaining orange solution was extracted into CH_2Cl_2 (75 mL) and washed with distilled water (2 x 50 mL). The organic

layer was dried over $MgSO_4$, filtered and reduced to dryness. The brown oil was purified by column chromatography (silica, petroleum ether (40 − 60 °C R_f = 0.00, then 95:5 petroleum ether (40-60 °C):ethyl acetate, R_f = 0.28) to give a buttercup yellow solid. Unfortunately the titular product and the trialkylated product eluted together in a 1:2 ratio by ^{1}H NMR. The mixed product, 1-bromododecane (0.25 mL, 0.32 g, 2.34 mmol) and K_2CO_3 (0.8071 g, 5.84 mmol) were heated to reflux in 2-butanone (75 mL) and methanol (25 mL) for 10 days, then cooled to room temperature and filtered. The pale yellow filtrate was reduced to dryness and purified *via* column chromatography (silica, petroleum ether (40 − 60 °C), R_f = 0.0, then 7:3 CH_2Cl_2:petroleum ether (40-60 °C):CH_2Cl_2, R_f = 0.59), then a second and third column (silica, :3 CH_2Cl_2:petroleum ether (40-60 °C): CH_2Cl_2, R_f = 0.59) to give an oil, which solidified on standing to give colourless crystals. Yield: 0.1506 g (7%)

^{1}H NMR (400 MHz, $CDCl_3$) δ^H ppm: 7.85 (2H, d, $^3J_{HH}$ = 8.0 Hz), 7.69 (1H, m), 7.59 (2H, d, $^4J_{HH}$ = 3.0 Hz), 6.93 (2H, d, $^3J_{HH}$ = 9.0 Hz), 6.87 (2H, dd, $^3J_{HH}$ = 8.8 Hz, $^4J_{HH}$ = 3.1 Hz), 3.99 (4H, t, $^3J_{HH}$ = 6.4 Hz), 3.95 (4H, t, $^3J_{HH}$ = 6.5 Hz), 1.74 (8H, m), 1.45 (8H, m), 0.96 (6H, t, $^3J_{HH}$ = 7.3 Hz), 0.92 (6H, t, $^3J_{HH}$ = 7.4 Hz).

2,5-[Hg]-C4: [Mercury(II)(2,6-*Bis*(2,5-dibutoxyphenyl)pyridine)chloride] and 2,5-[Hg₂]-C4: [DiMercury(II)(2,6-*Bis*(2,5-dibutoxyphenyl)pyridine)dichloride]
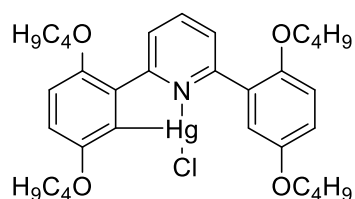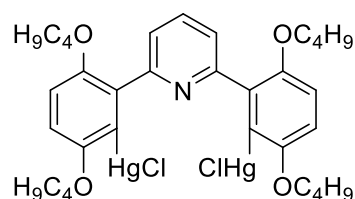
2,6-*Bis*(2,5-butoxyphenyl)pyridine (0.13 g, 0.22 mmol) and $Hg(OAc)_2$ (0.17 g, 0.53 mmol) were added to ethanol (50 mL) and heated to a vigorous reflux for 24 hr. The solution was cooled to 55 °C and a solution of LiCl (0.0259 g, 0.6109 mmol) in methanol (10 mL) was added. The resulting mixture was allowed to stir for 15 min. Distilled water (50 mL) was added and the resulting solution cooled to room temperature and filtered. The viscous gold oil precipitate was washed with copious amounts of water and air-dried. ^{1}H NMR spectroscopy indicates that **2,5-[Hg]-C4** and **2,5-[Hg₂]-C4** were formed in a 4:3 ratio. The products were separated by column chromatography (silica, 6:4

CH$_2$Cl$_2$:petroleum ether (40 – 60 °C)) to give **2,5-[Hg]-C4** as an oil, which solidified on standing to give colourless crystals and **2,5-[Hg$_2$]-C4** as an oil, which solidified on standing to give a white solid.

2,5-[Hg]-C4

Yield: 0.0516 g (43%)

^{1}H NMR (400 MHz, CDCl$_3$) δ^H ppm: 8.11 (1H, dd, $^3J_{HH}$ = 7.5 Hz, $^4J_{HH}$ = 0.6 Hz), 7.84 (1H, dd, $^3J_{HH}$ = 7.6 Hz, $^4J_{HH}$ = 1.1 Hz), 7.72 (1H, dd, $^3J_{HH}$ = 7.9 Hz, $^3J_{HH}$ = 7.9 Hz), 7.29 (1H, d, $^4J_{HH}$ = 2.8 Hz), 6.92 (4H, m), 3.98 (1H, t, $^3J_{HH}$ = 6.6 Hz), 3.97 (1H, t, $^3J_{HH}$ = 6.4 Hz), 3.94 (1H, t, $^3J_{HH}$ = 6.6 Hz), 3.94 (1H, t, $^3J_{HH}$ = 6.4 Hz), 1.74 (6H, m), 1.67 (2H, m), 1.47 (6H, m), 1.36 (2H, m), 0.94 (9H, t, $^3J_{HH}$ = 7.4 Hz), 0.90 (3H, t, $^3J_{HH}$ = 7.4 Hz).

^{13}C{^{1}H} NMR (100.6 MHz, CDCl$_3$) δ^C ppm: 155.57, 155.15, 154.95, 153.61, 152.48, 150.88, 142.80, 135.75, 133.31, 129.44, 124.30, 124.08, 117.35, 116.46, 115.00, 114.79, 112.56, 69.47, 69.43, 68.84, 68.54, 31.48, 31.43, 31.39, 19.39, 19.31, 19.23, 13.90, 13.82, 13.79.

R_f = 0.38 (6:4 CH$_2$Cl$_2$:petroleum ether (40 – 60 °C))

^{199}Hg{^{1}H} NMR (89.6 MHz, CDCl$_3$) δ^{Hg} ppm: -1008.68

2,5-[Hg$_2$]-C4

Yield: 0.0802 g (38%)

^{1}H NMR (400 MHz, CDCl$_3$) δ^H ppm: 8.03 (1H, d, $^3J_{HH}$ = 7.9 Hz), 7.74 (1H, t, $^3J_{HH}$ = 7.7 Hz), 6.94 (4H, s), 3.95 (4H, t, $^3J_{HH}$ = 6.5 Hz), 3.95 (4H, t, $^3J_{HH}$ = 6.5 Hz), 1.72 (8H, m), 1.44 (8H, m), 0.95 (6H, t, $^3J_{HH}$ = 7.4 Hz), 0.90 (6H, t, $^3J_{HH}$ = 7.4 Hz).

^{13}C{^{1}H} NMR (100.6 MHz, CDCl$_3$) δ^C ppm: 156.37, 155.27, 152.39, 143.19, 136.15, 133.27, 124.95, 116.01, 113.07, 70.08, 68.97, 31.39, 31.35, 19.31, 13.84, 13.79.

^{199}Hg{^{1}H} NMR (89.6 MHz, CDCl$_3$) δ^{Hg} ppm: -1010.38

$R_f = 0.46$ (6:4 CH$_2$Cl$_2$:petroleum ether (40 – 60 °C))

3,5-[L]-OMe: 2,6-*Bis*(3,5-dimethoxyphenyl)pyridine
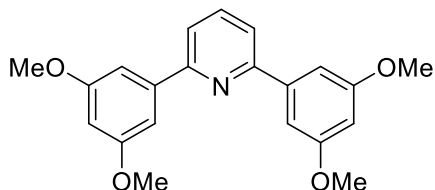
2,6-Dibromopyridine (6.74 g, 28.46 mmol) and 3,5-dimethoxyphenyl boronic acid (15.54 g, 85.37 mmol) were added to a flask containing [Pd$_2$(OAc)$_6$] (21.1 mg, 0.5 mol%) and K$_3$PO$_4$ (18.12 g, 85.37 mmol). Ethylene glycol (400 mL) was added, and the reaction mixture heated to 80 °C for 2 hr with vigorous stirring. The reaction mixture was cooled to room temperature, the solid precipitate isolated by filtration and washed with water (150 mL), after which it was air dried. The resulting grey solid was dissolved in warm CH$_2$Cl$_2$ (~100 mL) and filtered through Celite®. The filtrate was collected and the solvent removed under reduced pressure. The crystalline, off-white residue was recrystallised from the minimum amount of hot ethanol to give the pure product as white rhombic crystals. Yield = 8.92 g (89%)

^{1}H NMR (400 MHz, CDCl$_3$) δ^H ppm: 7.80 (1H, m), 7.66 (2H, d, $^3J_{HH}$ = 8.0 Hz), 7.32 (4H, d, $^4J_{HH}$ = 2.3 Hz), 6.56 (2H, t, $^4J_{HH}$ = 2.3 Hz), 3.89 (12H, s).

^{13}C{^{1}H} NMR (100.6 MHz, CDCl$_3$) δ^C ppm: 161.03, 156.32, 141.53, 137.45, 119.11, 105.10, 101.08, 55.43.

3,5-[L]-OH: 2,6-*Bis*(3,5-dihydroxyphenyl)pyridine
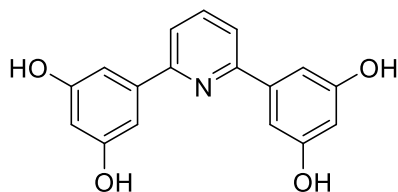
2,6-*Bis*(3,5-dimethoxyphenyl)pyridine (7.10 g, 20.20 mmol) was added to molten pyridinium chloride (29.47 g, 255.0 mmol) at 200 °C and stirred for 16 hr. The still molten mixture was carefully added to distilled water (200 mL) and the resulting red/pink

precipitate was isolated by filtration and air-dried. It was used without further purification. Yield: 7.13 g (120%, product contaminated with water)

^{1}H NMR (400 MHz, DMSO-d$_6$) δ^H ppm: 9.40 (2H, br s), 7.89 (1H, t, $^3J_{HH}$ = 7.9 Hz), 7.70 (2H, d, $^3J_{HH}$ = 7.8 Hz), 7.01 (4H, d, $^4J_{HH}$ = 2.6 Hz), 6.31 (2H, t, $^4J_{HH}$ = 2.6 Hz).

3,5-[L]: 2,6-Bis(3,5-didodecyloxyphenyl)pyridine
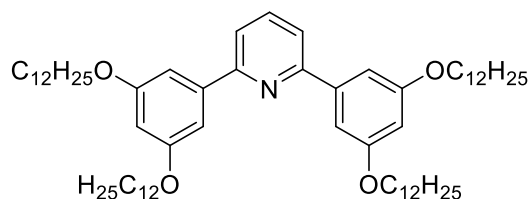
2,6-*Bis*(3,5-dihydroxyphenyl)pyridine (5.96 g, 20.18 mmol), 1-bromododecane (31 mL, 32.18 g, 125.11 mmol) and K$_2$CO$_3$ (48.81 g, 353.2 mmol) were heated to reflux in 2-butanone (300 mL) for 16 hr, then cooled to room temperature and filtered to isolate a brown filtrate, which was reduced to dryness. Methanol was added and the solution was cooled at 5 °C to give a brown solid, which was isolated by filtration and purified *via* column chromatography (silica, 95:5 petroleum ether (40-60 °C):ethyl acetate, R_f = 0.36) to give a pale orange oil, which solidified on standing to a pale pink crystalline solid. The solid was crystallised from hexane/ethyl acetate and a small amount of methanol to give off-white needle-like crystals, then from CH$_2$Cl$_2$/ethyl acetate to give white needle-like crystals. The residue was purified *via* column chromatography (silica, petroleum ether (40 – 60 °C), R_f = 0.0, then 9:1 petroleum ether (40-60 °C):ethyl acetate, R_f = 0.59), then recrystallised from CH$_2$Cl$_2$/ethyl acetate to give off-white crystals. Yield = 5.25 g (27%)

^{1}H NMR (400 MHz, CDCl$_3$) δ^H ppm: 7.87 (1H, m), 7.65 (2H, d, $^3J_{HH}$ = 7.8 Hz), 7.29 (4H, d, $^4J_{HH}$ = 2.3 Hz), 6.54 (2H, t, $^4J_{HH}$ = 2.3 Hz), 4.04 (8H, t, $^3J_{HH}$ = 6.5 Hz), 1.84 (8H, m), 1.48 (8H, m), 1.4-1.2 (64H, br m), 0.89 (12H, t, $^3J_{HH}$ = 6.8 Hz).

^{13}C{^{1}H} NMR (100.6 MHz, CDCl$_3$) δ^C ppm: 160.54, 156.42, 141.14, 137.30, 118.96, 105.56, 102.08, 68.12, 31.91, 31.89, 29.68, 29.64, 29.62, 29.60, 29.93, 29.35, 29.33, 26.09, 22.68, 14.11.

3,5-[Hg]: [Mercury(II)(2,6-*Bis*(3,5-didodecyloxyphenyl)pyridine)chloride] and 3,5-[Hg₂]]: [DiMercury(II)(2,6-*Bis*(3,5-dibutyloxyphenyl)pyridine)dichloride]

3,5-[Hg]

3,5-[Hg₂]
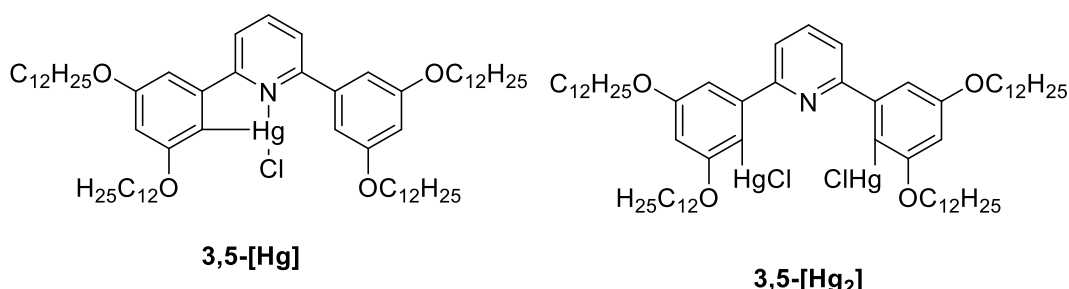
2,6-*Bis*(3,5-dodecyloxyphenyl)pyridine (3.07 g, 3.17 mmol) and Hg(OAc)₂ (1.98 g, 6.21 mmol) were added to ethanol (500 mL) and heated to a vigorous reflux for 24 hr. The resulting solution was cooled to 50 °C and a solution of LiCl (0.2635 g, 6.22 mmol) in methanol (50 mL) was added. The resulting mixture was allowed to stir for 15 min. Distilled water (200 mL) was added and the resulting solution cooled to room temperature and filtered. The resulting golden viscous oil was washed with copious amounts of water and air-dried. Yield: **3,5-[Hg]** = 0.35 g (9%), **3,5-[Hg₂]** = 0.21 g (3%)

1:0.5 **3,5-[Hg]**:**3,5-[Hg₂]** given by ^{1}H NMR.

^{1}H NMR (500 MHz, CDCl₃) δ^H ppm: 7.86 (0.5(1)H, t, $^3J_{HH}$ = 7.9 Hz), 7.85 (1H, d, $^3J_{HH}$ = 7.7 Hz), 7.81 (1H, d, $^3J_{HH}$ = 7.9 Hz), 7.72 (1(2)H, d, $^3J_{HH}$ = 7.6 Hz), 7.69 (1H, dd, $^3J_{HH}$ = 7.7 Hz, $^3J_{HH}$ =7.7 Hz), 7.04 (1.8 H, m), 6.97 (1H, d, $^4J_{HH}$ = 2.4 Hz), 6.59 (2.8H, m), 4.1 – 4.0 (12H, m), 1.47 (12H, m), 1.4-1.2 (104H, m), 0.89 (18H, m).

^{13}C{^{1}H} NMR (100.6 MHz, CDCl₃) δ^C ppm: 162.68, 162.53, 161.49, 160.50, 158.78, 157.76, 157.13, 144.82, 144.14, 140.15, 138.68, 138,08, 131.30, 129.79, 121.53, 121.07, 119.98, 106.35, 105.79, 102.43, 100.40, 100.04, 68.79, 68.53, 68.33, 68.27, 68.14, 31.89, 29.65, 29.61, 29.59, 29.57, 29.54, 29.43, 29.41, 29.39, 29.33, 29.30, 29.27, 26.16, 26.06, 26.04, 22.65, 14.08.

^{199}Hg{^{1}H} NMR (89.6 MHz, CDCl₃) δ^{Hg} ppm: -971.65, -954.42.

NMR data is for inseparable mixture and therefore non-integral ^{1}H NMR integrations reflect this. Data given in brackets reflects the 'true' integration values for the dimercury complex pyridyl system.

Attempted Synthesis of [Gold(III)(2,6-bis(3,5-didodecyloxyphenyl)pyridine)chloride (3,5-[Au]-Cl)
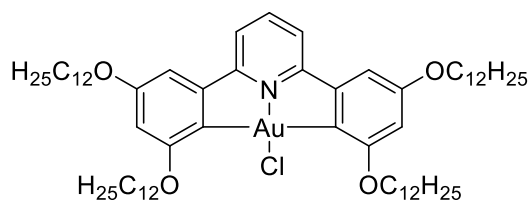
Na[AuCl$_4$] (0.1849 g, 0.46 mmol) and the mixed **3,5-[Hg]** product (0.56 g, 0.46 mmol) were heated to reflux in 1:1 chloroform:acetonitrile (200 mL) under a dinitrogen atmosphere for 24 hr. The reaction mixture was cooled to room temperature and reduced to dryness under reduced pressure, then the soluble salts extracted into acetonitrile (10 mL) to give a remaining viscous golden oil, which was determined by ^{1}H NMR spectroscopy to be the unreacted mercury(II) complexes.

6.3　　　Attempted Direct Auration

(Bu$_4$N)[AuCl$_4$]

H[AuCl$_4$] (0.4958 g, 1.4591 mmol) was dissolved in distilled water (25 mL) and solid (Bu$_4$N)Cl (0.4113 g, 1.4799 mmol) was added and stirred at room temperature for 3 hr in the dark. The resulting yellow precipitate was isolated by vacuum filtration, washed with distilled water (10 mL) and air dried. Yield = 0.680 g (80%)

^{1}H NMR (400 MHz, CDCl$_3$) δ^H ppm: 3.45 (8H, m), 1.83 (8H, m), 1.44 (8H, m), 0.98 (12H, t, $^3J_{HH}$ = 4.6 Hz).

Elemental Analysis: Found (%): C 33.0, H 6.1, N 2.2; Calc (%) for C$_{16}$H$_{36}$AuCl$_4$N: C 33.1, H 6.2, N 2.4.

6.3.1 Attempted Direct Auration using K[AuCl₄]
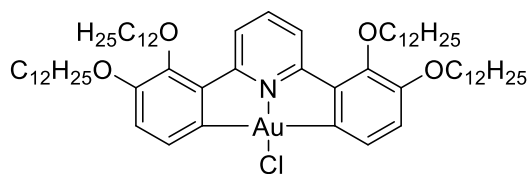
$$\text{K[AuCl_4]}$$

Attempt 1

K[AuCl₄] (0.1532 g, 0.4054 mmol) and 2,6-*bis*(2,3-didodecyloxyphenyl)pyridine (0.1532 g, 0.1582 mmol) in 1:1 chloroform:acetonitrile (200 mL) were heated to reflux under a dinitrogen atmosphere for 24 hr, then cooled to room temperature and reduced to dryness under reduced pressure. The residue was extracted into acetonitrile (25 mL) and the insoluble solid filtered off and washed with water (25 mL), then ethanol (15 mL) to give a pale orange solid, which was purified *via* column chromatography (silica, 95:5 petroleum ether (40 – 60 °C):ethyl acetate, then CH₂Cl₂).

APCI MS: m/z = 968.8414 [M + H]⁺ (free ligand)

^{1}H NMR spectroscopy indicated only free ligand present.

Attempt 2

2,6-*Bis*(2,3-didodecyloxyphenyl)pyridine (0.1456 g, 0.1511 mmol) and K[AuCl₄] (0.0784 g, 0.2075 mmol) in 1:1 chloroform:acetonitrile (50 mL) were heated to reflux under a dinitrogen atmosphere for 5 days, then cooled to room temperature and reduced to dryness under reduced pressure. The residue was extracted into acetonitrile (25 mL) and the insoluble solid filtered off and washed with water (25 mL), then ethanol (15 mL) to give a pale orange solid.

^{1}H NMR spectroscopy indicated only free ligand present.

6.3.2 Attempted Direct Auration using (Bu₄N)[AuCl₄]

Attempt 1

2,6-*Bis*(2,3-didodecyloxyphenyl)pyridine (0.4039 g, 0.4170 mmol) and (Bu₄N)[AuCl₄] (0.2428 g, 0.4054 mmol) in 1:1 chloroform:acetonitrile (200 mL) were heated to reflux under a dinitrogen atmosphere for 5 hr, then cooled to room temperature and reduced to dryness under reduced pressure. The residue was extracted into acetonitrile (25 mL) and

the insoluble solid filtered off and washed with ethanol (10 mL) to give a pale orange solid.

^{1}H NMR spectroscopy indicated only free ligand present.

Attempt 2

2,6-*Bis*(2,3-didodecyloxyphenyl)pyridine (0.1456 g, 0.1503 mmol) and $(Bu_4N)[AuCl_4]$ (0.1215 g, 0.2090 mmol) in 1:1 chloroform:acetonitrile (50 mL) were heated to reflux under a dinitrogen atmosphere for 5 days, then cooled to room temperature and reduced to dryness under reduced pressure. The residue was extracted into acetonitrile (25 mL) and the insoluble solid filtered off and washed with water (25 mL), then ethanol (15 mL) to give an off-white solid.

^{1}H NMR spectroscopy indicated only free ligand present.

Attempt 3

2,6-*Bis*(2,3-didodecyloxyphenyl)pyridine (0.2022 g, 0.2085 mmol), $(Bu_4N)[AuCl_4]$ (0.1212 g, 0.2085 mmol) and $(Bu_4N)(AcO)$ (0.0629 g, 0.2086 mmol) in acetone (50 mL) were heated to reflux under a dinitrogen atmosphere for 7 days, then cooled to room temperature and reduced to dryness under reduced pressure. The residue was extracted into acetonitrile (25 mL) and the insoluble solid filtered off and washed with acetonitrile to give an off-white solid.

^{1}H NMR spectroscopy indicated only free ligand present.

6.3.4   Attempted Direct Auration using H[AuCl$_4$]
Attempt 1

2,6-*Bis*(2,3-didodecyloxyphenyl)pyridine (0.1464 g, 0.1511 mmol) and $H[AuCl_4]$ (0.0712 g, 0.2095 mmol) in 1:1 chloroform:acetonitrile (50 mL) were heated to reflux under a dinitrogen atmosphere for 5 days, then cooled to room temperature and reduced to dryness under reduced pressure. The residue was extracted into acetonitrile (25 mL) and the insoluble solid filtered off and washed with water (25 mL), then ethanol (15 mL) to give a pale orange solid. ^{1}H NMR spectroscopy indicated only free ligand present.

6.3.5   Attempted Direct Auration *via* Lithium Species
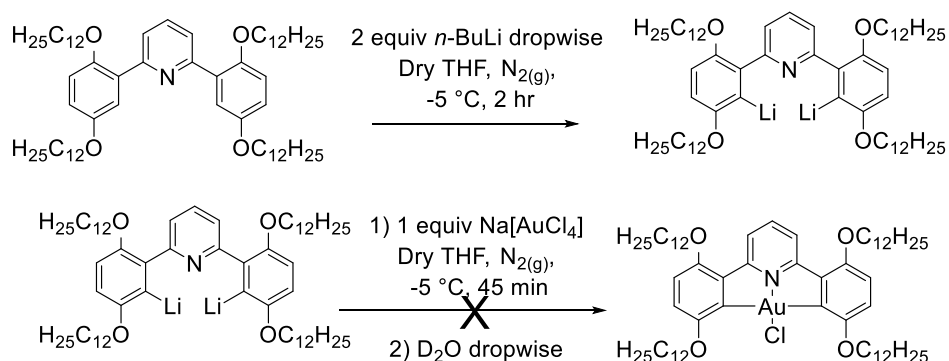
2,6-*Bis*(2,3-didodecyloxyphenyl)pyridine (0.1001 g, 0.1033 mmol) in dry THF (10 mL) was cooled in an ice/salt bath. *n*-BuLi (0.13 mL, 0.21 mmol, 1.6 M in hexanes) was added dropwise and the resulting solution stirred at <–5 °C for 2 hr under a dinitrogen atmosphere to give a dark brown solution. Na[AuCl$_4$] (0.0362 g, 0.0910 mmol) in dry THF (5 mL) was cooled in an ice/salt bath. The dilithium species solution was added dropwise and stirred at <-5 °C for 45 min under a dinitrogen atmosphere. The reaction was quenched by the addition of D$_2$O (10 mL) resulting in a dark solution, which was extracted into CH$_2$Cl$_2$ 950 mL). The organic layer was washed with distilled water (25 mL), then saturated brine (25 mL), before it was dried over MgSO$_4$, filtered and reduced to dryness to give an off-white solid. ^{1}H NMR indicated that only free ligand was present. Yield: 0.0 g (0%)

6.3.6   Unsuccessful Palladation Reactions

6.3.6.1 General Method

The ligand (3 equiv.) and K$_2$[PdCl$_4$] (2 equiv.) were heated to reflux in ethanol (50 mL) for 24 hr. The solution was cooled to room temperature and the resulting precipitate was isolated *via* filtration. The solid was washed with distilled water (25 mL), then ethanol (2.5 mL) and air dried.

3-[Pd₂]

3-[Pd2]
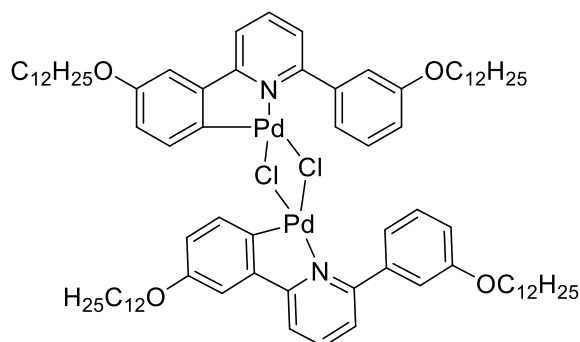
2,6-*Bis*(3-dodecylphenyl)pyridine (0.4995 g, 0.8325 mmol) and K₂[PdCl₄] (0.1817 g, 0.5566 mmol). ¹H NMR shows that only free ligand was isolated. Yield: 0.0 g (0%)

4-[Pd2]
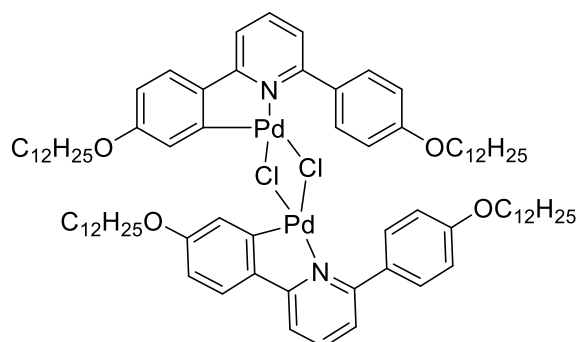
2,6-*Bis*(4-dodecylphenyl)pyridine (0.5011 g, 0.8353 mmol) and K₂[PdCl₄] (0.1862 g, 0.5704 mmol). ¹H NMR shows that only free ligand was isolated. Yield: 0.0 g (0%)

3,4-[Pd2]
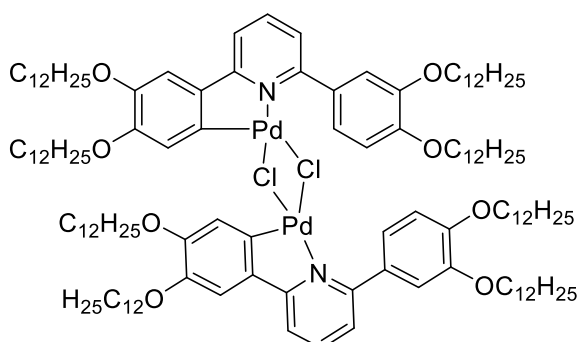
2,6-*Bis*(3,4-didodecylphenyl)pyridine (0.9993 g, 1.0317 mmol) and K₂[PdCl₄] (0.2291 g, 0.7018 mmol). ¹H NMR shows that only free ligand was isolated. Yield: 0.0 g (0%)

2,5-[Pd$_2$]
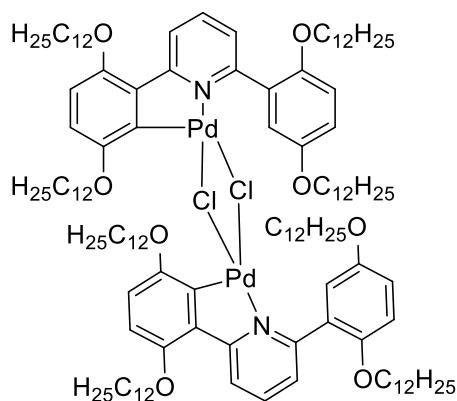
2,6-*Bis*(2,5-didodecylphenyl)pyridine (0.5014 g, 0.5177 mmol) and K$_2$[PdCl$_4$] (0.1126 g, 0.3450 mmol). ^{1}H NMR shows that only free ligand was isolated. Yield: 0.0 g (0%)

6.3.7 Unsuccessful Direct Auration *via* Rhodium Catalysis

6.3.7.1 General Method

Na[AuCl$_4$] (1.0 equiv.), NaOBz (1.2 equiv.) and [Cp*RhCl$_2$]$_2$ (2.5 mol%)) were added to a solution of 2,6-*bis*(2-dodecylphenyl)pyridine (1.2 equiv.) in ethyl acetate (20 mL) and heated at 60 °C for 18 hr. The resulting orange coloured solution was cooled to room temperature. The solid precipitate was isolated *via* filtration and washed with distilled water (20 mL), ethanol (2.5 mL) and air dried.

2-[Au]-Cl
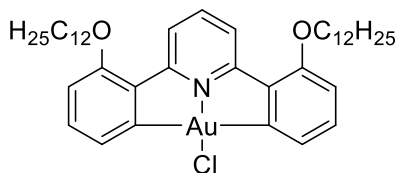
Na[AuCl$_4$] (0.1842 g, 0.2513 mmol), NaOBz (0.0452 g, 0.3136 mml), [Cp*RhCl$_2$]$_2$ (3.88 mg, 6.28 μmol) and 2,6-*bis*(2-dodecylphenyl)pyridine (0.1842 g, 0.3070 mmol). ^{1}H NMR shows no product present. Yield: 0.0 g (0%)

3-[Au]-Cl, 3/5-[Au]-Cl and 5-[Au]-Cl

3-[Au]-Cl   **3/5-[Au]-Cl**   **5-[Au]-Cl**
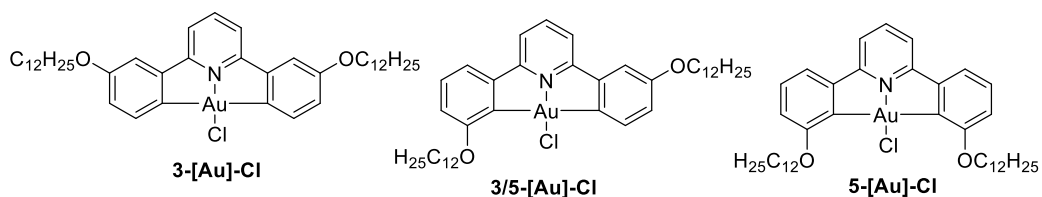
Na[AuCl$_4$] (0.1025 g, 0.2577 mmol), NaOBz (0.0435 g, 0.3244 mml), [Cp*RhCl$_2$]$_2$ (4.32 mg, 6.99 μmol) and 2,6-*bis*(3-dodecylphenyl)pyridine (0.1801 g, 0.3001 mmol). ^{1}H NMR shows that only free ligand was isolated. Yield: 0.0 g (0%)

4-[Au]-Cl
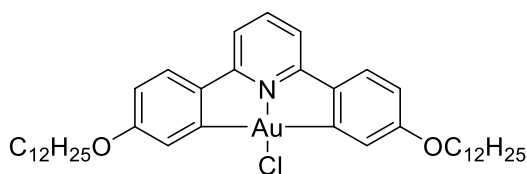
Na[AuCl$_4$] (0.1008 g, 0.2534 mmol), NaOBz (0.0438 g, 0.3039 mml), [Cp*RhCl$_2$]$_2$ (3.89 mg, 6.29 μmol) and 2,6-*bis*(4-dodecylphenyl)pyridine (0.1801 g, 0.3002 mmol). ^{1}H NMR shows that only free ligand was isolated. Yield: 0.0 g (0%)

3,4-[Au]-Cl
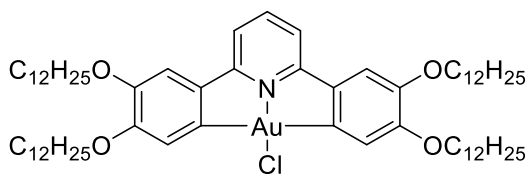
Na[AuCl$_4$] (0.1015 g, 0.2552 mmol), NaOBz (0.0462 g, 0.3206 mml), [Cp*RhCl$_2$]$_2$ (4.14 mg, 6.70 μmol) and 2,6-*bis*(3,4-didodecylphenyl)pyridine (0.2913 g, 0.3007 mmol). ^{1}H NMR shows that only free ligand was isolated. Yield: 0.0 g (0%)

363

2,5-[Au]-Cl
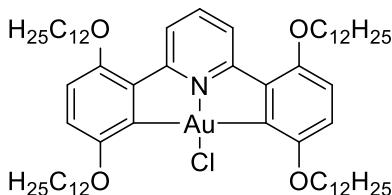
Na[AuCl$_4$] (0.1032 g, 0.2572 mmol), NaOBz (0.0465 g, 0.3227 mml), [Cp*RhCl$_2$]$_2$ (4.01 mg, 6.49 μmol) and 2,6-*bis*(2,5-didodecylphenyl)pyridine (0.2924 g, 0.3019 mmol). ^{1}H NMR shows no product present. Yield: 0.0 g (0%)

6.4   Successful Aurations

6.4.1   Auration *via* Palladium Complex Intermediate

2,3-[Pd$_2$]
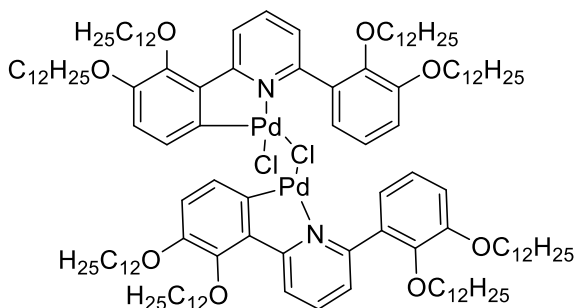
2,6-*Bis*(2,3-didodecylphenyl)pyridine (0.5004 g, 0.5166 mmol) and K$_2$[PdCl$_4$] (0.1125 g, 0.3446 mmol) were heated to reflux in ethanol (50 mL) for 24 hr. The solution was cooled to room temperature and the resulting yellow precipitate was isolated *via* filtration. The solid was washed by distilled water (15 mL), then ethanol (2.5 mL) and air dried. A second crop was isolated *via* the same method. The combined product was purified by column chromatography (silica, 95:5 petroleum ether (40 – 60 °C):ethyl acetate, R_f = 0.03, then 7:3 CH$_2$Cl$_2$: petroleum ether (40 – 60 °C), R_f = 0.47) to give a yellow oil, which solidified on standing to give a golden glassy solid. Yield: 0.1188 g (31%)

^{1}H NMR (400 MHz, CDCl$_3$) δ^H ppm: 8.48 (2H, d, $^3J_{HH}$ = 8.3 Hz), 7.89 (2H, t, $^3J_{HH}$ = 8.6 Hz), 7.46 (2H, t, $^3J_{HH}$ = 7.6 Hz), 7.38 (2H, d, $^3J_{HH}$ = 8.6 Hz), 7.16 (2H, dd, $^3J_{HH}$ = 7.4 Hz, $^3J_{HH}$ = 7.4 Hz), 7.04 (2H, d, $^3J_{HH}$ = 7.4 Hz), 6.97 (2H,d, $^3J_{HH}$ = 7.4 Hz), 6.66 (2H, d, $^3J_{HH}$

= 8.7 Hz), 4.07 (2H, br s), 4.00 (2H, br s), 3.92 (2H, t, $^3J_{HH}$ = 6.3 Hz), 1.80 (16H, m), 1.46 (16H, m), 1.4 – 1.0 (136H, br m), 0.86 (24H, m).

MALDI-TOF MS (m/z): Expected for $C_{130}H_{216}ClN_2O_8Pd_2$ = 2180.430948; Observed: 2180.435632 [M + H]$^+$ (Error = -0.2 mDa)

2,3-[Au]-Cl
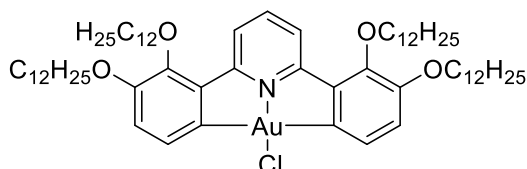
2,3-[Pd₂] (0.0995, 0.0448 mmol) and Na[AuCl₄] (0.0365 g, 0.0918 mmol) were heated to reflux in 1:1 chloroform:acetonitrile (50 mL) for 24 hr under a dinitrogen atmosphere. The solution was cooled to room temperature and reduced to dryness under reduced pressure. The off-white to purple solid was extracted into acetonitrile (15 mL) and the insoluble solid isolated *via* filtration, washed with acetonitrile (10 mL) and air dried. The purple solid was dissolved in CH_2Cl_2 and filtered through Celite$^®$ to remove elemental gold and the resulting yellow solution reduced to dryness. The remaining mustard yellow solid was recrystallised from CH_2Cl_2/hexane to give a pale yellow solid. Yield: 0.0467 g (48%)

^{1}H NMR (400 MHz, CDCl₃) δ^H ppm: 8.31 (2H, d, $^3J_{HH}$ = 8.1 Hz), 7.84 (1H, t, $^3J_{HH}$ = 8.5 Hz), 7.55 (2H, d, $^3J_{HH}$ = 7.9 Hz), 7.01 (2H, d, $^3J_{HH}$ = 9.1 Hz), 4.08 (4H, t, $^3J_{HH}$ = 7.0 Hz), 3.98 (4H, t, $^3J_{HH}$ = 6.8 Hz), 1.83 (8H, m), 1.47 (8H, m), 1.4-1.1 (68H, br m), 0.88 (6H, t, $^3J_{HH}$ = 6.9 Hz), 0.88 (6H, t, $^3J_{HH}$ = 6.9 Hz).

APCI MS (m/z): Expected for $C_{78}H_{122}AuNO_4$ = 1198.7627; Observed: 1198.7599 [M + H]$^+$ (Error = -2.8 mDa)

2-[Pd₂]
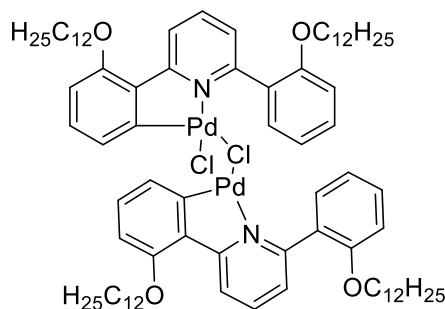
2,6-*Bis*(2-dodecylphenyl)pyridine (0.5014 g, 0.8358 mmol) and $K_2[PdCl_4]$ (0.1818 g, 0.5570 mmol) were heated to reflux in ethanol (50 mL) for 24 hr. The solution was cooled to room temperature and the resulting precipitate was isolated *via* filtration. The white solid was washed by distilled water (25 mL), then ethanol (2.5 mL) and air dried and shown by ^{1}H NMR spectroscopy to be the free ligand. A second crop of pale yellow crystals was isolated *via* the same method and was shown by ^{1}H NMR spectroscopy to be the impure product. The product was purified by column chromatography (silica, 95:5 petroleum ether (40 − 60 °C):ethyl acetate, R_f = 0.03, then 95:5 CH_2Cl_2: methanol, R_f = 0.82) to give a yellow oil, which solidified on standing to give a golden glassy solid. Yield: 0.0575 g (31%)

^{1}H NMR (400 MHz, CDCl₃) δ^H ppm: 8.46 (2H, dd, $^3J_{HH}$ = 8.3 Hz, $^4J_{HH}$ = 1.2 Hz), 7.89 (2H, dd, $^3J_{HH}$ = 8.2 Hz, $^3J_{HH}$ = 8.2 Hz), 7.47 (2H, ddd, $^3J_{HH}$ = 8.8 Hz, $^3J_{HH}$ = 7.3 Hz, $^4J_{HH}$ = 1.3 Hz), 7.40 (6H, m), 7.20 (4H, m), 6.95 (2H, dd, $^3J_{HH}$ = 8.2 Hz, $^3J_{HH}$ = 8.2 Hz), 6.66 (2H, dd, $^3J_{HH}$ = 7.4 Hz, $^4J_{HH}$ = 1.0 Hz), 4.56 (4H, t, $^3J_{HH}$ = 6.4 Hz), 4.08 (4H, t, $^3J_{HH}$ = 6.6 Hz), 1.90 (8H, m), 1.50 (4H, m), 1.39 (4H, m), 1.3 − 1.1 (64 H br m), 0.88 (6H, t, $^3J_{HH}$ = 6.8 Hz), 0.87 (6H, t, $^3J_{HH}$ = 7.2 Hz).

MALDI-TOF MS (m/z): Expected for $C_{82}H_{120}ClN_2O_4Pd_2$ = 1443.701559; Observed: 1443.701559 [M + H]$^+$ (Error = 1.7 mDa)

2-[Au]-Cl
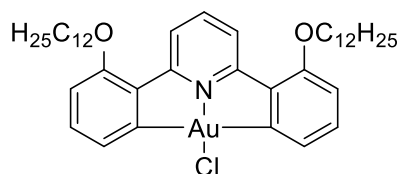
2-[Pd₂] (0.0531, 0.0358 mmol) and Na[AuCl₄] (0.0289 g, 0.0726 mmol) were heated to reflux in 1:1 chloroform:acetonitrile (50 mL) for 24 hr under a dinitrogen atmosphere. The solution was cooled to room temperature and reduced to dryness under reduced pressure. The off-white to purple solid was extracted into acetonitrile (20 mL) and the insoluble solid isolated *via* filtration, washed with distilled water (10 mL), then acetonitrile (5 mL) and air dried to give small yellow needles. Yield: 0.0177 g (30%)

^{1}H NMR (400 MHz, CDCl₃) δ^H ppm: 8.15 (2H, d, $^3J_{HH}$ = 8.2 Hz), 7.70 (1H, t, $^3J_{HH}$ = 8.2 Hz), 7.46 (2H, dd, $^3J_{HH}$ = 7.2 Hz, $^4J_{HH}$ = 1.0 Hz), 7.30 (2H, dd, $^3J_{HH}$ = 8.2 Hz, $^3J_{HH}$ = 7.2 Hz), 6.67 (2H, dd, $^3J_{HH}$ = 8.5 Hz, $^4J_{HH}$ = 1.0 Hz), 4.01 (4H, t, $^3J_{HH}$ = 6.9 Hz), 1.88 (4H, m), 1.50 (4H, m), 1.3-1.2 (32H, m), 0.88 (6H, t, $^3J_{HH}$ = 6.8 Hz).

APCI MS (m/z): Expected for $C_{41}H_{59}AuClNO_2$ = 830.39727; Observed: 830.3973 [M + H]$^+$ (Error = 4.7 mDa)

6.4.2   Auration *via* Rhodium Catalysis

[Cp*RhCl₂]₂

RhCl₃.3H₂O (2.5022 g, 9.5047 mmol) and 1,2,3,4,5-pentamethylcyclopentadiene (3.0 mL, 2.61 g, 19.26 mmol) were heated to reflux in methanol (100 mL) for 72 hours under a dinitrogen atmosphere. The resulting solution was cooled to room temperature and the brick-red precipitate isolated *via* filtration. The filtrate was concentrated to ~25 mL and the brick-red precipitate isolated *via* filtration. The combined solid was washed with diethyl ether (3 x 50 mL) and dried to give a brick-red solid. A third crop of red solid was isolated from the filtrate. Yield: 2.0606 g (35%)

^{1}H NMR (400 MHz, CDCl₃) δ^H ppm: 1.62 (15H, s).

2,3-[Au]-Cl
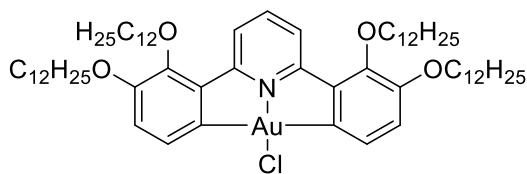
Na[AuCl$_4$] (0.1024 g, 0.2574 mmol), NaOBz (0.0447 g, 0.3102 mml) and [Cp*RhCl$_2$]$_2$ (4.14 mg, 6.70 μmol) were added to a solution of 2,6-*bis*(2,3-didodecylphenyl)pyridine (0.2951 g, 0.3047 mmol) in ethyl acetate (20 mL) and heated at 60 °C for 19 hr. The resulting cloudy straw coloured solution was cooled to room temperature and the light brown precipitate isolated *via* filtration and washed with distilled water (20 mL), ethanol (10 mL) and air dried. The solid was dissolved in chloroform and filtered through a Celite® plug to remove elemental gold and the resulting yellow solution reduced to dryness to give a pale yellow microcrystalline solid. Yield: 0.0316 g (11%)

^{1}H NMR (400 MHz, CDCl$_3$) δ^H ppm: 8.31 (2H, d, $^3J_{HH}$ = 8.2 Hz), 7.84 (1H, t, $^3J_{HH}$ = 8.4 Hz), 7.55 (2H, d, $^3J_{HH}$ = 8.0 Hz), 7.01 (2H, d, $^3J_{HH}$ = 8.0 Hz), 4.08 (4H, t, $^3J_{HH}$ = 6.9 Hz), 3.98 (4H, t, $^3J_{HH}$ = 6.4 Hz), 1.83 (8H, m), 1.47 (8H, m), 1.4-1.1 (68H, br m), 0.88 (6H, t, $^3J_{HH}$ = 6.8 Hz), 0.88 (6H, t, $^3J_{HH}$ = 6.8 Hz).

APCI MS (m/z): Expected for C$_{78}$H$_{122}$AuNO$_4$ = 1198.7627; Observed: 1198.7627 [M + H]$^+$ (Error = 6.7 mDa)

6.5   Synthesis of Phenylacetylene ligands

3,4,5-Tri(dodecyloxy)benzaldehyde
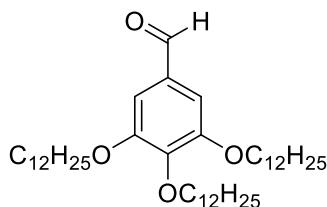
3,4,5-Trihydroxybenzaldehyde (0.5033 g, 3.2656 mmol), K$_2$CO$_3$ (1.4733 g, 10.6603 mmol) and 1-bromododecane (3.1 mL, 3.2 g, 10.9 mmol) were heated to reflux for 24 hr in 2-butanone (80 mL) under a nitrogen atmosphere. The reaction mixture was filtered through Celite® and reduced to dryness under reduced pressure. The resulting oil was purified by column chromatography (silica, 95:5 petroleum ether (40 − 60 °C):ethyl

acetate, $R_f = 0.40$) to give an oil that solidified on standing to give white crystals. Yield: 0.1087 g (5%)

^{1}H NMR (400 MHz, CDCl$_3$) δ^H ppm: 9.83 (1H, s), 7.08 (2H, s), 4.05 (2H, t, $^3J_{HH}$ = 6.6 Hz), 4.03 (4H, t, $^3J_{HH}$ = 6.8 Hz), 1.82 (4H, m), 1.74 (2H, m), 1.47 (6H, m), 1.4-1.2 (48H, broad m), 0.88 (6H, t, $^3J_{HH}$ = 7.0 Hz), 0.88 (3H, t, $^3J_{HH}$ = 7.0 Hz).

5-(2,2-Dibromovinyl)-1,2,3-tris(dodecyloxy)benzene
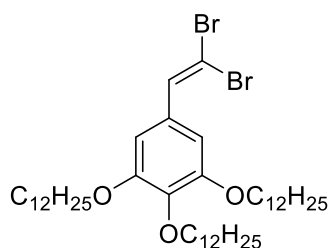
A solution of tetrabromomethane (0.1414 g, 0.4264 mmol) in dry CH$_2$Cl$_2$ (5 mL) under a nitrogen atmosphere and cooled to 0 °C was added to a solution of triphenylphosphine (0.2084 g, 0.7945 mmol) in dry CH$_2$Cl$_2$ (20 mL), while maintaining the temperature below 15 °C. After full addition the temperature was cooled to 0 °C and 3,4,5-tri(dodecyloxy)benzaldehyde (0.1000 g, 0.3015 mmol) and triethylamine (0.08 mL, 0.06 g, 0.3 mmol) in dry CH$_2$Cl$_2$ (20 mL) were added dropwise. The resulting solution was stirred at 0 °C under a nitrogen atmosphere for 30 min, then at room temperature for 1 hr. It was poured into hexane (100 mL), filtered through a Celite® plug and reduced to dryness to give am off-white solid, which was purified by column chromatography (silica, 1:1 Petroleum ether (40-60 °C): CH$_2$Cl$_2$, R_f = 0.57)) to give a yellow oil, which solidified on standing to give a white solid. Yield: 0.0862 g (35%)

^{1}H NMR (400 MHz, CDCl$_3$) δ^H ppm: 7.37 (1H, s), 6.76 (2H, s), 3.97 (2H, t, $^3J_{HH}$ = 6.5 Hz), 3.96 (4H, t, $^3J_{HH}$ = 6.5 Hz), 1.79 (4H, m), 1.73 (2H, m), 1.46 (6H, m), 1.4-1.2 (48H, br m), 0.88 (6H, t, $^3J_{HH}$ = 6.8 Hz), 0.88 (3H, t, $^3J_{HH}$ = 6.8 Hz).

5-Ethynyl-1,2,3-tris(dodecyloxy)benzene
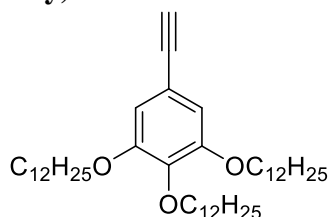
5-(2,2-Dibromovinyl)-1,2,3-tris(dodecyloxy)benzene (0.0815 g, 0.0815 mmol) was dissolved in dry THF (15 mL) under a dinitrogen atmosphere. A solution of EtMgBr (3M in diethyl ether, 0.05 mL, 0.02 g, 0.15 mmol) was added dropwise and the resulting reaction mixture was stirred for 2 hr at room temperature. Solid NH$_4$Cl (0.0473 g, 0.8843 mmol) was then added to quench the reaction. The resulting mixture was poured into hexane (50 mL), filtered through a Celite$^®$ plug and reduced to dryness under reduced pressure. The residue was purified by column chromatography (silica, 7:3 Petroleum ether (40-60 °C): CH$_2$Cl$_2$, R_f = 0.29)) to give an oil, which crystallised on standing to give white needles. Yield: 0.0475 g (73%)

^{1}H NMR (400 MHz, CDCl$_3$) δ^H ppm: 6.67 (1H, s), 3.94 (2H, t, $^3J_{HH}$ = 6.5 Hz), 3.93 (4H, t, $^3J_{HH}$ = 6.6 Hz), 1.78 (4H, m), 1.71 (2H, m), 1.44 (6H, m), 1.4-1.2 (48H, br m), 0.88 (6H, t, $^3J_{HH}$ = 6.9 Hz), 0.88 (3H, t, $^3J_{HH}$ = 6.9 Hz).

6.6 Synthesis of Perfluoro-ligands

1*H*,1*H*,2*H*,2*H*-perfluoro(dodecyl)trifluoromethanesulfonate
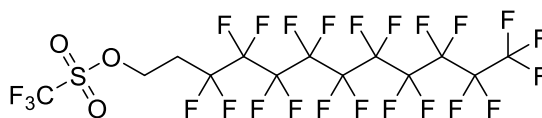
Triflic anhydride (1.8 mL, 3.0 g, 10.7 mmol) was added to dry CH$_2$Cl$_2$ (~20 mL) under dinitrogen and cooled to 0 °C. 1*H*,1*H*,2*H*,2*H*-perfluoroalkan-1-ol (4.64 g, 8.23 mmol) and pyridine (0.72 mL, 0.70 g, 8.86 mmol) were added in dry 2:1 1,4-dioxane:trifluoromethylbenzene (45 mL) over 15 min and the reaction was stirred at 0 °C under a dinitrogen atmosphere for 1 hr. The resulting precipitate was removed by filtration and the filtrate was reduced to dryness *in vacuo*. The purple residue was purified by flash column chromatography (silica, 8:2 CH$_2$Cl$_2$:petroleum ether(40-60), R_f = 0.84) to give an off-white solid. Yield 1.38 g (24%)

^{1}H NMR (400 MHz, CDCl$_3$) δ^H ppm: 4.79 (2H, t, $^3J_{HH}$ = 6.2 Hz), 2.69 (2H, m).

4-(1H,1H,2H,2H-perfluoro(dodecyloxy))benzaldehyde

$$O \diagup H$$

(structure)

$$O(CH_2)_2(CF_2)_9CF_3$$
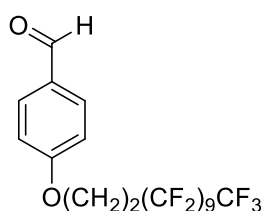
4-Hydroxybenzaldehyde (0.1353 g, 1.1079 mmol) and K_2CO_3 (0.1735 g, 1.2553 mmol) were dissolved in acetonitrile (20 mL) and stirred at room temperature. 1H,1H,2H,2H-perfluoro(dodecyl)trifluoromethanesulfonate (0.8484 g, 1.2186 mmol) dissolved in acetonitrile (30 mL) was added and the resulting solution stirred at room temperature for 16 hr. The solid precipitate was removed by filtration and washed with distilled water (50 mL) to remove K_2CO_2 and air dried. The filtrate was reduced to dryness under reduced pressure. The solid residue was dissolved in ethyl acetate (50 mL) and washed with NaOH (0.0910 g, 2.2750 mmol) in distilled water (30 mL). The aqueous layer was washed with ethyl acetate (2 x 30 mL) and the combined organic layers dried over $MgSO_4$, filtered and reduced to dryness. The combined product was purified by column chromatography (silica, 8:2 petroleum ether (40-60 °C):ethyl acetate, $R_f = 0.51$)to give an off-white solid. Yield: 0.5153 g (70%)

^{1}H NMR (400 MHz, CDCl$_3$) δ^H ppm: 9.91 (1H, s), 7.86 (2H, AA'XX', $J = 8.2$ Hz), 7.02 (2H, AA'XX', $J = 8.8$ Hz), 4.36 (2H, t, $^3J_{HH} = 6.8$ Hz), 2.70 (2H, m).

^{19}F NMR (379.5 MHz, CDCl$_3$) δ^F ppm: -80.60 (3F, t, $^3J_{FF} = 10.8$ Hz), -110.15 (2F, m), -121.62 (10F, m), -122.57 (2F, m), -123.35 (2F, m), -125.97 (2F, m).

4-(2,2-Dibromovinyl)-1-(1H,1H,2H,2H-perfluoro(dodecyloxy))benzene

$$Br$$
$$Br$$

(structure)

$$O(CH_2)_2(CF_2)_9CF_3$$
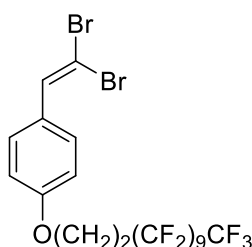
A solution of tetrabromomethane (0.4929 g, 1.4863 mmol) in dry CH_2Cl_2 (25 mL) under a nitrogen atmosphere and cooled to 0 °C was added to a solution of triphenylphosphine (0.7768 g, 2.9616 mmol) in dry CH_2Cl_2 (10 mL), while maintaining the temperature below 15 °C. After full addition the temperature was cooled to 0 °C and 4-(1H,1H,2H,2H-

perfluoro(dodecyloxy))benzaldehyde (0.7582 g, 1.1346 mmol) and triethylamine (0.30 mL, 0.22 g, 1.13 mmol) in dry CH_2Cl_2 (20 mL) was added dropwise. The resulting solution was stirred at 0 °C under a nitrogen atmosphere for 30 min, then at room temperature for 1 hr. It was poured into hexane (100 mL), filtered through a Celite® plug and reduced to dryness to give a white solid, which was purified by column chromatography (silica, 1:1 Petroleum ether (40-60 °C): CH_2Cl_2, R_f = 0.82)) to give a white solid. Yield: 0.4702 g (50%)

^{1}H NMR (400 MHz, CDCl$_3$) δ^H ppm: 7.52 (2H, AA'XX', J = 8.4 Hz), 7.41 (1H, s), 6.90 (2H, AA'XX', J = 8.9 Hz), 4.29 (2H, t, $^3J_{HH}$ = 6.7 Hz), 2.64 (2H, m).

^{19}F NMR (379.5 MHz, CDCl$_3$) δ^F ppm: -80.59 (3F, t, $^3J_{FF}$ = 10.2 Hz), -113.15 (2F, m), -121.60 (10F, m), -122.56 (2F, m), -123.36 (2F, m), -125.97 (2F, m).

1-(1H,1H,2H,2H-perfluoro(dodecyloxy))-4-ethynylbenzene
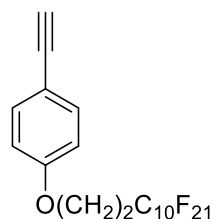
4-(2,2-Dibromovinyl)-1-(1H,1H,2H,2H-perfluoro(dodecyloxy))benzene (0.4702 g, 0.5706 mmol) was dissolved in dry THF (24 mL) under a dinitrogen atmosphere. A solution of EtMgBr (3M in diethyl ether, 0.28 mL, 0.11 g, 0.84 mmol) was added dropwise and the resulting reaction mixture was stirred for 2 hr at room temperature. Solid NH$_4$Cl (0.1901 g, 3.5539 mmol) was then added to quench the reaction. Excess and resultant salts were removed *via* filtration, and the filtrate reduced to dryness under reduced pressure. The residue was purified by column chromatography (silica, 6:4 petroleum ether (40-60 °C): ethyl acetate, R_f = 0.80)) to give a white solid. Yield: 0.2477 g (65%)

^{1}H NMR (400 MHz, CDCl$_3$) δ^H ppm: 7.44 (2H, AA'XX', J = 9.0 Hz), 6.85 (2H, AA'XX', J = 8.8 Hz), 4.28 (2H, t, $^3J_{HH}$ = 6.9 Hz), 3.01 (1H, s), 2.64 (2H, m).

^{19}F NMR (379.5 MHz, CDCl$_3$) δ^F ppm: -80.59 (3F, t, $^3J_{FF}$ = 9.5 Hz), -113.15 (2F, m), -121.54 (10F, m), -122.56 (2F, m), -123.37 (2F, m), -125.97 (2F, m).

6.7 Synthesis of [Gold(III)(C^N^C)(C≡C-R)]

2-[Au]-5 [Gold(III)(2,6-*bis*(2-dodecyloxyphenyl)pyridine)(1-ethynyl-4-pentylbenzene)]
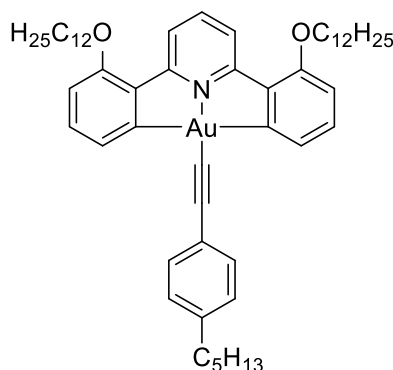
2-[Au]-Cl (0.1001 g, 0.1204 mmol), 1-ethynyl-4-pentylbenzene (0.03 mL, 0.0257 g, 0.1489 mmol) and CuI (0.0038 g, 0.0205 mmol) were degassed, then dry CH$_2$Cl$_2$ (~50 mL) and triethylamine (0.03 mL, 45 mol%) were added and the reaction stirred under a dinitrogen atmosphere at room temperature for 24 hr. The reaction mixture was filtered through Celite® and reduced to dryness under reduced pressure, then purified by column chromatography (silica; 1% ethyl acetate in CH$_2$Cl$_2$ (R_f = 0.05), then 1:1 CH$_2$Cl$_2$: petroleum ether (40 − 60 °C) (R_f = 0.72)) to give a yellow solid. Recrystallised from CH$_2$Cl$_2$/ethyl acetate to give yellow needle-like crystals. Yield = 0.0970 g (83%)

^{1}H NMR (500 MHz, CDCl$_3$) δ^H ppm: 8.22 (2H, d, $^3J_{HH}$ = 8.3 Hz), 7.72 (1H, t, $^3J_{HH}$ = 8.3 Hz), 7.71 (2H, dd, $^3J_{HH}$ = 7.1 Hz, $^4J_{HH}$ = 0.8 Hz), 7.53 (2H, AA'XX', J = 8.1 Hz), 7.29 (2H, dd, $^3J_{HH}$ = 8.3 Hz, $^3J_{HH}$ = 7.2 Hz), 7.14 (2H, AA'XX', J = 8.1 Hz), 6.72 (2H, dd, $^3J_{HH}$ = 8.4 Hz, $^4J_{HH}$ = 0.6 Hz), 4.06 (4H, t, $^3J_{HH}$ = 6.7 Hz), 2.61 (2H, t, $^3J_{HH}$ = 7.6 Hz), 1.90 (4H, m), 1.63 (2H, m), 1.51 (4H, m), 1.27 (36H, m), 0.91 (6H, t, $^3J_{HH}$ = 6.9 Hz), 0.88 (3H, t, $^3J_{HH}$ = 7.1 Hz).

^{13}C{^{1}H} NMR (125.8 MHz, CDCl$_3$) δ^C ppm: 167.71, 164.18, 158.05, 141.67,141.51, 136.42, 132.24, 131.60, 128.55, 128.11, 124.05, 121.58, 110.59, 100.63, 93.13, 68.33, 35.86, 31.92, 31.49, 31.07, 29.67, 29.66, 29.65, 29.60, 29.58, 24.40, 29.35, 29.21, 26.23, 22.68, 22.56, 14.11, 14.04.

APCI MS (m/z): Expected for $C_{54}H_{74}AuNO_2$ = 966.54801; Observed: 966.545801 [M + H]$^+$ (Error = -0.3 mDa)

Elemental Analysis: Found (%): C 66.7, H 7.8, N 1.2; Calc (%) for $C_{54}H_{74}AuNO_2$: C 67.1, H 7.7, N 1.5.

2-[Au]-8 [Gold(III)(2,6-*bis*(2-dodecyloxyphenyl)pyridine)(1-ethynyl-4-octylbenzene)]
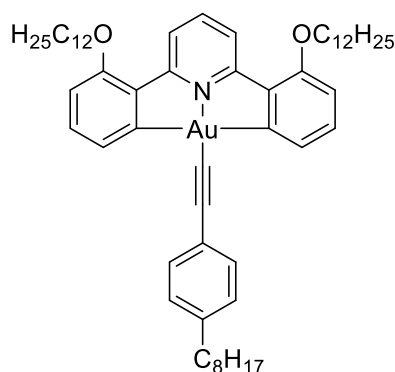
2-[Au]-Cl (0.1001 g, 0.1204 mmol), 1-ethynyl-4-octylbenzene (0.03 mL, 0.027 g, 0.13 mmol) and CuI (0.0047 g, 0.0247 mmol) were degassed, then dry CH_2Cl_2 (~50 mL) and triethylamine (0.03 mL, 45 mol%) added and the reaction stirred under a dinitrogen atmosphere at room temperature for 24 hr. The reaction mixture was filtered through Celite® and reduced to dryness under reduced pressure, then purified by column chromatography (silica; 1% ethyl acetate in CH_2Cl_2 (R_f = 0.05), then 1:1 CH_2Cl_2: petroleum ether (40 − 60 °C) (R_f = 0.79)), then on a second column (silica; 3:7 CH_2Cl_2: petroleum ether (40 − 60 °C) (R_f = 0.37)) to give an amorphous yellow solid. Crystallised from CH_2Cl_2/ethyl acetate and cooled at 5 °C to give yellow plate-like crystals. Yield = 0.0860 g (71%)

^{1}H NMR (500 MHz, CDCl$_3$) δ^H ppm: 8.26 (2H, d, $^3J_{HH}$ = 8.3 Hz), 7.76 (1H, t, $^3J_{HH}$ = 8.3 Hz), 7.70 (2H, dd, $^3J_{HH}$ = 7.1 Hz, $^4J_{HH}$ = 0.9 Hz), 7.53 (2H, AA'XX', J = 8.2 Hz), 7.33 (2H, dd, $^3J_{HH}$ = 8.3 Hz, $^3J_{HH}$ = 7.2 Hz), 7.13 (2H, AA'XX', J = 8.3 Hz), 6.77 (2H, dd, $^3J_{HH}$ = 8.4 Hz, $^4J_{HH}$ = 0.8 Hz), 4.09 (4H, t, $^3J_{HH}$ = 6.6 Hz), 2.60 (2H, t, $^3J_{HH}$ = 7.4 Hz), 1.92 (4H, m), 1.62 (2H, m), 1.51 (4H, m), 1.27 (36H, m), 0.89 (6H, t, $^3J_{HH}$ = 6.9 Hz), 0.88 (3H, t, $^3J_{HH}$ = 7.1 Hz).

^{13}C{^{1}H} NMR (125.8 MHz, CDCl$_3$) δ^C ppm: 167.72, 164.34, 158.10, 141.69,141.57, 136.47, 132.38, 131.61, 128.65, 128.12, 121.54, 110.70, 100.80, 83.89, 68.38, 35.89, 31.91, 31.39, 29.69, 29.66, 29.65, 29.58, 29.56, 29.49, 24.38, 29.35, 29.27, 29.22, 26.23, 22.68, 22.56, 14.11.

APCI MS (m/z): Expected for C$_{57}$H$_{80}$AuNO$_2$ = 1008.592751; Observed: 1008.592751 [M + H]$^+$ (Error = 0.0 mDa)

Found (%): C 67.2, H 7.7, N 1.3; Calc (%) for C$_{57}$H$_{80}$AuNO$_2$: C 67.9, H 8.0, N 1.4.

2-[Au]-1-10 [Gold(III)(2,6-*bis*(2-dodecyloxyphenyl)pyridine)(1-ethynyl-4-decyloxybenzene)]
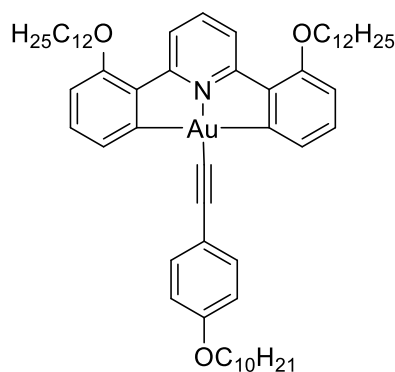
2-[Au]-Cl (0.0793 g, 0.0955 mmol), 1-ethynyl-4-decyloxybenzene (0.0380 g, 0.1471 mmol) and CuI (0.0025 g, 0.0131 mmol) were degassed, then dry CH$_2$Cl$_2$ (~50 mL) and triethylamine (0.01 mL, 45 mol%) was added and the reaction stirred under a dinitrogen atmosphere at room temperature for 48 hr. The reaction mixture was filtered through Celite® and reduced to dryness under reduced pressure, then purified by column chromatography (silica; 7:3 petroleum ether (40-60 °C): CH$_2$Cl$_2$ (R_F = 0.11), then 1:1 CH$_2$Cl$_2$: petroleum ether (40 − 60 °C) (R_f = 0.35)) to give a yellow crystalline solid. Recrystallised from CH$_2$Cl$_2$/ethyl acetate to give yellow needle-like crystals. Yield = 0.074 g (74%)

^{1}H NMR (400 MHz, CDCl$_3$) δ^H ppm: 8.26 (2H, d, $^3J_{HH}$ = 8.2 Hz), 7.76 (1H, t, $^3J_{HH}$ = 8.1 Hz), 7.75 (2H, dd, $^3J_{HH}$ = 7.1 Hz, $^4J_{HH}$ = 1.0 Hz), 7.54 (2H, AA'XX', J = 9.0 Hz), 7.34 (2H, dd, $^3J_{HH}$ = 8.4 Hz, $^3J_{HH}$ = 7.1 Hz), 6.85 (2H, AA'XX', J = 8.9 Hz), 6.77 (2H, dd, $^3J_{HH}$ = 8.5 Hz, $^4J_{HH}$ = 1.1 Hz), 4.09 (4H, t, $^3J_{HH}$ = 6.6 Hz), 3.97 (2H, t, $^3J_{HH}$ = 5.8 Hz), 1.92

(4H, m), 1.79 (2H, m), 1.6-1.2 (50H, br m), 0.89 (3H, t, $^3J_{HH}$ = 6.8 Hz), 0.88 (6H, t, $^3J_{HH}$ = 7.1 Hz).

^{13}C{^{1}H} NMR (100.6 MHz, CDCl$_3$) δ^C ppm: 167.71, 164.00, 158.02, 157.99, 141.6, 136.37, 133.00, 132.11, 128.41, 121.59, 119.03, 114.17, 110.46, 100.17, 92.13, 68.25, 68.01, 31.91, 31.89, 29.66, 29.60, 29.59, 29.56, 29.41, 29.35, 29.32, 29.29, 29.19, 26.21, 26.05, 22.68, 14.11.

APCI MS (m/z): Expected for C$_{59}$H$_{84}$AuNO$_3$ = 1052.6190; Observed: 1052.6172 [M + H]$^+$ (Error = 1.7 mDa)

Elemental Analysis: Found (%): C 67.5, H 8.1, N 1.3; Calc (%) for C$_{59}$H$_{84}$AuNO$_3$: C 67.3, H 8.1, N 1.3.

2-[Au]-2-10 [Gold(III)(2,6-*bis*(2-dodecyloxyphenyl)pyridine)(1-ethynyl-3,4-didecyloxybenzene)]
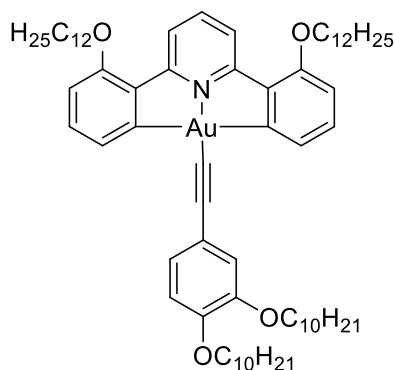
2-[Au]-Cl (0.1007 g, 0.1213 mmol), 1-ethynyl-3,4-di(decyloxy)benzene (0.0557 g, 0.1343 mmol) and CuI (0.0070 g, 0.0368 mmol) were degassed, then dry CH$_2$Cl$_2$ (~50 mL) and triethylamine (0.01 mL, 45 mol%) was added and the reaction stirred under a dinitrogen atmosphere at room temperature for 24 hr. The reaction mixture was filtered through Celite® and reduced to dryness under reduced pressure, then purified by column chromatography (silica; 7:3 Petroleum ether (40-60 °C): CH$_2$Cl$_2$ (R_f = 0.10), then 1:1 CH$_2$Cl$_2$: petroleum ether (40 − 60 °C) (R_f = 0.34)) to give a yellow crystalline solid. Recrystallised from CH$_2$Cl$_2$ /ethyl acetate to give bright yellow broad needle-like crystals. Yield = 0.130 g (89%)

^{1}H NMR (400 MHz, CDCl$_3$) δ^H ppm: 8.27 (2H, d, $^3J_{HH}$ = 8.2 Hz), 7.77 (1H, t, $^3J_{HH}$ = 8.2 Hz), 7.75 (2H, dd, $^3J_{HH}$ = 6.9 Hz, $^4J_{HH}$ = 1.0 Hz), 7.34 (2H, dd, $^3J_{HH}$ = 8.6 Hz, $^3J_{HH}$ = 7.4 Hz), 7.17 (1H, dd, $^3J_{HH}$ = 8.2 Hz, $^4J_{HH}$ = 1.6 Hz), 7.14 (1H, d, $^4J_{HH}$ = 1.8 Hz), 6.82 (1H, d, $^3J_{HH}$ = 8.2 Hz), 6.78 (2H, dd, $^3J_{HH}$ = 8.5 Hz, $^4J_{HH}$ = 1.2 Hz), 4.10 (4H, t, $^3J_{HH}$ = 6.5 Hz), 4.03 (2H, t, $^3J_{HH}$ = 6.6 Hz), 4.01 (2H, t, $^3J_{HH}$ = 6.8 Hz), 1.92 (4H, m), 1.83 (4H, m), 1.54-1.21 (64H, br m), 0.88 (12H, m).

^{13}C{^{1}H} NMR (125.8 MHz, CDCl$_3$) δ^C ppm: 167.77, 164.23, 158.07, 148.64, 148.49, 141.66, 136.43, 132.29, 128.59, 124.79, 121.56, 119.41, 117.26, 113.64, 110.63, 100.64, 91.78, 69.36, 69.26, 69.34, 31.92, 29.66, 29.65, 29.59, 29.57, 29.41, 29.39, 29.35, 29.33, 29.21, 26.23, 26.06, 26.04, 22.68, 14.11.

APCI MS (m/z): Expected for C$_{69}$H$_{104}$AuNO$_4$ = 1376.9582; Observed: 1376.9581 [M + H]$^+$ (Error = 0.1 mDa)

Elemental Analysis: Found (%): C 68.9, H 8.8, N 1.0; Calc (%) for C$_{69}$H$_{104}$AuNO$_4$: C 68.6, H 8.7, N 1.2.

2-[Au]-3-10 [Gold(III)(2,6-*bis*(2-dodecyloxyphenyl)pyridine)(1-ethynyl-3,4,5-tridecyloxybenzene)]
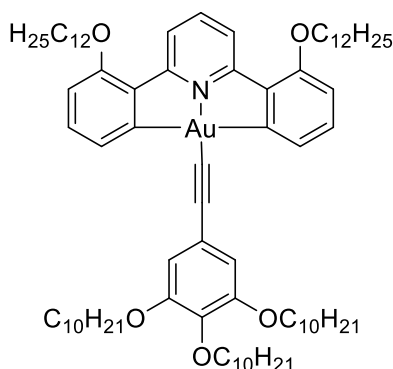
2-[Au]-Cl (0.0728 g, 0.0877 mmol), 1-ethynyl-3,4,5-tri(decyloxy)benzene (0.0471 g, 0.0825 mmol) and CuI (0.0022 g, 0.0217 mmol) were degassed, then dry CH$_2$Cl$_2$ (~50 mL) and triethylamine (0.01 mL, 45 mol%) was added and the reaction stirred under a dinitrogen atmosphere at room temperature for 24 hr. The reaction mixture was filtered through Celite$^®$ and reduced to dryness under reduced pressure, then purified by column chromatography (silica; 1:1 CH$_2$Cl$_2$: petroleum ether (40 − 60 °C) (R_f = 0.38)) to give a

yellow crystalline solid. Recrystallised from CH_2Cl_2/ethyl acetate and cooled at 5 °C to give yellow crystals. Yield = 0.076 g (69%)

^{1}H NMR (400 MHz, CDCl$_3$) δ^H ppm: 8.26 (2H, d, $^3J_{HH}$ = 8.3 Hz), 7.76 (1H, t, $^3J_{HH}$ = 8.3 Hz), 7.72 (2H, d, $^3J_{HH}$ = 7.1 Hz), 7.34 (2H, dd, $^3J_{HH}$ = 8.2 Hz, $^3J_{HH}$ = 8.2 Hz), 6.81 (2H, s), 6.77 (2H, d, $^3J_{HH}$ = 8.3 Hz), 4.09 (4H, t, $^3J_{HH}$ = 6.5 Hz), 4.00 (4H, t, $^3J_{HH}$ = 6.5 Hz), 3.96 (2H, t, $^3J_{HH}$ = 6.6 Hz), 1.92 (4H, m), 1.81 (4H, m), 1.75 (2H, m), 1.5-1.2 (78H, broad m), 0.88 (15H, m).

^{13}C{^{1}H} NMR (100.6 MHz, CDCl$_3$) δ^C ppm: 167.66, 164.23, 158.07, 152.74, 141.71, 137.86, 136.37, 132.31, 128.57, 121.57, 121.43, 110.64, 110.20, 100.92, 92.44, 77.21, 73.49, 69.06, 68.32, 31.94, 31.91, 30.33, 29.76, 29.36, 29.66, 29.64, 29.60, 29.58, 29.43, 29.41, 29.38, 29.35, 29.19, 26.21, 26.14, 26.11, 22.70, 22.68, 14.11.

APCI MS (m/z): Expected for $C_{79}H_{124}AuNO_3$ = 1364.9218; Observed: 1364.9218 [M + H]$^+$ (Error = 0.0 mDa)

Elemental Analysis: Found (%): C 69.7, H 9.3, N 1.2; Calc (%) for $C_{79}H_{124}AuNO_3$: C 69.5, H 9.2, N 1.0.

2-[Au]-3-14 [Gold(III)(2,6-*bis*(2-dodecyloxyphenyl)pyridine)(1-ethynyl-3,4,5-tri(tetradecyloxy)benzene)]
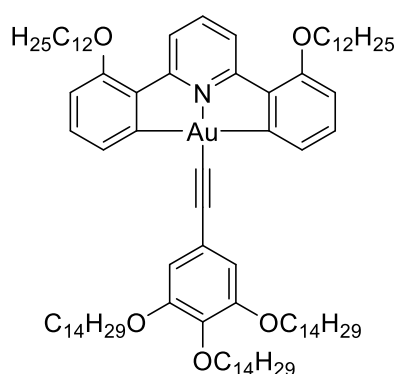
2-[Au]-Cl (0.0550 g, 0.0662 mmol), 1-ethynyl-3,4,5-tri(tetradecyloxy)benzene (0.0529 g, 0.0721 mmol) and CuI (0.0011 g, 0.0058 mmol) were degassed, then dry CH_2Cl_2 (~50 mL) and triethylamine (0.01 mL, 45 mol%) added and the reaction stirred under a dinitrogen atmosphere at room temperature for 5 hr. The reaction mixture was filtered through Celite® and reduced to dryness under reduced pressure, then purified by column

chromatography (silica; 4:1 petroleum ether (40 – 60 °C):ethyl acetate (R_f = 0.91)) to give an orange yellow solid, which was recrystallised from CH_2Cl_2/ethyl acetate to give a yellow microcrystalline solid. Yield: 0.0931 g (92%)

^{1}H NMR (400 MHz, CDCl$_3$) δ^H ppm: 8.26 (2H, d, $^3J_{HH}$ = 8.2 Hz), 7.77 (1H, t, $^3J_{HH}$ = 8.2 Hz), 7.72 (2H, dd, $^3J_{HH}$ = 7.1 Hz, $^4J_{HH}$ = 1.0 Hz), 7.33 (2H, dd, $^3J_{HH}$ = 8.4 Hz, $^3J_{HH}$ = 7.1 Hz), 6.81 (2H, s), 6.77 (2H, dd, $^3J_{HH}$ = 8.6 Hz, $^4J_{HH}$ = 1.2 Hz), 4.09 (4H, t, $^3J_{HH}$ = 6.6 Hz), 4.00 (4H, t, $^3J_{HH}$ = 6.6 Hz), 3.96 (2H, t, $^3J_{HH}$ = 6.6 Hz), 1.92 (4H, m), 1.80 (4H, m), 1.75 (2H, m), 1.5-1.2 (96H, broad m), 0.88 (6H, t, $^3J_{HH}$ = 6.8 Hz), 0.88 (3H, t, $^3J_{HH}$ = 6.8 Hz), 0.87 (6H, t, $^3J_{HH}$ = 7.0 Hz).

^{13}C{^{1}H} NMR (125.8 MHz, CDCl$_3$) δ^C ppm: 167.64, 164.24, 158.06, 152.72, 141.73, 137.79, 136.35, 132.33, 128.57, 121.57, 121.38, 110.63, 110.10, 100.94, 92.37, 73.47, 69.02, 68.31, 31.92, 30.32, 29.76, 29.71, 29.66, 29.57, 29.43, 29.37, 29.35, 29.18, 26.12, 26.69. 22.69, 14.12.

APCI MS (m/z): Expected for $C_{91}H_{148}AuNO_5$ = 1533.1096; Observed: 1533.1065 [M + H]$^+$ (Error = -3.1 mDa) Fragmentation in machine.

Elemental Analysis: Found (%): C 71.0, H 9.3, N 0.9; Calc (%) for $C_{91}H_{148}AuNO_5$: C 71.3, H 9.7, N 0.9.

2-[Au]-F10 [Gold(III)(2,6-*bis*(2-dodecyloxyphenyl)pyridine)(1-ethynyl-4--(1*H*,1*H*,2*H*,2*H*-perfluoro(decyloxy))benzene)]
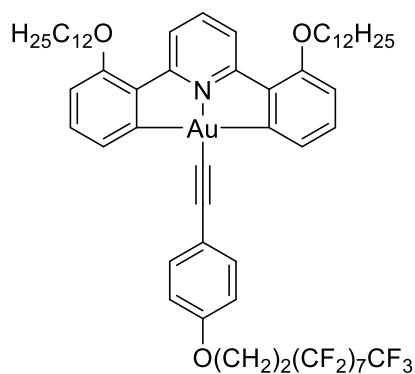
2-[Au]-Cl (0.0615 g, 0.0741 mmol), 1-(1*H*,1*H*,2*H*,2*H*-perfluoro(decyloxy))-4-ethynylbenzene (0.0446 g, 0.0790 mmol) and CuI (0.0034 g, 0.0179 mmol) were

degassed, then dry CH_2Cl_2 (~50 mL) and triethylamine (0.01 mL, 45 mol%) added and the reaction stirred under nitrogen at room temperature for 5 hr. The reaction mixture was filtered through Celite® and reduced to dryness under reduced pressure, then purified by column chromatography (silica; 3:7 CH_2Cl_2: petroleum ether (40 − 60 °C) (R_F = 0.22), then 1:1 CH_2Cl_2: petroleum ether (40 − 60 °C) (R_f = 0.74) to give a dirty yellow solid, which was recrystallised from CH_2Cl_2/acetonitrile to give yellow plates. Yield: 0.0704 g (70%)

^{1}H NMR (400 MHz, $CDCl_3$) δ^H ppm: 8.24 (2H, d, $^3J_{HH}$ = 8.2 Hz), 7.75 (1H, t, $^3J_{HH}$ = 8.4 Hz), 7.72 (2H, d, $^3J_{HH}$ = 7.1 Hz), 7.56 (2H, d, $^3J_{HH}$ = 8.8 Hz), 7.72 (2H, dd, $^3J_{HH}$ = 8.5 Hz, $^3J_{HH}$ = 8.5 Hz), 6.86 (2H, d, $^3J_{HH}$ = 8.8 Hz), 6.76 (2H, d, $^3J_{HH}$ = 8.1 Hz), 4.30 (2H, t, $^3J_{HH}$ = 7.0 Hz), 4.07 (4H, t, $^3J_{HH}$ = 6.5 Hz), 2.65 (2H, m), 1.91 (4H, m), 1.51 (4H, m), 1.4-1.2 (32H, broad m), 0.88 (3H, t, $^3J_{HH}$ = 6.8 Hz).

^{19}F NMR (376.5 MHz, $CDCl_3$) δ^F ppm: -80.61 (3F, t, $^3J_{FF}$ = 10.1 Hz), -113.16 (2F, m), -121.51 (4F, m), -121.77 (4F, m), -122.57 (2F, m), -123.38 (2F, m), -125.99 (2F, m).

^{13}C{^{1}H} NMR (100.6 MHz, $CDCl_3$) δ^C ppm: 167.67, 164.09, 158.04, 156.84, 141.67, 136.39, 133.15, 132.20, 128.42m 121.60, 120.16, 114.23, 110.56, 99.92, 92.76, 68.29, 59.99, 31.91, 29.66, 29.60, 29.58, 29.40, 29.35, 29.19, 26.21, 22.67, 14.10.

APCI MS (m/z): Expected for $C_{60}H_{67}AuF_{19}NO_3$ = 1358.4588; Observed: 1358.4565 [M + H]$^+$ (Error = 2.3 mDa) Fragmentation in machine.

Elemental Analysis: Found (%): C 51.2, H 5.0, N 1.0; Calc (%) for $C_{60}H_{67}AuF_{19}NO_3$: C 51.2, H 4.8, N 1.0.

2-[Au]-F12 [Gold(III)(2,6-*bis*(2-dodecyloxyphenyl)pyridine)(1-ethynyl-4--(1*H*,1*H*,2*H*,2*H*-perfluoro(dodecyloxy))benzene)]
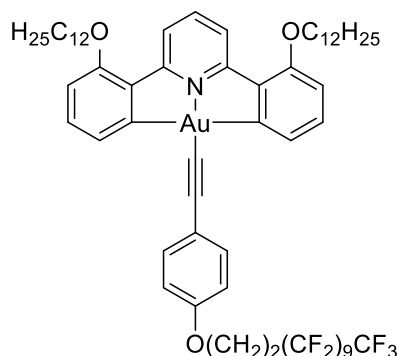
2-[Au]-Cl (0.0508 g, 0.0754 mmol), 1-(1*H*,1*H*,2*H*,2*H*-perfluoro(dodecyloxy))-4-ethynylbenzene (0.0569 g, 0.0686 mmol) and CuI (0.0036 g, 0.0356 mmol) were degassed, then dry CH_2Cl_2 (~50 mL) and triethylamine (0.01 mL, 45 mol%) added and the reaction stirred under a dinitrogen atmosphere at room temperature for 5 hr. The reaction mixture was filtered through Celite® and reduced to dryness under reduced pressure, then purified by column chromatography (silica; 3:7 CH_2Cl_2: petroleum ether (40 − 60 °C) (R_f = 0.41)) to give a dirty yellow solid, which was recrystallised from CH_2Cl_2/acetonitrile to give yellow microcrystals. Yield: 0.0669 g (67%)

R_f = 0.56 (CH_2Cl_2: petroleum ether 1:1)

^{1}H NMR (400 MHz, CDCl$_3$) δ^H ppm: 8.24 (2H, d, $^3J_{HH}$ = 8.2 Hz), 7.75 (1H, t, $^3J_{HH}$ = 8.3 Hz), 7.72 (2H, d, $^3J_{HH}$ = 7.1 Hz), 7.57 (2H, AA'XX', J = 7.9 Hz), 7.33 (2H, dd, $^3J_{HH}$ = 7.1 Hz, $^3J_{HH}$ = 7.1 Hz), 6.87 (2H, AA'XX', J = 7.9 Hz), 6.76 (2H, d, $^3J_{HH}$ = 8.6 Hz), 4.30 (2H, t, $^3J_{HH}$ = 7.0 Hz), 4.08 (4H, t, $^3J_{HH}$ = 6.4 Hz), 2.65 (2H, m), 1.91 (4H, m), 1.51 (4H, m), 1.39 (4H, m), 1.3-1.2 (28H, broad m), 0.88 (3H, t, $^3J_{HH}$ = 5.7 Hz).

^{19}F NMR (376.5 MHz, CDCl$_3$) δ^F ppm: -80.59 (3F, t, $^3J_{FF}$ = 10.1 Hz), -113.15 (2F, m), -121.60 (10F, m), -121.56 (2F, m), -122.37 (2F, m), -125.97 (2F, m).

^{13}C{^{1}H} NMR (100.6 MHz, CDCl$_3$) δ^C ppm: 167.68, 163.96, 157.99, 156.83, 141.64, 136.36, 133.13, 132.36, 133.13, 132.08, 128.35, 121.62, 120.26, 119.10, 114.23, 110.47, 99.78, 93.01, 68.26, 60.00, 31.92, 29.67, 29.61, 29.43, 29.36, 29.20, 26.21, 22.68, 14.08.

Elemental Analysis: Found (%): C 50.2, H 4.5, N 0.9; Calc (%) for $C_{61}H_{67}AuF_{21}NO_3$: C 50.3, H 4.6, N 1.0.

2-[Au]-CHO [Gold(III)(2,6-*bis*(2-dodecyloxyphenyl)pyridine)(4-ethynyl-benzaldhyde)]
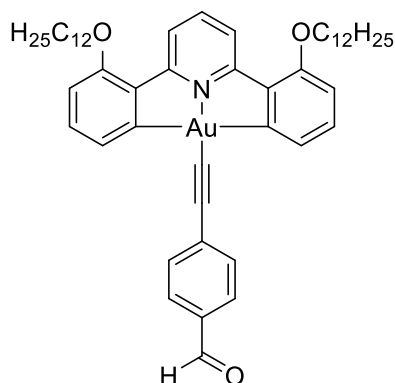
2-[Au]-Cl (0.1484 g, 0.1788 mmol), 4-(ethynyl)benzaldehyde (0.0256 g, 0.1967 mmol) and CuI (0.0046 g, 10 mol%) were degassed, then dry CH_2Cl_2 (~50 mL) and triethylamine (0.03 mL, 45 mol%) added and the reaction stirred under a dinitrogen atmosphere at room temperature for 5 hr. The reaction mixture was filtered through Celite® and reduced to dryness under reduced pressure, then purified by column chromatography (silica; 5% ethyl acetate in CH_2Cl_2 (R_f = 0.08), then 1:1 CH_2Cl_2: petroleum ether (40 – 60 °C) (R_f = 0.26), then 7:3 CH_2Cl_2: petroleum ether (40 – 60 °C) (R_f = 0.64)) to give a yellow solid. Crystallised from CH_2Cl_2/ethyl acetate and cooled at 5 °C to give a yellow microcrystalline solid. Yield = 0.131 g (79%)

^{1}H NMR (400 MHz, CDCl$_3$) δ^H ppm: 10.00 (1H, s), 8.27 (2H, d, $^3J_{HH}$ = 8.2 Hz), 7.84 (1H, d, $^3J_{HH}$ = 8.5 Hz), 7.79 (1H, t, $^3J_{HH}$ = 8.3 Hz), 7.73 (1H, d, $^3J_{HH}$ = 8.3 Hz), 7.68 (2H, dd, $^3J_{HH}$ = 7.1 Hz, $^4J_{HH}$ = 0.9 H), 7.35 (2H, dd, $^3J_{HH}$ = 8.3 Hz, $^3J_{HH}$ = 7.2 H), 6.79 (2H, dd, $^3J_{HH}$ = 8.5 Hz, $^4J_{HH}$ =0.8 Hz), 4.10 (4H, t, $^3J_{HH}$ = 6.5 Hz), 1.93 (4H, m), 1.53 (4H, m), 1.27 (32H, m), 0.88 (6H, t, $^3J_{HH}$ = 6.6 Hz).

APCI MS (m/z): Expected for $C_{50}H_{65}AuNO_3$ = 924.4625; Observed: 924.4584 [M + H]$^+$ (Error = 4.0 mDa)

2,3-[Au]-5 [Gold(III)(2,6-*bis*(2,3-didodecyloxyphenyl)pyridine)(1-ethynyl-4-pentylbenzene)]
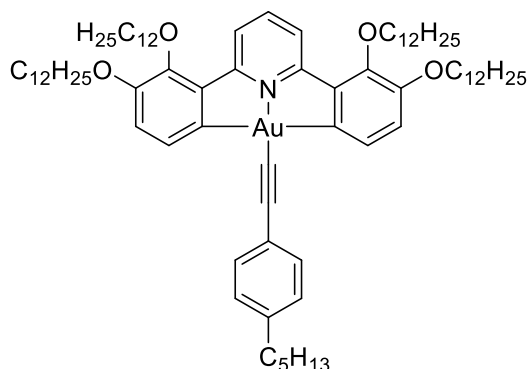
2,3-[Au]-Cl (0.0902 g, 0.0752 mmol), 1-ethynyl-4-pentylbenzene (0.02 mL, 0.0171 g, 0.0993 mmol) and CuI (0.0023 g, 0.0121 mmol) were degassed, then dry CH_2Cl_2 (~50 mL) and triethylamine (0.01 mL, 45 mol%) added and the reaction stirred under a dinitrogen atmosphere at room temperature for 24 hr. The reaction mixture was filtered through Celite® and reduced to dryness under reduced pressure, then purified by column chromatography (silica; 1% ethyl acetate in CH_2Cl_2 (R_f = 0.10), then 1:1 CH_2Cl_2: petroleum ether (40 – 60 °C) (R_f = 0.40)) to give a yellow to orange solid. Recrystallised from CH_2Cl_2/ethyl acetate to give fibrous pale-yellow needle-like crystals. Yield = 0.093 g (92%)

^1H NMR (400 MHz, CDCl$_3$) δ^H ppm: 8.32 (2H, d, $^3J_{HH}$ = 8.2 Hz), 7.83 (1H, t, $^3J_{HH}$ = 8.2 Hz), 7.73 (2H, d, $^3J_{HH}$ = 7.9 Hz), 7.50 (2H, d, $^3J_{HH}$ = 8.2 Hz), 7.12 (2H, d, $^3J_{HH}$ = 8.2 Hz), 6.96 (2H, d, $^3J_{HH}$ = 8.0 Hz), 4.07 (4H, t, $^3J_{HH}$ = 6.8 Hz), 3.98 (4H, t, $^3J_{HH}$ = 6.3 Hz), 2.60 (2H, t, $^3J_{HH}$ = 7.6 Hz), 1.83 (8H, m), 1.62 (2H, m), 1.48 (4H, m), 1.40-1.22 (68H, m), 0.88 (15H, m).

$^{13}C\{^1H\}$ NMR (100.6 MHz, CDCl$_3$) δ^C ppm: 164.21, 157.20, 151.40, 148.51, 142.02, 141.79, 141.49, 131.56, 131.49, 128.10, 124.01, 122.01, 116.56, 100.71, 91.72, 77.21, 73.26, 68.73, 35.83, 31.92, 31.47, 31.07, 30.36, 29.70, 29.66, 29.57, 29.47, 29.36, 26.23, 26.10, 22.68, 22.55, 14.11, 14.04.

APCI MS (m/z): Expected for $C_{78}H_{122}AuNO_4$ = 1334.9112; Observed: 1334.9120 [M + H]$^+$ (Error = -0.8 mDa)

Elemental Analysis: Found (%): C 70.0, H 9.1, N 0.9; Calc (%) for $C_{78}H_{122}AuNO_4$: C70.2, H 9.2, N 1.1.

2,3-[Au]-8 [Gold(III)(2,6-*bis*(2,3-didodecyloxyphenyl)pyridine)(1-ethynyl-4-octylbenzene)]
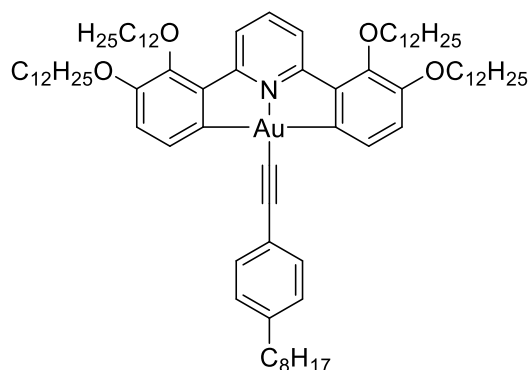
2,3-[Au]-Cl (0.0875 g, 0.0730 mmol), 1-ethynyl-4-octylbenzene (0.02 mL, 0.0171 g, 0.0993 mmol) and CuI (0.0025 g, 0.0131 mmol) were degassed, then dry CH_2Cl_2 (~50 mL) and triethylamine (0.01 mL, 45 mol%) added and the reaction stirred under a dinitrogen atmosphere at room temperature for 24 hr. The reaction mixture was filtered through Celite® and reduced to dryness under reduced pressure, then purified by column chromatography (silica; 1% ethyl acetate in CH_2Cl_2 (R_f = 0.13), then 1:1 CH_2Cl_2: petroleum ether (40 – 60 °C) (R_f = 0.35)) to give a glassy yellow solid. Recrystallised from CH_2Cl_2 /ethyl acetate and cooled at 5 °C to give a bright yellow solid. Yield = 0.093 g (93%)

^1H NMR (400 MHz, CDCl3) δ^H ppm: 8.32 (2H, d, $^3J_{HH}$ = 8.2 Hz), 7.83 (1H, t, $^3J_{HH}$ = 8.2 Hz), 7.72 (2H, d, $^3J_{HH}$ = 7.9 Hz), 7.50 (2H, d, $^3J_{HH}$ = 8.0 Hz), 7.12 (2H, d, $^3J_{HH}$ = 8.1 Hz), 6.96 (2H, d, $^3J_{HH}$ = 8.0 Hz), 4.07 (4H, t, $^3J_{HH}$ = 6.9 Hz), 3.98 (4H, t, $^3J_{HH}$ = 6.4 Hz), 2.60 (2H, t, $^3J_{HH}$ = 7.6 Hz), 1.84 (8H, m), 1.59 (2H, m), 1.48 (8H, m), 1.41-1.25 (74H, m), 0.88 (12H, t, $^3J_{HH}$ = 7.0 Hz), 0.88 (3H, t, $^3J_{HH}$ = 6.9 Hz).

$^{13}C\{^1H\}$ NMR (100.6 MHz, CDCl3) δ^C ppm: 164.21, 157.20, 151.40, 148.52, 142.02, 141.80, 141.50, 131.56, 131.49, 128.10, 124.01, 122.01, 116.57, 100.72, 91.72, 73.26, 68.73, 35.88, 31.92, 31.88, 31.40, 30.37, 29.70, 29.66, 29.57, 29.47, 29.37, 29.30, 26.27, 26.24, 26.11, 22.68, 22.67, 14.11.

APCI MS (m/z): Expected for $C_{78}H_{122}AuNO_4$ = 1376.9582; Observed: 1376.9581 [M + H]$^+$ (Error = 0.1 mDa)

Elemental Analysis: Found (%): C 71.0, H 9.6, N 0.8; Calc (%) for $C_{81}H_{128}AuNO_4$: C 70.7, H 9.4, N 1.0.

2,3-[Au]-1-10 [Gold(III)(2,6-b*is*(2,3-didodecyloxyphenyl)pyridine)(1-ethynyl-4-decyloxybenzene)]
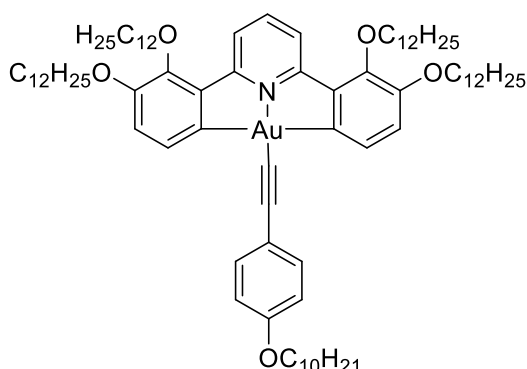
2,3-[Au]-Cl (0.0845 g, 0.0705 mmol), 1-ethynyl-4-decyloxybenzene (0.0522 g, 0.2020 mmol) and CuI (0.0030 g, 0.0296 mmol) were degassed, then dry CH_2Cl_2 (~50 mL) and triethylamine (0.01 mL, 45 mol%) was added and the reaction stirred under a dinitrogen atmosphere at room temperature for 48 hr. The reaction mixture was filtered through Celite® and reduced to dryness under reduced pressure, then purified by column chromatography (silica; 7:3 petroleum ether (40-60 °C): CH_2Cl_2 (R_f = 0.04), then 1:1 CH_2Cl_2: petroleum ether (40 − 60 °C) (R_f = 0.32)) to give a yellow crystalline solid. Recrystallised from CH_2Cl_2 /ethyl acetate and cooled at 5 °C to give bright yellow fibrous crystals. Yield = 0.085 g (85%)

^{1}H NMR (400 MHz, CDCl$_3$) δ^H ppm: 8.32 (2H, d, $^3J_{HH}$ = 8.3 Hz), 7.83 (1H, t, $^3J_{HH}$ = 8.2 Hz), 7.74 (2H, d, $^3J_{HH}$ = 7.9 Hz), 7.51 (2H, d, $^3J_{HH}$ = 8.8 Hz), 6.96 (2H, d, $^3J_{HH}$ = 8.0 Hz), 6.84 (2H, d, $^3J_{HH}$ = 8.8 Hz), 4.07 (4H, t, $^3J_{HH}$ = 6.9 Hz), 3.98 (4H, t, $^3J_{HH}$ = 6.5 Hz), 3.96 (2H, t, $^3J_{HH}$ = 6.2 Hz), 1.83 (10H, m), 1.4-1.2 (76H, broad m), 0.89 (3H, t, $^3J_{HH}$ = 6.8 Hz), 0.88 (12H, t, $^3J_{HH}$ = 7.1 Hz).

^{13}C{^{1}H} NMR (100.6 MHz, CDCl$_3$) δ^C ppm: 164.20, 158.01, 157.22, 151.39, 148.51, 142.00, 141.80, 132.98, 131.46, 122.00, 118.93, 116.56, 114.16, 100.39, 90.45, 73.26,

68.73, 68.00, 31.91, 31.89, 30.36, 29.70, 29.66, 29.56, 29.46, 29.40, 29.36, 29.31, 29.26, 26.23, 26.10, 26.03, 22.68, 14.11.

APCI MS (m/z): Expected for $C_{83}H_{132}AuNO_5$ = 1420.9844; Observed: 1420.9854 [M + H]$^+$ (Error = -1.0 mDa)

Elemental Analysis: Found (%): C 70.3, H 9.4, N 1.0; Calc (%) for $C_{83}H_{132}AuNO_5$: C 70.2, H 9.4, N 1.0.

2,3-[Au]-2-10 [Gold(III)(2,6-*bis*(2,3-didodecyloxyphenyl)pyridine)(1-ethynyl-3,4-didecyloxybenzene)]
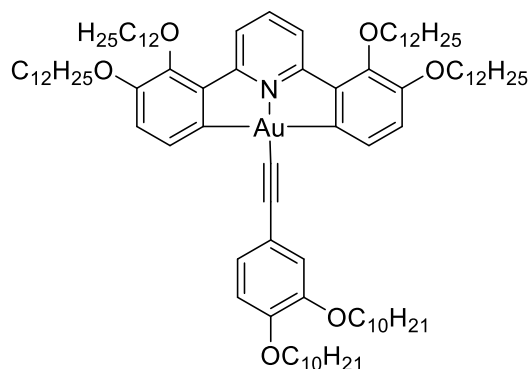
2,3-[Au]-Cl (0.0901 g, 0.0751 mmol), 1-ethynyl-3,4-di(decyloxy)benzene (0.0359 g, 0.0866 mmol) and CuI (0.0043 g, 0.0226 mmol) were degassed, then dry CH_2Cl_2 (~50 mL) and triethylamine (0.01 mL, 45 mol%) was added and the reaction stirred under a dinitrogen atmosphere at room temperature for 24 hr. The reaction mixture was filtered through Celite® and reduced to dryness under reduced pressure, then purified by column chromatography (silica; 7:3 petroleum ether (40-60 °C): CH_2Cl_2 (R_f = 0.06), then 1:1 CH_2Cl_2: petroleum ether (40 – 60 °C) (R_f = 0.25)) to give a yellow green glassy solid. Recrystallised from CH_2Cl_2 /ethyl acetate to give a yellow fibrous solid. Yield = 0.120 g (93%)

^{1}H NMR (400 MHz, CDCl$_3$) δ^H ppm: 8.32 (2H, d, $^3J_{HH}$ = 8.2 Hz), 7.83 (1H, t, $^3J_{HH}$ = 8.1 Hz), 7.73 (2H, d, $^3J_{HH}$ = 7.9 Hz), 7.14 (1H, dd, $^3J_{HH}$ = 8.3 Hz, $^4J_{HH}$ = 2.0 Hz), 7.11 (1H, d, $^4J_{HH}$ = 1.8 Hz), 6.96 (2H, d, $^3J_{HH}$ = 8.0 Hz), 6.81 (2H, d, $^3J_{HH}$ = 8.2 Hz), 4.07 (4H, t, $^3J_{HH}$ = 7.1 Hz), 4.02 (2H, t, $^3J_{HH}$ = 6.6 Hz), 4.00 (2H, t, $^3J_{HH}$ = 7.0 Hz), 3.98 (4H, t, $^3J_{HH}$ = 6.4 Hz), 1.85 (12H, m), 1.5-1.2 (100H, broad m), 0.88 (18H, m).

^{13}C NMR (125.8 MHz, CDCl$_3$) δ^C ppm: 164.24, 157.27, 151.42, 148.61, 148.56, 148.44, 142.00, 141.80, 131.50, 124.72, 122.01, 119.41, 117.21, 116.64, 113.63, 100.63, 90.40, 73.29, 69.36, 69.23, 68.79, 31.92, 30.37, 29.70, 29.59, 29.59, 29.57, 29.48, 29.47, 29.44, 29.36, 29.31, 26.24, 26.11, 26.05, 26.03, 22.68, 14.10.

APCI MS (m/z): Expected for C$_{93}$H$_{152}$AuNO$_6$ = 1577.1358; Observed: 1577.1375 [M + H]$^+$ (Error = -1.1 mDa)

Elemental Analysis: Found (%): C 70.9, H 9.7, N 0.7; Calc (%) for C$_{93}$H$_{152}$AuNO$_6$: C 70.8, H 9.7, N 0.9.

2,3-[Au]-3-10 [Gold(III)(2,6-*bis*(2,3-didodecyloxyphenyl)pyridine)(1-ethynyl-3,4,5-tridecyloxybenzene)]

2,3-[Au]-Cl (0.0993 g, 0.0828 mmol), 1-ethynyl-3,4,5-tri(decyloxy)benzene (0.0539 g, 0.0944 mmol) and CuI (0.0047 g, 0.0464 mmol) were degassed, then dry CH$_2$Cl$_2$ (~50 mL) and triethylamine (0.01 mL, 45 mol%) was added and the reaction stirred under nitrogen at room temperature for 24 hr. The reaction mixture was filtered through Celite$^®$ and reduced to dryness under reduced pressure, then purified by column chromatography (silica; 7:3 petroleum ether (40-60 °C): CH$_2$Cl$_2$ (R_f = 0.04), then 1:1 CH$_2$Cl$_2$: petroleum ether (40 − 60 °C) (R_f = 0.23)) to give a yellow crystalline solid. Recrystallised from CH$_2$Cl$_2$ /ethyl acetate and cooled at 5 °C to give bright yellow microcrystals. Yield = 0.120 g (84%)

^{1}H NMR (400 MHz, CDCl$_3$) δ^H ppm: 8.32 (2H, d, $^3J_{HH}$ = 8.2 Hz), 7.83 (1H, t, $^3J_{HH}$ = 8.1 Hz), 7.71 (2H, d, $^3J_{HH}$ = 7.9 Hz), 6.95 (2H, d, $^3J_{HH}$ = 8.2 Hz), 6.79 (2H,s), 4.07 (4H, t, $^3J_{HH}$ = 6.8 Hz), 3.97 (10H, m), 1.9-1.7 (14H, m), 1.5-1.4 (16H, m), 1.4-1.2 (98H, br m), 0.88 (21H, m).

$^{13}C\{^{1}H\}$ NMR (100.6 MHz, CDCl$_3$) δ^C ppm: 164.23, 157.15, 152.70, 151.43, 148.52, 142.05, 141.76, 137.78, 131.51, 122.02, 121.43, 116.53, 110.13, 100.96, 91.09, 73.20, 73.47, 73.26, 69.02, 68.72, 31.93, 31.91, 30.35, 30.31, 29.74, 2.69, 29.65, 29.62, 29.59, 29.55, 29.46, 29.41, 29.39, 29.35, 26.23, 26.12, 26.09, 22.69, 22.67, 14.10.

APCI MS (m/z): Expected for C$_{103}$H$_{172}$AuNO$_7$ = 1733.2872; Observed: 1733.2912 [M + H]$^+$ (Error = -2.3 mDa)

Elemental Analysis: Found (%): C 71.6, H 10.2, N 0.9; Calc (%) for C$_{103}$H$_{172}$AuNO$_7$: C 71.4, H 10.0, N 0.8.

2,3-[Au]-3-12 [Gold(III)(2,6-*bis*(2,3-didodecyloxyphenyl)pyridine)(1-ethynyl-3,4,5-tridodecyloxybenzene)]
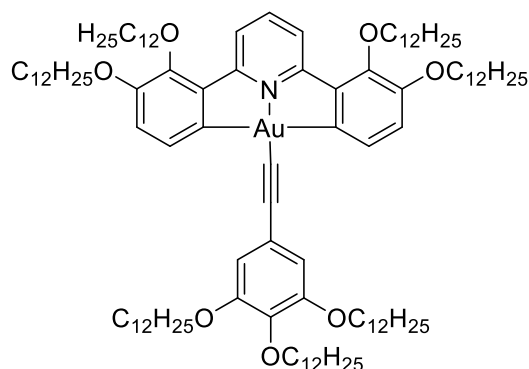
2,3-[Au]-Cl (0.0563 g, 0.0470 mmol), 1-ethynyl-3,4,5-tri(dodecyloxy)benzene (0.0367 g, 0.0560 mmol) and CuI (0.0026 g, 0.0257 mmol) were degassed by backfilling with nitrogen three times, then dry CH$_2$Cl$_2$ (~50 mL) and triethylamine (0.01 mL, 45 mol%) was added and the reaction stirred under a dinitrogen atmosphere at room temperature for 5 hr. The reaction mixture was filtered through Celite$^®$ and reduced to dryness under reduced pressure, then purified by column chromatography (silica; 7:3 petroleum ether (40-60 °C): CH$_2$Cl$_2$ (R_f = 0.00), then 1:1 CH$_2$Cl$_2$: petroleum ether (40 – 60 °C) (R_f = 0.38)) to give an orange/yellow glassy solid, then a second column (silica; 1:1 CH$_2$Cl$_2$: petroleum ether (40 – 60 °C) (R_f = 0.38)) to give an yellow solid. Recrystallised from CH$_2$Cl$_2$ /ethyl acetate to give a bright yellow solid. Yield = 0.0683 g (80%)

^{1}H NMR (400 MHz, CDCl$_3$) δ^H ppm: 8.32 (2H, d, $^3J_{HH}$ = 8.2 Hz), 7.83 (1H, t, $^3J_{HH}$ = 8.1 Hz), 7.71 (2H, d, $^3J_{HH}$ = 7.9 Hz), 6.95 (2H, d, $^3J_{HH}$ = 8.0 Hz), 6.79 (2H, s), 4.07 (4H, t,

$^3J_{HH}$ = 7.0 Hz), 3.98 (10H, m), 1.82 (14H, m), 1.57 (14H, m), 1.4-1.2 (112H, broad m), 0.88 (21H, m).

$^{13}C\{^1H\}$ NMR (100.6 MHz, CDCl$_3$) δ^C ppm: 164.25, 157.16, 152.71, 151.46, 148.54, 141.78, 137.81, 131.53, 122.04, 121.42, 116.56, 110.15, 101.00, 191.04, 73.48, 73.29, 69.04, 68.75, 31.94, 31.92, 30.36, 30.33, 29.76, 29.74, 29.70, 29.66, 29.57, 29.47, 29.43, 29.39, 29.37, 26.24, 26.14, 26.11, 22.69, 14.11.

APCI MS (m/z): Expected for C$_{169}$H$_{184}$AuNO$_7$ = 1817.3811; Observed: 1817.3847 [M + H]$^+$ (Error = 3.6 mDa)

Elemental Analysis: Found (%): C 71.6, H 9.7, N 0.6; Calc (%) for: C$_{169}$H$_{184}$AuNO$_7$: C 72.0, H 10.2, N 0.8.

2,3-[Au]-3-14 [Gold(III)(2,6-*bis*(2,3-ditetradecyloxyphenyl)pyridine)(1-ethynyl-3,4,5-tridecyloxybenzene)]
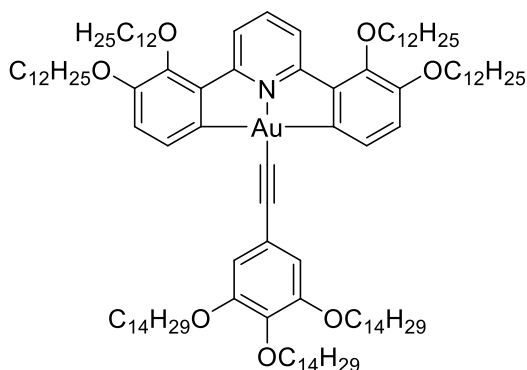
2,3-[Au]-Cl (0.0634 g, 0.0527 mmol), 1-ethynyl-3,4,5-tri(tetradecyloxy)benzene (0.0464 g, 0.0633 mmol) and CuI (0.0046 g, 0.0454 mmol) were degassed, then dry CH$_2$Cl$_2$ (~50 mL) and triethylamine (0.01 mL, 45 mol%) added and the reaction stirred under a dinitrogen atmosphere at room temperature for 4.5 hr. The reaction mixture was filtered through Celite$^®$ and reduced to dryness under reduced pressure, then purified by column chromatography (silica; 1:1 CH$_2$Cl$_2$: petroleum ether (40 – 60 °C) (R_f = 0.31)) to give an orange yellow solid, which was recrystallised from CH$_2$Cl$_2$/ethyl acetate to give a bright yellow microcrystalline solid. Yield: 0.0872 g (87%)

^{1}H NMR (400 MHz, CDCl$_3$) δ^H ppm: 8.32 (2H, d, $^3J_{HH}$ = 8.1 Hz), 7.83 (1H, t, $^3J_{HH}$ = 8.2 Hz), 7.71 (2H, d, $^3J_{HH}$ = 7.9 Hz), 6.95 (2H, d, $^3J_{HH}$ = 8.0 Hz), 6.79 (2H,s), 4.07 (4H, t,

$^3J_{HH}$ = 6.5 Hz), 3.99 (4H, t, $^3J_{HH}$ = 6.5 Hz), 3.97 (4H, t, $^3J_{HH}$ = 6.5 Hz), 3.95 (2H, t, $^3J_{HH}$ = 6.8 Hz), 1.9-1.7 (14H, m), 1.5-1.4 (16H, m), 1.4-1.2 (120H, broad m), 0.88 (21H, m).

$^{13}C\{^1H\}$ NMR (125.8 MHz, CDCl$_3$) δ^C ppm: 164.35, 157.27, 152.83, 148.65, 137.91, 122.14, 110.25, 73.39, 69.14, 68.85, 32.04, 30.48, 29.87, 29.82, 29.78, 29.68, 29.58, 29.55, 29.51, 29.48, 26.36, 26.22, 22.80, 14.23.

Elemental Analysis: Found (%): 72.4, H 10.2, N 0.8; Calc (%) for: C$_{115}$H$_{196}$AuNO$_7$: C 72.6, H 10.4, N 0.7.

2,3-[Au]-5-C4 [Gold(III)(2,6-*bis*(2,3-dibutyloxyphenyl)pyridine)(1-ethynyl-4-pentylbenzene)]
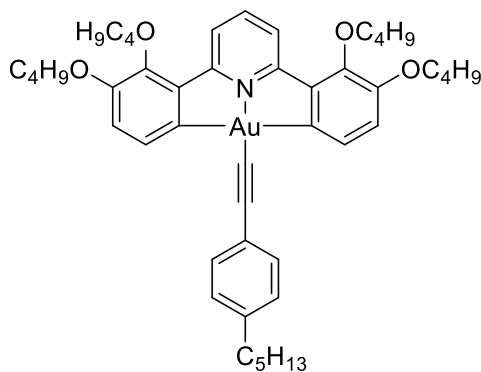
2,3-[Au]-Cl-C4 (0.0427 g, 0.0569 mmol), 1-ethynyl-4-pentylbenzene (0.015 mL, 0.0133 g, 0.0771 mmol) and CuI (0.0046 g, 0.0242 mmol) were degassed by backfilling with nitrogen three times, then dry CH$_2$Cl$_2$ (~50 mL) and triethylamine (0.01 mL, 45 mol%) was added and the reaction stirred under nitrogen at room temperature for 24 hours. Filtered through Celite® and reduced to dryness under reduced pressure. Purified by column chromatography (silica; 5% ethyl acetate in CH$_2$Cl$_2$, R_f = 0.13) to give a yellow to bronze solid. Recrystallised from CH$_2$Cl$_2$/ethanol to give fibrous pale-yellow needle-like crystals. Yield = 0.0225 g (45%)

^{1}H NMR (400 MHz, CDCl$_3$) δ^H ppm: 8.32 (2H, d, $^3J_{HH}$ = 8.3 Hz), 7.84 (1H, t, $^3J_{HH}$ = 8.2 Hz), 7.73 (2H, d, $^3J_{HH}$ = 7.9 Hz), 7.50 (2H, AA'XX', J = 8.4 Hz), 7.12 (2H, AA'XX', J = 8.4 Hz), 6.96 (2H, d, $^3J_{HH}$ = 7.9 Hz), 4.09 (4H, t, $^3J_{HH}$ = 6.89 Hz), 3.99 (4H, t, $^3J_{HH}$ = 6.6 Hz), 2.60 (2H, t, $^3J_{HH}$ = 7.6 Hz), 1.83(8H, m), 1.62 (2H, m), 1.53 (8H, m), 1.33 (4H, m), 1.00 (6H, t, $^3J_{HH}$ = 7.5 Hz), 1.00 (6H, t, $^3J_{HH}$ = 7.4 Hz), 1.00 (3H, t, $^3J_{HH}$ = 7.0 Hz).

2,5-[Au]-8 [Gold(III)(2,6-*bis*(2,5-didodecyloxyphenyl)pyridine)(1-ethynyl-4-octylbenzene)]
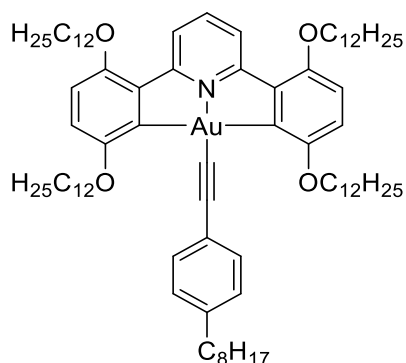
2,5-[Au]-Cl (0.0843 g, 0.0703 mmol), 1-ethynyl-4-octylbenzene (0.05 mL, 0.0428 g, 0.1994 mmol) and CuI (0.0024 g, 0.0237 mmol) were degassed, then dry CH_2Cl_2 (~50 mL) and triethylamine (0.01 mL, 45 mol%) added and the reaction stirred under a dinitrogen atmosphere at room temperature for 24 hr. The reaction mixture was filtered through Celite® and reduced to dryness under reduced pressure, then purified by column chromatography (silica; 1% ethyl acetate in petroleum ether ($R_f = 0.03$), then 7:3 CH_2Cl_2: petroleum ether (40 – 60 °C) ($R_f = 0.47$), then CH_2Cl_2 ($R_f = 0.95$)) to give a dirty yellow solid. Recrystallised from CH_2Cl_2 /ethyl acetate to give a bright yellow solid. Yield = 0.0793 g (82%)

^{1}H NMR (400 MHz, CDCl$_3$) δ^H ppm: 8.41 (2H, d, $^3J_{HH}$ = 8.4 Hz), 7.75 (1H, t, $^3J_{HH}$ = 8.2 Hz), 7.39 (2H, AA'XX', J = 8.2 Hz), 7.02 (2H, AA'XX', J = 8.2 Hz), 6.94 (2H, d, $^3J_{HH}$ = 9.1 Hz), 6.74 (2H, d, $^3J_{HH}$ = 9.0 Hz), 4.04 (4H, t, $^3J_{HH}$ = 6.8 Hz), 3.98 (4H, t, $^3J_{HH}$ = 7.4 Hz), 2.55 (2H, t, $^3J_{HH}$ = 7.8 Hz), 1.89 (4H, m), 1.6-1.5 (16H, m), 1.4-1.2 (68H, br s), 1.04 (4H, m), 0.88 (3H, t, $^3J_{HH}$ = 7.0 Hz), 0.88 (6H, t, $^3J_{HH}$ = 7.0 Hz), 0.88 (6H, t, $^3J_{HH}$ = 7.1 Hz).

^{13}C{^{1}H} NMR (100.6 MHz, CDCl$_3$) δ^C ppm: 164.16, 156.40, 154.63, 152.96, 140.96, 139.63, 137.12, 136.88, 127.57, 125.77, 121.90, 119.50, 112.14, 105.22, 83.48, 77.21, 71.46, 68.93, 35.85, 31.95, 31.93, 31.90, 31.51, 29.73, 29.71, 29.67, 29.67, 29.65, 29.64, 29.58, 29.56, 29.49, 29.45, 29.40, 29.34, 29.31, 26.26, 25.98, 22.70, 22.67, 14.11.

APCI MS (m/z): Expected for $C_{81}H_{128}AuNO_4$ = 1376.9582; Observed: 1376.9508 [M + H]$^+$ (Error = -5.3 mDa) Fragmentation in machine.

Elemental Analysis: Found (%): C 70.7, H 9.1, N 0.9; Calc (%) for $C_{81}H_{128}AuNO_4$: C 70.7, H 9.4, N 1.0.

2,5-[Au]-1-10 [Gold(III)(2,6-*bis*(2,5-didodecyloxyphenyl)pyridine)(1-ethynyl-4-decyloxybenzene)]
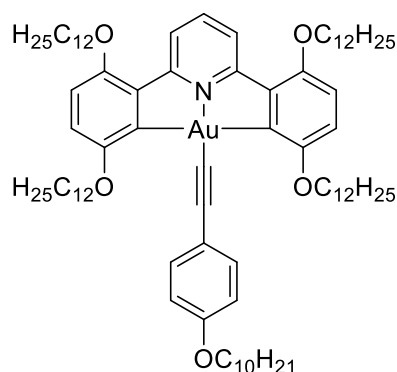
2,5-[Au]-Cl (0.0813 g, 0.0678 mmol), 1-ethynyl-4-(decyloxy)benzene (0.0446 g, 0.1726 mmol) and CuI (0.0023 g, 0.0227 mmol) were degassed, then dry CH_2Cl_2 (~50 mL) and triethylamine (0.01 mL, 45 mol%) added and the reaction stirred under nitrogen at room temperature for hr. The reaction mixture was filtered through Celite® and reduced to dryness under reduced pressure, then purified by column chromatography (silica; 3:7 CH_2Cl_2: petroleum ether (40 − 60 °C) (R_f = 0.08), then CH_2Cl_2 (R_f = 0.77)) to give an orange yellow solid, which was recrystallised from CH_2Cl_2/ethyl acetate to give a yellow microcrystalline solid. Yield: 0.0701 g (73%)

^{1}H NMR (400 MHz, CDCl$_3$) δ^H ppm: 8.41 (2H, d, $^3J_{HH}$ = 8.4 Hz), 7.75 (1H, t, $^3J_{HH}$ = 8.4 Hz), 7.41 (2H, AA'XX', J = 8.8 Hz), 6.94 (2H, d, $^3J_{HH}$ = 9.1 Hz), 6.76 (2H, AA'XX', J = 9.0 Hz), 6.74 (2H, d, $^3J_{HH}$ = 9.0 Hz), 4.03 (4H, t, $^3J_{HH}$ = 6.6 Hz), 3.92 (2H, t, $^3J_{HH}$ = 6.6 Hz), 3.90 (4H, t, $^3J_{HH}$ = 7.0 Hz), 1.89 (4H, m), 1.77 (2H, m), 1.61 (4H, m), 1.5-1.0 (90H, br m), 0.88 (3H, t, $^3J_{HH}$ = 7.0 Hz), 0.88 (6H, t, $^3J_{HH}$ = 7.0 Hz), 0.88 (6H, t, $^3J_{HH}$ = 7.0 Hz).

^{13}C{^{1}H} NMR (125.8 MHz, CDCl$_3$) δ^C ppm: 164.22, 156.96, 156.48, 154.78, 153.03, 137.18, 132.24, 121.89, 120.60, 119.81, 113.78, 112.22, 104.39, 71.60, 68.99, 67.96, 31.96., 31.91, 29.73, 29.71, 29.68, 29.65, 29.64, 29.60, 29.58, 29.56, 29.51, 29.48, 29.43, 29.40, 29.34, 29.33, 26.27, 26.12, 26.01, 22.70, 22.68, 14.12, 14.11.

APCI MS (m/z): Expected for $C_{83}H_{132}AuNO_5$ = 1420.9844; Observed: 1420.9812 [M + H]$^+$ (Error = -2.3 mDa) Fragmentation in machine.

Elemental Analysis: Found (%): C 70.1, H 9.3, N 0.8; Calc (%) for $C_{83}H_{132}AuNO_5$: C 70.2, H 9.4, N 1.0.

2,5-[Au]-1-12 Gold(III)(2,6-bis(2,5-didodecyloxyphenyl)pyridine)(1-ethynyl-4-dodecyloxybenzene)][§§]
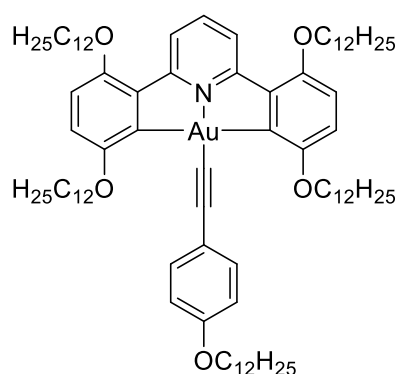
Synthesised using **2,5-[Au]-Cl** (0.0828 g, 0.0691 mmol) and 4-ethynyl-1-(dodecyloxy)benzene (0.0237 g, 0.0829 mmol). Yield: 0.0468 g (47%)[214]

^{1}H NMR (300 MHz, CDCl$_3$) δ^H ppm: 8.40 (2H, d, $^3J_{HH}$ = 8.3 Hz), 7.75 (1H, t, $^3J_{HH}$ = 8.2 Hz), 7.41 (2H, AA'XX', J = 8.9 Hz), 6.94 (2H, d, $^3J_{HH}$ = 9.0 Hz), 6.76 (2H, AA'XX', J = 8.9 Hz), 6.74 (2H, d, $^3J_{HH}$ = 9.2 Hz), 4.04 (1H, d, $^3J_{HH}$ = 6.6 Hz), 3.92 (2H, t, $^3J_{HH}$ = 6.5 Hz), 3.91 (4H, t, $^3J_{HH}$ = 7.5 Hz), 1.89 (4H, m), 1.77 (3H, m), 1.62 (4H, m), 1.5 − 1.0 (77H, broad m), 0.88 (6H, t, $^3J_{HH}$ = 6.9 Hz), 0.88 (6H, t, $^3J_{HH}$ = 6.9 Hz), 0.88 (3H, t, $^3J_{HH}$ = 6.9 Hz).

^{13}C{^{1}H} NMR (125.8 MHz, CDCl$_3$) δ^C ppm: 164.28, 156.54, 154.82, 153.11, 137.24, 132.34, 122.00, 121.11, 119.81, 113.86, 112.25, 71.65, 69.05, 32.07, 32.03, 29.83, 29.80, 29.77, 29.68, 29.63, 29.59, 29.52, 29.46, 29.42, 26.38, 26.11, 22.80, 14.24.

[§§] Synthesised under supervision by L. J. Curtis.

Elemental Analysis: Found (%): C 70.4, H 9.7, N 0.0; Calc (%) for: $C_{85}H_{136}AuNO_5$: C 70.5, H 9.5, N 1.0.

2,5-[Au]-1-14 Gold(III)(2,6-bis(2,5-didodecyloxyphenyl)pyridine)(1-ethynyl-4-tetradecyloxybenzene)][***]
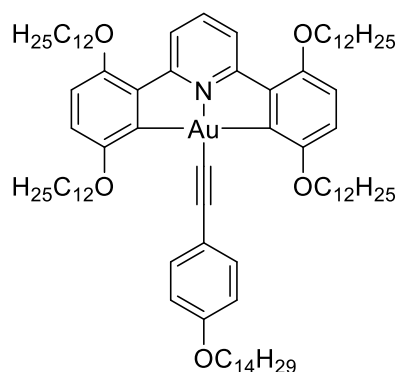
Synthesised using **2,5-[Au]-Cl** (0.0811 g, 0.0677 mmol) and 4-ethynyl-1-(tetradecyloxy)benzene (0.0255 mg, 0.0813 mmol). Yield: 0.0717 g (72%).[214]

^{1}H NMR (300 MHz, CDCl$_3$) δ^H ppm: 8.40 (2H, d, $^3J_{HH}$ = 8.3 Hz), 7.75 (1H, t, $^3J_{HH}$ = 8.2 Hz), 7.41 (2H, AA'XX', J = 8.9 Hz), 6.94 (2H, d, $^3J_{HH}$ = 9.0 Hz), 6.76 (2H, AA'XX', J = 8.9 Hz), 6.74 (2H, d, $^3J_{HH}$ = 9.2 Hz), 4.04 (1H, d, $^3J_{HH}$ = 6.6 Hz), 3.92 (2H, t, $^3J_{HH}$ = 6.5 Hz), 3.91 (4H, t, $^3J_{HH}$ = 7.5 Hz), 1.89 (4H, m), 1.77 (3H, m), 1.62 (4H, m), 1.5 − 1.0 (79H, broad m), 0.88 (6H, t, $^3J_{HH}$ = 6.9 Hz), 0.88 (6H, t, $^3J_{HH}$ = 6.9 Hz), 0.88 (3H, t, $^3J_{HH}$ = 6.9 Hz).

^{13}C{^{1}H} NMR (125.8 MHz, CDCl$_3$) δ^C ppm: 164.30, 156.54, 154.81, 153.11, 137.24, 132.34, 122.00, 113.86, 112.26, 71.66, 69.05, 32.07, 32.02, 29.84, 29.80, 29.76, 29.69, 29.67, 29.59, 29.52, 29.46, 26.37, 26.10, 22.82, 22.79, 14.23.

Elemental Analysis: Found (%): C 70.6, H 9.2, N 0.8; Calc (%) for: $C_{87}H_{140}AuNO_5$: C 70.8, H 9.6, N 1.0.

[***] Synthesised under supervision by L. J. Curtis.

2,5-[Au]-2-10 [Gold(III)(2,6-*bis*(2,5-didodecyloxyphenyl)pyridine)(1-ethynyl-3,4-didecyloxybenzene)]

2,5-[Au]-Cl (0.1001 g, 0.0835 mmol), 1-ethynyl-3,4-di(decyloxy)benzene (0.0415 g, 0.1002 mmol) and CuI (0.0021 g, 0.0208 mmol) were degassed, then dry CH_2Cl_2 (~50 mL) and triethylamine (0.01 mL, 45 mol%) added and the reaction stirred under a dinitrogen atmosphere at room temperature for 24 hr. The reaction mixture was filtered through Celite® and reduced to dryness under reduced pressure, then purified by column chromatography (silica; 5% ethyl acetate in petroleum ether (R_f = 0.08), then 7:3 CH_2Cl_2: petroleum ether (40 − 60 °C) (R_f = 0.53) to give an orange yellow solid, which was recrystallised twice from CH_2Cl_2/ethyl acetate to give a yellow microcrystalline solid. Yield: 0.0680 g (52%)

^{1}H NMR (400 MHz, $CDCl_3$) δ^H ppm: 8.41 (2H, d, $^3J_{HH}$ = 8.2 Hz), 7.75 (1H, t, $^3J_{HH}$ = 8.4 Hz), 7.06 (1H, d, $^4J_{HH}$ = 1.8 Hz), 7.02 (1H, dd, $^3J_{HH}$ = 8.2 Hz, $^4J_{HH}$ = 1.9 Hz), 6.94 (2H, d, $^3J_{HH}$ = 9.1 Hz), 6.74 (2H, d, $^3J_{HH}$ = 9.2 Hz), 6.74 (1H, d, $^3J_{HH}$ = 8.1 Hz), 4.04 (4H, t, $^3J_{HH}$ = 6.6 Hz), 3.96 (2H, t, $^3J_{HH}$ = 6.6 Hz), 3.95 (2H, t, $^3J_{HH}$ = 6.5 Hz), 3.91 (4H, d, $^3J_{HH}$ = 8.0 Hz), 1.89 (4H, m), 1.79 (4H, m), 1.62 (4H, m), 1.5-1.0 (100H, br s), 0.88 (18H, m).

^{13}C{^{1}H} NMR (100.6 MHz, $CDCl_3$) δ^C ppm: 164.20, 156.41, 154.70, 153.01, 148.34, 147.12, 137.13, 123.77, 121.89, 121.50, 119.71, 116.48, 113.54, 112.19, 104.94, 81.93, 71.51, 9.42, 68.95, 68.90, 31.96, 31.92, 31.90, 29.76, 29.72, 29.68, 29.65, 29.63, 29.57, 29.55, 29.50, 29.45, 29.41, 29.37, 29.35, 29.34, 29.30, 26.25, 26.09, 26.05, 22.69, 22.67, 14.11.

APCI MS (m/z): Expected for $C_{93}H_{152}AuNO_6$ = 1577.1358; Observed: 1577.1339 [M + H]$^+$ (Error = -1.2 mDa) Fragmentation in machine.

Elemental Analysis: Found (%): C 70.8, H 9.6, N 0.6; Calc (%) for $C_{93}H_{152}AuNO_6$: C 70.8, H 9.7, N 0.9.

2,5-[Au]-3-10 [Gold(III)(2,6-*bis*(2,5-didodecyloxyphenyl)pyridine)(1-ethynyl-3,4,5-tridecyloxybenzene)]
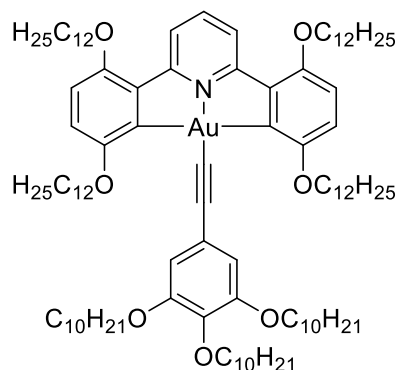
2,5-[Au]-Cl (0.0692 g, 0.0577 mmol), 1-ethynyl-3,4,5-tri(decyloxy)benzene (0.0380 g, 0.0666 mmol) and CuI (0.0022 g, 0.0217 mmol) were degassed, then dry CH_2Cl_2 (~50 mL) and triethylamine (0.01 mL, 45 mol%) added and the reaction stirred under nitrogen at room temperature for 24 hr. The reaction mixture was filtered through Celite® and reduced to dryness under reduced pressure, then purified by column chromatography (silica; 7:3 CH_2Cl_2: petroleum ether (40 – 60 °C) (R_f = 0.28) to give a glassy yellow solid. Recrystallised from CH_2Cl_2 /ethyl acetate to give bright yellow plate-like crystals. Yield: 0.0871 g (87%)

^{1}H NMR (400 MHz, CDCl$_3$) δ^H ppm: 8.41 (2H, d, $^3J_{HH}$ = 8.4 Hz), 7.75 (1H, t, $^3J_{HH}$ = 8.4 Hz), 6.94 (2H, d, $^3J_{HH}$ = 9.0 Hz), 6.74 (2H, d, $^3J_{HH}$ = 9.0 Hz), 6.74 (2H, s), 4.04 (4H, t, $^3J_{HH}$ = 6.6 Hz), 3.92 (10H, m), 1.90 (4H, m), 1.76 (6H, m), 1.63 (4H, m), 1.5-1.0 (114H, br s), 0.88 (21H, m).

^{13}C{^{1}H} NMR (100.6 MHz, CDCl$_3$) δ^C ppm: 164.22, 156.37, 154.60, 153.00, 152.33, 141.00, 137.10, 136.50, 123.34, 121.91, 119.57, 112.22, 109.41, 105.65, 82.82, 73.40, 71.43, 68.96, 68.83, 31.96, 31.92, 31.90, 30.39, 29.81, 29.74, 29.70, 29.65, 29.57, 29.55, 29.53, 29.48, 29.42, 29.38, 29.34, 29.30, 26.24, 26.21, 26.17, 26.12, 22.70, 22.68, 14.11.

APCI MS (m/z): Expected for $C_{103}H_{172}AuNO_7$ = 1733.2872; Observed: 1733.2795 [M + H]$^+$ (Error = 7.7 mDa) Fragmentation in machine.

Elemental Analysis: Found (%): C 71.4, H 9.9, N 0.5; Calc (%) for $C_{103}H_{172}AuNO_7$: C 71.4, H 10.0, N 0.8.

6.8   Synthesis of Acetylide Aldehydes

4-[(Trimethylsilyl)ethynyl)]benzaldehyde
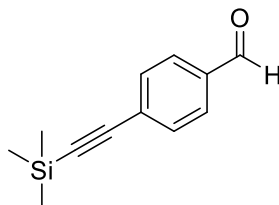
Via 4-iodobenzaldehyde

Degassed triethylamine (25 mL) was added to 4-iodobenzaldehyde (4.6481 g, 20.0 mmol), [PdCl$_2$(PPh$_3$)$_2$] (0.1009 g, 0.1438 mmol) and copper (I) iodide (0.0470 g, 0.2468 mmol) in dry THF (30 mL). Then degassed trimethylsilylacetylene (4.25 mL, 5.9944 g, 30.0 mmol) was added and stirred for 30 min at room temperature under a dinitrogen atmosphere. The reaction mixture was filtered, washed with ethyl acetate (~100 mL), concentrated and purified *via* column chromatography (silica, 5:9.5 to 1:9 ethyl acetate:petroleum ether (40-60 °C) Rf = 0.45 (petroleum ether: ethyl acetate 95:5)). The product fractions were combined and the solvent removed in vacuo. The resulting crystalline solid was recrystallised from hot acetone and dried *in vacuo* to give off-white, needle-like crystals. Yield: 3.296 g (81%)

Via 4-bromobenzaldehyde

Degassed triethylamine (25 mL) was added to 4-bromobenzaldehyde (3.7045 g, 20.0 mmol), [PdCl$_2$(PPh$_3$)$_2$] (0.1072 g, 0.1527 mmol) and copper(I) iodide (0.0481 g, 0.2526 mmol) in dry THF (30 mL). Then degassed trimethylsilylacetylene (4.25 mL, 5.9944 g, 30.0 mmol) and the resulting mixture stirred for 18 hr under a dinitrogen atmosphere at room temperature. The reaction mixture was filtered, washed with ethyl acetate (~100 mL), concentrated and purified *via* column chromatography (silica, 5:9.5 to 1:9 ethyl acetate:petroleum ether (40-60 °C), R_f = 0.45 (petroleum ether: ethyl acetate 95:5)). The resulting crystalline solid was recrystallised from hot acetone and dried *in vacuo* to give off-white, needle-like crystals. Yield: 3.856 g (95%)

^{1}H NMR (400 MHz, CDCl$_3$) δ^H ppm: 10.00 (1H, s), 7.82 (2H, AA'XX', J = 7.6 Hz), 7.60 (2H, AA'XX', J = 8.0 Hz), 0.27 (9H, s, $^2J_{SiH}$ = 120.2 Hz).

$^{13}\text{C}\{^1\text{H}\}$ NMR (100.6 MHz, CDCl$_3$) δ^{C} ppm: 19147, 135.53, 132.46, 129.43, 129.32, 103.79, 99.01, −0.24.

Elemental Analysis: Found (%): C 71.1, H 7.1, N 0.0; Calc (%) for C$_{12}$H$_{14}$OSi: C 71.2, H 7.0, N 0.0.

4-(Ethynyl)benzaldehyde
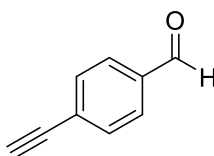
4-[(Trimethylsilyl)ethynyl)]benzaldehyde (1.5581 g, 7.70 mmol) and K$_2$CO$_3$ (3.1950 g, 23.12 mmol) were added to methanol (70 mL) and stirred for 3 hr at room temperature. The solvent was removed under reduced pressure and the orange residue extracted into CH$_2$Cl$_2$ (50 mL), which was washed with aqueous Na$_2$CO$_3$ (10%, 3 x 25 mL), and the organic layer dried over MgSO$_4$, filtered and reduced to dryness. Recrystallised from the minimum amount of hot hexane and isolated as a pale-yellow solid. Yield = 0.7106 g (71%)

^1H NMR (400 MHz, CDCl$_3$) δ^{H} ppm: 10.02 (1H, s), 7.85 (2H, AA'XX', J = 8.4 Hz), 7.64 (2H, AA'XX', J = 8.3 Hz), 3.30 (1H, s).

3-(Trimethylsilyl)-2-propynal
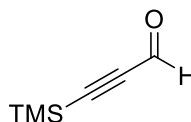
Trimethylsilylacetylene (5.6 mL, 3.97 g, 40.0 mmol) in dry THF (60 mL) was cooled to −78 °C under a dinitrogen atmosphere. n-BuLi (16.9 mL, 44.0 mmol, 2.6 M in hexane) was added dropwise and stirred at −78 °C for 30 min, after which the solution was warmed to room temperature and dry DMF (18.9 mL, 19.3 g, 44.0 mmol) in dry THF (40 mL) was added and the resulting solution stirred at room temperature for 1.5 hr. The reaction was quenched by adding HCl$_{(aq)}$ (37%, 80 mL), before extraction into diethyl ether (5 x

50 mL). The combined organic layers were dried over MgSO₄, filtered and the solvent removed under reduced pressure. The residue was extracted into hexane (3 x 50 mL) and each organic layer washed over distilled water (3 x 15 mL). The combined organic layers were dried over $MgSO_4$, filtered and solvent removed under reduced pressure to give a pale orange solution in hexane. Yield (10% hexane solution): 0.22 g (4%)

^{1}H NMR (400 MHz, CDCl₃) δ^H ppm: 9.17 (1H, s), 0.26 (9H, s).

3-(Triisopropylsilyl)-2-propynal
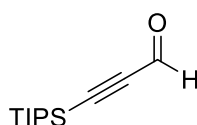
Triisopropylsilylacetylene (7.0 mL, 5.69 g, 31.2 mmol) in dry THF (60 mL) under a dinitrogen atmosphere was cooled to −78 °C. *n*-BuLi (13.5 mL, 35.1 mmol, 2.6 M in hexane) was added dropwise and stirred at −78 °C for 30 min, after which the solution was warmed to room temperature and dry DMF (19.0 mL, 19.3 g, 44.0 mmol) in dry THF (20 mL) added and the resulting solution stirred at room temperature for 1.5 hr. The reaction was quenched by adding HCl₍aq₎ (37%, 5.0 mL), then distilled water (80 mL) and extracted into diethyl ether (5 x 50 mL), dried over MgSO₄, filtered and the solvent removed under reduced pressure. The residue was extracted into hexane (50 mL) and washed over distilled H₂O (3 x 25 mL), dried over MgSO₄, filtered and the solvent removed under reduced pressure. The residue was purified *via* column chromatography (silica, petroleum ether 40-60 °C (R_F = 0.12), then 9.5:0.5 CH₂Cl₂:petroleum ether (R_F = 0.52)). The solvent was removed under reduced pressure to give a pale orange oil. Yield: 4.58 g (70%)

^{1}H NMR (400 MHz, CDCl₃) δ^H ppm: 9.20 (1H, s), 1.13 (3H, m), 1.10 (18H, d, $^3J_{HH}$ = 4.8 Hz).

6.9   Synthesis of Tetra-substituted Porphyrins

p-t-P: 5,10,15,20-Tetrakis[4-{(trimethylsilyl)ethynyl}phenyl)]porphyrin
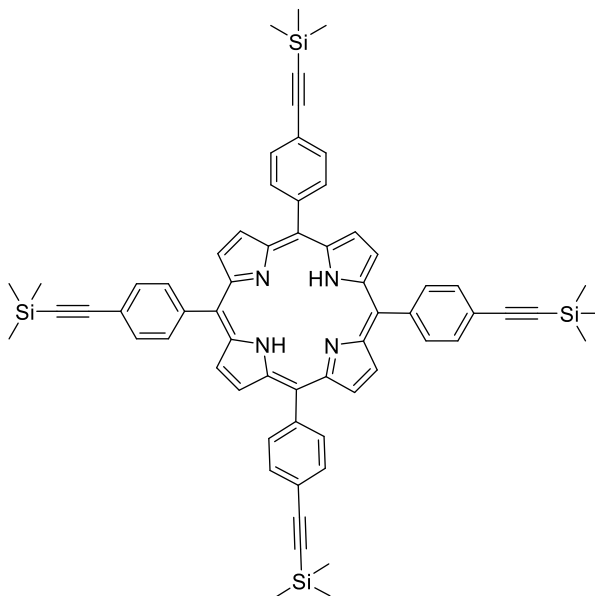
4-[(Trimethylsilyl)ethynyl)]benzaldehyde (0.4079 g, 2.0 mmol) was dissolved in CH_2Cl_2 (350 mL). Pyrrole (0.14 mL, 0.134 g, 2.0 mmol) and $BF_3(OEt_2)$ (0.070 mL, 0.0805 g, 0.57 mmol) were added and the resulting solution stirred under a dinitrogen atmosphere at room temperature for 3 hr. *p*-Chloranil (0.4926 g, 2.0 mmol) was added and the resulting black solution was heated to reflux, under a dinitrogen atmosphere, for 1 hr, then cooled to room temperature. The solution was concentrated and the resulting solid purified *via* column chromatography (silica, 7:3 CH_2Cl_2:petroleum ether (40-60 °C), $R_f =$ 0.98), dried *in vacuo* and recrystallised from CH_2Cl_2:methanol to give a purple crystalline solid. Elemental analysis proved unsuitable for characterisation of porphyrins giving a 14% error on carbon. Yield: 0.197 g (39%)

^{1}H NMR (400 MHz, CDCl$_3$) δ^H ppm: 8.82 (8H, s), 8.14 (8H, AA'XX', $J = 8.0$ Hz), 7.87 (8H, AA'XX', $J = 8.0$ Hz), 0.38 (36H, s, $^2J_{HH} = 120.2$ Hz), −2.86 (2H, s).

APCI MS (m/z): Expected for $C_{64}H_{63}N_4Si_4 = 999.4124$; Observed: 999.4092 [M + H]$^+$ (Error = -3.2 mDa)

Elemental Analysis: Found (%): C 62.6, H 4.3, N 4.0; Calc (%) for $C_{64}H_{62}N_4Si_4$: C 76.9, H 6.3, N 5.6. Issues with CHN combustion analysis due to nature of molecule.

t-P: 5,10,15,20-Tetrakis[4-(ethynyl)phenyl]porphyrin
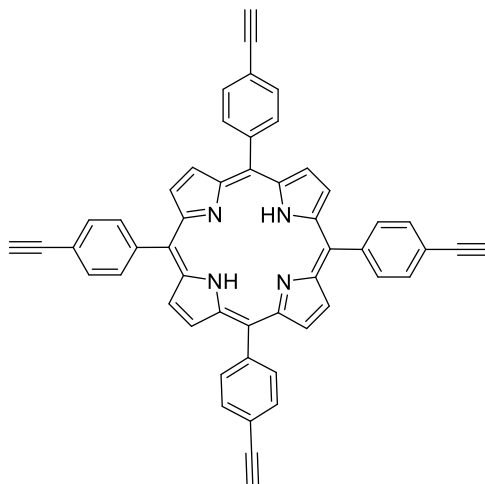
5,10,15,20-Tetrakis[4-{(trimethylsilyl)ethynyl}phenyl)]porphyrin (0.1765 g, 0.1758 mmol) was dissolved in CH_2Cl_2 (92.5 mL) and potassium carbonate (0.1334 g, 0.9652 mol) in methanol (38.5 mL) was added and the resulting solution stirred at room temperature for 23 hr. The solvent was removed under reduced pressure and the residue extracted into CH_2Cl_2 (1 x 75 mL), washed with aqueous $NaHCO_3$ (10%, 2 x 25 mL) and the combined aqueous layers washed with CH_2Cl_2 (4 x 25 mL). The organic layer was separated and dried over $MgSO_4$, filtered and reduced to dryness to give a dark purple crystalline solid. Yield: 0.114 g (92%)

^{1}H NMR (400 MHz, CDCl$_3$) δ^H ppm: 8.84 (8H, s), 8.17 (8H, AA'XX', J = 8.0 Hz), 7.90 (8H, AA'XX', J = 8.0 Hz), 3.33 (4H, s), −2.84 (2H, s).

Elemental Analysis: Found (%): C 87.5, H 4.2, N 7.4; Calc (%) for $C_{52}H_{30}N_4$: C 87.9, H 4.3, N 7.9. Issues with CHN combustion analysis due to nature of molecule.

APCI MS (m/z): Expected for $C_{52}H_{31}N_4$ = 711.254323; Observed: 711.253907 [M + H]$^+$ (Error = 0.4 mDa)

R_f = 0.76 (CH_2Cl_2:petroleum ether (40-60 °C) 7:3)

t-ZnP: Zinc(II) 5,10,15,20-tetrakis[4-(ethynyl)phenyl]porphyrin
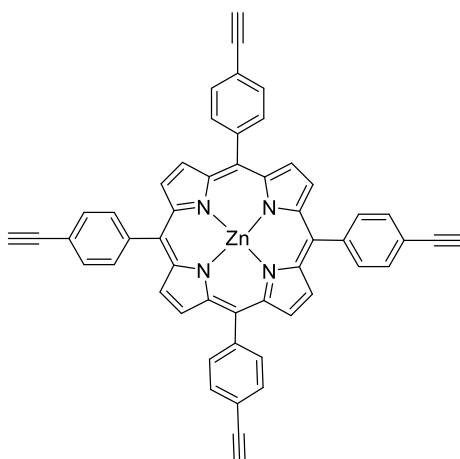
5,10,15,20- Tetra(4-ethynylphenyl)porphyrin (0.1050 g, 0.1477 mmol) was dissolved in CH_2Cl_2 (37 mL) and zinc acetate (0.0784 g, 0.4273 mmol) in methanol (13 mL) was added and the resulting solution stirred at room temperature for 20 hr. The solvent was removed and the residue extracted into CH_2Cl_2 (1 x 150 mL), washed with aqueous $NaHCO_3$ (10%, 2 x 25 mL) and the combined aqueous layers washed over CH_2Cl_2 (5 x 50 mL). The organic layer was separated and dried over $MgSO_4$, filtered and reduced to dryness. Recrystallised from CH_2Cl_2:methanol to give bright purple crystals. Yield: 0.093 g (81%)

^{1}H NMR (400 MHz, CDCl$_3$) δ^H ppm: 8.94 (8H, s), 8.18 (8H, AA'XX', J = 8.0 Hz), 7.90 (8H, AA'XX', J = 8.0 Hz), 3.32 (4H, s).

APCI MS (m/z): Expected for $C_{52}H_{29}N_4Zn$ = 773.167816; Observed: 773.169918 [M + H]$^+$ (Error = -2.1 mDa)

Elemental Analysis: Found (%): C 74.5, H 3.2, N 6.7; Calc (%) for $C_{52}H_{28}N_4Zn$: C 80.8, H 3.7, N 7.2. Issues with CHN combustion analysis due to nature of molecule.

TMS-CC-t-P: 5,10,15,20-Tetrakis[(trimethylsilyl)ethynyl]porphyrin
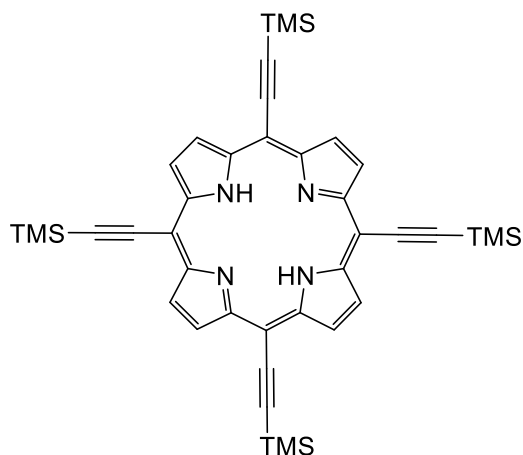
3-(Trimethylsilyl)-2-propynal (0.2236 g, 1.8 mmol, 3.25 mL, 10% hexane solution) was dissolved in CH_2Cl_2 (350 mL). Pyrrole (1.2 mL, 1.21 g, 18.0 mmol), then $BF_3(OEt_2)$ (0.070 mL, 0.0805 g, 0.57 mmol) were added and the resulting solution stirred under a dinitrogen atmosphere at room temperature for 3 hr. *p*-Chloranil (0.4426 g, 1.8 mmol) was added and the resulting dark solution heated to reflux under nitrogen, for 1 hr, then cooled to room temperature. The solution was concentrated and purified *via* column chromatography (silica, 7:3 CH_2Cl_2:petroleum ether (40-60 °C), R_f = 0.88) to give bright green 'wet' rectangular crystals. Yield: 0.016 g (5.0%)

^{1}H NMR (400 MHz, CDCl$_3$) δ^H ppm: 9.53 (8H, s), 0.62 (36H, s), −1.78 (s, 2H)

APCI MS (m/z): Expected for $C_{42}H_{39}N_4Si_4$ = 655.2708; Observed: 695.283909 [M + H]$^+$ (Error = -1.0 mDa)

TIPS-CC-t-P: 5,10,15,20-tetra(triisopropylsilyl)ethynyl)porphyrin
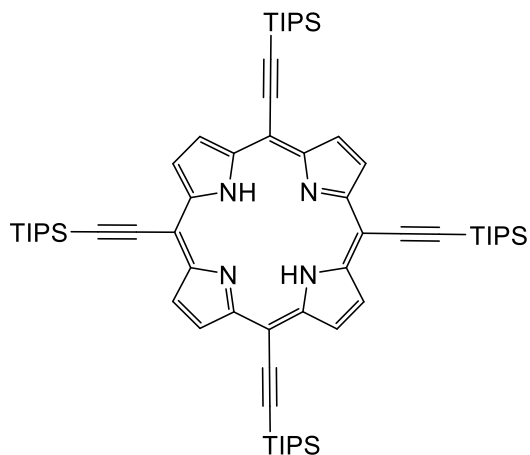
3-(Triisopropylsilyl)-2-propynal (0.42 g, 2.0 mmol) was dissolved in CH_2Cl_2 (350 mL). Pyrrole (1.4 mL, 0.13 g, 2.0 mmol), then $BF_3(OEt_2)$ (0.070 mL, 0.0805 g, 0.57 mmol) was added and the resulting solution stirred under a dinitrogen atmosphere at -20 °C for 2 hr, slowly warming to room temperature, then for a further hour at room temperature. *p*-Chloranil (0.4911 g, 2.0 mmol) was added and the resulting dark solution was heated to reflux under nitrogen for 1 hr. The solution was concentrated and purified *via* column chromatography (silica, 7:3 CH_2Cl_2:petroleum ether; $R_f = 0.94$), followed by a second and third column (silica, CH_2Cl_2; $R_f = 0.95$) and recrystallised from CH_2Cl_2/methanol to give a metallic purple crystalline solid, which is deep green in solution.. Yield = 0.060 (12%)

^{1}H NMR (400 MHz, CDCl$_3$) δ^H ppm: 9.57 (8H, s), 1.45 (84H, s), -1.68 (2H, s)

6.10 Synthesis of Disubstituted Porphyrins

Dipyrromethane
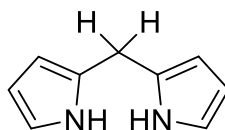
Via TFA:

A suspension of paraformaldehyde (1.7303 g, 57.5 mmol) in dry pyrrole (100 mL) was heated to 55 °C for 15 min under a dinitrogen atmosphere. The heat source was removed and TFA (0.45 mL, 0.68 g, 5.77 mmol) added, with the resulting solution stirred for 5 min. The reaction was quenched by addition of NaOH (6.03 g, 0.15 mol) and stirred for 1 hr in the dark, before filtering off the insoluble solid. The solvent was removed under reduced pressure and the residue extracted into 20% ethyl acetate/hexane (50 mL) and washed with distilled water (25 mL). The aqueous layer was washed with 20% ethyl acetate/hexane (4 x 50 mL) and the combined organic layers dried over $MgSO_4$, filtered and the solvent removed under reduced pressure to give an orange oil. The product was purified *via* column chromatography (silica, 100:1 CH_2Cl_2:triethylamine, $R_f = 0.55$, MnO_4 stain) to give an off-white solid. Yield: 0.724 g (9%)

Via InCl$_3$:

A suspension of paraformaldehyde (0.3032 g, 10.09 mmol) in dry pyrrole (100 mL, 96.7 g, 1.44 mol) was heated to 55 °C for 10 min under nitrogen, then InCl$_3$ (0.3159 g, 1.4282

mmol) was added and the resulting solution stirred for 2.5 hr at 55 °C, in the dark, to give a pale yellow solution. The reaction was quenched with NaOH (1.80 g, 45.0 mmol) and stirred for 1 hour in the dark. The solution was filtered and the solvent was removed under reduced pressure and the residue extracted into 20% ethyl acetate/hexane (50 mL) and washed with distilled water (25 mL). The aqueous layer was washed with 20% ethyl acetate/hexane (4 x 50 mL) and the combined organic layers dried over MgSO₄, filtered and the solvent removed under reduced pressure to give a red oil, which was titrated with petroleum ether (40-60 °C) (6 x 10 mL) to give white to red-orange needle-like crystals. Yield = 1.27 g (60%)

^{1}H NMR (400 MHz, CDCl₃) δ^H ppm: 7.93 (2H, br s), 6.68 (2H, m), 6.15 (2H, q, $^3J_{HH}$ = 3.0 Hz), 6.04 (2H, m), 4.00 (2H, s).

di-P: 5,15-*Bis*(4-[(trimethylsilyl)ethynyl)]phenyl)porphyrin
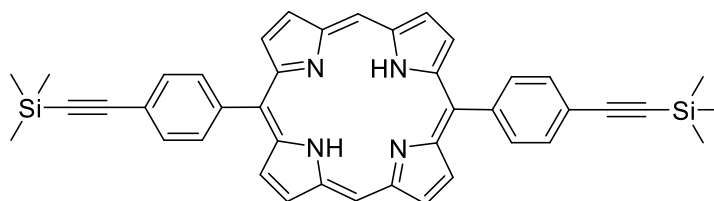
4-[(Trimethylsilyl)ethynyl)]benzaldehyde (0.4074 g, 2.0136 mmol) was dissolved in CH₂Cl₂ (~350 mL). Dipyrromethane (0.3078 g, 2.1055 mmol), then BF₃(OEt₂) (0.070 mL, 0.0805 g, 0.57 mmol) was added and the resulting solution stirred under a dinitrogen atmosphere at room temperature for 3 hr. *p*-Chloranil (0.4795 g, 1.9661 mmol) was added and the resulting dark red solution was heated to reflux under nitrogen for 1 hr, then cooled to room temperature. The solvent was removed under reduced pressure and the solid residue was purified *via* column chromatography (silica, 7:3 CH₂Cl₂:petroleum ether 40-60 °C, R_f = 0.77), then on a second column (silica, 7:3 CH₂Cl₂:petroleum ether 40-60 °C, R_f = 0.77) to give a purple crystalline solid. Recrystallised from CH₂Cl₂/MeOH to give a dark purple crystalline solid. Yield = 0.236 g (36%)

^{1}H NMR (400 MHz, CDCl₃) δ^H ppm: 10.34 (2H, s), 9.41 (4H, AA'XX', J = 4.6 Hz), 9.05 (4H, AA'XX', J = 4.6 Hz), 8.22 (4H, AA'XX', J = 8.0 Hz), 7.93 (8H, AA'XX', J = 8.1 Hz), 0.40 (18H, s, $^2J_{SiH}$ = 120.6 Hz), −3.14 (2H, s).

APCI MS (m/z): Expected for $C_{42}H_{39}N_4Si_2$ = 655.2708; Observed: 655.2699 [M + H]$^+$ (Error = -0.1 mDa)

di-PH2: 5,15-*Bis*(4-ethynylphenyl)porphyrin
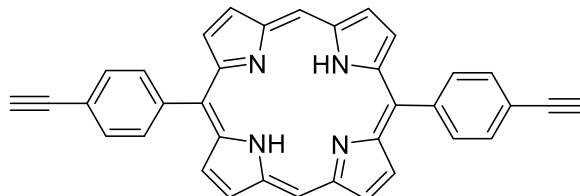
di-P (0.0568 g, 0.867 mmol) was dissolved in CH_2Cl_2 (40 mL) and potassium carbonate (0.1002 g, 0.7250 mmol) in methanol (10 mL) was added and the resulting solution stirred at room temperature for 19 hr. The solvent was removed under reduced pressure and the solid residue extracted into CH_2Cl_2 (50 mL), washed with 10% $NaHCO_{3(aq)}$ (2 x 25 mL) and the combined aqueous layers washed over CH_2Cl_2 (2 x 50 mL). Dried over $MgSO_4$, filtered and reduced to dryness under reduced pressure to give a purple crystalline solid. Yield: 0.0363 g (82%)

^{1}H NMR (400 MHz, CDCl$_3$) δ^H ppm: 10.34 (2H, s), 9.42 (4H, d, $^3J_{HH}$ = 4.6 Hz), 9.07 (4H, d, $^3J_{HH}$ = 4.5 Hz), 8.25 (4H, AA'XX', J = 7.9 Hz), 7.95 (4H, AA'XX', J = 8.1 Hz), 3.35 (2H, s), -3.14 (2H, br s).

p-di-ZnP: Zinc 5,15-*Bis*(4-[(trimethylsilyl)ethynyl)]phenyl)porphyrin
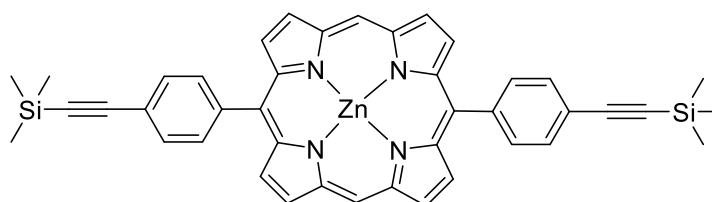
5,15-*Bis*(4-[(trimethylsilyl)ethynyl)]phenyl)porphyrin (0.2174 g, 0.3319 mmol) was dissolved in CH_2Cl_2 (112 mL) and zinc acetate (0.1770 g, 0. 9647 mmol) in methanol (37.5 mL) was added and the resulting solution stirred at room temperature for 16 hr. The solvent was removed under reduced pressure and the residue extracted into CH_2Cl_2 (1 x 150 mL), washed with aqueous $NaHCO_3$ (10%, 2 x 25 mL) and the combined aqueous layers washed over CH_2Cl_2 (4 x 50 mL). The organic layer was separated and dried over $MgSO_4$, filtered and reduced to dryness to give a purple crystalline solid. Yield: 0.2133 g (90%)

^{1}H NMR (400 MHz, CDCl$_3$) δ^H ppm: 10.35 (2H, s), 9.46 (4H, AA'XX', J = 4.5 Hz), 9.11 (4H, AA'XX', J = 4.5 Hz), 8.21 (4H, AA'XX', J = 8.0 Hz), 7.92 (8H, AA'XX', J = 8.1 Hz), 0.40 (18H, s, $^2J_{SiH}$ = 120.3 Hz).

APCI MS (m/z): Expected for C$_{36}$H$_{21}$N$_4$Si$_2$Zn = 717.1843; Observed: 717.1844 [M + H]$^+$ (Error = -0.1 mDa)

di-ZnP: Zinc 5,15-*Bis*(4-(ethynyl)phenyl)porphyrin
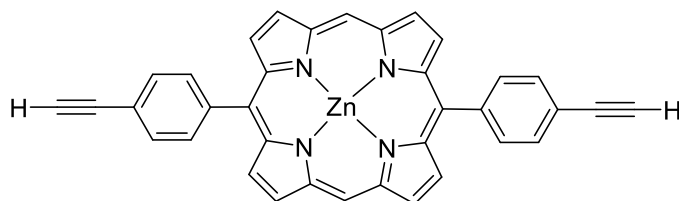
Zinc 5,15-*Bis*(4-[(trimethylsilyl)ethynyl)]phenyl)porphyrin (0.1129 g, 0.1572 mmol) was dissolved in CH$_2$Cl$_2$ (80 mL) and K$_2$CO$_3$ (0.1540 g, 1.1142 mmol) in methanol (20 mL) was added and the resulting solution stirred at room temperature for 18 hr. The solvent was removed under reduced pressure and the solid residue extracted into CH$_2$Cl$_2$ (1 x 75 mL), washed with aqueous NaHCO$_3$ (10%, 2 x 25 mL) and then the combined aqueous layers washed over CH$_2$Cl$_2$ (9 x 50 mL). The combined organic layers were dried over MgSO$_4$, filtered and reduced to dryness to give a purple crystalline solid. Yield: 0.086 g (96%)

^{1}H NMR (400 MHz, CDCl$_3$) δ^H ppm: 10.37 (2H, s), 9.48 (4H, AA'XX', J = 4.5 Hz), 9.14 (4H, AA'XX', J = 4.5 Hz), 8.24 (4H, AA'XX', J = 8.0 Hz), 7.94 (4H, AA'XX', J = 8.0 Hz), 3.35 (2H, s).

APCI MS (m/z): Expected for C$_{36}$H$_{21}$N$_4$Zn = 573.1052; Observed: 573.1051 [M + H]$^+$ (Error = 0.1 mDa)

R_f = 0.43 (CH$_2$Cl$_2$:petroleum ether 7:3)

CC-P: 5,15-*Bis*((triisopropylsilyl)ethynyl)porphyrin
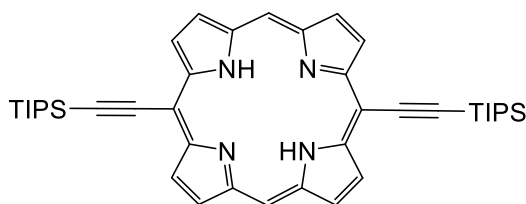
3-(Triisopropylsilyl)-2-propynal (1.5 mL, 1.422 g, 6.76 mmol) was dissolved in CH_2Cl_2 (~400 mL). Dipyrromethane (0.9843 g, 6.73 mmol), then $BF_3(OEt_2)$ (0.27 mL, 0.3108 g, 2.19 mmol) was added and the resulting solution stirred under a dinitrogen atmosphere at room temperature for 45 min. *p*-Chloranil (2.8918 g, 10.86 mmol) was added and the resulting dark solution was heated to reflux under nitrogen for 1 hr, then cooled to room temperature. The solvent was filtered through a silica plug and removed under reduced pressure. The solid residue was purified *via* column chromatography (silica, CH_2Cl_2, R_f = 0.82), followed by a subsequent four columns (silica, CH_2Cl_2, R_f = 0.82) and reduced to dryness to give a crystalline, dark purple solid. Recrystallised from CH_2Cl_2/MeOH to give green/purple cubic crystals. Yield = 1.026 g (45%)

^{1}H NMR (400 MHz, $CDCl_3$) δ^H ppm: 10.12 (2H, s), 9.71 (4H, d, $^3J_{HH}$ = 4.5 Hz), 9.30 (4H, d, $^3J_{HH}$ = 4.4 Hz), 1.53 (6H, m), 1.48 (36H, d, $^3J_{HH}$ = 5.5 Hz), -2.70 (2H, s).

APCI MS (m/z): Expected for $C_{42}H_{55}N_4Si_2$ = 671.3960; Observed: 671.3975 [M + H]$^+$ (Error = 1.5 mDa)

p-CC-ZnP: Zinc 5,15-*Bis*((triisopropylsilyl)ethynyl)porphyrin

5,15-*Bis*((triisopropylsilyl)ethynyl)porphyrin (0.1001 g, 0.1492 mmol) was dissolved in CH_2Cl_2 (37.5 mL) and zinc acetate (0.0820 g, 0.4470 mmol) in methanol (12.5 mL) was added and the resulting solution stirred at room temperature for 18 hr. The solvent was removed under reduced pressure and the residue extracted into CH_2Cl_2 (1 x 100 mL), washed with aqueous $NaHCO_{3(aq)}$ (10%, 2 x 25 mL) and the combined aqueous layers washed over CH_2Cl_2 (6 x 50 mL). The organic layer was separated and the combined

organic layers dried over MgSO$_4$, filtered and reduced to dryness to give an olive green solid. Yield: 0.1011 g (92%)

^{1}H NMR (400 MHz, CDCl$_3$) δ^H ppm: 10.02 (2H, s), 9.77 (4H, d, $^3J_{HH}$ = 4.4 Hz), 9.28 (4H, d, $^3J_{HH}$ = 4.4 Hz), 1.54 (6H, m), 1.52 (36H, d, $^3J_{HH}$ = 5.3 Hz).

APCI MS (m/z): Expected for C$_{42}$H$_{53}$N$_4$Si$_2$Zn = 733.3095; Observed: 733.3061 [M + H]$^+$ (Error = -3.3 mDa)

CC-ZnP: Zinc 5,15-*Bis*(ethynyl)porphyrin

Zinc 5,15-*Bis*((triisopropylsilyl)ethynyl)porphyrin (0.0898 g, 0.1223 mmol) was dissolved in THF (30 mL) and CH$_2$Cl$_2$ (10 mL) and TBAF (1.57 mL, 1.57 mmol, 1M in THF) was added and the resulting solution stirred at room temperature for 1 hr. Distilled water (25 mL) was added and the solution concentrated under reduced pressure. The insoluble dark purple solid was filtered off, washed with distilled water and dried. Yield: 0.0486 g (94%)

^{1}H NMR (400 MHz, d^6-DMSO) δ^H ppm: 10.35 (2H, s), 9.70 (4H, d, $^3J_{HH}$ = 4.3 Hz), 9.53 (4H, d, $^3J_{HH}$ = 4.4 Hz), 5.27 (2H, s).

APCI MS (m/z): Expected for C$_{24}$H$_{13}$N$_4$Zn = 421.042615; Observed: 421.042321 [M + H]$^+$ (Error = -0.3 mDa)

5-(1,1-Dimethylethyl)dipyrromethane
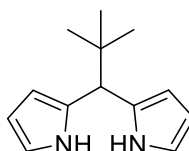
Pivaldehyde (1.7 mL, 1.29 g, 15.0 mmol) and TFA (0.1 mL, 0.16 g, 1.31 mmol) were added to dry pyrrole (50 mL, 48.4 g, 720.7 mmol) and was stirred at room temperature for 2 hr under a dinitrogen atmosphere. The reaction was quenched with NaOH (1.81 g,

45.3 mmol) and stirred for 45 min. The resulting green solution was filtered and the filtrate remove under reduced pressure to give a green crystalline solid, which was extracted into CH_2Cl_2 (150 mL), washed with distilled water (2 x 40 mL), dried over $MgSO_4$ and reduced to dryness to give a green crystalline solid. The crude product was recrystallised from CH_2Cl_2/hexane to give colourless white needle-like crystals. Yield: 1.60 g (53%)

^{1}H NMR (400 MHz, $CDCl_3$) δ^H ppm: 7.95 (2H, broad s), 6.62 (2H, m), 6.17 (2H, m), 6.13 (2H, m), 3.77 (1H, s), 1.01 (9H, s).

5,15-*Bis*(4-[(trimethylsilyl)ethynyl)]phenyl)-10,20-*bis*(*tert*-butyl)porphyrin
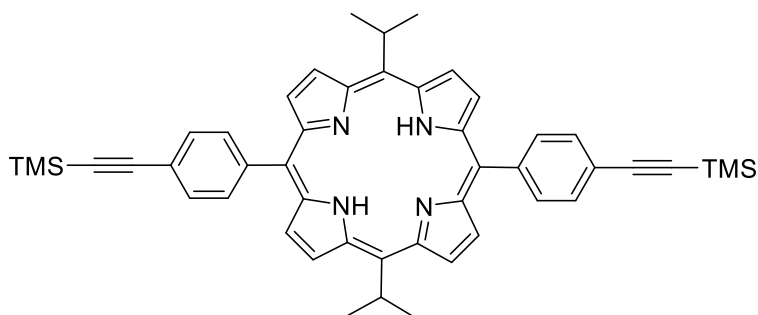
4-[(Trimethylsilyl)ethynyl)]benzaldehyde (0.4041 g, 2.0 mmol) was dissolved in CH_2Cl_2 (~350 mL). Dipyrromethane (0.4047 g, 2.0 mmol), then $BF_3(OEt_2)$ (0.070 mL, 0.0805 g, 0.57 mmol) was added and the resulting solution stirred under a dinitrogen atmosphere at room temperature for 3 hr. *p*-Chloranil (0.4883 g, 2.0 mmol) was added and the resulting dark red solution was refluxed under nitrogen for 1 hr, then cooled to room temperature. The solution was filtered through a silica plug, the solvent was removed under reduced pressure and the solid residue was purified *via* column chromatography (silica, CH_2Cl_2 (R_f = 0.91)), then second and third columns (silica, 1:1 CH_2Cl_2: petroleum ether (40 – 60 °C) (R_F = 0.5)) giving a purple crystalline solid, which was dissolved in methanol and the insoluble dark purple solid isolated by filtration. Recrystallised from CH_2Cl_2/MeOH to give a dark purple crystalline solid. Unable to fully purify and characterise.

5,15-*Bis*(4-(ethynyl)phenyl)-10,20-*bis*(*tert*-butyl)porphyrin
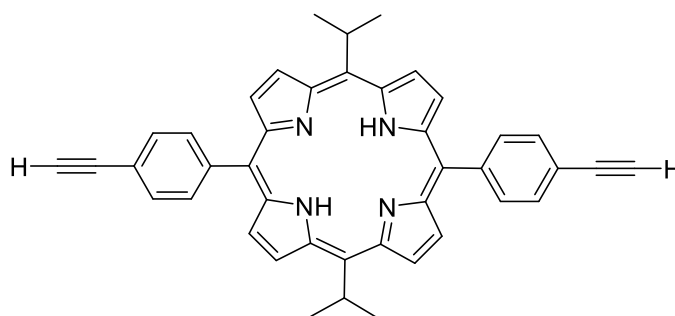
5,15-*Bis*(4-[(trimethylsilyl)ethynyl)]phenyl)-10,20-*bis*(*tert*-butyl)porphyrin (0.0154 g, 0.0201 mmol) was dissolved in CH_2Cl_2 (20 mL) and K_2CO_3 (0.0263 g, 0.1903 mmol) in methanol (5 mL) was added and the resulting solution stirred at room temperature for 18 hr. The solvent was removed under reduced pressure and the solid residue extracted into CH_2Cl_2 (50 mL), washed with 10% $NaHCO_{3(aq)}$ (2 x 25 mL) and the combined aqueous layers washed over CH_2Cl_2 (1 x 50 mL), dried over $MgSO_4$, filtered and reduced to dryness under reduced pressure to give a purple crystalline solid, which was purified *via* column chromatography (silica, 6:4 CH_2Cl_2:petroleum ether (40 – 60 °C) (R_f = 0.5)). Recrystallised from CH_2Cl_2 /methanol to give a dark purple solid. Unable to fully purify and characterise.

Zinc 5,15-*Bis*(4-[(trimethylsilyl)ethynyl)]phenyl)-10,20-*bis*(*tert*-butyl)porphyrin
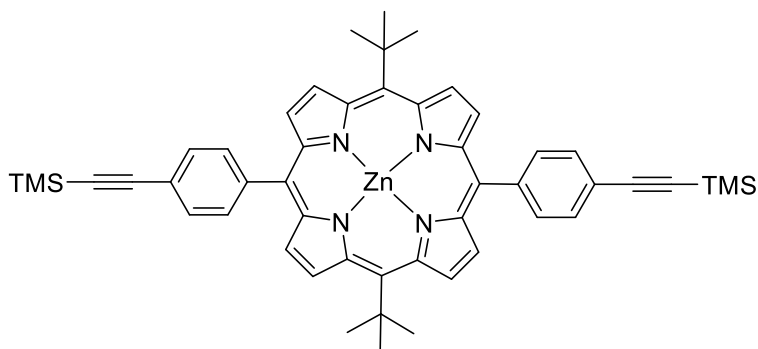
5,15-*Bis*(4-[(trimethylsilyl)ethynyl)]phenyl)-10,20-*bis*(*tert*-butyl)porphyrin (0.0265 g, 0.0345 mmol) was dissolved in CH_2Cl_2 (9 mL) and zinc acetate (0.0202 g, 0.1101 mmol) in methanol (3 mL) was added and the resulting solution stirred at room temperature for 20 hr. The solvent was removed under reduced pressure and the residue extracted into CH_2Cl_2 (1 x 25 mL), washed with aqueous $NaHCO_{3(aq)}$ (10%, 2 x 15 mL) and the combined aqueous layers washed over CH_2Cl_2 (4 x 25 mL). The organic layer was separated and the organic layers dried over $MgSO_4$, filtered and reduced to dryness to give a dark purple solid, which was recrystallised from CH_2Cl_2/MeOH to give a dark purple solid. Unable to fully purify and characterise.

5-(1-Methylethyl)dipyrromethane
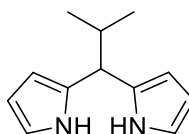
Isobutyraldehyde (1.4 mL, 1.1 g, 15.0 mmol) and TFA (0.1 mL, 0.16 g, 1.3 mmol) were added to dry pyrrole (50 mL, 48.4 g, 720.7 mmol) and was stirred at room temperature for 2 hr under a dinitrogen atmosphere. The reaction was quenched with NaOH (1.75 g, 46.8 mmol) and stirred for 45 min. The resulting pale yellow solution was filtered and the filtrate removed under reduced pressure to give a brown oil, which was extracted into CH_2Cl_2 (100 mL), washed with distilled water (2 x 40 mL), dried over $MgSO_4$ and reduced to dryness to give a brown oil, which was titrated with petroleum ether (40-60 °C) (5 x 10 mL) to give white to pale brown needle-like crystals, which was dissolved in minimum hexane and the insoluble solid isolated by filtration to give off-white small needle-like crystals. Yield: 1.843 g (64%)

^{1}H NMR (400 MHz, $CDCl_3$) δ^H ppm: 7.84 (2H, broad s), 6.64 (2H, m), 6.16 (2H, m), 6.06 (2H, m), 3.79 (1H, d, $^3J_{HH}$ = 6.8 Hz), 2.30 (1H, m), 0.94 (6H, d, $^3J_{HH}$ = 6.6 Hz).

iPr-P: 5,15-*Bis*(4-[(trimethylsilyl)ethynyl)]phenyl)-10,20-*bis*(*iso*-propyl)porphyrin
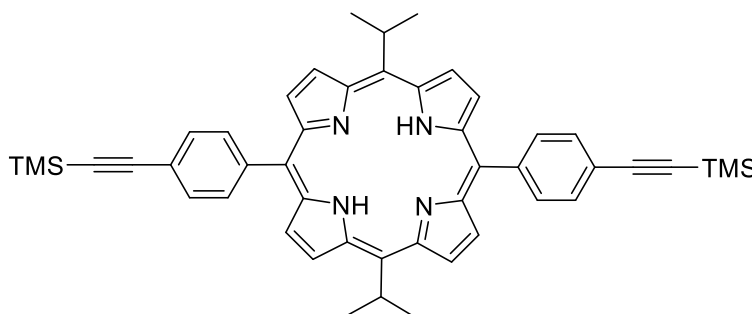
4-[(Trimethylsilyl)ethynyl)]benzaldehyde (0.4040 g, 2.0 mmol) was dissolved in CH_2Cl_2 (~350 mL). Dipyrromethane (0.3765 g, 2.0 mmol), then $BF_3(OEt_2)$ (0.070 mL, 0.0805 g, 0.57 mmol) was added and the resulting solution stirred under a dinitrogen atmosphere at room temperature for 2 hr. *p*-Chloranil (0.4622 g, 1.9 mmol) was added and the resulting dark red solution was refluxed under nitrogen for 1 hr, then cooled to room temperature. The solution was filtered through a silica plug, the solvent removed under reduced pressure and the solid residue purified *via* column chromatography (silica, CH_2Cl_2 (R_f = 0.93)), then a second column (silica, 7:3 CH_2Cl_2:petroleum ether (40 − 60 °C) (R_F = 0.76))

to give a purple crystalline solid, which was recrystallised from CH$_2$Cl$_2$/MeOH twice to give a dark purple crystalline solid. Yield: 0.0866 g (12%)

^{1}H NMR (400 MHz, CDCl$_3$) δ^H ppm: 9.54 (4H, d, $^3J_{HH}$ = 5.0 Hz), 8.76 (4H, d, $^3J_{HH}$ = 4.8 Hz), 8.11 (4H, AA'XX', J = 8.1 Hz), 7.86 (8H, AA'XX', J = 8.2 Hz), 5.61 (2H, m), 2.39 (12H, d, $^3J_{HH}$ = 7.2 Hz), 0.40 (18H, s, $^2J_{SiH}$ = 120.1 Hz), -2.47 (2H, s).

p-iPr-ZnP: Zinc 5,15-*Bis*(4-[(trimethylsilyl)ethynyl)]phenyl)-10,20-*bis*(*iso*-propyl)-porphyrin
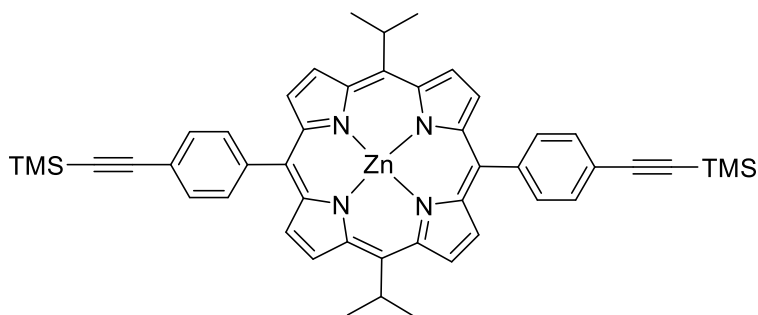
5,15-*Bis*(4-[(trimethylsilyl)ethynyl)]phenyl)-10,20-*bis*(*iso*-propyl)porphyrin in (0.0557 g, 0.0754 mmol) was dissolved in CH$_2$Cl$_2$ (37.5 mL) and zinc acetate (0.0450 g, 0.2453 mmol) in methanol (12.5 mL) was added and the resulting solution stirred at room temperature for 19 hr. The solvent was removed under reduced pressure and the residue extracted into CH$_2$Cl$_2$ (1 x 50 mL), washed with aqueous NaHCO$_{3(aq)}$ (10%, 2 x 25 mL) and the combined aqueous layers washed over CH$_2$Cl$_2$ (3 x 50 mL). The organic layer was separated and organic layers dried over MgSO$_4$, filtered and reduced to dryness to give a purple solid. Yield: 0.0557 g (92%)

^{1}H NMR (400 MHz, CDCl$_3$) δ^H ppm: 9.72 (4H, d, $^3J_{HH}$ = 4.8 Hz), 8.89 (4H, d, $^3J_{HH}$ = 4.8 Hz), 8.13 (4H, AA'XX', J = 7.9 Hz), 7.87 (8H, AA'XX', J = 8.2 Hz), 5.77 (2H, m), 2.44 (12H, d, $^3J_{HH}$ = 7.2 Hz), 0.40 (18H, s, $^2J_{SiH}$ = 120.3 Hz).

iPr-ZnP: Zinc 5,15-*Bis*(4-(ethynyl)phenyl)-10,20-*bis*(*iso*-propyl)-porphyrin
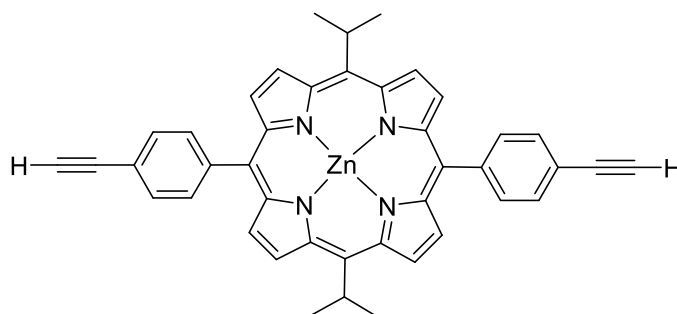
Zinc 5,15-*Bis*(4-[(trimethylsilyl)ethynyl)]phenyl)-10,20-*bis*(*iso*-propyl)-porphyrin (0.1593 g, 0.1985 mmol) was dissolved in CH_2Cl_2 (80.0 mL) and K_2CO_3 (0.2184 g, 1.5881 mmol) in methanol (20.0 mL) was added and the resulting solution stirred at room temperature for 18 hr. The solvent was removed under reduced pressure and the solid residue extracted into CH_2Cl_2 (50 mL), washed with 10% $NaHCO_{3(aq)}$ (2 x 25 mL) and the combined aqueous layers washed over CH_2Cl_2 (2 x 50 mL). The combined oragnice layers were dried over $MgSO_4$, filtered and reduced to dryness under reduced pressure to give a purple crystalline solid. The product was purified *via* column chromatography (silica, 7:3 CH_2Cl_2:petroleum ether (40 – 60 °C) (R_F = 0.70)), then a second column (silica, 1:1 CH_2Cl_2:petroleum ether (40 – 60 °C) (R_F = 0.23)) to give a dark purple solid. Yield: 0.0929 g (77%)

^{1}H NMR (400 MHz, $CDCl_3$) δ^H ppm: 9.73 (4H, d, $^3J_{HH}$ = 4.6 Hz), 8.91 (4H, d, $^3J_{HH}$ = 4.8 Hz), 8.15 (4H, AA'XX', J = 8.1 Hz), 7.90 (4H, AA'XX', J = 7.9 Hz), 5.77 (2H, m), 3.33 (2H, s), 2.45 (12H, d, $^3J_{HH}$ = 7.4 Hz).

6.11 Synthesis of Platinum(II) porphyrins

***cis*-[PtCl₂(PhCN)₂][12]**

A suspension of $PtCl_2$ (0.2590 g, 0.9738 mmol) in benzonitrile (20 mL) was stirred at room temperature for 18 hr to give a clear brown solution. On addition of hexane (>60 mL) a pale brown to pale yellow solid was precipitated and isolated by filtration and dried. Yield: 0.2153 g (47%)

^{1}H NMR (400 MHz, $CDCl_3$) δ^H ppm: 7.81 (2H, m), 7.75 (1H, tt, $^3J_{HH}$ = 7.7 Hz, $^4J_{HH}$ = 1.2 Hz), 7.57 (2H, dd, $^3J_{HH}$ = 7.9 Hz, $^3J_{HH}$ = 7.9 Hz).

[PtCl$_2$(DMSO)$_2$][13]

DMSO (0.25 mL, 0.28 g, 3.54 mmol) was added to a solution of K$_2$[PtCl$_4$] (0.4858 g, 1.1703 mmol) in water (25 mL) and stirred at room temperature for 30 min, before being left for 2 hr. The resulting white precipitate was isolated by filtration and washed with water (10 mL), then acetone (15 mL) and air dried to give the titular product as a white crystalline solid. Yield: 0.2198 g (44%)

^{1}H NMR (400 MHz, CDCl$_3$) δ^H ppm: 3.54 (12H, s, $^3J_{HPt}$ = 21.9 Hz).

Attempted Synthesis of Platinum(II) 5,10,15,20-Tetra*kis*[4-{(trimethylsilyl)-ethynyl}phenyl)]porphyrin
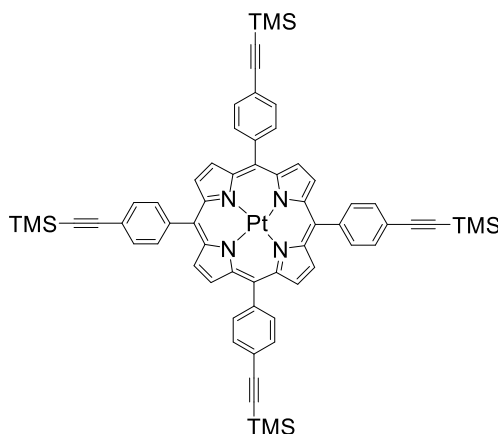
Attempt 1

p-t-P (0.3308 g, 0.3309 mmol) and PtCl$_2$ (0.1054 g, 0.3963 mmol) were heated to reflux in benzonitrile (40 mL) under a dinitrogen atmosphere for 4 hr. The solvent was removed under reduced pressure to give an insoluble, uncharacterisable black solid.

Attempt 2

p-t-P (0.1528 g, 0.1529 mmol), [PtCl$_2$(PhCN)$_2$] (0.1083 g, 0.2293 mmol) and sodium acetate (0.0635 g, 0.7741 mmol) were heated to reflux in chlorobenzene (4 mL) for 1.5 hr. The crude product was purified on a silica plug (chloroform) to give an insoluble, uncharacterisable black solid.

Platinum(II) 5,10,15,20-*p*-tolylporphyrin
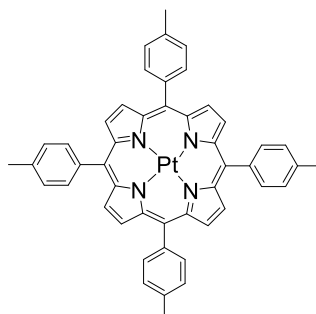
5,10,15,20-*p*-tolylporphyrin (0.0145 g, 0.0216 mmol), [PtCl$_2$(PhCN)$_2$] (0.0153 g, 0.0324 mmol) and sodium acetate (0.0095 g, 0.1158 mmol) were heated to reflux in chlorobenzene (1 mL) for 3 hr. The crude product was purified on a silica plug (chloroform, R_f = 0.78) to give an orange red solution, which was reduced to dryness under reduced pressure to give the product as a brown crystalline solid. Yield: 0.0162 g (87%)

^{1}H NMR (400 MHz, CDCl$_3$) δ^H ppm: 8.76 (8H, s), 8.08 (8H, AA'XX', J = 7.9 Hz), 7.55 (8H, AA'XX', J = 8.3 Hz), 2.70 (12H, s).

Attempted Synthesis of Platinum(II) 5,10,15,20-Tetra*kis*[4-ethynylphenyl)]porphyrin
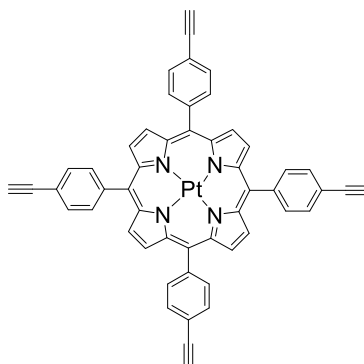
t-P (0.0093 g, 0.0013 mmol), [PtCl$_2$(PhCN)$_2$] (0.0101 g, 0.0214 mmol) and sodium acetate (0.0028 g, 0.0341 mmol) were heated to reflux in chlorobenzene (1 mL) for 1.5 hr. The crude product was purified on a silica plug (chloroform) to give an insoluble, uncharacterisable black solid.

Attempted Synthesis of Platinum(II) 5,15-*Bis*(4-[(trimethylsilyl)ethynyl)]phenyl)porphyrin
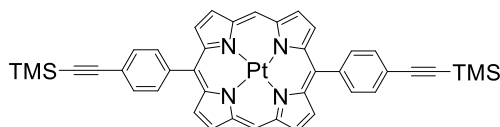
Attempt 1

di-P (0.0102 g, 0.0156 mmol), [PtCl$_2$(DMSO)$_2$] (0.0082 g, 0.0189 mmol) and sodium acetate (0.0084 g, 0.1024 mmol) were heated to reflux in dry acetonitrile (10 mL) under a dinitrogen atmosphere for 1 hr. The crude product was purified on a silica plug (chloroform) and reduced to dryness to give a red/purple solid which was shown by ^{1}H NMR spectroscopy to be the starting material.

Attempt 2

di-P (0.0100 g, 0.0153 mmol), [PtCl$_2$(DMSO)$_2$] (0.0122 g, 0.0288 mmol) and sodium acetate (0.0069 g, 0.0841 mmol) were heated to reflux in chloroform (10 mL) under a dinitrogen atmosphere overnight. The crude product was purified on a silica plug (chloroform) and reduced to dryness to give a red/purple solid which was shown by ^{1}H NMR spectroscopy to be the starting material.

Attempt 3

di-P (0.0104 g, 0.0159 mmol), [PtCl$_2$(PhCN)$_2$] (0.0106 g, 0.0224 mmol) and sodium acetate (0.0075 g, 0.0914 mmol) were heated to reflux in chloroform (10 mL) under a dinitrogen atmosphere for 6 hr. The crude product was purified on a silica plug (chloroform) and reduced to dryness to give a red/purple solid which was shown by ^{1}H NMR spectroscopy to be the starting material.

Attempt 4

di-P (0.0100 g, 0.0153 mmol), [PtCl$_2$(PhCN)$_2$] (0.0102 g, 0.0216 mmol) and sodium acetate (0.0078 g, 0.0950 mmol) were heated to reflux in chlorobenzene (1 mL) for 1 hr. The crude product was purified on a silica plug (chloroform) and reduced to dryness to give a red/purple solid which was shown by ^{1}H NMR spectroscopy to be the starting material.

Attempt 5

di-P (0.0101 g, 0.0154 mmol), [PtCl$_2$(PhCN)$_2$] (0.0185 g, 0.0392 mmol) and sodium acetate (0.0083 g, 0.1011 mmol) were heated to reflux in chlorobenzene (1 mL) for 4.5 hr. The crude product was purified on a silica plug (chloroform) to give an insoluble, uncharacterisable black solid.

Attempted Synthesis of Platinum(II) 5,15-*Bis*(4-ethynylphenyl)porphyrin
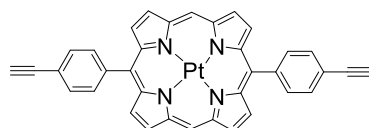
di-PH2 (0.0097 g, 0.0190 mmol), [PtCl$_2$(PhCN)$_2$] (0.0139 g, 0.0294 mmol) and sodium acetate (0.0088 g, 0.1073 mmol) were heated to reflux in chlorobenzene (1 mL) for 2.5 hr. The crude product was purified on a silica plug (chloroform) and reduced to dryness to give a red/purple solid which was shown by ^{1}H NMR spectroscopy to be the starting material and an insoluble, uncharacterisable black solid.

6.12   Attempted Synthesis of Tetra-Substituted Porphyrins Connected to Gold(III) C^N^C complexes

Attempted Synthesis of 4-[Au]-t-P
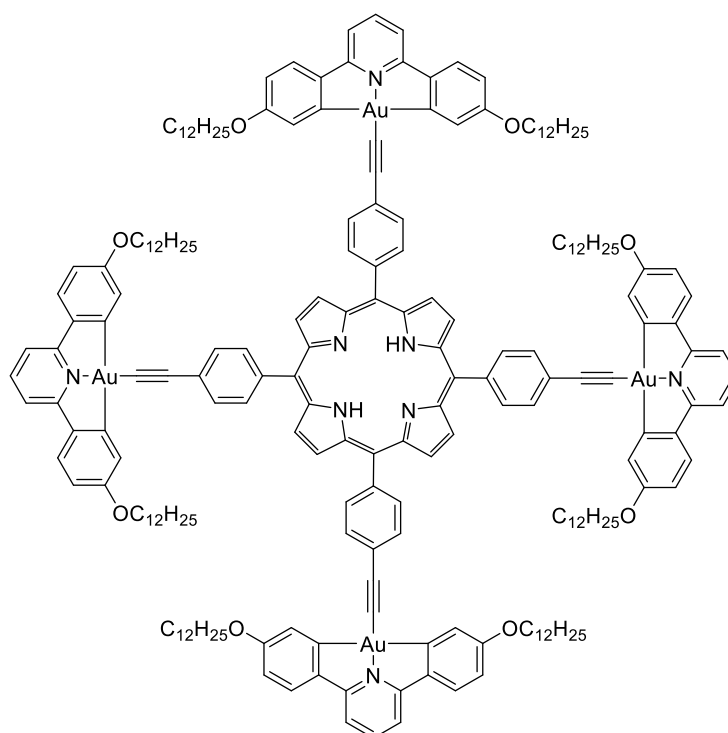
Dry CH_2Cl_2 (~45 mL) and triethylamine (2 μL, 45 mol%) were added under an atmosphere of dinitrogen to a degassed flask containing **4-[Au]-Cl** (0.1000 g, 0.1204 mmol), **t-P** (0.0211 g, 0.0294 mmol) and CuI (0.0039 g, 0.0205 mmol), and the reaction was stirred under nitrogen at room temperature for 120 hr. The reaction mixture was filtered through Celite® and reduced to dryness under reduced pressure, then purified by column chromatography (silica, CH_2Cl_2:petroleum ether (40-60 °C) 1:1, then 2:1). Co-elution occurred on most fractions therefore relevant fractions were passed down two more columns (silica, CH_2Cl_2:petroleum ether (40 − 60 °C)1:1, then CH_2Cl_2; silica CH_2Cl_2:petroleum ether 3:7, then 3:2, then CH_2Cl_2). No product was recovered, with ^{1}H NMR indicating Cu(II) insertion.

Attempted Synthesis of 2-[Au]-t-ZnP
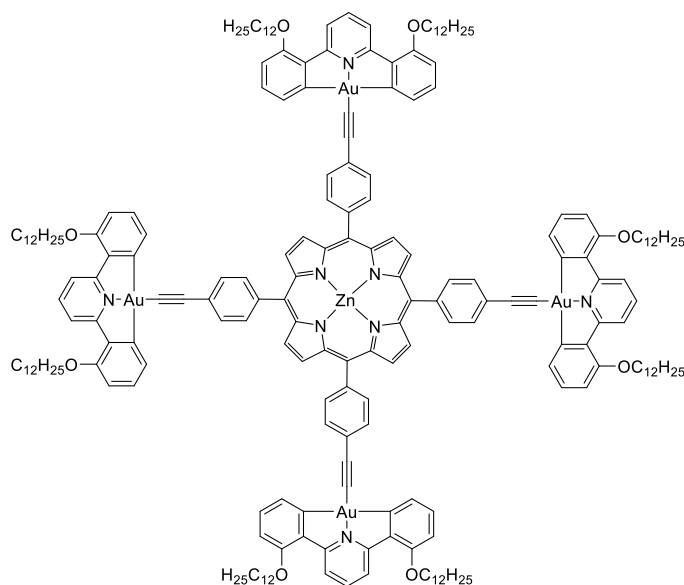
Attempt 1

Dry CH_2Cl_2 (50 mL) and triethylamine (10 μL, 45 mol%) were added under an atmosphere of dinitrogen to a degassed flask containing **2-[Au]-Cl** (0.1493 g, 0.1787 mmol), **t-ZnP** (0.0233 g, 0.0301 mmol) and CuI (0.0026 g, 0.0137 mmol), and the reaction was stirred under nitrogen at room temperature for 48 hr. The reaction mixture was filtered through Celite® and reduced to dryness under reduced pressure, then purified by column chromatography (silica, sequentially CH_2Cl_2:petroleum ether (40-60 °C) 4:6 (750 mL), 2:1 (500 mL), 7:3 (500 mL), CH_2Cl_2 (100 mL)). A purple solid was isolated, but was identified as a mixture of partly substituted products.

Dry CH₂Cl₂ (50 mL) and triethylamine (3 mL, 45 mol%) were added under an atmosphere of dinitrogen to a degassed flask containing **2-[Au]-Cl** (0.1508 g, 0.1816 mmol), **t-ZnP** (0.0235 g, 0.0525 mmol) and CuI (0.0079 g, 0.0415 mmol), and the reaction was stirred under nitrogen at room temperature for 48 hr. The reaction mixture was filtered through Celite® and reduced to dryness under reduced pressure, then purified by column chromatography (silica, sequentially CH₂Cl₂:petroleum ether (40-60 °C) 6:4, CH₂Cl₂:petroleum ether (40-60 °C) 6:4, CH₂Cl₂:petroleum ether (40-60 °C) 7:3, CH₂Cl₂:petroleum ether (40-60 °C) 8:2, CH₂Cl₂, CHCl₃). No product was recovered.

No product was recovered despite the procedure being repeated several times.

Attempted Synthesis of 2-[Au]-t-P
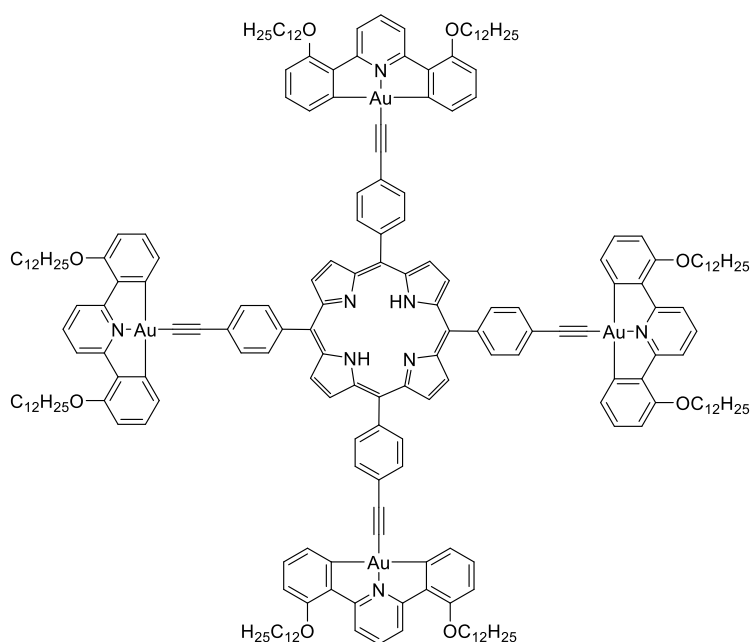
Attempt 1

2-[Au]-CHO (0.1021 g, 0.1105 mmol) was dissolved in dry CH₂Cl₂ (~75 mL) and pyrrole (0.075 mL, 0.0725 g, 1.0810 mmol), then BF₃(OEt₂) (0.03 mL) was added and the resulting solution stirred under a dinitrogen atmosphere at room temperature for 3 hr. *p*-Chloranil (0.0272 g, 0.1106 mmol) was added and the resulting dark solution was heated to reflux for 1 hr, then cooled to room temperature. The resulting reaction solution was concentrated and purified *via* column chromatography (silica, CH₂Cl₂:petroleum ether (40-60 °C) 7:3). No product was isolated.

Attempt 2

2-[Au]-CHO (0.2293 g, 0.2482 mmol) was dissolved in dry CH_2Cl_2 (~50 mL) and pyrrole (0.02 mL, 0.0193 g, 0.2877 mmol), then $BF_3(OEt_2)$ (0.02 mL) was added and the resulting solution stirred under a dinitrogen atmosphere at room temperature for 3 hr. *p*-Chloranil (0.0603 g, 0.2452 mmol) was added and the resulting dark solution was heated to reflux for 1 hr, then cooled to room temperature. Concentrated and purified *via* column chromatography (silica, CH_2Cl_2:petroleum ether (40-60 °C) 7:3) to give yellow tetrahedral crystals which were identified as the gold chloride from MALDI-MS.

No product was recovered despite the procedure being repeated several times.

6.13   Synthesis of Tetra-Substituted Porphyrins Connected to Gold(III) C^N^C complexes

2,3-[Au]-t-ZnP
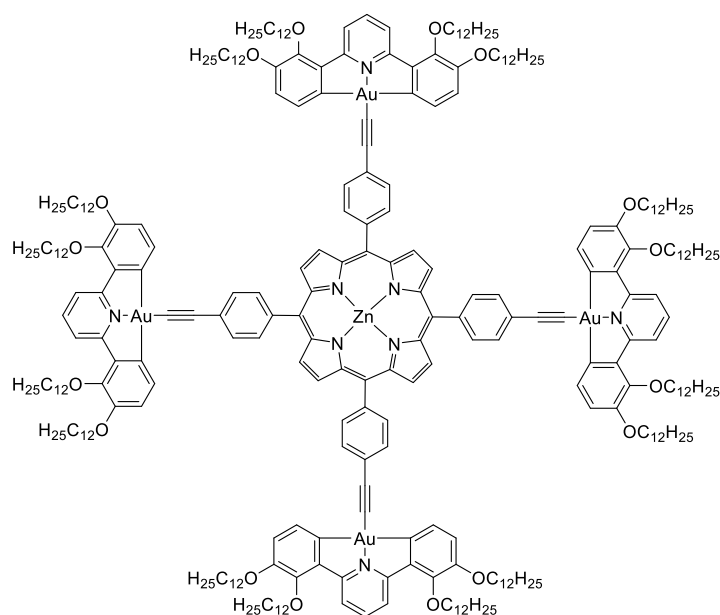
2,3-[Au]-Cl (0.1004 g, 0.0837 mmol), **t-ZnP** (0.0146 g, 0.0189 mmol) and CuI (0.0050 g, 0.0263 mmol) were dissolved in dry CH_2Cl_2 (50 mL) and triethylamine (0.1 mL, 180 mol%) was added and the reaction stirred under a dinitrogen atmosphere at room temperature for 20 hr. Filtered through Celite® and reduced to dryness under reduced pressure. Purified by column chromatography (silica, CH_2Cl_2:petroleum ether (40-60 °C) 4:6, $R_f = 0.10$, CH_2Cl_2:petroleum ether (40-60 °C) 3:7, $R_f = 0.58$, the CH_2Cl_2, $R_f = 0.96$)

to give a dark purple solid, which was then recrystallised from CH_2Cl_2/MeOH to give a burgundy solid. Yield: 0.0684 g (72%)

^{1}H NMR (400 MHz, CDCl$_3$) δ^H ppm: 9.08 (8H, s), 8.38 (8H, d, $^3J_{HH}$ = 8.2 Hz), 8.20 (8H, AA'XX', J = 8.2 Hz), 8.00 (8H, AA'XX', J = 8.2 Hz), 7.96 (8H, d, $^3J_{HH}$ = 7.9 Hz), 7.88 (4H, t, $^3J_{HH}$ = 8.4 Hz), 7.09 (8H, d, $^3J_{HH}$ = 8.2 Hz), 4.12 (16H, t, $^3J_{HH}$ = 6.9 Hz), 4.04 (16H, t, $^3J_{HH}$ = 6.5 Hz), 1.87 (32H, m), 1.5 – 1.2 (288H, br m), 0.89 (24H, t, $^3J_{HH}$ = 6.9 Hz), 0.86 (24H, t, $^3J_{HH}$ = 6.9 Hz).

2,3-[Au]-t-ZnP-C4
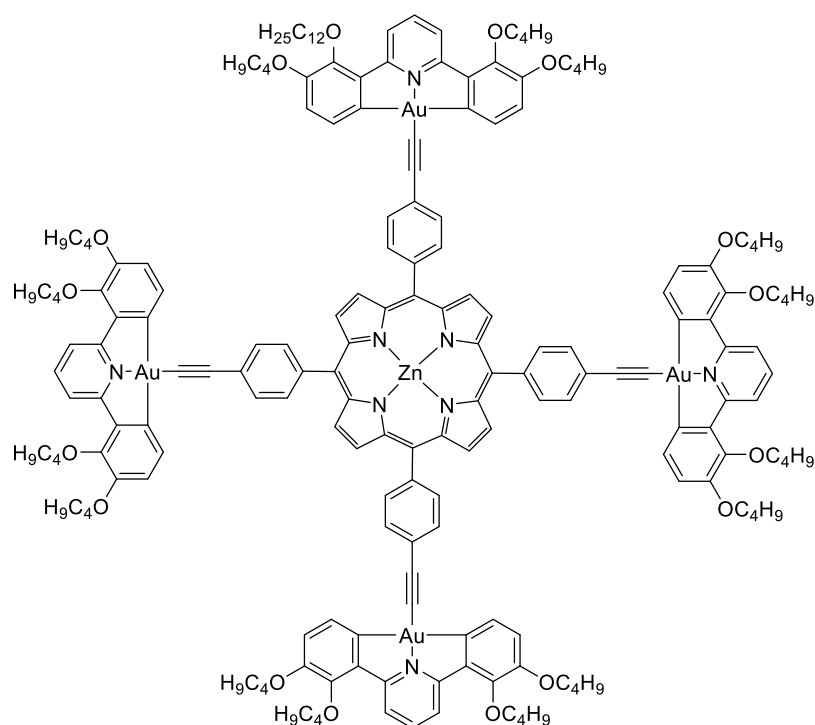
2,3-[Au]-Cl-C4 (0.1018 g, 0.1357 mmol), **t-ZnP** (0.0237 g, 0.0306 mmol) and CuI (0.0034 g, 0.0179 mmol) were degassed, then dry CH_2Cl_2 (~50 mL) and triethylamine (0.1 mL, 180 mol%) was added and the reaction stirred under a dinitrogen atmosphere at room temperature for 22 hr. The reaction mixture was filtered through Celite® and reduced to dryness under reduced pressure, then purified by column chromatography (silica, CH_2Cl_2:petroleum ether (40-60 °C) 1:1, $R_f = 0.00$, then CH_2Cl_2, $R_f = 0.79$) to give a dark purple solid, which was then recrystallised from CH_2Cl_2/MeOH to give a dark purple solid. Yield: 0.0297 g (37%)

^{1}H NMR (400 MHz, CDCl₃) δ^H ppm: 9.08 (8H, s), 8.38 (8H, d, $^3J_{HH}$ = 8.2 Hz), 8.20 (8H, AA'XX', J = 8.2 Hz), 8.00 (8H, AA'XX', J = 8.2 Hz), 7.95 (8H, d, $^3J_{HH}$ = 8.1 Hz), 7.89 (4H, t, $^3J_{HH}$ = 8.4 Hz), 7.09 (8H, d, $^3J_{HH}$ = 8.1 Hz), 4.14 (16H, t, $^3J_{HH}$ = 6.8 Hz), 4.05 (16H, t, $^3J_{HH}$ = 6.5 Hz), 1.86 (32H, m), 1.56 (32H, br m), 1.03 (24H, t $^3J_{HH}$ = 7.2 Hz), 1.01 (24H, t, $^3J_{HH}$ = 7.2 Hz).

2,3-[Au]-t-P
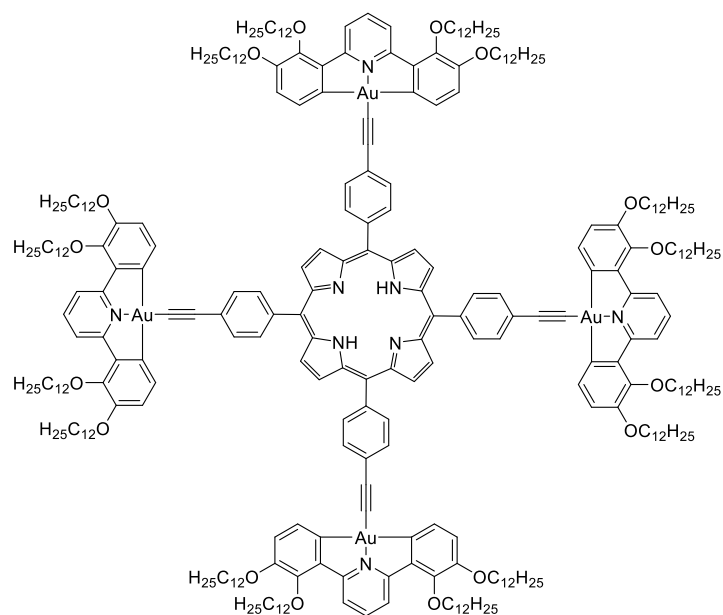
2,3-[Au]-t-ZnP (0.0325 g, 0.0064 mmol) was dissolved in CH_2Cl_2 (25 mL) and trifluoroacetic acid (0.02 mL, 0.030 g, 0.26 mmol) was added and the resulting solution stirred at room temperature for 1 hr. The reaction was quenched by addition of triethylamine (0.07 mL, 0.050 g, 0.26 mmol) and stirred for a further 15 min. The solution was washed with distilled water (25 mL), then brine (25 mL). The combined aqueous layers were washed with CH_2Cl_2 (2 x 10 mL) and the combined organic layers dried over $MgSO_4$, filtered and reduced to dryness to give a red/purple solid, which was recrystallised from CH_2Cl_2/MeOH to give a burgundy solid. Yield: 0.0281 g (88%)

^{1}H NMR (400 MHz, CDCl3) δ^H ppm: 8.97 (8H, s), 8.38 (8H, d, $^3J_{HH}$ = 8.2 Hz), 8.20 (8H, AA'XX', J = 7.4 Hz), 8.00 (8H, AA'XX', J = 7.9 Hz), 7.94 (8H, d, $^3J_{HH}$ = 7.7 Hz), 7.88 (4H, t, $^3J_{HH}$ = 8.4 Hz), 7.08 (8H, d, $^3J_{HH}$ = 8.1 Hz), 4.12 (16H, t, $^3J_{HH}$ = 6.5 Hz), 4.03 (16H, t, $^3J_{HH}$ = 7.0 Hz), 1.87 (32H, m), 1.54 (32H, m), 1.4 – 1.2 (256H, br m), 0.90 (24H, t, $^3J_{HH}$ = 7.0 Hz), 0.87 (24H, t, $^3J_{HH}$ = 7.0 Hz), -2.71 (2H, br s).

2,3-[Au]-t-P-C4
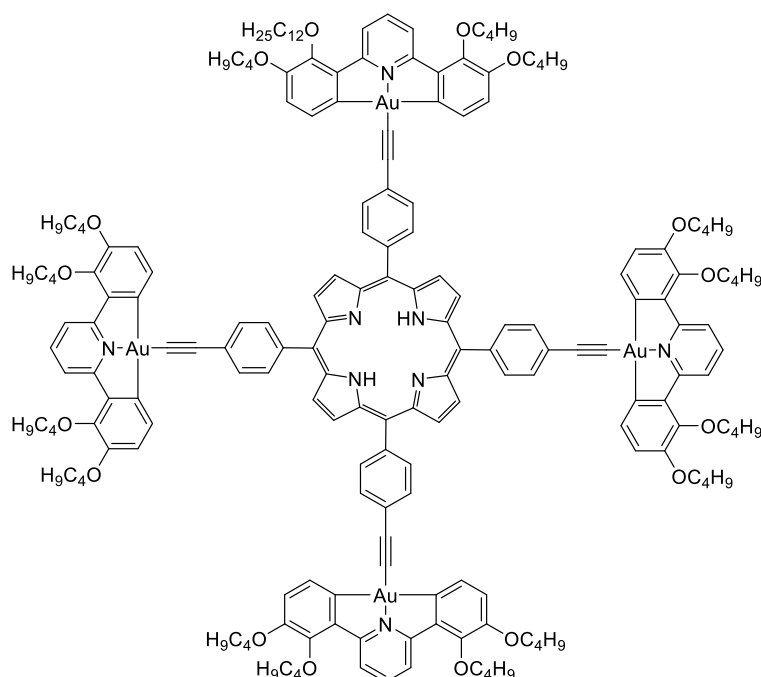
2,3-[Au]-t-ZnP-C4 (0.0192 g, 0.0053 mmol) was dissolved in CH_2Cl_2 (25 mL) and trifluoroacetic acid (0.01 mL, 0.015 g, 0.13 mmol) was added and the resulting solution stirred at room temperature for 1 hr. The reaction was quenched by addition of triethylamine (0.04 mL, 0.029 g, 0.15 mmol) and stirred for a further 15 min. The solution was washed with distilled water (25 mL), then brine (25 mL). The combined aqueous layers were washed with CH_2Cl_2 (2 x 10 mL) and the combined organic layers dried over $MgSO_4$, filtered and reduced to dryness to give a dark purple solid. Yield: 0.0148 g (79%)

^{1}H NMR (400 MHz, CDCl$_3$) δ^H ppm: 8.97 (8H, s), 8.38 (8H, d, $^3J_{HH}$ = 8.2 Hz), 8.20 (8H, AA'XX', J = 8.0 Hz), 8.00 (8H, AA'XX', J = 8.2 Hz), 7.95 (8H, d, $^3J_{HH}$ = 7.9 Hz), 7.89 (4H, t, $^3J_{HH}$ = 9.2 Hz), 7.09 (8H, d, $^3J_{HH}$ = 8.2 Hz), 4.14 (16H, t, $^3J_{HH}$ = 7.0 Hz), 4.05 (16H, t, $^3J_{HH}$ = 6.5 Hz), 1.85 (32H, m), 1.55 (32H, br m), 1.03 (24H, t, $^3J_{HH}$ = 7.2 Hz), 1.01 (24H, t, $^3J_{HH}$ = 7.4 Hz), -2.72 (2H, br s).

2,5-[Au]-t-ZnP
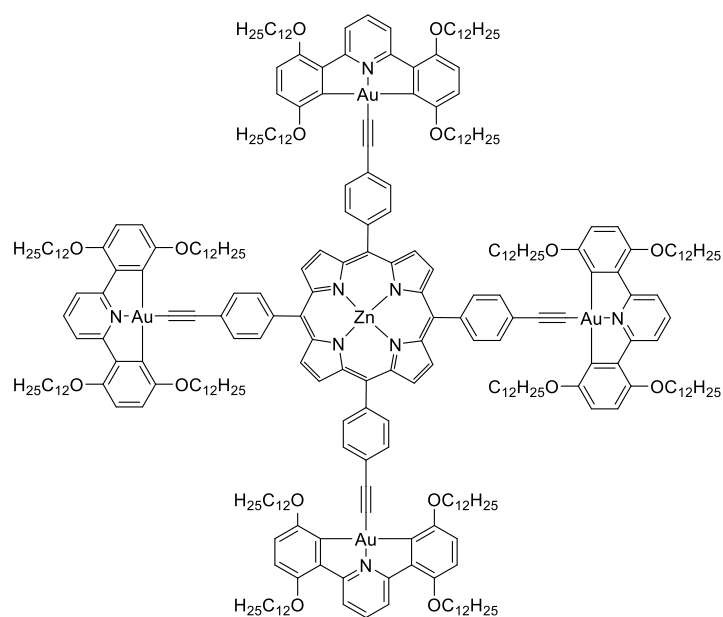
2,5-[Au]-Cl (0.1003 g, 0.0837 mmol), **t-ZnP** (0.0149 g, 0.0192 mmol) and CuI (0.0019 g, 0.0100 mmol) were dissolved in dry CH_2Cl_2 (50 mL) and triethylamine (0.1 mL, 180 mol%) was added and the reaction stirred under a dinitrogen atmosphere at room temperature for 20 hr. The reaction mixture was filtered through Celite® and reduced to dryness under reduced pressure. Then, purified by column chromatography (silica, CH_2Cl_2 R_f = 0.03, 5% MeOH in CH_2Cl_2, R_f = 0.96) twice to give a dark purple solid, which was then recrystallised from CH_2Cl_2/MeOH to give a dark purple solid. Yield: 0.0655 g (68%, impure)

^{1}H NMR (400 MHz, CDCl$_3$) δ^H ppm: 9.05 (8H, m)), 8.47 (8H, d, $^3J_{HH}$ = 8.3 Hz), 8.13 (8H, m), 7.91 (8H, AA'XX', J = 8.1 Hz), 7.81 (4H, t, $^3J_{HH}$ = 8.3 Hz), 7.07 (8H, d, $^3J_{HH}$ = 9.6 Hz), 6.82 (4H, d, $^3J_{HH}$ = 9.3 Hz), 4.16 (16H, m), 4.10 (16H, t, $^3J_{HH}$ = 6.4 Hz), 1.954 (32H, m), 1.6 – 1.3 (224H, br m), 1.0 - 0.8 (64H, br m), 0.89 (24H, t, $^3J_{HH}$ = 6.9 Hz), 0.52 (24H, t, $^3J_{HH}$ = 7.1 Hz).

6.14 Synthesis of Disubstituted Porphyrins Connected to Gold(III) C^N^C complexes

2,3-[Au]-di-ZnP
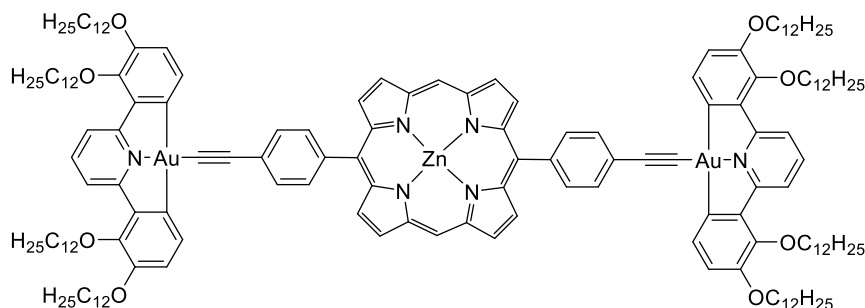
2,3-[Au]-Cl (0.1003 g, 0.0837 mmol), **di-ZnP** (0.0209 g, 0.0364 mmol) and CuI (0.0020 g, 0.0105 mmol) were degassed, then dry CH_2Cl_2 (50 mL) and triethylamine (0.1 mL, 90 mol%) was added and the reaction stirred under a dinitrogen atmosphere at room temperature for 23 hr. The reaction mixture was filtered through Celite® and reduced to dryness under reduced pressure, then purified by column chromatography (silica, CH_2Cl_2:petroleum ether (40-60 °C) 7:3, (R_f = 0.28)), then recrystallised from CH_2Cl_2/MeOH to give a reddish purple solid. Yield = 0.0828 g (78%)

^{1}H NMR (400 MHz, CDCl$_3$) δ^H ppm: 10.29 (2H, s), 9.44 (4H, d, $^3J_{HH}$ = 4.5 Hz), 9.23 (4H, d, $^3J_{HH}$ = 4.5 Hz), 8.34 (4H, d, $^3J_{HH}$ = 8.3 Hz), 8.24 (4H, d, $^3J_{HH}$ = 8.1 Hz), 8.04 (4H, d, $^3J_{HH}$ = 8.1 Hz), 7.93 (4H, d, $^3J_{HH}$ = 7.9 Hz), 7.87 (2H, t, $^3J_{HH}$ = 8.3 Hz), 7.07 (4H, d, $^3J_{HH}$ = 8.1 Hz), 4.10 (8H, t, $^3J_{HH}$ = 6.7 Hz), 4.03 (8H, t, $^3J_{HH}$ = 6.4 Hz), 1.87 (16H, m), 1.51 (16H, m) 1.40-1.25 (128H, br m), 0.90 (12H, t, $^3J_{HH}$ = 6.7 Hz), 0.88 (12H, t, $^3J_{HH}$ = 7.1 Hz).

2,3-[Au]-di-ZnP-C4
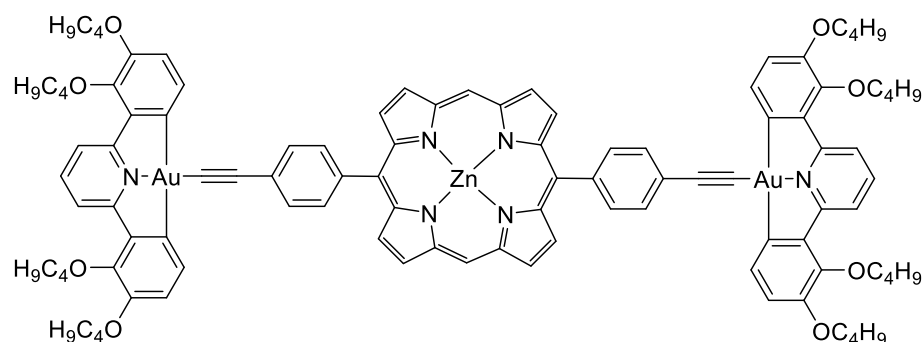
2,3-[Au]-Cl-C4 (0.1003 g, 0.1072 mmol), **di-ZnP** (0.0271 g, 0.0472 mmol) and CuI (0.0049 g, 0.0257 mmol) were degassed, then dry CH_2Cl_2 (50 mL) and triethylamine (0.1 mL, 45 mol%) was added and the reaction stirred under a dinitrogen atmosphere at room temperature for 22 hr. The reaction mixture was filtered through Celite® and reduced to dryness under reduced pressure, then purified by column chromatography (silica, CH_2Cl_2:petroleum ether (40-60 °C) 1:1, $R_f = 0.0$, then CH_2Cl_2:petroleum ether (40-60 °C) 7:3, $R_f = 0.12$, then CH_2Cl_2, $R_f = 0.87$) to give a red/pink solid, which was then recrystallised from CH_2Cl_2/MeOH, to give a reddish pink solid. Yield = 0.0826 g (87%)

^{1}H NMR (400 MHz, CDCl$_3$) δ^H ppm: 10.27 (2H, s), 9.42 (4H, d, $^3J_{HH}$ = 4.6 Hz), 9.22 (4H, d, $^3J_{HH}$ = 4.6 Hz), 8.33 (4H, d, $^3J_{HH}$ = 8.2 Hz), 8.25 (4H, AA'XX', J = 8.0 Hz), 8.04 (4H, AA'XX', J = 8.1 Hz), 7.92 (4H, d, $^3J_{HH}$ = 8.1 Hz), 7.86 (2H, t, $^3J_{HH}$ = 8.4 Hz), 7.06 (4H, d, $^3J_{HH}$ = 8.1 Hz), 4.10 (8H, t, $^3J_{HH}$ = 6.8 Hz), 4.03 (8H, t, $^3J_{HH}$ = 6.5 Hz), 1.86 (16H, m), 1.56 (16H, m), 1.04 (12H, t, $^3J_{HH}$ = 7.4 Hz), 1.03 (12H, t, $^3J_{HH}$ = 7.4 Hz).

2,5-[Au]-di-ZnP
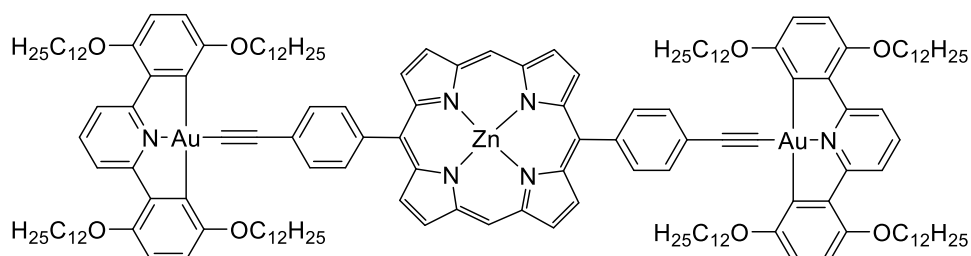
2,5-[Au]-Cl (0.0979 g, 0.0817 mmol), **di-ZnP** (0.0215 g, 0.0375 mmol) and CuI (0.0025 g, 0.0131 mmol) were degassed, then dry CH_2Cl_2 (50 mL) and triethylamine (0.1 mL, 90 mol%) was added and the reaction stirred under a dinitrogen atmosphere at room temperature for 5 hr. The reaction mixture was filtered through Celite® and reduced to dryness under reduced pressure, then purified by column chromatography (silica, CH_2Cl_2

($R_f = 0.03$), then 10% MeOH in CH_2Cl_2 ($R_f = 0.96$)) to give a plum red solid, which was then recrystallised from CH_2Cl_2 /MeOH to give a reddish purple solid. Yield = 0.0800 g (74%)

^{1}H NMR (400 MHz, CDCl$_3$) δ^H ppm: 10.33 (2H, s), 9.44 (4H, d, $^3J_{HH}$ = 4.6 Hz), 9.22 (4H, d, $^3J_{HH}$ = 4.5 Hz), 8.44 (4H, d, $^3J_{HH}$ = 8.2 Hz), 8.17 (4H, AA'XX', J = 8.2 Hz), 7.96 (4H, AA'XX', J = 8.1 Hz), 7.79 (2H, t, $^3J_{HH}$ = 8.2 Hz), 7.08 (4H, d, $^3J_{HH}$ = 8.9 Hz), 6.81 (4H, d, $^3J_{HH}$ = 9.0 Hz), 4.17 (8H, t, $^3J_{HH}$ = 7.4 Hz), 4.08 (8H, t, $^3J_{HH}$ = 6.5 Hz), 1.95 (16H, m), 1.52 (16H, m), 1.4 – 1.3 (82H, br m), 1.21 (8H, m), 1.12 (8H, m), 1.0 – 0.8 (30H, br m), 0.90 (12H, t, $^3J_{HH}$ = 6.9 Hz), 0.60 (12H, t, $^3J_{HH}$ = 6.9 Hz).

2-[Au]-di-ZnP
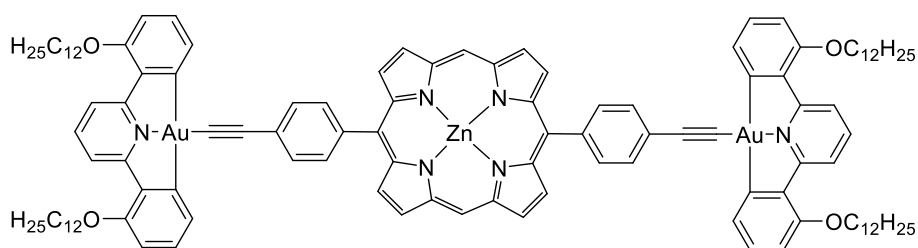
2-[Au]-Cl (0.0639 g, 0.0770 mmol), **di-ZnP** (0.0211 g, 0.0368 mmol) and CuI (0.0017 g, 0.0089 mmol) were degassed, then dry CH_2Cl_2 (50 mL) and triethylamine (0.05 mL, 90 mol%) added and the reaction stirred under a dinitrogen atmosphere at room temperature for 22 hr. The reaction mixture was filtered through Celite® and reduced to dryness under reduced pressure, then purified by column chromatography (silica, CH_2Cl_2:petroleum ether (40-60 °C) 6:4 (R_f = 0.23), then CH_2Cl_2:petroleum ether (40-60 °C) 6:4 (R_f = 0.52), then CH_2Cl_2 (R_f = 0.97)) to give a reddish purple solid. Recrystallised from CH_2Cl_2/methanol to give a reddish pink solid. Yield: 0.0157 g (21%)

^{1}H NMR (400 MHz, CDCl$_3$) δ^H ppm: 10.30 (2H, s), 9.44 (4H, d, $^3J_{HH}$ = 4.3 Hz), 9.24 (4H, d, $^3J_{HH}$ = 4.5 Hz), 8.28 (4H, d, $^3J_{HH}$ = 8.4 Hz), 8.26 (4H, d, $^3J_{HH}$ = 8.2 Hz), 8.07 (4H, d, $^3J_{HH}$ = 8.2 Hz), 7.94 (4H, dd, $^3J_{HH}$ = 6.8 Hz, $^4J_{HH}$ = 1.2 Hz), 7.80 (2H, t, $^3J_{HH}$ = 8.2 Hz), 7.43 (4H, dd, $^3J_{HH}$ = 8.2 Hz, $^3J_{HH}$ = 6.1 Hz), 6.81 (4H, dd, $^3J_{HH}$ = 8.2 Hz, $^4J_{HH}$ = 1.2 Hz), 4.21 (8H, t, $^3J_{HH}$ = 6.8 Hz), 1.96 (8H, m), 1.40-1.25 (72H, br m), 0.89 (12H, t, $^3J_{HH}$ = 7.2 Hz).

4-[Au]-ZnP
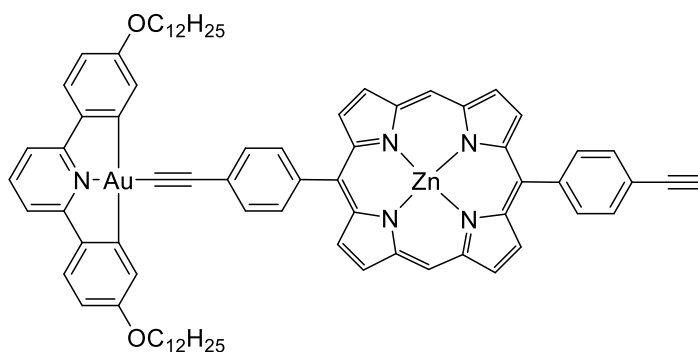
4-[Au]-Cl (0.0641 g, 0.0772 mmol), **di-ZnP** (0.0204 g, 0.0355 mmol) and CuI (0.0022 g, 0.0116 mmol) were degassed, then dry CH_2Cl_2 (50 mL) and triethylamine (0.05 mL, 90 mol%) added and the reaction stirred under a dinitrogen atmosphere at room temperature for 22 hr. The reaction mixture was filtered through Celite® and reduced to dryness under reduced pressure, then purified by column chromatography (silica, CH_2Cl_2:petroleum ether (40-60 °C) 6:4 (R_f = 0.23), then CH_2Cl_2:petroleum ether (40-60 °C) 6:4 (R_f = 0.50), then CH_2Cl_2 (R_f = 0.97)), then on a second column (silica, CH_2Cl_2:petroleum ether (40-60 °C) 6:4 (R_f = 0.50), then CH_2Cl_2 (R_f = 0.94)), to give a reddish purple solid. Recrystallised from CH_2Cl_2/methanol to give a reddish purple solid. Yield: 0.0092 g (19%)

^{1}H NMR (400 MHz, CDCl$_3$) δ^H ppm: 10.31 (2H, s), 9.46 (2H, d, $^3J_{HH}$ = 4.5 Hz), 9.44 (2H, d, $^3J_{HH}$ = 4.6 Hz), 9.25 (2H, d, $^3J_{HH}$ = 4.6 Hz), 9.10 (2H, d, $^3J_{HH}$ = 4.6 Hz), 8.25 (2H, d, $^3J_{HH}$ = 8.2 Hz), 8.04 (2H, d, $^3J_{HH}$ = 8.1 Hz), 7.80 (2H, d, $^4J_{HH}$ = 2.7 Hz), 7.67 (1H, t, $^3J_{HH}$ = 7.0 Hz), 6.65 (2H, dd, $^3J_{HH}$ = 9.4 Hz, $^4J_{HH}$ = 1.5 Hz), 4.15 (4H, t, $^3J_{HH}$ = 6.7 Hz), 3.35 (1H, s), 1.88 (4H, m), 1.4-1.1 (36H, br m), 0.71 (6H, t, $^3J_{HH}$ = 7.2 Hz).

3,4-[Au]-ZnP
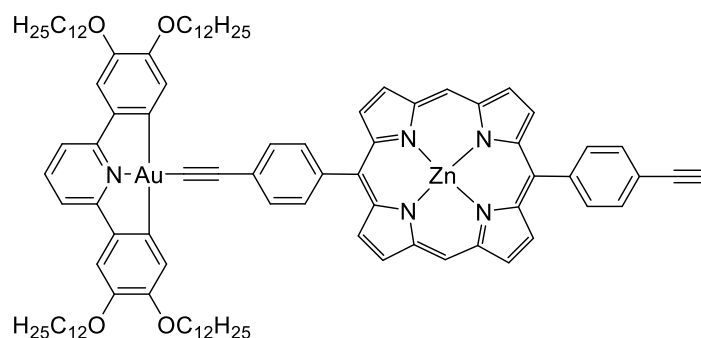
3,4-Au-Cl (0.1010 g, 0.0842 mmol), **di-ZnP** (0.0218 g, 0.0380 mmol) and CuI (0.0021 g, 0.0110 mmol) were degassed, then dry CH_2Cl_2 (50 mL) and triethylamine (0.05 mL, 90 mol%) added and the reaction stirred under a dinitrogen atmosphere at room temperature for 48 hr. The reaction mixture was filtered through Celite® and reduced to dryness under reduced pressure, then purified by column chromatography (silica, CH_2Cl_2:petroleum ether (40-60 °C) 6:4 (R_f = 0.20), then CH_2Cl_2:petroleum ether (40-60 °C) 6:4 (R_f = 0.50), then CH_2Cl_2 (R_f = 0.94)), then on a second column (silica, CH_2Cl_2:Petroleum ether (40-60 °C) 6:4 (R_f = 0.50), then CH_2Cl_2 (R_f = 0.94)), before recrystallising from CH_2Cl_2/MeOH to give a reddish purple solid. Yield: 0.0464 g (70%)

^{1}H NMR (400 MHz, CDCl$_3$) δ^H ppm: 10.30 (2H, s), 9.44 (2H, d, $^3J_{HH}$ = 4.6 Hz), 9.43 (2H, d, $^3J_{HH}$ = 4.8 Hz), 9.22 (2H, d, $^3J_{HH}$ = 4.5 Hz), 9.11 (2H, d, $^3J_{HH}$ = 4.5 Hz), 8.25 (2H, d, $^3J_{HH}$ = 8.4 Hz), 8.25 (2H, d, $^3J_{HH}$ = 8.4 Hz), 8.01 (2H, d, $^3J_{HH}$ = 8.1 Hz), 7.95 (2H, d, $^3J_{HH}$ = 8.0 Hz), 7.79 (2H, d, $^3J_{HH}$ = 7.0 Hz), 7.65 (1H, t, $^3J_{HH}$ = 7.0 Hz), 7.09 (2H, d, $^3J_{HH}$ = 8.2 Hz), 7.03 (2H, s), 4.02 (4H, t, $^3J_{HH}$ = 6.7 Hz), 4.02 (4H, t, $^3J_{HH}$ = 6.7 Hz), 3.35 (1H, s), 1.94 (4H, m), 1.84 (4H, m), 1.5-0.9 (72H, broad m), 0.88 (6H, t, $^3J_{HH}$ = 6.7 Hz), 0.66 (6H, t, $^3J_{HH}$ = 7.2 Hz).

2,3-[Au]-iPr-ZnP
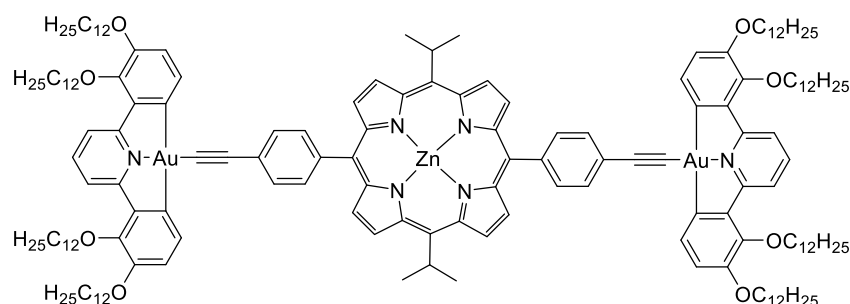
di-ZnP (0.0888 g, 0.0737 mmol), **2,3-[Au]-Cl** (0.0220 g, 0.0334 mmol) and CuI (0.0025 g, 0.0247 mmol) were degassed, then dry CH_2Cl_2 (50 mL) and triethylamine (0.1 mL, 90 mol%) was added and the reaction stirred under a dinitrogen atmosphere at room temperature for 23 hr. The reaction mixture was filtered through Celite® and reduced to dryness under reduced pressure, then purified by column chromatography (silica, 1:1 CH_2Cl_2:petroleum ether (40-60 °C), R_f = 0.14, then 7:3 CH_2Cl_2:petroleum ether (40-60 °C), R_f = 0.5) to give a red-purple solid, which was then recrystallised from CH_2Cl_2/MeOH to give a reddish purple solid. Yield = 0.0383 g (38%)

^{1}H NMR (400 MHz, CDCl3) δ^H ppm: 9.73 (4H, d, $^3J_{HH}$ = 5.0 Hz), 9.02 (4H, d, $^3J_{HH}$ = 4.8 Hz), 8.38 (4H, d, $^3J_{HH}$ = 8.2 Hz), 8.14 (4H, AA'XX', J = 8.1 Hz), 7.98 (4H, AA'XX', J = 8.0 Hz), 7.95 (4H, d, $^3J_{HH}$ = 8.0 Hz), 7.88 (2H, t, $^3J_{HH}$ = 8.2 Hz), 7.09 (4H, d, $^3J_{HH}$ = 8.1 Hz), 5.79 (2H, m), 4.13 (8H, t, $^3J_{HH}$ = 6.7 Hz), 4.04 (8H, t, $^3J_{HH}$ = 6.5 Hz), 2.47 (12H, d, $^3J_{HH}$ = 7.2 Hz), 1.87 (16H, m), 1.51 (16H, m), 1.4-1.2 (56H, br m), 0.89 (12H, t, $^3J_{HH}$ = 5.2 Hz), 0.87 (12H, t, $^3J_{HH}$ = 6.7 Hz).

2,5-[Au]-iPr-ZnP
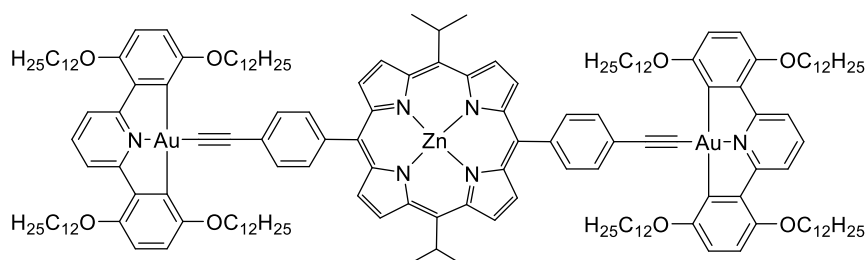
di-ZnP (0.0952 g, 0.0794 mmol), **2,5-[Au]-Cl** (0.0234 g, 0.0356 mmol) and CuI (0.0039 g, 0.0385 mmol) were degassed, then dry CH_2Cl_2 (50 mL) and triethylamine (0.1 mL, 90 mol%) was added and the reaction stirred under a dinitrogen atmosphere at room temperature for 23 hr. The reaction mixture was filtered through Celite® and reduced to dryness under reduced pressure, then purified by column chromatography (silica, CH_2Cl_2,

$R_f = 0.21$, then 1% MeOH in CH_2Cl_2, $R_f = 0.90$) to give a purple solid, which was then recrystallised from CH_2Cl_2/MeOH to give a burgundy solid. Yield = 0.0466 g (44%)

^{1}H NMR (400 MHz, CDCl$_3$) δ^H ppm: 9.69 (4H, d, $^3J_{HH}$ = 5.2 Hz), 9.99 (4H, d, $^3J_{HH}$ = 4.6 Hz), 8.45 (4H, d, $^3J_{HH}$ = 8.2 Hz), 8.07 (4H, AA'XX', J = 8.2 Hz), 7.89 (4H, AA'XX', J = 8.0 Hz), 7.80 (4H, t, $^3J_{HH}$ = 8.4 Hz), 7.08 (2H, d, $^3J_{HH}$ = 8.6 Hz), 6.82 (4H, d, $^3J_{HH}$ = 9.1 Hz), 5.77 (2H, m), 4.16 (8H, t, $^3J_{HH}$ = 7.2 Hz), 4.09 (8H, t, $^3J_{HH}$ = 6.5 Hz), 2.46 (16H, d, $^3J_{HH}$ = 7.1), 1.94 (16H, m), 1.4-1.2 (98H, broad m), 1.0-0.8 (46H, br m), 0.88 (12H, t, $^3J_{HH}$ = 6.9 Hz), 0.61 (12H, t, $^3J_{HH}$ = 7.2 Hz).

2,3-[Au]-CC-ZnP
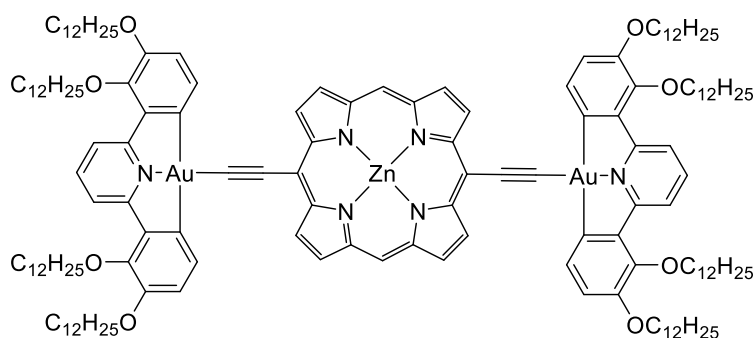
2,3-[Au]-Cl (0.1002 g, 0.0836 mmol), **CC-ZnP** (0.0162 g, 0.0379 mmol) and CuI (0.0030 g, 0.0158 mmol) were degassed, then dry CH_2Cl_2 (50 mL) and triethylamine (0.01 mL, 90 mol%) added and the reaction stirred under a dinitrogen atmosphere at room temperature for 23 hr. The reaction mixture was filtered through Celite® and reduced to dryness under reduced pressure, then purified by column chromatography (silica, CH_2Cl_2:petroleum ether (40-60 °C) 7:3 (R_f = 0.08), then CH_2Cl_2 (R_f = 0.92), to give a green solid. Yield: 0.0055 g (6%)

^{1}H NMR (400 MHz, CDCl$_3$) δ^H ppm: 9.84 (2H, s), 8.30 (4H, d, $^3J_{HH}$ = 8.3 Hz), 7.83 (2H, t, $^3J_{HH}$ = 8.3 Hz), 7.54 (4H, d $^3J_{HH}$ = 8.1 Hz), 7.52 (4H, d, $^3J_{HH}$ = 5.7 Hz), 7.01 (4H, d, $^3J_{HH}$ = 8.4 Hz), 4.08 (8H, t, $^3J_{HH}$ = 6.7 Hz), 3.98 (8H, t, $^3J_{HH}$ = 6.2 Hz), 1.83 (16H, m), 1.4 − 1.2 (144H, br m), 0.88 (12H, t, $^3J_{HH}$ = 7.2 Hz), 0.88 (12H, t, $^3J_{HH}$ = 7.2 Hz).

Unable to locate one pyrrolic C-H signal, which is likely to be hidden under the CHCl$_3$ peak.

2,3-[Au]-di-P
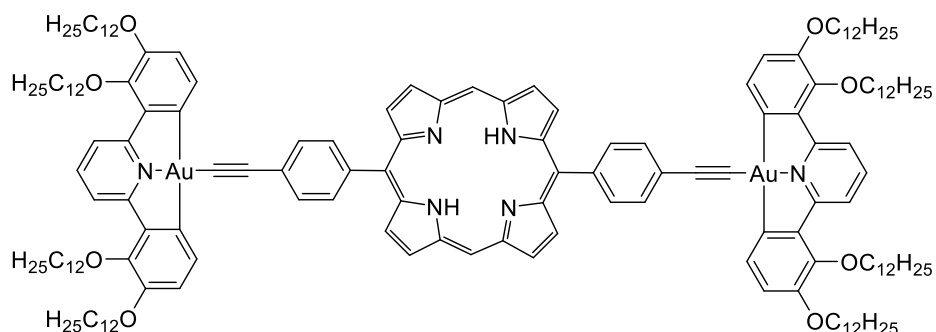
2,3-[Au]-di-ZnP (0.0522 g, 0.0180 mmol) was dissolved in CH_2Cl_2 (25 mL) and trifluoroacetic acid (0.01 mL, 0.015 g, 0.13 mmol) was added and the resulting solution stirred at room temperature for 1 hr. The reaction was quenched by addition of triethylamine (0.04 mL, 0.029 g, 0.15 mmol) and stirred for a further 15 min. The solution was washed with distilled water (25 mL), then brine (25 mL). The combined aqueous layers were washed with CH_2Cl_2 (2 x 10 mL) and the combined organic layers dried over $MgSO_4$, filtered and reduced to dryness. Recrystallised from CH_2Cl_2/MeOH to give a red/purple solid. Yield: 0.0442 g (99.5%)

^{1}H NMR (400 MHz, $CDCl_3$) δ^H ppm: 10.34 (2H, s), 9.43 (4H, d, $^3J_{HH}$ = 4.6 Hz), 9.17 (4H, d, $^3J_{HH}$ = 4.6 Hz), 8.39 (4H, d, $^3J_{HH}$ = 8.2 Hz), 8.24 (4H, AA'XX', J = 8.0 Hz), 8.05 (4H, AA'XX', J = 8.0 Hz), 7.96 (4H, d, $^3J_{HH}$ = 7.9 Hz), 7.89 (2H, t, $^3J_{HH}$ = 8.2 Hz), 7.10 (4H, d, $^3J_{HH}$ = 8.2 Hz), 4.14 (8H, t, $^3J_{HH}$ = 6.9 Hz), 4.05 (8H, t, $^3J_{HH}$ = 6.5 Hz), 1.89 (16H, m), 1.52 (16H, m), 1.4-1.2 (128H, br m), 0.90 (12H, t, $^3J_{HH}$ = 6.9 Hz), 0.88 (12H, t, $^3J_{HH}$ = 7.0 Hz), -3.07 (2H, br s).

2,3-[Au]-di-P-C4
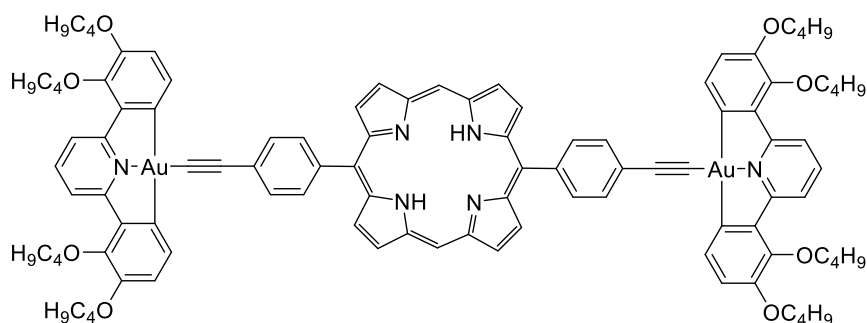
2,3-[Au]-di-ZnP-C4 (0.0515 g, 0.0257 mmol) was dissolved in CH_2Cl_2 (25 mL) and trifluoroacetic acid (0.01 mL, 0.015 g, 0.13 mmol) was added and the resulting solution

stirred at room temperature for 1 hr. The reaction was quenched by addition of triethylamine (0.04 mL, 0.029 g, 0.15 mmol) and stirred for a further 15 min. The solution was washed with distilled water (25 mL), then brine (25 mL). The combined aqueous layers were washed with CH_2Cl_2 (2 x 10 mL) and the combined organic layers dried over $MgSO_4$, filtered and reduced to dryness. The product war recrystallised from CH_2Cl_2/MeOH to give a dark purple solid. Yield: 0.0498 g (100%)

^{1}H NMR (400 MHz, CDCl₃) δ^H ppm: 10.34 (2H, s), 9.43 (4H, d, $^3J_{HH}$ = 4.6 Hz), 9.17 (4H, d, $^3J_{HH}$ = 4.4 Hz), 8.38 (4H, d, $^3J_{HH}$ = 8.2 Hz), 8.25 (4H, AA'XX', J = 8.0 Hz), 8.05 (4H, AA'XX', J = 8.0 Hz), 7.96 (4H, d, $^3J_{HH}$ = 7.9 Hz), 7.90 (2H, t, $^3J_{HH}$ = 8.4 Hz), 7.10 (4H, d, $^3J_{HH}$ = 8.2 Hz), 4.15 (8H, t, $^3J_{HH}$ = 6.8 Hz), 4.06 (8H, t, $^3J_{HH}$ = 6.5 Hz), 1.87 (16H, m), 1.57 (16H, m), 1.04 (12H, t, $^3J_{HH}$ = 7.2 Hz), 1.03 (12H, t, $^3J_{HH}$ = 7.5 Hz), -3.07 (2H, br s).

2,5-[Au]-di-P
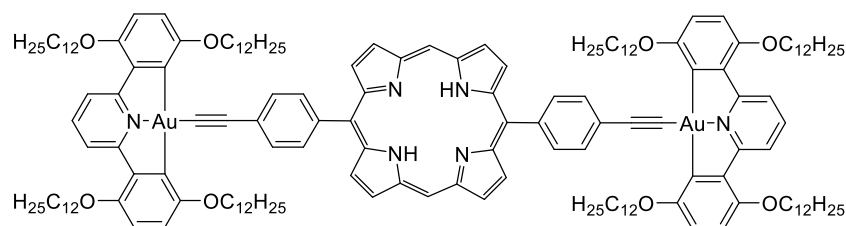
2,5-[Au]-di-ZnP (0.0132 g, 0.0046 mmol) was dissolved in CH_2Cl_2 (25 mL) and trifluoroacetic acid (0.01 mL, 0.015 g, 0.13 mmol) was added and the resulting solution stirred at room temperature for 1 hr. The reaction was quenched by addition of triethylamine (0.01 mL, 0.0073 g, 0.0381 mmol) and stirred for a further 15 min. The solution was washed with distilled water (25 mL), then brine (25 mL). The combined aqueous layers were washed with CH_2Cl_2 (2 x 10 mL) and the combined organic layers dried over $MgSO_4$, filtered and reduced to dryness to give a red/purple solid. Yield: 0.0094 g (83%)

^{1}H NMR very difficult to assign.

2,3-[Au]-iPr-P
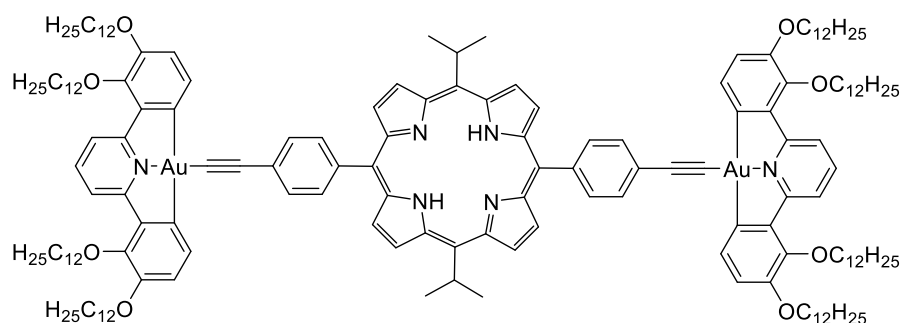
2,3-[Au]-iPr-ZnP (0.0181 g, 0.0061 mmol) was dissolved in CH_2Cl_2 (15 mL) and trifluoroacetic acid (0.01 mL, 0.015 g, 0.13 mmol) was added and the resulting solution stirred at room temperature for 1 hr. The reaction was quenched by addition of triethylamine (0.09 mL, 0.025 g, 0.34 mmol) and stirred for a further 15 min. The solution was washed with distilled water (2 x 25 mL), then brine (25 mL). The combined aqueous layers were washed with CH_2Cl_2 (2 x 10 mL) and the combined organic layers dried over $MgSO_4$, filtered and reduced to dryness. The product was recrystallised from CH_2Cl_2/MeOH to give a red/purple solid. Yield: 0.0134 g (75%)

^{1}H NMR (400 MHz, $CDCl_3$) δ^H ppm: 9.56 (4H, d, $^3J_{HH}$ = 4.7 Hz), 9.89 (4H, d, $^3J_{HH}$ = 4.87 Hz), 8.39 (4H, d, $^3J_{HH}$ = 8.1 Hz), 8.13 (4H, AA'XX', J = 8.1 Hz), 7.98 (4H, AA'XX', J = 8.1 Hz), 7.96 (4H, d, $^3J_{HH}$ = 8.1 Hz), 7.89 (2H, t, $^3J_{HH}$ = 8.3 Hz), 7.10 (4H, d, $^3J_{HH}$ = 8.3 Hz), 5.64 (2H, m), 4.13 (8H, t, $^3J_{HH}$ = 6.7 Hz), 4.05 (8H, t, $^3J_{HH}$ = 6.6 Hz), 2.42 (12H, d, $^3J_{HH}$ = 6.6 Hz), 1.89 (16H, m), 1.4-1.2 (88H, br m), 0.90 (12H, t, $^3J_{HH}$ = 6.9 Hz), 0.88 (12H, t, $^3J_{HH}$ = 7.1 Hz), -2.40 (2H, br s).

2,5-[Au]-iPr-P
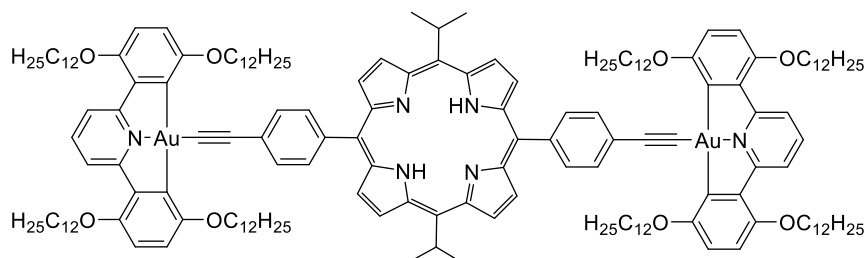
2,5-[Au]-iPr-ZnP (0.0126 g, 0.0042 mmol) was dissolved in CH_2Cl_2 (15 mL) and trifluroacetic acid (0.01 mL, 0.015 g, 0.13 mmol) was added and the resulting solution stirred at room temperature for 1 hr. The reaction was quenched by addition of triethylamine (0.09 mL, 0.025 g, 0.34 mmol) and stirred for a further 15 min. The solution was washed with distilled water (2 x 25 mL), then brine (25 mL). The combined aqueous

layers were washed with CH_2Cl_2 (2 x 10 mL) and the combined organic layers dried over $MgSO_4$, filtered and reduced to dryness. The product was recrystallised from CH_2Cl_2/MeOH to give a red/purple solid. Yield: 0.0115 g (94%)

^{1}H NMR very difficult to assign.

6.15   Computational Methods

Density function theory (DFT), followed by time-dependent density functional theory (TD-DFT) calculations were carried out on the ligand and gold complexes using Gaussian16[14] on the University of York Viking Computing Cluster and visualised using GaussView 6.0.[15] The structures of the complexes were optimised, and the IR frequencies calculated, at the bp86/def2-SV(P) level of theory.[16-18] A lack of negative frequencies indicated optimisation to a true minima. Modified single crystal structures, with replacement of long chains with methoxy and ethyl chains to save computational power, were used first as the input geometries and solvation was modelled through a PCM dichloromethane solvent mask.[19-22] A superfine grid was used for **2,3-[Au]-1-OMe** in order to gain convergence within 48 hours. TD-DFT calculations were carried out at the pbe0/def2-TZVPP level of theory,[23, 24] The zero-point energy of each complex was calculated by optimising the structure at the pbe0/def2-SV(P) level of theory,[23, 18] with an ultrafine grid applied, and then the energy calculated at the pbe0/def2-TZVPP level of theory, with, again, an ultrafine grid applied.[23, 24] NTOs were calculated at the pbe0/def2-TZVPP[23, 24] level of theory. The first singlet excited state structure was calculated at the pbe0/def2-TZVPP level of theory.[23, 24] The geometry of the lowest energy triplet state structure was calculated at the pbe0/def2-SV(P) level of theory,[23, 18] and then the single point energy calculated at the pbe0/def2-TZVPP level of theory,[23, 24] with the optimised singlet excited state used as the input geometry.

6.16   References

1.   R. R. Parker, PhD Thesis, University of York, 2019.
2.   L. J. Curtis, MChem Thesis, University of York, 2021.
3.   G. Johansson, V. Percec, G. Ungar and J. P. Zhou, *Macromolecules*, 1996, **29**, 646-660.
4.   G. Johansson, V. Percec, G. Ungar and K. Smith, *Chem. Mater.*, 1997, **9**, 164-175.
5.   O. V. Dolomanov, L. J. Bourhis, R. J. Gildea, H. J. A. K. and H. Puschmann, *J. Appl. Crystallogr.*, 2009, **42**, 339-341.

6. G. Sheldrick, *Acta Crystallogr. A*, 2008, **64**, 112-122.
7. A. S. Brewster, D. G. Waterman, J. M. Parkhurst, R. J. Gildea, I. D. Young, L. J. O'Riordan, J. Yano, G. Winter, G. Evans and N. K. Sauter, *Acta Crystallogr D Struct Biol*, 2018, **74**, 877-894.
8. G. M. Sheldrick, *Acta Crystallogr. Sect. A*, 2015, **71**, 3-8.
9. G. M. Sheldrick, *Acta Crystallogr. Sect. C*, 2015, **71**, 3-8.
10. L. Peng, *Micrron*, 1999, **30**, 625-648.
11. T. Gruene, H. W. Hahn, A. V. Luebben, F. Meilleur and G. M. Sheldrick, *J. Appl. Crystallogr.*, 2014, **47**, 462-466.
12. U. Toshihiko, T. Yoshio, N. Yukio, M. Toshio and K. Shinichi, *Bull. Chem. Soc. Japan*, 1981, **54**, 181-185.
13. V. Y. Kukushkin, A. J. L. Pombeiro, C. M. P. Serreira and L. I. Elding, *Inorg. Synth.*, 2002, **33**, 189-196.
14. M. J. Frisch, G. W. Trucks, H. B. Schlegel, G. E. Scuseria, M. A. Robb, J. R. Cheeseman, G. Scalmani, V. Barone, G. A. Petersson, H. Nakatsuji, M. C. X. Li, A. V. Marenich, J. Bloino, B. G. Janesko, R. Gomperts, B. Mennucci, H. P. Hratchian, J. V. Ortiz, A. F. Izmaylov, J. L. Sonnenberg, D. Williams-Young, F. Ding, F. Lipparini, F. Egidi, J. Goings, B. Peng, A. Petrone, T. Henderson, D. Ranasinghe, V. G. Zakrzewski, N. R. J. Gao, G. Zheng, W. Liang, M. Hada, M. Ehara, K. Toyota, R. Fukuda, J. Hasegawa, M. Ishida, T. Nakajima, Y. Honda, O. Kitao, H. Nakai, T. Vreven, K. Throssell, J. J. A. Montgomery, J. E. Peralta, F. Ogliaro, M. J. Bearpark, J. J. Heyd, E. N. Brothers, K. N. Kudin, V. N. Staroverov, T. A. Keith, R. Kobayashi, J. Normand, K. Raghavachari, A. P. Rendell, J. C. Burant, S. S. Iyengar, J. Tomasi, M. Cossi, J. M. Millam, M. Klene, C. Adamo, R. Cammi, J. W. Ochterski, R. L. Martin, K. Morokuma, O. Farkas, J. B. Foresman and D. J. Fox, GAUSSIAN 16 (Revision G16W), Gaussian, Inc., Wallingford CT, 2016.
15. R. Dennington, T. A. Keith and J. M. Millam, GAUSSVIEW 6.0, Semichem Inc., Shawnee Mission, KS, 2016.
16. J. P. Perdew, *Phys Rev B Condens Matter*, 1986, **33**, 8822-8824.
17. A. D. Becke, *Phys Rev A Gen Phys*, 1988, **38**, 3098-3100.
18. F. Weigend and R. Ahlrichs, *Phys. Chem. Chem. Phys.*, 2005, **7**, 3297-3305.
19. S. Miertus, E. Scrocco and J. Tomasi, *Chem. Phys.*, 1981, **55**, 117-129.
20. S. Miertus and J. Tomasi, *Chem. Phys.*, 1982, **65**, 239-245.
21. J. L. Pascual-Ahuir, E. Silla and I. Tunon, *J. Comput. Chem.*, 1994, **15**, 1127-1138.
22. J. Tomasi, B. Mennucci and R. Cammi, *Chem. Rev.*, 2005, **105**, 2999−3093.
23. A. D. Becke, *J. Chem. Phys.*, 1993, **98**, 5648-5652.
24. F. Weigend, *Phys. Chem. Chem. Phys.*, 2006, **8**, 1057-1065.

Abrevations

ADP: Atomic Displacement Parameters

APCI-MS: Atmospheric Pressure Chemical Ionisation-Mass Spectrometry

Col: Columnar Liquid Crystal Phase

COSY: Correlation Spectroscopy

Crys: Crystalline Solid Phase

CSA: Chemical Shift Anisotropy

DCM: Dichloromethane

DEPT: Distortionless Enhancement by Polarisation Transfer

DLS: Dynamic Light Scattering

DMF: Dimethylformaldehyde

DMSO: Dimethylsulfoxide

DSC: Differential Scanning Calorimetry

EQE: External Quantum Efficiency

Gn: Generation of dendrimer, where n is the generation number.

HAE: Heavy Atom Effect

HMBC: Heteronuclear Multiple-Bond Correlation

HOMO: Highest-Occupied Molecular Orbital

HSQC: Heteronuclear Single-Quantum Correlation

IL: Intraligand

ILCT: Intraligand Charge Transfer

IC: Internal Conversion

ISC: Intersystem Crossing

Iso: Isotropic Liquid

LC: Liquid Crystal

LLCT: Ligand-to-Ligand Charge Transfer

LUMO: Lowest-Occupied Molecular Orbital

mes: Mesitylene (1,3,5-trimethylbenzene)

MALDI-TOF: Matrix-Assisted Laser Desorption/Ionization-Time of Flight

MircoED: Microcrystal Electron Diffraction

MOF: Metal Organic Framework

MS: Mass Spectrometry

N: Nematic Liquid Crystal

NHC: *N*-heterocyclic carbene

NOE: Nuclear Overhauser Effect

NMR: Nuclear Magnetic Resonance

PCM: Polarizable Continuum Model

PLQY: Photoluminescent Quantum Yield

PMMA: Poly(methyl methacrylate)

POM: Polarising Optical Microscopy

rISC: Reverse Intersystem Crossing

SAXS: Small-Angle X-ray Scattering

Sm: Smectic Liquid Crystal Phase

SOC: Spin-Orbit Coupling

TADF: Thermally Activated Delayed Florescence

TBAF: Tetra-*n*-butylammonium fluoride

TEM: Transition Electron Microscopy

TFA: Trifluoroacetic Acid

THF: Tetrahydrofuran

TIPS: Triisopropylsilyl

TLC: Thin Layer Chromatography

TMS: Trimethylsilyl

Ts: Tosyl (toluenesulfonyl)

TSDP: Thermally Stimulated Delayed Phosphorescence

XRD: X-Ray Diffraction